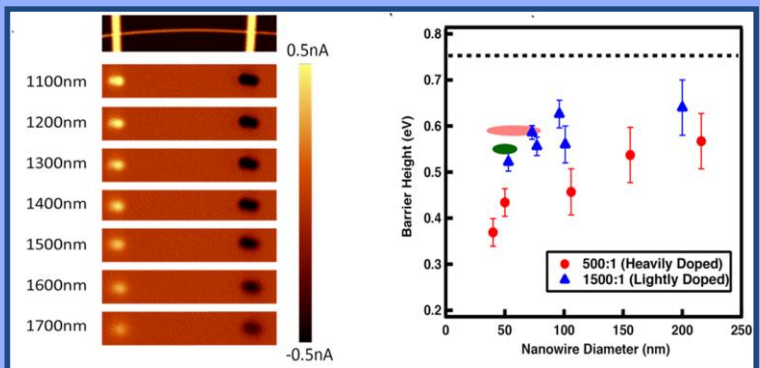
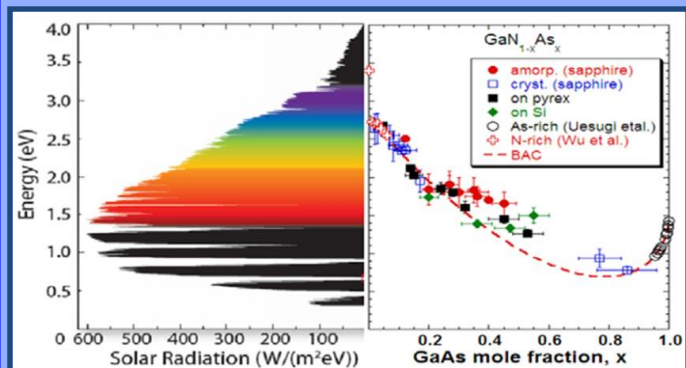
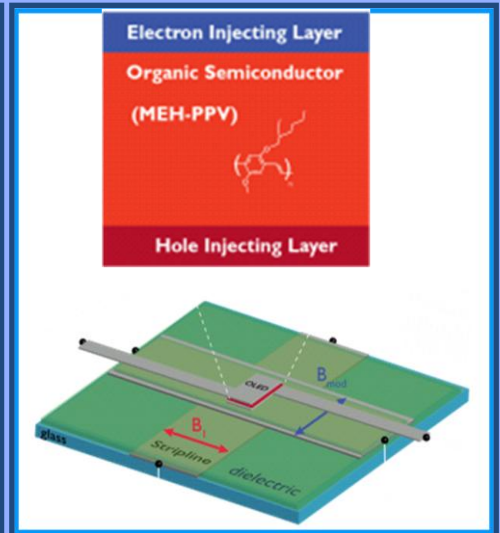
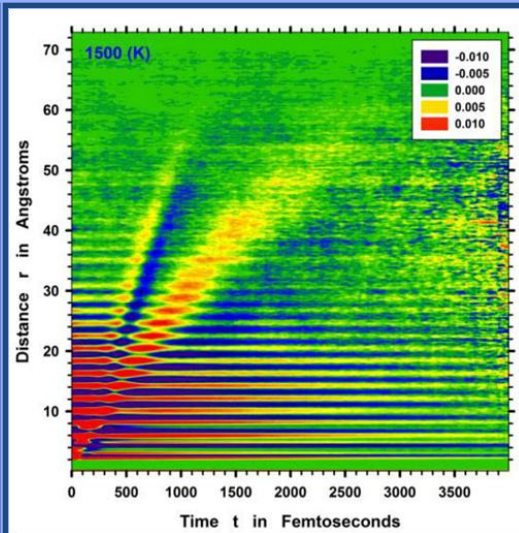
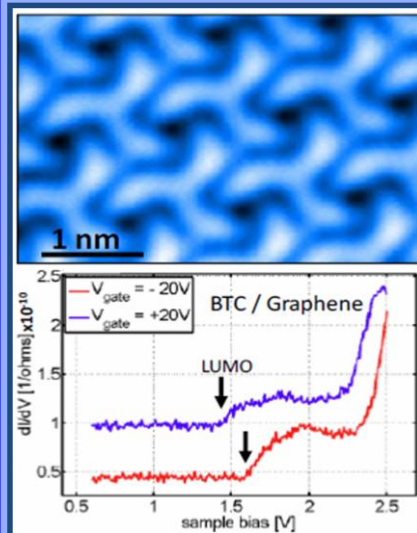
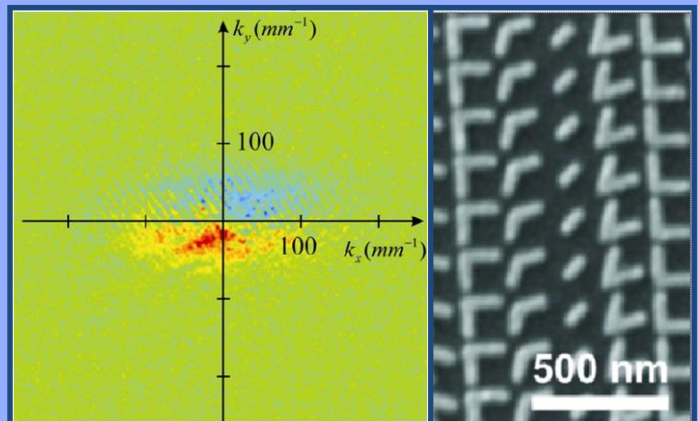
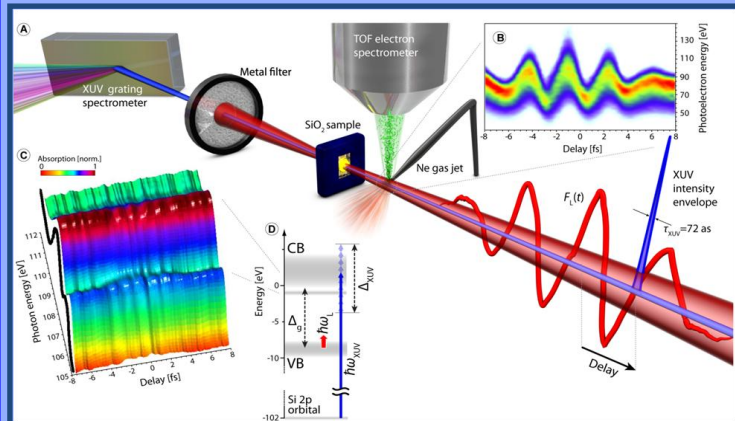


# DOE – BES PI Meeting

# Physical Behavior of Materials

Bolger Center, Potomac, MD, April 14-17, 2013  
*Program and Abstracts*

*Chairs: Puru Jena (VCU), Takeshi Egami (ORNL)*



U.S. Department of Energy  
 Office of Science – Basic Energy Sciences  
 Division of Materials Sciences and Engineering



## COVER

**Top Left** – Simultaneous attosecond absorption and streaking spectroscopy. (A) Illustration of the experimental setup; (B) Attosecond streaking spectrogram of an isolated attosecond XUV pulse and a near-single-cycle NIR pulse; (C) Attosecond transient absorption spectrogram of a 125-nm-thick SiO<sub>2</sub> membrane as a function of delay between the XUV pulse and the NIR pulse (black line: Synchrotron-XANES absorption data for comparison); (D) Schematic energy level diagram of SiO<sub>2</sub>. The blue arrow represents the XUV absorption (Si L-states to the SiO<sub>2</sub> conduction band). *Mark Stockman (Georgia State University)*

**Top Right** – A giant photonic Spin Hall effect is discovered when light is propagated through a metamaterial comprised of V-shaped antennas with a variety of arm configurations (right image). The light follows a curved trajectory that drags light with different circular polarization in opposite transverse directions. *Xiang Zhang (Lawrence Berkeley National Laboratory)*

**Middle Left** – An STM image demonstrating that BTC molecules form a well-ordered monolayer on a gated graphene/BN device (BTC = 3,3',3''-(Benzene-1,3,5-triyl)tris(2-cyanoacrylonitrile), BN = boron nitride). STM spectroscopy of BTC reveals that the LUMO state of this molecule can be controllably tuned (i.e., shifted relative to E<sub>F</sub>) via application of a backgate potential. Top: STM image of BTC molecules on gated graphene device. Bottom: STM spectroscopy shows LUMO shift with gate voltage. *Michael Crommie (Lawrence Berkeley National Laboratory)*

**Middle Center** – How atoms communicate with each other. This figure is the correlation function of atomic-level stresses in space and time. Horizontal streaks reflect the quasistatic atomic correlation, and two diagonal lines represent sound waves. *Takeshi Egami (Oak Ridge National Laboratory)*

**Middle Right** – An accurate magnetometer device has been invented, based on a low cost, thin-film organic semiconductor diode. The device is most useful for intermediate magnetic field strengths (millitesla range), where it yields better accuracies than existing sensor devices (e.g. Hall sensors). *Christoph Boehme (University of Utah)*

**Bottom Left** – A comparison of the measured band gap of GaN<sub>1-x</sub>As<sub>x</sub> as a function of composition with the values predicted by the band anticrossing model (right). Alloys in the composition range of 0.10 < x < 0.8 are amorphous but exhibit sharp, well defined absorption edge. *(Ali Javey et.al., Lawrence Berkeley National Laboratory)*

**Bottom Right** – Internal photoemission measurement of Schottky barrier height of contact to semiconductor nanowire. At left is an image of the nanowire between two ohmic contacts, followed by photocurrent images at increasing wavelength (3 x 15 μm<sup>2</sup>). The barrier height is extracted from dependence of the photocurrent yield on energy. At right, the measured barrier heights are plotted as a function of nanowire diameter for different doping densities. *Lincoln Lauhon (Northwestern University)*

This document was produced under contract number DE-AC05-06OR23100 between the U.S. Department of Energy and Oak Ridge Associated Universities.

The research grants and contracts described in this document are supported by the U.S. DOE Office of Science, Office of Basic Energy Sciences, Materials Sciences and Engineering Division.

## FOREWORD

This extended-abstract booklet summarizes the scientific content of the 2013 “Physical Behavior of Materials” Principal Investigators’ meeting that is sponsored by the Division of Materials Sciences and Engineering (DMS&E) of the Department of Energy, Office of Basic Energy Sciences (BES), held on April 14–17, 2013, at the Bolger Conference Center in Potomac, Maryland. The primary purpose of the meeting is to provide an environment for the exchange of new information and ideas among participants, and to foster synergistic activities among researchers in the Physical Behavior Program. For the grantees and BES, it facilitates an overview of the program useful to define future directions for the program and identify promising new research areas. These meetings are designed to stimulate crosscutting and inspiring of new ideas, as it brings together leading experts in diverse fields of interest to our program.

The Physical Behavior of Materials program covers a broad range of research activities. Being at the crossroads of physics and materials sciences, it has the mission to support fundamental science and use-inspired basic research that promise to bring a better understanding to fundamentals of many exciting fields of research and support out agency’s mission. The physical behavior of electrons and other charge carriers, photons, phonons, plasmons and other elementary excitations, as well as their mutual interactions in different material environments are all among the primary scientific interests of the program. The program has a rich portfolio in many ground-breaking, high-risk high-reward projects using both experimental and theoretical approaches.

This year’s Principal Investigators’ meeting is chaired by Puru Jena of the Virginia Commonwealth University, and Takeshi Egami of the Oak Ridge National Laboratory. It is attended by over 90 scientists, with 32 oral presentations in 10 sessions and 55 poster presentations in two poster sessions. We organized this year’s presentations into ten separate sessions grouped in similar topical research areas. New this year, we have organized three special sessions that focus on several recent national initiatives that have strong connections to the Physical Behavior of Materials program. Titles of the presentations in these special sessions are “Critical Materials Initiative,” BESTAR, EFRC–“Solid-State Solar-Thermal Energy Conversion Center,” EFRC–“Light-Material Interactions in Energy Conversion,” and the “SunShot Initiative.”

The contributions of all the participants are gratefully acknowledged, for their investment of time and for their willingness to share their ideas with other meeting participants. We also gratefully acknowledge the outstanding support of Tammy Click and Joreé O’Neal from the Oak Ridge Institute for Science and Education, and Teresa Crockett of the DMS&E, and the staff of the Bolger Conference Center.

Refik Kortan, Ph.D.  
Program Manager,  
Division of Materials Sciences  
and Engineering  
Office of Basic Energy Sciences  
Department of Energy  
April 2013



## Table of Contents

<b>Foreword</b> .....	i
<b>Table of Contents</b> .....	iii
<b>Agenda</b> .....	xi

### Session I

<b>Sub-wavelength Metamaterial Design, Physics and Applications</b> <i>Xiang Zhang, Eli Yablonovitch, Yuen-Ron Shen</i> .....	1
<b>Quantum Nanoplasmonics Theory</b> <i>Mark I. Stockman</i> .....	5
<b>Metamaterials as a Platform for the Development of Novel Materials for Energy Applications</b> <i>Willie J. Padilla</i> .....	8

### Session II

<b>Electronic Materials Program</b> <i>Ali Javey, Joel W. Ager, Daryl C. Chrzan, Oscar D. Dubón, Wladek Walukiewicz, Kin Man Yu, and Junqiao Wu</i> .....	13
<b>Control of Semiconductor Surfaces with Soft Gates</b> <i>Joel W. Ager</i> .....	17
<b>Acceptor Defects in ZnO and Related Materials</b> <i>Matthew D. McCluskey and Leah Bergman</i> .....	21

### Session III

<b>Critical Materials</b> <i>Karl A. Gschneidner Jr.</i> .....	25
<b>The Materials Project</b> <i>Kristin Persson</i> .....	26

## Session IV

<b>Nanometer-Scale Surface and Interface Phenomena</b> <i>Gary Kellogg, Norman Bartelt, Farid El Gabaly, Peter Feibelman, Kevin McCarty, Nancy Missert, Taisuke Ohta, Brian Swartzentruber, Konrad Thürmer, and Kevin Zavadil</i> .....	29
<b>Make VO<sub>2</sub> Work: Micro Solid Engine and Nano Powermeter</b> <i>Junqiao Wu, R. Ramesh, D. C. Chrzan, C. P. Grigoropoulos, A. Minor, and K. M. Yu</i> .....	33
<b>In-Situ Scanning Probe Studies of Interface Evolution on Model LiMn<sub>2</sub>O<sub>4</sub> Cathodes for Li Ion Batteries</b> <i>Nancy Missert, Jeyavel Velmurugan, and Robert Garcia</i> .....	37
<b>Spatially Resolved Ionic Diffusion and Electrochemical Reactions in Solids— A Biased View at Lithium Ion Batteries</b> <i>Nina Balke</i> .....	41

## Session V

<b>High Performance Nano-Crystalline Oxide Fuel Cell Materials: Defects, Structures, Interfaces, Transport, and Electrochemistry</b> <i>S. A. Barnett, L. D. Marks, T. O. Mason, K. Poepelmeier, P. W. Voorhees</i> .....	45
<b>Experimental and Theoretical Pursuit of the Ultimate Conductivity in ZnO</b> <i>David C. Look</i> .....	49
<b>Energy Transport in Graphene</b> <i>Li Shi and Stephen Cronin</i> .....	53
<b>Defect Studies of CZTSSe and Related Thin Film Photovoltaic Materials</b> <i>Mike Scarpulla</i> .....	57

## Session VI

<b>Frequency Dependent Properties of Magnetic Nanoparticle Crystals</b> <i>Sara Majetich</i> .....	61
<b>Understanding the Spin-Lattice Coupling in Multiferroic Oxides</b> <i>Trevor A. Tyson</i> .....	65
<b>Enhancement of Magnetoelectric Coupling in Nanoengineered Oxide Films and Heterostructures by Laser MBE</b> <i>Xiaoxing Xi</i> .....	69

## Session VII

<b>Solid-State Solar-Thermal Energy Conversion Center (S<sup>3</sup>TEC Center)</b> <i>Gang Chen, M. S. Dresselhaus, E. A. Fitzgerald, P. Jarillo-Herrero, J. Joannopoulos, S.-G. Kim, K. A. Nelson, Y. Shao-Horn, C. A. Schuh, M. Soljacic, E. N. Wang, D. Broido, C. P. Opeil, Z. F. Ren, O. Delaire, D. J. Singh, G. Ramanath, and T. Borca-Tasciuc</i> .....	73
<b>Light Material Interactions Energy Frontier Research Center</b> <i>Harry A. Atwater</i> .....	77

## Session VIII

<b>Atomic and Mesoscopic Study of Metallic Glasses</b> <i>T. Egami</i> .....	79
<b>Domain Microstructures and Mechanisms for Large, Reversible and Anhysteretic Strain Behaviors in Phase Transforming Ferroelectric Materials</b> <i>Yu U. Wang</i> .....	83
<b>Mesoscale Interfacial Dynamics in Magnetoelectric Nanocomposites</b> <i>Dwight Viehland, Shashank Priya, and Armen Khachaturyan</i> .....	87
<b>Prediction of Thermal Transport Properties of Multiscale-Structured Crystalline Materials</b> <i>Youping Chen</i> .....	91

## Session IX

<b>Evaluating the Oxidative, Photothermal and Electrical Stability of Colloidal Nanocrystal Solids</b> <i>Matt Law</i> .....	95
<b>Polymer Multiferroics</b> <i>Shenqiang Ren and Manfred Wuttig</i> .....	99
<b>p-Type Dye Sensitized Solar Cells: Materials and Charge Carrier Dynamics</b> <i>Yiyang Wu</i> .....	100
<b>Charge Transfer Across the Boundary of Photon-Harvesting Nanocrystals</b> <i>Frank Wise, Tobias Hanrath, and Jim Engstrom</i> .....	104
<b>Exceeding the Planck Free-Space Energy Transfer Limit through Photonic Density of States Control and Near Field Coupling</b> <i>Ting S. (Willie) Luk</i> .....	108

<b>Crystallization and Thermoelectric Transport in Silicon Microstructures and Nanostructures under Extreme Electrical Stress</b> <i>Ali Gokirmak and Helena Silva</i> .....	112
<b>Session X</b>	
<b>DOE SunShot Initiative</b> <i>Lidija Sekaric</i> .....	117
<b>Poster Sessions</b>	
<b>Poster Session I</b> .....	119
<b>Poster Session II</b> .....	121
<b>Poster Abstracts</b>	
<b>Light-Stimulated Epitaxy of Novel Semiconductor Alloys and Heterostructures</b> <i>Kirstin Alberi</i> .....	125
<b>Understanding Compound Phase Transitions in New Heusler Alloy Giant Magnetocaloric Materials: Extension to Multifunctional Materials</b> <i>Naushad Ali and Shane Stadler</i> .....	127
<b>Plasmonic Photovoltaics</b> <i>Harry A. Atwater</i> .....	131
<b>Coherent Control of Spin States in Organic Electronics – Manipulation of Electron-Spin Interactions for Organic Electronics and Spintronics</b> <i>Christoph Boehme and John M. Lupton</i> .....	135
<b>First Principles Determination of Structure, Thermodynamics, and Transport in Metals and Oxides</b> <i>Gerbrand Ceder</i> .....	139
<b>Near-Field Thermal Radiation between Two Objects at Extreme Separations</b> <i>Gang Chen and Mehran Kardar</i> .....	143
<b>Electrochemically-Driven Phase Transitions in Battery Storage Compounds</b> <i>D. B. Ravnsbaek, K. Xiang, W. Xing, C. Carter, M. Tang, and Y. M. Chiang</i> .....	147
<b>Materials, Physics, and Nanostructures for Next Generation Spintronics</b> <i>C. L. Chien</i> .....	151

<b>Extreme Thermoelectric Behavior in Low-Dimensional Oxide Conductors</b> <i>Joshua L. Cohn</i> .....	153
<b>In Situ NMR to Understand Hydrogen Storage Chemistry</b> <i>Mark S. Conradi</i> .....	157
<b>Characterization of Functional Nanomachines</b> <i>M. F. Crommie, C. Bustamante, M. L. Cohen, S. G. Louie, G. Marriott, and A. Zettl</i> .....	161
<b>Energy Transport in Graphene</b> <i>Stephen Cronin and Li Shi</i> .....	165
<b>Proximity Effects in Charged Oxide Heterostructures</b> <i>J. A. Eastman, P. Zapol, D. D. Fong, and P. H. Fuoss</i> .....	169
<b>Nanophotonics-Enhanced Solar Cells</b> <i>Shanhui Fan and Mark Brongersma</i> .....	173
<b>Elucidation of Hydrogen Desorption Mechanisms from Complex Metal Hydrides Interacting with Carbon Nanostructures</b> <i>Purusottam Jena</i> .....	177
<b>Superhalogens and Beyond – Bare and Supported Clusters</b> <i>Purusottam Jena</i> .....	179
<b>Optical and Electrical Properties of III-Nitrides and Related Materials</b> <i>Hongxing Jiang and Jingyu Lin</i> .....	183
<b>Light Trapping and Solar Energy Harvesting with Photonic Crystals</b> <i>Sajeev John</i> .....	185
<b>Bridging Atomistic and Continuum Scales in Phase-Field Modeling of Stressed Polycrystalline Materials</b> <i>Alain Karma</i> .....	189
<b>Electron Dynamics in Nanostructures in Strong Laser Fields</b> <i>Matthias F. Kling</i> .....	193
<b>Coupling Electrons, Phonons, and Photon for Nonequilibrium Transport Simulation</b> <i>Irena Knezevic</i> .....	197
<b>Functional Imaging of Hybrid Nanostructures: Visualization of Mechanisms for Solar Energy Utilization</b> <i>Lincoln J. Lauhon</i> .....	200

<b>Hydrogen Absorption in Pd-Based Nanostructures</b> <i>David Lederman</i> .....	204
<b>Physical Chemistry of Inorganic Nanostructures</b> <i>Stephen R. Leone, A. Paul Alivisatos, and Peidong Yang</i> .....	208
<b>Superconducting Materials</b> <i>Qiang Li</i> .....	212
<b>Light Trapping, Guiding and Concentration for Maximizing Solar Energy Conversion</b> <i>Shawn-Yu Lin</i> .....	216
<b>Physical Behavior Associated with Mechanical Strain and Quantum Electronic Stress</b> <i>Feng Liu</i> .....	220
<b>Study of p-Type ZnO and MgZnO Thin Films for Solid State Lighting</b> <i>Jianlin Liu</i> .....	224
<b>Amorphous Structures and Polymorphs of the Phase-Change Ge<sub>2</sub>Sb<sub>2</sub>Te<sub>5</sub> Alloy</b> <i>E. Ma</i> .....	228
<b>Surface Engineering by Simultaneous Action of Multiple External Fields</b> <i>Dimitrios Maroudas</i> .....	232
<b>Using Multiaxial Magnetic Fields to Drive Emergent Behavior in Magnetic Platelet Suspensions</b> <i>James E. Martin and Kyle Solis</i> .....	236
<b>Electronic Processes in Solid State Organic Electronic Materials</b> <i>Richard L. Martin, Enrique Batista, and Darryl Smith</i> .....	240
<b>Electronic and Optical Processes in Novel Semiconductors for Energy Applications</b> <i>Angelo Mascarenhas</i> .....	244
<b>Interfaces in Electronic and Structural Materials</b> <i>Yuri Mishin</i> .....	248
<b>Optically Active 3-Dimensional Semiconductor Quantum Dot Assemblies in Heterogeneous Nanoscale Hosts</b> <i>A. V. Nurmikko and Jung Han</i> .....	252

<b>Complex Hydrides – A New Frontier for Future Energy Applications</b> <i>V. K. Pecharsky, D. D. Johnson, M. Pruski, and L.S. Chumbley</i> .....	256
<b>Extraordinary Responsive Magnetic Rare Earth Materials</b> <i>V. K. Pecharsky, K. A. Gschneidner, Jr., G. J. Miller, and L. S. Chumbley</i> .....	260
<b>High Performance Bulk Thermoelectric Materials</b> <i>Zhifeng Ren</i> .....	264
<b>Nanostructured Materials for Thermoelectric Energy Conversion</b> <i>Rachel Segalman</i> .....	267
<b>Study of Materials and Interface Properties for High-Efficiency Spin Injection</b> <i>Jing Shi</i> .....	271
<b>Phase Transformations in Confined Nanosystems</b> <i>Jeffrey E. Shield</i> .....	276
<b>Magnetic Frustration and Cooperative Phenomena in Correlated Electron Oxide Materials</b> <i>Hariharan Srikanth, M. H. Phan, Anis Biswas, Nicholas Bingham, and Paula Lampen</i> .....	280
<b>Spin Polarized Functionality through Complex Oxide Heteroepitaxy</b> <i>Yuri Suzuki</i> .....	284
<b>Electrochemically Driven Phase Transitions in Battery Storage Compounds</b> <i>Ming Tang, Yet-Ming Chiang, and W. Craig Carter</i> .....	288
<b>Thermodynamic, Kinetic and Electrochemical Studies on Mixed Proton, Oxygen Ion, and Electron (Hole) Conductors</b> <i>Anil V. Virkar</i> .....	292
<b>Nanocrystal-Based Dyads for Solar to Electric Energy Conversion</b> <i>David Waldeck, D. N. Beratan, and Ron Naaman</i> .....	296
<b>Fundamental Piezotronic and Piezo-phototronic Effects in Nanowires</b> <i>Zhong Lin Wang and Wenzhuo Wu</i> .....	300
<b>Synthesis and Characterization of Nanomaterial Heterostructures and Assemblies: Investigation of Charge and Energy Flow at Nanostructured Interfaces</b> <i>Stanislaus S. Wong, James A. Misewich, M. Y. Sfeir, R. M. Konik, Y. Zhu, and J. Appenzeller</i> .....	304

<b>Interband Cascade Photovoltaic Cells</b> <i>Rui Q. Yang, Michael B. Santos, Matthew B. Johnson, J. F. Klem, R. T. Hinkey, L. Li, H. Loffi, Z. Tian, J. C. Keay, H. Ye, S. Rassel, L. Zhao, C. Niu, and T. D. Mishima</i> .....	308
<b>Near-Field Thermal Radiation between Flat Surfaces with a Nanogap</b> <i>Zhuomin Zhang</i> .....	312
<b>Elucidation of Hydrogen Interaction Mechanisms with Metal Doped Carbon Nanostructures</b> <i>Ragaiy Zidan, Joseph A. Teprovich, Jr., Douglas A. Knight, Brent Peters, and Puru Jena</i> .....	316
<b>Author Index</b> .....	321
<b>Participant List</b> .....	323

**Physical Behavior of Materials  
Principal Investigators' Meeting  
April 15–17, 2013  
Bolger Center, Potomac, MD**

***Meeting Chairs: Puru Jena (VCU) and Takeshi Egami (ORNL)***

<b>Sunday, April 14, 2013</b>	
3:00 – 6:00 pm	Registration
6:00 – 7:00 pm	Reception (No Host, Pony Express Bar & Grill )
7:00 pm	*** Dinner (Osgood's Restaurant – On your own) ***
<b>Monday, April 15, 2013</b>	
7:00 – 8:00 am	*** Breakfast ***
8:00 – 8:15 am	<b>Welcome, Meeting Chairs</b>
<b>Session I</b>	<b>Chair: Sajeev John (Univ. Toronto)</b>
8:15 – 8:45 am	Eli Yablonovitch (LBNL) <i>"Sub-wavelength Metamaterial Design, Physics and Applications"</i>
8:45 – 9:15 am	Mark Stockman (Georgia State Univ.) <i>"Quantum Nanoplasmonics Theory"</i>
9:15 – 9:45 am	Willie Padilla (Boston College) <i>"Metamaterials as a Platform for the Development of Novel Materials for Energy Applications"</i>
9:45 – 10:15 am	*** Break ***
<b>Session II</b>	<b>Chair: Gerbrand Ceder (MIT)</b>
10:15 – 10:45 am	Ali Javey (LBNL) <i>"Electronic Materials Program"</i>
10:45 – 11:15 am	Joel Ager (LBNL) <i>"Control of Semiconductor Surfaces with Soft Gates"</i>
11:15 – 11:45 pm	Matthew McCluskey (Washington State Univ.) <i>"Acceptor Defects in ZnO and Related Materials"</i>
11:45 – 12:45 pm	** Working Lunch (poster introductions: session I) **
<b>Session III</b>	<b>Chair: Puru Jena (VCU)</b>
12:45 – 1:30 pm	<b>"Division and Program Updates"</b> Linda Horton, Director, Division of Materials Science and Engineering Refik Kortan, Program Manager, Physical Behavior of Materials

1:30 – 2:00 pm	<b>Karl Gschneidner (AMES) - Critical Materials</b>
2:00 – 2:30 pm	<b>Kristin Persson (LBNL) – BESTAR</b>
2:30 – 3:00 pm	*** Break ***
3:00 – 5:30 pm	<b>Poster Session I</b>
5:30 – 6:30 pm	*** Dinner (Scientific Highlights of the Day: Discussion and Input from Attendees) ***

<b>Session IV</b>	<b>Chair: Yet-Ming Chiang (MIT)</b>
-------------------	-------------------------------------

6:30 – 7:00 pm	Gary Kellogg (SNL) <i>"Nanometer-Scale Surface and Interface Phenomena"</i>
7:00 – 7:30 pm	Junqiao Wu (LBNL) <i>"Make VO<sub>2</sub> Work: Micro Solid Engine and Nano Powermeter"</i>
7:30 – 8:00 pm	Nancy Missert (SNL) <i>"In Situ Scanning Probe Studies of Interface Evolution on Model LiMn<sub>2</sub>O<sub>4</sub> Cathodes for Li Ion Batteries"</i>
8:00 – 8:30 pm	Nina Balke (ORNL) <i>"Spatially Resolved Ionic Diffusion and Electrochemical Reactions in Solids"</i>

8:30 – 10:00 pm	<b>Continuation of Poster Session I</b>
-----------------	---

<b>Tuesday, April 16, 2013</b>	
--------------------------------	--

7:30 – 8:30 am	*** Breakfast ***
----------------	-------------------

<b>Session V</b>	<b>Chair: Ragaiy Zidan (SRNL)</b>
------------------	-----------------------------------

8:30 – 9:00 am	Peter Voorhees (Northwestern Univ.) <i>"High Performance Nano-Crystalline Oxide Fuel Cell Materials: Defects, Structures, Interfaces, Transport, and Electrochemistry"</i>
9:00 – 9:30 am	David Look (Wright State Univ.) <i>"Experimental and Theoretical Pursuit of the Ultimate Conductivity in ZnO"</i>
9:30 - 10:00 am	Li Shi (Univ. Texas) <i>"Energy Transport in Graphene"</i>
10:00 – 10:30 am	Michael Scarpulla (Univ. Utah) <i>"Defect Studies of CZTSSe &amp; Related Thin Film Photovoltaic Materials"</i>
10:30 – 11:00 am	*** Break ***

<b>Session VI</b>	<b>Chair: Srikanth Hariharan (Univ. South Florida)</b>
11:00 – 11:30 am	Sara Majetich ( <i>Carnegie Mellon Univ.</i> ) "Frequency Dependent Properties of Magnetic Nanoparticle Crystals"
11:30 – 12:00 pm	Trevor Tyson ( <i>NJIT</i> ) "Exploring Electric Polarization Mechanisms in Multiferroic Oxides"
12:00 – 12:30 pm	Xiaoxing Xi ( <i>Temple Univ.</i> ) "Enhancement of Magnetoelectric Coupling in Nanoengineered Oxide Films and Heterostructures by Laser MBE"
12:30 – 1:30 pm	** Working Lunch ( <i>poster introductions: session II</i> ) **
<b>Session VII</b>	<b>Chair: Takeshi Egami (ORNL)</b>
1:30 – 2:00 pm	<b>Gang Chen, EFRC – "Solid-State Solar-Thermal Energy Conversion Center"</b>
2:00 – 2:30 pm	<b>Harry Atwater, EFRC – "Light-Material Interactions in Energy Conversion"</b>
2:30 – 3:00 pm	*** Break ***
3:00 – 5:30 pm	<b>Poster Session II</b>
5:30 – 6:30 pm	*** Dinner (Scientific Highlights of the Day: Discussion and Input from Attendees) ***
<b>Session VIII</b>	<b>Chair: Richard Martin (LANL)</b>
6:30 – 7:00 pm	Takeshi Egami ( <i>ORNL</i> ) "Atomic and Mesoscopic Study of Metallic Glasses"
7:00 – 7:30 pm	Yu Wang ( <i>Michigan Tech Univ.</i> ) "Domain Microstructures and Mechanisms for Large, Reversible and An hysteretic Strain Behaviors in Phase Transforming Ferroelectric Materials"
7:30 – 8:00 pm	Dwight Viehland ( <i>VA Polytechnic Inst.</i> ) "Mesoscale Interfacial Dynamics in Magnetoelectric Nanocomposites"
8:00 – 8:30 pm	Youping Chen ( <i>Univ. Florida</i> ) "Prediction of Thermal Transport Properties of Multiscale-Structured Crystalline Materials"
8:30 – 10:00 pm	<b>Continuation of Poster Session II</b>

## Wednesday, April 17, 2013

7:30 – 8:30 am \*\*\* Breakfast \*\*\*

### Session IX

**Chair: Michael Crommie (LBNL)**

8:30 – 9:00 am Matthew Law (*UC Irvine*)  
*"Evaluating the Oxidative, Photothermal and Electrical Stability of Colloidal Nanocrystal Solids"*

9:00 – 9:30 am Manfred Wuttig (*Univ. MD*)  
*"Polymer Multiferroics"*

9:30 – 10:00 am Yiyang Wu (*Ohio State*)  
*"p-Type Dye-Sensitized Solar Cells: Materials and Charge Carrier Dynamics"*

10:00 – 10:30 am Frank Wise (*Cornell Univ.*)  
*"Charge Transfer Across the Boundary of Photon-Harvesting Nanocrystals"*

10:30 – 11:00 am \*\*\* Break \*\*\*

11:00 – 11:30 am Ting Luk (*SNL*)  
*"Exceeding the Planck Free-Space Energy Transfer Limit through Photonic Density of States Control and Near Field Coupling"*

11:30 – 12:00 pm Ali Gokirmak (*Univ. Connecticut*)  
*"Crystallization and Thermoelectric Transport in Silicon Microstructures and Nanostructures Under Extreme Electrical Stress"*

12:00 – 1:00 pm \*\* Working Lunch (Scientific Highlights of the Day: Discussion and Input from Attendees) \*\*

### Session X

**Chairs: Puru Jena (VCU) – Takeshi Egami (ORNL)**

1:00 – 1:30 pm **Lidija Sekaric, EERE – "SunShot Initiative"**

1:30 – 2:00 pm Closing Remarks by Meeting Chairs and PM

# **Session I**



## Program Title: Sub-wavelength Metamaterial Design, Physics and Applications

**Principal Investigator: Xiang Zhang, Co-Investigators: Eli Yablonovitch, Yuen-Ron Shen**  
**Mailing Address: Materials Sciences Division, Lawrence Berkeley National Laboratory, 1 Cyclotron Road, Berkeley, CA 94720**  
**E-mail: [xzhang4@lbl.gov](mailto:xzhang4@lbl.gov)**

### Program Scope

Metamaterials, that mimic the order in matter have opened an exciting gateway to reach unprecedented physical properties and functionality, unattainable from naturally existing materials. The “atoms” and “molecules” in meta-materials can be tailored, the lattice constant and inter-atomic interaction can be precisely tuned, and “defects” can be designed and placed at desired locations. Besides our current effort in high spatial resolution imaging with the optical metamaterial hyperlens [2, 14], an indefinite metamaterial with hyperbolic isofrequency contour [6, 10], and reconfigurable metamaterials [22, 23], this program sets to explore the revolutionary physics of subwavelength metamaterials, covering new metamaterial design with symmetry considerations, an inverse electromagnetic algorithm, new control approaches for reconfigurable metamaterials, and new physics with conformal transformation in the metamaterial hyperlens. The unique properties arising from the specific configurations of the metamaterials open up exciting new venues for the device development for DOE missions. Moreover, the intrinsic resonant and broadband electromagnetic responses of metamaterials make them the outstanding candidate to control and manipulate ultrafast optical pulses at unprecedented small time and length scales, advancing the ultrafast photon science research at LBNL - one of the key DOE grand challenges.

The power of metamaterials in manipulating light lies in the flexibility in designing each individual artificial atom with properties far beyond the reach of natural materials. The artificial atoms as building blocks can be assembled into metamaterials in a similar way that real atoms form natural materials. This analogy can be carried on further to categorize metamaterials into gas and solid phases. In the gas phase, the artificial atoms interact weakly with each other, and the overall material properties are solely determined by the sharp resonance features of each individual artificial atom. Whereas in the solid phase, the artificial atoms strongly interact to form crystal like properties, and the sharp resonance of each individual artificial atom evolves into band structure. Thus, designing the level of coupling among the artificial atoms provides a powerful mean to engineer the dispersion of the metamaterials. In addition, a few artificial atoms of different types can also be combined to form artificial molecules with distinct properties from each of the constituent artificial atoms. This further enriches the optical properties in the optical metamaterials. Our project explores the novel design of both of the individual artificial

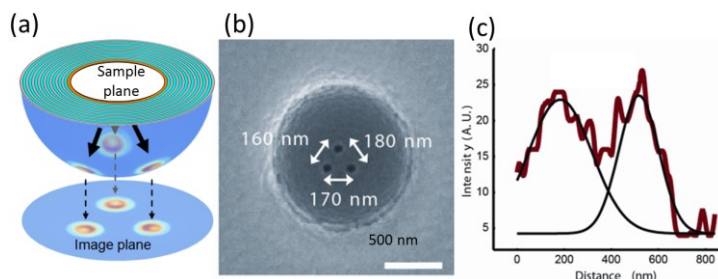


**Figure 1.** (a) Schematic of optical hyperlens. (b) Scanning electron microscope (SEM) image of nano-scale object. (c) Cross-sectional analysis of the image taken of the object being magnified by the hyperlens. The sub-diffraction-limited objects were clearly resolved by the spherical hyperlens showing  $\times 2.1$  magnification.

atoms and their interaction to achieve the desired metamaterial optical properties, and investigates the emergent and unique wave phenomena.

## Recent progress

***High Spatial Resolution Imaging with the Optical Metamaterial Hyperlens.*** The fundamental diffraction limit restricts optical imaging resolution to about half of the wavelength scale. It was once regarded as an insurmountable obstacle toward extension to the nano-scale for practical applications. By careful theoretic design and simulation, we have realized a *3D spherical hyperlens* configuration with broadband response and high far-field resolution [2]. The limited resolution of a conventional optical imaging system stems from the fact that the fine feature information of an object is carried by evanescent waves, which exponentially decay in space and thus cannot reach the imaging plane. The Metamaterial hyperlens has shown the ability to overcome this limit by employing carefully engineered plasmonic metamaterials. As shown in Figure 1, hyperlenses not only carry the subwavelength information contained in evanescent waves across the lens, but also magnify them, thereby convert them into propagating waves such that the information travels macroscopic distances also outside the lens. The new design also extends the working wavelength into visible range.

***Indefinite Metamaterial with Hyperbolic Isofrequency Contour.*** Using finite materials, we have realized the smallest optical cavity known to date [6, 10], as shown in Fig. 2. As a result of the open-curved hyperboloid dispersion, the medium allows a wave with an extremely large wave vector to propagate, and the giant momentum mismatch between the metamaterial and air causes total internal reflection at the interface. By cutting the metamaterial into subwavelength dimensions, a three-dimensional optical Fabry–Perot cavity can be formed with a very large effective refractive index. Unprecedented capabilities in miniaturizing optical components and in studying quantum electrodynamics on a metamaterial platform arise from these unique properties. The metal-dielectric stacks form square-based pyramids 100~200 nanometers across and exhibit an extremely large refractive index of 17.4. Importantly, we found as cavity size reduces, the radiation quality factor increases dramatically, following the fourth power scaling law of the resonating wave vector. These unique properties will significantly increase the photon density of states and enhance light–matter interactions, which may make these cavities valuable for high-performance optical devices.

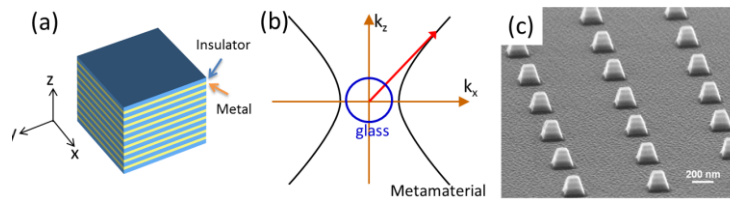


**Figure 2.** (a) Schematic of multilayer indefinite metamaterial structure and its hyperboloid IFC. The permittivity components are negative along the x- and y-directions and positive along the z-direction. (b) Hyperboloid IFC (black) of the multilayer metamaterial calculated from the dispersion relation and the spherical isotropic IFC of air (blue). (c) SEM image of an indefinite optical cavity array.

***Reconfigurable Metamaterials.*** Molecules of different handedness exhibit dramatically different physiological properties and pharmacological effects. Working with terahertz (THz), we fashioned a delicate artificial chiral meta-molecule incorporating with a photoactive silicon medium [23], as shown in Fig. 3. Through photoexcitation of the metamolecules with an external beam of infrared light, handedness flipping in the form of circularly polarized THz emission has been successfully observed. Furthermore, the photoexcitation enables chirality

flipping and the circular polarization of THz light can be dynamically controlled at high speed. The team has also demonstrated electrical controlled plasmonic resonance using the graphene-metal structure as a model hybrid system [22]. The demonstration of tunable plasmonic resonance in the composite structure opens up a new paradigm for tunable metamaterials.

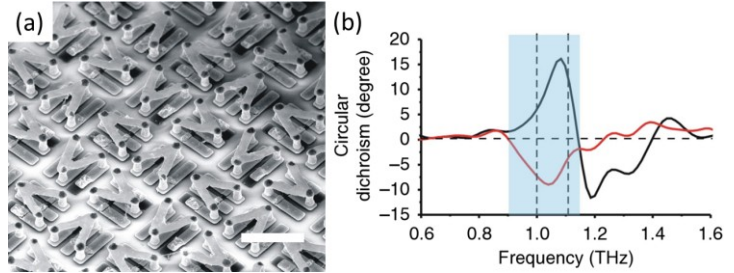


**Figure 3.** (a) SEM images of the fabricated metamaterial. Scale bar is 25  $\mu\text{m}$ . (b) The circular dichroism from the transmission spectra without (black) and with photoexcitation (red).

## Future Plans

The future research directions outlined below must be seen in the backdrop of the close collaboration of our subwavelength metamaterial team over the past 3 years. The major goals are to explore exciting optical properties and to develop promising applications of subwavelength metamaterials. This will go hand-in-hand with advances of metamaterial design with symmetry considerations and inverse electromagnetic algorithm. Major developments will also include fabricating reconfigurable metamaterials with new control approaches, and study of new physics with conformal transformation in metamaterial hyperlens.

Symmetries play a fundamental role in the linear and non-linear response of materials. We propose *a new way to achieve negative index with closed ring metamaterials* that overcomes the limitations of previous designs and paves the way to isotropic metamaterials because it is based on discrete elements. The unique influence of symmetry breaking on the dispersion of the metamaterials provides unprecedented degrees of freedom in engineering the optical properties of the system. A computational algorithm called Inverse Design, is capable of automatically designing optimal geometries of dielectric or metal components will be employed to optimize the metamaterials.

Based on our previous work on chiral metamaterials [23] and tunable graphene hybrid metamaterial [22], we propose to develop *new control approaches of reconfigurable metamaterials by electrical gating and mechanical reconfiguration*. We expect that substantial gate-induced persistent switching and linear modulation of light can be achieved in the two-dimensional metamaterial, into which an atomically thin, gated two-dimensional graphene layer is integrated. We also propose to develop reconfigurable metamaterials with integrated mechanical controls. By reshaping the geometry within the metamaterial unit cell, the electric and magnetic response can be remarkably tuned for realizing adaptive metamaterials with novel electromagnetic functionalities.

Following our success in realizing a hyperlens with two dimensional magnification through a spherical shape, the team will work together to *explore new physics in metamaterial hyperlens with on-demand external shapes for various applications*. We propose to use newly developed methodology, conformal transformation of the electromagnetic space, for the study and development of subwavelength ray optics with curved ray trajectories at deep subwavelength scales. This unusual manipulation of light can be carried out by cascading multiple metamaterials-based elements with the ability to direct light or bend it. The flexibility in

designing the metamaterial hyperlens opens up a broad range of new applications in dispersion and diffraction management, particularly in the deep sub-wavelength scale.

### References (which acknowledge DOE support)

1. T. Zentgraf, S. Zhang, R. F. Oulton, and X. Zhang, "Ultrannarrow coupling-induced transparency bands in hybrid plasmonic systems" *Physical Review B*, Vol. 80, 195415, 2009
2. J. Rho, Z. Ye, Y. Xiong, et al., "Spherical hyperlens for two-dimensional sub-diffractive imaging at visible frequencies", *Nature Communications*, Vol. 1, 143, 2010
3. X. Yang, Y. Liu, R.F. Oulton, et al., "Optical Forces in Hybrid Plasmonic Waveguides", *Nano Letters*, Vol. 11, 321, 2011
4. Cang Hu, Anna Labno, Changgui Lu, Xiaobo Yin, Ming Liu, Christopher Gladden, Yongmin Liu, and Xiang Zhang, "Probing the electromagnetic field of a 15-nanometre hotspot by single molecule imaging", *Nature*, Vol. 469, 385, 2011
5. Xiaodong Yang, Atsushi Ishikawa, Xiaobo Yin, and Xiang Zhang, "Hybrid Photonic-Plasmonic Crystal Nanocavities", *ACS Nano*, Vol. 5, 2831, 2011
6. J. Yao, X. Yang, X. Yin, et al., "Three-dimensional nanometer-scale optical cavities of indefinite medium", *Proceedings of the National Academy of Sciences*, Vol. 108, 11327, 2011
7. Boubacar Kante, Kevin O'Brien, Avi Niv, Xiaobo Yin, and Xiang Zhang, "Proposed isotropic negative index in three-dimensional optical metamaterials", *Physical Review B*, Vol. 85, 041103(R), 2011
8. Y. R. Shen, "Surface Nonlinear Optics", *J. Opt. Soc. Am. B* 28, A56, 2011.
9. M. Staffaroni, J. Conway, S. Vedantam, J. Tang, and E. Yablonovitch "Circuit Analysis in Metal-Optics", *Photonics and Nanostructures*, 10, 166, 2012.
10. Xiaodong Yang, Jie Yao, Junsuk Rho, et al. "Experimental realization of three-dimensional indefinite cavities at the nanoscale with anomalous scaling laws", *Nature Photonics*, 6, 450, 2012
11. Zhaowei Liu, Yuan Wang, Jie Yao, Hyesog Lee, Werayut Srituravanich and Xiang Zhang, "Broad Band Two-Dimensional Manipulation of Surface Plasmons" *Nano Letters*, 9, 462, 2009
12. Atsushi Ishikawa, Shuang Zhang, Dentcho A. Genov, et al. "Deep Subwavelength Terahertz Waveguides Using Gap Magnetic Plasmon" *Physical Review Letters*, Vol.102, 043904, 2009
13. Jason Valentine, Jensen Li, Thomas Zentgraf, Guy Bartal and Xiang Zhang, "An optical cloak made of dielectrics" *Nature Materials*, Vol. 8, 568, 2009
14. Yi Xiong, Zhaowei Liu, and Xiang Zhang, "A simple design of flat hyperlens for lithography and imaging with half-pitch resolution down to 20 nm" *Applied Physics Letters* 94, 203108, 2009
15. Ming Liu, Thomas Zentgraf, Yongmin Liu, Guy Bartal, and Xiang Zhang, "Light-driven nanoscale plasmonic motors", *Nature Nanotechnology*, Vol. 5, 570, 2010
16. Chih-Wei Chang, Ming Liu, Sunghyun Nam, Shuang Zhang, Yongmin Liu, Guy Bartal, and Xiang Zhang, "Optical Mobius Symmetry in Metamaterials", *Physical Review Letters*, Vol.105, 235501, 2010
17. P. Kolchin, R.F. Oulton, X. Zhang, "Nonlinear Quantum Optics in a Waveguide: Distinct Single Photons Strongly Interacting at the Single Atom Level" *Physical Review Letters*, 106, 113601, 2011
18. S.C. Kher, Y.M. Liu, L.W. Martin, et al., "Near-field examination of perovskite-based superlenses and superlens-enhanced probe-object coupling", *Nature Communications*, Vol. 2, 249, 2011
19. Shuang Zhang, Yi Xiong, Guy Bartal, Xiaobo Yin, and Xiang Zhang, "Magnetized Plasma for Reconfigurable Subdiffraction Imaging", *Physical Review Letters*, Vol. 106, 243901, 2011
20. T.J. Seok, A. Jamshidi, M. Kim, et al. "Radiation Engineering of Optical Antennas for Maximum Field Enhancement", *Nano Letters* Vol. 11 pp. 2606-2610, 2011
21. J. Horng, C.F. Chen, B. Geng, et al, "Drude conductivity of Dirac fermions in graphene", *Phys. Rev. B*, 83, 165113, 2011.
22. L. Ju, B.S. Geng, J. Horng, et al. "Graphene Plasmonics for Tunable TeraHertz Metamaterials", *Nature Nanotechnology*, Vol 6, 630-624, 2011.
23. S. Zhang, J. Zhou, Y.S. Park, et al., "Photoinduced handedness switching in terahertz chiral metamolecules", *Nature Communications*, Vol. 3, 942, 2012

# Quantum Nanoplasmonics Theory

Mark I. Stockman

Department of Physics and Astronomy, Georgia State University, 29 Peachtree Center Avenue,  
Atlanta, GA 30303, USA

Grant DE-FG02-11ER46789

## 1. PROGRAM SCOPE

The program is aimed at fundamental theoretical investigations of a wide range of phenomena where quantum properties of matter and surface plasmon excitations are of primary importance. Among phenomena where quantum behavior of surface plasmons defines their fundamental physics is spaser (quantum generation and amplification of nanoscopic optical fields). An example of such a phenomenon is the recently predicted effect of metallization of dielectrics or spaser. Matter in ultrastrong and ultrafast optical fields is another research field of this Program where quantum phenomena play dominating role.

## 2. PUBLICATIONS RESULTING FROM THE GRANT

Overall during this grant period, the grant provided a major support that resulted in publications of Refs. [1-7]. Also, the following publications received a supplemental support from the grant: Refs. [8-10].

## 3. HIGHLIGHTS OF RECENT RESULTS

### ***3.1. Predicted Ultrafast Dynamic Metallization of Dielectric Nanofilms by Strong Single-Cycle Optical Fields [1]***

In this article [1], we predict a dynamic metallization effect where an ultrafast (single-cycle) optical pulse with a  $\lesssim 1 \text{ V/\AA}$  field causes plasmonic metal-like behavior of a dielectric film with a few-nm thickness. This manifests itself in plasmonic oscillations of polarization and a significant population of the conduction band evolving on a  $\sim 1 \text{ fs}$  time scale. These phenomena are due to a combination of both adiabatic (reversible) and diabatic (i.e., irreversible) pathways.

### ***3.2. Loss Compensation by Gain and Spasing [2]***

In this work [2], we present a theory of the effective dielectric response of optical metamaterials containing optical gain. We demonstrate analytically that the conditions of spaser generation and the full loss compensation in a dense resonant plasmonic-gain metamaterial are identical. Consequently, attempting the full compensation or overcompensation of losses by gain will lead to an instability and a transition to a spaser state. This will limit (clamp) the inversion and eliminate the net gain. As a result, the full loss compensation (overcompensation) in such metamaterials is impossible. The criterion of the loss overcompensation, leading to the instability and spasing, is given in an analytical and a universal (independent from system geometry) form.

### ***3.3. Plasmonic Generation of Ultrashort Extreme-Ultraviolet Light Pulses [3]***

Ultrashort extreme-ultraviolet pulses are a key tool in time-resolved spectroscopy for the investigation of electronic motion in atoms, molecules, and solids. High-harmonic generation is a well-established

process for producing ultrashort extreme-ultraviolet pulses by direct frequency upconversion of femtosecond near-infrared pulses. However, elaborate pump–probe experiments performed on the attosecond timescale require continuous efforts to improve the spatiotemporal coherence and also the repetition rate of the generated pulses.

In this article [3], we employ a three-dimensional metallic waveguide for the plasmonic generation of ultrashort extreme-ultraviolet pulses by means of field enhancement using surface-plasmon polaritons. The intensity enhancement factor reaches a peak of  $\sim 350$ , allowing generation up to the 43<sup>rd</sup> harmonic in xenon gas, with a modest incident intensity of  $\sim 1 \times 10^{11} \text{ Wcm}^{-2}$ . The pulse repetition rate is maintained as high as 75 MHz without external cavities. The plasmonic waveguide is fabricated on a cantilever microstructure and is therefore suitable for near-field spectroscopy with nanometer-scale lateral selectivity.

### ***3.4. Electric Spaser in the Extreme Quantum Limit [6]***

Active or gain nanoplasmonics was introduced by spaser (Surface Plasmon Amplification by Stimulated Emission of Radiation). The spaser is a nanoscale quantum-plasmonic generator and ultrafast nanoamplifier of coherent localized optical fields. Among the observed spasers, most are with optical pumping, including all the spasers with the strong 3D confinement. Only few surface-plasmon polariton spasers, whose confinement and losses are not strong, are with electric pumping.

In this article [6], We consider theoretically the spaser excited electrically via a nanowire with ballistic quantum conductance. We show that in the extreme quantum regime, i.e., for a single conductance-quantum nanowire, the spaser with the core made of common plasmonic metals, such as silver and gold, is fundamentally possible. For ballistic nanowires with multiple-quanta or non-quantized conductance, the performance of the spaser is enhanced in comparison with the extreme quantum limit. The electrically-pumped spaser is promising as an optical source, nanoamplifier, and digital logic device for optoelectronic information processing with speed  $\sim 100 \text{ GHz}$  to  $\sim 100 \text{ THz}$ .

### ***3.5. Semi-metallization of Dielectrics in Strong Ultrafast Optical Fields [7]***

The time it takes to switch on and off electric current determines the rate at which signals can be processed and sampled in modern information technology. Field-effect transistors are able to control currents at frequencies  $\geq 100 \text{ GHz}$ , but electric interconnects may hamper progress towards reaching the terahertz ( $10^{12} \text{ Hz}$ ) range. All-optical injection of currents through interfering photoexcitation pathways or photoconductive switching of terahertz transients has made it possible to control electric current on a subpicosecond timescale in semiconductors. Insulators have been deemed unsuitable for both methods, because of the need for either ultraviolet light or strong fields, which induce slow damage or ultrafast breakdown, respectively.

In this paper [7], we report the feasibility of electric signal manipulation in a dielectric due to *laser field-induced quantum transition of the dielectric to a semimetallic state*. A few-cycle optical waveform reversibly increases—free from breakdown—the a.c. conductivity of amorphous silicon dioxide (fused silica) by more than 18 orders of magnitude within  $\leq 1$  femtosecond, allowing electric currents to be driven, directed and switched by the instantaneous light field. Thus the dielectric, for  $\sim 1 \text{ fs}$  acquires properties of semimetal, without any damage or longer-lasting changes of electronic or optical properties. This work opens up the way to extending electronic signal processing and high-speed metrology into the petahertz ( $10^{15} \text{ Hz}$ ) domain.

#### 4. FUTURE PLANS

We intend to capitalize on the progress achieved and further develop the field of quantum nanoplasmonics theory. One of the promising directions in the future research will be incorporation of graphene as a nanoplasmonic medium. In particular, we will develop quantum theory of graphene-based spaser. Another direction of research will be quantum theory of graphene in strong ultrafast laser fields. We will also continue developing quantum theory of conventional materials in strong fields including metals. There is a preliminary indication that metals will turn into semi-metals with  $\sim 1$  fs time interval reversibly in fields on the order of a few V/Å.

#### References

1. M. Durach, A. Rusina, M. F. Kling, and M. I. Stockman, *Predicted Ultrafast Dynamic Metallization of Dielectric Nanofilms by Strong Single-Cycle Optical Fields*, Phys. Rev. Lett. **107**, 0866021-5 (2011).
2. M. I. Stockman, *Loss Compensation by Gain and Spasing*, Phil. Trans. R. Soc. A **369**, 3510-3524 (2011).
3. I.-Y. Park, S. Kim, J. Choi, D.-H. Lee, Y.-J. Kim, M. F. Kling, M. I. Stockman, and S.-W. Kim, *Plasmonic Generation of Ultrashort Extreme-Ultraviolet Light Pulses*, Nat. Phot. **5**, 677-681 (2011).
4. S. H. Chew, F. Sussmann, C. Spath, A. Wirth, J. Schmidt, S. Zherebtsov, A. Guggenmos, A. Oelsner, N. Weber, J. Kapaldo, A. Gliserin, M. I. Stockman, M. F. Kling, and U. Kleineberg, *Time-of-Flight-Photoelectron Emission Microscopy on Plasmonic Structures Using Attosecond Extreme Ultraviolet Pulses*, Appl. Phys. Lett. **100**, 051904-4 (2012).
5. M. I. Stockman, *Nanoplasmonics: Past, Present, and Glimpse into Future*, Opt. Express **19**, 22029-22106 (2011).
6. D. Li and M. I. Stockman, *Electric Spaser in the Extreme Quantum Limit*, arXiv:1211.0366 [cond-mat.mes-hall] (2012); Phys. Rev. Lett. (**In Print**), 1-4 (2013).
7. A. Schiffrin, T. Paasch-Colberg, N. Karpowicz, V. Apalkov, D. Gerster, S. Muhlbrandt, M. Korbman, J. Reichert, M. Schultze, S. Holzner, J. V. Barth, R. Kienberger, R. Ernstorfer, V. S. Yakovlev, M. I. Stockman, and F. Krausz, *Optical-Field-Induced Current in Dielectrics*, Nature **493**, 70-74 (2013).
8. V. Apalkov and M. I. Stockman, *Theory of Dielectric Nanofilms in Strong Ultrafast Optical Fields*, Phys. Rev. B **86**, 165118-1-13 (2012).
9. V. Apalkov and M. I. Stockman, *Metal Nanofilm in Strong Ultrafast Optical Fields*, arXiv:1209.2245 [cond-mat.mes-hall], 1-5 (2012).
10. M. Schultze, E. M. Bothschafter, A. Sommer, S. Holzner, W. Schweinberger, M. Fiess, M. Hofstetter, R. Kienberger, V. Apalkov, V. S. Yakovlev, M. I. Stockman, and F. Krausz, *Controlling Dielectrics with the Electric Field of Light*, Nature **493**, 75-78 (2013).

# Metamaterials as a Platform for the Development of Novel Materials for Energy Applications

Willie J. Padilla

Boston College, 140 Commonwealth Ave., Chestnut Hill, MA 02467

[willie.padilla@bc.edu](mailto:willie.padilla@bc.edu)

## Program Scope

The goal of the program is to explore the fundamental properties of metamaterials (MMs) and their potential for energy applications in support of the mission of the Department of Energy and the office of Basic Energy Sciences. The advent of metamaterials provides novel electromagnetic responses and enables study of exotic materials – particularly in the microwave through THz and up into far IR parts of the electromagnetic (EM) spectrum – providing an ideal platform to explore a rich variety of science, from optics, condensed matter physics, materials science, to nanoscience. We propose to advance the understanding of these materials through fundamental investigations of the experimental and theoretical properties of metamaterials and to provide a knowledge base for the discovery, prediction and design of new materials with novel structures, functions, and properties. The proposed research activities emphasize the computational design and fabrication of the materials, and the characterization of their electromagnetic properties. Shown in Fig. 1 are some typical examples of metamaterials with exotic responses – particularly relevant for fundamental energy investigations – and which have been developed in our prior research effort.

## Recent Progress

The research effort has resulted in papers published in high impact journals as well as several papers submitted. We have realized a number of novel results including: first demonstration of a metamaterial absorber (MMA) detector,<sup>1</sup> discovery and characterization of surface electromagnetic waves on metamaterial absorbers<sup>2</sup> and first demonstration of a tunable metamaterial absorber.<sup>3</sup> We have also completed a review paper which was recently published in *Advanced Materials*.<sup>4</sup> In this review we

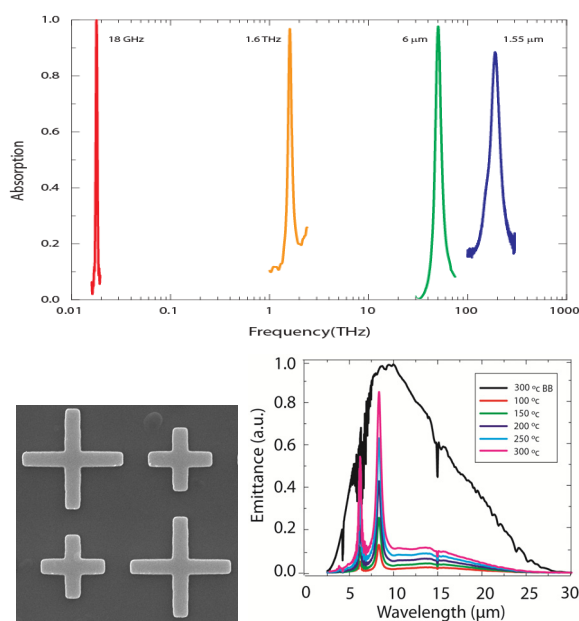


Figure 1. Top: Experimental realizations of MM absorbers across the electromagnetic spectrum – microwave (18GHz), terahertz (1.6THz), infrared (6μm) and optical (1.55μm). Bottom left shows a scanning electron microscope image of a dual-band infrared MM emitter. Bottom right shows experimental emittance of the dual-band MM as a function of temperature (colored curves) compared to an ideal black body emitter (black curve).

made a significant effort to review and cite *every single publication* on metamaterial absorbers published to date - the paper had nearly 180 references.

In one particular investigation we carried out a series of off-normal angular dependent measurements on large area samples of the reflectance for both transverse electric (TE) and transverse magnetic (TM) polarizations. We also calculated the experimental specular absorption,  $A_s=1-R$ , for both TE (dashed black curves) and TM (solid grey curves) at incident angles of 15, 30, 45, and 60 degrees which are shown in the left panels of Fig. 2. At near normal incidence (15 degrees) the spectral characteristics of  $A_s$  are similar for both polarizations. The main absorptive feature due to the MMA is observed near  $6\mu\text{m}$  other identifiable absorptive signatures are also seen. Proceeding to larger incident angles we observe that, for the TE polarized case, the amplitude of the main peak drops noticeably from 90% at 15 degrees to 75% at 60 degrees.

However, for TM polarization the peak in  $A_s$  remains high for all angles investigated, but notably two distinct signatures are revealed for larger incidence angles. One of these absorptive features – which we term here Mode A – is independent of incident angle and occurs at a wavelength of  $4.83\mu\text{m}$ . The other feature – termed Mode B – is observed to shift to longer wavelengths as angle is increased (as noted by the red arrows in Fig. 2). In order to gain insight into the various absorptive features observed in the experimental results presented above, we performed 3D full wave electromagnetic field simulations. The MMA was simulated with dimensions identical to that of the fabricated sample. Simulations provide the complex scattering parameters and we calculate the specular absorption as  $A_s = 1-R = 1-|S_{11}|^2$ . The right panels of Fig. 2 show  $A_s$  for various incident angles and good agreement with experimental results is evident - notably both Modes A and B are also observed.

We next discuss the implications of the experimental and computational results and focus first on Mode B. We note that Mode B only appears in the TM polarization and its peak redshifts as a function of incident angle. It is well-known that periodic structures can support spoof surface-

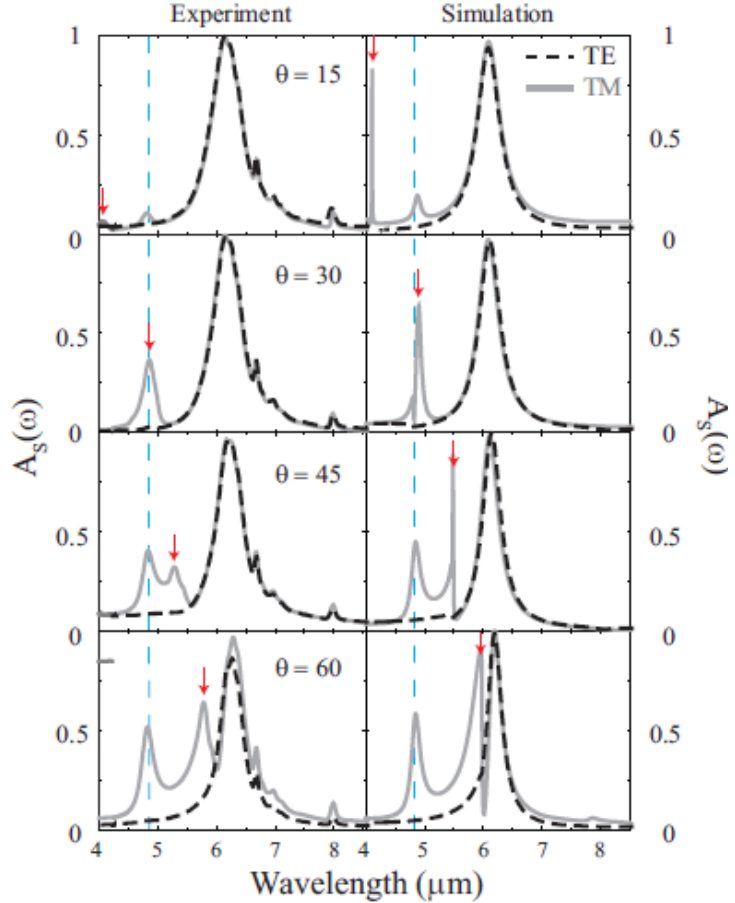


Figure 2. Experimental (left panels) and simulated (right panels) frequency dependent specular absorption for various incident angles ( $\theta$ ) in both TM (grey solid curves) and TE (black dash curves) polarizations.

plasmon-polaritons (SPPs) for TM polarization incident waves. Excitation of SPPs requires the momentum of incident light,  $k_i$ , to match that of the SPP, i.e.  $k_{spp} = k_i + k_G$ , where  $k_{spp}$  and  $k_G$  are  $k$ -vectors of SPP and the Bloch wave (reciprocal lattice vector), respectively. By re-writing  $k_i$  in terms of free space light  $k_0$  as  $k_i = k_0 \sin \theta$ , a strong angular dependence of such SPPs is evident. If Mode B is indeed a SPP, then its peak value should be a function of  $\sin(\theta)$ . We perform a linear fit to our experimental data, (not shown) and find that our  $y$ -intercept,  $k_G = 2\pi/a$ , equals a value of  $1.71 \times 10^6 \text{ (m}^{-1}\text{)}$ . A linear fit to the curve reveals a value of  $a = 3.65 \text{ }\mu\text{m}$ , which agrees qualitatively with the lattice spacing ( $3.2\mu\text{m}$ ) of the fabricated samples. Thus, we attribute the angular dependent feature, (Mode B), as a Bloch wave or spoof SPP, related to the periodicity of the metamaterial.

The other absorptive feature, (Mode A), is independent of incident angle and is seen to always occur near  $4.83\mu\text{m}$ . Notably, Mode A seems to increase in strength as a function of increasing incident angle. Through simulation (not shown) we found that the TM incident wave is coupling to the surface of the metamaterial and both a decaying surface wave and a free space component are observed. Although quantitatively the TE and TM polarized waves show disparate behavior, our simulations further allowed us to extract quantitative information by approximating both the wave number and loss of the surface wave. We find that the surface wave yields a wavelength of about  $4.72\mu\text{m}$  while the free space wavelength is  $4.83\mu\text{m}$ .

The end result of the above study was that scattering was found to be negligible near the primary metamaterial absorption  $\lambda_0$ , and only became appreciable at shorter wavelengths. Two surface modes were found to exist on metamaterial absorbers, when incident light is TM polarized, one due to the periodicity of the unit cell and the other due to the effective optical constants of the MMA. The latter occurs at  $\lambda_0$ , is highly lossy and is responsible for the good angular dependence of absorption in TM polarization.

## Future Plans

The proposed project explores the fundamental properties of metamaterials and their potential for energy applications. There are three main materials which will be investigated:

**1) Metamaterial absorbers** – We have demonstrated, in the previous effort, tailored metamaterial absorbers. There are, however, a number of fundamental unexplored phenomena regarding the absorption process. We will continue investigation of the electromagnetic properties of metamaterial absorbers, initially at infrared wavelengths, then moving on to both longer (THz) and shorter (optical) wavelengths. The ability to tune the angular dependence and/or polarization state of the absorption process, for example, will be explored.

**2) Multi-band / broadband metamaterial emitters** – Metamaterials consisting of multi sub-unit cells can be utilized to tune emission over a broadband. However, the impact of scattering and generation of surface electromagnetic waves are examples of phenomena which may occur with periodicity and / or larger unit cell sizes, and remain unexplored. We will investigate the feasibility to which multiple unit-cell can contribute to emission while still maintaining desired electromagnetic properties. Iteration of various designs will take place within computation space in order to optimize metamaterials for a given energy range.

**3) Metamaterials for super blackbody emission** – For surfaces at a certain temperature the maximum emission is set by Planck’s radiation law, i.e. it cannot be greater than an ideal blackbody. However for bodies or surfaces heated by a given constant input power, a tailored metamaterial surface can emit more power, in a narrow band, than an ideal blackbody surface. The physics underlying such a response will be theoretically and experimentally investigated and the extent that this phenomena can be utilized for potential energy applications will be explored.

## References

---

<sup>1</sup> David Shrekenhamer, Wangren Xu, Suresh Venkatesh, David Schurig, Sameer Sonkusale, and Willie J. Padilla, *Experimental Realization of a Metamaterial Detector Focal Plane Array*, Phys. Rev. Lett. **109**, 177401 (2012).

<sup>2</sup> Wen-Chen Chen, Machhindra Koirala, Xianliang Liu, Talmage Tyler, Kevin G. West, Christopher M. Bingham, Tatiana Starr, Anthony F. Starr, Nan M. Jokerst and Willie J. Padilla, *Characterization of Surface Electromagnetic Waves and Scattering on Infrared Metamaterial Absorbers*, in review at Physical Review Letters. Available at <http://arxiv.org/pdf/1212.2868.pdf>

<sup>3</sup> David Shrekenhamer, Wen-Chen Chen, and Willie J. Padilla, *Liquid Crystal Tunable Metamaterial Perfect Absorber*, accepted for publication - Physical Review Letters. Available at <http://arxiv.org/pdf/1206.4214.pdf>

<sup>4</sup> Claire M. Watts, Xianliang Liu, Willie J. Padilla, *Metamaterial Electromagnetic Wave Absorbers*, Advanced Materials **24**, OP98 (2012)



# **Session II**



**Program Title****Electronic Materials Program**

Materials Sciences Division  
Lawrence Berkeley National Laboratory  
Berkeley, CA 94720

**Principal Investigator**

Ali Javey

**Co-principal Investigators**

Joel W. Ager, Daryl C. Chrzan, Oscar. D. Dubón,  
Wladek Walukiewicz, Kin Man Yu

**Collaborating Investigator**

Junqiao Wu

**Program Scope**

The Electronic Materials Program (EMAT) is focused on the basic materials science of semiconductors. Our research links atomic-scale phenomena with nano-, meso- and macro-scale materials properties and functionalities. There are three research themes:

- *Semiconductor quantum membranes: Spatial confinement, probing, and functionalization;*
- *Band structure and interface tuning on command: Engineering band structures in semiconductor alloys, and electronic and structural properties at interfaces;*
- *Control of phase transitions at the nanoscale.*

Common to these research themes is a synthetic strategy that allows to control structure and phase transitions at the nanoscale. In the case of quantum membranes, our ability to make and control 2-D versions of an arbitrary semiconductor enables to study the interplay of electronic structure and carrier transport at a fundamental level. Our control of materials composition via highly non equilibrium synthesis techniques allows us to tune band structures and interface properties on command. By exploiting new insights in the nanoscale control of phase transitions, we can synthesis new functional structures.

**Semiconductor quantum membranes***Recent progress*

Two-dimensional (2-D) electronic materials such as graphene have seen intense research interest over the last decade. We have identified an opportunity to generalize the use of single layer and few-layer 2-D systems (we will call them quantum membranes, QMs) by using not only naturally occurring layered materials (e.g., MoS<sub>2</sub>, WSe<sub>2</sub>) and but also compound semiconductor layers isolated via transfer processes (e.g., InAs, **Fig. 1**). These ultrathin QMs are not subject to the constraints of lattice-matched heterostructures. Moreover, it appears possible to stack them in arbitrary order and transfer them to almost any substrate.

An important consideration for the fundamental study of QMs whether surface effects will dominate the charge transport. We are finding that developing methods to form low resistance contacts to these ultrathin structures and also controlling carrier scattering by reducing surface roughness are key factors. We are

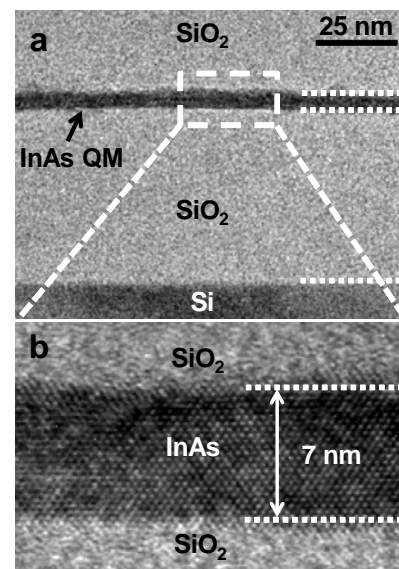


**Fig. 1.** TEM analyses of InAs quantum membranes (QMs). (a) Low magnification and (b) high resolution TEM images of a 7 nm InAs QM capped with SiO<sub>2</sub> on a Si/SiO<sub>2</sub> substrate.

discovering that transport in QMs can be near bulk like: led InAs ultrathin membranes transferred to Si substrates have excellent field-effect electron mobilities (peak effective mobility of  $\sim 5000 \text{ cm}^2/\text{V}\cdot\text{s}$ )<sup>1</sup> and *monolayer* WSe<sub>2</sub> Si/SiO<sub>2</sub> substrates has  $\sim 250 \text{ cm}^2/\text{V}\cdot\text{s}$  hole mobility.<sup>2</sup>

### Future work

The ability to place 2D semiconductor membranes on a user-defined substrate enables exploration of a range of fundamental studies that were previously inaccessible due to the constraints of the growth substrate. Figure 2 shows absorbance spectra for InAs membranes with different thicknesses (3-19 nm which reveal *for the first time*, the existence of a quantum unit of absorbance,  $A_Q$ , where the

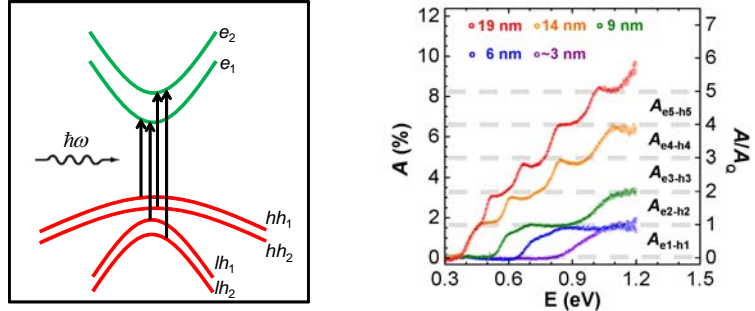


**Fig.2.** Qualitative band structure schematic of a 2-D InAs QM, with arrows indicating the allowed optical interband transitions between valence and conduction sub-bands. Absorbance spectra of InAs QMs with thickness of  $L_z \sim 3, 6, 9, 14,$  and  $19 \text{ nm}$  at room temperature, showing universal absorbance steps of  $A_Q \sim 1.5\%$  in magnitude

magnitude of absorbance due to interband transitions for any 2D semiconductor is shown to be independent of thickness and most material specific parameters (including the effective mass). We plan to perform similar optical studies on II-VI and dichalcogenide QMs where we expect to find excitonic effects in addition to band to band absorption.

Developing doping methods to controls the charge density in QMs is a fundamental challenge. Our initial work suggests a few promising pathways. Ultrathin ( $\sim 5 \text{ nm}$  in thickness) InAs and dichalcogenide QMs can be readily doped n-type with high carrier concentration ( $\sim 10^{19} \text{ cm}^{-3}$ ) by placing K atoms on the surface. For hole doping, we have shown NO<sub>2</sub> molecules on WSe<sub>2</sub> can cause strong p-doping. However there are a number of unanswered questions. For K the activation appears to be near unity while it is less than 0.1% for NO<sub>2</sub>. Furthermore, K doping exhibits a relatively high stability in air which suggests a strong binding energy to the surface of QMs, especially dichalcogenides.

The ability to transfer one QM onto another presents a unique opportunity to form *van der Waals (vdW) heterojunctions* where one can, in principle, combine any two semiconductors without lattice mismatch constraints. This opens an entirely new spectrum of heterojunctions with unique functionalities via tailored surfaces and interfaces including controlled band offsets. We will begin by pursuing two such structures:

1. InAs n-layer/WSe<sub>2</sub> p-layer. Based on the bulk band alignments, this would be expected to form a high rectifying p-n junction.
2. WSe<sub>2</sub> p-layer/SnS<sub>2</sub> n-layer. This is expected to lead to a Type II heterojunction with efficient carrier tunneling.

## Band structure and interface tuning on command

### Recent progress

Highly mismatched alloys (HMAs) formed through alloying of distinctly different semiconductors enable one to use these interactions to modify the band structure in a predictive

way by using the band anticrossing (BAC) interaction between the localized states of the substituted element and the extended states of the matrix.

The mismatched alloy  $\text{GaN}_{1-x}\text{As}_x$  HMAs was synthesized over the whole composition range and both  $p$ -type and  $n$ -type doping was achieved.<sup>3,4</sup> The wide range of band gaps accessible using this material (Fig. 3) makes it promising for solar conversion devices. Our work opens opportunities for possibly functionalizing this material and other amorphous III-V alloys, as well as the fundamental study of defect physics in amorphous III-V semiconductors. Recently we were also able to synthesize  $\text{GaN}_{1-x}\text{Bi}_x$  alloys an extreme HMAs in which large metallic Bi replaces small electronegative N atoms.<sup>5</sup>

#### *Future work*

For most metal oxides, only one type of conductivity can be obtained. This is primarily due to the location of the conduction and valence band edges with respect to the common energy reference represented by the average energy of native defects located at about 4.9 eV below the vacuum level. For example, reliable  $p$ -type doping in ZnO and CdO have not been reported since, as the valence band of ZnO and CdO is very low. However, adding a small amount of Se to ZnO pushes the valence up by  $\sim 1$  eV to the localized nature of the Se state in ZnO. Hence it is expected that O-rich ZnSeO can be doped  $p$ -type with the incorporation of an acceptor such as Cu, P or As. At the same time the conduction band of ZnOSe is low enough for a good  $n$ -type doping in the whole composition range. We will utilize this valence band anticrossing effect for achieving  $n$  and/or  $p$ -type doping in semiconductors where only one type of conductivity is otherwise commonly observed.

The extremely low conduction band edge of CdO provides a wide tunability range of the conduction band edge when alloyed with other metal oxides, particular oxides with different crystallographic structure. Most recently we have synthesized alloys  $\text{Zn}_{1-x}\text{Cd}_x\text{O}$  alloys which show very unique properties close to the wurtzite-rock salt phase transition at  $x=0.69$ . Depending on the crystal structure, alloys at this transition have either high (2.4 eV) or low (1.6 eV) band gap. The “border line” alloys are both highly conducting, with electron concentration of more than  $10^{20} \text{ cm}^{-3}$  and optically active with relatively sharp, intense photoluminescence. An abrupt 4 fold increase of the electron mobility at the transition point is clearly associated with structure induced abrupt modification of the electronic band structure and potential phase separation.

## **Control of phase transitions at the nanoscale**

### *Recent progress*

Phase transitions and their underlying physics lie at the heart of materials science. While simple melting point depression with decreasing size has been well established, recent work has shown that the range of phase transition behaviors at the nanoscale can be considerably more rich. As an exciting recent example, we have fabricated GeAu, GeSn<sup>6</sup> and more recently, GeAg

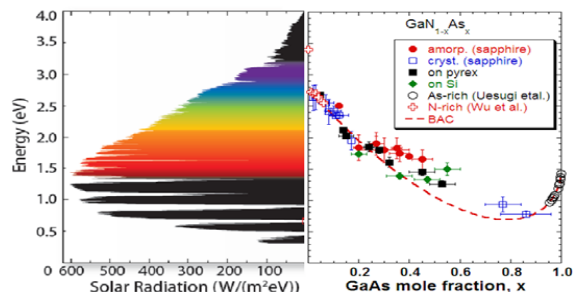


**Fig. 3** A comparison of the measured band gap of  $\text{GaN}_{1-x}\text{As}_x$  as a function of composition with the values predicted by the band anticrossing model (right). Alloys in the composition range of  $0.10 < x < 0.8$  are amorphous but exhibit sharp, well-defined absorption edge

particles (and in the case of GeAu, nanowires) with diameters in the range of 10-50 nm embedded within silica. These binary eutectic alloy nanoclusters (BEANs) synthesized in EMAT are, perhaps, the smallest half metal, half-semiconductor particles synthesized to date.**Error! Bookmark not defined.** We have already demonstrated interesting phenomenology within our binary eutectic alloy nanostructures (BEANs). For example, in the case of GeSn and GeAu nanoclusters, we have tuned phase transformation kinetics to switch the BEANs between amorphous metallic and Schottky barrier configurations.

#### Future work

We will now implement these concepts in functional structures. For example, we will use our interfacial free energy mediated control of melting/solidification transition temperatures and kinetics to engineer the heat capacity of an embedded nanoclusters, which might then serve as a means to store and transport thermal energy. Interfacial free energies also play a substantial role in the development of thin film processing routes capable of producing high quality films (*e.g.* InP films on Mo underneath silica, or large-area silicene), and we will further explore these applications. We have promising initial calculations that imply we will be able to stabilize liquid inclusions of relatively high melting point metals (*e.g.* Au) at room temperature. As the melting point is a function of interface energy and geometry, we can envision 2-D structures with alternating liquid and solid sections.

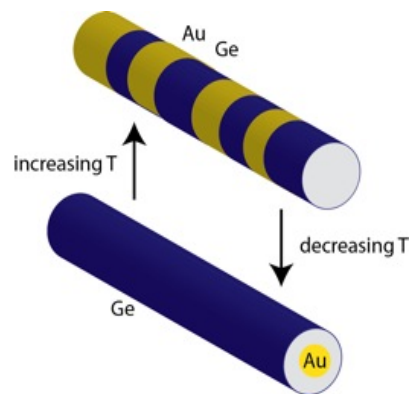


**Fig. 4.** 1-D BEANs offer the potential for interesting switching behavior. It might be possible, for example, to switch between multilayer and core/shell morphologies, using either temperature or exploiting.

## References to DOE-supported work

- 1 Takei, K.; Chuang, S.; Fang, H.; Kapadia, R.; Liu, C.-H.; Nah, J.; Kim, H. S.; Plis, E.; Krishna, S.; Chueh, Y.-L. & Javey, A. Benchmarking the performance of ultrathin body InAs-on-insulator transistors as a function of body thickness *Applied Physics Letters*, 2011, 99, 103507
- 2 Fang, H.; Chuang, S.; Chang, T. C.; Takei, K.; Takahashi, T. & Javey, A. High-Performance Single Layered WSe<sub>2</sub> p-FETs with Chemically Doped Contacts *Nano Letters*, 2012, 12, 3788-3792
- 3 K. M. Yu, S. V. Novikov, R. Broesler, I. N. Demchenko, J. D. Denlinger, Z. Liliental-Weber, F. Luckert, R. W. Martin, W. Walukiewicz, and C. T. Foxon, "Highly Mismatched GaN<sub>1-x</sub>As<sub>x</sub> Alloys in the Whole Composition Range," *J. Appl. Phys.* **106**, 103709 (2009).
- 4 A. X. Levander, S. V. Novikov, Z. Liliental-Weber, R. dos Reis, O. D. Dubon, J. Wu, C. T. Foxon, K. M. Yu, and W. Walukiewicz, "Doping of GaN<sub>1-x</sub>As<sub>x</sub> with High As content," *J. Appl. Phys.* **110**, 093702 (2011).
- 5 A. X. Levander, K. M. Yu, S. Novikov, A. Tseng, W. Walukiewicz, C. T. Foxon, O. D. Dubon, J. Wu, "GaN<sub>1-x</sub>Bi<sub>x</sub>: Extremely Mismatched Semiconductor Alloys," *Appl. Phys. Lett.* **97**, 141919 (2010).
- 6 Shin, S. J.; Guzman, J.; Yuan, C.-W.; Liao, C. Y.; Boswell-Koller, C. N.; Stone, P. R.; Dubon, O. D.; Minor, A. M.; Watanabe, M.; Beeman, J. W.; Yu, K. M.; Ager, J.; Chrzan, D. C. & Haller, E. E. Embedded binary eutectic alloy nanostructures: a new class of phase change materials. *Nano Lett*, 2010, 10, 2794-2798

**Control of Semiconductor Surfaces with Soft Gates**  
**Electronic Materials Program at LBNL**

Joel W. Ager

Lawrence Berkeley National Laboratory, Materials Sciences Division, MS 2R0200,  
 1 Cyclotron Road, Berkeley, CA 94720

**Program Scope**

The insulating double layer (Helmholtz layer) formed by a liquid electrolyte can be used to create electric fields at the surface of a semiconductor. Here, we are using electrolyte gating to control surface carrier properties for fundamental transport studies.

Our work with indium nitride (InN) illustrates some of the benefits of this approach. The Group III-nitride alloy band gaps span from the infrared InN ( $E_g=0.675$  eV or more than 1800 nm) to well into the ultraviolet GaN ( $E_g=3.4$  eV or 365 nm), AlN ( $E_g=6.1$  eV or 203 nm), a range that includes not only the entire visible but virtually the entire solar spectrum. InN has the smallest bandgap in this alloy system. It also has an exceptionally large ( $> 5.5$  eV) electron affinity which creates a strong thermodynamic driving force for the formation of native donor defects both in the bulk and at the surface. For example, undoped InN thin films are always n-type and all as-grown InN surfaces, regardless of polarity, crystal orientation, or doping, have an accumulation layer of electrons (Fig. 1). The surface electron layer had prevented the study of the fundamental transport properties of InN by standards method such as Hall effect.

In prior work, we discovered that electrolyte gating can be used to deplete the surface electron accumulation. This allowed the acceptor nature of Mg to be confirmed by capacitance voltage techniques and enabled the surface layer contribution to be “turned off” in Hall effect measurements. We also used thermopower measurements to assess hole transport directly in Mg-doped InN, finding a hole mobility of up to  $60 \text{ cm}^2 \text{ V}^{-1} \text{ s}^{-1}$  for a hole concentration of  $1\text{-}3 \times 10^{18} \text{ cm}^{-3}$ .

**Recent Progress**

Calculations of the expected electron and hole accumulation in InN for cathodic and anodic biases, respectively, are shown in Fig. 1. Most recently, we have shown that

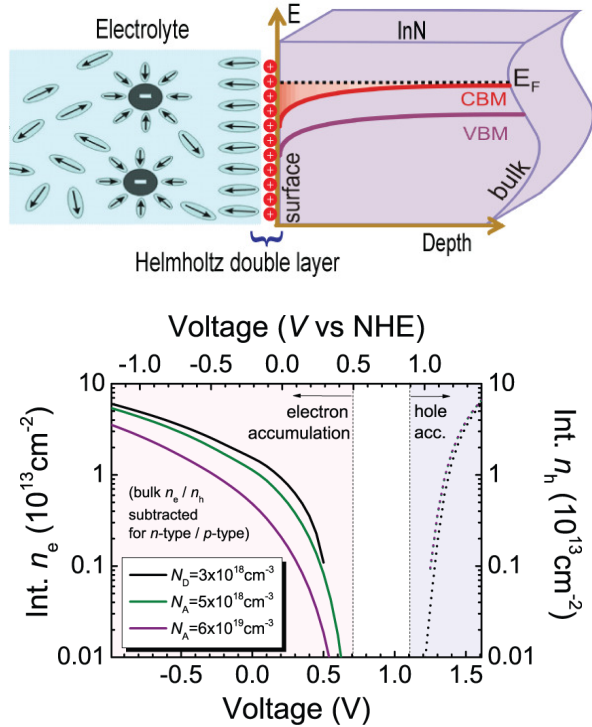


**Fig. 1.** Calculated surface sheet electron (left) and hole (right) concentrations for InN with bulk donor or acceptor doping in contact with an electrolyte. Negative applied voltages to the semiconductor increase the electron accumulation while positive voltages decrease it and eventually invert the surface. Calculations by E. Alarcón-Lladó.

electrolyte gating can not only reduce surface electron accumulation but also invert the surface and accumulate holes.

As shown in Fig. 2, we used *in-situ* Seebeck coefficient measurements detect the change in the surface carriers in InN under electrolyte control. The increasing Seebeck coefficient at large positive bias shows the accumulation of holes at the surface [Ager and Miller, 2012].

Despite nearly a decade of effort worldwide, a rectifying pn junction had not been demonstrated in InN as the electron accumulation layer discussed above had prevented direct contact to the p-type regions of Mg-doped InN films. By using a device a similar to a field effect transistor in which the insulating double layer of the ionic liquid serves as the gate dielectric, we reduced the electron accumulation on the surface of p-type InN, thus forcing the carriers to flow through the pn junction created between the n-type surface layer and the p-type bulk. In the absence of gating or when a positive voltage is applied to the gate, accumulating electrons, the current preferentially flows through the n type regions at the surface and at the interface with the substrate, and linear current-voltage (IV) behavior is observed. However, when a negative voltage gate is applied, as shown in Fig. 3, surface electrons are depleted and current flows through the p-type bulk. This creates an n-p-n structure and a characteristic non-linear IV curve is observed, which is well explained by an np-pn equivalent circuit and clearly demonstrates pn junction rectification in InN. [Alarcón-Lladó *et al.*, 2011].

The aqueous and ionic liquid electrolytes we use are transparent to visible light and thus allow facile access for optical spectroscopy. We are developing *in-situ* micro-Raman spectroscopy techniques to probe surface and near-surface carrier properties under soft gate control. The origin of the

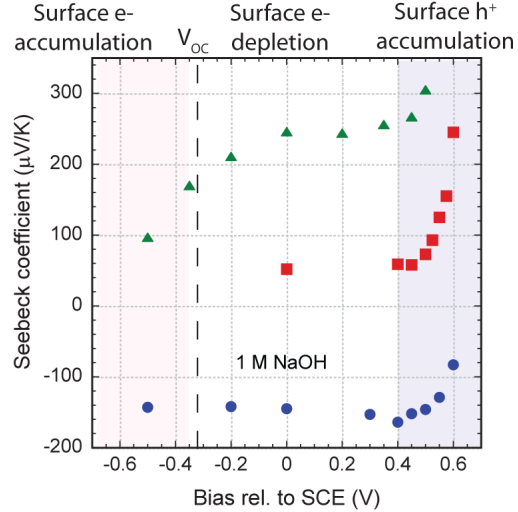


**Fig. 2.** Seebeck coefficient ( $S$ ) of Mg-doped, p-type (green and red) and n-type (blue) InN films as a function of bias, 1 M NaOH in aqueous solution. Positive Seebeck coefficients for the Mg-doped films indicate bulk p-type conduction. Surface hole accumulation is revealed by the increasing Seebeck coefficients at positive (anodic) bias. In Mg-doped samples, an increase in electron accumulation at large negative bias can also be produced.

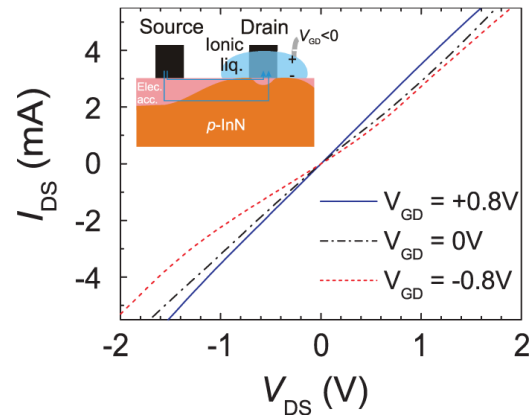


**Fig 3.** Gating produces no effect in n-type InN. Similarly increasing electron accumulation in p-type InN with a positive gate also has little effect. However, depleting the electron accumulation with a negative gate produces an S-shaped IV curve of a npn structure, clearly demonstrating rectification in InN.

intense peak appearing in the resonance Raman spectrum of wurtzite InN films in the vicinity of the expected ( $E_{1,A_1}$ ) longitudinal optical (LO) frequency has been of considerable interest for the last decade. Specifically, it had not been clear whether the observed excitation energy dispersion of this feature is due to wavevector non-conservation due to impurities or is a bulk effect. Our in-situ measurements performed under electrolyte gate control find that as the surface condition is tuned from electron depletion to accumulation and back, Raman scattering near the expected position of the longitudinal optical (LO) near  $590\text{ cm}^{-1}$  shifts to lower frequency and back in a completely reversible manner (Fig. 4). This is the first experimental evidence of the relation between the LO feature in InN and free electron accumulation at its surface.

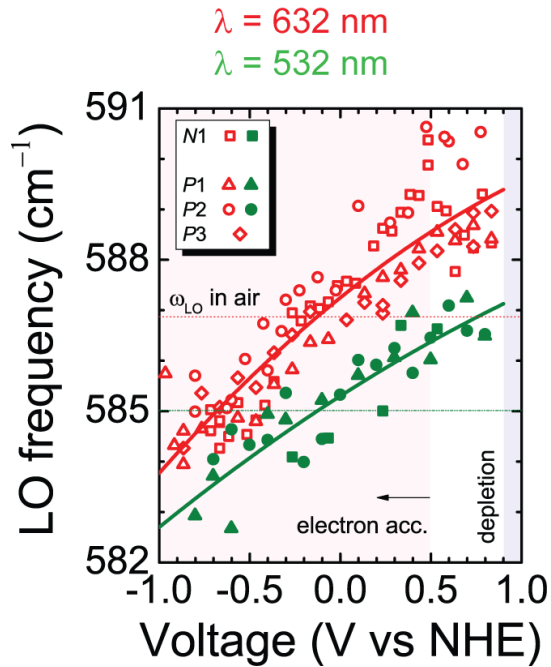


Fig. 4. As the surface condition is tuned from electron depletion to accumulation and back, Raman scattering near the expected position of the longitudinal optical (LO) near  $590\text{ cm}^{-1}$  shifts to lower frequency in a completely reversible manner.

### Future Work

We will apply our *in-situ* optical spectroscopy techniques to low dimensional structures such as nanowires and 2-D semiconductors. We have already utilized the conformal nature of the electrolyte gate to control the surface electron concentration in InN nanowires and have observed reversible phonon feature shifts similar to those discussed above for the bulk. In initial work, we have begun to investigate optical signatures of band filling and carrier lifetime effects in electrolyte-gated 2-D semiconductors.

### BES-supported publications, 2011-2013

- K. Wang, N. Miller, R. Iwamoto, T. Yamaguchi, M.A. Mayer, T. Araki, Y. Nanishi, K.M. Yu, E.E. Haller, W. Walukiewicz, and J.W. Ager III, "[Mg doped InN and confirmation of free holes in InN](#)," *Appl. Phys. Lett.* **98**, 042104 (2011).
- N. Miller, E.E. Haller, G. Koblmüller, C. Gallinat, J.S. Speck, W.J. Schaff, M.E. Hawkrige, K.M. Yu, and J.W. Ager III, "[Effect of charged dislocation scattering on electrical and electrothermal transport in n-type InN](#)," *Phys. Rev. B* **84**, 075315 (2011).
- E. Alarcon-Llado, M.A. Mayer, B.W. Boudouris, R.A. Segalman, N. Miller, T. Yamaguchi, K. Wang, Y. Nanishi, E.E. Haller, and J.W. Ager, "[PN junction](#)"

[rectification in electrolyte gated Mg-doped InN](#),” Appl. Phys. Lett. **99**, 102106 (2011).

J. W. Ager III and N. R. Miller, “[Taming transport in InN](#),” Phys. Status Solidi A **209**, 83–86 (2012).

## Acceptor defects in ZnO and related materials

Matthew D. McCluskey<sup>1,\*</sup> and Leah Bergman<sup>2,\*\*</sup>

<sup>1</sup>Department of Physics and Astronomy, Washington State University, Pullman, WA 99164-2814

<sup>2</sup>Department of Physics, University of Idaho, Moscow, ID 83844-0903

### PROGRAM SCOPE

Zinc oxide (ZnO) is a potentially important material in electronic devices, including transparent contacts in solar cells, transparent anodes in polymer light-emitting diodes, and active materials in solid-state white lighting. ZnO nanocrystals provide wavelength tunability via quantum confinement and may be useful in dye-sensitized solar cells. Despite the large amount of research performed on semiconductor nanoparticles in general, the fundamental properties of dopants in nanocrystals are only beginning to be understood. *P*-type doping, required for most practical device applications, has been elusive.

The program utilizes a range of experimental techniques to elucidate the microscopic structure, charge state, and concentrations of defects and dopants in ZnO nanocrystals. The effect of particle size on these properties is investigated from the nanometer to micron regimes. To probe energy levels, the band gaps will be tuned by systematically varying quantum confinement, alloy composition, and hydrostatic pressure. By controlling defects and dopants, we aim to achieve *p*-type conductivity in ZnO nanocrystals. Reliable *p*-type doping would be transformative, enabling a range of new applications.

Specific aims of the project include:

- Investigate the fundamental electrical and optical properties of acceptors in oxide semiconductors.
- Use alloying to tune the band structure and convert deep acceptors into shallow ones.
- Elucidate the role of surface states in doped ZnO nanocrystals and thin films.
- Demonstrate reliable, repeatable *p*-doping of ZnO and/or ternary alloys.

Optical spectroscopy, performed at Washington State University (WSU) and University of Idaho (UI), is complemented by work at DOE user facilities at Pacific Northwest National Laboratory (PNNL) and Lawrence Berkeley National Laboratory (LBNL).

### RECENT PROGRESS

#### ZnO:Cu ceramics

ZnO:Cu ceramic samples were created via a sintering process that involves hard-pressing followed by an annealing procedure. Samples of 0, 0.5, 1, and 5% copper were studied. The room-temperature UV PL of the samples have an interesting correlation to the percentage of Cu in the samples. The pure ZnO sample has a strong PL centered at ~ 3.3 eV. As the percentage of Cu increases, a significant decrease in the PL intensity is observed. Due to the diminishing intensity of the PL, up to *nine orders of the longitudinal optical (LO) mode* are observable for the Cu doped samples (Fig. 1). Our results suggest that the low PL intensity is due to non-radiative centers of Cu-related complexes.

The multiple LO modes give us unparalleled insight into anharmonic vibrational processes. We are currently investigating the effect of pressure on the anharmonicity, and the fundamental role it plays in phase transitions. MgZnO alloys are also being investigated (Fig. 2).

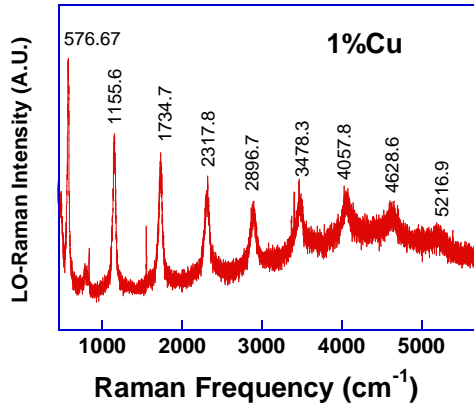


Fig. 1. Raman spectrum of the 1% Cu doped ceramic ZnO sample. The PL is completely quenched. Similar spectra were observed for the 5% sample.

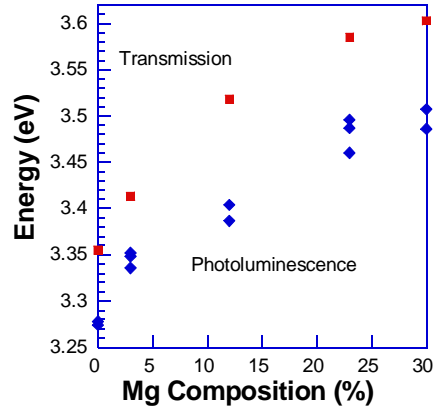


Fig. 2. PL and the absorption edge of MgZnO as a function of Mg composition.

### Nitrogen: A deep acceptor in ZnO?

Zinc oxide (ZnO) is a promising material for energy-efficient white lighting, among other applications. A suitable *p*-type dopant is, however, a fundamental problem for realizing its potential. Nitrogen substituting for oxygen ( $N_O$ ) has been proposed as a shallow acceptor. Numerous reports claim that nitrogen doping can produce *p*-type ZnO. Theoretical work suggests that nitrogen is actually *deep* acceptor. Our experiments show that nitrogen is, in fact, a deep acceptor and therefore cannot produce *p*-type ZnO. A broad photoluminescence (PL) emission band near 1.7 eV, with an excitation onset of  $\sim 2.2$  eV, was observed, in agreement with the deep-acceptor model of the nitrogen defect (Fig. 3). A proposed solution to this problem is to push the ZnO valence band upward, by alloying with chalcogens (S, Se, Te). This may reduce the acceptor binding energy of nitrogen and enable *p*-type doping.

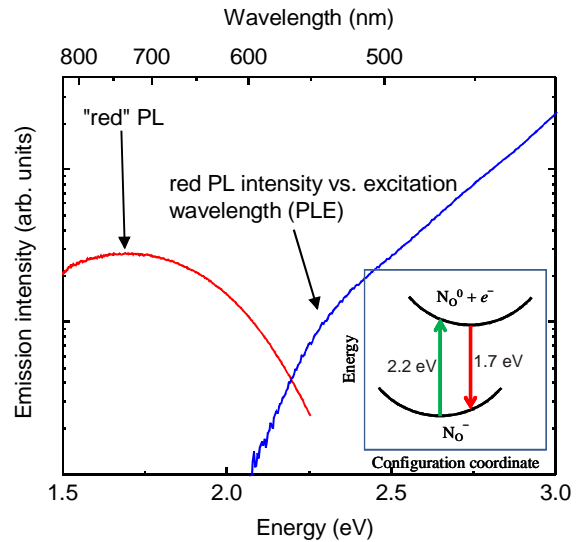


Fig. 3. PL and PLE spectra from nitrogen acceptors in ZnO. Photons (energy  $> 2.2$  eV) excite an electron from nitrogen ( $N_O^-$ ) to the conduction band. When the electron is recaptured by the nitrogen, a red photon (1.7 eV) is emitted.

### Acceptors and surface states in ZnO nanocrystals

Our optical studies of ZnO nanocrystals ( $\sim 20$  nm diameter) show that they contain acceptors as grown. Because ZnO nanocrystals have a high surface-to-volume ratio, surface effects become

especially important. From the results of optical spectroscopy, we have proposed a unified model that explains acceptor *and* surface states in ZnO nanocrystals. The energy levels of these states are shown in Fig. 4. While the acceptor level (0.46 eV) is not shallow, to our knowledge it is shallower than any other acceptor in ZnO. Our EPR results suggest that the acceptor may be a zinc-vacancy complex.

At liquid-helium temperatures, we observed a series of sharp IR absorption peaks that arise from the acceptor. In analogy with a hydrogen atom, a hole orbits the negatively charged acceptor. IR light excites the hole into higher-energy orbits, resulting in spectral lines similar to the  $1s$ -to- $2p$  transitions in hydrogen. When sample warms up, though, the peaks disappear (Fig. 5). From the temperature dependence, we determined that the hole is thermally excited into surface states that lie slightly above the valence band.

To probe the surface states further, we performed PL experiments. In these experiments, electrons and holes are created by exposing the sample to an excitation light source. Some of the electrons fall to the acceptor level, emitting violet light. Other electrons and holes recombine on the surface, emitting red light. The PL energies are consistent with the energy-level diagram in Fig. 4.

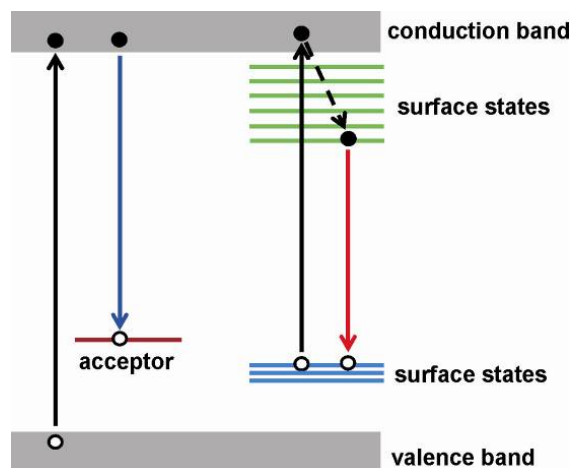


Fig. 4. Energy-level for acceptor and surface states in ZnO.

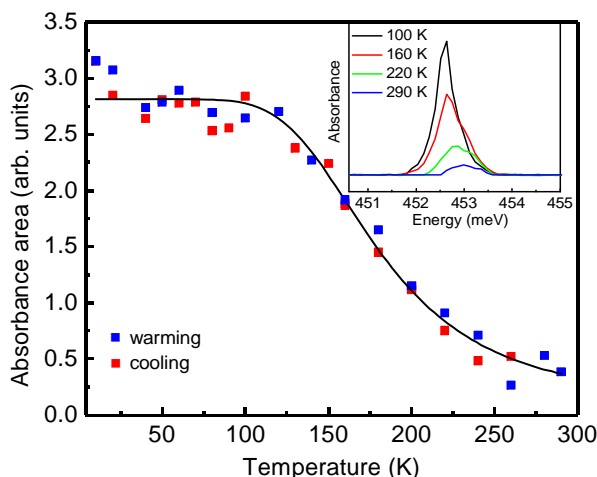


Fig. 5. Temperature-dependent IR absorbance area of the acceptor excited-state peak upon cooling and warming of the sample. Inset: IR absorption spectra of an acceptor peak, showing a decrease with temperature.

## Future Plans

Future research will provide a fundamental understanding of defects in ZnO that could lead to reliable  $p$ -type conductivity. First, alloying ZnO with the chalcogens sulfur, selenium, or tellurium will raise the valence band. By tuning the valence band, one may realize a reduced nitrogen acceptor binding energy. This approach can be summarized as “if you cannot bring the acceptor to the valence band, bring the valence band to the acceptor.” Alkali dopants (lithium and sodium), which have lower binding energies than nitrogen, could prove especially fruitful. A second strategy for  $p$ -type doping is suggested by studies on ZnO nanocrystals, which show evidence for an acceptor level 0.46 eV above the valence-band maximum. The identity of this acceptor is currently unknown, and identifying it is a goal of our research.

## Publications of DOE-sponsored research (2010-2012)

- S.J. Jokela and M.D. McCluskey, “Structure and stability of N-H complexes in single-crystal ZnO,” *J. Appl. Phys.* **107**, 113536:1-5 (2010).
- W.M. Hlaing Oo, M.D. McCluskey, J. Huso, J.L. Morrison, L. Bergman, M.H. Engelhard, and L.V. Saraf, “Incorporation of Cu acceptors in ZnO nanocrystals,” *J. Appl. Phys.* **108**, 064301:1-3 (2010).
- W.M. Hlaing Oo, S. Tabatabaei, M.D. McCluskey, J.B. Varley, A. Janotti, and C.G. Van de Walle, “Hydrogen donors in SnO<sub>2</sub> studied by infrared spectroscopy and first-principles calculations,” *Phys. Rev. B* **82**, 193201:1-4 (2010).
- M.C. Tarun and M.D. McCluskey, “Hydrogen-related defects in strontium titanate,” *J. Appl. Phys.* **109**, 063706:1-4 (2011).
- L. Bergman, J. Huso, J.L. Morrison, and G.M. Norton, “Luminescent ZnO and MgZnO,” in *Handbook of Photoluminescent Semiconductor Materials*, ed. Leah Bergman and Jeanne L. McHale (Taylor & Francis 2011).
- M.C. Tarun, M. Zafar Iqbal, and M.D. McCluskey, “Nitrogen is a deep acceptor in ZnO,” *AIP Advances* **1**, 022105:1-7 (2011).
- F.A. Selim, M.C. Tarun, D.E. Wall, L.A. Boatner, and M.D. McCluskey, “Cu-doping by nuclear transmutation,” *Appl. Phys. Lett.* **99**, 202109:1-3 (2011).
- S.T. Teklemichael, W.M. Hlaing Oo, M.D. McCluskey, E.D. Walter, and D.W. Hoyt, “Acceptors in ZnO nanocrystals,” *Appl. Phys. Lett.* **98**, 232112:1-3 (2011).
- S.T. Teklemichael and M.D. McCluskey, “Acceptor and surface states of ZnO nanocrystals: A unified model,” *Nanotechnology* **22**, 475703:1-4 (2011).
- G.J. Hanna, S.T. Teklemichael, M.D. McCluskey, L. Bergman, and J. Huso, “Equations of state for ZnO and MgZnO by high pressure x-ray diffraction,” *J. Appl. Phys.* **110**, 073511:1-5 (2011).
- U. Sahaym, M.G. Norton, J. Huso, J.L. Morrison, H. Che, and L. Bergman, “Microstructure evolution and photoluminescence in nanocrystalline MgZnO thin films,” *Nanotechnology* **22**, 425706:1-9 (2011).
- J. Huso, J.L. Morrison, H. Che, W.-J. Yeh, and L. Bergman, “ZnO and MgZnO nanocrystalline flexible films: Optical and material properties,” *Journal of Nanomaterials* **2011**, 691582:1-7 (2011).
- J.L. Morrison, J. Huso, H. Che, D. Thapa, M. Huso, M. G. Norton, and L. Bergman, “The formation of MgZnO luminescent ceramics,” *J. Mater. Science: Mater. Electron.* **23**, 437-444 (2012).
- M.D. McCluskey, M.C. Tarun, and S.T. Teklemichael, “Hydrogen in oxide semiconductors,” *J. Mater. Res.* **27**, 2190-8 (2012).
- H. Che, J. Huso, J.L. Morrison, D. Thapa, M. Huso, W. Jiang Yeh, M.C. Tarun, M.D. McCluskey, and L. Bergman, “Optical properties of ZnO-alloyed nanocrystalline films,” *Journal of Nanomaterials* **2012**, 963485:1-7 (2012).

\* E-mail: mattmcc@wsu.edu

\*\* E-mail: lbergman@uidaho.edu

# **Session III**



## Critical Materials

Karl A. Gschneidner Jr.  
Ames Laboratory, DOE and  
Department of Materials Science and Engineering  
Iowa State University  
Ames, IA 50011-3020  
cagey@ameslab.gov

In 2010-2011 China mined 95-97% of the rare earths consumed in the world, by 2012 it fell to about 85% with Molycorp Mount Pass' mine coming into full production. China's rare earth cartel posed a big threat to the USA's energy and military security, but with Molycorp's and Lynas' (Australia) production of rare earths coming on stream in 2012 and 2013, respectively, this situation has been ameliorated to some extent. However, these two non-Chinese mines produce only the light rare earths, and China still controls ~100% of the production of the heavy rare earths, which means that the energy critical elements, Eu, Tb, Dy and Y, still is a problem for the non-Chinese countries. This shortage will not be relieved until 2014-2015 when non-Chinese mines containing appreciable heavy rare earth elements become operational.

The slowdown of the world's economics in 2011-2012 has resulted in a reduction of the demand of rare earth materials and chemicals, and thus contributed to a reduction of the criticality. But this is only a temporary pause.

The second problem is the lack of the intellectual capital of scientists, engineers and technicians with a background in the rare earths in the USA. This is slowly being resolved, but it will take the USA 5 to 10 more years before we fully recover the number of these trained personnel as in the 1990s.

Although there seems to be a lull in the crisis today, price wars will arise again in and after 2015. The price war will not be at the low end of the supply chain (i.e. ores, concentrates and separated rare earth chemicals), but it will be at or near the high end of the supply chain (i.e. magnets, phosphors, CFL and LED lamps, computers, speakers, high end electronics, etc.). The USA needs to be ready for these price wars.

The newly established DOE critical energy materials hub, i.e. the Center for Materials Institute, CMI, headed by the Ames Laboratory, will help overcome the critical materials crisis. The four CMI focus areas are: diversifying supply, developing substitutes, reuse and recycling, and crosscutting research. Also included in CMI mission are outreach and professional education programs. The CMI consortium consists of four national DOE laboratories (the Ames Laboratory, Idaho National Laboratory, Lawrence Livermore National Laboratory and Oak Ridge National Laboratory), seven academic institutions and seven industrial organizations.

# The Materials Project

Kristin Persson  
Lawrence Berkeley National Laboratory  
1 Cyclotron Rd  
Berkeley, Ca 94720  
Phone: 510-486-7218  
Email: [kapersson@lbl.gov](mailto:kapersson@lbl.gov)

Today, it takes 18 years on average from materials conception to commercialization. One of the foremost reasons for the long process time in materials discovery is the lack of comprehensive knowledge about materials, organized for easy analysis and rational design. Google has demonstrated the value of organizing data and making the data available and searchable to large communities. In June 2011, the Materials Genome Initiative was launched to leverage improved, large-scale computations and data organization to aid and accelerate future materials design.



**Figure 3** Web page for the Materials Project showing the current data coverage and the available analysis and design tools

In spirit of Materials Genome Initiative, the recently BES-funded Materials Project aims to leverage the information age for materials design. The goal of the Materials Project (online at <http://www.materialsproject.org>), see Fig. 1, is to accelerate materials discovery and education through advanced scientific computing and innovative design methods, scale those computations to inorganic compounds and beyond, and disseminate that information and design tools to the larger materials community. We envision a future where computable properties of most compounds will be known, can be searched easily, where the variation of properties across the universe of composition and structure is

better understood, and where rapid design cycles can be achieved. Such an effort, to expose “the Materials Genome”, requires substantial cross-disciplinary and collaborative efforts in materials theory, high-throughput computing, experimental and application specific materials knowledge, computer science, data mining, and database science.

The goal of the Materials Project is to provide a such a Materials Genomic nucleus for both experimentalists and theorists to have access to materials properties to search for suitable chemistries, analyze the results and ultimately inspire novel materials development (see Fig. 2). The Project was launched online in October 2011 and since then we have computed and imported > 30,000 inorganic compounds into the database, which can now be freely accessed and searched over through the web interface for structural properties, local environments and coordination, XRD, electronic structure and more. NERSC has been a tremendously supportive partner and we execute most of our calculations as well as store our database on NERSC hardware. A sophisticated software infrastructure [1]

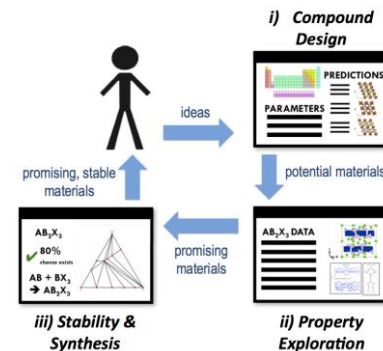


**Figure 4** Iterative materials design capability available at the Materials Project

encompassing an automatic workflow

(‘Fireworks’) that monitors and manages the calculations, a document-based MongoDB database [3], a public python library [2] (‘Pymatgen’) for data analysis and a web-based dissemination powers the Project. Different ‘apps’ which process the raw Schrodinger data according to different specifications, such as Li-ion battery applications, electronic structure, reaction chemistry, phase stability etc are available to browse the data. Interactive tools for structure prediction for a given chemistry using datamining algorithms and crystal structure manipulation are also available. High-throughput computing is always vulnerable to data pollution and inaccuracies. While several automatic data accuracy algorithms are in place, such as energy, volume and bond length sanity checks, more data validation and provenance tools are on the way. Today, 1.5 year after launch, the Materials Project has attracted over 3,500 registered users and the average usage of any site app is around 200-300 per month. A RESTful interface allows high-volume users to bypass the web interface and download large amounts of data efficiently for customized analysis and datamining. In the last month alone, 18,000 materials records were downloaded through this interface.

Nine core PIs are working to enhance and add more materials properties and analysis tools to the Project while others are contributing on a voluntary collaborative basis using the Project’s publicly available codes and infrastructure. Future data sets planned to be made available include defect prediction, higher-order electronic structure descriptions, temperature-dependent properties such as phonons, phase diagrams, thermal expansion and surfaces. Future data interactive capabilities include computations on demand, dissemination of published compound data and enhanced crowd sourcing for data provenance and validation. We invite scientists, teachers and materials engineers and to join us, to add data, analysis tools and expertise to the Project.

In summary, the Materials Project Center aims to leverage accurate materials property and structure prediction with high-performance computing and data mining to realize an efficient materials design platform. Many property requirements transcend a particular application (e.g., band gap, charge transport, stability, predicting point defects), which means that gathering all properties in one place, will maximize the impact on the materials community. Indeed, its largest impact will not come from the people who calculate and organize the data, but from the tens of thousands of scientists in academia and industry who design and develop new materials.

1. Anubhav Jain, Geoffroy Hautier, Charles J. Moore, Shyue Ping Ong, Christopher C. Fischer, Tim Mueller, Kristin A. Persson, Gerbrand Ceder, *A High-Throughput Infrastructure for Density Functional Theory Calculations*, *Comp. Mat. Sci.* **50**, 2295–2310 (2011).
2. Shyue Ping Ong, William Davidson Richard, Gerbrand Ceder, Anubhav Jain, Michael Kocher, Shreyas Cholia, Daniel Gunter, Kristin A. Persson, Geoffroy Hautier, and Vincent L. Chevrier, *Python Materials Genomics (pymatgen) : A Robust, Open-Source Python Library for Materials Analysis*, *Computational Materials Science* Volume 68, pg. 314–319 (2013).
3. Dan Gunter, Shreyas Cholia, Anubhav Jain, Michael Kocher, Kristin Persson, Lavanya Ramakrishnan, Shyue Ping Ong, Gerbrand Ceder, 5th Workshop on Many-Task Computing on Grids and Supercomputers (MTAGS) 2012, Conference proceedings.



# **Session IV**



## Nanometer-Scale Surface and Interface Phenomena

Gary Kellogg\* (PI), Norman Bartelt, Farid El Gabaly, Peter Feibelman, Kevin McCarty, Nancy Missert, Taisuke Ohta, Brian Swartzentruber, Konrad Thürmer and Kevin Zavadil  
Sandia National Laboratories, Albuquerque, NM and Livermore, CA

\*Mailing address: Mail Stop 1415, Albuquerque, NM 87185 email: gkello@sandia.gov

### Program Scope

The purpose of this program is to develop an atomic/molecular-scale understanding of technologically important processes occurring at solid surfaces, internal interfaces and solid-liquid interfaces. Our ultimate goal is to provide the fundamental information needed to understand and control surface/interface properties for materials applications with emphasis on energy-related technologies. Our approach combines state-of-the-art experimental capabilities with first-principles, kinetic and thermodynamic modeling to determine how atomic-scale processes relate to the longer-range interactions that control interfacial behavior. Specific materials systems are chosen for their relevance to national needs, notably energy-related materials. Our four major tasks are designed to investigate a set of increasingly reactive environments from clean surfaces in ultrahigh vacuum, to liquid-solid interfaces, to metallic and oxide nanostructures in electrochemical environments:

1) *Atomistic dynamics of surfaces* – This task's goal is to determine the mechanisms and energetics of atom transport across the surface and into the interior of solids. Experimental tools include STM and LEEM. Theoretical approaches to interpreting our observations include density functional theory (DFT), molecular dynamics/Monte Carlo simulations and thermodynamic modeling. Our current areas of emphases are: (1) the molecular structure of water on metal surfaces; (2) oxide-on-oxide thin film growth; and (3) the bonding and transport of carbon, notably graphene, on metals and on SiC.

2) *Collective phenomena in surface dynamics* – This task strives to quantify the collective processes that govern the surface structures and morphologies of functional materials. We measure (STM, LEEM) the time-evolution of surface structure on nanometer length scales and develop equations of motion that account for the observed time dependences precisely. This general approach often reveals unanticipated surface dynamical mechanisms and has been a rich source of insight into materials behavior. Using it we have: 1) shown that unexpected diffusion processes, such as cluster diffusion and bulk/surface mass exchange, can affect materials growth; 2) identified new kinetic pathways that promote film instability; 3) quantitatively determined the forces that stabilize self-assembling patterns.

3) *Materials at interfaces: structural and electronic properties* – Task 3 focuses on how interfaces affect the macroscopic mechanical and electronic properties of materials. We combine newly acquired surface microscopies (qPlus AFM and spectroscopic LEEM-PEEM) with modeling studies to determine microscopic interface structure. Current emphases include investigations of the properties of water at interfaces, how the electronic structure of graphene is affected by its interaction with a metal or another graphene sheet and the relationship between structure and magnetism in thin metal oxide films.

Task 4) *Nanoscale electrochemistry* – The primary focus of this task is to develop a quantitative understanding of the mechanisms of localized corrosion initiation in passive metals and to quantify the critical parameters governing ion transport and nanostructure formation in model systems for energy storage applications. Our approach is based on the novel and unique application of nanofabrication techniques to produce tailored surfaces and to simulate specific defect types on controlled substrates in well-defined locations. We shed light on corrosion, ion

transport, and nanostructure-formation mechanisms using in-situ and advanced electrochemical, morphological, chemical and structural analytical tools.

### **Recent Progress**

Task 1 Our recent progress includes: 1) determining the molecular structure of water on the (111) surfaces of Pt, Pd, and Ru; 2) identifying the stoichiometry, domain structure and growth dynamics of ultrathin iron oxide films on YSZ(001); 3) investigating the details of Pt-cluster binding and stability with respect to CO gas exposure of Pt-cluster arrays on the graphene moiré on Ir(111); 4) characterizing the interaction between and orientation of graphene islands on Au(111); 5) discovering the essential role of carbon's surface diffusion in graphene growth on SiC; and 8) developing a combined STM-LEEM system for examining surface features from atoms to microns.

Task 2 Our recent progress includes: 1) elucidating the complex relationship between hexagonal ice and cubic ice by examining film morphology at various growth stages; 2) establishing an underlayer growth mechanism for graphene on Ir, Ru, and Cu and during CVD; 3) understanding the factors that control graphene growth on the coinage metals Cu and Au; 4) determining how O<sub>2</sub> etches graphene from Ru and Ir; 5) characterizing the growth and structure of Mg and Pd films and the mechanism of metal-hydride formation; 6) identifying the order of phase transitions on iron oxide surfaces and films; 7) creating defect-free, self-assembled stripe patterns over dimensions of several microns, and 8) examining how the step structure of the quasicrystal *i*-Al-Pd-Mn evolves during growth.

Task 3 Our recent progress includes: 1) calculating the viscosity of ultrathin water films confined between oxide surfaces; 2) imaging (STM) 2-D ice islands on ice surfaces and interpreting their shapes in terms of surface-step energies that depend on proton order; 3) upgrading our existing UHV variable-temperature STM system to incorporate qPlus sensor AFM; 4) investigating the electronic structures of two rotational variants of epitaxial, single-layer graphene on Ir(111); 5) using spatially resolved measurements of electron reflectivity in LEEM to determine the work functions of six different rotational variants of graphene on Pd(111); 6) measuring an azimuthal effect on work function of graphene on Ir(111) by thermionic emission in LEEM; 7) developing methods to produce and characterize twisted bilayer graphene (TBG) with varying degrees of rotation between the sheets; 8) measuring the valence band structure of TBG and interpreting the results using first-principles calculations; and 9) determining that magnetite remains magnetic even at a film thickness of two unit cells.

Task 4 Our recent progress includes: 1) combining microelectrochemical cells with precision electrochemistry to map the early stages of pitting in aluminum; 2) using in-situ fluorescence microscopy to study the early stages of pit initiation on five individual pure Al thin film electrodes, each containing a single engineered Cu particle; 3) optimizing the growth of smooth, large-grained, (111) oriented, spinel LiMn<sub>2</sub>O<sub>4</sub> thin films and showing that surface layer formation depends upon the initial microstructure; 4) probing electrochemical alloying by passing 1.8 pA of current into and out of a 10 μm length of a 150 nm diameter Si nanowire immersed in a Li<sup>+</sup> based ionic liquid; and 5) combining oxidation-state-sensitive X-ray microscopy and morphological observations to quantify the local state-of-charge of 450 Li<sub>x</sub>FePO<sub>4</sub> particles over the entire electrode thickness.

### **Future Plans**

Task 1 Our future plans include adding studies of: 1) proton mobility in ice films; 2) intermixing at oxide-oxide interfaces; 3) the structure of complex metal oxides; and 4) intercalation of metal atoms under and between graphene sheets.

Task 2 We plan new studies of: 1) water films on metals and metal-oxides; 2) cooperative mechanisms of material growth, including those that cause graphene to grow by cluster addition; and 3) the stability of thin films, including the conversion of ice from amorphous to crystalline.

Task 3 Future work will explore how lattice mismatch or rotational misalignment affects the electronic properties of stacked 2-D crystals. The strong in-plane atomic bonding and weak interlayer interaction due to incommensurability offers opportunities to create novel electronic devices by tuning material properties.

Task 4 In future work we will build on our use of tailored surfaces and in-situ diagnostics to explain mechanisms governing materials properties in electrochemical environments. Our recent work on corrosion initiation, ion transport, and nanostructure formation has shown the importance of the evolution of interfacial structures at the electrode surface. Our goal is to understand the link between evolving nanostructure and the stability of the electrode surface in electrochemical environments under potential control.

### DOE Sponsored Publications 2010-2012

1. P. J. Feibelman, "The first wetting layer on a solid," *Physics Today* **63**, 34-39 (2010).
2. P. J. Feibelman, N. C. Bartelt, S. Nie and K. Thürmer, "Interpretation of high-resolution images of the best-bound wetting layers on Pt(111)," *Journal of Chemical Physics* **133**, 154703 (2010).
3. S. Nie, P. J. Feibelman, N. C. Bartelt and K. Thürmer, "Pentagons and Heptagons in the First Water Layer on Pt(111)," *Physical Review Letters* **105**, 026102 (2010).
4. T. Ohta, N. C. Bartelt, S. Nie, K. Thürmer and G. L. Kellogg, "Role of carbon surface diffusion on the growth of epitaxial graphene on SiC," *Phys Rev B* **81**, 121411 (2010).
5. J. M. Wofford, S. Nie, K. F. McCarty, N. C. Bartelt and O. D. Dubon, "Graphene islands on Cu foils: the interplay between shape, orientation and defects," *Nano Letters* **10**, 4890 (2010).
6. T. Herranz, K. F. McCarty, B. Santos, M. Monti and J. de la Figuera, "Real space observations of magnesium hydride formation and decomposition," *Chemistry of Materials* **22**, 1291 (2010).
7. B. Santos, J. M. Puerta, J. I. Cerda, T. Herranz, K. F. McCarty and J. de la Figuera, "Structure of ultrathin Pd films determined by low-energy electron microscopy and diffraction," *New Journal of Physics* **12**, 023023 (2010).
8. E. Starodub, N. C. Bartelt and K. F. McCarty, "Oxidation of graphene on metals," *Journal of Physical Chemistry C* **114**, 5134 (2010).
9. Y. Sato, B. Unal, T. A. Lograsso, P. A. Thiel, A. K. Schmid, T. Duden, N. C. Bartelt and K. F. McCarty, "Periodic step arrays on the aperiodic i-Al-Pd-Mn quasicrystal surface at high temperature," *Phys Rev B* **81**, 161406 (2010).
10. P. J. Feibelman, "DFT Versus the "Real World" (or, Waiting for Godft)," *Topics in Catalysis* **53**, 417-422 (2010).
11. Y. Murata, E. Starodub, B. B. Kappes, C. V. Ciobanu, N. C. Bartelt, K. F. McCarty and S. Kodambaka, "Orientation-dependent work function of graphene on Pd(111)," *App. Phys. Lett.* **97**, 143114 (2010).
12. J. Soltis, D. P. Krouse, N. J. Laycock and K. R. Zavadil, "Automated processing of electrochemical current noise in the time domain: I. Simulated signal," *Corros Sci* **52**, 838-847 (2010).
13. P. J. Feibelman, G. A. Kimmel, R. S. Smith, N. G. Petrik, T. Zubkov and B. D. Kay, "A unique vibrational signature of rotated water monolayers on Pt(111): Predicted and observed," *Journal of Chemical Physics* **134**, 204702 (2011).
14. E. Bussmann, I. Ermanoski, P. J. Feibelman, N. C. Bartelt and G. L. Kellogg, "Buried Pd slows self-diffusion on Cu(001)," *Phys Rev B* **84**, 245440 (2011).
15. S. Nie, J. M. Wofford, N. C. Bartelt, O. D. Dubon and K. F. McCarty, "Origin of the mosaicity in graphene grown on Cu(111)," *Phys Rev B* **84**, 155425 (2011).
16. T. Herranz, B. Santos, K. F. McCarty and J. de la Figuera, "Real-space study of the growth of magnesium on ruthenium," *Surface Science* **605**, 903-911 (2011).
17. S. Nie, A. L. Walter, N. C. Bartelt, E. Starodub, E. Bostwick, E. Rotenberg and K. F. McCarty, "Growth from Below: Graphene Bilayers on Ir(111)," *ACS Nano* **5**, 2298-2306 (2011).
18. I. Ermanoski, N. C. Bartelt and G. L. Kellogg, "Self-assembly of defect-free nanostripe arrays on B-doped Si(001)," *Phys Rev B* **83**, 205432 (2011).

19. E. Starodub, A. Bostwick, L. Moreschini, S. Nie, F. El Gabaly, K. F. McCarty and E. Rotenberg, "In-plane orientation effects on the electronic structure, stability, and Raman scattering of monolayer graphene on Ir(111)," *Phys. Rev. B* **83** (2011).
20. S. Nie, N. C. Bartelt and K. Thürmer, "Evolution of proton order during ice-film growth: An analysis of island shapes," *Phys Rev B* **84**, 035420 (2011).
21. A. Mascaraque, T. O. Mentès, K. F. McCarty, J. F. Marco, A. K. Schmid, A. Locatelli and J. de la Figuera, "Valence band circular dichroism in non-magnetic Ag/Ru(0001) at normal emission," *J. Phys.-Cond. Mat.* **23**, 305006 (2011).
22. A. L. Walter, S. Nie, A. Bostwick, K. S. Kim, L. Moreschini, Y. J. Chang, D. Innocenti, K. Horn, K. F. McCarty and E. Rotenberg, "Electronic structure of graphene on single-crystal copper substrates," *Phys Rev B* **84**, 195443 (2011).
23. D. A. Schmidt, T. Ohta and T. E. Beechem, "Strain and charge carrier coupling in epitaxial graphene," *Phys Rev B* **84**, 235422 (2011).
24. A. Seyeux, G. S. Frankel, N. Missert, K. A. Unocic, L. H. Klein, A. Galtayries and P. Marcus, "TOF-SIMS Imaging Study of the Early Stages of Corrosion in Al-Cu Thin Films," *Journal of the Electrochemical Society* **158**, C165-C171 (2011).
25. S. Maier, I. Stass, T. Mitsui, P. J. Feibelman, K. Thuermer and M. Salmeron, "Adsorbed water-molecule hexagons with unexpected rotations in islands on Ru(0001) and Pd(111)," *Phys Rev B* **85**, 155434 (2012).
26. S. Nie, N. C. Bartelt, J. M. Wofford, O. D. Dubon, K. F. McCarty and K. Thürmer, "Scanning tunneling microscopy study of graphene on Au(111): Growth mechanisms and substrate interactions," *Phys Rev B* **85**, 205406 (2012).
27. J. Knudsen, P. J. Feibelman, T. Gerber, E. Granas, K. Schulte, P. Stratmann, J. N. Andersen and T. Michely, "Clusters binding to the graphene moire on Ir(111): X-ray photoemission compared to density functional calculations," *Phys Rev B* **85** (2012).
28. S. Nie, W. Wu, S. Xing, Q. Yu, J. Bao, S. Pei and K. F. McCarty, "Growth from Below: Bilayer Graphene on Copper by Chemical Vapor Deposition," *New Journal of Physics* **14**, 093028 (2012).
29. N. C. Bartelt and K. F. McCarty, "Graphene growth on metal surfaces," *MRS Bulletin* **37**, 1158 - 1165 (2012).
30. C.-F. Lin, A. B. H. Hammouda, H.-C. Kan, N. C. Bartelt and R. J. Phaneuf, "Directing self-assembly of nanostructures kinetically: Patterning and the Ehrlich-Schwoebel barrier," *Phys Rev B* **85**, 085421 (2012).
31. J. I. Cerda, B. Santos, T. Herranz, J. M. Puerta, J. de la Figuera and K. F. McCarty, "CO-Assisted Subsurface Hydrogen Trapping in Pd(111) Films," *Journal of Physical Chemistry Letters* **3**, 87-91 (2012).
32. E. Starodub, N. C. Bartelt and K. F. McCarty, "Viable thermionic emission from graphene-covered metals," *Applied Physics Letters* **100** (2012).
33. T. Ohta, J. T. Robinson, P. J. Feibelman, A. Bostwick, E. Rotenberg and T. E. Beechem, "Evidence for Interlayer Coupling and Moire Periodic Potentials in Twisted Bilayer Graphene," *Physical Review Letters* **109** (2012).
34. T. Ohta, T. E. Beechem, J. T. Robinson and G. L. Kellogg, "Long-range atomic ordering and variable interlayer interactions in two overlapping graphene lattices with stacking misorientations," *Phys Rev B* **85**, 075415 (2012).
35. Y. Murata, S. Nie, A. Ebnoussir, E. Starodub, B. B. Kappes, K. F. McCarty, C. V. Ciobanu and S. Kodambaka, "Growth structure and work function of bilayer graphene on Pd(111)," *Phys Rev B* **85**, 181604 (2012).
36. B. Santos, S. Gallego, A. Mascaraque, K. F. McCarty, A. Quesada, A. T. N'Diaye, A. K. Schmid and J. de la Figuera, "Hydrogen-induced reversible spin-reorientation transition and magnetic stripe domain phase in bilayer Co on Ru(0001)," *Phys Rev B* **85**, 134409 (2012).
37. M. Monti, B. Santos, A. Mascaraque, O. Rodriguez de la Fuente, M. Angel Nino, T. O. Mentès, A. Locatelli, K. F. McCarty, J. F. Marco and J. de la Figuera, "Magnetism in nanometer-thick magnetite," *Phys Rev B* **85**, 020404 (2012).
38. N. Missert, R. G. Copeland, C. M. Johnson and J. C. Barbour, "Current Measurements from Multiple Pitting Sites in Engineered Aluminum Electrodes," *Journal of the Electrochemical Society* **159**, C259-C264 (2012).
39. N. Murer, N. A. Missert and R. G. Buchheit, "Finite Element Modeling of the Galvanic Corrosion of Aluminum at Engineered Copper Particles," *Journal of the Electrochemical Society* **159**, C265-C276 (2012).
40. K. R. Zavadil, "Correlating pit initiation in aluminum with passive oxide defect structure," *ECS Transactions* **41**, 133 (2012).
41. J. T. Robinson, W. Schmucker, C. B. Diaconescu, J. P. Long, J. C. Culbertson, T. Ohta, A. L. Friedman and T. E. Beechem, "Electronic Hybridization of Large-Area Stacked Graphene Films," *ACS Nano* **7**, 637 (2013).
42. W. C. Chueh, F. E. Gabaly, J. D. Sugar, N. C. Bartelt, K. R. Fenton, K. R. Zavadil, T. Tyliszczak, W. Lai and K. F. McCarty, "Intercalation Pathway in Many-Particle LiFePO<sub>4</sub> Electrode Revealed by Nanoscale State-of-Charge Mapping," *Nano Lett.*, available online: <http://pubs.acs.org/doi/full/10.1021/nl3031899> (2012).

## Make VO<sub>2</sub> work: micro solid engine and nano powermeter

PI: Junqiao Wu

University of California, Berkeley, and Lawrence Berkeley National Laboratory

Email: [wuj@berkeley.edu](mailto:wuj@berkeley.edu)

BES / Physical Behavior of Materials Program

Collaborators: R. Ramesh, D. C. Chrzan, C. P. Grigoropoulos, A. Minor, K. M. Yu

### Recent Progress

In the past several years, we have pioneered the investigation of domain [1] and size effects [2] on the metal (M) - insulator (I) phase transition (MIT) of vanadium dioxide (VO<sub>2</sub>) and related materials. Strain-free VO<sub>2</sub> undergoes the first-order MIT at ~ 67°C with a drastic change in conductivity and optical reflection, accompanied with a structural transition that involves a large (1~2%) spontaneous strain.

Recently we have demonstrated that the MIT of VO<sub>2</sub> can be engineered to offer: (1) high-amplitude, high-speed and energy-efficient micro actuation [3]. Based on this, we propose a phase-transition driven microscale solid engine ( $\mu$ SE) that would be complementary to or replacing existing micro-actuation technologies [4]; and (2) quantitative test of nanoscale light absorption [5]. We hence develop a nanoscale powermeter that would allow easy characterization of absorption and transport of heat and light in individual nanostructures [6].

The  $\mu$ SE exploits the high phase transition strain in VO<sub>2</sub>, in analogy to the steam engine invoking large volume expansion in a liquid-vapor phase transition. Figure 1 shows the property

and operation of VO<sub>2</sub>-based  $\mu$ SE. It can be seen that the MIT of VO<sub>2</sub> provides a work density up to 7 J/cm<sup>3</sup>, superior to most other actuation materials (This number is surpassed only by some special shape memory alloys, but the latter are limited by poor micro-scale processability). These other actuation mechanisms typically offer either large-amplitude or high-force actuation, but not both. The high work density in VO<sub>2</sub> enables micro-actuation with simultaneously high amplitude, high force, and at high speed (> 4 kHz) [3]. The energy efficiency of the devices is calculated to be equivalent to thermoelectrics with figure of merit  $ZT = 2$  at the working temperatures [4], and much higher than other bimorph actuators. The bimorph  $\mu$ SE can be easily scaled down to the nanoscale, and operates with high

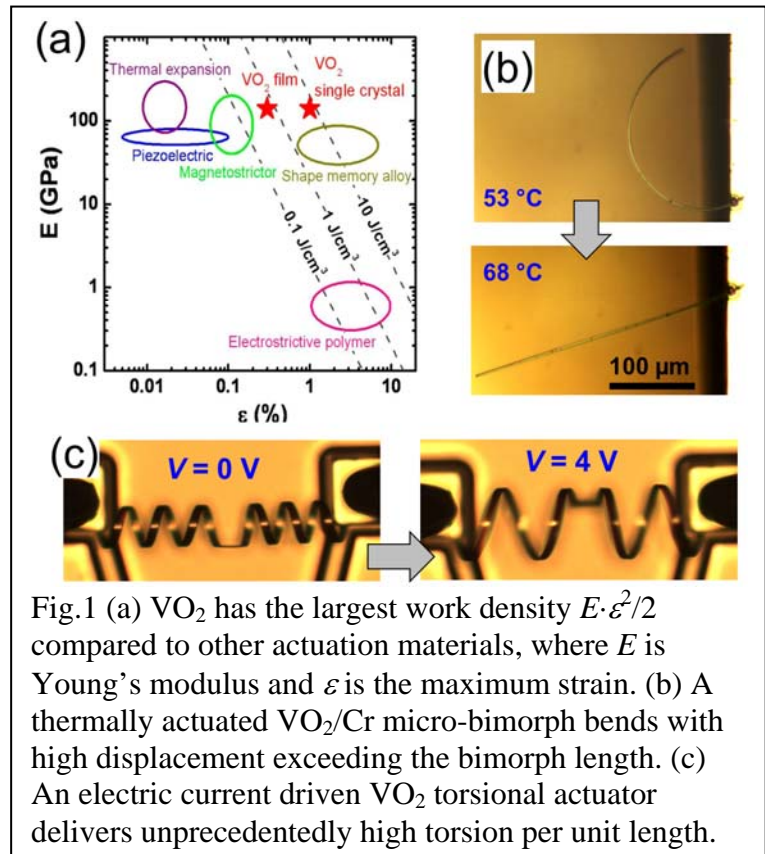


Fig.1 (a) VO<sub>2</sub> has the largest work density  $E \cdot \epsilon^2/2$  compared to other actuation materials, where  $E$  is Young's modulus and  $\epsilon$  is the maximum strain. (b) A thermally actuated VO<sub>2</sub>/Cr micro-bimorph bends with high displacement exceeding the bimorph length. (c) An electric current driven VO<sub>2</sub> torsional actuator delivers unprecedentedly high torsion per unit length.

stability in near-room-temperature, ambient or aqueous conditions. Based on the  $\mu$ SE, we demonstrate a macroscopic smart composite of  $\text{VO}_2$  bimorphs embedded in a polymer that produces high-amplitude actuation at and above the millimeter scale [4]. Combining the superior performance, high durability, diversity in responsive stimuli, versatile working environments, and microscale manufacturability, these actuators offer potential applications in microelectromechanical systems, microfluidics, robotics, drug delivery, and artificial muscles.

The second project seeks to quantify the efficiency of light capture and heat transfer in individual nanostructures. These processes play a key role in nanomaterials-based energy conversion devices such as solar cells, thermoelectric modules and antennas. However, it has been extremely challenging to quantify because of the length scales involved are comparable to or below the light wavelength or acoustic phonon mean free path. For example, it is known that a nanowire could absorb and trap light more efficiently than a smooth thin film, a desired effect for photovoltaics, but a direct measurement of light absorption by a single nanowire has been lacking; It is known that heat transfer would be hindered along channels with width smaller than phonon mean free path, a desired property for thermoelectrics, but size effect of thermal conductivity has been elusive. To address these problems, we develop a near-field, nanoscale powermeter based on the MIT in  $\text{VO}_2$  nanowires. The M and I phases can be clearly resolved with a simple optical microscope.

Therefore, an individual  $\text{VO}_2$  nanowire (Fig.2b) acts as an optically readable, nanoscale thermometer. When a cantilevered  $\text{VO}_2$  nanowire is bonded to another nanowire (e.g., a Si nanowire as in Fig.2), the optical energy absorbed by the single Si nanowire can be calculated from the M/I domain wall position along the  $\text{VO}_2$  nanowire. Shown in Fig.2 are the light absorbance of a single Si nanowire as a function of its radius (c) and engineered surface roughness (d). It can be seen that when the surface roughness is below the light wavelength, the nanowire absorbance is significantly enhanced due to near-field optical effects. The optical absorbance of single semiconductor nanowires is quantified for the first time.

### Future Plans

Based on these achievements, we plan to investigate the

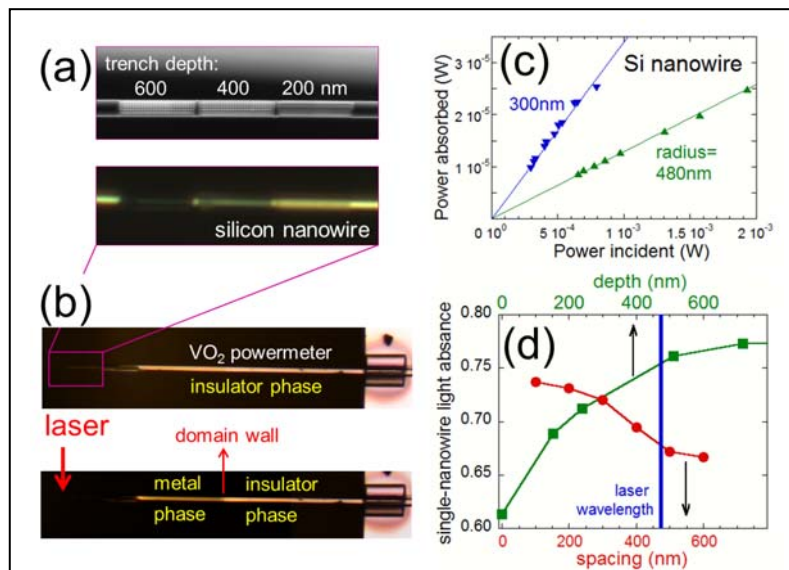


Fig.2 (a) Surface of a Si nanowire engraved with trenches to achieve different sub-wavelength roughness. Upper is SEM image, and bottom is optical image. Different surface roughness yields different light reflection coefficient. (b) The Si nanowire bonded to a  $\text{VO}_2$  nanowire as a nanoscale powermeter. Laser power absorbed by the Si nanowire can be quantified by measuring the M/I domain wall position along the  $\text{VO}_2$  nanowire. (c) Measured light power absorbed by smooth Si nanowire as a function of incident laser power. (d) Light absorbance of a single Si nanowire as a function of spacing and depth of the engraved trenches on the surface.

following topics.

#### (1) Mechanical Memdevices

Recent development and understanding of memristors [7] have opened a completely new approach to information processing: neuromorphic computing [8]. These memristors can be fabricated with MIT in transition metal oxides [9] including VO<sub>2</sub>. However, mechanically active memdevices are needed for implementation of the still-missing circuit elements of meminductors and memcapacitors [10], as well as integrating the memristors with microelectromechanical systems. The first-order MIT in VO<sub>2</sub> offers a natural mechanism for memory devices, and the demonstrated VO<sub>2</sub>-based  $\mu$ SE adds a new dimension of mechanical activity to the memory functionality. We will design and fabricate, for the first time, two-terminal meminductors and memcapacitors using VO<sub>2</sub>, and ultimately design and assemble new circuits with these memdevices.

#### (2) Near-field energy transfer

We will explore, on the individual nanostructure level, the effect of plasmonic enhancement in semiconductor light absorption. Plasmonic excitation at the interface between a metal and a semiconductor can be used to boost light absorption in photovoltaics and optoelectronics [11]. However, the near-field length scale and geometrical complication hamper direct characterization of these effects. Our VO<sub>2</sub>-based nano powermeter would be an ideal tool to probe the fundamental plasmonic interactions between metal and semiconductor nanostructures.

In addition to light absorption, other physical properties of single nanostructures can also be quantified using this VO<sub>2</sub> nano powermeter, such as thermal conductivity, heat capacity and thermal diffusivity. For example, the thermal conductivity of the Si nanowire in Fig.2(b) can be calculated from the absorbed laser power. This not only presents a platform to measure thermal conductivity of individual nanowires in a much simpler [12] or more accurate [13] way than existing methods, but also allows in situ measurements of nanowire thermal properties in response to stress or bending. As preliminary data, we recently found that the thermal conductivity of a single Si nanowire remains unchanged if it is bent within elastic deformation, but rapidly decreases when the bending angle exceeds the elastic limit such that dislocations are generated [6].

In summary, by exploiting the MIT of VO<sub>2</sub>, we seek to develop novel, nano-micro scale tools and devices to achieve unprecedented functionalities or capabilities for various energy technologies.

## References

(highlighted in **bold** are our related publications of DOE sponsored research in 2010-2012):

- [1] J. Cao, E. Ertekin, V. Srinivasan, W. Fan, S. Huang, H. Zheng, J. W. L. Yim, D. R. Khanal, D. F. Ogletree, J. C. Grossman and J. Wu, Strain engineering and one-dimensional organization of metal-insulator domains in single-crystal VO<sub>2</sub> beams, *Nature Nanotech.* **4**, 732-737 (2009).
- [2] **Z. Tao, T. T. Han, S. D. Mahanti, P. M. Duxbury, F. Yuan, C. Y. Ruan, K. Wang and J. Wu, Decoupling of structural and electronic phase transitions in VO<sub>2</sub>, *Phys. Rev. Lett.* **109**, 166406 (2012).**

- [3] K. Liu, C. Cheng, Z. Cheng, K. Wang, R. Ramesh and J. Wu, **Giant-Amplitude, High-Work Density Microactuators with Phase Transition Activated Nanolayer Bimorphs**, *Nano Lett.* **12**, 6302 (2012).
- [4] K. Wang, C. Cheng, E. Cardona, J. Guan, K. Liu and J. Wu, **Performance limits of micro-actuation with vanadium dioxide as a solid engine**, *ACS Nano*, in press (2013).
- [5] C. Cheng, W. Fan, J. Cao, C. P. Grigoropoulos and J. Wu, **Heat Transfer across the Interface between Nanoscale Solids and Gas**, *ACS Nano* **5**, 10102 (2011).
- [6] C. Cheng and J. Wu, Phase transition-based nano powermeter, In preparation. (2012).
- [7] D. B. Strukov, G. S., D. R. Stewart and R. S. Williams, **The missing memristor found**, *Nature* **453**, 80 (2008).
- [8] S. Afshar, O. Kavehei, A. van Schaik, J. Tapson, S. Skafidas and T. J. Hamilton, **Emergence of Competitive Control in a Memristor-Based Neuromorphic Circuit**, *IEEE WCCI* (2012).
- [9] M. D. Pickett and R. S. Williams, **Sub-100 fJ and sub-nanosecond thermally driven threshold switching in niobium oxide crosspoint nanodevices**, *Nanotech.* **23**, 215202 (2012).
- [10] M. D. Ventra, Y. V. Pershin and L. O. Chua, **Circuit Elements with Memory: Memristors, Memcapacitors, and Meminductors**, *Proc. IEEE* **97**, 1717 (2009).
- [11] V. E. Ferry, J. N. Munday and H. A. Atwater, **Design Considerations for Plasmonic Photovoltaics**, *Adv. Mater.* **22**, 4794 (2010).
- [12] P. Kim, L. Shi, A. Majumdar and P. McEuen, **Thermal Transport Measurements of Individual Multiwalled Nanotubes**, *Phys. Rev. Lett.* **87**, 215502 (2001).
- [13] G. S. Doerk, C. Carraro and R. Maboudian, **Single Nanowire Thermal Conductivity Measurements by Raman Thermography**, *ACS Nano* **4**, 4908 (2010).

## **In-situ scanning probe studies of interface evolution on model $\text{LiMn}_2\text{O}_4$ cathodes for Li ion batteries**

Nancy Missert, Jeyavel Velmurugan, and Robert Garcia  
Sandia National Laboratories, Albuquerque, NM 87185-1415  
[namisse@sandia.gov](mailto:namisse@sandia.gov)

Nanometer Scale Surface and Interface Phenomena: Nanoscale Electrochemistry

**Program Scope:** The primary focus of this program is to develop a quantitative understanding of the mechanisms of localized corrosion initiation in passive metals and to quantify the critical parameters governing ion transport and nanostructure formation in model systems for energy storage applications. Our approach is based on the novel and unique application of nanofabrication techniques to produce tailored surfaces and to simulate specific defect types on controlled substrates in well-defined locations. We shed light on corrosion, ion transport, and nanostructure-formation mechanisms using in-situ and advanced electrochemical, morphological, chemical and structural analytical tools. We have identified three critical areas where further, detailed knowledge is needed: 1) the chemical/structural description of the nano-scale site responsible for pit initiation, 2) the role of microstructure in pit initiation and stabilization 3) the role of surface properties in ion transport and electrochemically controlled nanostructure formation. The evolution of the passive oxide up to the point of pit initiation is under investigation using microscale electrochemical characterization combined with analytical electron microscopy. The role of microstructure during the early stages of pitting is studied using in-situ fluorescence microscopy, modeling, and mapping of surface oxide electronic properties and composition. Ion transport and nanostructure formation on model systems in electrochemical environments is being examined using in-situ and ex-situ scanning probes and transmission electron microscopy. Our future work will employ the novel in-situ techniques we've developed in this program to identify interfacial structure responsible for nucleation of electrochemical reactions on ideal, controlled materials relevant for understanding corrosion initiation and surface phenomena in energy storage materials.

**Recent Progress:** Optimization of energy storage technologies is a critical goal for the DOE. For transportation applications, Li ion batteries are one of the most promising solutions. Although this technology has advanced significantly in recent years, further improvements in cost, performance, cycling life, calendar life, and safety must all be addressed. Due to the complexity of typical multi-component batteries and battery electrodes, gaining fundamental understanding of the nanoscale processes governing ion transport and surface reactions has been extremely challenging. We have used ideal electrodes and high-resolution scanning probes to investigate the evolution of interfacial layers inhibiting Li ion transport. These studies advance our understanding of the factors governing the performance and lifetime of materials for Li ion batteries. Our results will provide the essential guidance needed for optimization of materials, interfacial structure and properties in order to produce reliable solutions for future energy storage needs.

Li-Mn-based oxide materials look very promising in terms of cost and safety for the next-

generation of batteries for electric vehicles. However, their performance, cycling life and calendar life all appear to be limited by the growth of a interfacial layer that forms during cycling due to electrolyte oxidation and reaction with the surface at high potentials [1-22]. The interfacial layer on cathode materials has proven much more challenging to study than the solid electrolyte interface (SEI) on the graphite anode, because it is thought to be a few nanometers thick and often does not passivate the surface, but continues to evolve with cycling. In addition, the complex composite nature of the typical cathode electrode (active material powder plus conductive carbon and binder) makes it very difficult to distinguish the properties of the interfacial layer and identify the reaction mechanisms.

The spinel  $\text{LiMn}_2\text{O}_4$  is an ideal system for these studies, where surface layer formation is known to inhibit charge transport, leading to an increase in cell impedance, while consumption of the active material leads to a loss in cell capacity. We have optimized growth of smooth, large-grained, (111) oriented, spinel  $\text{LiMn}_2\text{O}_4$  thin films containing a variety of nanostructural features including terraces, step-edges, and exposed facets using pulsed laser deposition (PLD) as shown in Figure 1a. Our laboratory has established the capability to perform EC-AFM measurements in an Ar glovebox with a sealed electrochemical cell using a Bruker Multimode microscope. Our initial measurements (in EC:DMC: $\text{LiPF}_6$  electrolytes) on these films show clear formation of nanoscale reaction products that result from potential cycling, mostly concentrated near faceted grains as seen in Figure 1b. We find that surface layer formation depends upon the initial microstructure, where (111) planes are the most stable, while off-(111) axis facets are the most reactive, Figure 1c. These results indicate that the initial surface morphology is critical in formation of the interfacial layer, where reactions with the electrolyte occur at preferential sites. Future work will expand on these findings.

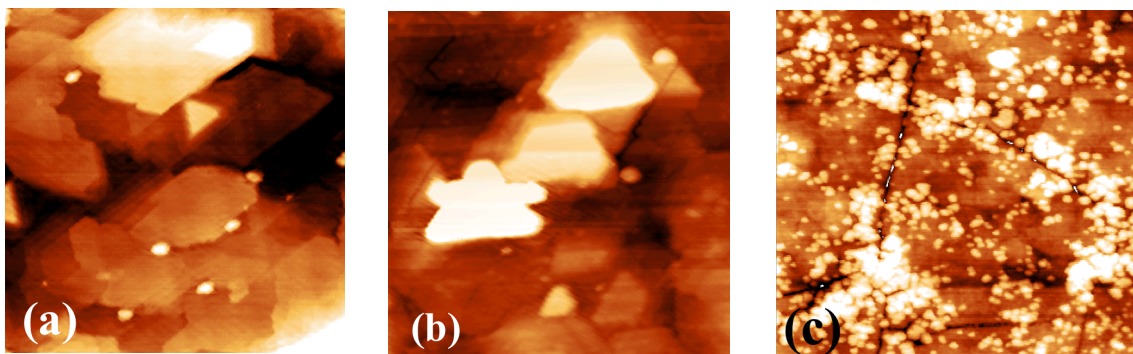


Figure 1. 500 x 500 nm AFM images of (a) (111) oriented  $\text{LiMn}_2\text{O}_4$  showing (111) terraces (b) appearance of surface reaction products following potential cycling adjacent to high-faceted grains (c) film with high off-(111) facet density following potential cycling showing surface covered with reaction products.

**Future plans:** In future work we will build on our use of tailored surfaces and in-situ diagnostics to explain mechanisms governing materials properties in electrochemical environments. Our goal is to understand the link between evolving nanostructure and the stability of the electrode surface in electrochemical environments under potential control. Our previous EC-AFM studies of interfacial evolution on ideal spinel  $\text{LiMn}_2\text{O}_4$  electrodes showed that the microstructure at the electrode surface has an enormous impact on interfacial layer formation. Further studies are needed in order to determine where these reactions initiate, how they evolve with cycling parameters, and how they depend upon the structure of the electrode surface and the components in the electrolyte. We propose to extend our initial work described above to the high voltage cathode spinel  $\text{LiNi}_{0.5}\text{Mn}_{1.5}\text{O}_4$  (LNMS) due to its higher energy density and reasonable cycling capability [23-30]. So far, it is not known how the presence of Ni influences these surface reactions. Furthermore, the increase in operating voltage from 4.0 V for the Mn spinel to 4.7 V for the Ni/Mn spinel further complicates the surface reactions due to electrolyte oxidation at the higher potentials [31]. We will use our PLD capability to grow high quality thin films of LNMS as ideal electrodes for interfacial evolution studies. EC-AFM will obtain three-dimensional images of surface reaction products on ideal cathode surfaces where precisely defined crystallographic features have been created. The nanometer scale resolution, combined with electrochemical control of charge transport, will allow us to determine, for the first time, the answers to the following questions: (1) How does surface nanostructure (crystal orientation, exposed facets, terraces and step edges) influence surface reactions; (2) How do these reactions initiate and evolve with cycling (state of charge, charge/discharge rate); (3) How do promising electrolyte additives and electrode coatings alter or inhibit surface film formation. Reaction product constituents will be identified with ex-situ XPS and TEM measurements. Obtaining such a detailed understanding of surface layer formation and evolution should provide clear guidance for future optimization of cathode surface properties, electrolyte additives, and coatings that ensure facile charge transport, leading to the enhanced reliability needed for transportation applications.

#### References

- [1] F. Simmen, A. Foelske-Schmitz, P. Verma, M. Horisberger, T. Lippert, P. Novak, C. W. Schneider and A. Wokaun, *Electrochimica Acta* **56**, 8539-8544 (2011).
- [2] D. Aurbach, *J. Power Sources* **89**, 206-218 (2000).
- [3] D. Aurbach, K. Gamolsky, B. Markovsky, G. Salitra, Y. Gofer, U. Heider, R. Oesten and M. Schmidt, *J. Electrochem. Soc.*, **147**, 1322-1331 (2000).
- [4] D. Ostrovskii, F. Ronci, B. Scrosati and P. Jacobsson, *J. Power Sources* **103**, 10-17 (2001).
- [5] C. Wu, Y. Bai and F. Wu, *J. Power Sources* **189**, 89-94 (2009).
- [6] J. L. Lei, L. J. Li, R. Kosteki, R. Muller and F. McLarnon, *J. Electrochem. Soc.* **152**, A774-A777 (2005).
- [7] S. S. Zhang, T. R. Jow, K. Amine and G. L. Henriksen, *J. Power Sources* **107**, 18-23 (2002).
- [8] T. Eriksson, A. M. Andersson, C. Gejke, T. Gustafsson and J. O. Thomas, *Langmuir* **18**, 3609-3619 (2002).

- [9] J. Vetter, P. Novak, M. R. Wagner, C. Veit, K. C. Moller, J. O. Besenhard, M. Winter, M. Wohlfahrt-Mehrens, C. Vogler and A. Hammouche, *J. Power Sources* **147**, 269-281 (2005).
- [10] K. Edstrom, T. Gustafsson and J. O. Thomas, *Electrochim. Acta* **50**, 397-403 (2004).
- [11] J. M. Tarascon and M. Armand, *Nature* **414**, 359-367 (2001).
- [12] T. Eriksson, A. M. Andersson, A. G. Bishop, C. Gejke, T. Gustafsson and J. O. Thomas, *J. Electrochem. Soc.*, **149**, A69-A78 (2002).
- [13] G. Amatucci and J. M. Tarascon, *J. Electrochem. Soc.*, **149**, K31-K46 (2002).
- [14] K. Sato, D. M. Poojary, A. Clearfield, M. Kohno and Y. Inoue, *J. Solid State Chemistry* **131**, 84-93 (1997).
- [15] R. Chromik and F. Beck, *Electrochimica Acta* **45**, 2175-2185 (2000).
- [16] D. H. Jang and S. M. Oh, *Electrochimica Acta* **43**, 1023-1029 (1998).
- [17] Du Pasquier, A. Blyr, P. Courjal, D. Larcher, G. Amatucci, B. Gerand and J. M. Tarascon, *J. Electrochem. Soc.*, **146**, 428-436 (1999).
- [18] D. H. Jang, Y. J. Shin and S. M. Oh, *J. Electrochem. Soc.*, **143**, 2204-2211 (1996).
- [19] D. H. Jang and S. M. Oh, *J. Electrochem. Soc.*, **144**, 3342-3348 (1997).
- [20] A. Blyr, A. Du Pasquier, G. Amatucci and J. M. Tarascon, *Ionics* **3**, 321-331 (1997).
- [21] S. J. Wen, T. J. Richardson, L. Ma, K. A. Striebel, P. N. Ross and E. J. Cairns, *J. Electrochem. Soc.*, **143**, L136-L138 (1996).
- [22] D. Aurbach, B. Markovsky, Y. Talyossef, G. Salitra, H. J. Kim and S. Choi, *J. Power Sources* **162**, 780-789 (2006).
- [23] K. Amine, H. Tukamoto, H. Yasuda and Y. Fujita, *J. Electrochem. Soc.*, **143**, 1607-1613 (1996).
- [24] B. Markovsky, Y. Talyossef, G. Salitra, D. Aurbach, H. J. Kim and S. Choi, *Electrochem. Comm.* **6**, 821-826 (2004).
- [25] H. Xia, Y. S. Meng, L. Lu and G. Ceder, *J. Electrochem. Soc.* **154**, A737-A743 (2007).
- [26] P. G. Bruce, B. Scrosati and J. M. Tarascon, *Angewandte Chemie-International Edition* **47**, 2930-2946 (2008).
- [27] R. Santhanam and B. Rambabu, *J. Power Sources* **195**, 5442-5451 (2010).
- [28] K. Ariyoshi, Y. Maeda, T. Kawai and T. Ohzuku, *J. Electrochem. Soc.* **158**, A281-A284 (2011).
- [29] T. F. Yi, Y. Xie, M. F. Ye, L. J. Jiang, R. S. Zhu and Y. R. Zhu, *Ionics* **17**, 383-389 (2011).
- [30] F. Zhou, X. M. Zhao, A. van Bommel, X. Xia and J. R. Dahn, *J. Electrochem. Soc.*, **158**, A187-A191 (2011).
- [31] K. Xu, *Chem. Rev.*, **104**, 4303-4417 (2004).

**Spatially resolved ionic diffusion and electrochemical reactions in solids -  
a biased view at lithium ion batteries  
(ERKCZ12)**

Nina Balke (PI)  
Oak Ridge National Laboratory  
1 Bethel Valley Road  
P.O. Box 2008, MS-6487  
Oak Ridge, TN 37831-6487  
Email: balken@ornl.gov

**Scope**

The functionality of energy storage systems, such as Li-ion batteries, is based on and ultimately limited by the rate and localization of ion flows through the device on different length scales ranging from atoms over grains to interfaces. The fundamental gap in understanding ionic transport processes on these length scales strongly hinders the improvement of current and development of future battery technologies. The goal of this proposal is to create, through nanometer-resolution imaging of ionic flows, fundamental understanding of the local mechanisms which define a rechargeable battery. Using Electrochemical Strain Microscopy, which utilizes the intrinsic link between unit cell volume and Li-ion concentration, it is possible to separate and characterize transport processes in the electrodes and across electrode/electrolyte interfaces, allowing us to decipher the single stages of ionic transport through the battery. With this knowledge it will be possible to identify and overcome the bottlenecks which lead to predominant limitations in present battery technology such as low energy storage density or capacity loss during cycling.

**Recent Progress**

Electrochemical Strain Microscopy (ESM) is a unique technical development to study ionic transport on the nanoscale through strain. This has been demonstrated to work for single battery elements, such as cathode or anode, and for all-solid batteries. The recent progress can be separated in four main research lines: 1) Role of measurement environment on the ESM signal, 2) correlation of ionic transport and microstructure, 3) extraction of quantitative parameters describing the ionic transport, and 4) connecting information from the nanoscale with the macroscale.

*1) Role of measurement environment on the ESM signal*

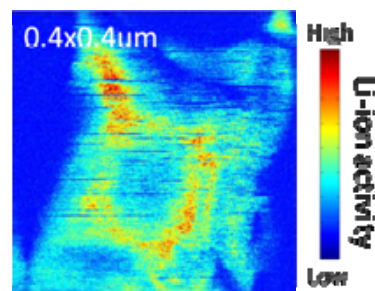
In order to understand and correctly interpret the ESM signal we need to understand the signal generating mechanism and the influence of the measurement environment. ESM was established to measure ionic transport in Li-ion electrode materials in a non-liquid environment. If the measurements are performed in air, the humidity of the air can significantly influence the locally applied fields due to thin water layers on the surface. The strength of this effect was investigated by performing a variety of ESM experiments in air and under Ar in a glove box. It was found that measurements in air allowed Li-ions to be extracted from the electrode due to the water surface layers which act as electrolytes. This strongly decreases the ESM signal when compared to measurements in the glove box. We also extended this study to identify the role of

mechanical and electrical tip properties used to probe the local ionic transport in electrode materials. In the future, these results will provide guidance on ESM signal interpretation.

### 2) Correlation of ionic transport and microstructure

The microstructure of a thin film electrode can actively influence the ionic transport. The understanding of this function-structure relationship is essential to design battery electrodes with improved electrochemical performance. Here, Vector-ESM was performed on  $\text{LiCoO}_2$  thin films with grains of different orientation to separate ionic transport parallel and perpendicular to the sample surface. By comparing the results from the Vector-ESM image with analytical modeling, the crystallographic orientation of each grain can be estimated based on the strong transport anisotropy in  $\text{LiCoO}_2$ . Not only the grain orientation, also the grain morphology can play a significant role in ionic transport. The layered structure of  $\text{LiCoO}_2$  results in a surface morphology which exhibits a lot of step edges. Spatially resolved ESM measurements showed an enhanced ionic transport along the step edges (Fig. 1) which can be explained by lateral transport induced by the biased tip. The correlation between surface morphology and ionic transport will be very valuable in the future to optimize battery electrode materials.

**Figure 1:** ESM map for a  $400 \times 400 \text{ nm}^2$  area across step edges in  $\text{LiCoO}_2$  thin films.



### 3) Extraction of quantitative parameters describing the ionic transport

Typical parameters to describe the ionic transport are the activation energy and diffusivity. The goal was to design ESM-based experiments to extract or estimate these parameters on a local scale. Therefore, temperature dependent ESM has been performed. Here, the sample was placed on a heated sample stage and was heated and equilibrated before each ESM measurement. At higher temperatures the ions are more mobile and the ESM signal increases. On an Arrhenius-type plot, the data for each pixel followed a linear relationship, which was linearly fitted to extract the activation energy for each pixel. The resulting map is shown in Fig. 2 overlaid with the sample topography. Interestingly, the average activation energy is around 0.3 eV and seems to be independent of the absolute ESM value. This activation energy agrees very well with macroscopic measurements and theoretical calculations of around 0.3 eV for  $\text{LiCoO}_2$  with high Li content.

The local diffusivity is estimated through time spectroscopy ESM. Here, a short voltage pulse is applied to the ESM tip which induces a strong concentration gradient in the probed volume. Once the voltage is turned off, the Li-ions diffuse back which can be tracked by

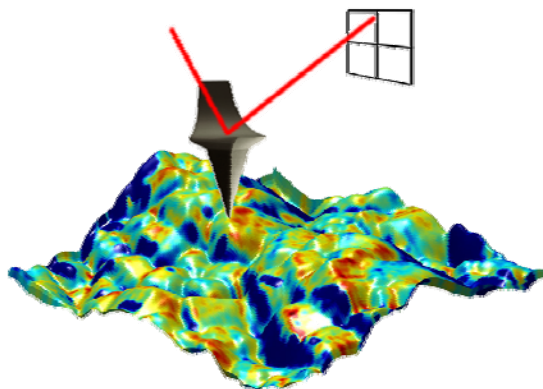


**Figure 2:** Activation energy map from temperature-dependent ESM images after application of a Gaussian filter to reduce pixel noise overlaid with the sample topography. The scan size was  $3 \times 3 \mu\text{m}^2$ .

measuring ESM as function of time. The relaxation curves can be fitted with a simple exponential decay and the extracted relaxation time can be used to estimate the diffusivity. ESM time spectroscopy was performed on a spatially resolved map and strong variations in separate grains were observed. The average relaxation time in the investigated area can be used to estimate an average diffusivity. Here we assume that the length scale  $L$  over which Li-ions diffuse during the experiment is in the order of the tip radius, which is typically a good assumption for SPM-type experiments and is around 30 nm.  $D$  can be estimated to  $4 \times 10^{-14}$   $\text{m}^2/\text{s}$  (Fig. 3). This value fits well within the reported range of diffusivities for  $\text{LiCoO}_2$  samples from  $10^{-14}$  to  $10^{-12}$   $\text{m}^2/\text{s}$ .

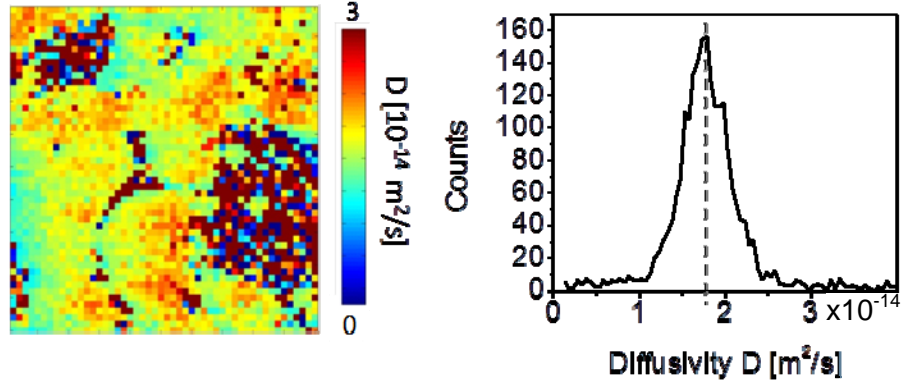


**Figure 3:** Map and histogram of the estimated diffusivity extracted from time dependent ESM measurements for a  $1 \times 1 \mu\text{m}^2$  area in  $\text{LiCoO}_2$  thin films.

#### 4) Connecting information from the nanoscale with the macroscale

The key to the future success of ESM is the connection of the nanoscale information gained by ESM and the macroscopic material parameters and performance. The idea is to identify nanoscale fingerprints of a good battery electrode which can then be used to screen newly developed materials. For that, two important directions are established:

1) Correlation of local ESM signal with macroscopic battery performance. Here,  $\text{LiCoO}_2$  thin films with a different ion distribution were investigated. The as-grown  $\text{LiCoO}_2$  thin films exhibit randomly distributed Li and Co atoms ( $\gamma\text{-LiCoO}_2$ ) and the electrochemical performance is poor. After annealing,  $\alpha\text{-LiCoO}_2$  is formed with good electrochemical performance. The ESM experiments performed on these two different materials show some similarities and differences which need to be interpreted.

2) The ESM signal contains information about both, ionic mobility and concentration. It is known from macroscopic measurements, that during charge and discharge the ionic concentration in the electrode changes which results in a strong change in the diffusivity. To explore the correlation between this macroscopic change and the development of the ESM signal, ESM of  $\text{LiCoO}_2$  thin films of different charging state were studied. This was done by performing ex-situ experiments after charging in an electrochemical cell inside the AFM. The ESM signal shows the trend of higher signal strength for sample with lower ion concentration, as expected from macroscopic measurements.

#### Future Plans

So far, ESM experiments focused strongly on well known  $\text{LiCoO}_2$  electrode materials. In the future, ESM will be tested for a variety of electrode materials including spinel and phase change materials to compare them to layered Li-ion intercalation materials. Preliminary studies have shown that other electrode material exhibit different strain mechanism which are not always

connected to Li-ion motion. We will study these new mechanisms and identify materials suitable for ESM studies.

The second focus will be the implementation of in situ ESM. Here the ESM measurements will be performed in liquid environment and, therefore, can be performed during charge and discharge. This will allow studying the interfacial transport and the formation of SEI layer. However, the transition of air to liquid is non-trivial and further technique development will be necessary. However, first experiments of electromechanical characterization of ferroelectrics in highly conductive liquids were successful and open the pathway to study ESM in liquid for battery materials.

### **Publications (July 2011-2012)**

1. N. Balke, A. Tselev, T. A. Arruda, S. Jesse, Y.-H. Chu, and S. V. Kalinin, "Probing Local Electromechanical Effects in Highly Conductive Electrolytes", **ACS Nano** DOI: 10.1021/nn3038868 (2012).
2. S. V. Kalinin, Y. Kim, A. Kumar, e. Strelcov, N. Balke, T. M. Arruda, S. Jesse, D. Leonard, and A. Borisevich, "Electrochemical strain microscopy: probing electrochemical transformations in nanoscale volumes", **Miroscopy Today** 20, 10-15 (2012).
3. N. Balke, E. A. Eliseev, S. Jesse, S. Kalnaus, C. Daniel, N. J. Dudney, A. N. Morozovska, and S. V. Kalinin, "Three-dimensional Vector Electrochemical Strain Microscopy", **J. Appl. Phys.** 112, 052020 (2012).
4. N. Balke, D. Bonnell, D. S. Ginger, M. Kemerink, "Scanning probes for new energy materials: Probing local structure and function", **MRS Bulletin** 37, 633-637 (2012).
5. N. Balke, S. Kalnaus, N. J. Dudney, C. Daniel, S. Jesse, and S. V. Kalinin, "Local detection of activation energy for ionic transport in lithium cobalt oxide", **Nano Lett.** 12, 3399-3403 (2012).
6. N. Balke, S. Jesse, Y.-H. Chu, S. V. Kalinin, "High frequency electromechanical imaging of ferroelectrics in a liquid environment", **ACS Nano** 6, 5559-5565 (2012).
7. S. V. Kalinin, A. Kumar, N. Balke, M. McCorkle, S. L. Guo, T. Arruda, and S. Jesse, "ESM of ionic and electrochemical phenomena on the nanoscale", **Adv. Mater. Processes** 169, 30-34 (2011).
8. S. Jesse, N. Balke, E. Eliseev, A. Tselev, N. J. Dudney, A. N. Morozovska, "Direct Mapping of Ionic Transport in a Si Anode on the Nanoscale: Time Domain Electrochemical Strain Spectroscopy Study", **ACS Nano** 5, 9682-9695 (2011).
9. S. V. Kalinin, N. Balke, S. Jesse, A. Tselev, A. Kumar, T. M. Arruda, S. Guo, and R. Proksch, "Li-ion dynamics and reactivity on the nanoscale", **Materials Today** 14, 548-558 (2011).
10. S. V. Kalinin, S. Jesse, A. Tselev, A. P. Baddorf, and N. Balke, "The role of electrochemical phenomena in scanning probe microscopy of ferroelectric thin films", **ACS Nano** 5, 5683-5691 (2011).
11. D.-W. Chung, N. Balke, S. V. Kalinin, and R. E. García, "Virtual electrochemical strain microscopy of polycrystalline LiCoO<sub>2</sub> films", **J. Electrochem. Soc.** 158, A1083-A1089 (2011).
12. S. Guo, S. Jesse, S. Kalnaus, N. Balke, C. Daniel, and S. V. Kalinin, "Direct mapping of ion diffusion times on LiCoO<sub>2</sub> surfaces with nanometer resolution", **J. Electrochem. Soc.** 158, A982-A990 (2011).
13. S. V. Kalinin and N. Balke, "Local electrochemical functionality in energy storage materials and devices by scanning probe microscopies: status and perspectives", **Adv. Mater.** 22, E193-E209 (2010).

# **Session V**



# High Performance Nano-Crystalline Oxide Fuel Cell Materials: Defects, Structures, Interfaces, Transport, and Electrochemistry

S.A. Barnett, L.D. Marks, T.O. Mason, K. Poepelmeier, P.W. Voorhees

Northwestern University

2220 Campus Drive

Evanston, IL 60208

Phone: 847 491 2447; FAX: 847 491 7820

s-barnett@northwestern.edu

DOE Program Officer: Refik Kortan

301/903-3308; refik.kortan@science.doe.gov

## Program Scope

Solid oxide cells (SOCs) are versatile electrochemical devices with applications including clean efficient electricity generation, chemical production, renewable fuel production, and electricity storage. Solid oxide fuel cells are nearing commercial viability, but fundamental challenges remain, especially reducing operating temperature and improving long-term durability. Operating temperature is important not only for making the technology viable, but for enabling new uses such as transportation and portable generation. SOC's can also be used to complement renewable sources by providing a means for storing energy as a chemical fuel such as hydrogen or methane.

This project aims to parlay our improving understanding of the enhanced electronic and ionic transport properties of nano-scale oxides and surfaces to address electrode performance and durability issues that limit the utility of SOC's. The focus is on the fundamental problems limiting reduced-temperature SOC's. The scientific focus is on the dynamics of mixed nano- and micron-scale structures in electrochemical cells. New methods for fabrication and characterization of novel SOC materials have been developed. In addition, we are working towards a fundamental understanding of transport properties, polarization behavior, and degradation phenomena.

## Recent Progress

Oxygen tracer diffusion ( $D^*$ ) and chemical diffusion ( $D^{\sim}$ ) were measured in dense  $\text{Sr}_{0.5}\text{Sm}_{0.5}\text{CoO}_{3-\delta}$  (SSC) ceramics by Isotope Exchange Depth Profiling/Secondary Ion Mass Spectrometry and electrical conductivity relaxation. As shown in Figure 1, SSC exhibits higher oxygen chemical diffusivity than other reported solid oxide cell cathodes. Oxygen surface exchange rates have also been measured (not shown) and are amongst the best among known materials.

This same high performance

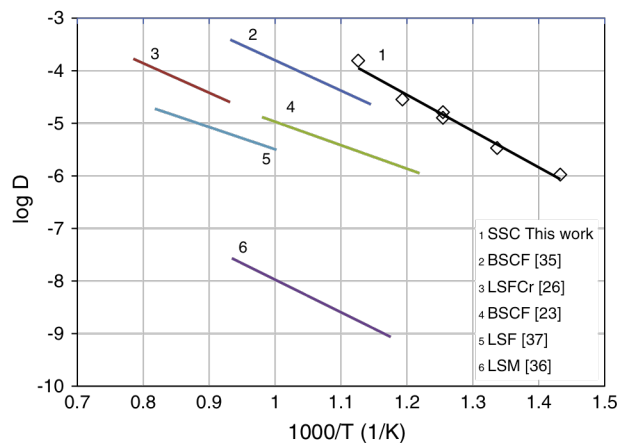
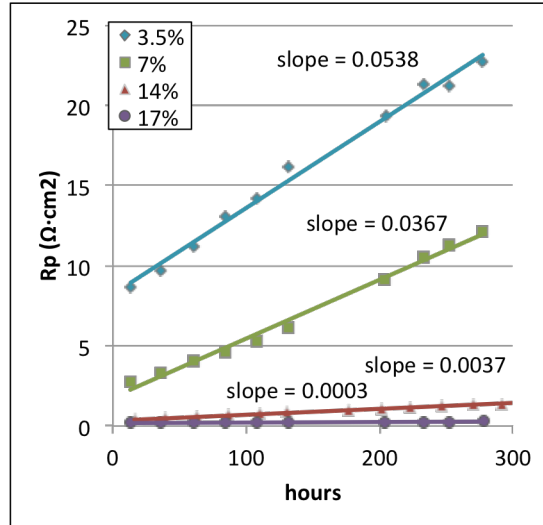


Figure 1. Chemical diffusivities of the SSC material (data points) compared with literature values for other high performance SOC air-electrode materials.

material has been explored in realistic electrodes, producing amongst the lowest reported air-electrode polarization resistances, low enough to enable excellent cell performance well below 600°C. However, the long-term stability of such highly active nano-scale cathodes has not previously been studied and remains a potential show-stopper (solid state ionic devices such as fuel cells that should operate at temperature for > 40,000 h). We have thus carried out accelerated testing studies of the of nano-scale SSC cathode materials. Figure 2 shows how the cathode polarization resistance measured at 600°C in air, for SSC infiltrated into Gd-doped Ceria (GDC) scaffolds, varies with time at 800°C, a temperature high enough to accelerate degradation. The decrease in polarization resistance with increasing loading has been observed previously, and is believed due to improved connectivity between SSC nanoparticles. The dramatic decrease in degradation rate with increasing loading is a new observation suggesting that much of the degradation at low loading is due to increased isolation of SSC nanoparticles with increasing annealing time. This is an important result for achieving low degradation rates. Another interesting observation is that the resistance increases linearly with time, different than in our prior studies of LSCF cathodes where the degradation followed a power law dependence. Work is under way to understand these new observations.

Infiltration of one material into a scaffold, such as the SSC infiltration into GDC mentioned above, is an important avenue for increasing the performance of a SOFC. The infiltrate size scale and interconnectivity, which have a major effect on the polarization resistance, are related to the size and location of the liquid droplets that are present on the scaffold surface following the evaporation of the liquid. We have developed a model that predicts the size of these droplets. Their size scale, ~50 nm (Figure 3) is reasonably consistent with experiments. The model is not limited to a planar surface, and thus can be used to assess the development of the infiltrated phase upon subsequent loadings.

Due to the nanoscale size of the oxide particles, these particles can be subject to stress that is not relieved as the temperature is changed from room temperature to the operating temperature of the SOFC. We have developed a model for the effects of stress on the surface-exchange limited chemical capacitance, vacancy formation energy, and the degree of oxygen nonstoichiometry in the



**Figure 2. Cathode polarization resistance measured at 600°C in air, for SSC infiltrated into Gd-doped Ceria (GDC) scaffolds, varies with time at 800°C.**

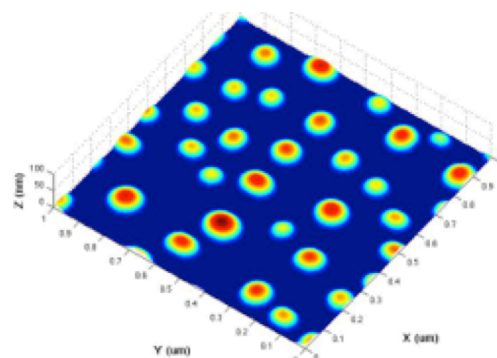


**Figure 3. A simulation of the liquid film evaporation process, showing the formation of liquid droplets on a surface.**

oxide. The theory shows that the oxygen nonstoichiometry is a linear function of the trace of the stress, and can change significantly with stress.

We have also explored novel oxide anode materials where catalytic nano-particles nucleate during SOC operation and greatly enhance electrochemical kinetics. Figure 4 shows TEM images of  $(\text{La}_{0.8}\text{Sr}_{0.2})(\text{Fe}_{0.5}\text{Cr}_{0.3}\text{Ru}_{0.2})\text{O}_3$  particles that were exposed to hydrogen at elevated temperature resulting in self-assembly of surface Ru nano-particles that greatly improve anode performance. The image shown is just one of a rotation series being reconstructed to produce a 3D image – such imaging will allow us quantify particle nucleation and growth and thereby understand their role in electrochemical processes.

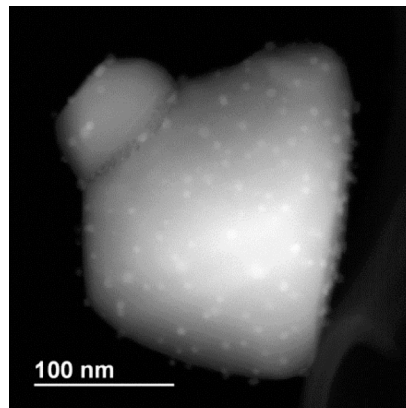


**Figure 4. Z-contrast TEM image of a  $(\text{La,Sr})(\text{Fe,Cr,Ru})\text{O}_3$  particle decorated with Ru nano-particles.**

Electrochemical measurements of these new perovskite anodes show substantially lower polarization resistance than prior oxide anode materials, apparently by taking advantage of both mixed conductivity and nanoparticle catalysts. A picture of the electrochemical rate-limiting steps is beginning to emerge based on detailed impedance spectroscopy studies. Figure 5 illustrates an example of impedance data from a cell with a  $(\text{La}_{0.33}\text{Sr}_{0.67})(\text{Fe}_{0.67}\text{Cr}_{0.33})\text{O}_3$  anode under varying  $\text{H}_2$  partial pressures  $P_{\text{H}_2}$  (balance Ar with 3%  $\text{H}_2\text{O}$ ).

The Bode plot shows a main electrochemical process with a peak frequency at 2 Hz that varies strongly with  $P_{\text{H}_2}$ . (The process at  $\sim 1000$  Hz is mainly due to the cathode.) While a low-frequency response with a strong  $P_{\text{H}_2}$  dependence is often associated with gas diffusion, this is not the case here because the response is strongly temperature dependent. On the other hand, such a response, along with the limiting-current behavior seen in current-voltage characteristics, can be explained well by a  $\text{H}_2$  dissociative adsorption rate-limiting process.

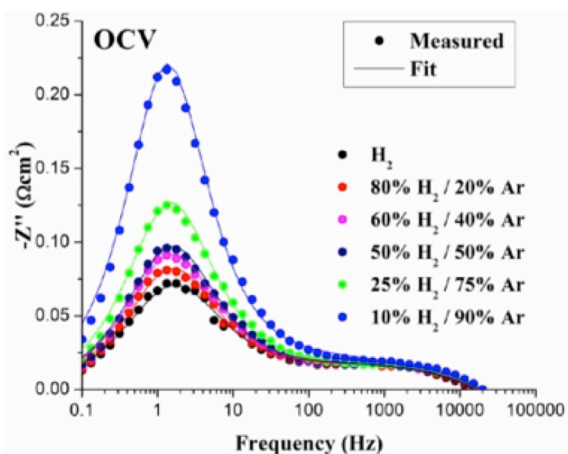


**Figure 5. Bode plots of impedance spectra measured from a SOFC at  $800^\circ\text{C}$  at open circuit voltage with different  $\text{H}_2$  partial pressures. Fits are also shown.**

When Ru is added to the perovskite oxide anode such that Ru nanoparticles form, the anode polarization resistance is reduced, the dependence on  $P_{\text{H}_2}$  becomes weaker, and the limiting-current behavior disappears – these are all indications of the elimination  $\text{H}_2$  adsorption as a rate limiting step. In this case, the new rate-limiting step appears to be hydrogen electrochemical oxidation. This can be understood by figuring that the Ru nanoparticles act as catalysts for  $\text{H}_2$  dissociation with subsequent spillover of H atoms onto the adjacent oxide surface, where the oxidation process is thereby enhanced.

It has been possible to implement some of the above materials in novel reduced-temperature solid oxide cells that provide a real demonstration of their effectiveness.

Figure 6 shows the electrical testing results of such a cell. The cell resistances are remarkably low and power densities high – above 1 W/cm<sup>2</sup> at 550°C. This represents unprecedented performance at these temperatures for a solid oxide fuel cell.

### Future Plans

Much of the work described above will be continued in the short term. The combined

experimental/theoretical approach to understanding nano-structure evolution, and its impact on electrochemical performance, will be continued, with new input from 3D

TEM observations. For cathodes, the emphasis will be on obtaining nano-structures that yield both low resistance and good durability. Accelerated testing will continue to the point where realistic degradation models can be developed and used to predict long-term durability. For anodes, the emphasis will be on improving low-temperature performance and on materials that exhibit regenerative behavior. Novel oxide anode studies will be continued to develop quantitative models of hydrogen electrochemical oxidation kinetics.

### Publications of DoE-Sponsored Research (in the past year)

1. Z. Zhan, D. Han, T. Wu, X. Ye, S. Wang, T. Wen, S. Cho and S.A. Barnett, "A solid oxide cell yielding high power density below 600 °C," *RSC Advances* **2** (2012) 4075
2. J.D. Nicholas, L. Wang, A.V. Call and S.A. Barnett, "Use of the Simple Infiltrated Microstructure Polarization Loss Estimation (SIMPLE) model to describe the performance of nano-composite solid oxide fuel cell cathodes," *Phys Chem Chem Phys* 10.1039/c2cp43370b (2012)
3. J.M. Haag, D.M. Bierschenk, S.A. Barnett and K.R. Poeppelmeier, "Structural, chemical, and electrochemical characteristics of LaSr<sub>2</sub>Fe<sub>2</sub>CrO<sub>9-δ</sub>-based solid oxide fuel cell anodes," *Solid State Ionics* **212** (2012) 1-5
4. S. Cho, D. Fowler, E.C. Miller, J.S. Cronin, K.R. Poeppelmeier and S.A. Barnett, "Fe-substituted SrTiO<sub>3+δ</sub> / Ce<sub>0.9</sub>Gd<sub>0.1</sub>O<sub>1.95</sub> composite anodes for solid oxide fuel cells," *PCCP in press* (2013)
5. D.M. Bierschenk, J.M. Haag, K.R. Poeppelmeier and S.A. Barnett, "Performance and Stability of LaSr<sub>2</sub>Fe<sub>2</sub>CrO<sub>9-δ</sub>-Based Solid Oxide Fuel Cell Anodes in Hydrogen and Carbon Monoxide," *Journal of The Electrochemical Society* **160** (2012) F90-F93
6. D.M. Bierschenk and S.A. Barnett, "Electrochemical characteristics of La<sub>0.8</sub>Sr<sub>0.2</sub>Cr<sub>0.82</sub>Ru<sub>0.18</sub>O<sub>3-δ</sub>-Gd<sub>0.1</sub>Ce<sub>0.9</sub>O<sub>2</sub> solid oxide fuel cell anodes in H<sub>2</sub>-H<sub>2</sub>O-CO-CO<sub>2</sub> fuel mixtures," *Journal of Power Sources* **201** (2012) 95-102
7. S.A. Barnett, "Solid Oxide Fuel Cells: Direct Hydrocarbon Type," *Encyclopedia of Electrochemistry / High-Temperature Electrochemistry*, Springer, 2012
8. T.C. Yeh, J.L. Routbort and T.O. Mason, "Oxygen transport and surface exchange properties of Sr<sub>0.5</sub>Sm<sub>0.5</sub>CoO<sub>3-δ</sub>," *Solid State Ionics* **232** (2013) 138-143

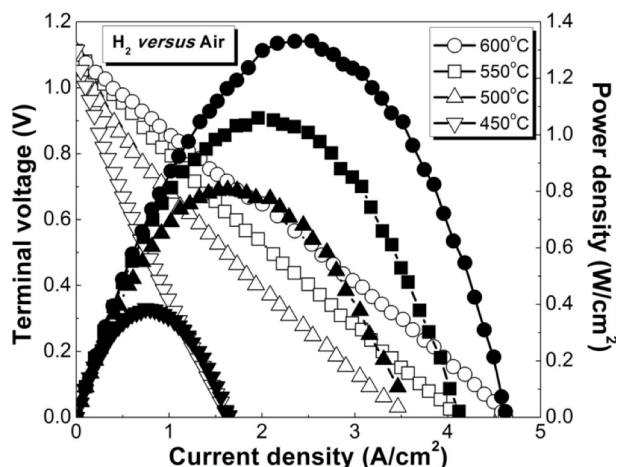


**Figure 6. Voltage and power density versus current density for a solid oxide fuel cell operated at various temperatures in air and humidified H<sub>2</sub> fuel.**

# Experimental and theoretical pursuit of the ultimate conductivity in ZnO

DE-FG02-11ER46820

16April2013

**PI:** David C. Look

**Mailing address:** Semiconductor Research Center, 134 Oelman Hall, Wright State University,  
3640 Col. Glenn Hwy., Dayton, OH 45435

**Telephone number:** 937-528-8741

**E-mail:** [david.look@wright.edu](mailto:david.look@wright.edu)

## Purpose and Goals

The main purpose of this program is to develop highly conductive ZnO as a replacement for In<sub>2</sub>O<sub>3</sub>:Sn (ITO) in transparent electrode applications, such as solar cells, flat-panel displays, and light-emitting diodes. Pursuant to this purpose, the main goal was to test the limits of conductivity for ZnO to see if it could truly compete with ITO. A secondary goal was to test stability, sometimes an issue for materials doped beyond their thermodynamic solubility limits. A third goal was to compare different growth methods, especially pulsed laser deposition and sputtering. During the course of this research, it has also been realized that our highly doped ZnO has plasmonic resonances in the infrared regime and thus can enable functionality not available with the usual metal plasmonics. This possibility generates a new goal, to determine the limits of plasmonic resonance wavelengths in ZnO.

## Recent progress

The lowest resistivity ever achieved in ZnO is  $\rho = 0.8 - 0.9 \times 10^{-4} \Omega\text{-cm}$ , reported by two different groups 6 - 10 years ago. However, there are serious inconsistencies in each of these papers, rendering their results questionable. Another recent, more convincing, paper reports  $\rho = 1.1 \times 10^{-4} \Omega\text{-cm}$ , and that, in our opinion, should be taken as the mark to shoot for. So far, our best value is  $\rho = 1.2 \times 10^{-4} \Omega\text{-cm}$ , within 10% of the record. However, we have achieved this through a well quantified and easily repeatable methodology, and this is our major contribution so far. Just prior to the beginning of the present program in Sept2011, we had developed two unique tools that greatly aided our efforts: (1) the use of pure Ar ambient in the pulsed-laser-deposition growth of Ga-doped ZnO that allowed us to consistently achieve a resistivity of  $\rho = 2.0 \times 10^{-4} \Omega\text{-cm}$ ; and (2) formulation of a degenerate mobility theory that permitted donor  $N_D$

and acceptor  $N_A$  concentrations to be calculated from experimental values of mobility  $\mu$  and concentration  $n$  at any temperature. Applying the theory we quickly learned that the most useful strategy in reducing  $\rho$  was not to increase  $N_D$ , already near its maximum, but to reduce  $N_A$ . This strategy required identification of the dominant acceptor, and we showed that it was not any impurity at all, but instead the Zn vacancy  $V_{Zn}$ . We then devised an annealing procedure to reduce  $[V_{Zn}]$ , placing the sample face down on Zn foil and annealing in a tube furnace for 10 min at 550 °C in flowing gas, and we achieved  $\rho = 1.2 \times 10^{-4} \Omega\text{-cm}$ . For this sample our theory gives:  $N_D = 1.52 \times 10^{21} \text{ cm}^{-3}$  and  $N_A = 0.048 \times 10^{21} \text{ cm}^{-3}$ , giving an extremely small compensation ratio  $K = N_A/N_D = 0.03$ . It might be said that this procedure thwarts thermodynamics, i.e., it overcomes the crystal's attempt to lower its energy by creating native acceptors to compensate the added Ga donors. Of course, given enough time the crystal would accomplish just that, especially if the temperature were raised significantly. In that regard, we have shown that a 10-min anneal in air at 500 °C increases  $\rho$  by only xx %, demonstrating the excellent stability of this material.

Interestingly, however, increasing the annealing temperature to 600 °C produces a huge change in  $\rho$ , to about  $1\Omega\text{-cm}$ , clearly rendering the TCO useless as a transparent electrode. However, while carrying out this set of experiments, we realized that we could *control*  $\rho$ , or more importantly  $n$  and  $\mu$ , over a wide range by simply choosing the appropriate annealing temperature. Since, for high enough  $\mu$ , the plasmonic resonance frequency is given by  $\omega_{p,\text{res}} = (e^2 n / m^* \epsilon_\infty)^{1/2}$ , our control of  $n$  becomes a control of  $\omega_{p,\text{res}}$ , or equivalently of  $\lambda_{p,\text{res}} = 2\pi c / \omega_{p,\text{res}}$ , the plasmon resonance wavelength,. For a concentration  $n = 1.46 \times 10^{21} \text{ cm}^{-3}$  (this study),  $\lambda_{p,\text{res}} = 1.06 \mu\text{m}$ , while annealing in air produces lower  $n$  and thus higher  $\lambda_{p,\text{res}}$ . As practical examples, we have easily created samples with  $\lambda_{p,\text{res}} = 1.30$  and  $1.55 \mu\text{m}$ , the major telecommunication wavelengths. Indeed, this new field of semiconductor plasmonics opens up a wide variety of applications in the infrared that cannot be addressed by metal plasmonics.

### Future plans

Another problem for thin films is the thickness dependence of  $\rho$ ,  $\mu$ , and  $n$  for layers grown on lattice-mismatched substrates. For example, when 3%Ga-doped ZnO is grown by PLD on  $\text{Al}_2\text{O}_3$ , a dead layer (no conduction) of thickness  $d_{\text{dead}} = 15 \text{ nm}$  is typical, and roughly the same  $d_{\text{dead}}$  is found for 2%Al-doped ZnO grown by RF sputtering on quartz glass. Thus, this phenomenon is rather universal and results in an electrical thickness  $d_{\text{el}}$  that is less than the metallurgical thickness  $d$ ; i.e.,  $d_{\text{el}} = d - d_{\text{dead}}$ . A consequence is that the *apparent* concentration  $n_{\text{meas}}$  is going to be less than the *real* concentration  $n$  by a factor  $d_{\text{el}}/d$ , which can be appreciable for thicknesses  $d = 50 \text{ nm}$  or less. While  $n_{\text{meas}}$  is nearly always observed to be dependent on thickness,  $n$  itself may actually be independent of thickness if it is properly normalized to  $d_{\text{el}}$  instead of  $d$ . However, even if  $n$  is *independent* of  $d$ , mobility will *always* be *dependent* on  $d$  if the dead layer is charged, which is usually the case. This is because the conduction electrons

will spend more time close to the interface in thinner layers, and therefore will be more effectively scattered by the interface charge. A similar argument holds if the interface is rough. We are collaborating on buffer development with a group at the University of Kyushu in Japan that has developed a good buffer layer that mitigates the thickness dependence of  $\mu$ . In fact, we have already characterized a set of buffered and unbuffered layers received from them in early December 2012, and have just had a paper accepted on our results. In the paper, we introduce a new figure of merit (FoM) for buffer efficacy, a parameter  $d^*$  that is defined as the thickness at which interface scattering and bulk scattering are equal. This parameter is a useful FoM because it is easily measurable and is obviously meaningful; i.e., good conductance demands  $d > d^*$  so low  $d^*$  is desirable. The Kyushu group has just received an AOARD grant to continue our collaboration, and their proposal contains two new goals: (1) grow *single-crystalline* undoped ZnO on Al<sub>2</sub>O<sub>3</sub>; and (2) grow polycrystalline highly-doped ZnO on quartz glass with a resistivity of  $2 \times 10^{-4} \Omega\text{-cm}$  or less in a layer of thickness 100 nm or less. Neither of these goals has ever been achieved, to our knowledge.

#### **Publications associated with this DOE grant (begun in Sept 2011)**

1. Buguo Wang, Matthew Mann, Michael Snure, Michael J. Callahan, and David C. Look, "Hydrothermal growth and characterization of bulk Ga-doped and Ga/N codoped ZnO crystals", Proc. of SPIE Vol. 8263, 828305-1 (2012). Mar12
2. D.C. Look and K.D. Leedy, "Making highly conductive ZnO: creating donors and destroying acceptors", Proc. of SPIE Vol. 8263, 828302-1 (2012). Mar12
3. J. T-Thienprasert, S. Rujirawat, W. Klysubun, J.N. Duenow, T.J. Coutts, S.B. Zhang, D.C. Look, and S. Limpijumnong, "Compensation in Al-doped ZnO by Al-Related Acceptor Complexes: Synchrotron X-ray Absorption Spectroscopy and Theory", Phys. Rev. Lett. **110**, 055502 (2013) Jan13.
4. D.C. Look, T.C. Droubay, and S.C. Chambers, "Stable highly conductive ZnO via reduction of Zn vacancies", Appl. Phys. Lett. **101**,102101 (2012). Aug12
5. Leonard J. Brillson, Yufeng Dong, Filip Tuomisto, Bengt G. Svensson, Andrei Yu. Kuznetsov, Daniel Douth, H. Lee Mosbacker, Gene Cantwell, Jizhi Zhang, Jin Joo Song, Z.-Q. Fang, and David C. Look, "Interplay of native point defects with ZnO Schottky barriers and doping", J. Vac. Sci. Technol. B **30**, 050801 (2012). Oct12
6. B. Wang, J.M. Mann, B. Claflin, M. Snure, and D.C. Look, "Hydrothermal growth and characterization of bulk Al-doped ZnO bulk crystals", Proc. of SPIE Vol. 8626, 862607-1 (2013). Mar13
7. M.S. Allen, J.W. Allen, B.R. Wenner, D.C. Look and K.D. Leedy, "Application of highly conductive ZnO to plasmonics", Proc. of SPIE Vol. 8626, 862604-1 (2013). Mar13

8. B. Claflin, K.D. Leedy, and D.C. Look “Dopant profiles in heavily doped ZnO”, Proc. of SPIE Vol. 8626, 862605-1 (2013). Mar13
9. D.C. Look, K.D. Leedy, A. Kiefer, B. Claflin, N. Itagaki, K. Matsushima, and I. Surhariadi, “Model for thickness dependence of mobility and concentration in highly conductive ZnO”, Proc. of SPIE Vol. 8626, 862601-1 (2013). Mar13
10. D.C. Look, K.D. Leedy, A. Kiefer, B. Claflin, N. Itagaki, K. Matsushima, and I. Surhariadi, “Model for thickness dependence of mobility and concentration in highly conductive ZnO”, Optical Engineering, accepted.
11. D.C. Look and K.D. Leedy, “ZnO plasmonics for telecommunications”, APL (submitted)
12. D.C. Look, T.C. Droubay, and S.A. Chambers, “Optical/electrical correlations in ZnO: The plasmonic resonance phase diagram”, Physica Status Solidi, submitted (*7<sup>th</sup> Int. Workshop on ZnO and Related Materials*, Nice, France, 12Sept2012)

Program Title: Energy Transport in Graphene  
 Principal Investigator: Li Shi  
 Institution: The University of Texas at Austin  
 Address: 204 E. Dean Keeton Street, Austin, TX 78712  
 Email: lishi@mail.utexas.edu  
 DOE Grant Number: DE-FG02-07ER46377  
 Collaboration: Prof. Stephen Cronin, University of Southern California

### Program Scope or Definition

The objective of this proposed research is to develop a better understanding of phonon transport and coupled electron-phonon transport in graphene. As a monatomic layer of  $sp^2$  carbon atoms, graphene is a promising material for future-generation energy-efficient electronic devices and thermal management solutions because of its superior charge mobility, mechanical strength, and thermal conductivity. This project aims to

- (i) Clarify whether the flexural vibration modes make an important or negligible contribution to thermal conductivity of graphene.
- (ii) Investigate the effects of inter-layer coupling, substrate interaction, stress and morphology on phonon transport in suspended and supported single- and few-layer graphene.
- (iii) Characterize the interfacial thermal transport between supported graphene and underlying dielectric, metallic, and polymeric substrates.
- (iv) Evaluate interfacial thermal transport between graphene and its surrounding gas environment;
- (v) Determine whether or not coupled electron-phonon transport in graphene is highly non-equilibrium as in carbon nanotubes.
- (vi) Reveal the effects of inter-layer coupling, substrate interaction, stress, morphology, and gas environment on electron-phonon coupling in graphene.

### Recent Progress

In this collaborative project with Prof. Cronin, we have established experimental methods based on micro-Raman and electrical resistance thermometry to probe phonon transport in suspended and supported graphene as well as ultrathin-graphite foams. In addition, Scanning Thermal Microscopy (SThM) and spatially resolved Raman spectroscopy have been combined to probe temperature distributions of different phonon populations and reveal bias-dependent hot spots in electrically biased graphene devices.

**Raman Measurements of Thermal Transport in Suspended and Supported Graphene:** We have established a micro-Raman spectroscopy method to probe thermal transport above room temperature in a graphene monolayer grown by chemical vapor deposition (CVD) and suspended over holes with different diameters. The Raman laser beam of varied spot sizes was focused either at the center of the suspended graphene monolayer or on the graphene region supported on the  $Au/SiN_x$  membrane. The optical absorption by the graphene was obtained by measuring the laser powers incident on and transmitted through the suspended graphene. The Raman G peak and 2D peak positions of graphene down shift with increasing temperature, and were

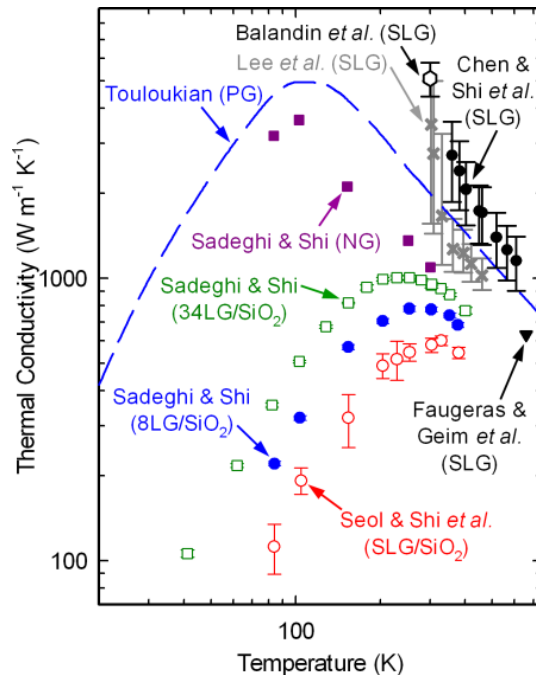


**Figure 1.** Experimental basal plane thermal conductivity results reported by different groups for (i) suspended single-layer graphene (SLG), (ii) SLG, 8-layer graphene (8LG) and 34-layer graphene (34LG) supported on  $SiO_2$ , (iii) the natural graphite (NG) source where the supported SLG and FLG were exfoliated from, and (iv) high-quality pyrolytic graphite (PG).

used to determine the temperature rise of the optically heated graphene. An analytical solution of the heat diffusion equation was developed to obtain the thermal conductivities of the suspended and supported regions of the graphene samples, as well as the thermal interface conductance between the graphene and the Au/SiN<sub>x</sub> membrane. A comparison of the measurement results conducted in vacuum and different gas environment further yielded the heat transfer coefficient between the graphene and surrounding gas molecules. The main findings of this series of experiments include the observation of considerably lower thermal conductivity in the supported region than the suspended region of the same graphene, and that Umklapp phonon scattering results in decreasing thermal conductivity of the suspended graphene with increasing temperature above room temperature (see the data by Chen & Shi et al. in Fig. 1).

### Substrate and Polymer Residue Scattering of Phonons in Graphene:

We have fabricated different micro-bridge devices with sensitive resistance thermometers to measure the graphene thermal conductivity at different temperatures. Compared to the natural graphite (NG) source where the graphene samples were exfoliated from, a large suppression in the basal-plane thermal conductivity was found in the graphene samples supported on an amorphous SiO<sub>2</sub> or suspended graphene samples contaminated by polymer residue on the surface. The suppression is especially pronounced at low temperatures (see the data by Sadeghi & Shi, and Seol & Shi et al in Fig. 1). A theoretical calculation found that flexural phonons make a large contribution to the thermal conductivity of clean suspended graphene at 300 K and below, and interface interaction with an amorphous material results in considerable damping of their contribution.

Moreover, such interface scattering was found to yield increasing thermal conductivity with increasing layer thickness of multi-layer graphene (Fig. 2), opposite to the trend suggested for clean suspended graphene, as well as a decreasing temperature for the peak thermal conductivity with increasing layer thickness (see the data by Sadeghi and Shi, and Seol & Shi et al. in Fig. 1). The interface scattering effect was found to be effective in suppressing the thermal conductivity of multi-layer graphene as thick as 34 layers. This long range effect is attributed to the long intrinsic phonon mean free path in graphite, and explained by a model of interface scattering of phonons in anisotropic multi-layer graphene. These findings are useful for the design of multi-layer graphene heat spreaders and graphene-polymer nanocomposites for thermal management, and indicate a need for obtaining ultra-clean suspended graphene samples for studies of their intrinsic thermal properties.

**Thermal Transport in Ultrathin-Graphite Foams:** In this work, we have conducted temperature-dependent electron and phonon transport measurements of three-dimensional (3D) foam structures consisting of few-layer graphene (FLG) and ultrathin graphite (UG) building blocks synthesized through the use of methane CVD on reticulated nickel foam that was subsequently removed. At a very low solid concentration of ~0.45 vol %, the thermal conductivity of the freestanding ultrathin-graphite foam (UGF) processed with a gentle Ni etchant can be increased to 1.7 Wm<sup>-1</sup>K<sup>-1</sup> at room temperature, showing a quadratic dependence on temperature between 11 and 75 K, peaking at about 150 K where the solid thermal conductivity of the FLG and UG constituents reached about 1000 Wm<sup>-1</sup>K<sup>-1</sup> (Fig. 3). The finding suggests that the covalently bonded continuous UGF structure is an effective approach to overcoming the

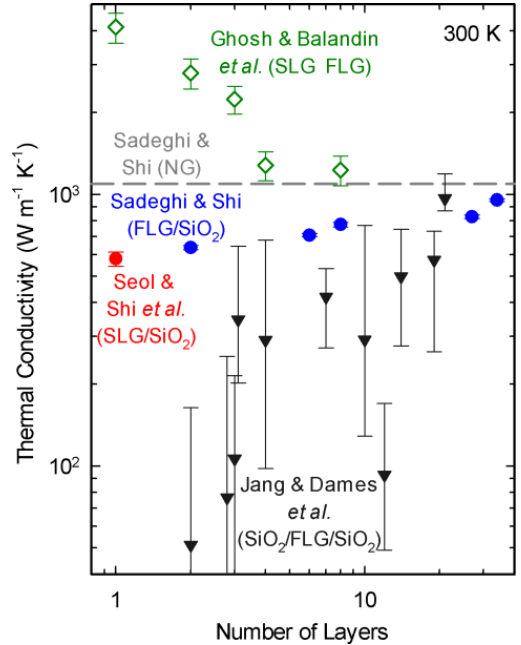


**Figure 2.** Room-temperature basal plane thermal conductivity measured by different groups for suspended SLG and FLG, and FLG encased in SiO<sub>2</sub>, SLG and FLG supported on SiO<sub>2</sub>, and the natural graphite (NG) source where the supported SLG and FLG samples were exfoliated from.

contact thermal resistance bottleneck found in other 3D networks of van der Waals bonded carbon nanomaterials developed for thermal management.

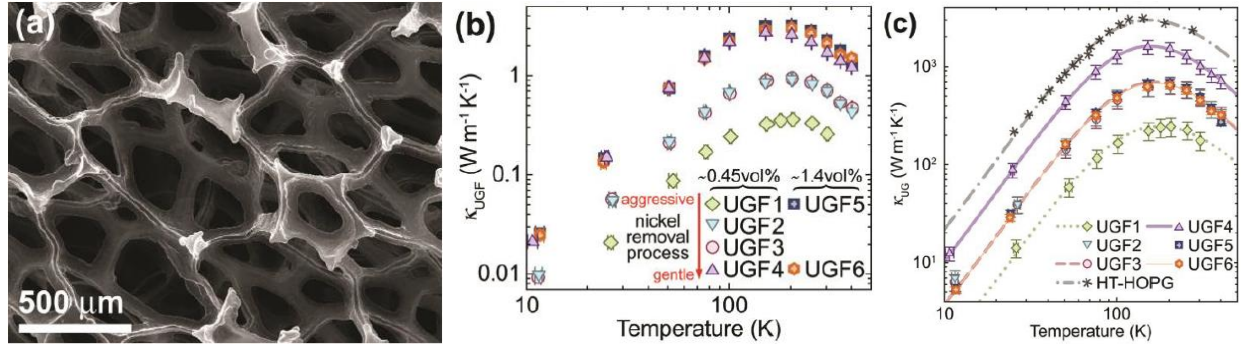


**Figure 3.** (a) Scanning electron micrograph, (b) measured effective thermal conductivity, and (c) extracted solid strut wall thermal conductivity of UGFs grown by CVD on sacrificial Ni foams, which were removed by different wet etchants to yield UGFs of 0.45 vol% or 1.4 vol% solid concentration.

### Low-Frequency Acoustic Phonon Temperature Distribution in Electrically Biased Graphene:

With the use of a combined contact mode and lift mode operation of a SThM tip, we were able to measure the low-frequency acoustic phonon temperature profiles in electrically biased graphene devices with a spatial resolution better than 100 nm. The obtained temperature maps (Fig. 4a) reveal bias-dependent hot spots in the operating graphene devices that were considerably smaller than those reported by infrared (IR) thermal imaging measurements. In addition, the high temperature sensitivity of the SThM technique allows us to examine the thermal behavior of the graphene device in the low-power density regime that was not accessible by the optical techniques due to limited temperature sensitivity. The measured acoustic phonon temperature was close to the intermediate frequency phonon temperature determined from the Raman peak shift on the same sample (Fig. 4b).

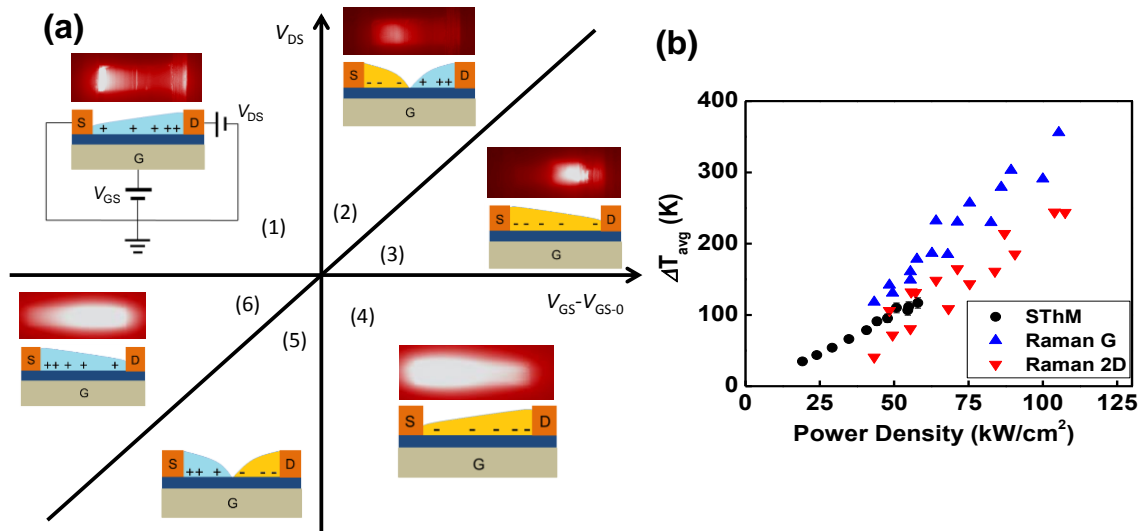


**Figure 4.** (a) Thermal images of a graphene device under different source-drain ( $V_{DS}$ ) and gate bias ( $V_G$ ) conditions, which result in different charge carrier distributions along the 6.7- $\mu\text{m}$  long graphene. (b) Average graphene temperature rise measured by SThM and Raman G and 2D peak as a function of power density in the device.

### Future Plans

In the remaining funding period of this project, we will explore polymer-free transfer method to prepare clean graphene samples for investigating the intrinsic thermal transport properties of graphene, and measure the temperature distribution in electrically biased graphene supported on h-BN.

**References to publications of DOE sponsored research that have appeared in 2010-2012 or that have been accepted for publication.**

This research has resulted in the following twelve journal publications [1-12] and three book chapters [13-15]:

- [1] J. H. Seol, I. Jo, A. L. Moore, L. Lindsay, Z. H. Aitken, M. T. Pettes, X. S. Li, Z. Yao, R. Huang, D. Broido, N. Mingo, R. S. Ruoff, and L. Shi, "Two-Dimensional Phonon Transport in Supported Graphene," *Science* 328, 213-216, 2010.
- [2] W. W. Cai, A. L. Moore, Y. W. Zhu, X. S. Li, S. S. Chen, L. Shi, and R. S. Ruoff, "Thermal Transport in Suspended and Supported Monolayer Graphene Grown by Chemical Vapor Deposition," *Nano Letters* 10, 1645-1651, 2010.
- [3] I. K. Hsu, M. T. Pettes, M. Aykol, L. Shi, and S. B. Cronin, "The Effect of Gas Environment on Electrical Heating in Suspended Carbon Nanotubes," *Journal of Applied Physics* 108, 084307, 2010.
- [4] S. S. Chen, A. L. Moore, W. W. Cai, J. W. Suk, J. H. An, C. Mishra, C. Amos, C. W. Magnuson, J. Y. Kang, L. Shi, and R. S. Ruoff, "Raman Measurements of Thermal Transport in Suspended Monolayer Graphene of Variable Sizes in Vacuum and Gaseous Environments," *ACS Nano* 5, 321-328, 2011.
- [5] I. K. Hsu, M. T. Pettes, M. Aykol, C. C. Chang, W. H. Hung, J. Theiss, L. Shi, and S. B. Cronin, "Direct Observation of Heat Dissipation in Individual Suspended Carbon Nanotubes using a Two-laser Technique," *Journal of Applied Physics* 110, 044328, 2011.
- [6] I. Jo, I. K. Hsu, Y. J. Lee, M. M. Sadeghi, S. Kim, S. Cronin, E. Tutuc, S. K. Banerjee, Z. Yao, and L. Shi, "Low-Frequency Acoustic Phonon Temperature Distribution in Electrically Biased Graphene," *Nano Letters* 11, 85-90, 2011.
- [7] J. H. Seol, A. L. Moore, L. Shi, I. Jo, and Z. Yao, "Thermal Conductivity Measurement of Graphene Exfoliated on Silicon Dioxide," *Journal of Heat Transfer-Transactions of the Asme* 133, 022403, 2011.
- [8] M. T. Pettes, I. S. Jo, Z. Yao, and L. Shi, "Influence of Polymeric Residue on the Thermal Conductivity of Suspended Bilayer Graphene," *Nano Letters* 11, 1195-1200, 2011.
- [9] M. T. Pettes, H. Ji, R. S. Ruoff, and L. Shi, "Thermal Transport in Three-Dimensional Foam Architectures of Few-Layer Graphene and Ultrathin Graphite," *Nano Letters* 12, 2959-2964, 2012.
- [10] M. M. Sadeghi, M. T. Pettes, and L. Shi, "Thermal Transport in Graphene," *Solid State Communications* 152, 1321-1330, 2012.
- [11] L. Shi, "Thermal and Thermoelectric Transport in Nanostructures and Low-Dimensional Systems," *Nanoscale and Microscale Thermophysical Engineering* 16, 79-116, 2012.
- [12] I. Jo, M. T. Pettes, J. Kim, K. Watanabe, T. Taniguchi, Z. Yao, and L. Shi, "Thermal Conductivity and Phonon Transport in Suspended Few-Layer Hexagonal Boron Nitride," *Nano Letters* 13, 550-554, 2013.
- [13] L. Shi, "Thermal Conductance of Carbon Nanotubes," in *Handbook of Nanophysics*, K. D. Sattler, Ed., ed: Taylor & Francis, 2010, pp. 4.1-4.14
- [14] L. Shi, "Thermal and Thermoelectric Characterization of Individual Nanostructures and Thin Films," in *Thermoelectrics and Its Energy Harvesting*, in *Thermoelectrics and Its Energy Harvesting*, D. Rowe, Ed., ed: Taylor & Francis 2012, pp. 21.1-21.25.
- [15] L. Shi, "Scanning Thermal Microscopy," in *Encyclopedia of Nanotechnology*, B. Bhushan, Ed., ed: Springer 2012, pp. 2293-2301.

**Program Title:** Defect Studies of CZTSSe & Related Thin Film Photovoltaic Materials  
**PI:** Mike Scarpulla  
**Mail address:** MSE & ECE Departments, University of Utah, RM 3280 MEB, 50 S. Central Campus Dr., Salt Lake City, UT 84112  
**E-mail:** scarpulla@eng.utah.edu

**Program Scope:**

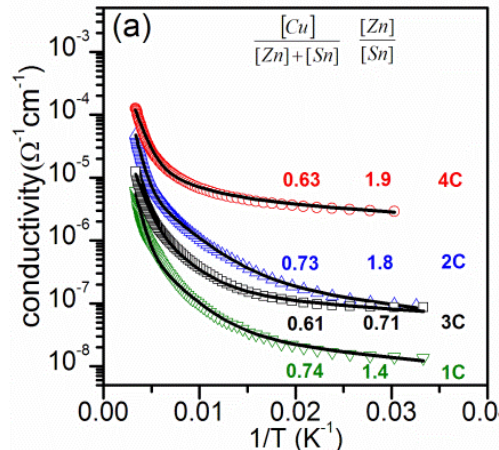
The past five years have brought thin film photovoltaics (TFPV) ever closer to realizing their potential for economical large-scale renewable electrical generation. The thin film PV designs with the highest power conversion efficiencies ( $\eta$ ) remain CdTe/CdS ( $\eta > 18\%$ ) and Cu(In,Ga)Se<sub>2</sub>/CdS (CIGSe,  $\eta > 20\%$ ). In the same time frame, Cu<sub>2</sub>ZnSn(S,Se)<sub>4</sub> (CZTSSe) has emerged as the first possibly credible alternative material for TFPV absorbed layers especially after demonstrations of  $\eta > 11\%$ . Whereas both CdTe and CIGSe technologies may face scale-up limitations within approximately 2 decades based on the geological and industrial availabilities of In and Te especially, CZTS does not because its constituents are abundant by design. Thus basic science investigating the fundamental properties of CZTSSe is of great importance to enable this material to be used at terawatt levels in the future. The study of CZTSSe also provides more data towards the general questions surrounding the use of polycrystalline semiconductors in minority carrier devices. Studying a different material class such as CZTSSe, whether or not in the end it has the potential for TFPV efficiencies near 20%, will help to understand how materials such as CdTe and CIGSe do in fact work at these levels despite their crystalline and electronic imperfections.

The research objectives of this project center around investigations of the basic properties of Cu<sub>2</sub>ZnSn(S,Se)<sub>4</sub> thin films, especially the electronic defects in the bulk and at the polycrystalline grain boundaries. We specify five sub activities for our efforts: **1)** measuring and understanding the electrical and compositional properties of grain boundaries in CZTSSe; **2)** measuring and understanding electronic defects in CZTS, CZTSSe, and CZTSe thin films using electrical spectroscopies; **3)** modeling the point defect equilibrium in CZTSSe; **4)** spatially-resolving interdiffusion and reaction during CZTSSe annealing using synchrotron techniques; and **5)** high-resolution Raman studies on CZTS, CZTSSe and CZTSe as functions of composition to elucidate peak shifts related to point defects and nanoscale phase separation.

The potential impact of this research will be to generate basic but critical materials knowledge about an emerging alloy system that may be capable of photovoltaic efficiency on par with CdTe and CIGS but at lower cost and having the benefit of avoiding constraints on scale-up from rare and expensive elements.

**Recent Progress:**

**Physics of Electrical Conductivity in Polycrystalline CZTS Thin Films**



We have investigated the through-thickness conductivity of our polycrystalline CZTS films having grain size less than the film thickness from 30-300 K [1]. Three regimes of behavior were found which we ascribe to grain boundary barrier surmounting at high temperature, nearest neighbor hopping at intermediate temperatures, and Mott variable range hopping at low temperatures. Interestingly, for rather Cu-poor films we find that the GB barrier height varies sensitively with  $[Cu]/([Zn]+[Sn])$  ratio ( $\gamma$ ), but is independent of  $[Zn]/[Sn]$  ratio ( $\delta$ ). For  $\gamma \approx 0.62$  the GB

**Figure 1** - Conductivity vs.  $1/T$  for a series of CZTS samples with different compositions. Solid lines represent fits to 3-regime model described in text.

barrier is approximately 110 meV while for  $\gamma \geq 0.74$  it is near 150 meV. These observations point to Cu-related point defects as being dominant for doping at grain boundaries and/or in the grain interiors. Cu vacancies ( $V_{Cu}$ ) and Cu on antisites ( $Cu_{Zn}$ ) are believed to dominate the p-doping in CZTS. The  $V_{Cu}$  acceptor is calculated to be a more traditional acceptor with 20 meV binding energy and formation enthalpy  $< 1$  eV which changes intuitively with Cu-poorness [2,3]. The details of how and why the GB barrier height changes as it does is somewhat uncertain – a simple picture in which the number of GB defects and their density of states remains constant with  $\gamma$  decreasing cannot explain the data unless we posit that for very Cu-poor films ( $\gamma < 0.7$ ) the GB states are completely filled by holes and the Fermi level becomes un-pinned thus reducing the GB barrier height. This does not seem likely, as from our calculations of CZTS defect equilibrium, we find that the net doping stays relatively constant with variation of  $\gamma$  because  $[Cu_{Zn}]$  increases while  $[V_{Cu}]$  decreases as  $\gamma$  increases. Thus it seems possible that the dominant effects of Cu variation actually occur through modification of the GB states and not the doping in the grains (specifically, Cu poorness below  $\gamma \sim 0.7$ ) either reduces the number of pinning states in the GB or moves the centroid of the density of states at the GB towards the valence band edge. A third possibility is that different phase(s) are involved at the GBs. Thus there are many open questions still in this area and we will continue to attempt to identify the correct dominant physics.

### Modeling CZTSSe Defect Equilibrium

In this sub project, defect equilibrium in CZTS and CZTSe is calculated from a system of quasi-chemical reactions based on the change in free energy (Gibbs or Helmholtz) of formation. Many ab-initio electronic structure calculations of defect formation energies have appeared in the literature, however these are always performed at 0 Kelvin (Born-Oppenheimer approximation). For defect formation at film processing temperatures of hundreds of Celsius the vibrational energy of formation can be the dominant term. It is only recently that computational power and efficient codes have begun to allow ab-initio calculations of phonons in (possibly) meaningfully-large supercells containing point defects to simulate dilute concentrations. Therefore we have initiated a collaboration with Prof. Andrei Postnikov at Lorraine University in Metz, France [4,5] to investigate the effects of vibrational energy on defect concentrations in semiconductors and especially CZTSSe. We find indications that in CZTS the vibrational free energy leads to potentially 1000-fold changes in the final defect concentrations and most importantly affects different defects in different ways. Thus, understanding the effects of vibrational free energy for different defects is imperative for understanding doping, compensation, band tails, and recombination in CZTS. This question is obviously general to all semiconductors and we will continue to investigate this avenue of inquiry.

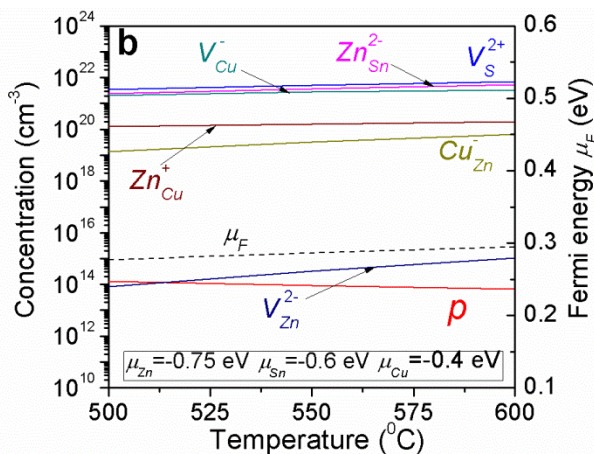


**Figure 2** - Concentrations at room temperature for ionized point defects and Fermi energy in CZTS and Fermi energy calculated for  $\mu_{Zn} = -0.75$  eV,  $\mu_{Sn} = -0.6$  eV, and  $\mu_{Cu} = -0.4$  eV as a function of annealing temperature. The sulfur chemical potential is set by the equilibrium  $S_2$  vapor pressure – i.e. the calculation is for static gas one-zone annealing conditions.

We have computed the equilibrium for the six most dominant native point defects in CZTS using formation enthalpies from Chen et al., [2,3] and the vibrational density of states computed by Prof. Postnikov. Our model can accommodate a range of different situations, however we first undertook to predict the defect equilibrium for a case of annealing CZTS in the presence of a saturated  $S_2$  vapor in a one-zone situation.

Figure 2 presents the results of a calculation of the net doping and all 6 defects concentrations as a function of annealing temperature for the case of quenching to room temperature using chemical potentials for the metals

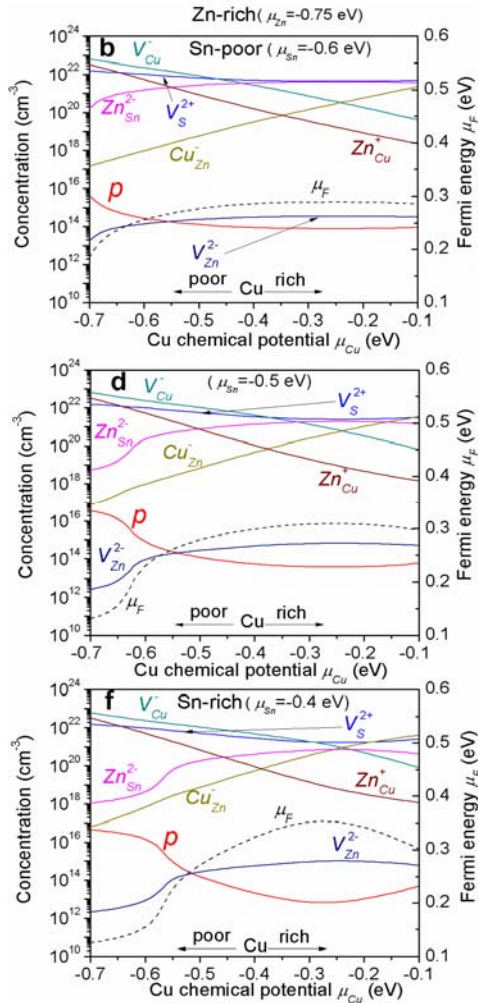


**Figure 3** - Calculations of point defect equilibrium after quenching too room temperature from 550 °C annealing temperature for CZTS annealed in one-zone conditions.

thought to correspond to typical film growth (Zn-rich, Cu-poor). The most important finding from this figure (and the computations in general) is that under such annealing conditions, CZTS which is observed to be p-doped in experiments should be nearly completely compensated by  $V_S$  and  $Zn_{Sn}$  donors because of the lowering of their formation energies by the low Fermi level. The net carrier concentration is thus many orders of magnitude below the concentrations of five of the six types of native defects considered. The compensation may be reduced by increasing the sulfur chemical potential which in experiment corresponds to supplying S vapor at a higher temperature or via another species such as  $H_2S$  and by supplying Sn overpressure – both trends are consistent with the literature. Effects such as these are not captured in the pure ab-initio computational works which typically only present the computed formation enthalpies. Therefore it is imperative compute the full equilibrium to fully understand the system.

Typically, CZTSSe films which work well in devices have  $\gamma \approx 0.5$  and  $\delta \approx 1.2$ . Figure 3 shows the model predictions for quenching from 550 °C annealing to room temperature for Zn-rich conditions as functions of Cu and Sn chemical potentials. These results may help to further understand this trend as it is clear that p-type doping in the  $10^{16} /cm^3$  range results from conditions where the Cu chemical potential is lower than the Sn chemical potential. Of course, the chemical potentials do not translate exactly into final film compositions however we are continuing to try to map out these relationships

between chemical potentials and final film compositions.

### Observation of Defects in CZTSSe using Electrical Spectroscopy Techniques

We are also using electrical and optoelectronic spectroscopy techniques to observe the defect energy levels resulting from defects in this complex alloy system. The holy grail will be to observe, identify, and determine how to suppress deep defects acting as recombination centers. Figure 4 shows our data on the density of states of p-type traps from a CZTSe solar cells with efficiency  $\sim 7\%$  and grain size spanning the film thickness from Dr. Ingrid Repins at NREL. The data suggests the admittance response is dominated by a trap state located near 140 meV above the valence which may be the  $Cu_{Zn}$  deep acceptor according to leading computations [2,3]. Our capacitance voltage profiling shows that these CZTSe layers have nearly-uniform net dopant concentrations in the low  $10^{16} /cm^3$  range for all temperatures, while this DOS extracted has a net area of roughly  $10^{15} /cm^3$ . Therefore our data seems to indicate that the net doping is not dominated by the  $Cu_{Zn}$  acceptors. This may be a significant finding because it is being commonly observed that CZTSSe solar cells display series resistance with  $\sim 150$  meV which has been ascribed to this defect in the literature. We will continue to pursue this issue.

We have also used deep level transient spectroscopy to measure both minority (electron) and majority (hole) trap states in the CZTSe layers. We have found the signature of a minority trap near mid gap which may be acting as a recombination center. This is a very significant finding as all other work to date has reported only majority trap

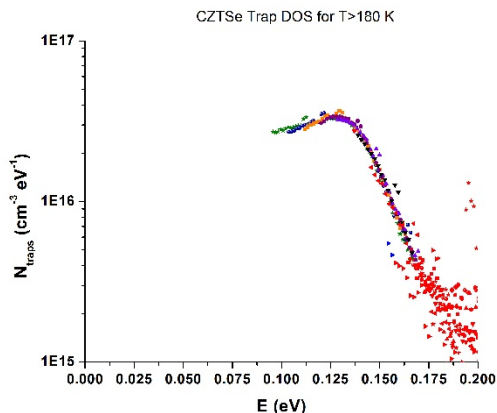


**Figure 4** – Density of trap states extracted from admittance spectroscopy measurements on a solar cell with a CZTSe absorber layer fabricated by Dr. Ingrid Repins at NREL.

states, which are not necessarily related to minority carrier lifetime and thus device efficiency changes. We are working to publish these results quickly.

#### Future Plans:

We plan to continue investigating these themes in CZTSSe and related materials, as well as pursuing measurements of cation disordering and phase formation using synchrotron based experiments. These results will be critical to understanding if CZTSSe can ever provide device efficiencies on par with CdTe and CIGSe and thus fulfil its potential as an earth abundant photovoltaic material.

#### References:

- [1] V. Kosyak, M. A. Karmarkar, and M.A. Scarpulla, *Temperature-dependent conductivity of polycrystalline  $\text{Cu}_2\text{ZnSnS}_4$  thin films*, Applied Physics Letters, **100** 263903 (2012).
- [2] S. Chen, X.G. Gong, A. Walsh, and S.-H. Wei, *Defect physics of the kesterite thin-film solar cell absorber  $\text{Cu}_2\text{ZnSnS}_4$* . Applied Physics Letters, **96** 021902 (2010).
- [3] S. Chen, J.-H. Yang, X.G. Gong, A. Walsh, and S.-H. Wei, *Intrinsic point defects and complexes in the quaternary kesterite semiconductor  $\text{Cu}_2\text{ZnSnS}_4$* . Physical Review B, **81** 245204 (2010).
- [4] N.B. Mortazavi Amiri and A. Postnikov, *Electronic structure and lattice dynamics in kesterite-type  $\text{Cu}_2\text{ZnSnSe}_4$  from first-principles calculations*. Physical Review B, **82**(20) 205204 (2010).
- [5] A. Postnikov and N.B. Mortazavi Amiri, *Ab initio phonons in kesterite and stannite-type  $\text{Cu}_2\text{ZnSnSe}_4$* . Japanese Journal of Applied Physics, **50** 05FE04 (2011).

#### DOE-sponsored Research Publications:

V. Kosyak, M. A. Karmarkar, and M.A. Scarpulla, Temperature-dependent conductivity of polycrystalline  $\text{Cu}_2\text{ZnSnS}_4$  thin films, Applied Physics Letters, **100** 263903 (2012). Doi: 10.1063/1.4731875

E.A. Lund and M.A. Scarpulla, Photovoltaic heterojunctions of earth abundant semiconductors: band alignments in the defective limit, Materials Science and Engineering B, **177** 1436– 1440 (2012) Doi: 10.1016/j.mseb.2012.02.015

W.M. Hlaing Oo, J.L. Johnson, A. Bhatia, E.A. Lund, M.M. Nowell, and M.A. Scarpulla, Grain Size and Texture of  $\text{Cu}_2\text{ZnSnS}_4$  Thin Films Synthesized by Co-sputtering Binary Sulfides and Annealing: Effects of Processing Conditions and Sodium, J. Electronic Materials **40**(11) 2214-2221 (2011)

K. Hartman, J.L. Johnson, M.I. Bertoni, D. Recht, M.J. Aziz, M.A. Scarpulla, and T. Buonassisi, SnS thin-films by RF sputtering at room temperature, Thin Solid Films **519**(21) 7421-7424 (2011)

H. Du, F. Yan, M. Young, B. To, C.S. Jiang, G. Teeter, E.A. Lund, D.C. Hancock, W.M. Hlaing Oo, M.A. Scarpulla, and Z. Chi, Investigation of the Crystalline Morphology of  $\text{Cu}_2\text{ZnSnS}_4$  Thin Films using Combinatorial Co-evaporation Growth Method at 325°C, *In Review* (2012)

# **Session VI**



**Project Title: Frequency Dependent Properties of Magnetic Nanoparticle Crystals**

PI: **Sara Majetich**, Physics Department, Carnegie Mellon University, Pittsburgh, PA 15213-3890, [sara@cmu.edu](mailto:sara@cmu.edu)

**Program Scope:**

This research program is investigating the frequency-dependent response of magnetic nanoparticle assemblies. Magnetostatic interactions are long-range and anisotropic, leading to complex behavior in dense nanoparticle assemblies, particularly in their time- and frequency-dependent properties. In analogy to the blocking temperature of an ensemble of superparamagnetic particles, we predict the existence of a blocking frequency, below which the spins can be treated as frozen. When superparamagnetic properties are ordered into dense assemblies, we have shown in static measurements that there are long-range correlations between the particle moments,<sup>1,2</sup> and that there is a collective phase transition from a dipolar ferromagnet to a superparamagnetic state over a narrow temperature window.<sup>3</sup> We seek to learn if there is collective transition over a narrow frequency range as well. If so, such assemblies could be designed for high frequency applications requiring high permeability but low eddy current losses. Grain size, intergrain separation, and porosity are expected to be important parameters for the nanocomposite structure.

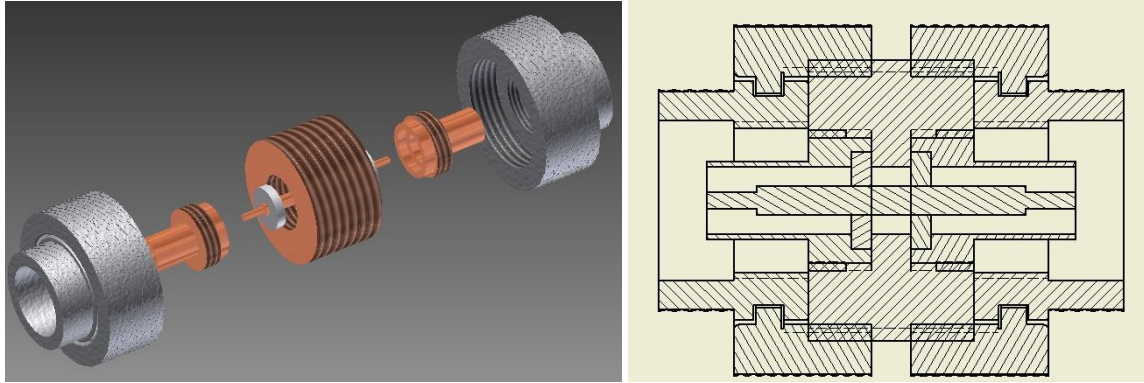
**Recent Progress:**

The main activities in the first year have involved the construction of a sample cell for high frequency measurements, testing of the measurement system and analysis algorithms on bulk-like powder samples, the development of software to predict the composite properties, and the preliminary testing of composite samples as a function of the main design parameters.

Development of Measurement Capabilities Up to 10 GHz

A coaxial transmission line design was developed for measurements up to 10 GHz using an Agilent Technologies 85071 vector network analyzer. In the sample holder, the magnetic nanocomposite toroid replaces the dielectric around the center electrode (Figure 1). At the maximum frequency, the sample length must be less than one-quarter of the radiation wavelength. For high frequencies this limits the sample length to 1-2 millimeters. In order to increase the signal-to-noise ratio, the outer diameter of the sample toroid was increased.

A two port vector network analyzer is used to measure the complex impedance, and therefore the electric permittivity and magnetic permeability as a function of frequency. Here the sample is inserted between two ports. A signal at a given frequency is emitted from Port 1, and its reflection back to this port and transmission to Port 2 are characterized by the scattering matrix parameters  $S_{11}$  and  $S_{21}$ , respectively. The connections to the sample are designed to match the 50  $\Omega$  impedance of the ports, so that the amplitude and phase differences arise only from the sample. The  $S$  parameters relate the magnitude and phase of traveling waves through the microwave network, and so the reference planes for the phase must be specified.



(a)

(b)

**Figure 1.** Sample Holder. (a) Schematic showing two symmetric port extensions (gray) that screw onto the central region (brown) housing the toroidal sample at the center. (b) Cross-section of sample holder. Here the shaded regions are metallic. The “sideways H”- shaped region at the center corresponds to the brown sample housing in (a). The unshaded region at the center of the H is the sample toroid. The other pieces screw onto the sample housing and enable it to mate to coaxial cables connected to the ports of the vector network analyzer.

The shift in reference plane, relative to each port, can be determined. Here the reference planes are chosen to be symmetric on either side of the magnetic sample. With transmission line techniques the measured results are very sensitive to losses in the lines themselves, and therefore a precise calibration procedure is needed to remove systematic errors due to these losses outside the sample. For a one-port calibration from reflection measurements, this is done by measuring the empty sample holder under three conditions: open circuit, short circuit, and load.

The complex electrical permittivity  $\epsilon(f) = \epsilon' - i\epsilon''$  and magnetic permeability  $\mu(f) = \mu' - i\mu''$  are determined from the complex  $S$  parameters. There are different algorithms for determining permittivity and permeability from the  $S$  parameters.<sup>4-6</sup> This is a non-trivial process because of the ambiguity in the phase determination, since  $\theta$  and  $\theta + 2\pi n$  yield the same mathematical result. These algorithms help in extracting the physically meaningful values. Our results use the Nicholson-Ross algorithm in a program written using *MatLab*<sup>TM</sup> software.

### High Frequency Permeability and Permittivity Results and Analysis

High frequency inductors are made of magnetic insulators because of their eddy current losses. To help calibrate our system, we began by measuring the properties of composites made from large grain nickel powder. Increasing volume fraction led to increased magnetic permeability (Figure 2 *a,b*).

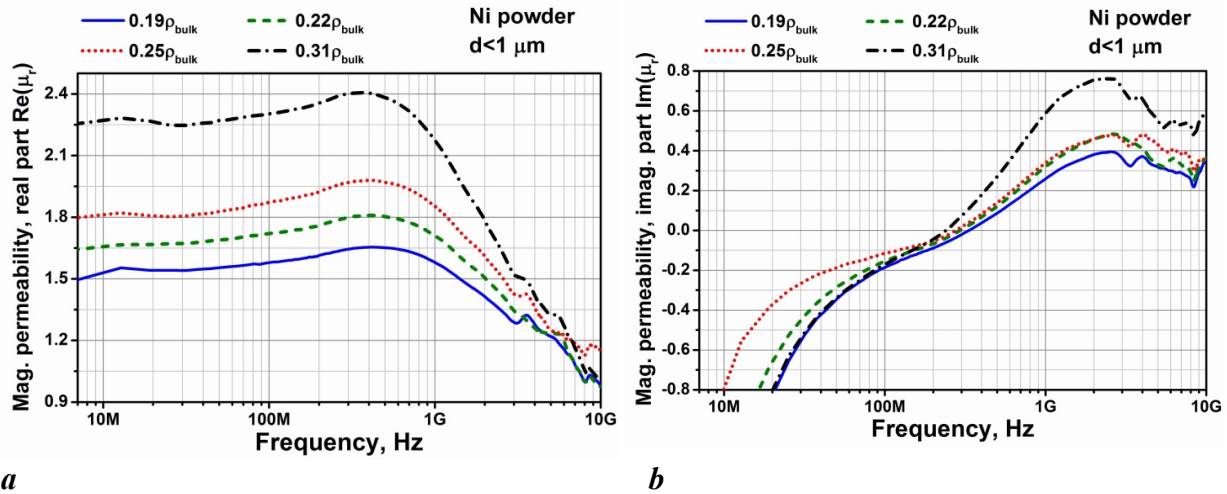


Fig. 2. Frequency dependence of the real (*a*) and imaginary (*b*) parts of the magnetic permeability for nickel powder with grain size less than 1  $\mu\text{m}$  at different volume fractions.

To study the grain size influence on the permeability we carried out measurements with three different nickel powders having grain sizes less than 150 micrometers, <1 micrometer and <100 nanometer, respectively, with approximately the same volume fraction of powders in the sample holder. Since the grains have similar oxide layer thicknesses, the smaller the grain size, the greater the influence of the oxide on the overall permeability values (Figure 3 *a, b*). However, for the nickel powder with grain size less than 100 nm we observed surprisingly high values of the real part of the permittivity, and a peak at 5.8 GHz for the imaginary part.

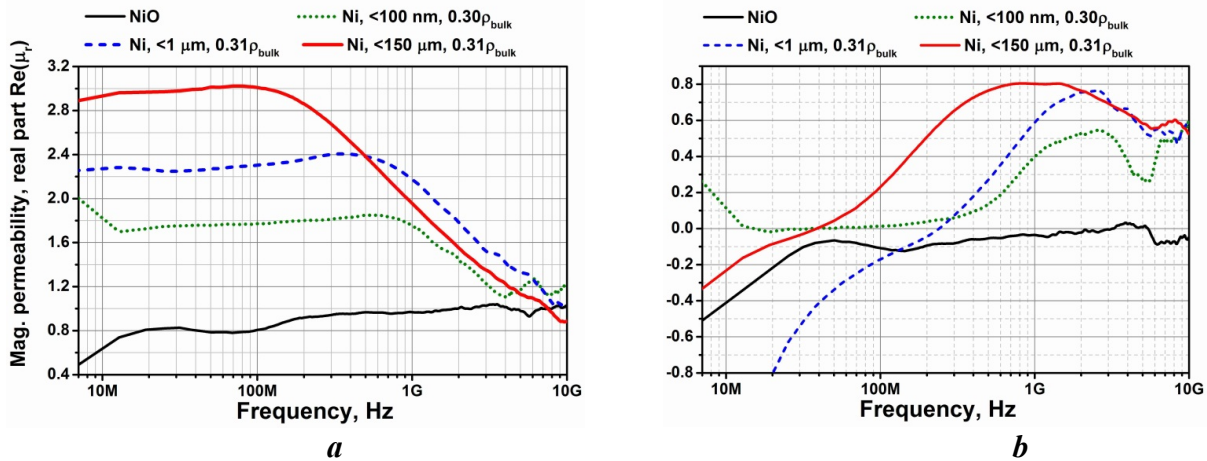


Fig. 3. Frequency dependence of real (*a*) and imaginary (*b*) parts of magnetic permeability for nickel powders having different grain size.

Monodisperse 8 nm diameter surfactant-coated Co nanoparticles were washed and dried to form a nanopowder, and the magnetic permeability and dielectric permittivity were then measured from 300 kHz to 10 GHz. To observe the influence of nanoparticle oxidation on air, the powder was left in the sample holder for 5 days. Oxidation decreased the real part of the

permeability, and the decrease in the imaginary part of the permeability was likely due to decreasing eddy current losses

1. K. Yamamoto, S. A. Majetich, M. R. McCartney, M. Sachan, S. Yamamuro, and T. Hirayama, *Appl. Phys. Lett.* **93**, 082502 (2008).
2. M. Sachan, C. Bonnoit, S. A. Majetich, Y. Ijiri, P. O. Mensah-Bonsu, J. A. Borchers, and J. J. Rhyne, *Appl. Phys. Lett.* **92**, 152503 (2008).
3. K. Yamamoto, C. R. Hogg, S. Yamamuro, T. Hirayama, S. A. Majetich, *Appl. Phys. Lett.* **98**, 072509 (2011).
4. A. M. Nicholson and G. F. Ross, *IEEE Trans. Instrum. Meas.* **19**, 377-382 (1970)
5. W. B. Weir, *Proc. IEEE* **62**, 33-36 (1974)
6. J. Baker-Jarvis, E. J. Vanzura, W. A. Kissick, *IEEE Trans. Microwave Theory and Techniques* **38** 1096-1103 (1990).
7. A. Sharma and M. N. Afsar, *J. Appl. Phys.* **109**, 07A503 (2011).

### **Future Plans:**

Work will continue on high frequency measurements on nanoparticle composites, with emphasis on increasing the volume fraction and minimizing porosity in order to increase the permeability and enable testing of the blocking frequency model. We will also investigate frequency-dependent magnetoresistance measurements of individual particles and assemblies up to 50 MHz to characterize the medium frequency behavior in greater detail.

### **Publications Supported by DOE Research 2010-2012:**

*Polarization-analyzed small-angle neutron scattering. II. Mathematical angular analysis*, K. Krycka, J. Borchers, Y. Ijiri, R. Booth, and S. Majetich, *J. Appl. Crystallogr.* **45**, 554-565 (2012).

*The Magnetocaloric Effect in Thermally Cycled Polycrystalline Ni-Mn-Ga*, Ryan A. Booth and Sara A. Majetich, *J. Appl. Phys.* **111**, 07A933 (2012).

*Internal Magnetic Structure of Magnetite Nanoparticles Below Their Blocking Temperature*, K. L. Krycka, J. A. Borchers, R. Booth, C. R. Hogg, Y. Ijiri, W. C. Chen, S. M. Watson, M. Laver, T. R. Gentile, S. Harris, L. R. Dedon, J. J. Rhyne, and S. A. Majetich, *J. Appl. Phys.* **107**, 09B525 (2010).

*Preferential Crystallographic Alignment in Polycrystalline MnP*, R. A. Booth, M. Marinescu, J. F. Liu, and S. A. Majetich, *J. Magn. Magn. Mater.* **322**, 2571-2574 (2010).

*Visualizing Core-Shell Magnetic Interplay within Iron Oxide Nanoparticles*, K. L. Krycka, J. A. Borchers, J. A. Borchers, Y. Ijiri, W. C. Chen, S. M. Watson, M. Laver, T. R. Gentile, S. Harris, L. R. Dedon, J. J. Rhyne, and S. A. Majetich, *Phys. Rev. Lett.* **104** 207203 (2010).

*Error analysis for small angle neutron scattering datasets using Bayesian inference*, Chip Hogg, Sara Majetich, Joseph B. Kadane, and Jong-Soo Lee, *Bayesian Analysis* **5**, 1-34 (2010).

# Understanding the Spin-Lattice Coupling in Multiferroic Oxides

Trevor A. Tyson, Department of Physics  
New Jersey Institute of Technology, Newark NJ 07102-1982  
Email: tyson@adm.njit.edu

**Abstract and Program Scope:** Multiferroic oxides (such as  $RMnO_3$  and  $RMn_2O_5$  (RE=rare earth, Sc, Y)) are a class of materials which are simultaneously ferroelectric and ferromagnetic. The possibility of coupling the magnetic and electric properties will enable new functions. These capabilities will possibly lead to devices in which ferroelectric memory can be written with magnetic fields or magnetic bits can be written by an electric field. However, the detailed mechanism behind the coupling of the spin and atomic degrees of freedom in these materials is not well understood. In this proposal we are conducting structural measurements on multiple length scales in the presence of magnetic and electrical fields in order to ascertain the mechanism behind the spin-lattice coupling. In this phase of the project, we have focused on the small ion  $RMnO_3$  systems such as  $InMnO_3$  and  $ScMnO_3$  with high  $T_N$  values. The corresponding E-type perovskite phases of the same materials are also being synthesized (under high pressure) and studied. DFT simulations have been conducted to ascertain the ground state magnetic structures. The stable magnetic ground states at different pressures and total polarization have been predicted. The detailed origin of the onset of ferroelectricity in hexagonal  $RMnO_3$  was determined by combined local structural measurements and molecular dynamics simulation at high temperature. **This work is supported by DOE Grants DE-FG02-07ER46402.**

## Results from Research on Multiferroics

### A. Observation Electric Polarization in $InMnO_3$

The hexagonal manganites are part of a class of materials which exhibit coupled ferromagnetism and ferroelectricity (multiferroic systems). Hexagonal phase  $RMnO_3$  is found for small radius ions ( $R=Ho, Er, Tm, Yb, Lu$  and also  $Y$  and  $Sc$ ). From an application's perspective, these materials have attracted much attention as data storage media in nonvolatile random access memory. These devices have the advantage of low power consumption and decreased memory cell size over existing technology because the electric charge induced by the remnant polarization controls the conductivity of the Si substrate where they are deposited. The  $YMnO_3$  system has been studied extensively and is currently being utilized in device applications.

Tuning this  $RMnO_3$  system by replacing the R ion with other species or multiple species serves as a possible path to enhance the ferroelectric properties of these materials. One system which is being studied is the  $R = In$  system. However, the room temperature structure and ferroelectric properties of  $InMnO_3$  are still not well understood. Structural measurement on polycrystalline materials have yielded conflicting results.

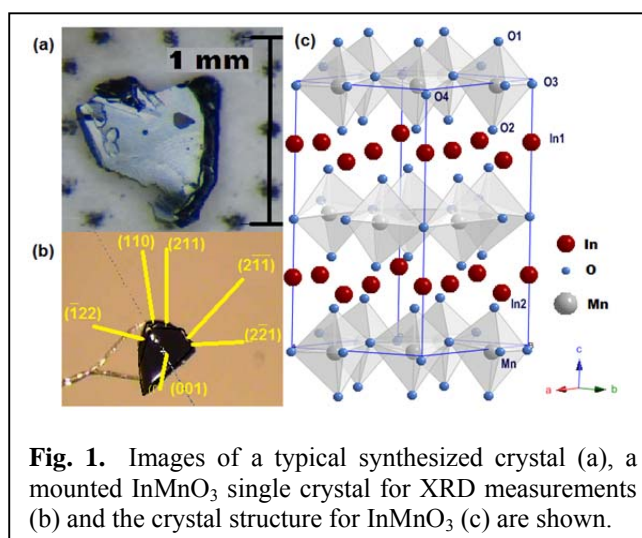


**Fig. 1.** Images of a typical synthesized crystal (a), a mounted  $InMnO_3$  single crystal for XRD measurements (b) and the crystal structure for  $InMnO_3$  (c) are shown.

To fully understand the properties of the  $\text{InMnO}_3$  system, single crystal samples were grown and the structure as well as the thermal and electronic properties was studied. The space group of single crystal material is found to be consistent with the previous neutron powder diffraction measurements and a material with a  $\text{P6}_3\text{cm}$  polar space group [Fig. 1(c)] is revealed. Magnetic ordering temperatures are identified by heat capacity measurements. Polarization measurements show a finite value of polarization for the first time. Point charge and density functional theory calculations of the electric polarization reveal an upper limit of  $7.8 \mu\text{C}/\text{cm}^2$  on the electrical polarization, which is 26% larger than that for  $\text{YMnO}_3$ .

Fig. 2(a) shows the near edge x-ray absorption spectra of a series of hexagonal  $\text{RMnO}_3$  systems ( $\text{R}=\text{Sc}, \text{Y}$  and  $\text{Lu}$ ) compared to  $\text{InMnO}_3$ . Note the similarity in shape of all of the spectra indicating equivalent local structure and local symmetry. Compared to the other samples, no additional peaks appear in the  $\text{R}=\text{In}$  spectrum. However, the  $\text{InMnO}_3$  spectrum has lower amplitude and is broadened. This indicates a lower level of long-range order. Note the shift in the position of the main peak of the  $\text{ScMnO}_3$  to higher energy compared to the other samples. This shift shows that the Mn-O bond distance is shorter in this system than the others according to the ‘‘Natoli’s Rule’’ ( $E_p - E_0$ ) $R^2 = \text{const.}$ ).

Single crystal structure solution was conducted after the data were corrected for absorption by face indexing. Refinements with respect to  $\text{P-3c}$ ,  $\text{P3c1}$  and  $\text{P6}_3\text{cm}$  space groups were conducted. Use of the non-polar space group  $\text{P-3c}$  yielded  $R_1 = 6.12\%$  and  $wR_2 = 15.6\%$  with ratio of number of  $F_0 > 4 \sigma(F_0)$  values to free parameters of  $199/21 = 9.5$  while the polar space group  $\text{P3c1}$  yielded  $R_1 = 4.81\%$  and  $wR_2 = 12.8\%$  and ratio of number of  $F_0 > 4 \sigma(F_0)$  values to free parameters of  $371/40 = 9.3$ . Analysis of the coordinates revealed that this space group solution ( $\text{P3c1}$ ) corresponded to the higher space group  $\text{P6}_3\text{cm}$ .

Polarization hysteresis loops were calculated by integrating the total transferred charge during application of a bipolar triangular voltage waveform, then dividing the remanent charge by the projected area. We examined a large range of electric fields from 64 kV/cm to 216 kV/cm and displaying the P-E loops, which give a remanent polarization (Pr) of  $\sim 4.4 \mu\text{C}/\text{cm}^2$  for the saturated loop at room temperature shown in Fig. 3. The remanent polarization exhibits negligible frequency dependence in the range 500 Hz to 2000 Hz. The polarization was estimated by the point-charge model with the experimental structure derived above and using DFT to estimate the reference paraelectric structure. The polarization amplitude of  $7.8 \mu\text{C}/\text{cm}^2$  on  $\text{InMnO}_3$  single crystal was obtained indicating a theoretical upper limit  $\sim 26\%$  larger than that for  $\text{YMnO}_3$  (near  $6.2 \mu\text{C}/\text{cm}^2$ ). Our measurement gave a value of  $\sim 4.4 \mu\text{C}/\text{cm}^2$  for the remanent

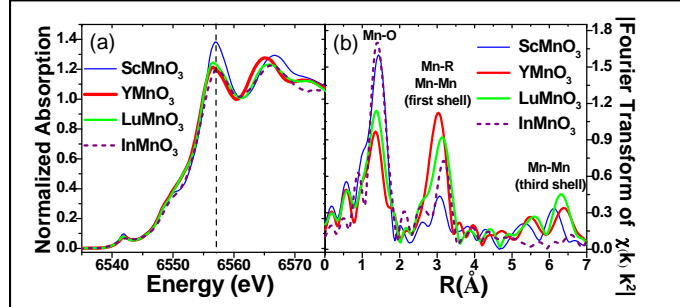


**Fig. 2.** (a) Comparison of the Mn K-edge near-edge spectra of  $\text{RMnO}_3$  ( $\text{R}=\text{Sc}, \text{Y}, \text{Lu}, \text{In}$ ) showing the similar structure for the entire series of compounds with  $\text{InMnO}_3$  (powdered single crystals) as dashed line. (b) Local structure at the Mn sites from the extended x-ray absorption data. Note the reduced amplitude for the In systems for the distant shells (Mn-Mn third shell).

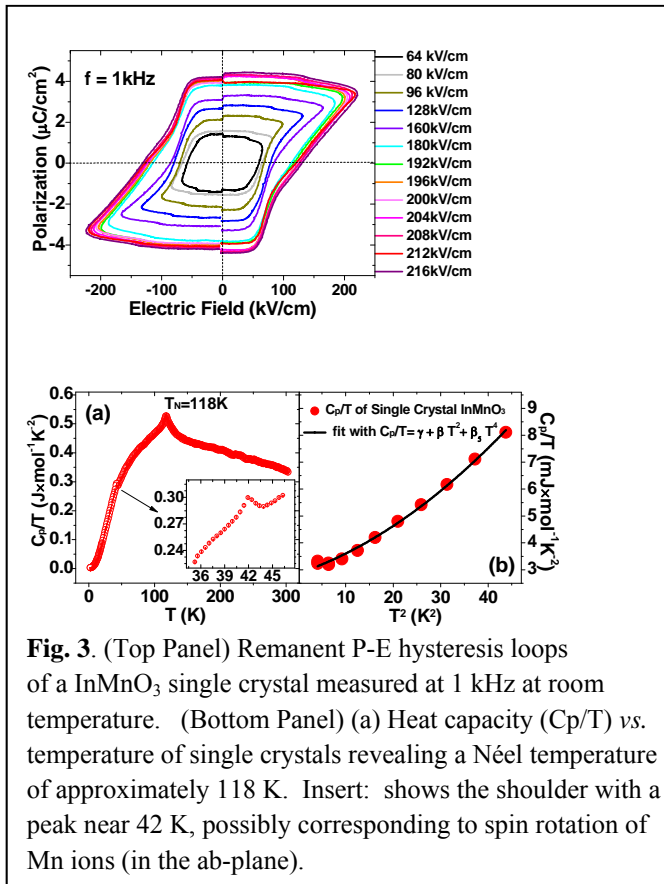


**Fig. 3.** (Top Panel) Remanent P-E hysteresis loops of a  $\text{InMnO}_3$  single crystal measured at 1 kHz at room temperature. (Bottom Panel) (a) Heat capacity ( $C_p/T$ ) vs. temperature of single crystals revealing a Néel temperature of approximately 118 K. Insert: shows the shoulder with a peak near 42 K, possibly corresponding to spin rotation of Mn ions (in the ab-plane).

polarization at room temperature. The smaller value is possibly due to defect/voids formed during the quenching procedure.

Finally, for comparison with other systems, the heat capacity of  $\text{InMnO}_3$  single crystals was measured giving a Néel temperature near 118 K. We have also found a peak near 42 K consistent with the spin rotation on Mn seen in  $\text{HoMnO}_3$ . However, we note that nanoscale  $\text{LuMnO}_3$  with a closed 4f shell at the R site exhibits the same reorientation transition near 42 K and indicates the spin orientation may not be only driven by the Mn-R spin interactions as suggested by earlier studies.

## B. Perovskite $\text{RMnO}_3$

The orthorhombic perovskite materials with small ion size (such as  $\text{HoMnO}_3$  and  $\text{LuMnO}_3$ ) have become a topic of keen interest because of the possible existence of mainly electronically driven ferroelectricity and is a topic of intense study. However, no detailed structural studies have been conducted on these systems assessing the relative weights of the charge and ion displacement components of ferroelectricity in these systems. Examining the full range of systems as a function of R ion size may lead to the discovery of an optimal system with high electric polarization.

We report a new monoclinic  $\text{ScMnO}_3$  phase with perovskite type structure synthesized from hexagonal  $\text{ScMnO}_3$  under high-pressure and high-temperature conditions. Phase transition behavior of this monoclinic  $\text{ScMnO}_3$  were examined by in-situ x-ray diffraction on heating from room temperature to 1400 K. Three phase transitions, monoclinic  $\rightarrow$  orthorhombic  $\rightarrow$  hexagonal, were identified. Based on combined room temperature XRD structural measurements on single crystals and DFT simulations, we predict a polarization value in this system approaching that of  $\text{HoMnO}_3$  and  $\text{LuMnO}_3$  without the need for rare earth ions. Overall, perovskite phase  $\text{HoMnO}_3$ ,  $\text{LuMnO}_3$  and  $\text{ScMnO}_3$  have been synthesized. DFT studies are in progress to evaluate the most stable phase of this system for a broad range on ion sizes. The pressure dependence of the stable magnetic phase is being evaluated by combined high pressure structural measurements and DFT simulations. Preliminary results suggest the E-type phase stability is enhanced with pressure or for small ion size.

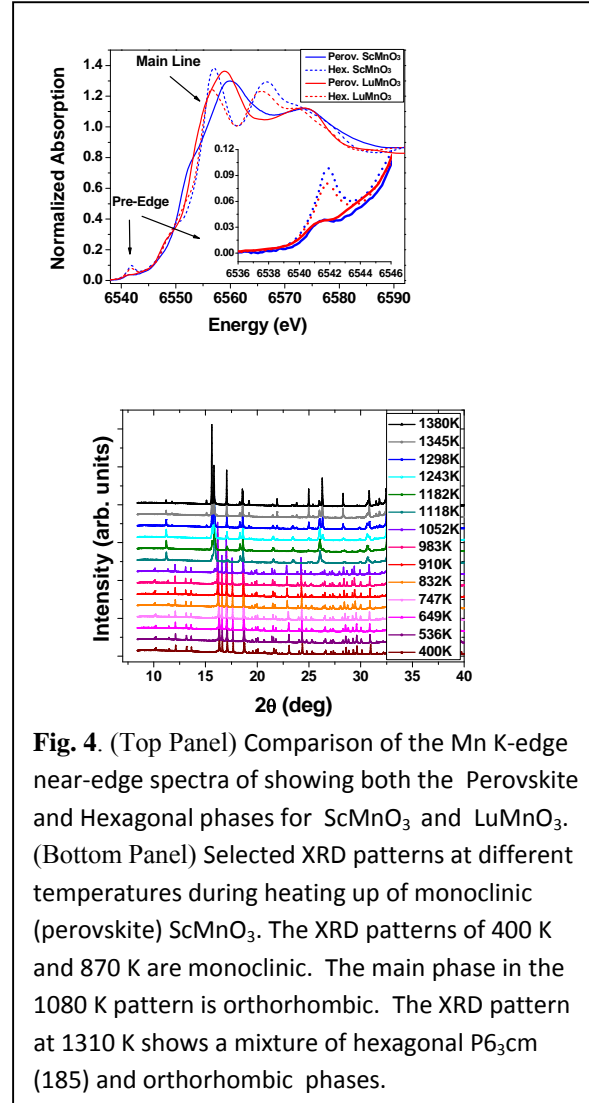


**Fig. 4.** (Top Panel) Comparison of the Mn K-edge near-edge spectra of showing both the Perovskite and Hexagonal phases for  $\text{ScMnO}_3$  and  $\text{LuMnO}_3$ . (Bottom Panel) Selected XRD patterns at different temperatures during heating up of monoclinic (perovskite)  $\text{ScMnO}_3$ . The XRD patterns of 400 K and 870 K are monoclinic. The main phase in the 1080 K pattern is orthorhombic. The XRD pattern at 1310 K shows a mixture of hexagonal  $P6_3cm$  (185) and orthorhombic phases.

## Application of Developed Methods to Superconductors and complex oxide Thermoelectrics $\text{K}_{0.8}\text{Fe}_{1.6+x}\text{Se}_2$ Superconductor

We have utilized the techniques developed for this project to study the relation between the structure and superconductivity in  $\text{K}_{0.8}\text{Fe}_{1.6+x}\text{Se}_2$  as a collaboration with Dr. Q. Li (Brookhaven Nat. Lab.). Temperature dependent measurements at the Fe sites show that the Fe-Se atomic correlation follows that of the Fe-As correlation in the superconductor  $\text{LaFeAsO}_{0.89}\text{F}_{0.11}$  - having the same effective Einstein temperature (stiffness). In  $\text{K}_{0.8}\text{Fe}_{1.6+x}\text{Se}_2$ , the nearest neighbor Fe-Fe bonds has a lower Einstein temperature and higher structural disorder than in  $\text{LaFeAsO}_{0.89}\text{F}_{0.11}$ . The moderate Fe site and high K site structural disorder is consistent with the high normal state resistivity seen in this class of materials. For higher shells, an enhancement of the second nearest neighbor Fe-Fe correlation is found just below  $T_c$  possibly due to changes in magnetic or local structural ordering.

### Thermoelectric $[\text{Ca}_2\text{CoO}_3][\text{CoO}_2]_{1.61}$ (referred to as $\text{Ca}_3\text{Co}_4\text{O}_9$ )

The tools developed were also applied to the thermoelectric system  $\text{Ca}_3\text{Co}_4\text{O}_9$ . Temperature dependent electrical resistivity, crystal structure and heat capacity measurements reveal a resistivity drop and

metallic to insulating transition corresponding to first order structural phase transition near 400 K in  $\text{Ca}_3\text{Co}_4\text{O}_9$ . Reduced resistivity associated with this first order phase transition from metallic to insulating behavior enhances the thermoelectric properties at high temperatures and points to the metallic to insulating transition as a mechanism for improved  $ZT$  in this high temperature thermoelectric oxide.

Resistivity and Seebeck coefficient measurements on  $\text{Ca}_3\text{Co}_{4-x}\text{Fe}_x\text{O}_9$  ( $x=0, 0.05, 0.1, 0.2$  and  $0.25$ ) reveal enhanced thermoelectric performance with an optimal  $x$  value of  $0.2$ . X-ray diffraction measurements show continuous Fe doping into the host lattice while X-Ray absorption experiments reveal that Fe substitutes for Co in the  $\text{Ca}_2\text{CoO}_3$  (rock salt) block as  $\text{Fe}^{3+}$  which results in electron doping and decreases the carrier concentration. The competition between carrier concentration and mobility induced by electron doping and structural change results in the lowest resistivity at  $x=0.2$ . materials with improved  $ZT$  in complex oxide systems.

### **Future Plans for this Project**

We plan to complete continue our exploration of the dependence of magnetic ordering temperature on the structure of the hexagonal  $\text{RMnO}_3$  system by examining the temperature dependent structure of the small ion systems such as hexagonal  $\text{InMnO}_3$  ( $T_N \sim 120$  K) and  $\text{ScMnO}_3$  ( $T_N \sim 130$  K, compared with  $\text{YMnO}_3$  with  $T_N \sim 70$  K) and their alloys in order to find ways to increase  $T_N$  and the coupling between the magnetization and electric polarization. The effect of pressure (hydrostatic pressure) and strain (from film substrates) on the electric polarization of orthorhombic phase  $\text{RMnO}_3$  (E-type magnetic order) is being evaluated to determine methods to enhance electric polarization. DFT simulations of the magnetic ordering as a function pressure will be conducted. A new system recently being discovered to have strong coupling of the magnetization and electric polarization  $\text{HoAl}_3(\text{BO}_3)_4$  will be examined for the nature of the coupling via magnetic field dependent structural measurements, heat capacity and magnetization studies to elucidate the mechanism for the high low temperature electrical polarization at high field ( $\sim 7$  T). To understand the longer range structure in this materials, total x-ray and Neutron scattering (diffuse + Bragg Scattering) on powder samples will be conducted between 4 K and 300 K to complement the XAFS studies already carried out. Modeling of the data will be used to determine the correct unit cells, space groups and local distortions as a function of temperature from the low temperature magnetic ordered phases. DFT based simulations of phonon DOS will be compared with inelastic neutron scattering measurements to look for low energy phonons and also identify the closely lying magnetic excitation (at the same energy)

### **Publications under this Grant**

1. T. A. Tyson, T. Wu, H. Y. Chen, J. Bai, K. H. Ahn, K. I. Pandya, S. B. Kim and S. W. Cheong, "Measurements and ab initio molecular dynamics simulations of the high temperature ferroelectric transition in hexagonal  $\text{RMnO}_3$ ", *J. Appl. Phys.* **110**, 084116 (2011).
2. T. A. Tyson, T. Yu, S. J. Han, M. Croft, G. D. Gu, I. K. Dimitrov and Q. Li, "Local structure of the superconductor  $\text{K}_0.8\text{Fe}_{1.6+x}\text{Se}_2$ : evidence of large structural disorder", *Phys. Rev. B* **85**, 024504 (2012).
3. T. Wu, T. A. Tyson, H. Chen, J. Bai, H. Wang, and C. Jaye, "A structural change in  $\text{Ca}_3\text{Co}_4\text{O}_9$  associated with enhanced thermoelectric properties", *J. Phys. Cond. Mat.* **24**, 455602 (2012).
4. X. Luo, Y. S. Oh, A. Sirenko, P. Gao, T. A. Tyson, K. Char, and S. W. Cheong, "High Carrier Mobility in Transparent  $\text{Ba}_{1-x}\text{La}_x\text{SnO}$  Crystals with Wide Band Gap", *Appl. Phys. Lett.* **100**, 172112 (2012).
5. P. Gao, Z. Chen, T. A. Tyson, T. Wu, K. H. Ahn, Z. Liu, R. Tappero, S. B. Kim and S. W. Cheong, "High-pressure structural stability of multiferroic hexagonal  $\text{RMnO}_3$  ( $R = \text{Y, Ho, Lu}$ )", *Phys. Rev. B: Condens. Matter Mater. Phys.* **83**, 224113/224111-224113/224119 (2011).
6. P. Gao, H. Y. Chen, T. A. Tyson, Z. X. Liu, J. M. Bai, L. P. Wang, Y. J. Choi and S. W. Cheong, "Observation of anomalous phonons in orthorhombic rare-earth manganites", *Applied Physics Letters* **97** (26), 262905 (2010).
7. T. A. Tyson, T. Wu, K. H. Ahn, S.-B. Kim and S.-W. Cheong, "Local spin-coupled distortions in multiferroic hexagonal  $\text{HoMnO}_3$ ", *Phys. Rev. B: Condens. Matter Mater. Phys.* **81**, 054101 (2010).
8. V. V. Poltavets, K. A. Lokshin, A. H. Nevidomskyy, M. Croft, T. A. Tyson, J. Hadermann, G. Van Tendeloo, T. Egami, G. Kotliar, N. ApRoberts-Warren, A. P. Dioguardi, N. J. Curro and M. Greenblatt, "Bulk Magnetic Order in a Two-Dimensional  $\text{Ni}^{1+}/\text{Ni}^{2+}$  ( $d_9/d_8$ ) Nickelate, Isoelectronic with Superconducting Cuprates", *Physical Review Letters* **104** (20), 206403 (2010).
9. T. A. Tyson, T. Wu, J. C. Woicik, B. Ravel, A. Ignatov, C. L. Zhang, Z. Qin, T. Zhou and S. W. Cheong, "Temperature-dependent local structure of  $\text{LaFeAsO}_{1-x}\text{Fx}$ : Probing the atomic correlations", *Journal of Applied Physics* **108** (12), 123715 (2010).
10. T. A. Tyson, T. Wu, K. H. Ahn, S.-B. Kim and S.-W. Cheong, "Local spin-coupled distortions in multiferroic hexagonal  $\text{HoMnO}_3$ ", *Phys. Rev. B: Condens. Matter Mater. Phys.* **81**, 054101 (2010).

## **Program Title: Enhancement of Magnetoelectric Coupling in Nanoengineered Oxide Films and Heterostructures by Laser MBE**

**Principle Investigator: Xiaoxing Xi**

**Address: Temple University, Barton Hall, 1900 N. 13th Street, Philadelphia, PA 19122**

**Email: xiaoxing@temple.edu**

### **Program Scope**

The objective of this project is the enhancement of magnetoelectric coupling in nanoengineered oxide films and heterostructures that are predicted to show strong magnetoelectric coupling via control of oxygen octahedron rotations. The main focuses of the project are the  $(\text{BaTiO}_3)_n/(\text{CaMnO}_3)_n$  short-period superlattices, which have been predicted to exhibit interface-induced giant magnetoelectric coupling.

According to a first-principles calculation,  $\text{BaTiO}_3$ , which is highly resistant to oxygen octahedral rotations and strongly ferroelectric, suppresses the  $\text{MnO}_6$  octahedral rotation in  $\text{CaMnO}_3$ , leading to a ferroelectric ground state whose polarization depends strongly on the magnetic ordering. The enhancement of the magnetoelectric coupling is the strongest for the shortest superlattice period  $n = 1$ . This mechanism is different from the enhancement of magnetoelectric coupling by the strain and charge mediation at oxide interfaces, which has been studied extensively. It represents a new and novel paradigm in the search for strong multiferroic materials.

The  $(\text{BaTiO}_3)_n/(\text{CaMnO}_3)_n$  short-period superlattices will be grown by laser MBE from separate oxide targets. This approach is different from laser MBE practiced in most other labs, where compound targets are used to grow films (for example, growing  $\text{SrTiO}_3$  films from a  $\text{SrTiO}_3$  target). In our research, targets of  $\text{BaO}$ ,  $\text{TiO}_2$ ,  $\text{CaO}$ , and  $\text{MnO}_2$  will be used and ablated alternately to deposit one atomic layer at a time. For example, the basic sequence of the atomic layer deposition for a  $(\text{BaTiO}_3)_1/(\text{CaMnO}_3)_1$  superlattices will be  $\text{BaO-TiO}_2\text{-CaO-MnO}_2$ , which repeats itself. The atomic layer-by-layer mode of the laser MBE growth is superior to the conventional laser MBE in achieving stoichiometry control and more suitable for the synthesis of the short-period superlattices and layered perovskites.

### **Recent Progress**

#### *1. Atomic layer-by-layer growth of $\text{SrTiO}_3$ by laser MBE from separate targets*

A technical key element for this project is the atomic layer-by-layer growth of the nanoscale heterostructure by laser MBE from separate targets. This is a completely different approach of laser MBE from the common practices. It mimics the alternate monolayer growth in reactive MBE. For example, to grow  $\text{SrTiO}_3$  films, separate  $\text{SrO}$  and  $\text{TiO}_2$  targets are used. The targets are switched back and forth to be ablated by the pulsed laser beam alternately, thus depositing one atomic layer at a time. As in reactive MBE, the intensity oscillation of the RHEED diffraction streak is used to help achieve atomic level control. Figure 1 shows RHEED intensity oscillation taken from the 1st order (#2, #3) and 2nd order (#4, #5) diffraction spots

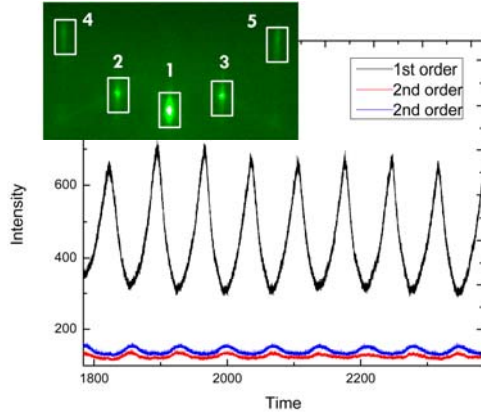


Fig. 1 RHEED intensity oscillation taken from the 1st order (#2, #3) and 2nd order (#4, #5) diffraction spots during the growth of a  $\text{SrTiO}_3$  film from SrO and  $\text{TiO}_2$  targets.

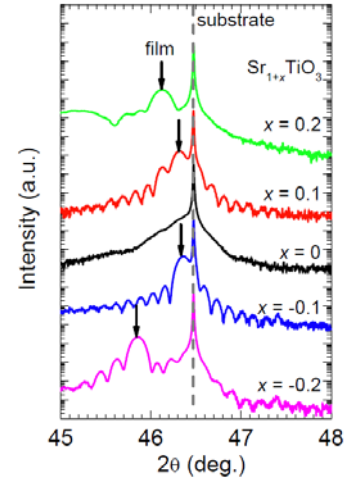


Fig. 2 XRD  $\theta$ - $2\theta$  scans around the (200) peak of 5  $\text{Sr}_{1+x}\text{TiO}_3$  films.

during the growth of a  $\text{SrTiO}_3$  film from SrO and  $\text{TiO}_2$  targets. Each time the SrO target is ablated, the RHEED intensity increases. When the  $\text{TiO}_2$  layer is being deposited, the RHEED intensity decreases.

Figure 2 shows x-ray diffraction  $\theta$ - $2\theta$  scans around the (200) peak of five  $\text{Sr}_{1+x}\text{TiO}_3$  films of different compositions controlled by the different numbers of laser pulses on the SrO and  $\text{TiO}_2$  targets, respectively. When the exact 1:1 Sr/Ti ratio is achieved, the film peak overlaps with that of the substrate. Off-stoichiometric films show lattice expansion and smaller film diffraction angles. However, UV Raman spectroscopy shows that strong first-order Raman peaks are observed even in the stoichiometric film (Sr/Ti ratio is 1:1), which indicates that there exists broken inversion symmetry in the films. The problem is most likely the atomic layer coverage. Even though the 1:1 stoichiometry is achieved, each atomic layer may not be 100% covered: more or less material than required by a complete atomic layer may be delivered to the substrate.

To achieve 100% coverage, we have pursued the active control of the number of laser pulses based on the close real time inspection of the RHEED intensity oscillation. We varied the number of laser pulses during growth of each layer to prevent beating of the RHEED intensity. Figure 3 shows the number of laser pulses on each target for one atomic layer of SrO or  $\text{TiO}_2$  as the film grew to more layers. For example, the number of laser pulses for each SrO layer was around 270 at the beginning, dropped to around 180, and drifted down to around 130. This may arise from the fluctuation of the laser energy or the nonuniformity of the targets, as issue to be addressed in the future research. Such active control has achieved much better quality films. Figure 4 shows XRD  $\theta$ - $2\theta$  scans for several stoichiometric  $\text{SrTiO}_3$  films in comparison to the  $\text{SrTiO}_3$  substrate diffraction peak. The sample GZ101 did not employ the active control of laser pulses, and its spectrum shows a shoulder around the substrate peak, indicating defects. The bottom three samples are grown with the active control of laser pulses. They show better quality, in particular sample 121016a, whose diffraction spectrum is indistinguishable from that of the substrate peak.

## 2. Atomic layer-by-layer growth of $\text{LaAlO}_3$ by laser MBE from separate targets

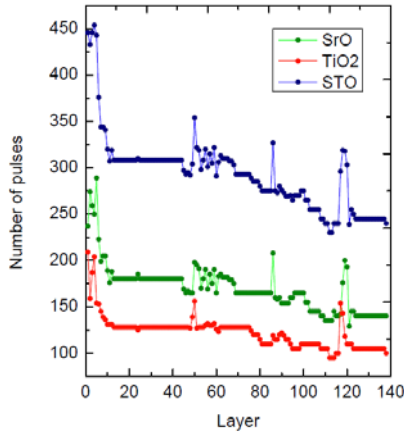


Fig. 3 Adjustment of the number of laser pulses on SrO and TiO<sub>2</sub> targets to achieve 100% atomic layer coverage.

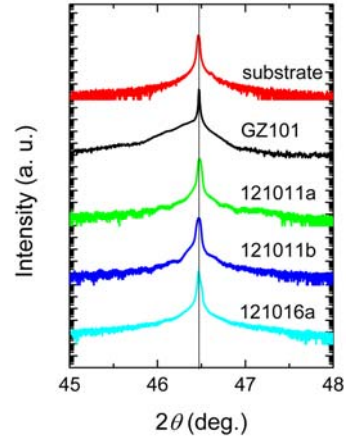


Fig. 4 XRD spectra of stoichiometric SrTiO<sub>3</sub> films grown by laser MBE from separate oxide targets.

The atomic layer-by-layer growth by laser MBE from separate oxide targets is further used for LaAlO<sub>3</sub> films. La<sub>2</sub>O<sub>3</sub> and Al<sub>2</sub>O<sub>3</sub> targets are used and switched back and forth to be ablated by the pulsed laser beam alternately, thus depositing one atomic layer at a time. Figure 5 shows RHEED intensity oscillation taken during the growth. Each time the Al<sub>2</sub>O<sub>3</sub> target is ablated, the RHEED intensity increases. When the LaO layer is being deposited, the RHEED intensity decreases. Figure 6 shows an XRD spectrum of a stoichiometric LaAlO<sub>3</sub> film grown by laser MBE from separate oxide targets and compared to that of the LaAlO<sub>3</sub> substrate. The film peak overlaps with that of the substrate, indicating stoichiometry in the film.

### 3. Stoichiometry of SrTiO<sub>3</sub> films grown by pulsed laser deposition

Pulsed laser deposition (PLD) is one of the most widely used growth techniques for oxide thin films to a large extent because of the ease of reproducing the target composition in films.

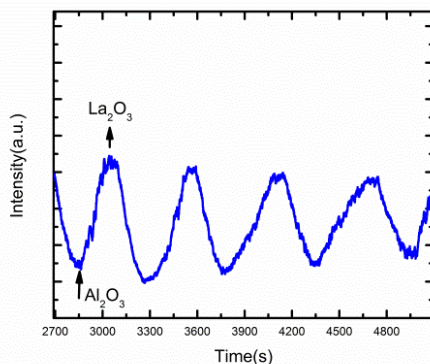


Fig. 5 RHEED intensity oscillation from the diffraction spots during the growth of LaAlO<sub>3</sub> from LaO and Al<sub>2</sub>O<sub>3</sub> targets.

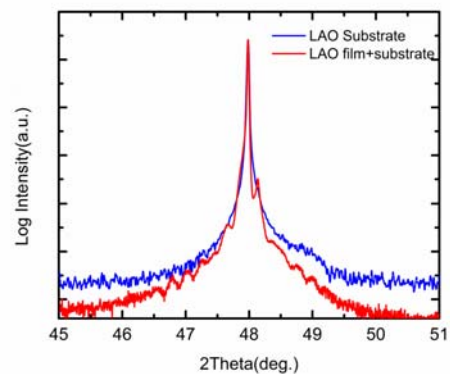


Fig. 6 XRD spectrum of stoichiometric LaAlO<sub>3</sub> film grown by laser MBE from separate oxide targets.

However, it has been shown that stoichiometric SrTiO<sub>3</sub> films can only be obtained under certain conditions. We have investigated the effects of laser energy density and oxygen pressure on the cation stoichiometry of homoepitaxial (001) SrTiO<sub>3</sub> thin film grown by pulsed laser deposition. Figure 7 shows the results for 25 samples in a contour map of the lattice expansion  $\Delta c$  as functions of laser energy density and oxygen pressure. Further, using the published result of the relationship between the  $c$ -axis expansion and the Sr off-stoichiometry  $x$ , the  $|x|$  values in Sr<sub>1+x</sub>TiO<sub>3</sub> are also shown in the figure. From the figure, we find that all the films deposited at 10<sup>-1</sup> Torr have  $|x| < |0.04 \pm 0.05|$ , and all the films deposited with a laser energy density of 0.9 J/cm<sup>2</sup> have  $|x| < |0.05 \pm 0.05|$ .

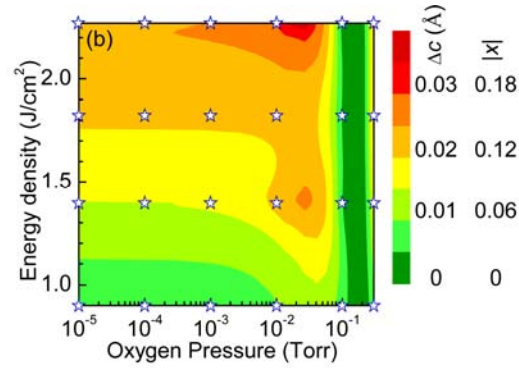


Fig. 7 Contour map of  $c$ -axis expansion  $\Delta c$  and Sr off-stoichiometry  $|x|$  in Sr<sub>1+x</sub>TiO<sub>3</sub> films for different laser energy densities and oxygen pressures.

### Future Plan

Continue the establishment of atomic layer-by-layer growth of oxide films by laser MBE from separate targets. Use prototypical materials such as SrTiO<sub>3</sub> and LaAlO<sub>3</sub> to firmly establish the growth methodology in terms of RHEED intensity oscillation-assisted active growth control.

Atomic layer-by-layer growth of BaTiO<sub>3</sub> and CaMnO<sub>3</sub> films by laser MBE from separate targets. The behaviors of the RHEED intensity oscillation, in particular for CaMnO<sub>3</sub>, will be established.

Growth of (BaTiO<sub>3</sub>)<sub>n</sub>/(CaMnO<sub>3</sub>)<sub>n</sub> short-period superlattices by laser MBE from separate targets. Structural, electrical, and magnetic characterizations of the superlattice samples.

### Publications of DOE sponsored research (2011-2012)

1. A. Bruchhausen, A. Fainstein, S. Tinte, A. Soukiassian, D. G. Schlom, X. X. Xi, Coupling between Light and Terahertz-Frequency Acoustic Phonons in Ferroelectric BaTiO<sub>3</sub>/SrTiO<sub>3</sub> Superlattices, *Chin. J. Phys.* 49, 159 (2011).
2. G. Z. Liu, Q. Y. Lei, and X. X. Xi, Stoichiometry of SrTiO<sub>3</sub> films grown by pulsed laser deposition, *Appl. Phys. Lett.* 100, 202902 (2012).
3. Q. Y. Lei, G. Z. Liu, and X. X. Xi, Structural characterization of homoepitaxial SrTiO<sub>3</sub> films grown by pulsed laser deposition, to appear in *Integrated Ferroelectrics*.
4. M. Golalikhani, Q. Y. Lei, G. Chen, J. E. Spanier, H. Ghassemi, C. L. Johnson, M. L. Taheri, and X. X. Xi, Stoichiometry of LaAlO<sub>3</sub> films grown on SrTiO<sub>3</sub> by pulsed laser deposition, to appear in *J. Appl Phys.*

# **Session VII**



**SOLID-STATE SOLAR-THERMAL ENERGY CONVERSION CENTER  
(S<sup>3</sup>TEC CENTER)**

**DOE Grant Number: DE-SC0001299/ DE-FG02-09ER46577**

**Massachusetts Institute of Technology (Lead Institution):** Gang Chen (PI and Director), M.S. Dresselhaus, E.A. Fitzgerald, P. Jarillo-Herrero, J. Joannopoulos, S.-G. Kim, K. A. Nelson, Y. Shao-Horn, C.A. Schuh, M. Soljacic, E.N. Wang  
**Boston College:** D. Broido, C.P. Opeil, Z.F. Ren  
**Oak Ridge National Laboratory:** O. Delaire, D.J. Singh  
**Rensselaer Polytechnic Institute:** G. Ramanath, T. Borca-Tasciuc

**Scope:** The S<sup>3</sup>TEC Center aims at advancing fundamental science and developing materials to harness heat from the sun and convert this heat into electricity via solid-state thermoelectric (Fig. 1a) and thermophotovoltaic (Fig.1b) technologies. Solar thermophotovoltaics (STPV) first uses solar radiation to raise the temperature of a terrestrial object, which then emits photons optimized to the bandgap of a photovoltaic cell to generate electricity. Solar thermoelectric energy conversion uses solar radiation to create a temperature difference across a solid-state material to generate electricity. These technologies have transformative potentials: solar thermophotovoltaics has a theoretical maximum efficiency of 85% with a single junction photovoltaic cell, while solar thermoelectrics could potentially reduce solar electricity generation cost. Thermoelectrics can also be used in combination with current solar technologies. Both thermoelectric and thermophotovoltaic technologies can be applied to terrestrial heat sources, for example, geothermal, waste heat from industrial processes, transportation and buildings. Thermoelectric devices can also be used for refrigeration and air-conditioning without producing any greenhouse gases.

The efficiency of solar thermoelectric generators (STEG) depends on spectrally selective surfaces with a high absorptance to the solar radiation and a low emittance in the infrared range. It also depends on the availability of thermoelectric materials with high figure of merit, which is linearly proportional to the electrical conductivity, the square of the Seebeck coefficient, and inversely proportional to the thermal conductivity. The S<sup>3</sup>TEC center aims at advancing thermoelectric materials through detailed experimental and theoretical studies of electron and phonon transport in nanostructures and bulk materials. Optical pump-probe and neutron

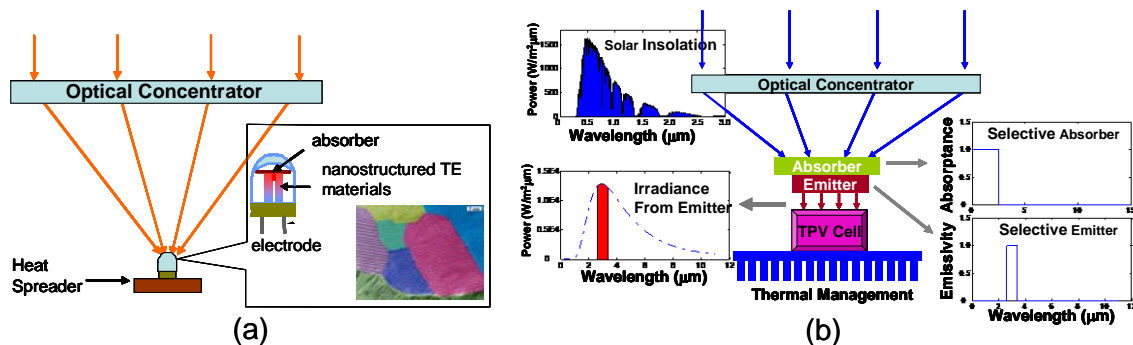


Figure 1 Solid-state solar-thermal energy conversion technologies to be pursued at the S<sup>3</sup>TEC Center (a) low-cost solar thermoelectric generators (STEGs) built from high performance nanostructured thermoelectric materials, and (b) high efficiency solar thermophotovoltaics achieved via precision spectral control.

scattering will be used to understand phonon transport, together with quantum and classical simulations of phonon transport in bulk and nanostructured materials. Electron spectroscopy will be performed in both thermoelectric materials and at the electrical contact regions, together with transport modeling. Both thin films and bulk nanostructures will be investigated, aiming at eventual large scale applications. Proof-of-principle prototypes will be built to demonstrate the concepts and the potential of the solar thermoelectric generation. Neutron spectrometers and STEM at Oak Ridge National Laboratory will be used for phonon spectroscopy and high-resolution imaging of interfacial structures. Fundamental studies will be conducted to understand high temperature stability of nanostructured materials and electrodes to thermoelectric materials.

Spectral control is not only important for STEG, but also crucial for STPV. Ideal selective absorbers should absorb all solar radiation, but not lose heat via their own thermal emission. In a solar TPV, broadband solar insolation is first absorbed by a surface, which heats the absorber to 1000-2000 °C. On the other side of the absorber is an emitter, which reradiates photons that are optimized to match a photovoltaic cell. The maximum efficiency of such solar TPV converters is 85.4%, very close to that of multi-junction cells with an infinite number of stages (86.8%), but it can be achieved with a single junction cell. Selective surfaces for solar TPV are more challenging due to their higher operational temperature. Key questions for solar TPV are: (1) How can we push structure design to reach the theoretical limit for selective absorbers and emitters? (2) Will the structure be stable at operational temperature? (3) How can we achieve high performance selective surfaces at low cost? Finally, (4) how can we deliver high photon flux in a narrow spectral band? Our proposed research includes selective absorber and emitter design, fabrication, testing, high temperature stability studies for both thermoelectric materials and spectral control structures, and solar TPV prototyping. Other novel concepts taking advantages of the high-temperature photonic spectral control are also being exploited.

### **Recent Progress:**

**Task 1: Thermoelectric Transport Simulation and Materials Design.** This task aims at understanding electron and phonon transport in thermoelectric materials and identifies promising materials and nanostructures. The theoretical and numerical works are closely coupled to experimental work in thermoelectric materials synthesis, optical and neutron spectroscopy, and transport measurements to provide closed loop feedback to the experimental effort. Key progress made includes: (1) using density functional theory (DFT) to guide the search of materials with promising thermoelectric figure-of-merit  $ZT$ ;<sup>1,2</sup> (2) developing first-principles based simulation approaches to compute phonon thermal conductivity<sup>3</sup> and successfully applying it to thermoelectric materials,<sup>4</sup> revealing details of the phonon scattering mechanisms; and (3) conceiving new concepts to improve electron performance such as modulation doping<sup>5</sup> and electron cloaking<sup>6</sup>, and experimentally demonstrating the modulation doping concept in 3D random nanostructures.

**Task 2: Spectroscopy.** The aim of this task is to probe the details of phonon and electron transport experimentally. There is an especially dire need for tools that better characterize phonons. Thermal conductivity measurements alone are not enough because the measured values are integral effects of contributions from many phonons. Experimental effort in this group is closely coupled to simulations in task 1 and to materials synthesis in task 3. Major achievements in this task are as follows. (1) Neutron spectroscopy in PbTe highlights the role of the proximity of PbTe to a ferroelectric lattice instability, which results in strongly anharmonic

phonons.<sup>7,8</sup> Experimental data for phonon linewidths in PbTe have been used to compare with first-principles computations of phonon lifetimes performed and showed good agreement.<sup>9</sup> (2) Two optical techniques to determine contributions from phonons with different mean free path values to the total thermal conductivity have been developed, one based on pump-probe thermoreflectance technique and the other based on transient grating experiment.<sup>10</sup> (3) Our team has recently observed coherent phonon heat conduction contribution in superlattices, opening up a potential way to further engineer thermal conductivity.<sup>11</sup>

**Task 3: Thermoelectric Materials Synthesis and Characterization.** Fundamental understandings on phonon and electron transports described in task 1 and task 2 provide guidance to engineer better thermoelectric materials. The thermoelectric materials synthesis and characterization efforts are geared towards developing materials synthesis methods and structural and property characterization tools to achieve anticipated enhancement in the thermoelectric figure of merit. Structure and property characterizations also provide feedback to theoretical and experimental efforts described in previous sections. Major achievements include (1) developing a microwave based wet-chemistry approach to synthesize nanoparticles and achieving high ZT values;<sup>12</sup> (2) experimental demonstration of the modulation concept; (3) improving the ZT values of half-Heuslers to above one;<sup>13,14</sup> (4) observation of resonant states in PbSe-based materials; and (5) fundamental understanding on materials stability and grain growth.<sup>15</sup>

**Task 4: High Temperature Photonics and Solar Thermophotovoltaic.** For solar TPV, the key is to control the absorption and re-emission of light. Selective absorbers that maximize the absorption and minimize the emission of thermal energy are needed on the side facing the sun, for both STPV and STEGs, and selective emitters are needed to emit photons near the bandgap of photovoltaic cells. A challenge is to maintain the stability of nanostructures fabricated for photon control during their high temperature operation. Major achievements include (1) designing and fabricating photon control structures that are stable at high temperatures,<sup>16,17</sup> (2) developing the angular photonic crystal concept for emission control.<sup>18,19</sup>

**Task 5 Prototyping of Proof-of-Principle Devices.** Device prototyping is important to S<sup>3</sup>TEC for several reasons. First, material properties will ultimately be validated through device performance. Second, thermoelectrics and TPV energy conversion are not proven technologies. Proof-of-principle demonstrations are therefore crucial to establish their viability for future solar energy conversion systems. In addition, fundamental challenges exist in engineering electrodes for thermoelectric devices since the interfaces are subject to high thermomechanical stresses and device performance demands low electrical and thermal contact resistance with strong interfacial bonding. Major achievements include (1) demonstration of a prototype solar thermoelectric generator with 4.6% efficiency at AM1.5 illumination condition without any optical concentration,<sup>20</sup> and (2) modeling and developing a STPV prototype device testing platform.

### **Journal Publications (over 110 publications from 2011-2012, only cited ones are listed)**

<sup>1</sup> Q. Zhang, F. Cao, K. Lukas, W. S. Liu, K. Esfarjani, C. Opeil, D. Broido, D. Parker, D. J. Singh, G. Chen, Z.F. Ren, "Study of the thermoelectric properties of lead selenide doped with boron, gallium, indium, or thallium," JACS, 134, 17731, 2012.

<sup>2</sup> D. Parker and D.J. Singh, "Very heavily electron-doped CrSi<sub>2</sub> as a high performance high-temperature thermoelectric material", New J. Phys. 14, 033045, 2012.

<sup>3</sup> K. Esfarjani, G. Chen, H. T. Stokes, "Heat Transport in Silicon from First-principles Calculations," Phys. Rev. B 84, 085204, 2011.

- <sup>4</sup> J. Shiomi, K. Esfarjani, G. Chen, "Thermal Conductivity of Half-Heusler Compounds from First Principle Calculations," *Phys. Rev. B* 84, 104302, 2011.
- <sup>5</sup> M. Zebarjadi, G. Joshi, G. Zhu, B. Yu, A. Minnich, Y. Lan, X. Wang, M. S. Dresselhaus, Z. F. Ren, G. Chen, "Power Factor Enhancement by Modulation Doping in Bulk Nanocomposites," *Nano Letters*, 11, 2225, 2011.
- <sup>6</sup> B. L. Liao, M. Zebarjadi, K. Esfarjani, G. Chen, "Cloaking core-shell nanoparticles from conducting electrons in solids," *Phys. Rev. Lett.*, 109, 126806, 2012.
- <sup>7</sup> O. Delaire, J. Ma, K. Marty, A. F. May, M. A. McGuire, M. H. Du, D. J. Singh, A. Podlesnyak, G. Ehlers, M. D. Lumsden, B. C. Sales, "Giant Anharmonic Phonon Scattering in PbTe", *Natural Materials*, 10, 614-619 (2011).
- <sup>8</sup> O. Delaire, K. Marty, M. B. Stone, P. R. C. Kent, M. S. Lucas, D. L. Abernathy, D. Mandrus, B. C. Sales, "Phonon Softening and Metallization of a Narrow-gap Semiconductor by Thermal Disorder," *PNAS*, 108, 4725, 2011.
- <sup>9</sup> T. Shiga, J. Shiomi, O. Delaire, K. Esfarjani, G. Chen, "Microscopic mechanism of low thermal conductivity in lead-telluride," *Phys. Rev. B*, 85, 155203, 2012..
- <sup>10</sup> A. J. Minnich, J. A. Johnson, A. J. Schmidt, K. Esfarjani, M. S. Dresselhaus, K. A. Nelson, G. Chen, "Thermal Conductivity Spectroscopy Technique to Measure Phonon Mean Free Paths," *Phys. Rev. Lett.* 107, 095901, 2011.
- <sup>11</sup> M. Luckyanova, J. Garg, K. Esfarjani, A. Jandl, M. Bulsara, A.J. Schmidt, A.J. Minnich, S. Chen, M. Dresselhaus, Z.F. Ren, E.A. Fitzgerald, G. Chen, "Coherent Phonon Heat Conduction in Superlattice," *Science* 338, 936, 2012.
- <sup>12</sup> R. J. Mehta, Y.L. Zhang, C. Karthik, B. Singh, R. W. Siegel, T. Borca-Tasciuc, G. Ramanath, "A new class of doped nanobulk high-figure-of-merit thermoelectrics by scalable bottom-up assembly," *Nature Materials*, 11, 233, 2012.
- <sup>13</sup> X. Yan, W. Liu, H. Wang, S. Chen, J. Shiomi, K. Esfarjani, H. Wang, D. Wang, G. Chen, Z.F. Ren, "Stronger phonon scattering by larger differences in atomic mass and size in p-type half-Heuslers  $\text{Hf}_{1-x}\text{Ti}_x\text{CoSb}_{0.8}\text{Sn}_{0.2}$ ", *Energy Environ. Sci.* 5, 7543-7548, 2012.
- <sup>14</sup> G. Joshi, X. Yan, H. Z. Wang, W. S. Liu, G. Chen, Z. F. Ren, "Enhancement in Thermoelectric Figure-Of-Merit of an N-Type Half-Heusler Compound by the Nanocomposite Approach," *Adv. Energy Materials* 1, 643, 2011.
- <sup>15</sup> C. Deng, C. A. Schuh, "Atomistic Simulation of Slow Grain Boundary Motion," *Phys. Rev. Lett.*, 106, 045503, 2011.
- <sup>16</sup> Y. X. Yeng, M. Ghebrebrhan, P. Bermel, W. R. Chan, J. D. Joannopoulos, M. Soljagic, and I. Celanovic, "Enabling high-temperature nanophotonics for energy applications" *PNAS*, 109, 2280, 2012.
- <sup>17</sup> V. Rinnerbauer, S. Ndao, Y.X. Yeng, J.J. Sendevich, K.F. Jensen, J.D. Joannopoulos, M. Soljagic, I. Celanovic, "Large-area fabrication of high aspect ratio tantalum photonic crystals for high-temperature selective emitters," *J. Vac. Sci. Techn. B*, 31, 011802-1, 2013.
- <sup>18</sup> P. Bermel, M. Ghebrebrhan, M. Harradon, Y. X. Yeng, I. Celanovic, J. D Joannopoulos, M. Soljagic. "Tailoring Photonic Metamaterial Resonances for Thermal Radiation", *Nanoscale Res. Lett.* 6, 549, 2011.
- <sup>19</sup> J. Bravo-Abad, J.D. Joannopoulos, M.Soljagic, "Enabling single-mode behavior over large areas with photonic Dirac cones" *PNAS*, 109, 9761, 2012.
- <sup>20</sup> D. Kraemer, B. Poudel, H.-P. Feng, J. C. Caylor, B. Yu, X. Yan, Y. Ma, X. Wang, D. Wang, A. Muto, K. McEnaney, M. Chiesa, Z. Ren, G. Chen, "High-performance flat-panel solar thermoelectric generators with high thermal concentration," *Nature Materials* 10, 532, 2011.

**Program Title:** Light Material Interactions Energy Frontier Research Center

**Principal Investigator:** Harry A. Atwater,

**Mailing Address:** California Institute of Technology, Thomas J. Watson Laboratories of Applied Physics, MS 128-95, Pasadena, CA 91125

**e-mail:** [haa@caltech.edu](mailto:haa@caltech.edu)

The "Light-Material Interactions in Energy Conversion" Energy Frontier Research Center (LMI-EFRC) is a national resource for fundamental optical principles and phenomena relevant to solar energy conversion, and for design of the optical properties of materials and devices used for energy conversion. The LMI-EFRC features a team that spans the campuses of Caltech, Berkeley, Illinois, and Harvard, and creates a foundational partnership between scientific leaders in optical properties of matter with experts in solar energy conversion and innovators in the design and fabrication of novel electronic and photonic materials.

To improve energy conversion efficiency with photonic design and materials requires the simultaneous development of theoretical methods (new photonic principles, mathematical methods, electromagnetic designs and computational approaches) and experimental methods (synthetic methods for nano- and micro-scale fabrication of materials with controlled refractive index profiles and complex two- and three-dimensional architectures). The confluence of these new photonic methods, the performance requirements for solar energy conversion and scientific opportunity has framed the challenges that define the research groups in the LMI-EFRC:

- i) **Full Spectrum Conversion:** The most substantial near-term opportunity for increase in solar energy conversion efficiency is via exploitation of the full solar spectrum. Researchers are investigating designs and materials that utilize the entire solar spectrum, including phenomena such as up-conversion, down-conversion, down-shifting, and spectrum splitting.
- ii) **Spontaneous Emission and Absorption Enhancement:** Solar cells suffer substantial efficiency losses due to incomplete light trapping. While the principles of light trapping in the ray optical regime are well-established, wave optical light trapping principles are largely undeveloped and are the focus of current intensive worldwide effort. Initial work from RG-2 has identified new optical designs for light trapping beyond the ray optical light trapping limit, using both scattering structures and also by exploiting internal photon recycling via spontaneous emission.
- iii) **Transformation Optics for Photovoltaics:** Transformation optics is a recent approach to control electromagnetic power flow in materials in which the complex dielectric function is spatially inhomogeneous in an optical medium. This paradigm has already led to cloaking of two dimensional scattering objects and transformation optical designs suggest the possibility to create a 'black hole' perfect broadband light absorber using materials with spatially inhomogeneous refractive index profiles.
- iv) **Complex Architecture and Self-Architected Absorbers:** New synthetic methods have enabled complex three-dimensional solar absorber architectures that were previously not possible to make. As an example, arrays of high aspect ratio semiconductor structures such as photonic crystals and Si microwire arrays give rise to unusual optical properties not found in conventional bulk or thin film solar absorbers. Perhaps the ultimate method to control light absorption in materials is to utilize light absorption itself to regulate material growth, another area of current LMI-EFRC focused research.



# **Session VIII**



# Atomic and Mesoscopic Study of Metallic Glasses

T. Egami ([egami@utk.edu](mailto:egami@utk.edu))

Joint Institute for Neutron Sciences, University of Tennessee, Knoxville, TN 37996  
Oak Ridge National Laboratory, Oak Ridge, TN 37831

## Program Scope

The goal of this project is to gain a fundamental understanding of the science of metallic liquids and glasses and provide guides to the experimental development of new bulk metallic glasses (BMG) with superior properties. The recent development of BMG has greatly improved the potential for application of metallic glasses as a structural material. However, the basic science of metallic glasses at the atomistic level remains poorly developed. In this program we will advance a fundamental understanding of structural and dynamic properties in metallic liquids and glasses through combination of tightly-coupled simulation, theory and experiment. The computational effort includes molecular dynamics simulations and the first-principles calculation of atomic level stresses. Experimental studies include neutron scattering using the superior power of the Spallation Neutron Source, synchrotron x-ray scattering and nanoscale mechanical testing. The ultimate goal is to develop a general atomistic understanding of deformation, dynamics and the glass transition in metallic glasses. This project makes full use of excellent scientific and technical expertise of the co-PI's and the PI, and outstanding facilities at ORNL and other DOE laboratories.

## Recent Progress

### 1. Atomic Mechanism of Flow in Liquid

Earlier we found that the mechanical failure of metallic glasses is a consequence of shear-induced glass transition [P1]. Even well below the glass transition temperature applied shear stress melts a glass into a liquid if it is strong enough. We proceeded to determine the atomic mechanism of flow under shear. We found that if the flow direction is  $x$  and the velocity increases along  $z$ , an atomic bond near the  $[10\bar{1}]$  direction (A-B) gets cut, and soon after a new bond (C-D) is formed along  $[101]$  (inset of Fig. 1). The time between cutting the bond and forming the bond is of the order of  $1/\nu_D$  ( $\nu_D$  is Debye frequency) as shown in Fig. 1 [P3], so the two actions can be regarded as one action of bond exchange. This bond-exchange was observed also for anelastic creep deformation by x-ray diffraction [1], suggesting it may be the universal atomistic mechanism of deformation in metallic glasses.

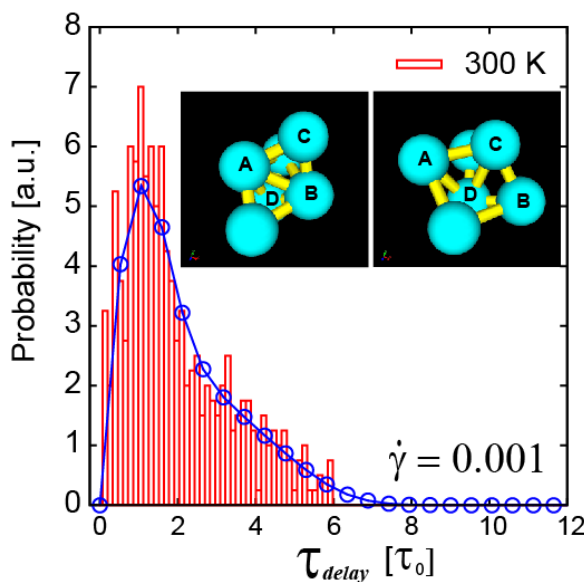


Fig. 1 Histogram of the time delay between the bonds cut (A-B) and formed (C-D), in the unit of  $\tau_0 = 0.7 \times 10^{-13}$  sec. The inset shows the bond-exchange mechanism [P3].

## 2. Non-local Nature of Viscosity

Viscosity  $\eta$  can be expressed in terms of the auto-correlation function of the shear stress,  $\sigma_{xy}(t)$ , by the Green-Kubo equation,

$$\eta = \frac{kT}{V} \int \langle \sigma_{xy}(0) \sigma_{xy}(t) \rangle dt$$

We re-expressed the stress in terms of the atomic-level shear stress,  $\sigma_i^{xy}$  [2, P11] as,

$$\sigma_{xy} = \sum_i \frac{\Omega_i}{V} \sigma_i^{xy}$$

where  $\Omega_i$  is the atomic volume of the  $i$ -th atom. Fig. 2 shows the spatial and temporal correlation function of atomic-level shear stresses [P3]. The stresses are correlated over surprisingly large space and time, showing the non-local nature of the viscosity. In Fig. 2 diagonal streaks are due to shear waves, and horizontal lines reflect the atomic pair-distribution function (PDF).

## 3. Elementary Excitation and Origin of Viscosity in High Temperature Liquid

It has long been assumed that the atomic motion in high temperature liquid was totally random and atoms diffuse almost freely [3]. However, viscosity shows thermally activated Arrhenian behavior above the crossover temperature,  $T_A$  [4]. By examining the viscosity of various alloy liquids by MD simulation we found that the Maxwell relaxation time,  $\tau_M$ , is equal to the time-scale for local configurational excitation (LCE), an action for an atom to lose or gain ONE nearest neighbor,  $\tau_{LC}$  [P5], at temperatures above  $T_A$ , as shown in Fig. 3 [5]. Thus LCE determines viscosity, and they are the elementary excitation in liquids. Here not only the composition was varied but the potentials and methods are different (a pairwise soft potential for Fe, Lennard-Jones potential for KA, EMA for Zr-Cu and Zr-Cu-Al, and *ab-initio* MD for Zr-Cu), suggesting that this result is universal. We also determined the origin of the crossover phenomenon in terms of localization of the transverse sound wave. Above  $T_A$   $\tau_{LC}$  is shorter than the time for the transverse phonon with the velocity  $c_T$  to travel one atomic distance  $a$ ,  $c_T a$ , so LCE's cannot communicate to each other. But below  $T_A$  they can interact with each other, and the rapid increase in viscosity below  $T_A$  could be described in terms of the interactions among LCE's.  $\tau_{LC}$  is not the same for each atom, and is dependent on the local coordination number,  $N_C$ . From this dependence we determined the local energy landscape as a function of  $N_C$  [5].

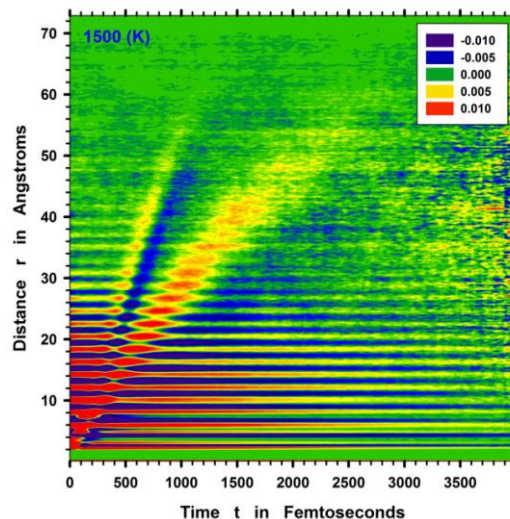


Fig. 2 Spatial and temporal correlation function of the atomic-level shear stress [P3].

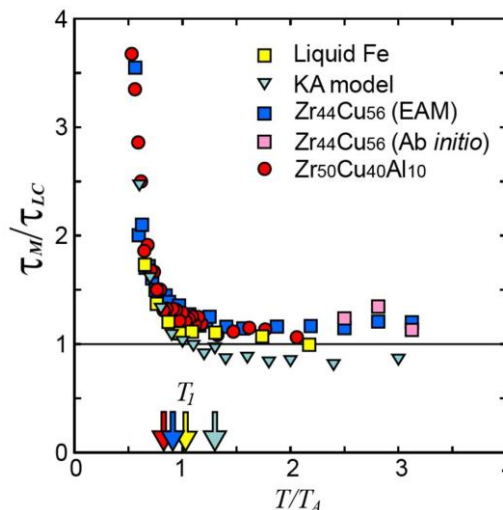


Fig. 3 The ratio,  $\tau_M/\tau_{LC}$ , is nearly unity for  $T > T_A$ , suggesting that the LCE determines the viscosity of a liquid [5].

Other achievements include the experimental determination of the structure of a metallic glass under elastic stress by x-ray anisotropic PDF method [P2] which confirmed the prediction of local anelasticity [6], the nano-indentation study to identify the critical role of surface defects in initiating the shear bands and thus determining the strength of metallic glasses [P10], the first *ab-initio* calculation of the atomic-level stresses using the density functional theory [P14], and the extension of the STZ theory to explain the viscous behavior of liquid [P19].

### Future Plans

We have recently built an electro-static liquid levitator for neutron scattering in collaboration with K. Kelton of Washington University. We plan to carry out a study of the structure and dynamics of metallic liquid without contact with a container, thus enabling deep supercooling, using this method. We will use this system with NOMAD (SNS) to study the structure, and with ARCS (SNS) to study the dynamics. The levitator will give us clean scattering data with less background, which will be helpful in obtaining the dynamic PDF with less noise. We hope to confirm the LCE in the liquid described above using this levitator using the dynamic PDF method. Theoretical and simulation study will focus on the supercooled liquid at  $T < T_A$ , and attempt to elucidate the rapid increase in viscosity toward the glass transition in terms of the interaction among LCE's, in an effort to resolve the long-standing theoretical challenge, the question of why a liquid becomes a glass.

### References

1. Y. Suzuki, J. Haimovich and T. Egami, "Bond-Orientational Anisotropy in Metallic Glasses Observed by X-Ray Diffraction", *Phys. Rev. B* **35**, 2162 (1987).
2. T. Egami, K. Maeda and V. Vitek, "Structural Defects in Amorphous Solids: A Computer Simulation Study", *Phil. Mag. A* **41**, 883 (1980).
3. P. Debenedetti and F. H. Stillinger, "Supercooled liquids and the glass transition", *Nature* **410**, 259 (2001).
4. C. A. Angell, "Formation of glasses from liquids and biopolymers", *Science* **267**, 1924 (1995).
5. T. Iwashita and T. Egami, "Elementary excitation and crossover phenomena in liquids", *unpublished*.
6. Y. Suzuki and T. Egami, "Shear Deformation of Glassy Metals: Breakdown of Cauchy Relationship and Anelasticity", *J. Non-Cryst. Solids* **75**, 361 (1985).

### Publications ('10-'12)

- P1. P. Guan, M.-W. Chen and T. Egami, "On the Stress-Temperature Scaling for Steady-State Flow in Metallic Glasses," *Phys. Rev. Lett.*, **104**, 205701 (2010).
- P2. W. Dmowski, T. Iwashita, C.-P. Chuang, J. Almer and T. Egami, "Elastic Heterogeneity in Metallic Glasses," *Phys. Rev. Lett.* **105**, 205502 (2010).
- P3. V. A. Levashov, J. R. Morris and T. Egami, "Viscosity and Atomic Level Stress Correlation in a Supercooled Liquid," *Phys. Rev. Lett.* **106**, 115703 (2011).
- P4. E. Bouchbinder and J. S. Langer, "Linear Response Theory for Hard and Soft Glassy Materials," *Phys. Rev. Lett.* **106**, 148301 (2011).
- P5. T. Iwashita and T. Egami, "Atomic Mechanism of Flow in Simple Liquids under Shear", *Phys. Rev. Lett.*, **108**, 196001 (2012).

- P6. W. Dmowski, Y. Yokoyama, A. Chuang, Y. Ren, M. Umemoto, K. Tsuchiya, A. Inoue, and T. Egami, "Structural Rejuvenation in a Bulk Metallic Glass Induced by Severe Plastic Deformation," *Acta Materialia*, **58**, 429 (2010).
- P7. T. Egami, "Understanding the Properties and Structure of Metallic Glasses at the Atomic Level," *Journal of Metals*, **62**, 2, 70 (2010).
- P8. T. Egami, V. A. Levashov, J. R. Morris and O. Haruyama, "Statistical Mechanics of Metallic Glasses and Liquids," *Mater. Trans. A*, **41**, 1628 (2010).
- P9. L. J. Peng, J. R. Morris and R.S. Aga, "A quantitative comparison of simulated crystal nucleation for the Lennard-Jones system with classical nucleation theory," *J. Chem. Phys* **133**, 084505 (2010).
- P10. H. Bei, Z. P. Lu, S. Shim, G. Chen, and E. P. George, "Specimen Size Effects on Zr-based Bulk Metallic Glasses Investigated by Uniaxial Compression and Spherical Nanoindentation," *Metall. Mater. Trans.* **41** A 1735-1742 (2010).
- P11. T. Egami, "Atomic Level Stresses," *Progr. Mater. Sci.* **56**, 637 (2011).
- P12. T. Egami, "Mechanical Failure and Glass Transition in Metallic Glasses," *J. Alloys and Compounds*, **509S**, S82 (2011).
- P13. M. Ojha, D. M. Nicholson, B. Radhakrishnan, R. E. Stoller and T. Egami, "Crystalline and Amorphous Models of Highly Damaged Fe," *MRS Symp. Proc.* **1363**, 05-32 (2011).
- P14. T. Egami, M. Ojha, D. M. Nicholson, D. Louzguine-Luzgin, N. Chen and A. Inoue, "Glass Formability and Al-Au System", *Phil. Mag. A*, **92**, 655 (2012).
- P15. C. Fan, H. G. Yan, C. T. Liu, H. Q. Li, P. K. Liaw, Y. Ren and T. Egami, "Changes in the Atomic Structure through Glass Transition Observed by X-Ray Scattering", *Intermetallics*, **23**, 111 (2012).
- P16. V. Wessels, A.K. Gangopadhyay, K.K. Sahu, R.W. Hyers, S.M. Canepari, J.R. Rogers, M.J. Kramer, A.I. Goldman, D. Robinson, J. W. Lee, J.R. Morris, K.F. Kelton, "Reply to "Comment on 'Rapid chemical and topological ordering in supercooled liquid Cu<sub>46</sub>Zr<sub>54</sub>'", *Phys. Rev. B* **85**, 066102 (2012).
- P17. T. Egami and W. Dmowski, "Dynamic Pair-Density Function Method for Neutron and X-Ray Inelastic Scattering", *Z. Kristallogr.*, **227**, 233 (2012).
- P18. Bin Wu, Boutheïna Kerkeni, Takeshi Egami, Changwoo Do, Yun Liu, Yongmei Wang, Lionel Porcar, Kunlun Hong, Sean C. Smith, Emily L. Liu, Gregory S. Smith and Wei-Ren Chen, "Structured Water in Polyelectrolyte Dendrimers: Understanding Small Angle Neutron Scattering Results through Atomistic Simulation", *J. Chem. Phys.*, **136**, 144901 (2012).
- P19. J. S. Langer and T. Egami, "Glass Dynamics at High Strain Rates", *Phys. Rev. E*, **86**, 011502 (2012).
- P20. B. Wu, W.-R. Chen, T. Egami, X. Li, Y. Liu, Y. Wang, C. Do, L. Porcar, K. Hong, L. Liu, G. Smith and S. Smith, "Molecular dynamics and neutron scattering study of the dependence of polyelectrolyte dendrimer conformation on counterion behavior", *J. Chem. Phys. B*, **137**, 064902 (2012).
- P21. M. Ojha, D. M. Nicholson, Kh. Odbadrakh, Bala. Radhakrishnan, R. E. Stoller and T. Egami, "The Use of Atomic Level Stress to Characterize the Structure of Irradiated Iron", *J. Phys.: Conf. Ser.* **402**, 012010 (2012).
- P22. B-G Yoo, J-Y Kim, Y-J Kim, I-Ch Choi, S. Shim, T.Y. Tsui, H. Bei, U. Ramamurty, J-I Jang, "Increased time-dependent room temperature plasticity in metallic glass nanopillars and its size-dependency", *International Journal of Plasticity*, **37**, 108-118 (2012).

**Program Title:** Domain Microstructures and Mechanisms for Large, Reversible and An hysteretic Strain Behaviors in Phase Transforming Ferroelectric Materials  
**Principal Investigator:** Yu U. Wang  
**Mailing Address:** Michigan Technological University, Materials Science & Engineering Department, 405 M&M Building, 1400 Townsend Drive, Houghton, MI 49931  
**E-mail:** wangyu@mtu.edu

### **Program Scope**

This project performs theoretical and computational studies of fundamental principles and mechanisms and their synergistic operations for achieving advanced strain behaviors in phase transforming ferroelectric materials. The research aims to advance the fundamental understanding of field-induced strain behaviors to achieve desired combination of advanced attributes of large, reversible and anhysteretic strains (these strain attributes usually compromise each other, leading to trade-offs that limit material's applicability). The objectives are to: (i) develop phase field approach-based computational tools and perform simulation studies of domain microstructures and mechanisms for achieving advanced strain behaviors; (ii) develop nanodomain diffraction analysis technique, identify domain microstructures and mechanisms from diffraction experiments, and correlate computations and experiments; (iii) investigate domain microstructure engineering to exploit the full potential of phase transforming ferroelectric materials; and (iv) advance state-of-the-art understanding of strain behaviors of ferroelectric materials, and shed light on other phase transforming materials such as magnetostrictive materials, conventional and magnetic shape memory alloys.

### **Recent Progress**

Our recent studies focus on understanding the microstructure and property relations in ferroelectric polycrystals and develop nanodomain diffraction analysis. The effects of crystallographic texture and grain shape on polycrystal properties are studied. It is found that grain shape plays a minor effect, crystallographic texturing significantly improves the polycrystal properties, and the critical degree of texturing is determined to achieve single crystal-like behaviors. Templated grain growth and texture development in ferroelectric polycrystals are simulated to investigate the effects of template seed volume fraction and sizes on final grain structures and textures. It is found that reducing template size and shortening seed distance is critical to achieve higher texture at lower template volume fraction. Two-phase ferroelectric composites consisting of template seeds and textured matrix grains are modeled to study the competing effects of grain texture and interfacial clamping. It is found that while a higher template volume fraction increases grain texturing, it also tends to erode away the advantage of textured polycrystals due to inferior properties of the template seeds, thus achieving higher texture at lower template volume fraction is critical for property improvement. Diffraction analysis of nanodomain microstructures is developed, which is integrated into phase field modeling to calculate diffraction patterns of simulated microstructures. Three-dimensional diffuse scattering technique is developed to characterize phonon domains in high-static-symmetry phase prior to phase transformations.

#### (1) Effect of Crystallographic Texture and Grain Shape on Polycrystal Properties

We performed computer simulations to study the effects of crystallographic texture and grain shape on dielectric and piezoelectric properties of polycrystals. As shown in Figure 1, it is found that, while grain shape plays a minor effect, crystallographic texturing significantly improves the polycrystal

properties, and a critical degree of texturing, i.e., about 15° in [001] uniaxial texture, is required to achieve dielectric and piezoelectric properties in polycrystals approaching that of single crystals.

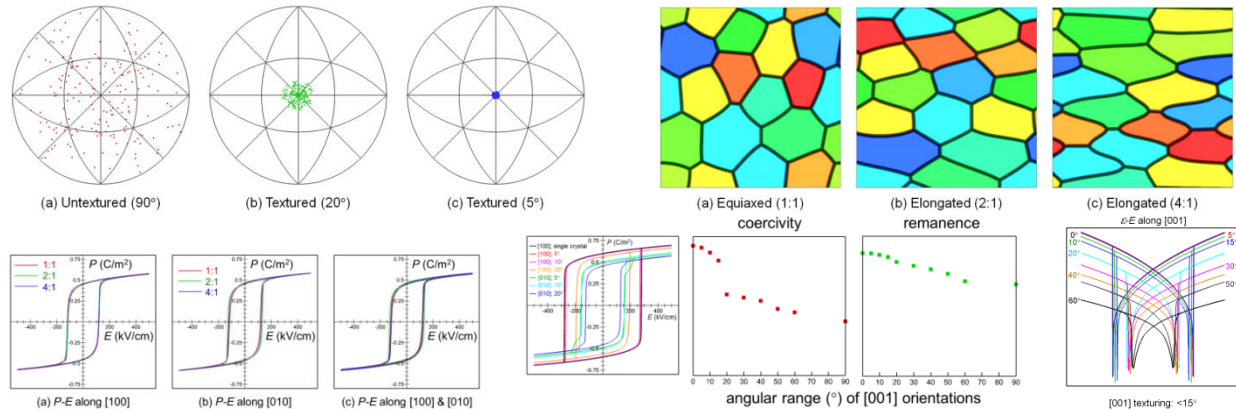


**Figure 1.** Simulation study of the effects of crystallographic texture and grain shape anisotropy on dielectric and piezoelectric properties of polycrystals.

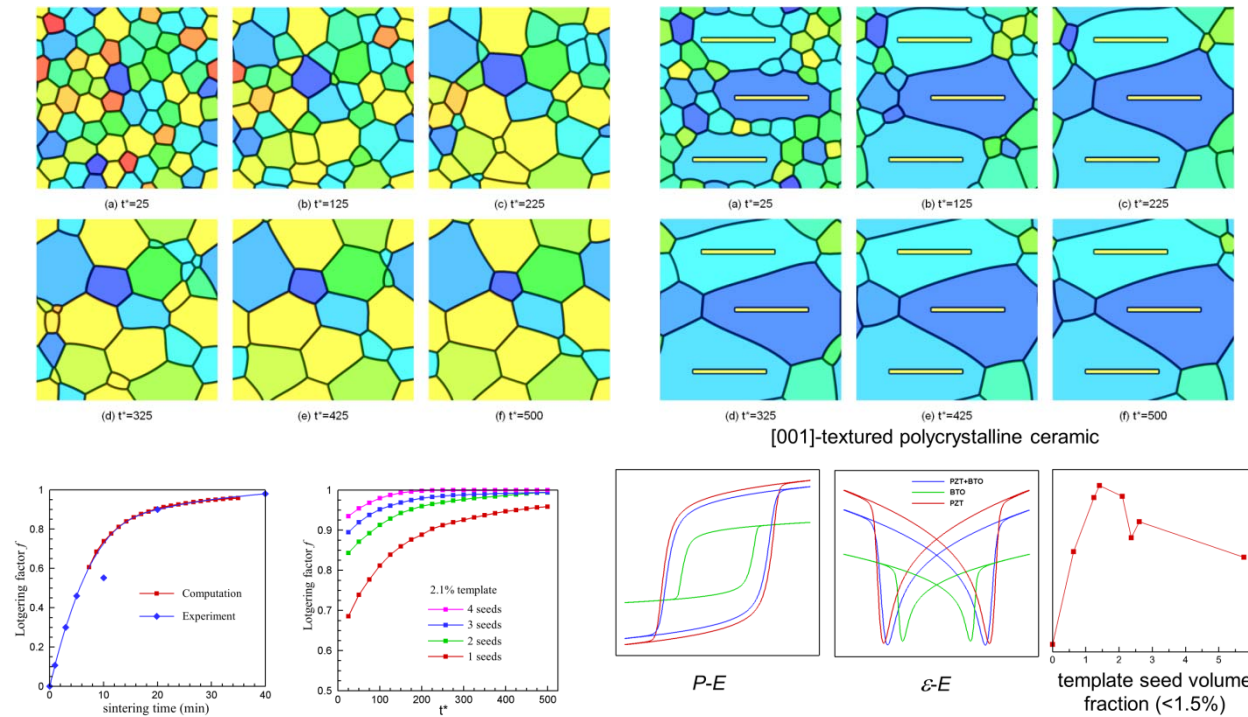


**Figure 2.** Simulation study of templated grain growth, texture development, and effects of template seed volume fraction and template dimensions on the structures and properties of matrix-template two-phase polycrystal composites.

## (2) Ferroelectric Composites Textured by Templated Grain Growth

Templated grain growth process for texture development in ferroelectric polycrystals is studied by computer simulation to find ways and understand the mechanisms to achieve higher uniaxial texture with lower template volume fraction, which is desired for improved piezoelectric properties. Diffraction peak intensities of the simulated polycrystals are computed during grain structure evolution to provide a direct

link to experiments. Texture development is characterized by the evolution of Lotgering factor. The effects of template seed volume fraction and template dimensions on the final grain structure and texture are investigated. As shown in Figure 2, it is found that, while the degree of crystallographic texture increases with increasing template volume fraction, the average template seed distance also plays an important role, and reducing the template size and shortening the seed distance is an effective way to achieve higher texture at lower template volume fraction.

To study the competing effects of grain texture and interfacial clamping in templated grain grown polycrystals, two-phase ferroelectric composites consisting of template seeds and textured matrix grains are modeled. As shown in Figure 2, it is found that, while a higher template volume fraction increases grain texturing, it also tends to erode away the advantage of crystallographic texturing due to inferior properties of the template seeds, thus achieving higher texture at lower template volume fraction is critical for property improvement.

### (3) Diffraction Analysis of Heterogeneous Nanodomains

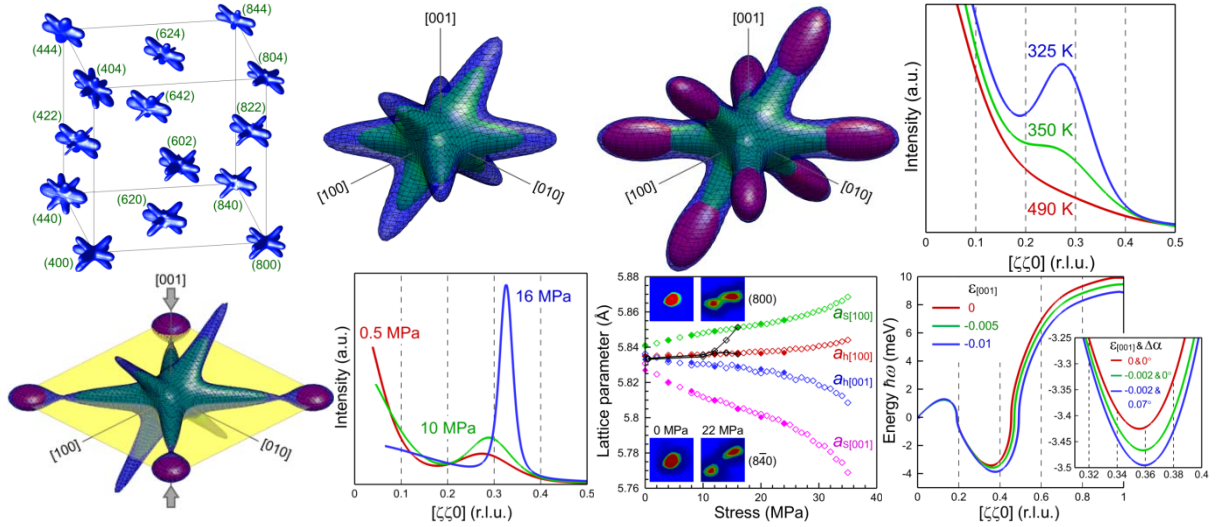


**Figure 3.** Diffuse scattering of softened phonons and first principles density functional perturbation theory calculation of phonon dispersion under stress.

To characterize nanodomain microstructures and identify domain mechanisms, diffraction analysis is developed, which is not only integrated into phase field modeling of microstructure evolutions but also combined with synchrotron diffraction experiments. Taking untransformed crystal lattice as a reference state, a nanodomain microstructure is characterized by a displacement field  $\mathbf{u}(\mathbf{r})$ , which in diffraction produces the scattering intensity distribution as a sum of coherent and diffuse intensities:

$$I(\mathbf{k}) = I_{\text{coh}}(\mathbf{k}) + I_{\text{diff}}(\mathbf{k}) \quad , \quad \text{where} \quad I_{\text{coh}}(\mathbf{k}) = \frac{N}{V} \sum_{\mathbf{G}} |\tilde{n}_0(\mathbf{G})|^2 [1 - (\mathbf{G} \otimes \mathbf{G}) : \langle \mathbf{u} \otimes \mathbf{u} \rangle_{\mathbf{R}}] \delta(\mathbf{k} - \mathbf{G}) \quad \text{and}$$

$$I_{\text{diff}}(\mathbf{k}) = \frac{1}{V^2} |\tilde{n}_0(\mathbf{k})|^2 (\mathbf{k} \otimes \mathbf{k}) : [\tilde{\mathbf{u}}(\mathbf{k}) \otimes \tilde{\mathbf{u}}(-\mathbf{k})].$$

In particular, the diffuse scattering intensity distribution around a fundamental reflection point  $\mathbf{G}$  (i.e., a Bragg peak) can be rewritten as

$$I_{\text{diff}}(\mathbf{G} + \boldsymbol{\rho}) = \frac{1}{V^2} |\tilde{n}_0(\mathbf{G} + \boldsymbol{\rho})|^2 [(\mathbf{G} + \boldsymbol{\rho}) \otimes (\mathbf{G} + \boldsymbol{\rho})] : [\tilde{\mathbf{u}}(\boldsymbol{\rho}) \otimes \tilde{\mathbf{u}}(-\boldsymbol{\rho})], \quad \text{where} \quad \boldsymbol{\rho} = \mathbf{k} - \mathbf{G}.$$

This analytical result can be extended to dynamic atomic displacements and explains the experimentally observed three-

dimensional diffuse scattering of softened phonons: as shown in Figure 3, each diffuse scattering rod corresponds to one branch of softened transverse acoustic  $TA_2$  phonons with  $\langle 110 \rangle$  wavevectors and  $\langle 1\bar{1}0 \rangle$  polarizations, where systematic extinction of diffuse rods arises from  $\mathbf{G} \cdot \mathbf{u}$ . The temperature and stress dependences of phonon diffuse scattering reveal existence of nanoscale phonon domains in high-symmetry phase prior to phase transformations. First principles density functional perturbation theory calculations of phonon dispersion are carried out, which agree with the experimental observation and theoretical interpretation.

### Future Plans

We will perform further computational study of the diffraction effects of various simulated nanodomain microstructures. The above diffraction intensity formula can be integrated into the phase field modeling to calculate the scattering intensity distributions and diffraction patterns. Figure 4 illustrates some representative nanodomain microstructures as simulated by phase field modeling, which consist of multiple domains and/or multiple phases. Due to coherent scattering and interference effects important for nanoscale domain microstructures, the diffraction patterns are difficult to predict, and computational approach is highly desired, which is able to explicitly treat the domain microstructures. The computational diffraction study not only augments the domain microstructure simulations but also, more importantly, correlates modeling and simulation to experiments and help investigate new domain-level mechanisms. Such domain-level computational diffraction has not been implemented in existing works thus represents an advancement in computational materials science.

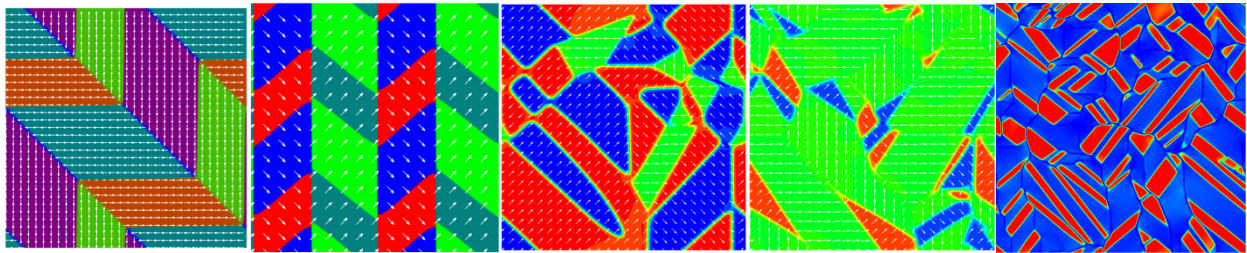


**Figure 4.** Representative nanodomain microstructures as simulated by phase field modeling, whose scattering intensity distributions will be calculated to study the diffraction effects.

### References

- [1] W.F. Rao, K.W. Xiao, T.L. Cheng, J.E. Zhou, Y.U. Wang, "Control of Domain Configurations and Sizes in Crystallographically Engineered Ferroelectric Single Crystals: Phase Field Modeling," *Appl. Phys. Lett.*, **97**, 162901, 2010.
- [2] W.F. Rao, T.L. Cheng, Y.U. Wang, "Aging-Stabilization of Ferroelectric Domains and Internal Electric Field due to Short-Range Ordering of Charged Point Defects: Phase Field Modeling," *Appl. Phys. Lett.*, **96**, 122903, 2010.
- [3] J.E. Zhou, T.L. Cheng, Y.U. Wang, "Correlated Nucleation and Self-Accommodating Kinetic Pathway of Ferroelectric Phase Transformation," *J. Appl. Phys.*, **111**, 024105, 2012.
- [4] T.L. Cheng, F.D. Ma, J.E. Zhou, G. Jennings, Y. Ren, Y.M. Jin, Y.U. Wang, "In-Situ Three-Dimensional Reciprocal-Space Mapping of Diffuse Scattering Intensity Distribution and Data Analysis for Precursor Phenomenon in Shape-Memory Alloy," *JOM*, **64**, 167, 2012.
- [5] Y.M. Jin, Y.U. Wang, "Diffuse Scattering Intensity Distribution Associated with Static and Dynamic Atomic Position Fluctuations," *JOM*, **64**, 161, 2012.

**Title:** Mesoscale Interfacial Dynamics in Magnetolectric Nanocomposites

**Principal Investigators:** Dwight Viehland, Shashank Priya, and Armen Khachaturyan

**Mailing Address:** 201 Holden Hall, Dept. Materials Science and Engineering, Virginia Tech, Blacksburg, VA 24061.

**Email:** [viehland@mse.vt.edu](mailto:viehland@mse.vt.edu); [spriya@vt.edu](mailto:spriya@vt.edu); [khach@jove.rutgers.edu](mailto:khach@jove.rutgers.edu)

**Problem Scope:** Multiferroic materials have a coexistence of at least two ferroic orders (ferroelectric, ferromagnetic, or ferroelastic). In multiferroic materials, the coupling interaction between the different order parameters can produce new phenomena, such as the magnetoelectric (ME) effect. The ME response is the appearance of an electric polarization  $P$  upon applying a magnetic field  $H$ , and/or the appearance of a magnetization  $M$  upon applying an electric field  $E$ . Magnetoelectricity has been observed as an intrinsic effect in some natural materials at low temperature; however, such single phase materials suffer from extremely weak ME exchange. Better alternatives are two-phase composites consisting of magnetostrictive and piezoelectric phases, which have been shown to have large ME coefficients. Said composites exploit a unique product ME tensor property that depends upon the individual strictions of the piezoelectric and magnetostrictive phases, the elastic stiffness and integrity of the interphase interfaces, the phase distribution and the dimensionality of its connectivity, and any elastic constraint; amongst other things. The specific objectives of this program are as following (i) development of new self-assembled morphologies and anisotropies in two phase ME epitaxial layers; (ii) determine microstructure of the interfaces between magnetic and piezoelectric phases, using electron microscopies; (iii) find the correlation between local and bulk magnetoelectric responses, the interfacial microstructure for fine scale composites of various phase connectivities, and (iv) develop a 3D Phase Field model of spontaneously self-organizing nano-scale microstructures.

### Recent progress:

(i) **Engineered Magnetic Shape Anisotropy in BiFeO<sub>3</sub>-CoFe<sub>2</sub>O<sub>4</sub> Self-Assembled Thin Films:** We have deposited BFO-CFO self-assembled thin films on three differently oriented STO substrates with different phase architectures. An example of our results are shown in Figure 1 for layers grown on (001) STO. CFO forms rectangular nanopillars on (001) STO with a lateral size of around 100 nm, where the aspect ratio can be manipulated by the height of the nanopillars. An easy axis rotation from in-plane to out-of-plane direction was shown as the film thickness was increased from 300 nm to 500 nm. Complete magnetization switching in each CFO nanopillar was observed in the MFM images. In addition, nanostriped CFO was also deposited on (110) STO substrates with an in-plane aspect ratio of R=5:1. An easy axis was found in the length direction with strong magnetic shape anisotropy. An intractable in-plane easy axis indicated a strong demagnetization field induced by a large magnetization gradient in each triangular pillar along the in-plane direction. These results illustrate an important relationship between magnetic properties with specific shapes and aspect ratios for BFO-CFO self-assembled heterostructures. Development of ferromagnetic artificial patterns of nanometer size with controllable magnetic anisotropy may offer application in high-density perpendicular storage.

(ii) **Engineered microstructures and grain morphologies in oriented BTO films for ME composites:** We have made significant progress towards the understanding of the self-assembled microstructures and morphology evolution of the (111) orientated BaTiO<sub>3</sub> films grown by pulsed laser deposition on platinized silicon substrate. This understanding is important for the integration of multiferroic system with silicon. Based on the

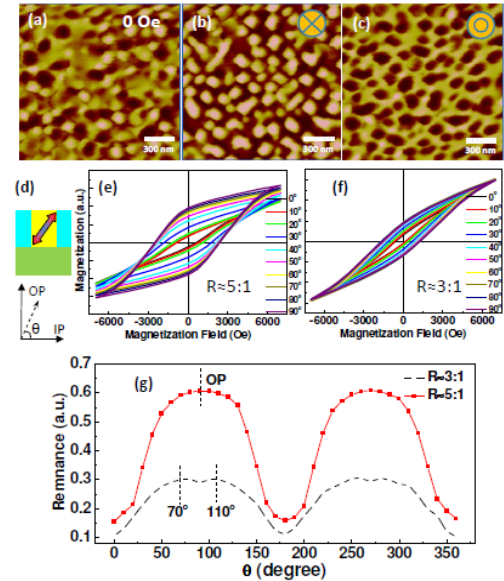


**Figure 1.** (a-c) MFM images of single domain CFO nanopillars after applying different magnetic fields. (d-f) M-H loops for different measurement angles of CFO nanopillars with different aspect ratios. (g) Remnant magnetization as a function of in-plane to out-of-plane rotation angle.

detailed scanning probe microscopy and high resolution transmission electron microscopy investigations (Fig. 2), a model was developed to explain the growth process and the surface morphology transformation from pyramid to hexagram. At the beginning of the growth process, (111)-faceted BTO nuclei were favorably formed on the (111) Pt surface to minimize the interfacial energy. The strain caused by the lattice mismatch between the BTO and Pt can be accommodated by the elastic deformation as the film is thinner than the critical thickness. During the initial stages, epitaxial growth occurs where grain growth was mainly along the thickness direction because the lateral growth was restricted by the competing neighboring grains and the substrate itself. Subsequently, the film assumes a columnar structure while maintaining the pyramid shape surface morphology given by (111) orientation. As the thickness of the film increased, the influence of the substrate will decrease and a competitive grain growth between different orientations occurs. According to the Drift's "evolutionary selection theory", the fast growing grains keep growing, while the slow growing grains do not grow continuously. Thus, the grains above the plane growing along the equivalent directions of  $\langle 111 \rangle$  orientation possess higher growth rate, but the growth velocity is higher along the normal-to-plane direction due to the less competition from the neighboring grains. There are 8 possible  $\langle 111 \rangle$  growth directions: 2 normal-to-plane, 3 above the plane and 3 below the plane along the diagonal axis. Once the film thickness increases beyond the critical dimensions, the grain structure with high aspect ratio attempts to achieve equiaxed configuration which has higher thermodynamically stability. This results in coarsened columnar structure where surface morphology changes from pyramid to hexagrams. If further grain growth occurred, then the final shape would be (111)-faceted single crystal rod. HRTEM investigations were able to identify the role of the twin lamellae's in controlling the nucleation and growth of oriented structure.

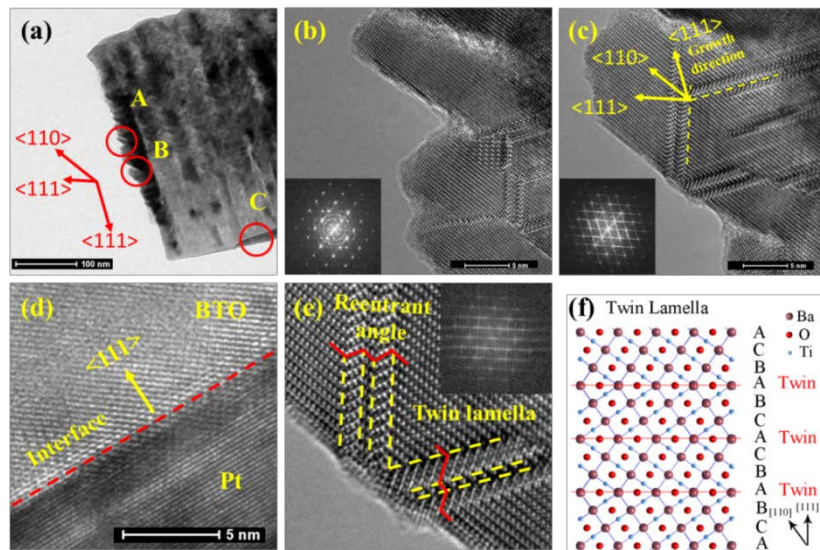


**Figure 2.** TEM characterization of BTO thin film synthesized by pulse laser deposition at 800°C on platinized silicon substrate (a) Bright field image of the BTO thick film; (b) HRTEM image of BTO film in Region A, the image corresponding to the region marked as 'A' in (a); (c) An HRTEM image corresponding to the region marked as 'B' in (a); (d) The lattice fringe of the BTO and Pt interface, which corresponding to the region marked as 'C' in (a); (e) HRTEM image depicting magnified view of lamella twins, inset is showing FFT pattern corresponding to twin lamella regions; (f) Simulated twin lamella structure.

(iii) **Domain rotation induced strain effect on the magnetic and magnetoelectric response in  $\text{CoFe}_2\text{O}_4/\text{Pb}(\text{Mg,Nb})\text{O}_3\text{-PbTiO}_3$  heterostructures:** We have observed good control of both magnetic and electric properties with electric and magnetic fields, respectively, for epitaxial  $\text{CoFe}_2\text{O}_4$  (CFO) films on  $\text{Pb}(\text{Mg,Nb})\text{O}_3\text{-PbTiO}_3$  (PMN-PT). X-ray reciprocal space mapping (see Fig.3) revealed a transformation between *a*- and *c*-domains in the PMN-PT under electric field (E). Magnetic hysteresis loop (Fig.4a-4b) and magnetic force microscopy (MFM) measurements showed a considerable change in the magnetic properties in specific

areas of CFO layers poled by MFM probe tips. Furthermore, a pulsed electric field applied to the substrate was found to switch the magnetization of CFO between high and low values (Fig.4c), depending on the polarity of E.

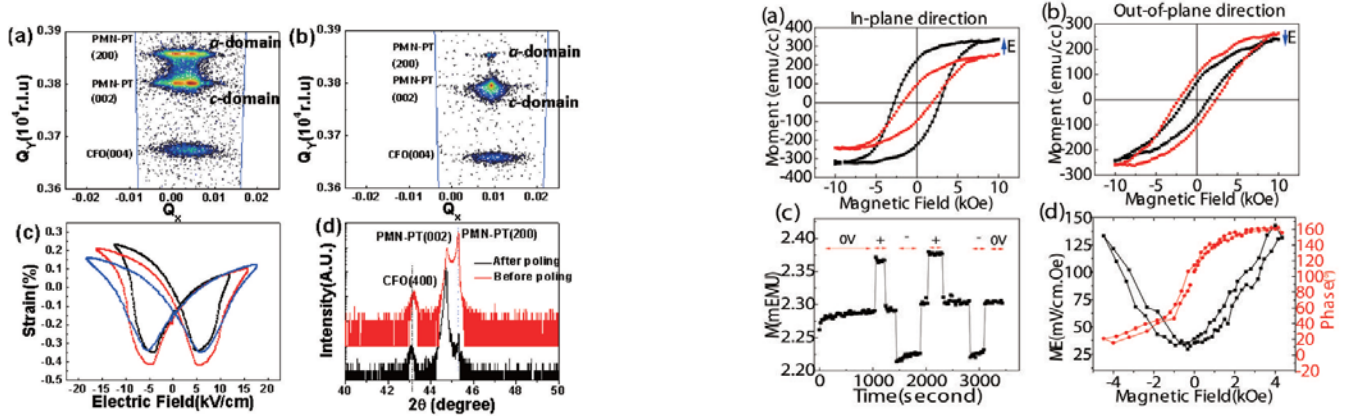
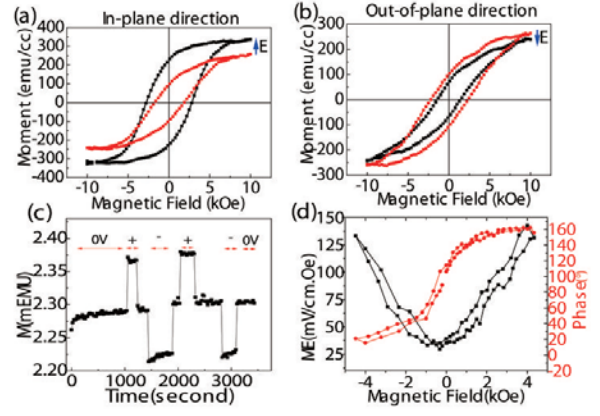


**Figure 2.** (a) Reciprocal space map of CFO/PMN-PT heterostructure with multi-domain structure; (b) Reciprocal space map with different domain configuration in the in-plane map of CFO/PMN-PT heterostructure with quasi single c-domain; (c) Strain-electric field curve of Magnetization step change under square wave electric piezoelectric PMN-PT substrate; (d) XRD line scans of CFO/PMN-PT before and after electric field poling.



(iv) **Giant piezoelectric responses in soft matrix with hard inclusions:** A giant strain response of the ferroelectrics near MPB of the ferroelectric solid solution is considered. The effect is associated with low polar anisotropy against a coherent rotation of the polarization. The abnormally low polar anisotropy near MPB follows from both general thermodynamic arguments and first principle calculations. However, an easiness of rotation of polarization of the matrix near MPB results in a reduction of the blocking force. To prevent this detrimental effect, we investigated a possibility of the use of the same concept as in the development of Spring Ferromagnetics. This is the use of a composite material consisting of "soft" ferroelectric matrix with the low dipolar anisotropy and inclusions of a "hard" ferroelectric material with high dipolar anisotropy. In this situation, the polar inclusions generate built-in fixed electric and stress fields caused by the crystal lattice misfit. They align the polarization of soft matrix along this local field, which results in the large macroscopic shape change (extrinsic piezoelectric strain). If the precipitates are randomly oriented and initial state is not poled, the resultant polarization of non-poled state vanishes. Poling aligns the polarization of the inclusions along the poling direction if the poling field is sufficiently strong. This, in turns, aligns the inclusion-induced polarization of the matrix along the same direction producing the net dipole moment.

Application of the external electric field rotates the polarization of the soft matrix from their local energy-minimizing orientations. This rotation induces an abnormally large strain, which is large because it is of the order of crystal lattice misfit between the tetragonal and rhombohedral phases, i.e. it is of the order of percents. Therefore, in this case, the application of the external field generates a large strain response, which is a piezoelectric effect. However, the most important circumstances are that this electric field-induced strain is recoverable and blocking force is increased: a removal of the external field should results in a

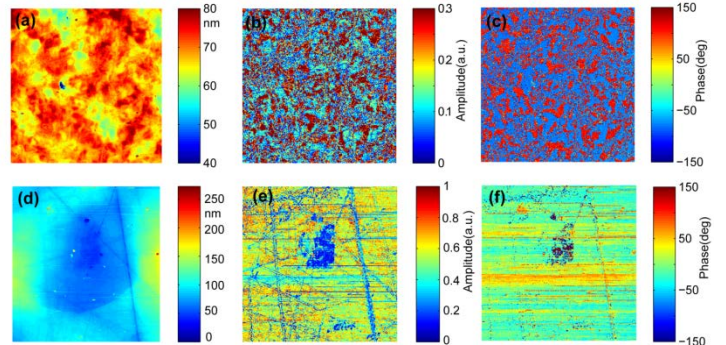


**Figure 5:** Scanning probe microscopy experiments on PZT-based ceramics embedded with and without hard inclusions.

recovery of the initial energy-minimizing state (and strain) by the reverse rotation of local polarization of the matrix. The driving force of the recovery is not a weak intrinsic polar anisotropy of the matrix but a strong coupling of the matrix/inclusion polarizations provided by the strain and dipolar interaction of the inclusions and matrix. A hysteresis of such a system upon application of the cycling electric field should be small as long as the applied electric field is not sufficient to switch the polarization of the hard ferroelectric inclusions. However, the hysteresis should be high if the electric field is sufficiently high to switch polarization of hard ferroelectric inclusion, which will be followed by the corresponding rotation of the polarization of the matrix coupled with the polarization of the matrix by the high electrostatic and stress-induced interactions. The coercive electric field significantly increases because a very reason for coercivity in this case is not the intrinsic polar anisotropy, which is small for the matrix, but the strong electrostatic and stress-induced interaction of polarization of the matrix with the built-in static polarization of the inclusions. To investigate this effect, we carried out the computer modeling assuming, for certainty, that the soft ferroelectric matrix is a generic PZT system near the morphotropic boundary and hard particles are described by the free energy with high polar anisotropy. Experimental validation is being conducted by synthesizing PZT-based ceramics with controlled microstructure and using scanning probe microscopy to measure the changes in local polarization and piezoelectric response. These changes are being compared with the matrix without any inclusions to quantify stress-induced interactions.

**Future Plans:** We will try to develop smoother and flatter atomic surfaces on substrates that have been terminated for the deposition of two phase thin layers with nanostructures. Such finely tuned substrates could have significant implications in controlling the size, shape and phase distribution of vertically integrated ME nanocomposites and ME nano-chessboard structures. With highly ordered nano-structure aligned in out-of-plane direction, the elastic coupling between two phases are expected much stronger than any other two phase ME composites in use. We will continue to conduct experiments on self-assembled multiferroic structures on silicon and novel microstructures consisting of hard inclusions. These manuscripts are under preparation.

**References: list of papers (already published, in press, submitted) in which DOE support is acknowledged.**

1. Z. Wang, Y. Li, R. Viswan, B. Hu, V. G. Harris, J. F. Li and D. Viehland, "Engineered magnetic shape anisotropy in BiFeO<sub>3</sub>-CoFe<sub>2</sub>O<sub>4</sub> self-assembled thin films" (submitted).
2. R. Viswan, J. J. Yao, D. Berry, R. Varghese, Z. Wang, S. Priya, J. F. Li and D. Viehland, "Direct and converse magnetoelectric effects in PbZr<sub>0.52</sub>Ti<sub>0.48</sub>O<sub>3</sub> films deposited on Metglas substrates", (submitted).
3. Y. Yan, K. Cho, D. Maurya, A. Kumar, S. Kalinin, A. Khachatryan and S. Priya, "High performance textured piezoelectric ceramics" *Appl. Phys. Lett.* **102**, 042903 (2013).
4. A. Kumar, J. Kumar, and S. Priya, "Defect and adsorbate induced ferromagnetic spin-order in magnesium oxide nanocrystallites." *Applied Physics Letters* **100**, 192404 (2012).
5. C. Park, A. Khachatryan, and S. Priya, "Giant magnetoelectric coupling in laminate thin film structure grown on magnetostrictive substrate" *Applied Physics Letters* **100**, 192904 (2012).
6. C. Park, D. Avirovik, M. Burchurin, V. Petrov, and S. Priya, "Tunable magnetoelectric response of dimensionally gradient laminate composites" *Applied Physics Letters* **100**, n 21, 212901 (2012).
7. Z. Wang, Y. Li, R. Viswan, B. Hu, V. G. Harris, J. F. Li and D. Viehland, " Self-assembled NaNbO<sub>3</sub>-Nb<sub>2</sub>O<sub>5</sub> (ferroelectric-semiconductor) heterostructures grown on LaAlO<sub>3</sub> substrates", *Appl. Phys. Lett.* **101**, 132902 (2012).
8. Z. Wang, R. Viswan, B. Hu, V. G. Harris, J. F. Li, D. Viehland, "Tunable magnetic anisotropy of CoFe<sub>2</sub>O<sub>4</sub> nanopillar arrays released from BiFeO<sub>3</sub> matrix", *Phys. Stat. Solidi (RRL)* **6**, 92 (2012).
9. Z. Wang, R. Viswan, B. Hu, J. F. Li, V. G. Harris, and D. Viehland, "Domain rotation induced strain effect on the magnetic and magneto-electric response in CoFe<sub>2</sub>O<sub>4</sub>/Pb(Mg,Nb)O<sub>3</sub>-PbTiO<sub>3</sub> heterostructures" *J. Appl. Phys.* **111**, 034108 (2012).
10. Z. Wang, R. Viswan, B. Hu, J. F. Li, V. G. Harris, and D. Viehland, "Phase-controlled epitaxial growth of iron oxide thin films on MgO(001) and LaAlO<sub>3</sub>(001) substrates", *Phys. Stat. Solidi (RRL)* **6**, 89 (2012).
11. Wei-Feng Rao and Armen G. Khachatryan, "Giant quasi-elastic responses in decomposed two-phase nanodispersions: Phase field modeling," *Acta Mater.*, **60**, 443, Jan. 2012.
12. Wei-Feng Rao and Armen G. Khachatryan, "Giant quasi-elastic responses in decomposed two-phase nanodispersions: Phase field modeling," *Acta Mater.*, **60**, 443, (2012).

# Prediction of Thermal Transport Properties of Multiscale-Structured Crystalline Materials

Youping Chen, ypchen2@ufl.edu  
Department of Mechanical and Aerospace Engineering  
University of Florida, Gainesville Florida 32611

## Program Scope

The ability to design and control the microstructure of materials promises revolutionary advances in new materials development. In addition to the processing technology for precise control of materials microstructure at the nanometer to micron scales, the most formidable challenge in developing this ability is to predict the material properties from its chemical composition and multiscale microstructural features. *No simulation tool currently exists for such prediction.* This project aims to meet this challenge by (a) establishing a concurrently coupled atomistic-continuum methodology that can be used to understand and design materials with microstructural complexity, and (b) demonstrating the methodology through predicting the mechanical and thermal transport properties of thermoelectric materials. In pursuit of this goal, we have planned the following research tasks:

- (1) Reformulate the classical statistical mechanical theory of transport processes to unify atomistic and continuum descriptions of balance laws.
- (2) Recast the governing equations to facilitate coarse-scale finite element simulation of discontinuous material behavior
- (3) Establish a concurrent atomistic-continuum (CAC) simulation tool to simultaneously study microstructural, mechanical, and phonon transport properties of materials
- (4) Test the formulation and simulation tool through comparison of CAC simulations with fully atomistic simulations
- (5) Validate through comparing simulation results of existing thermoelectric materials ( $\text{Bi}_2\text{Te}_3$ , nanostructured BiSbTe alloy, and nanostructured SiGe alloy) with experimental measurements
- (6) Predict the lowest possible phonon thermal conductivity in SrTiO<sub>3</sub> ceramics

## Recent Progress

- (1) Fundamental to the development of a concurrent atomistic-continuum methodology is a unified formulation of atomistic and continuum representation of balance laws. We have generalized Kirkwood's statistical mechanical theory of transport processes to have a two-level structural description of general crystalline materials. The new formulation describes the structure of a crystalline material in terms of a continuously-distributed lattice cells, but with a group of discrete atoms situated in each lattice cell at sub-

structural level, in exactly the same way with the Solid State Physics approach in describing the structure of all crystals; correspondingly, the atomic deformation is expressed as the sum of the lattice deformation and the subscale internal deformation relative to the lattice, which is consistent with lattice dynamics description of the dynamics of atoms in crystals. This concurrent two-level material description then leads to (1) a new formalism by which fluxes (stress and heat flux) consist of components representing the distortions of lattice cells and the rearrangement of atoms within the cells, and (2) a new mathematical representation of balance laws that can be used to solve for both the motion of the continuously-distributed lattice cells and the internal motion of atoms within each lattice cell. Under elastic distortion, the new balance equations can fully reproduce the phonon dispersion relations. The information of the arrangements of atoms as well as the interaction of atoms in the crystal is thus all built in the new formulation. As a result, this new formulation enables us to model a general crystalline material as a continuous collection of lattice cells, but embedded within each material point is a group of discrete atoms. These coupled continuum-atomistic features make this formulation distinct from all existing coarse-grained atomistic or multiscale formulations.

- (2) The continuum representation of conservation equations involves spatial derivatives. The presence of these spatial derivatives requires continuity of the material. Therefore, defects within a material have to be treated as surface boundaries of the material. This means that the obstacle in continuum modeling of defects lies in the mathematical framework. To overcome this obstacle, we have been working to seek a different mathematical representation of the conservation equations, including the balance equations of linear momentum and the conservation equations of energy. The balance equations of linear momentum have been rewritten in terms of internal force density and kinetic temperature, this the allow simulations of defects, including dislocations and cracks to emerge as a consequence of the governing equations. We are still working on the energy equations.
- (3) The numerical implementation of our new formulation leads to the concurrent atomistic-continuum (CAC) models in which non-uniform FE meshes can be employed for a concurrent multi-resolution simulation and coarse-grained (CG) atomistic simulation when uniform coarse FE meshes are used. We use standard Gauss integration along with linear interpolation within each element to reduce the computational cost. We have developed a preliminary version of the CAC simulation tool. We have simulated the mechanical behavior of Cu, Al, Si, and SrTiO<sub>3</sub>, and have compared the accuracy and efficiency with respect to MD simulations in simulation of the dynamics of defects. The CAC simulations have shown to allow dislocation loops to grow from several nanometers to 45 nm~75 nm in radius, significantly larger than that have been modeled using existing MD simulations (Fig.1), and comparable with that observed in experiments. We have also started to model phonon thermal transport and the phonon-dislocation interactions in crystalline materials.

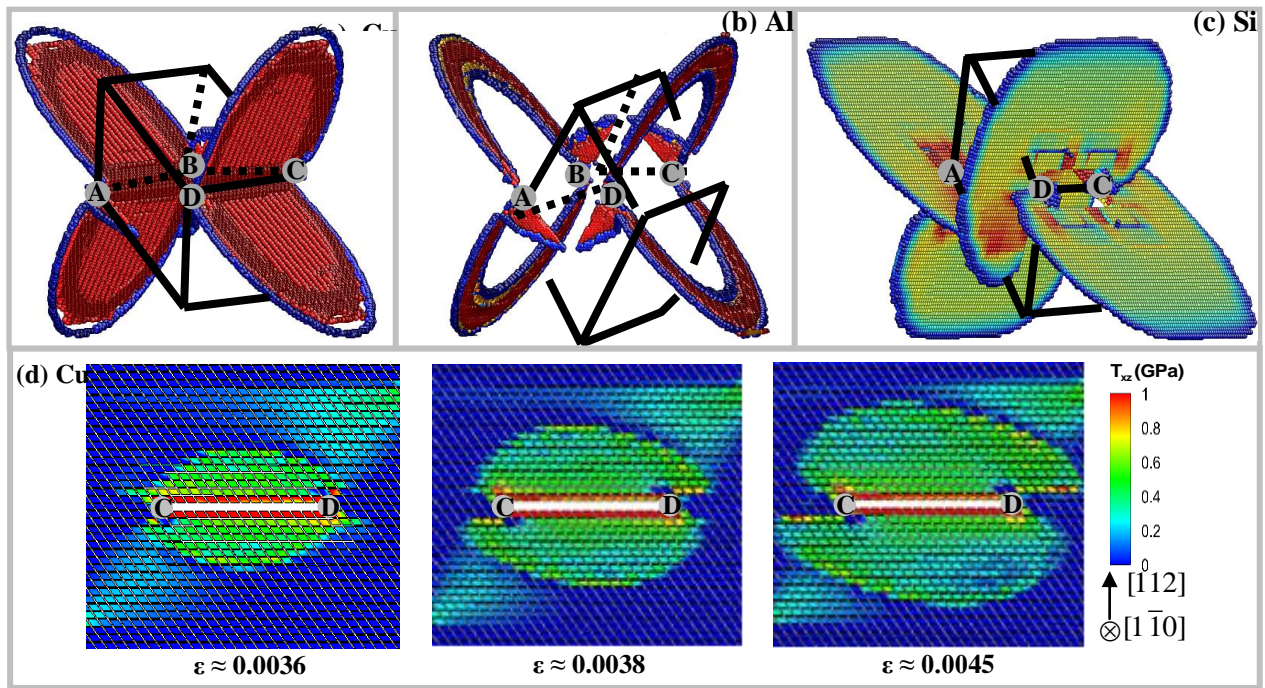


Fig. 1. Dislocation loops and stacking fault structures in (a) Cu, (b) Al, (c) Si and (d) strain sequences of snapshots of mesh deformation and shear stress distributions in Cu under tension from CG simulations.

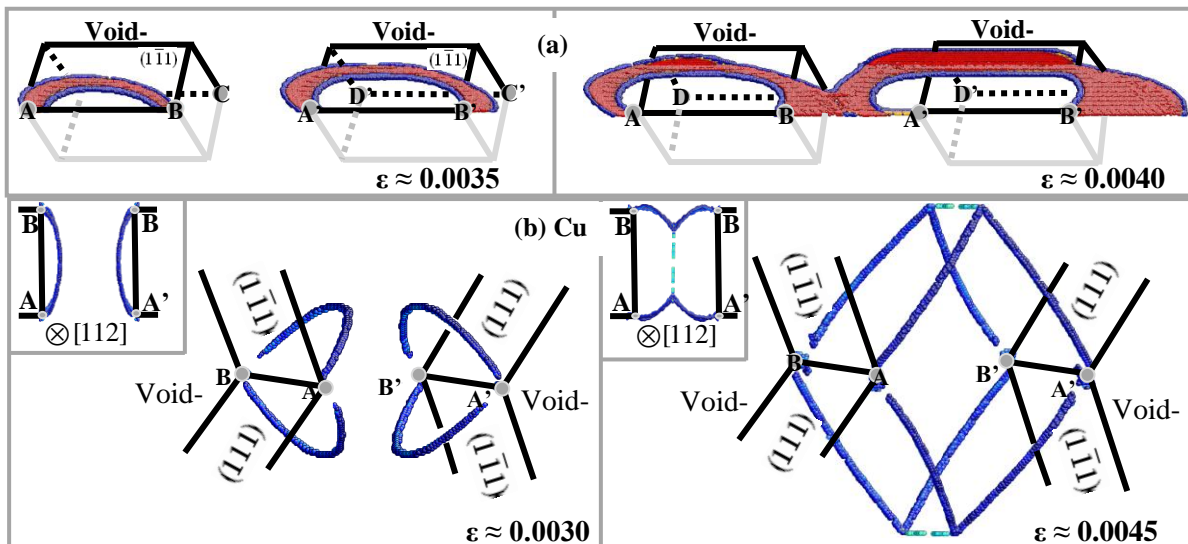


Fig. 2. Strain sequences of snapshots of loop interactions in (a) Al and (b) Cu from CG simulations.

## Future Plans

A key objective of this research project is to reformulate the energy equation from atomistics to allow heat to pass from atomistic to continuum region. This will enable measurement of thermal conductivity in materials with dislocations, grain boundaries and phase boundaries through concurrent atomistic-continuum simulations. We are currently working on one method based on phonon dynamics and another formulation based on the thermostating formalism.

The ability to represent higher frequency lattice vibrations is typically compromised via coarse-graining, which influences anharmonic effects and temperature, because the usual linear-shape function in the traditional FE method will cut off waves whose wavelengths are smaller than the element size. We will formulate a new shape function to overcome this problem. Our strategy is to add the displacements that having been cut off by the size of a linear finite element back to the displacement interpolated via standard finite element method interpolation.

Like the length scale problem, the time scale problem is also a significant challenge to mutliscale methods. Multiple time-scale algorithms developed for atomistic simulations may be utilized in the numerical implementation of CAC. One particularly algorithm that fits well with CAC is the “reversible reference system propagator algorithm”. We plan to adapt the reversible reference system propagator algorithm according to the different time scales and the dynamic characteristics of the CAC models. We expect the multiscale computation will be partitioned into several portions with different time steps assigned.

Finally, we will perform CAC simulations of thermoelectric materials Bi<sub>2</sub>Te<sub>3</sub>, nanostructured SiGe alloy, and ceramics SrTiO<sub>3</sub>, and then compare the simulation results with existing experimental measurements. We will predict the lowest possible phonon thermal conductivity in SrTiO<sub>3</sub> ceramics through simulations of SrTiO<sub>3</sub> ceramics with different nano/microstructures.

## References to publications of DOE sponsored research (07/2011-02/2013)

1. Shengfeng Yang, Liming Xiong, Qian Deng, Youping Chen (2013), “Concurrent atomistic and continuum simulation of strontium titanate”, *Acta Materialia*, Volume 61, Issue 1, January 2013, Pages 89–102.
2. Liming Xiong, David L. McDowell, Youping Chen (2012), “Nucleation and growth of dislocation loops in Cu, Al and Si by a concurrent atomistic-continuum method”, *Scripta Materialia*, Volume 67, Issues 7–8, October 2012, Pages 633–636.
3. Liming Xiong, Qian Deng, Garritt Tucker, David L. McDowell, Youping Chen (2012), “A concurrent scheme for passing dislocations from atomistic to continuum domains”, *Acta Materialia*, Volume 60, Issue 3, February 2012, Pages 899–913 .
4. Liming Xiong, Qian Deng, Garritt Tucker, David L. McDowell, Youping Chen (2012), “Coarse-grained atomistic simulations of dislocations in Al, Ni and Cu crystals”, *International Journal of Plasticity*, Volume 38, November 2012, Pages 86–101 .
5. Liming Xiong and Youping Chen, “Coarse-grained atomistic modeling and simulation of inelastic material behavior”, *Acta Mechanica Solida Sinica*, Volume 25, Issue 3, June 2012, Pages 244–261.

# **Session IX**



**Program Title:** Evaluating the Oxidative, Photothermal and Electrical Stability of Colloidal Nanocrystal Solids

**Principal Investigator:** Matt Law

**Address:** Department of Chemistry and Chemical Engineering and Materials Science, University of California, Irvine, Irvine, CA. 92697

**Email:** lawm@uci.edu

## Program Scope

IV-VI quantum dot (QD) solids are a novel class of granular electronic materials with great technological potential (e.g., in photodetectors, field-effect transistors (FETs), and solar cells), but their oxidative and thermal instability present a barrier to practical applications. Poor stability is a fundamental issue facing many nanoscale materials. Basic studies are needed to elucidate the most important mechanisms of degradation and develop robust countermeasures if QD materials are to become technologically important.

This project aims to determine the degradation mechanisms of IV-VI QD solids (primarily PbSe and PbS) and to introduce new chemical strategies to drastically improve their operating lifetimes and overall performance. The approach is based on (1) detailed testing of QD thin film materials (principally FETs and solar cells) as a function of oxidative and thermal stress, and (2) using organic and inorganic approaches to (i) link the QDs into strongly electronically coupled, high-mobility films, (ii) prevent their oxidation and (iii) eliminate internal degrees of freedom that lead to film degradation.

Stability against oxidation and thermal degradation is the major focus of this project. We are evaluating the stability of QD thin films and interfaces at temperatures less than 100°C (the regime most relevant to applications). Low-temperature, long-term oxidation and sintering of QD films are investigated using current-voltage, capacitance-voltage, SKPM, Fourier transform infrared spectroscopy (FTIR), and X-ray photoelectron spectroscopy (XPS) techniques. Scanning Kelvin probe microscopy (SKPM) is being used to map the potential profiles of operating QD FETs and solar cells as a function of air exposure, illumination and temperature, which will provide detailed information on how the work functions, potential drops and charge concentrations within these materials change with oxidation and other factors. We are pursuing two strategies to fabricate QD films with stable electrical characteristics: (1) the use of robust molecular surface ligands, and (2) “matrix engineering,” the creation of inorganic matrices by low-temperature atomic layer deposition (ALD) that function to passivate surface states, prevent oxidation, lock the QDs into position, inhibit diffusion, and tune the height and width of the inter-QD potential barriers that govern charge transport.

Poor stability is a common feature of nanoscale electronic materials, yet stability is all too rarely the focus of basic research. Fundamental studies are therefore needed to elucidate the most important mechanisms of degradation and develop simple yet effective countermeasures. By revealing both how QD solids degrade in response to environmental stresses (oxidative, photothermal, and electric) and how to prevent this degradation, the project is greatly improving our ability to develop practical QD materials for real-world applications.

## Recent Progress

***Oxidative and Photothermal Degradation of PbS QD Films.*** We combined optical absorption spectroscopy, transmission electron microscopy (TEM) imaging, and variable-temperature measurements to study the effect of ultraviolet (UV) light and heat treatments on ethanedithiol-treated PbS quantum dot (QD) films as a function of ambient atmosphere, temperature, and QD size. Film aging occurs mainly by oxidation or ripening and sintering depending on QD size and the presence of oxygen. We can stop QD oxidation and greatly suppress ripening by infilling the films with amorphous Al<sub>2</sub>O<sub>3</sub> using room-temperature ALD (Figure 1).

We have found that UV illumination causes preferential oxidation of large QDs but preferential ripening/sintering of small QDs. This difference is due to the greater driving force for ripening/sintering of smaller QDs. The main mechanism of UV action is not simple film heating; instead, it seems that UV-generated electron-hole pairs (i) cause photo-oxidation and (ii) create hotspots that trigger diffusion and ripening/sintering (particularly in small QDs). We can completely freeze out UV-induced ripening/sintering in inert gas by cooling films to 80 K, which suggests that ripening/sintering are strongly activated processes. However, UV-induced oxidation could not be eliminated even at temperatures as low as 110 K. From the temperature dependence, we identify two stages of oxidation, with self-terminating oxidation of the outermost monolayer of surface atoms occurring at low temperature and strongly activated subsurface oxidation important at higher temperature. We also find that moisture is responsible for most of the increase in size distribution of PbS QD films aged in air. Our results will be useful in ongoing efforts to fabricate truly stable QD films for next-generation solar cells.

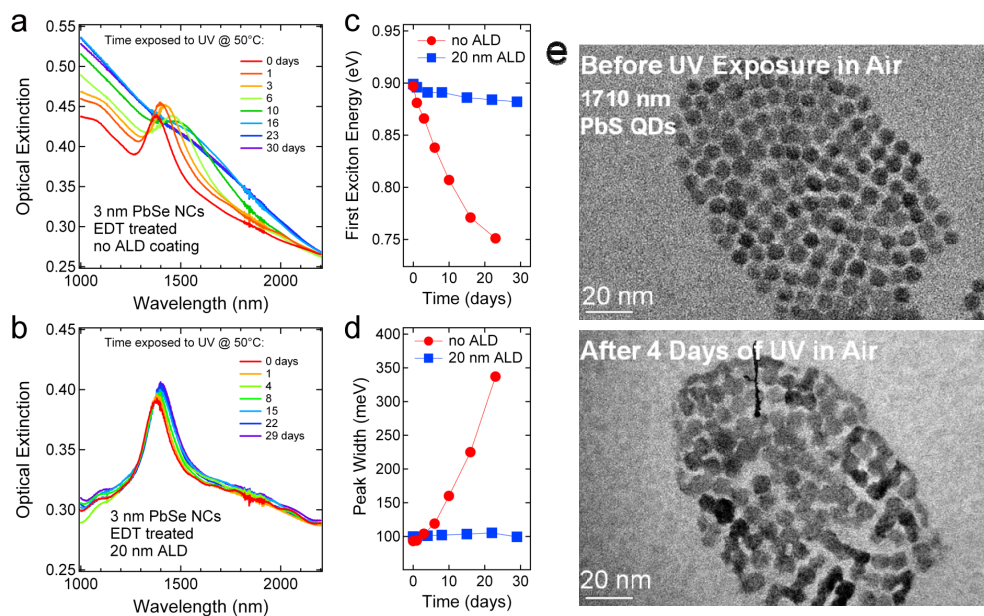


**Figure 1.** **a**, Optical absorption spectra of an uncoated, EDT-treated film of 3 nm PbSe NCs exposed to UV light ( $365 \text{ nm}$ ,  $1.4 \text{ mW cm}^{-2}$ ) at  $50^\circ\text{C}$  in a glovebox ( $1\text{-}5 \text{ ppm O}_2$  and  $\text{H}_2\text{O}$ ) for one month. **b**, Spectra of an identical film infilled with  $20 \text{ nm}$  of  $\text{Al}_2\text{O}_3$  at  $27^\circ\text{C}$ . **c**, Energy and, **d**, width of the first exciton absorption peak over time for both samples. The ALD matrix greatly suppresses UV-induced ripening/sintering of the NCs. **e**, TEM images of EDT-treated PbS NCs (no ALD treatment) before and after four days of UV exposure in air.

**Robust, high-performance QD devices by ALD infilling.** The fabrication of practical solar cells based on films of PbX QDs depends on preventing oxidation, surface diffusion, ripening, sintering, and other unwanted physicochemical changes that plague these metastable materials. We used low-temperature ALD to infill conductive PbSe QD films with amorphous alumina to produce inorganic nanocomposites in which the QDs are locked in place and protected against oxidative and photothermal damage (Figure 2). ALD infilling stops oxidation, prevents internal atomic and molecular motion, and modifies inter-QD barrier heights, surface trap densities, and other electronic characteristics of QD films. Infilling yields PbSe QD field-effect transistors and solar cells that operate with enhanced performance indefinitely in air. ALD infilling with ZnO lowers the height of the inter-NC tunnel barrier for electron transport, yielding PbSe NC films with electron mobilities of  $1 \text{ cm}^2 \text{ V}^{-1} \text{ s}^{-1}$ . ALD infilling is a general, manufacturable approach to making truly robust QD films for next-generation solar cells. The unrivaled ability of ALD to

conformally coat nanostructured substrates with functional materials, including semiconductors, metals, and catalyst layers, offers many exciting opportunities to fabricate high-performance, robust nanomaterials for optoelectronics.

This approach has been hugely successful in overcoming most of the stability problems associated with QD films. In many ways, the success of ALD infilling has altered the course of the rest of our research program, steering it away from more basic studies of degradation to focus instead on non-stability performance improvements.

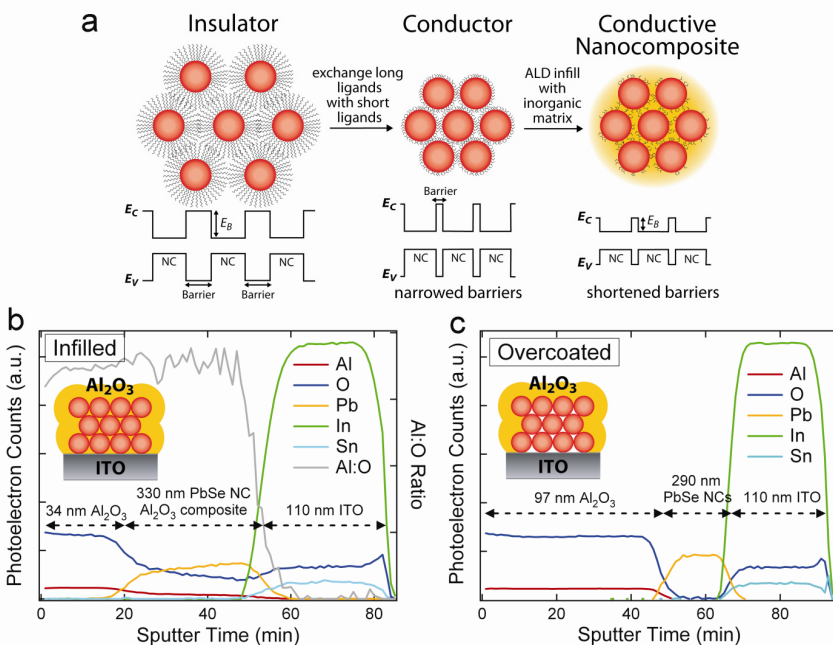


**Figure 2.** **a**, Conductive QD films made by ligand exchange with short-chain organic molecules are infilled with metal oxides/sulfides by low-temperature ALD, creating stable inorganic nanocomposites. **b**, XPS depth profile of a PbSe QD film infilled with ALD Al<sub>2</sub>O<sub>3</sub> at 70°C. **c**, XPS profile of an EDT-treated QD film overcoated (not infilled) with CVD Al<sub>2</sub>O<sub>3</sub> at 70°C in the same deposition chamber.

**QD Films with Air-Stable Electron Mobilities above  $7 \text{ cm}^2 \text{ V}^{-1} \text{ s}^{-1}$ .** In order to produce high photocurrent and efficiency, a solar cell must normally have a minority carrier diffusion length (the characteristic distance that an electron or hole moves before recombining) that is longer than the thickness of the active layer. A critical challenge in the field of QD solar cells is that the diffusion length of existing QD films is too short by a factor of 10-20, limiting currents and forcing the use of optically thin active layers (“depleted heterojunctions”) that will never achieve high efficiency. Increasing the diffusion length depends on increasing the carrier mobility-lifetime product as much as possible, which calls for new strategies to simultaneously maximize interdot electronic coupling and minimize disorder and recombination. The electron mobility of QD films used in solar cells is less than  $0.1 \text{ cm}^2 \text{ V}^{-1} \text{ s}^{-1}$  (about 10 times smaller than the value for amorphous silicon). We have achieved electron mobilities above  $7 \text{ cm}^2 \text{ V}^{-1} \text{ s}^{-1}$  in ambipolar PbSe QD FETs by using ALD infilling of amorphous alumina ( $\text{a-Al}_2\text{O}_3$ ) to tune the carrier concentration and reduce the trap density in QD films prepared via dip coating with sodium sulfide ( $\text{Na}_2\text{S}$ ) ligand exchange (Figure 3). Sulfide capping results in a very small interdot distance, strong electronic coupling, and high-conductance  $p$ -channel FETs prior to infilling. Alumina infilling is found to systematically lower the free hole concentration by eliminating acceptors at the QD surface. As a result, the FETs evolve from  $p$ -channel to ambipolar and then to dominant  $n$ -channel behavior, with linear electron mobilities of  $4\text{-}5 \text{ cm}^2 \text{ V}^{-1} \text{ s}^{-1}$  and  $6\text{-}8 \text{ cm}^2 \text{ V}^{-1} \text{ s}^{-1}$  for fully-infilled devices made at ALD temperatures of  $54^\circ\text{C}$  and  $75^\circ\text{C}$ , respectively. Using partial ALD infilling, we can for the first time control the dominant carrier type and equilibrium film conductivity to make  $p$ -type films that feature high minority carrier mobilities, favorable for efficient thin-film QD solar cells. Since the high electron mobility is achieved partly by passivating surface defects, the mobility-lifetime product and diffusion length should be especially large in these films. Moreover, the ALD coating renders the FETs indefinitely

stable in air. These sulfide-treated, ALD-infilled PbSe QD FETs are the first high mobility, air stable PbX QD solids and should be useful in the development of high-performance QD solar cells.

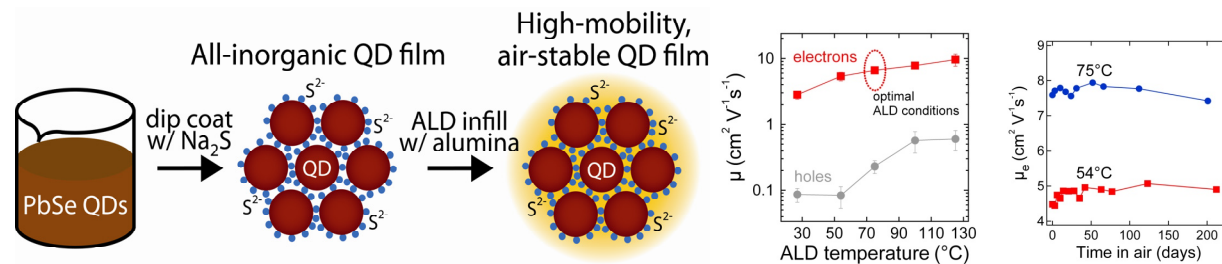


**Figure 3.** High-mobility, air-stable QD solids. **(left)** Fabrication scheme for ALD-infilled, sulfide-capped PbSe QD films. **(middle)** Electron mobility of QD field-effect transistors as a function of ALD temperature. Mobility reaches 6-8 cm<sup>2</sup> V<sup>-1</sup> s<sup>-1</sup> at a deposition temperature of 75°C. **(right)** Electron mobility versus time in air for two films, one made at 54°C and another at 75°C, showing that the FET performance is stable indefinitely in air.

### Future Plans

Our major efforts over the next year will include completing SKPM and EFM studies of working QD solar cells to determine their mechanisms of operation and to probe the real-time effects of oxidation, heat, light, and electric fields on the internal physics of such cells. We will also use our high-mobility, air-stable QD films made by ALD infilling to fabricate *p-n* heterojunction QD solar cells with record photocurrent and efficiency, with a short-term target of over 8%. This work will likely involve outdoor stability testing at our Amonix two-axis tracking tower testing facility at UCI. Finally, we are interested in combining electronic and spectroscopic measurements to study the surface states that limit carrier mobility, increase recombination rates, and promote oxidative degradation of PbX QD films, both in the QD film bulk and at the interfaces between QDs and metals or other semiconductors. These efforts will occupy us through the end of the project period and beyond.

### References to DOE-Sponsored Publications (2010-2012)

1. p-Type PbSe and PbS quantum dot solids prepared with short-chain acids and diacids. Zarghami, M. H., Liu, Y., Gibbs, M., Gebremichael, E., Webster, C., Law, M. *ACS Nano* **4**, 2475-2485 (2010).
2. Dependence of carrier mobility on nanocrystal size and ligand length in PbSe nanocrystal solids. Liu, Y., Gibbs, M., Puthussery, J., Gaik, S., Ihly, R., Hillhouse, H. W., Law, M. *Nano Letters* **10**, 1960-1969 (2010).
3. Robust, functional nanocrystal solids by infilling with atomic layer deposition. Liu, Y., Gibbs, M., Perkins, C. L., Zarghami, M. H., Bustamante, Jr., J., Law, M. *Nano Letters* **11**, 5349-5355 (2011).
4. The photothermal stability of PbS quantum dot solids. Ihly, R., Tolentino, J., Liu, Y., Gibbs, M., Law, M. *ACS Nano* **5**, 8175-8186 (2011).
5. Pseudodielectric function and critical point energies of iron pyrite. Choi, S. G., Hu, J., Abdallah, L. S., Limpinsel, M., Zhang, Y. N., Zollner, S., Wu, R. Q., Law, M. *Physical Review B* **86**, 115207 (2012).
6. PbSe quantum dot field-effect transistors with air-stable electron mobilities above 7 cm<sup>2</sup> V<sup>-1</sup> s<sup>-1</sup>. Liu, Y., Tolentino, J., Gibbs, M., Ihly, R., Perkins, C. L., Liu, Y., Crawford, N., Hemminger, J. C., Law, M. *Nano Letters*, ASAP (2013).

## POLYMER MULTIFERROICS

Shenqiang Ren\* and Manfred Wuttig\*\*

\* Department of Chemistry, University of Kansas, Lawrence, KS

\*\* Department of Materials Science, University of Maryland, College Park, MD

Excitonic semiconducting polymers are interesting and promising materials because of their fundamental physical properties and potential for photovoltaic applications utilizing the charges created by the controlled dissociation of photoinduced excitons. However, until now, coupling of exciton with magnetic and mechanical degrees of freedom has been elusive, although exciton magnetism is a well-known property. Here, we report on the observation of substantial visible light-, electrically and mechanically induced changes of the magnetization of an organic exciton multiferroic consisting of single crystal P3HT doped with C<sub>60</sub>. An electric field of 5 MVm<sup>-1</sup> switches the room temperature saturation magnetization on and off, resulting in a magnetoelectric coupling coefficient of 40 mV/cm Oe at 100 Oe. Illumination of the composite with 615 nm light increases the room temperature magnetization about two fold. Stress changes the magnetization by  $\left. \frac{\partial M}{\partial \sigma} \right|_{H,T} \approx 4 \cdot 10^{-6} \text{ Oe}^{-1}$ , [1] significantly more than that of crystalline metallic ferromagnets.

Morphology control of the active layer is crucial to achieve high magnetoelectric coupling efficiency. It can be exercised through decomposition of polymer blends or ordering of block copolymers (BCPs)[2] with appropriate blocks which could spontaneously self-assemble into nanostructured films. This can be achieved by block polythiophenes with not only crystallinity contrast but also distinct electronic properties of the two blocks further demonstrating the potential of this mode of morphology control toward a new type of organic exciton multiferroics. Our strategy is to deposit nanostructured films from all conjugated block copolymer solutions.[3] The bicontinuous network formed within two distinct electronic blocks will facilitate high charge separation yielding efficient charge transport and excitonic magnetism. The multiferroic devices prepared using this strategy display high ME coupling coefficient of 79.6 V/cm Oe, achieved at a hexagonal block ratio (3:1).

<sup>1</sup> S. Ren, M. Wuttig, *Adv. Mater.* 24, 724, 2012

<sup>2</sup> S. Ren, R. Briber and M. Wuttig, *Appl. Phys. Lett.* 93, 173507, 2008

<sup>3</sup> J. Lohrman, S. Duan, Y. Liu, X. Zhao, M. Wuttig and S. Ren, *Adv. Mater.* 25, 783, 2013

**p-type Dye-Sensitized Solar Cells: Materials and Charge Carrier Dynamics**  
(DE-FG02-07ER46427)

PI: Yiyi Wu

Address: 100 W 18th Avenue, The Ohio State University, Columbus, OH 43210

e-mail: wu@chemistry.ohio-state.edu

**Program Scope**

Conventional Grätzel cells are called n-type dye-sensitized solar cells or n-DSCs because n-type semiconductors such as TiO<sub>2</sub> are used as the support for accepting electrons injected from photoexcited sensitizers. These sensitized photoanodes have been studied extensively in the last two decades. In contrast, much less work has been done on cells based on dye-sensitized photocathodes, which use p-type semiconductors as the support for accepting photo-injected holes.<sup>3</sup> They are called p-DSCs in this proposal. A tandem DSC, consisting of a dye-sensitized TiO<sub>2</sub> photoanode and a dye-sensitized photocathode, represents an attractive structure for achieving a high energy-conversion efficiency (see Fig. 1). Currently, the efficiency of a tandem DSC is limited by the relatively poor performance of the p-DSC side. *Therefore, the focus of this proposal is to identify and synthesize new p-type semiconductors and dye molecules, and to understand the fundamental charge transport and transfer processes at the p-semiconductor/dye/electrolyte interfaces.*

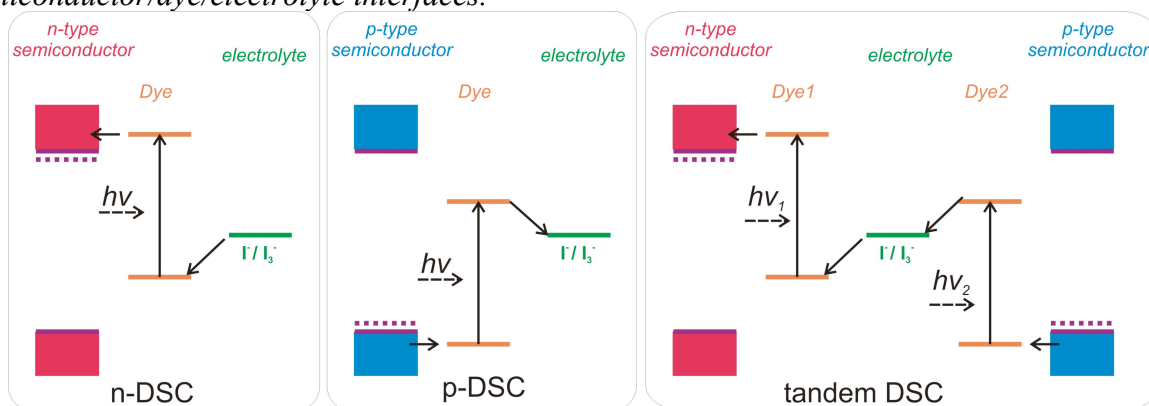


**Figure 1.** Schematic operation principle of n-DSC (left), p-DSC (middle), and the tandem DSC (right). The passive counter-electrode in the n-DSC and p-DSC is not shown. The arrows show the direction of electron flow.

**Summary of our achievements**

This project has three aspects of activities: (1) designing new dye sensitizers for p-DSCs, (2) synthesizing new nanostructured p-type semiconductors with proper valence band (VB) position, high visible transparency and high hole mobility, and (3) investigating the charge carrier kinetics of the solar cells. We have made significant progresses in all three aspects in the past three years.

**a: Dye sensitizers**

Dye sensitizers are a key component in a DSC for the efficient light harvesting and charge separation. In the past three years, we have synthesized 10 cyclometalated Ru(II) dyes that allow us to tune the HOMO/LUMO positions and the regeneration/recombination kinetics. We have also synthesized three new organic donor-acceptor dyes with different linker groups. For example, we have designed and synthesized the first series of cyclometalated ruthenium complexes as sensitizers for NiO p-DSCs (see Fig. 2). We have also carried out femtosecond (fs) transient absorption (TA) to study the interfacial charge injection and recombination rate at the sensitizer/NiO interface. The results suggest that hole injection from the excited dye to NiO occurs within sub-ps time window. Due to the heterogeneous nature of the NiO/dye interface, multiple exponential charge recombination processes, spanning from ps to ns, were observed (Fig. 3). In addition, the charge recombination rate decreases as the spacer length increases. The correlation of the charge recombination rate is further analyzed in terms of attenuation factor  $\beta$  according to the equation:

$k_{et} = k_0 \exp(-\beta r)$ , where  $k_{et}$  is the electron transfer rate,  $k_0$  is the rate constant, and  $r$  is the distance for electron transfer.

**b. CuGaO<sub>2</sub> Nanoplates for high-photovoltage p-DSCs**

The p-type wide-bandgap semiconductor is another key component in a p-DSC. It supports the adsorption of a monolayer of dye molecules, collects the holes injected from the photoexcited dye molecules and transports the injected holes to the conductive substrate. Till date, the predominant p-type semiconductor used in p-DSCs is NiO. An exciting finding from our prior studies is the first application of delafossite CuGaO<sub>2</sub> nanoplates for p-DSCs. The reason we have selected CuGaO<sub>2</sub> is its high hole mobility due to the mixing between the Cu-3d<sup>10</sup> orbitals and the oxygen-2p<sup>6</sup> orbitals at the valence band maximum. It is also more transparent than NiO, because it does not contain partially occupied d-orbitals. The white-yellowish CuGaO<sub>2</sub> nanoplates (~200nm in size) barely compete with the dye sensitizers for visible light absorption (Fig. 4). Saturation photovoltage of 464 mV and open-circuit voltage V<sub>oc</sub> of 357mV under 1sun AM 1.5

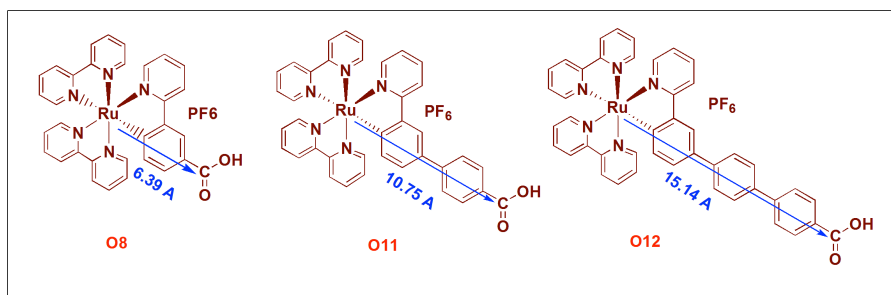


**Figure 2.** The structures of sensitizer O8, O11, and O12

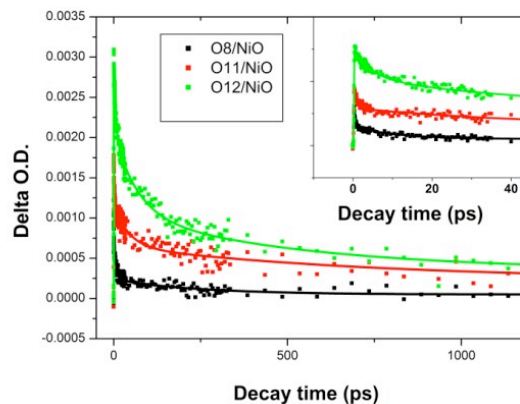


**Figure 3.** The kinetic traces of O8/NiO, O11/NiO, and O12/NiO probed at 681 nm, 679 nm, and 684 nm respectively.

The p-type wide-bandgap semiconductor is another key component in a p-DSC. It supports the adsorption of a monolayer of dye molecules, collects the holes injected from the photoexcited dye molecules and transports the injected holes to the conductive substrate. Till date, the predominant p-type semiconductor used in p-DSCs is NiO. An exciting finding from our prior studies is the first application of delafossite CuGaO<sub>2</sub> nanoplates for p-DSCs. The reason we have selected CuGaO<sub>2</sub> is its high hole mobility due to the mixing between the Cu-3d<sup>10</sup> orbitals and the oxygen-2p<sup>6</sup> orbitals at the valence band maximum. It is also more transparent than NiO, because it does not contain partially occupied d-orbitals. The white-yellowish CuGaO<sub>2</sub> nanoplates (~200nm in size) barely compete with the dye sensitizers for visible light absorption (Fig. 4). Saturation photovoltage of 464 mV and open-circuit voltage V<sub>oc</sub> of 357mV under 1sun AM 1.5

illumination have been obtained from CuGaO<sub>2</sub>-based p-DSCs. These are among the highest values that have been reported for p-DSCs. This area will be the focus of our future work.

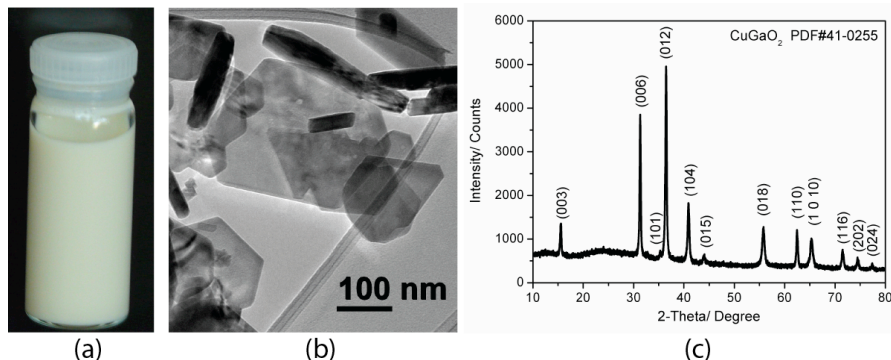


**Figure 4.** CuGaO<sub>2</sub> nanoplates: (a) a digital photo of the CuGaO<sub>2</sub> particles dispersed in water; (b) TEM image and (c) XRD pattern of the CuGaO<sub>2</sub> nanoplates.

### c. Understanding NiO p-DSCs

NiO is a magnetic insulator. Ni<sup>2+</sup> has the partially filled and localized 3d-orbitals. The band picture resulting from the orbital overlap is not accurate for describing the electronic properties of NiO. Some basic questions of NiO have not been well elucidated, despite its common use in p-DSCs. What controls the photovoltage of NiO-based p-DSCs? How to describe the hole-transport in NiO? Is the transport a bulk property or just a surface property of NiO? Therefore, in our study of p-DSCs, *we not only pursue new semiconductors such as CuGaO<sub>2</sub> delafossite, but also try to establish a better understanding and control of NiO.*

A major effort is to use impedance spectroscopy to probe the device physics of the NiO p-DSCs. *We have carried out the first systematic electrochemical impedance spectroscopy (EIS) study of the NiO based p-DSCs and measured the key parameters in the charge recombination processes including the recombination resistance, chemical capacitance, and the hole lifetime.* From the measured resistances, we have quantitatively interpreted the shape of the current-voltage J-V curves of NiO p-DSCs and identified the overwhelming recombination of the photo-injected holes with the reduced dye anions as the factor responsible for the *low fill factor in NiO p-DSCs* (Fig. 5). We have also used atomically deposited alumina to slow down the recombination reactions in NiO p-DSCs, and used cation doping to tune the valence-band edge of NiO. The transport mechanism in NiO has also been explained.

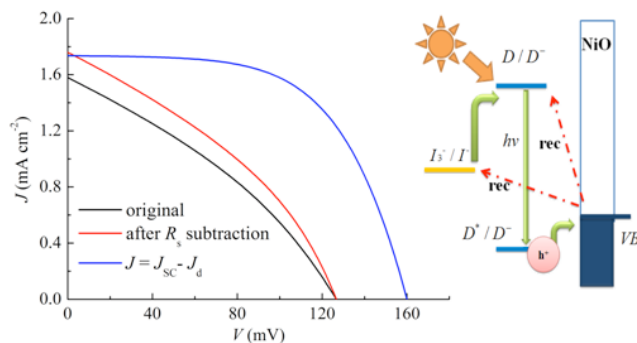


**Figure 5:**  $J$ - $V$  curve of a typical NiO p-DSC, before and after eliminating the series resistance and the recombination with reduced dye.

#### **d: A list of papers from 2010 - 2012**

1. P. Hasin, M. A. Alpuche-Aviles, Y. Wu\*. “Electrocatalytic activity of graphene multilayers towards  $I^-/I_3^-$ : effect of preparation conditions and polyelectrolyte modification” *J. Physical Chemistry C* 114(37), 15857 (2010).
2. G. Natu, Y. Wu\*. “Photoelectrochemical Study of the Ilmenite Polymorph of  $CdSnO_3$  and its Photoanodic Application in Dye-Sensitized Solar Cells” *J. Physical Chemistry C*, **114** (14), 6802 (2010).
3. Z. Ji, G. Natu, Z. Huang and Y. Wu\*, “Linker effect in organic donor-acceptor dyes on p-type NiO dye sensitized solar cells” *Energy & Environmental Science*, 2011, **4**, pp 2818-2821.
4. Z. Huang, G. Natu, Z. Ji, P. Hasin and Y. Wu\*, “P-type Dye-Sensitized NiO Solar Cells: A Study by Electrochemical Impedance Spectroscopy” *Journal of Physical Chemistry C*, 2011, **115** (50), pp 25109–25114.
5. G. Natu, Z. Ji and Y. Wu\*, “The Effect of an Atomically Deposited Layer of Alumina on NiO in P-type Dye-Sensitized Solar Cells”, *Langmuir*, 2012, **28** (1), pp 950–956.
6. M. Yu, G. Natu, Z. Ji and Y. Wu\*, “p-Type Dye-Sensitized Solar Cells Based on Delafossite  $CuGaO_2$  Nanoplates with Saturation Photovoltages Exceeding 460 mV” *Journal of Physical Chemistry letters*, 2012, **3**, pp 1074–1078.
7. Z. Ji, G. Natu, Z. Huang, O. Kokhan; X. Zhang\*, and Yiyang Wu\*, " Synthesis, Photophysics and Photovoltaic Studies of Ruthenium Cyclometalated Complexes as Sensitizers for P-Type NiO Dye-Sensitized Solar Cells”, *Journal of Physical Chemistry C*, 2012, **116** (32) pp 16854-16863.
8. Z. Huang, G. Natu, Z. Ji, M. He, M. Yu, and Y. Wu\*, “ Probing the low fill factor of NiO p-Type dye-sensitized solar cells” *Journal of Physical Chemistry C*, 2012, **116**, pp 26239-26246.
9. G. Natu, P. Hasin, Z. Huang, Z. Ji, M. He and Y. Wu\*, “Valence Band-edge engineering of nickel oxide nanoparticles via cobalt doping for application in p-type dye-sensitized solar cells” *ACS Applied Materials and Interfaces*, 2012, **4**(11) pp 5922-5929.

#### **e: Future plan.**

Our prior results have clearly shown that  $CuGaO_2$  holds a great promise as the p-type semiconductor in p-DSCs. Therefore, in our future plan, we will systematically investigate Cu(I)-based p-type delafossite semiconductors including  $CuAlO_2$ ,  $CuGaO_2$  and  $CuScO_2$ . The goal is to understand the basic chemistry and crystallization process in the hydrothermal synthesis of these delafossite nanocrystals, determine their band energies, and measure the charge carrier dynamics at the semiconductor/dye/electrolyte interface. The results are expected to have an impact to the fundamental materials science of delafossites. The knowledge will establish an understanding of the crystallization of delafossite nanocrystals, and also the physical properties of the delafossite/electrolyte junctions. Moreover, these delafossites have the technologically important applications as the p-type transparent conducting oxides. Our results will have an impact not only to p-DSCs, but also to other areas such as transparent electronics and photoelectrochemical reduction of water and  $CO_2$ .

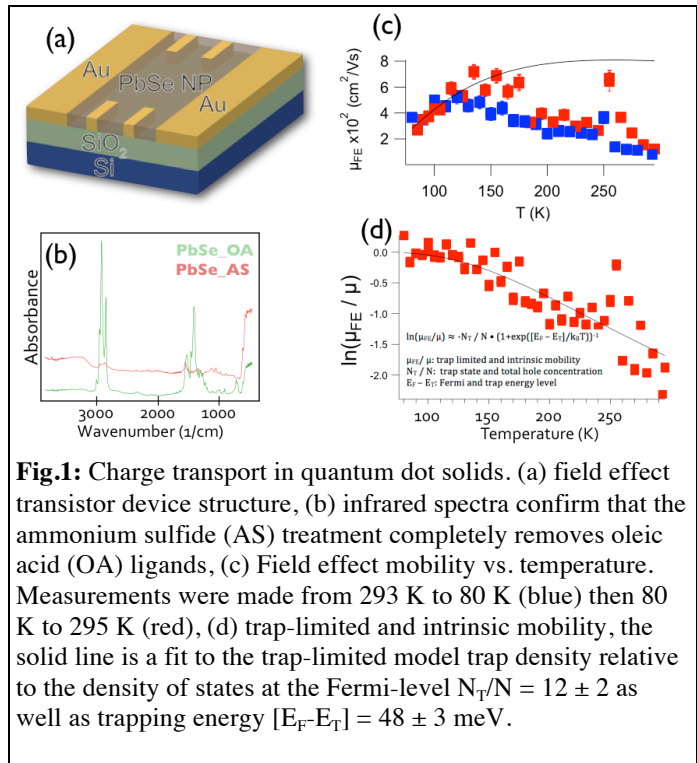
**Charge Transfer Across the Boundary of Photon-Harvesting Nanocrystals**  
**Frank Wise (PI)**  
**Department of Applied Physics**  
**Tobias Hanrath, Jim Engstrom**  
**Department of Chemical and Biochemical Engineering**  
**Cornell University**  
**Ithaca, NY 14853**

**Recent Progress**

A central goal of this project is to understand the mechanisms that govern extraction of photogenerated charge from quantum-confined nanocrystals and the transport to external electrodes. In the context of photovoltaic devices, we seek to gain a deeper understanding of how photogenerated excitons dissociate and the subsequent transport of free electrons and holes from the site of generation to the external contacts. We have performed studies of charge transport in the thin films of nanocrystals, and we have also made advances in the charge-transport layers adjacent to the nanocrystal film. A highlight is the demonstration of confined-but-connected films of semiconductor nanocrystals.

**Quantum-dot solids**

We studied charge transport in PbSe nanocrystal films deposited onto prefabricated field effect transistor structures (Fig. 1a). Nanocrystals were coupled by chemical treatment with ammonium sulfide, which completely removed the original oleic acid ligand (Fig. 1b). Temperature-dependent transport measurements revealed positive and negative correlation between mobility and temperature (Fig. 1c). At low temperature we observe thermally activated transport. The solid line in Fig. 1c represents the mobility predicted for nearest-neighbor hopping with an activation energy of 22 meV, particle diameter of 5.2 nm, wavefunction decay parameter of  $1 \text{ \AA}^{-1}$ , and hopping distance of 5  $\text{\AA}$ . Mobility measurements revealed decreasing mobility with increasing temperature (Fig. 1). The negative correlation between temperature and mobility has previously been interpreted as ‘band-like’ charge transport through delocalized states. Given the extent of electronic disorder prevailing in nanocrystal films, we have adopted alternative models. The transport data are well described by models adopted from transport in disordered solid. We can describe the ratio of trap-limited mobility (at high temperature) to the intrinsic mobility as a function of the trap density relative to the density of states at the Fermi level and the trapping energy (Fig. 1d). An alternate model of charge transport in polycrystalline thin films describes the charge transport limitation in context of grain boundary scattering. This model predicts charge transport limited by acoustic phonon scattering at high temperatures and a  $T^{-5/2}$  temperature dependence; at low temperatures grain boundary scattering dominates. Our current work focuses on refining this hypothesis by testing a range of grain sizes, which we can tailor by changing the diameter of the nanocrystals.



### ***Nanorod solids***

Nanorods may offer some advantages over spherical nanocrystals for photovoltaics. They have larger absorption cross-sections, which is significant because very thin layers of nanostructures may be required by the electron transport in the layer. There will be much interest in nanorods for solar cells, because carrier multiplication is significantly stronger in nanorods than in dots [1,2]. As a first step toward making nanorod cells, we studied films of 4x30-nm PbSe nanorods. An interesting aspect in nanorod thin films is the preferred orientation of the rod axis relative to the plane of the film. We have investigated thin film formation by drop-casting and spin-casting and are characterizing the film structure by electron microscopy and X-ray scattering. We have investigated optical signatures of inter-rod charge transport. With long-chain oleic-acid ligands, mixtures of two diameters of nanorods exhibit clear signatures of resonant energy transfer (Fig. 2). This information will be critical as we start to study charge transfer in nanorod films.

### ***Confined-but-connected quantum dots***

The presence of long-chain organic ligands on the surface of colloidal quantum dots has presented a long-standing challenge to achieve efficient electronic coupling between proximate dots. Several ligand exchange methods have been developed to displace ligands and ‘cross-link’ the dots. Unfortunately, these methods generally disrupt the orientational and translational order of the quantum dot assembly. We have recently discovered a novel ligand exchange method that balances the dynamics of ligand exchange and particle assembly in a way to yield confined-but-connected structures. Importantly, quantum dots in these structures are coupled in specific crystallographic directions (*i.e.*,  $\langle 100 \rangle$ ). We have confirmed the confined-but-connected structure using electron microscopy and X-ray scattering (Fig. 3). Absorbance spectra reveal excitonic peaks, which confirm that the electronic structure of the treated films is still quantum confined. The ability to create confined-but-connected ‘quantum grid’ structures presents an interesting experimental platform for optical and electronic measurements.

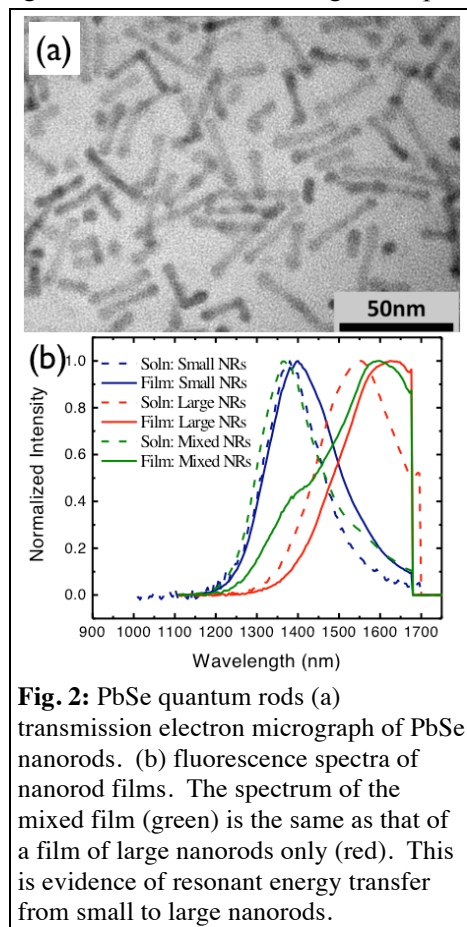


**Fig. 2:** PbSe quantum rods (a) transmission electron micrograph of PbSe nanorods. (b) fluorescence spectra of nanorod films. The spectrum of the mixed film (green) is the same as that of a film of large nanorods only (red). This is evidence of resonant energy transfer from small to large nanorods.

### ***All-inorganic nanocrystal photovoltaics***

Organic materials such as PEDOT are commonly used as hole-transport layers in photovoltaics. We are eager to improve on the performance of PEDOT, and for stability it is desirable to eliminate organic materials and organic/inorganic interfaces. We are assessing NiO for this purpose. First, we confirmed that charge transfer from PbS nanocrystals to NiO occurs, by monitoring the fluorescence of PbS nanocrystals linked to nanoparticles of NiO. Fast quenching of the nanocrystal fluorescence (Fig. 4) is the signature of charge transfer.

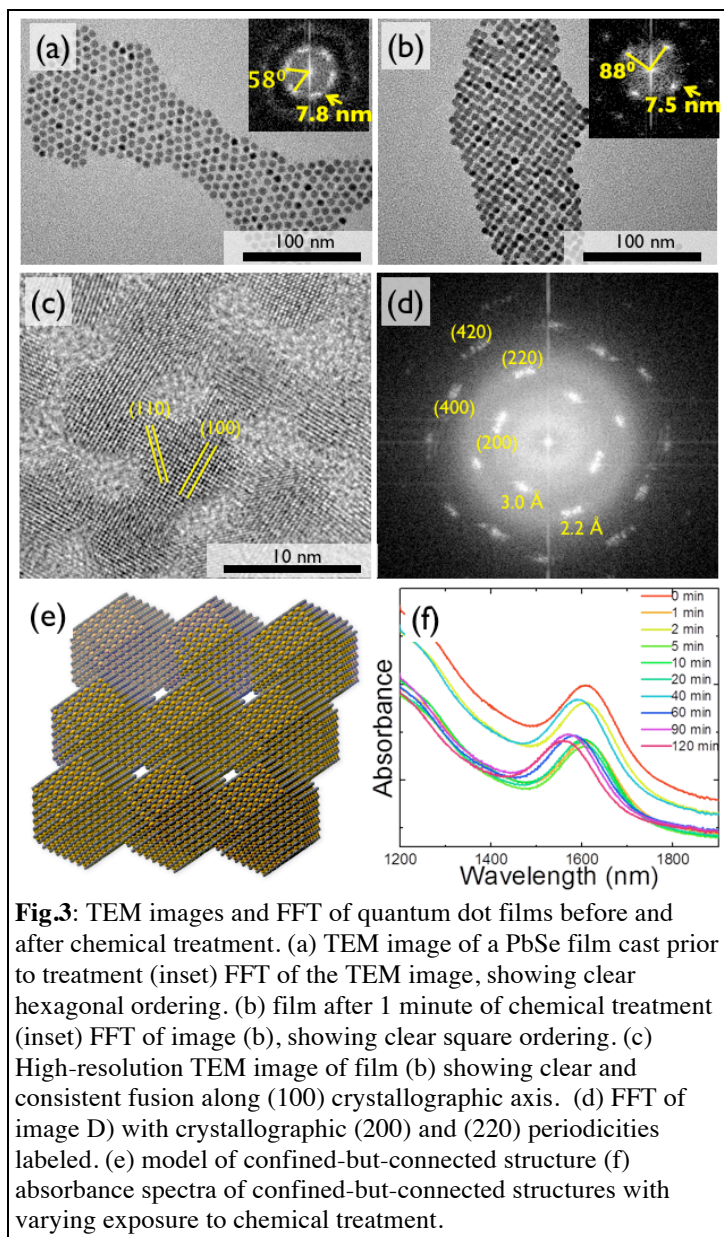


**Fig.3:** TEM images and FFT of quantum dot films before and after chemical treatment. (a) TEM image of a PbSe film cast prior to treatment (inset) FFT of the TEM image, showing clear hexagonal ordering. (b) film after 1 minute of chemical treatment (inset) FFT of image (b), showing clear square ordering. (c) High-resolution TEM image of film (b) showing clear and consistent fusion along (100) crystallographic axis. (d) FFT of image D) with crystallographic (200) and (220) periodicities labeled. (e) model of confined-but-connected structure (f) absorbance spectra of confined-but-connected structures with varying exposure to chemical treatment.

Our typical prototype solar-cell structure is shown in Fig. 4. The design of the device stack is guided by an optical model employing a transfer matrix formalism to calculate the reflected and transmitted waves at each interface in the device stack. Solar cells made with sol-gel NiO hole-transport layers produce encouraging results, reaching 2.5% efficiency. However, the sol-gel film requires thermal treatment, which increases the resistivity of the ITO contact layer. Furthermore, thermal treatment will be a problem for the creation of tandem cells. Finally, it is difficult to control the thickness of sol-gel films adequately. We are currently investigating room-temperature sputtering as a possible route to production of the films. We have succeeded in sputtering NiO and ZnO films for the structure of Fig. 4. Energy conversion efficiency above 5% has been reached (Fig. 4). Although it has not been completely optimized, this all-inorganic structure offers performance that is not far from the best reported for a nanocrystal solar cell, which is 7% efficiency [3].

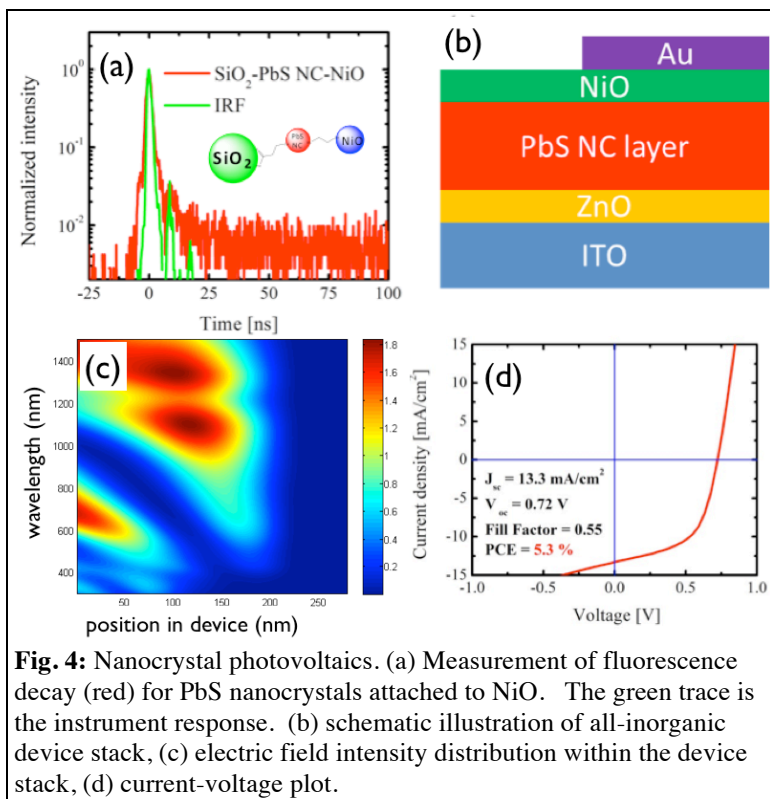
### ***Development of atomic layer deposition***

We are working on methods to infiltrate thin films of semiconducting nanocrystals with inorganic materials, preferably semiconductors. This will require investigation of methods to remove the organic ligands, along with methods to fill the interstitial spaces with inorganic

materials using atomic layer deposition. To develop a better understanding of these processes, we are developing a high-pressure probe/reaction cell. This cell will enable the investigation of vapor phase deposition processes under realistic reaction conditions, and direct *in situ* analysis in UHV without exposing the thin film to the atmosphere.

The design of the cell consists of a central channel where the reactants are input. This central channel is surrounded by an annular region where these reactants are pumped out. Separately, a purge flow is also introduced in the surrounding UHV chamber, and this flow is also pumped through the annular region. This surrounding purge flow acts to minimize the contact of reactant gases with the inner walls of the UHV chamber, thus preserving UHV conditions once the (inert) purge gas is pumped away.

We have developed a design for a high-pressure probe/reaction cell that can produce realistic reaction conditions ( $p \sim 1$  Torr) and fast cycle times for ALD ( $< 10$  s), and this design results in minimal exposure of the inner walls of the UHV chamber to reactive gases ( $< 10^{-6}$  Torr). Components of the cell have been ordered, and we expect construction of the cell to commence in May of 2013.



### ***Publications under DoE Support***

None yet.

### ***Future Plans***

Our plans for the near future include the following:

- Ligand exchange on lead-salt nanorods, and investigation of the resulting films
- Fabrication and characterization of solar cells with PbSe nanorods
- Systematic structural, electronic, and optical characterization of the quantum-grid structures
- Calculation of the electronic states of the quantum-grid structures
- Construction of high-pressure cell for studies of ligand removal and filling interstitial spaces in nanocrystal solids
- Characterization of nanocrystal solids treated by atomic layer deposition

### ***References***

1. P. D. Cunningham *et al.*, “Enhanced multiple exciton generation in quasi-one-dimensional semiconductors,” *Nano Lett.* 11, 3476 (2011).
2. L. A. Padilha *et al.*, “Aspect ratio dependence of Auger recombination and carrier multiplication in PbSe nanorods,” *Nano Letters*, Articles ASAP.
3. A. H. Ip *et al.*, “Hybrid passivated colloidal quantum dot solids,” *Nature Nanotech.* 7, 577 (2012).

**Program title:**

Exceeding the Planck free-space energy transfer limit through photonic density of states control and near field coupling.

**Principle investigator:**

Ting S. (Willie) Luk.

**Mailing address:**

Sandia National Laboratories, P.O. Box 5800, Albuquerque, NM 87185.

[tsluk@sandia.gov](mailto:tsluk@sandia.gov)

**Program scope or definition:**

The overarching goal of this project is to achieve a fundamental understanding of light-matter interaction through engineering material properties at the subwavelength scale. This enables tailoring of electronic and photonic density of states, and the phase-space of light and matter. The ultimate goal is to control the flow of energy between photons, phonons and electrons in ways that are not possible with natural materials. We seek to achieve a fundamental understanding of how the electromagnetic phase space and density of states can be engineered to tailor the spectral content of electromagnetic energy at the surface and interior to nanostructured photonic materials. The objective of this research effort is to exploit the design flexibility offered by nanostructured materials to produce advanced electromagnetic materials with enhanced properties and functionalities. We will also study the dynamical behavior of energy transport between nanostructure materials. Specifically, we studied surface plasmon polariton (SPP) and epsilon-near-zero modes as a mean to enhance photonic density of states in Indium Tin Oxide and hyperbolic metamaterial systems.

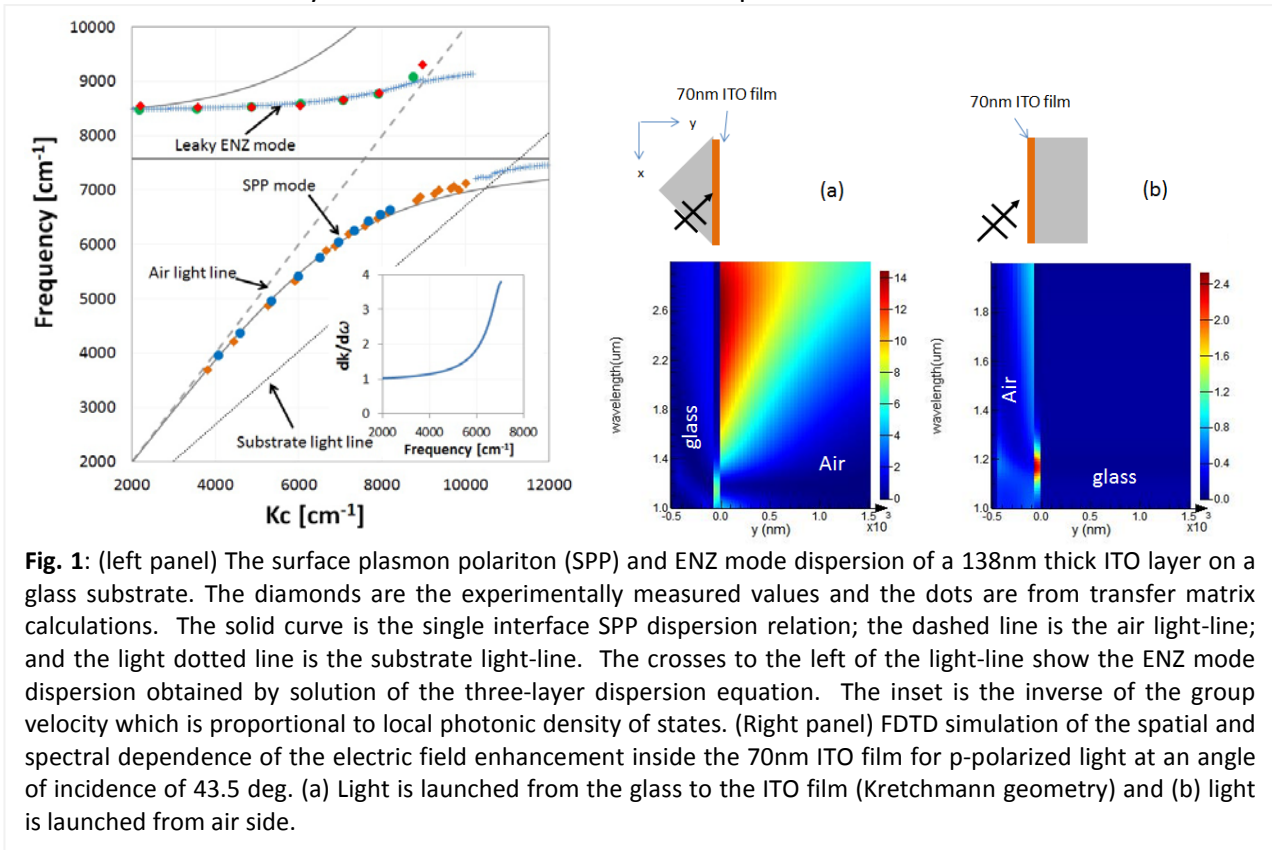
**Recent Progress:***High photonic density of states surface plasmon polariton and epsilon-near-zero (ENZ) modes*

Photonic nanostructures supporting large momentum photonic modes can store more electromagnetic energy than conventional materials, since the phase space for such modes can be quite large, leading to a large *total number of modes*. Furthermore, spectral content of the electromagnetic energy can be tailored by manipulating the photonic *density of modes*. A large photonic density of states can be achieved using high Q photonic crystal cavities, however, such structures do not lead to large photonic momentum because the lattice constant is comparable to the wavelength[1]. The SPP mode has both a large photonic momentum and a large photonic density of states due to its flat dispersion property near the surface plasmon frequency. This optical mode has been studied for many years and continues to be of interest. Indeed recent investigations of SPP modes have shown: strong interaction of quantum dots (QD) with SPPs[2]; and using the SPPs field profile to enhance the mode confinement of nanowire lasers[3]. However, demonstrations of good plasmonic materials and tuning the surface plasmon frequency have been limited. Photonic nanostructures offer a route to the development of better infrared and near-infrared plasmonic materials that can form the basis for a new regime of electronic and photonic density of states control.

Indium tin oxide (ITO) is a well-known transparent conductive oxide that is widely used in many optoelectronic devices. ITO is accurately described by a simple Drude model, and has a plasma frequency that is located in the near infrared (1.3-1.6 $\mu\text{m}$ ). To accurately determine the density of states enhancement at the SPP frequency, we performed a comprehensive

experimental characterization of high quality ITO films. The results of these characterization efforts are presented in Figure 1 which shows the measured dispersion curves for the ITO film. We observe the SPP dispersion lying to the right of the light-line and tending towards horizontal as the parallel wavevector is increased. From the slope of the dispersion curve we can determine the group velocity index of the SPP mode which provides us with a measure of the density of states enhancement. We experimentally determine this enhancement to be approximately 4.

In addition to the SPP dispersion, we also measure the dispersion of the epsilon-near-zero mode in detail for the first time. Importantly, as seen in Fig. 1, this mode exhibits a very flat dispersion behavior suggesting this mode will be associated with a high photonic density of states. The measured dispersion is in excellent agreement with the complex frequency solution to the thin-film eigenvalue equation. Enhancement of the electromagnetic energy at the ENZ frequency can also be realized when the material is in contact with a high index material by virtue of the boundary condition that the normal displacement field is continuous. In this



manner, thermally excited fields, QD or quantum well emissions in the substrate are enhanced in the ENZ material by a factor of  $\epsilon_2/\epsilon_{ENZ}$ , where  $\epsilon_2$  and  $\epsilon_{ENZ}$  are the dielectric constant of the substrate and material respectively at the ENZ frequency. Based on finite difference time domain simulations (Fig. 1), the  $|E|^2$  enhancement factor is 7 for a 70nm ITO film on a glass substrate, where E is the normal component of the electric field. The enhancement factor can be significantly higher using Si as a substrate or using a high index metamaterial substrate[4].

### SPP and ENZ modes from hyperbolic metamaterials

Hyperbolic metamaterials (HMM), also known as indefinite metamaterials, have very rich optical properties. These materials are characterized by a permittivity tensor which contains both positive and negative values on the diagonal. As a result, the iso-frequency surfaces of these materials are open hyperboloids, rather than the customary ellipsoids of conventional materials (see Fig. 2). This is of great significance since the open surfaces allow modes over a large span of wavevectors, and leads to a large number of modes for each frequency. Since the equipartition theorem states that each mode will possess  $kT/2$  energy in thermal equilibrium, it is anticipated that large energy densities can be achieved within these materials. This type of metamaterial material can be designed to support surface

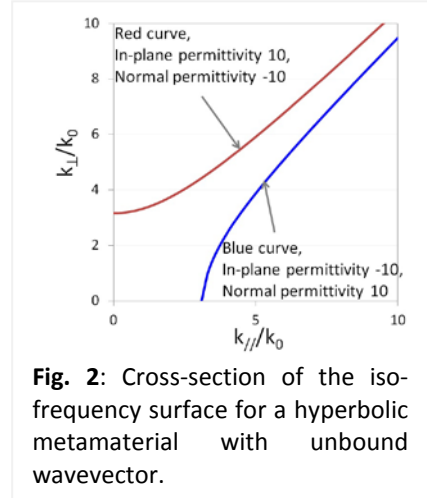
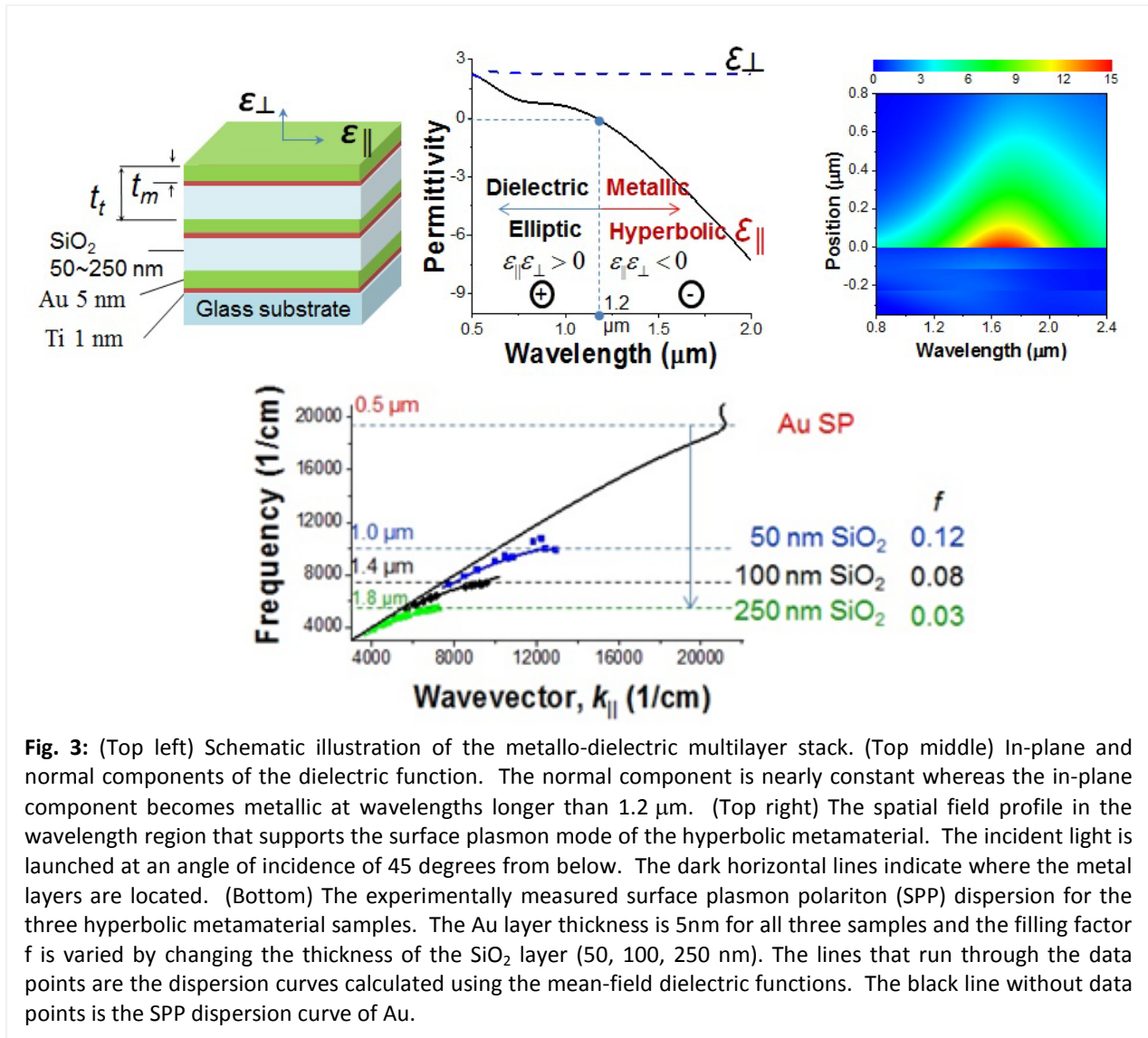


**Fig. 2:** Cross-section of the iso-frequency surface for a hyperbolic metamaterial with unbound wavevector.



plasmon polaritons and ENZ modes also and these modes can be tuned with the metal filling fraction as shown in Fig. 3. We demonstrated this property by using subwavelength periodic metallo-dielectric thin film stack of Au and SiO<sub>2</sub>. These results have been submitted for publication [5].

*Dynamical energy transport by high photonic momentum states*  
 In order to liberate electromagnetic energy stored in spectrally controlled high-photonic momentum states, a nanophotonic antenna is needed. For complex nanophotonic antenna structures, such calculations are typically quite involved. We have developed a theoretical formalism which combines the fluctuation-dissipation theorem and temporal coupled mode theory (CMT) to arrive at simple formulas for the emission properties of resonant thermal emitters. This work was recently published in Applied Physics Letters[6]. The comparison of this formalism and the Finite Difference Time Domain (FDTD) calculations is shown in Fig. 4.

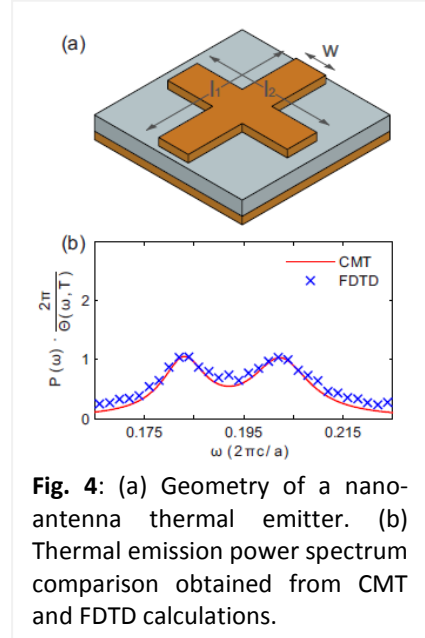


**Fig. 4:** (a) Geometry of a nano-antenna thermal emitter. (b) Thermal emission power spectrum comparison obtained from CMT and FDTD calculations.

#### Future plan

1. Since ENZ and SPP modes both have large photonic density of states, emission properties of QDs interacting with these modes will be studied.
2. Low loss SPP and ENZ states in the infrared region can be tuned using highly-doped semiconductor. Angular dependence study of ENZ emission will be performed.
3. Energy coupling and relaxation behavior of high photonic momentum states to free-space will be studied through nano-antenna.

#### References

- [1] T. S. Luk, S. Xiong, W. W. Chow, X. Miao, G. Subramania, P. J. Resnick, A. J. Fischer, and J. C. Brinker, "Anomalous enhanced emission from PbS quantum dots on a photonic-crystal microcavity," *J. Opt. Soc. Am. B*, vol. 28, pp. 1365-1373, 2011.
- [2] D. E. Gómez, K. C. Vernon, P. Mulvaney, and T. J. Davis, "Surface Plasmon Mediated Strong Exciton-Photon Coupling in Semiconductor Nanocrystals," *Nano Letters*, vol. 10, pp. 274-278, 2010.
- [3] R. F. Oulton, V. J. Sorger, T. Zentgraf, R.-M. Ma, C. Gladden, L. Dai, G. Bartal, and X. Zhang, "Plasmon lasers at deep subwavelength scale," *Nature*, vol. advance online publication, 2009.
- [4] T. S. Luk, Y. C. Jun, I. Kim, T. Tiwald, S. W. Howell, M. B. Sinclair, P. B. Catrysse, and S. Fan, "Epsilon-near-zero and surface plasmon polariton modes in ITO," *In preparation*.
- [5] T. S. Luk, I. Kim, S. Campione, S. W. Howell, G. Subramania, R. K. Grubbs, I. Brener, H.-T. Chen, S. Fan, and M. B. Sinclair, "Near-infrared surface plasmon polariton dispersion control with hyperbolic metamaterials," *submitted*, 2013.
- [6] L. Zhu, S. Sandhu, C. Otey, S. Fan, M. B. Sinclair, and T. S. Luk, "Temporal coupled mode theory for thermal emission from a single thermal emitter," *Applied Physics Letters*, vol. to be published, 2013.

## Crystallization and Thermoelectric Transport in

### Silicon Microstructures and Nanostructures Under Extreme Electrical Stress

Ali Gokirmak ([gokirmak@engr.uconn.edu](mailto:gokirmak@engr.uconn.edu)), Helena Silva ([hsilva@engr.uconn.edu](mailto:hsilva@engr.uconn.edu))

Electrical & Computer Engineering, University of Connecticut, 371 Fairfield Way, Storrs CT 06269-2157

**Program Scope:** To study *a)* crystallization of silicon structures at small scales through self-heating; *b)* thermoelectric phenomena in silicon micro- and nano-structures under extreme electrical stress (which play an important role in the crystallization process).

#### Recent Progress:

- Experimental and computational analysis of the high temperature thermoelectric phenomena that lead to significant asymmetric self-heating; contribution of minority carrier generation-transport-recombination is identified as the main cause<sup>(1)</sup>;
- Extraction of high-temperature electrical resistivity and thermal conductivity of nano-crystalline (nc) Si up to high-temperatures and under extreme thermal gradients (up to  $\sim 1700$  K,  $\sim 1$  K/nm)<sup>(2)</sup>;
- Computational granularity models for percolation and nanoscale filament formation<sup>(3)</sup>;
- Analysis of crystallization of silicon micro/nano-structures through self-heating and impact of thermoelectric effects on crystallization (relative importance of Joule and thermoelectric heating)<sup>(4, 5)</sup>;
- Development of high-temperature measurement setups for resistivity and Seebeck coefficient ( $\sim 30$  C - 600 C) and Hall carrier mobility and concentration ( $\sim 30$  C to  $\sim 450$  C) for thin films<sup>(1, 6)</sup>;
- Application of some of the developed electrothermal models to phase-change memory devices<sup>(7, 8)</sup>;
- Training of students in experimental and computational methods related to crystallization and electrothermal transport at small scales.

*High-Temperature Thermoelectric Transport at Small Scales:* Electrothermal phenomena have been typically studied in the context of thermoelectric energy conversion or solid-state cooling<sup>(9)</sup> using large-scale devices, and electronic transport at small-scales has been mostly studied in the lower temperature range ( $< 400$  K) where the behavior of the charge carriers can be understood by examining the potential energy profiles. Thermoelectric studies at high-temperatures ( $\sim 1000$  K), where the thermal energy of the carriers in semiconductors becomes comparable to their potential energy, and under extreme thermal

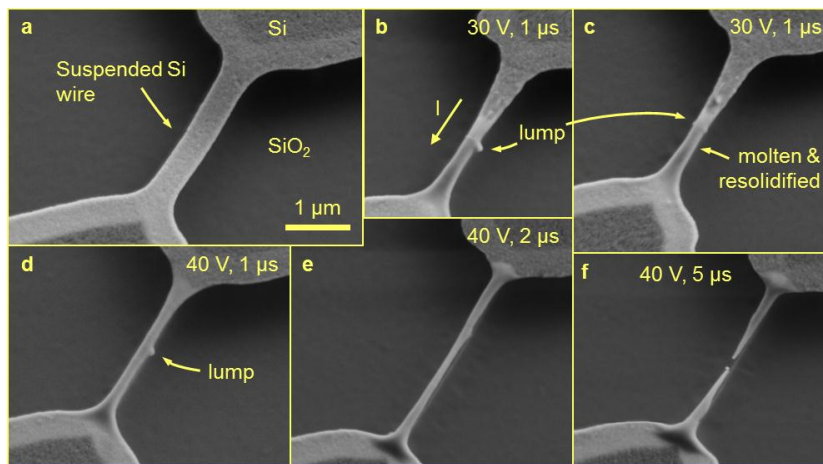


Figure 1. SEM images of (a) an as-fabricated suspended n-type Si wire and (b-f) five wires pulsed using indicated durations and amplitudes. Moderately pulsed wires (b-c) show melting on the source side, whereas larger amplitude pulses (d-f) result in complete melting, sagging and breaking. SEM acceleration 2.5 kV.

gradients ( $> 1$  K/nm), which lead to uncommon electrothermal phenomena, have been limited due to difficulties in performing controlled experiments. We have shown the significance of thermoelectric effects for high-temperature electronics through self-heating of current-carrying highly-doped silicon wires which consistently start melting at one end. This extreme asymmetry in melting reveals the significance of energy transport by drift of thermally

generated minority carriers and their recombination downstream. This minority-carrier *generation-transport-recombination (GTR)* process is a distinct behavior in highly-doped semiconductors under extreme thermal gradients at high temperatures and opposes the direction of the electronic-convective heat flow which dominates in semiconductors at lower temperatures and in metals. These results are directly applicable to emerging electrothermal nanoscale devices such as phase-change memories in which thermal gradients even greater than those in our experiments are expected. Studies on electrothermal effects at high-temperatures and small scales can contribute to large scale implementation of such devices and utilization of their full capacity for information processing.

The experiments were performed with highly doped ( $n \sim 6 \times 10^{19} \text{ cm}^{-3}$ ) silicon microwires self-heated to very high temperatures (up to melting,  $\sim 1690 \text{ K}$ ) (Figure 1)<sup>(1, 10)</sup>. These wires with large contact extensions were lithographically defined and the  $\text{SiO}_2$  layer was partially removed, suspending the wires between the contact-extensions anchored to the substrate. Tungsten probes were used to make electrical contact at these large extension regions. Extremely asymmetric partial melting of these symmetric nc-Si wires is observed for voltage levels and durations that are not sufficient to melt the whole wires (Figure 1b,c). Melting is consistently observed closer to the lower potential end, where the electrons (majority carriers) enter the wires. We attribute this extreme asymmetry to thermoelectric effects that come into play due to high current densities ( $2 - 7 \text{ MA/cm}^2$ ) resulting in steep thermal gradients ( $\sim 1 \text{ K/nm}$ ). The polarity of the asymmetry – hottest point is where the majority charge carriers enter the wire – is in agreement with our optical observations of asymmetric self-heating in *n*- and *p*-type silicon wires<sup>(10)</sup> as well as other similar observations on silicon micro-structures and PCM nano-bridges, all attributed to thermoelectric Thomson heat<sup>(11, 12)</sup>. However, there has been very little or no explanation in the literature for the underlying physical phenomena giving rise to this asymmetry, largely due to difficulties in performing reliable and repeatable measurements at elevated temperatures.

The thermoelectric effects, Seebeck and Peltier effects due to junctions of two different materials, and Thomson effect (heat) in uniform materials experiencing a thermal gradient and electric current, are the results of the energy exchange between the charge carriers and the lattice<sup>(13)</sup>. The average total energy of a charge carrier, or the magnitude of the Peltier coefficient  $\Pi(T)$ , is the product of the Seebeck coefficient  $S(T)$  of the material and the local temperature. Strong  $\Pi(T)$  gradients lead to increased energy exchange between the carriers and the lattice as the carriers move along the temperature gradient (large Thomson effect). The contribution of this thermoelectric transport can be modeled as a Seebeck field ( $-\nabla T$ ) in the electronic drift-diffusion model and as a thermoelectric heat drift term ( $-\nabla \cdot (JST)$ ) in the thermal model<sup>(14)</sup>.

We have performed 3D finite element simulations using COMSOL Multiphysics including temperature dependent experimental, extracted and calculated material parameters<sup>(1, 2)</sup>. The simulation results show melting of approximately one half of a  $2.5 \mu\text{m}$  long wire at the source (lower potential) side for  $1 \mu\text{s}$  pulses, in agreement with the experiments, the experimental asymmetry being stronger. Our modeling results (Figure 2) show that thermoelectric transport is the dominant mechanism leading to the observed asymmetric heating. The charge carriers transport energy in their flow directions, which increases with temperature for electrons ( $TS_e$ ) and decreases for holes ( $TS_h$ ) as the Fermi level approaches mid-gap and the band-gap shrinks (Figure 2e,f). On the other hand, the minority carrier concentration increases exponentially with temperature. Hence, the net energy transported by the charge carriers ( $TS_e \sigma_e/\sigma + TS_h \sigma_h/\sigma$ ) sharply decreases as the material turns intrinsic, diminishing to metallic values upon melting ( $\text{Si } T_{\text{melt}} = 1690 \text{ K}$ ). The contribution of the minority carriers becomes significant at elevated

temperatures for highly doped semiconductors (at  $\sim 1300$  K for *n-type* Si with  $[N_D] = 6 \times 10^{19} \text{ cm}^{-3}$ ), leading to a shift of the hottest spot towards the drain for minority carriers.

**Future Plans:** Continue our studies on electrothermal behavior under extreme conditions on Si (large area electronics, photovoltaics) and expand these to other high-temperature electronic materials - SiGe (thermoelectrics), SiC (power electronics) and GeSbTe (phase-change memory).

Specific future planned activities include:

- High-temperature characterization of relevant materials (including metal contacts, interfacial and insulation layers); electrical and thermal conductivities, Seebeck, carrier mobility and concentration;
- High-speed device-level characterization of metastable amorphous and crystalline phases, crystallization and amorphization dynamics, melting and crystalline growth-from-melt;
- Non-homogeneous materials (such as p-n junctions) under extreme thermal gradients;
- Extraction of thermal conductivity under large thermal gradients, as a function of structure size (hence thermal gradient) to study ballistic thermal transport (expected at  $\sim 1$  K/nm and larger);
- Light emission from various types of structures to probe thermal profiles at micro-scale;
- Investigation of an integrated CCD technique to probe thermal profiles at nano-scale utilizing the identified role of generation-transport-recombination of minority carriers in self-heated structures;
- Expanded computational model to include self-consistent solution of Poisson charge equation (together with current and heat equations currently solved) for improved accuracy of role of bipolar conduction;
- Crystallization model incorporating experimentally determined nucleation rates and growth velocities to enable simulation of grain growth, growth-from-melt, filament formation and retention;
- Short range ( $\sim 10$  nm) electrothermal effects at interfaces: traps, bilayers, thermal boundary resistances;
- Alternative crystallization techniques such as high-frequency continuous wave and microwave anneal.

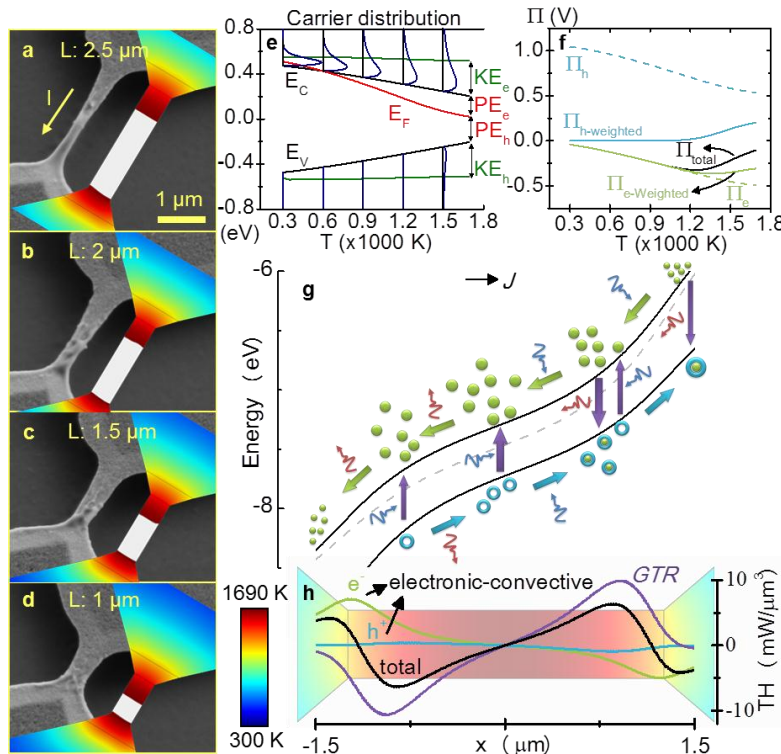


Figure 2. (a-d) Partially crystallized wires with indicated lengths after 30 V, 1  $\mu$ s pulse, and corresponding simulated temperature profiles (white  $> T_{\text{melt}} = 1690$  K). The current direction is indicated in (a). (e) Calculated energy-band diagram of  $6 \times 10^{19} \text{ cm}^{-3}$  doped *n-type* Si with electron and hole distributions from 300 to 1500 K. (f) Calculated electron, hole (both unweighted and weighted) and total Peltier coefficients (sum of weighted  $\Pi_h$  and  $\Pi_e$ ). (g) Cartoon illustration of carrier generation, transport and recombination (*GTR*), and energy exchange with lattice for a hypothetical wire with initially symmetric temperature profile. (h) Breakdown of thermoelectric heat (*TH*) leading to asymmetric melting: convective transport by electrons, by holes, and *GTR* of holes.

## Publications related to this project:

### *Journal articles*

- [6] N. Kanan, A. Faraclas, N. Williams, H. Silva and A. Gokirmak, "Computational Analysis of Rupture Oxide Phase Change Memory Cells," IEEE Trans. on Electron Devices, accepted with minor revisions.
- [5] K. Cil, Y. Zhu, J. Li, C. H. Lam, H. Silva, "Assisted cubic to hexagonal phase transition in GeSbTe thin films on silicon nitride," *Thin Solid Films*, accepted with minor revisions.
- [4] G. Bakan, L. Adnane, A. Gokirmak, H. Silva, "Extraction of temperature dependent electrical resistivity and thermal conductivity from silicon microwires self-heated to melting temperature," *Journal of Applied Physics* 112, 063527 (2012).
- [3] N. Williams, H. Silva, A. Gokirmak, "Finite Element Analysis of Scaling of Micro Thermoelectric Generators," *AIP Journal of Renewable and Sustainable Energy* 4, 043110 (2012).
- [2] H. Silva, G. Bakan, A. Cywar, N. Williams, N. Henry, F. Dirisaglik, A. Gokirmak, "Crystallization of silicon microstructures through rapid self-heating for high-performance electronics on arbitrary substrates," *Nanoscience and Nanotechnology Letters* 4, 10, pp. 970-976(7) (2012).
- [1] G. Bakan, N. Khan, A. Cywar, K. Cil, M. Akbulut, A. Gokirmak and H. Silva, "Self-heating of silicon microwires: Crystallization and thermoelectric effects," *Journal of Materials Research*, 26: 1061-1071, *Invited Feature Paper* (2011).

### *Conference proceedings articles*

- [6] S. Fischer, C. Osorio, N. Williams, H. Silva, A. Gokirmak, "Finite element modeling of current-induced filaments in nanocrystalline silicon", IEEE 2011 Intl. Semiconductor Device Research Symposium (2011).
- [5] A. Cywar, G. Bakan, A. Gokirmak, H. Silva, "Silicon nanowire-based oscillator achieved through solid-liquid phase switching," IEEE 2011 Intl. Semiconductor Device Research Symposium (2011).
- [4] F. Dirisaglik, G. Bakan, A. Gokirmak, H. Silva, "Modeling of thermoelectric effects in phase change memory cells," IEEE 2011 Intl. Semiconductor Device Research Symposium (ISDRS) (2011).
- [3] A. Faraclas, N. Williams, G. Bakan, A. Gokirmak, H. Silva, "Comparison of Instantaneous Crystallization and Metastable Models in Phase Change Memory Cells," Proc. 2012 IEEE Device Research Conference (2012).
- [2] N. Williams, A. Gokirmak, H. Silva, "Finite Element Simulations on Scaling Effects of 3D SiGe Thermoelectric Generators," Mater. Res. Soc. Symp. Proc. Vol. 1388 (2012).
- [1] G. Bakan, N. Khan, H. Silva and A. Gokirmak, "Thermoelectric effects in current induced crystallization of silicon microstructures," in *MEMS and Nanotechnology*, 4, pp. 9-16, *Springer* (2011).

## References

- [1] G. Bakan, et al., To be submitted (2013).
- [2] G. Bakan, et al., J. Appl. Phys. 112, 063527 (2012).
- [3] S. Fischer, et al., submitted to Applied Physics Letters (2013).
- [4] H. Silva, et al., Nanoscience and Nanotechnology Letters 4, 970 (2012).
- [5] G. Bakan, A. Gokirmak and H. Silva, in preparation.
- [6] L. Adnane, et al., Bulletin of the American Physical Society (2012).
- [7] K. Cil, et al., submitted to Thin Solid Films (2012).
- [8] N. Kan'an, et al., IEEE Trans. on Electron Devices (accepted, 2013).
- [9] F. J. DiSalvo, Science 285, 703 (1999).
- [10] G. Bakan, et al., J. Mater. Res. 26, 1061 (2011).
- [11] C. H. Mastrangelo, J. H. J. Yeh and R. S. Muller, IEEE Trans. Elect. Dev. 39, 1363 (1992).
- [12] D. T. Castro, et al., IEEE International Electron Devices Meeting, 315 (2007).
- [13] D. M. Rowe, *Thermoelectrics Handbook: Macro to Nano*, (DRC, 2006).
- [14] L. D. Landau, L. P. Pitaevskii and E. M. Lifshitz, *Electrodynamics of Continuous Media*, 2nd edn. (Butterworth-Heinemann, Burlington, MA, 1984).



# **Session X**



## **DOE SunShot Initiative**

**Lidija Sekaric, *DOE - EERE***

The U.S. Department of Energy's (DOE) SunShot initiative is a collaborative, national effort to reduce the total cost of solar-generated electricity to become cost-competitive with other energy sources by 2020. When the price of solar electricity reaches about \$0.06 per kilowatt-hour over its lifetime, it will be cost-competitive with other non-renewable forms of electricity. This in turn will enable solar-generated power to grow from less than .05% of the current electricity supply to roughly 14% by 2030 and 27% by 2050, as projected in the SunShot Vision Study.

The SunShot initiative builds on the Department's significant research and development (R&D) efforts in solar energy over the past decade, conducted in partnership with American universities, national laboratories, and the private sector. In the last ten years, DOE has invested more than \$1 billion in solar energy research that has been leveraged with significant private industry funding to support more than \$2 billion in total solar R&D projects. This includes investments by DOE's Office of Science, Solar Energy Technologies Program, and ARPA-E, the Advanced Research Projects Agency-Energy. Innovations in both science and technology have driven the cost of solar down 60% since 1995, and have yielded a number of critical breakthroughs in solar technologies' performance and cost.

Since the SunShot Initiative was announced in February 2011, the Solar Office has funded more than 150 projects in the areas of photovoltaics, concentrating solar power, balance of systems costs and systems and grid integration. Past and future programs will be described and their role in achieving the overall grid-parity metrics. Through its programs, SunShot is supporting a range of key activities by private companies, academia, and national laboratories.

In addition to investing in the activities that drive down the cost of solar installations, an important SunShot initiative mission is revitalization of U.S. solar industry. As recently as 1995, the United States maintained a dominant position in the solar marketplace, manufacturing 43% of the world's PV panels. The U.S. market share has steadily declined in recent years, shrinking to 27% by 2000 and to 3% by 2012. SunShot aims to help re-establish American technological and market leadership, improve the nation's energy security, and strengthen U.S. economic competitiveness.



# Poster Sessions



# Physical Behavior of Materials Principal Investigators' Meeting

## POSTER SESSION I

*Monday, April 15, 3:00–5:30 pm & 8:30–10:00 pm*

- 1) Physical Chemistry of Inorganic Nanostructures  
Stephen Leone, Lawrence Berkeley National Laboratory
- 2) Synthesis and Characterization of Nanomaterial Heterostructures and Assemblies:  
Investigation of Charge and Energy Flow at Nanostructure Interfaces  
Stanislaus Wong, Brookhaven National Laboratory
- 3) Superconducting Materials  
Qiang Li, Brookhaven National Laboratory
- 4) Electronic and Optical Processes in Novel Semiconductors for Energy Applications  
Angelo Mascarenhas, National Renewable Energy Laboratory
- 5) Light-Stimulated Epitaxy of Novel Semiconductor Alloys and Heterostructures  
Kirstin Alberi, National Renewable Energy Laboratory
- 6) Proximity Effects in Charged Oxide Heterostructures  
Jeffery Eastman and Peter Zapol, Argonne National Laboratory
- 7) Electronic Processes in Solid State Organic Electronic Materials  
Richard Martin, Los Alamos National Laboratory
- 8) Plasmonic Photovoltaics  
Harry Atwater, California Institute of Technology
- 9) Nanocrystal-Based Dyads for Solar to Electric Energy Conversion  
David Waldeck, University of Pittsburgh
- 10) Light Trapping, Guiding and Concentration for Maximizing Solar Energy Conversion  
Shawn-Yu Lin and Kuang Ping, Rensselaer Polytechnic Institute
- 11) Energy Transport in Graphene  
Stephen Cronin, University of Southern California
- 12) Nanophotonics-Enhanced Solar Cells  
Shanhui Fan, Stanford University

- 13) Light Trapping and Solar Energy Harvesting with Photonic Crystals  
Sajeev John, University of Toronto
- 14) Optically Active 3-Dimensional Semiconductor Quantum Dot Assemblies in Heterogeneous Nanoscale Hosts  
Arto Nurmikko, Brown University
- 15) Study of p-Type ZnO and MgZnO Thin Films for Solid State Lighting  
Cuong Dang, Brown University
- 16) Interband Cascade Photovoltaic Cells  
Rui Yang, University of Oklahoma
- 17) Optical and Electrical Properties of III-Nitrides and Related Materials  
Hongxing Jiang, Texas Tech
- 18) Coupling Electrons, Phonons, and Photon for Nonequilibrium Transport Simulation  
Irena Knezevic, University of Wisconsin-Madison
- 19) Interfaces in Electronic and Structural Materials  
Yuri Mishin, George Mason University
- 20) Amorphous Structures and Polymorphs of the Phase-Change  $\text{Ge}_2\text{Sb}_2\text{Te}_5$  Alloy  
Evan Ma, Johns Hopkins University
- 21) Surface Engineering by Simultaneous Action of Multiple External Fields  
Dimitrios Maroudas, University of Massachusetts, Amherst
- 22) Spin Polarized Functionality through Complex Oxide Heteroepitaxy  
Yuri Suzuki, Stanford University
- 23) Physical Behavior Associated with Mechanical Strain and Quantum Electronic Stress  
Feng Liu, University of Utah

## Physical Behavior of Materials Principal Investigators' Meeting

### POSTER SESSION II

*Tuesday, April 16, 3:00–5:30 pm & 8:30–10:00 pm*

- 1) Complex Hydrides – A New Frontier for Future Energy Applications  
Vitalij Pecharsky, Ames Laboratory
- 2) Extraordinary Responsive Magnetic Rare Earth Materials  
Vitalij Pecharsky, Ames Laboratory
- 3) Elucidation of Hydrogen Interaction Mechanisms with Metal Doped Carbon Nanostructures  
Ragaiy Zidan, Savannah River National Laboratory
- 4) Elucidation of Hydrogen Desorption Mechanisms from Complex Metal Hydrides Interacting with Carbon Nanostructures  
Purusottam Jena, Virginia Commonwealth University
- 5) Using Multiaxial Magnetic Fields to Drive Emergent Behavior in Magnetic Platelet Suspensions  
James Martin, Sandia National Laboratories, New Mexico
- 6) Nanostructured Materials for Thermoelectric Energy Conversion  
Jeff Urban, Lawrence Livermore National Laboratory
- 7) Characterization of Functional Nanomachines  
Michael Crommie, University of California, Berkeley
- 8) Electrochemically Driven Phase Transitions in Battery Storage Compounds  
Ming Tang, Lawrence Livermore National Laboratory
- 9) First Principles Determination of Structure, Thermodynamics, and Transport in Metals and Oxides  
Gerbrand Ceder, Massachusetts Institute of Technology
- 10) Thermodynamic, Kinetic and Electrochemical Studies on Mixed Proton, Oxygen Ion, and Electron (Hole) Conductors  
Anil Virkar, University of Utah
- 11) Superhalogens and Beyond – Bare and Supported Clusters  
Purusottam Jena, Virginia Commonwealth University

- 12) *In Situ* NMR to Understand Hydrogen Storage Chemistry  
Mark Conradi, Washington University of Saint Louis
- 13) Hydrogen Absorption in Pd-Based Nanostructures  
David Lederman, West Virginia University
- 14) Study of Materials and Interface Properties for High-Efficiency Spin Injection  
Jing Shi, University of California, Riverside
- 15) Materials, Physics, and Nanostructures for Next Generation Spintronics  
Chia-Ling Chien, Johns Hopkins University
- 16) Magnetic Frustration and Cooperative Phenomena in Correlated Electron Oxide Materials  
Hariharan Srikanth, University of South Florida
- 17) Coherent Control of Spin States in Organic Electronics – Manipulation of Electron-Spin Interactions for Organic Electronics and Spintronics  
Christoph Boehme, University of Utah
- 18) Near-Field Thermal Radiation between Flat Surfaces with a Nanogap  
Zhuomin Zhang, Georgia Institute of Technology
- 19) Near-Field Thermal Radiation between Two Objects at Extreme Separations  
Gang Chen, Massachusetts Institute of Technology
- 20) Bridging Atomistic and Continuum Scales in Phase-Field Modeling of Stressed Polycrystalline Materials  
Alain Karma, Northeastern University
- 21) Understanding Compound Phase Transitions in New Heusler Alloy Giant Magnetocaloric Materials: Extension to Multifunctional Materials  
Naushad Ali, Southern Illinois University
- 22) High Performance Bulk Thermoelectric Materials  
Zhifeng Ren, University of Houston
- 23) Fundamental Piezotronic and Piezo-phototronic Effects in Nanowires  
Zhong Lin Wang and Wenzhuo Wu, Georgia Institute of Technology

- 24) Electron Dynamics in Nanostructures in Strong Laser Fields  
Matthias Kling, Kansas State University
- 25) Electrochemically Driven Phase Transitions in Battery Storage Compounds  
Yet-Ming Chiang, Massachusetts Institute of Technology
- 26) Extreme Thermoelectric Behavior in Low-Dimensional Oxide Conductors  
Joshua Cohn, University of Miami
- 27) Phase Transformations in Confined Nanosystems  
Jeffrey Shield, University of Nebraska-Lincoln
- 28) Functional Imaging of Hybrid Nanostructures: Visualization of Mechanisms for Solar Energy Utilization  
Lincoln Lauhon, Northwestern University



# **Poster Abstracts**



# Light-Stimulated Epitaxy of Novel Semiconductor Alloys and Heterostructures

Kirstin Alberi

National Renewable Energy Laboratory, 1617 Cole Blvd., Golden, CO 80401

Kirstin.Alberi@nrel.gov

## Project Scope and Recent Progress

New semiconductor alloys and heterostructures are currently under exploration to meet the needs of a variety of energy-related applications, including photovoltaics and solid-state lighting. However, the synthesis of many semiconductors, especially those composed of a mixture of disproportionately large/small atoms, is often challenging and limits our ability to investigate their inherent properties or incorporate them into devices. The objective of this program is to investigate the interaction of light with a growth surface as a means to selectively manipulate processes that enhance adatom kinetics and enable the growth of new semiconductor material systems. Absorption of light can affect the growth surface through three primary pathways: photo-dissociation of bonds and species, local enhancement of thermal energy, and generation of free carriers, which can influence bonding processes and surface reconstructions. Some of these processes are shown in Fig. 1. Exploration of the fundamental mechanisms by which photons may alter the growth of a material is intended to deliver further insight into the physical processes that impact the growth surface and expand our understanding of alloy synthesis and heterovalent interface formation.

Light-stimulated growth is carried out in a dual chamber III-V/II-VI molecular beam epitaxy (MBE) system that is specifically designed with near-normal optical access to the substrate. A broadband Xe halogen lamp (with optical filters) and a KrF excimer laser (ns pulsed, 248 nm) are coupled to the growth chambers as the primary light sources, allowing for adjustment of the excitation conditions. Recent work has focused on understanding the how the growth surface responds to external stimulation with light in well-known material systems, including GaAs and  $\text{Al}_x\text{Ga}_{1-x}\text{As}$ . Reflection high-energy electron diffraction, atomic force microscopy and photoluminescence have been used to study the growth rate, surface morphology

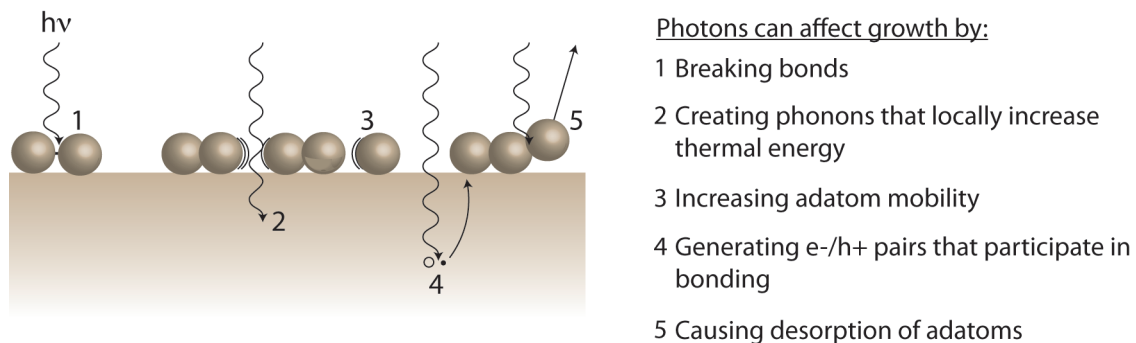


**Figure 1.** Possible photo-assisted processes that affect the growth of a semiconductor.

and defect characteristics as a function of MBE growth conditions and illumination characteristics. This work will set the stage for future work on light-stimulated growth of metastable semiconductor alloys and heterostructures.

### **Future Work**

Developing advanced *in-situ* measurement techniques to probe the growth surface will be critical for studying how light modifies growth mechanisms. To this end, we plan to build and incorporate light and He ion scattering measurement setups into the MBE growth chambers. Detection of scattered photons/He ions by adatoms will provide complementary information about the surface roughness on the micron (photon) and nanometer (He ion) scale that can be used to monitor surface coverage, step edge densities and the evolution of the surface morphology. These measurement capabilities will enhance our ongoing efforts to understand the mechanisms by which photons may affect adatom mobility, dimer dissociation rates, and the desorption of surface species.

Two types of material systems are targeted for further investigation. The first category consists of semiconductors alloyed with dilute concentrations of isovalent anions with much larger or smaller atomic radii than that of the host. Examples include  $\text{GaAs}_{1-x}\text{N}_x$  and  $\text{GaAs}_{1-x}\text{Bi}_x$ . The relatively low growth temperatures required for these species to incorporate into the lattice can affect the adatom mobility and promote the formation of high concentrations of point defects. Strain due to the atomic size mismatch is also known to drive clustering, which further degrades the optical and electrical quality of these alloys. Light-induced cluster dissolution will be studied as a function of growth and illumination conditions. In this case, light will be investigated as a medium for controlling growth as well as a tool for exploring the less well-understood incorporation of large/small atoms into an alloy. The synthesis of alloys with a high degree of compositional uniformity will also allow us to probe their intrinsic properties rather than those dominated by defects.

The second material category under investigation is III-V/II-VI heterostructures. Heterovalent interfaces are difficult to form due to the need to achieve a delicate electrostatic balance of mixed anion-cation bonding that preserves charge neutrality. Consequently, they are often initiated by three-dimensional growth, which makes the interface more diffuse and can lead to higher defect densities. Future work will investigate the role that photons and photogenerated carriers can play in attaining favorable surface reconstructions for fabricating abrupt III-V/II-VI heterostructures.

# Understanding compound phase transitions in new Heusler alloy giant magnetocaloric materials: Extension to multifunctional materials

(Grant No. USDOE-DE-FG02-06ER46291)

Naushad Ali

*Southern Illinois University, Department of Physics, Carbondale, IL 62901 (nali@physics.siu.edu)*

Shane Stadler

*Louisiana State University, Department of Physics & Astronomy, Baton Rouge, LA 70808 (stadler@phys.lsu.edu)*

## SCOPE/DEFINITION

The central goal of this project is to identify and understand the physical mechanisms responsible for large magnetocaloric effects observed in Heusler alloys and other intermetallic systems that undergo magnetostructural phase transitions near room temperature. The practical importance of this research is connected to the advancement of magnetic refrigeration technologies, which are both more efficient and more environmentally friendly than conventional, gas-compression technologies.

The complex, magnetostructural phase transitions observed in many of these compounds are often responsible not only for large magnetocaloric effects (normal and inverse), but also a throng of other pronounced physical properties including magnetoelasticity, large Hall effects, giant magnetoresistance, high spin polarization, and exchange bias. Some systems exhibit two or more of these properties (often in the same temperature regime), and are therefore defined to be **multifunctional materials**. The multi-properties are often a consequence of a common magnetostructural phase transition, and are therefore connected to each other. Identifying the connections between these properties, and their relationships to the phase transitions, is the primary objective of this project, as such advances will help us to better understand the origins of magnetocaloric effects, and to develop new magnetocaloric and multifunctional materials.

## RECENT PROGRESS

Here we report some recent advances in understanding: (i) the role of Ni-Mn hybridization in Heusler alloys; (ii) the origin of strong electron correlations in a Heusler alloy near in the proximity of a non-collinear ferromagnetic state; and (iii) the effects of stress on the magnetostructural phase transitions in Heusler alloy **thin films**.

### (i) Ni-Mn hybridization in Mn-rich Heusler alloys

We have performed an experimental study on  $\text{Ni}_{50}\text{Mn}_{37-x}\text{Cr}_x\text{Sb}_{13}$  and  $\text{Ni}_{50-x}\text{Mn}_{37-x}\text{Sb}_{13}$  Heusler alloys in order to determine the physical origins of the martensitic phase transitions in this system.[1] It is commonly accepted that the martensitic transition temperatures in Ni-Mn-Z (Z = Ga, In, Sb, Sn) based Heusler alloys directly depend on the valence electron concentration,  $e/a$ . Our work on Mn-rich systems shows that, regardless of the change in  $e/a$ , the martensitic transition temperatures ( $T_M$ ) decrease with increasing Cr or Ni concentration. These results support the notion that it is the hybridization between the Ni atoms and the Mn atoms in the Z sites that plays the dominant role in driving the martensitic transformation.

We have determined in this study that it is likely that the driving force behind the martensitic transformation in these Mn-rich Heusler alloys is the hybridization between the Ni 3d  $e_g$  states and the 3d states of the excess Mn atoms on the Sn sites. In such a scenario, once the maximum hybridization is established, any change in the Ni or Mn content will tend to weaken the hybridization, and result in a decrease in the martensitic temperature  $T_M$ . This idea is supported by the data in Fig. 1, where the dependence of  $T_M$  on  $e/a$  and Cr/Ni content is shown. It is clear in Fig. 1 that  $T_M$  does not depend monotonically on  $e/a$ , but rather upon the Cr or Ni content (i.e., reducing the number of excess Mn atoms that are likely located on the Sb sites).

### (ii) $Mn_{1-x}Fe_xCoGe$ : a strongly correlated metal near a noncollinear ferromagnetic state

In recent years, considerable attention has been devoted to studies of MnCoGe-based systems due to the giant magnetocaloric effects observed in these materials near room temperature. It was therefore of interest to conduct a deeper study of these systems, perhaps to elucidate the physical origin of their pronounced physical behaviors. Specifically, we set out to closely examine the rarely studied experimental electronic properties of MnCoGe-based systems. The major outcome of this work suggests that  $Mn_{1-x}Fe_xCoGe$  is not a *normal metal*, but rather a new type of *strongly correlated metal* in the proximity of a noncollinear ferromagnetic (FM) state.\*

The development of strong electron correlations in  $Mn_{1-x}Fe_xCoGe$  arises when it passes through the noncollinear FM state for  $x = 0.2$ , as evidenced from our  $C_p(T)$  and  $\rho(T)$  data (Fig. 2). The zero-field  $C_p(T)$  data for  $x = 0.2$  is shown in Fig. 2(a). The low-temperature data as shown in the inset of Fig. 2(a) was fitted by the standard expression,  $C_p = \gamma T + \beta T^3$ , and the fitted values of  $\gamma$  and  $\beta$  were found to be 27.6 mJ/mol K<sup>2</sup> and 0.164 mJ/mol K<sup>4</sup>, respectively. The large value of  $\gamma$  indicates the formation of heavy quasiparticles with a mass enhancement of approximately 30 times that of free electrons. The Debye temperature obtained from the  $\beta$  value is 306 K. The DOS at  $E_F$  estimated from the  $\gamma$  value is  $D_0(E_F) = 16.5$  states/eV/f.u. Previously it had been shown that, in the case of the CoMnX (X = P, Si, Ge), the noncollinear ground states (antiferromagnetic or ferromagnetic) are energetically preferable compared to the collinear FM phase, as characterized by the low total density of states at the Fermi level. A high number of states can make the collinear FM state unstable and promote a noncollinear magnetic arrangement in these types of compounds. Therefore, the more than three-fold increase in  $D_0(E_F)$  for  $Mn_{0.8}Fe_{0.2}CoGe$  relative to that of the parent MnCoGe ( $D_0(E_F) = 5$  states/eV/f.u.) indicates the instability of the collinear FM state in this composition, and promotes the formation of a stable noncollinear FM state. A noncollinear magnetic state can be stabilized in any alloys or compounds through the formation of a hybridization gap at the Fermi energy.

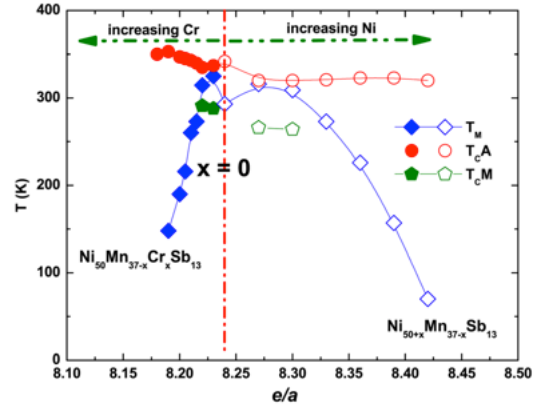


**Fig. 1.** The transition temperatures as a function of  $e/a$  of  $Ni_{50}Mn_{37-x}Cr_xSb_{13}$  and  $Ni_{50+x}Mn_{37-x}Sb_{13}$  alloys. Taken from  $M(T)$  measurements in an applied magnetic field of  $H = 1$  kOe,  $T_M$  is the martensitic transitions temperature, and  $T_{CA}$  and  $T_{CM}$  are the Curie temperatures of the austenitic and martensitic phases, respectively.

\*  $Mn_{1-x}Fe_xCoGe$ : a strongly correlated metal in the proximity of a noncollinear ferromagnetic state, T. Samanta, I. Dubenko, Abdiel Quetz, J. Prestigiacomo, P. W. Adams, S. Stadler, and N. Ali (Submitted to Phys. Rev. Lett. 2013).

The low-temperature  $\rho(T)$  data for  $x = 0.2$  was fitted by  $\rho(T)=\rho_0 + AT^2$ , suggesting a dominant electron-electron scattering behavior (inset of Fig. 2(b)). The value of  $A$  obtained from the fit is  $0.0324 \mu\Omega\cdot\text{cm}\cdot\text{K}^{-2}$ . Therefore, the Kadowaki–Woods ratio for  $x = 0.2$  is  $\text{KWR} = A/\gamma^2=43 \mu\Omega\cdot\text{cm}\cdot\text{mol}^2\cdot\text{K}^2\cdot\text{J}^{-2}$ . This value is much larger than the value  $A/\gamma^2\sim 10 \mu\Omega\cdot\text{cm}\cdot\text{mol}^2\cdot\text{K}^2\cdot\text{J}^{-2}$  reported for a number of heavy fermion compounds, suggesting that  $\text{Mn}_{0.8}\text{Fe}_{0.2}\text{CoGe}$  is a strongly correlated metal. Although the studied materials were synthesized from isotropic end-members ( $\text{MnCoGe}$  and  $\text{FeCoGe}$ ) similar to that of heavy fermion compounds, the development of strong electron correlation in  $\text{Mn}_{0.8}\text{Fe}_{0.2}\text{CoGe}$  has an unexpected and unique anisotropic origin. In this case, interlayer transport of heavy quasiparticles due to the formation of a layered structure is the origin of the strong electron correlation. This has been explained in the context of the unified model developed by Jacko *et al.* [Nature Physics, **5**, 422 (2009)] to describe the KWR by considering a dimensional analysis. Our findings can be extended to predict strong electron correlation effects in other classes of materials that stabilize in a noncollinear state.

### (iii) Magnetostructural transitions in thin films

We have used pulsed laser deposition to grow thin films from  $\text{Ni}_{50}\text{Mn}_{35}\text{In}_{15}$  and  $\text{Ni}_{50}\text{Mn}_{35}\text{In}_{14}\text{Al}$  targets on Si, MgO, and SrTiO<sub>3</sub> (STO) substrates.[2,3] The  $M(T)$  curve of a  $\text{Ni}_{50}\text{Mn}_{35}\text{In}_{15}$  film grown on MgO (100) (see Fig. 3) is similar to those observed for bulk off-stoichiometric alloys. As the temperature increases, the first sharp magnetization decrease is observed at  $T_{\text{CM}} = 286$  K, indicating a magnetic, second-order phase transition in the martensitic phase. At  $T_{\text{A}} = 320$  K, a first-order phase transition occurs that is associated with the onset of the austenite phase. At this temperature, the magnetization sharply increases and then falls again at the Curie temperature  $T_{\text{C}} = 334$  K. With subsequent cooling, the martensitic phase re-establishes at  $T_{\text{M}} = 314$  K, yielding a 6 K temperature hysteresis, confirming that the phase transition is of first order. The inverse susceptibility increases linearly with increasing temperature above 334 K (see Fig. 3, right axis), confirming the paramagnetic state of the sample above 334 K. These results show promising avenues for studying magnetostructural phase transitions, and corresponding physical properties, in thin films and multilayers.

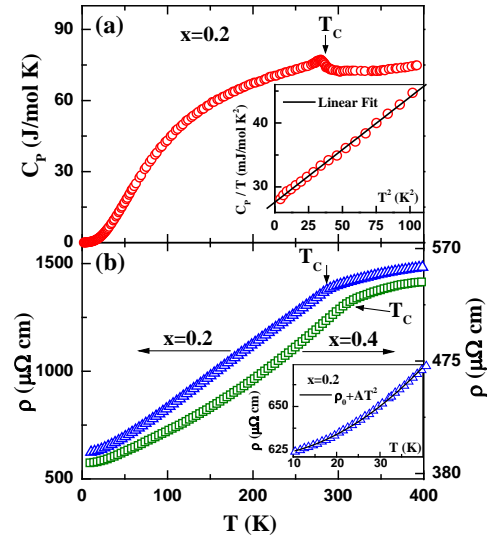


**Fig. 2.** (a) Heat capacity  $C_p$  versus temperature  $T$  for  $x = 0.2$ . Inset: the linear fit of  $C_p/T$  versus  $T^2$ . (b) Electrical resistivity ( $\rho$ ) as a function of  $T$  with  $x = 0.2$  and  $0.4$ , respectively. Inset: the fit of  $\rho(T)$  by  $\rho(T)=\rho_0 + AT^2$  for  $x=0.2$  as indicated by the solid curve.

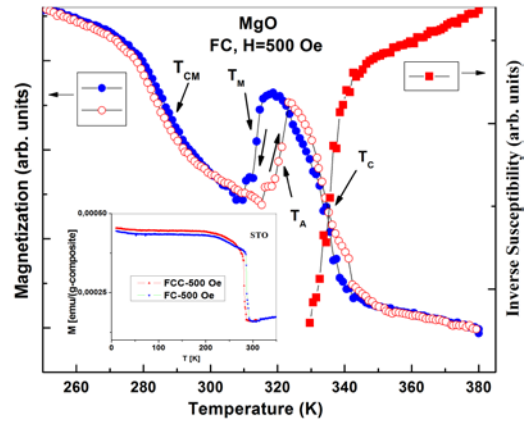


**Fig. 3.**  $M(T)$  for a 10 nm  $\text{Ni}_{50}\text{Mn}_{35}\text{In}_{15}$  film grown on a MgO (100) substrate, clearly showing a martensitic transition at about  $T=320$  K. (Inset)  $M(T)$  for the same film grown on STO (100).

## FUTURE PLANS

We plan to carry out the following activities in the future: (i) study the effects of compositional variations and isoelectronic vacancies on the phase transitions and physical properties of  $\text{Ni}_{50}\text{Mn}_{50-x}\text{In}_x$  and  $\text{Ni}_{2-x}\text{M}_x(\text{Mn,Al})$  Heusler alloys; (ii) Develop new metamagnets  $\text{MnTX}$  ( $T = \text{Ni, Co, Cu}$  and  $X = \text{Si,Ge}$ ) and investigate the magnetocaloric effects in these systems; (iii) grow Heusler alloy and  $\text{MnTX}$  thin films and understand the ramifications of size-scale effects on the phase transitions and physical properties (including magnetocaloric effects); and (iv) synthesize new carbon nanotube/magnetic nanoparticle composites with the hope of revealing new and novel physical properties.

## REFERENCES PUBLISHED OR ACCEPTED (2010-Present)

- [1] M. Khan, J. Jung, S.S. Stoyko, A. Mar, A. Quetz, T. Samanta, I. Dubenko, N. Ali, S. Stadler, K. H. Chow, *Appl. Phys. Lett.* **100**, 172403 (2012). [DOI: 10.1063/1.4705422]
- [2] A. Sokolov, Le Zhang, I. Dubenko, T. Samanta, S. Stadler, and N. Ali, *Appl. Phys. Lett.* **102**, 072407 (2013).
- [3] A. Sokolov, Le. Zhang, I. Dubenko, T. Samanta, S. Stadler, and N. Ali, accepted to *J. Appl. Phys.* (2013).
- [4] A. Quetz, I. Dubenko, T. Samanta, H. Vinson, S. Talapatra, N. Ali, and S. Stadler, accepted to *J. Appl. Phys.* (2013).
- [5] I. Dubenko, T. Samanta, A. Quetz, A. Kazakov, I. Rodionov, D. Mettus, V. Prudnikov, S. Stadler, P. Adams, J. Prestigiacomo, A. Granovsky, A. Zhukov, and N. Ali, *Appl. Phys. Lett.* **100**, 192402 (2012). [doi: 10.1063/1.4714539]
- [6] T. Samanta, I. Dubenko, A. Quetz, S. Stadler, N. Ali, accepted to *J. Appl. Phys.* (2013).
- [7] T. Samanta, I. Dubenko, A. Quetz, S. Stadler, N. Ali, *J. Magn. Magn. Mat.* **330**, 88 (2013).
- [8] Gucua, A. Ozdemir, I. Dubenko, T. Samanta, N. Ali, N. Kervan, and S. Kervan, *J. Magn. Mag. Mat.* **327**, 7 (2013).
- [9] T. Samanta, I. Dubenko, A. Quetz, S. Stadler, and N. Ali, *Appl. Phys. Lett.* **101** 242405 (2012). <http://dx.doi.org/10.1063/1.4770379>.
- [10] I. Dubenko, T. Samanta, A. K. Pathak, A. Kazakov, V. Prudnikov, S. Stadler, A. Granovsky, A. Zhukov, and N. Ali, *J. Magn. Magn. Mat.* **324**, 353 (2012). [DOI: 10.1016/j.jmmm.2012.02.082]
- [11] I. Dubenko, T. Samanta, A. Quetz, A. Kazakov, I. Rodionov, D. Mettus, V. Prudnikov, S. Stadler, P.W. Adams, J. Prestigiacomo, A. Granovsky, A. Zhukov, and N. Ali, *IEEE Trans. Magn.* **48** 3738 (2012).
- [12] T. Samanta, I. Dubenko, A. Quetz, S. Stadler, and N. Ali, *Appl. Phys. Lett.* **101**, 242405 (2012).
- [13] A. Kazakov, V. Prudnikov, A. Granovsky, N. Perov, I. Dubenko, A. K. Pathak, T. Samanta, S. Stadler, N. Ali, A. Zhukov, M. Ilyin, J. Gonzalez, *Journal of Nanoscience and Nanotechnology*, **12** 1 (2012).
- [14] T. Samanta, I. Dubenko, A. Quetz, S. Temple, S. Stadler, and N. Ali, *J. Appl. Phys. Lett.* **100**, 052404 (2012). doi:10.1063/1.3681798.
- [15] P. Hill, I. Dubenko, T. Samanta, A. Quetz and N. Ali, *J. Appl. Phys.* **111**, 07E333 (2012): doi: 10.1063/1.3677658.
- [16] A. Özdemir, I. Dubenko, T. Samanta, N. Ali, F. Güçlü, S. Kervan, and N. Kervan, *J. Magn. Magn. Mat.* **324**, 1258 (2012). [DOI:10.1016/j.jmmm.2011.11.024]
- [17] T. Samanta, I. Dubenko, V.I. Krylov, A.V. Tsvyashenko, L.N. Fomicheva, R.A. Sadykov, and N. Ali, *Solid State Phenomena* **190**, 351 (2012). [DOI: 10.4028/www.scientific.net/SSP.190.351]
- [18] A. K. Pathak, I. Dubenko, S. Stadler, and N. Ali, *Journal of Alloys and Compounds* **509** (4), 1106-1110 (2011). [DOI: 10.1016/j.jallcom.2010.09.174]
- [19] A. K. Pathak, I. Dubenko, Y. Xiong, P. W. Adams, S. Stadler, and N. Ali, *J. Appl. Phys.* **109** (7), 07A916 (1-3) (2011). [DOI: 10.1063/1.3540696]
- [20] A. K. Pathak, I. Dubenko, S. Stadler, and N. Ali, *J. Magn. Magn. Mater.* **323** (20), 2436-2440 (2011). [DOI: 10.1016/j.jmmm.2011.04.020]
- [21] A. K. Pathak, I. Dubenko, S. Stadler, and N. Ali, *J. Appl. Phys.* **109** (7), 07A913 (103) (2011). [DOI: 10.1063/1.3544509]
- [22] A. P. Kazakov, V. N. Prudnikov, A. B. Granovsky, A. P. Zhukov, J. Gonzales, I. Dubenko, A. K. Pathak, S. Stadler, and N. Ali, *Appl. Phys. Lett.* **98** (13), 131911 (1-3) (2011). [DOI: 10.1063/1.3574088].
- [23] A. K. Pathak, I. Dubenko, S. Stadler, and N. Ali, *Journal of Alloys and Compounds* **509** (4), 1106-1110 (2011).
- [24] V. N. Prudnikov, A. P. Kazakov, I. S. Titov, Ya.N. Chovarskii, N. S. Perov, A. B. Granovskii, I.S. Dubenko, A. K. Pathak, N. Ali, A. P. Zhukov, and J. Gonzales, **53**, (2011) 3490–493.
- [25] N. Prudnikov, A. P. Kazakov, I. S. Titov, N. S. Perov, A. B. Granovskii, I. S. Dubenko, A. K. Pathak, N. Ali, A. P. Zhukov, and J. Gonzales, *JETP Letters*, **92**, (2010) 666–670.
- [26] A. K. Pathak, I. Dubenko, H. E. Karaca, S. Stadler, and N. Ali, *Appl. Phys. Lett.* **97** 062505 (2010). DOI:10.1063/1.3467460.
- [27] I. Dubenko, A. K. Pathak, N. Ali, Ya. Kovarskii, V. N. Prudnikov, N. S. Perov, and A. B. Granovsky, *J. Phys.: Conf. Ser.* **200** 052005 (2010)
- [28] I. Dubenko, A. K. Pathak, S. Stadler, Ya. Kovarskii, V.N. Prudnikov, N.S. Perov, A.B. Granovsky and N. Ali, *J. Phys.: Conf. Ser.*, **200**, 052005 (2010).
- [29] A. K. Pathak, I. Dubenko, C. Pueblo, S. Stadler, and N. Ali, *IEEE Trans. Magn.* **46** (2010) 1444-1446. DOI: 10.1109/TMAG.2010.2043924
- [30] A. K. Pathak, I. Dubenko, C. Pueblo, S. Stadler, and N. Ali, *Appl. Phys. Lett.* **96** 172503 (2010). [DOI: 10.1063/1.3422483]
- [31] A. K. Pathak, I. Dubenko, C. Pueblo, S. Stadler, and N. Ali, *J. Appl. Phys.* **107** 09A907 (2010).
- [32] A. K. Pathak, P. Basnyat, I. Dubenko, S. Stadler, and N. Ali, *J. Magn. Magn. Mater.* **322** (2010) 692.

## Program Title: Plasmonic Photovoltaics

**Principal Investigator:** Harry A. Atwater,

**Mailing Address:** California Institute of Technology, Thomas J. Watson Laboratories of Applied Physics, MS 128-95, Pasadena, CA 91125

**e-mail:** [haa@caltech.edu](mailto:haa@caltech.edu)

### Program Scope

There is at present great worldwide scientific interest in nanophotonic mechanisms for light management and trapping in solar energy conversion. Researchers have recognized that many of the wave optical phenomena encountered in e.g., atomic physics, guided wave optics and quantum confined semiconductors have important manifestations for solar energy conversion. A very intriguing recent finding is that in the wave optic regime, the optical intensity and material absorption can greatly exceed their corresponding values in the ray optic limit. This has further concentrated interest on photonic structures for light trapping. Our project has concentrated on developing a comprehensive understanding of light trapping by plasmonic structures of interest for photovoltaics. Major themes include efforts to:

- i) Investigate the role of the spatial frequencies and spatial correlations in light incoupling by textured back reflectors for thin photovoltaics.
- ii) Develop a framework for the maximum intensity enhancement in the wave optics regime based on the local density of optical states (LDOS). Notably this LDOS approach allowed us to make specific predictions about conditions where, in the wave optic regime, the maximum intensity and absorption can exceed the  $4n^2$  ray optical light trapping limit set by detailed balance considerations.
- iii) Understand plasmon excitation in conducting ‘half-metallic’ oxides, which represents a promising direction to pursue the mitigation of metallic losses in plasmonic materials. Conducting oxides and other materials with electron densities intermediate between noble metals and semiconductors also have considerable promise for giant optical nonlinearities; we demonstrated unity-order modulation of refractive index by field effect modulation of the carrier density in indium tin oxide.
- iv) Develop a concept framework for resonant guided wave networks, a new class of metamaterials that enable optical dispersion control in wavelength-scale structures.

### Recent Progress

#### 1. Light Trapping Structure Roughness: Power Spectral Density and Spatial Correlations

Thin and ultra-thin film solar cells are attractive candidates for low-cost replacement of thick, wafer-based devices. To achieve full absorption of the solar spectrum with ultra-thin semiconductor volumes, light trapping is required over a broad spectral and angular range. To date, several light trapping geometries based on nanowires, nanocones, photonic crystals, nanoparticles, gratings, and random textures have been demonstrated. While many researchers have demonstrated increased photocurrent due to scattering-mediated light trapping, the role of spatial correlations and surface topography of random or periodic arrangements of the scattering nanostructures has remained unclear. In work in press, we have identified the relation between these key parameters and the photocurrent spectrum for high efficiency (> 9.5%) ultra-thin (< 100 nm thick absorber) film a-Si:H solar cells containing both integrated plasmonic and Mie

scattering nanostructures. The enhanced performance of the nanostructure arrays signals a new direction for enhanced absorption in which light trapping nanopatterns, defined by their spatial coherence spectral density, are designed for broadband and isotropic response.

## **2. Exceeding the $4n^2$ Light Trapping Limit: A Local Density of States Perspective**

In 1982, Yablonovitch proposed a thermodynamic limit on light trapping within homogeneous semiconductor slabs using a statistical ray optics treatment. This limit imposes an upper bound on the intensity and absorption enhancement of  $4n^2$ , where  $n$  is the refractive index, within the semiconductor. This model implies a bound on both the minimum amount of material needed to fully absorb the solar spectrum and the photovoltaic efficiency. However, this limit is not valid for a new generation of wavelength-scale and subwavelength solar absorbers with modified geometries, such as ultrathin or inhomogeneously structured solar cells, wire-based solar cells, photonic crystal based solar cells, and plasmonic solar cells. In this reporting period, we demonstrated that the conventional or so-called ergodic light trapping limit can in fact be exceeded by designing an elevated local density of optical states (LDOS) for the absorber, if the optical modes of the structure can be appreciably populated via an appropriate incoupling mechanism. Moreover, for any semiconductor we showed that it is always possible to exceed the  $4n^2$  enhancement and illustrated how the photonic design imperative to exceed  $4n^2$  depends on the thickness and wavelength under consideration. Using these principles, we articulated a number of new solar absorber designs that have the potential to exceed the ergodic light trapping limit. Our results imply that there is no fundamental limit to the maximum absorption enhancement nor a minimum amount of semiconductor material needed to fully absorb the solar spectrum, opening new avenues for solar cell design and cost reduction.

## **3. Reducing Metallic Losses in Plasmonic Structures**

Noble metals have traditionally been the material of choice for plasmonic structures, but they suffer from high resistive losses—even metals with the highest conductivities, silver and gold, exhibit excessive losses at optical frequencies that restrict the development of devices in this frequency range. A different approach would be the discovery of better plasmonic materials that have a negative real part of dielectric permittivity, by improving the optical properties of the existing metallic materials via doping, or alloying and careful band structure engineering. The material losses are not the only consideration—the real part of the dielectric permittivity is critical because it determines the optical performance of the system. For example, although negative real permittivity is required for any plasmonic structure, an extremely negative value is not desirable for many applications. Both the loss issue and the ability to tune the real part of the dielectric permittivity are factors to consider when searching for alternative plasmonic materials. Materials can be classified on the basis of carrier concentration and carrier mobility. The carrier concentration has to be high enough to provide a negative real permittivity, but it also must be tunable so that larger negative values would be accessible with further increases in carrier concentration. Lower carrier mobilities translate to higher material losses. We have identified materials, such as conducting oxides, which by virtue of simultaneously high carrier density and carrier mobility, have potential for reducing metallic losses in plasmonic and metamaterial structures.

## **4. Unity-Order Modulation of Refractive Index in Conducting Oxides**

We have developed a method for obtaining unity-order refractive index changes in the accumulation layer of a metal-oxide semiconductor (MOS) heterostructure with a conducting indium-tin oxide (ITO) layer as the active ‘semiconductor’ material. Under applied field, carrier

concentrations at the dielectric/conducting oxide interface increase from  $1 \times 10^{21}/\text{cm}^3$  to  $2.8 \times 10^{22}/\text{cm}^3$ , resulting in a local refractive index change of 1.39 at 800 nm. When this structure is modeled as a plasmonic slot waveguide, the change corresponds to a modal index change of  $n = 0.08$  for the plasmonic mode. This finding has stimulated investigation of heavily doped semiconductors and half-metallic oxides as potential candidates for low loss plasmonic and highly nonlinear materials.

## 5. Resonant Guided Wave Networks

In 2010, we introduced the concept of a resonant guided wave networks, which is an optical material design consisting of power-splitting elements arranged at the nodes of a waveguide network. The resulting wave dispersion depends on the network layout due to localized resonances at several length scales in the network. We showed that these structures exhibit both localized resonances with a Q similar to 80 at 1550 nm wavelength as well as photonic bands and band gaps in large periodic networks at infrared wavelengths. In this period, we investigated *inhomogeneous* resonant guided wave networks. Photonic functions (spectrum splitting, Boolean algebra, etc) can be programmed by manipulating wave interference in inhomogeneous resonant guided wave networks composed of power-splitting elements arranged at the nodes of a *non-uniform* waveguide network. Using a compact, yet comprehensive, scattering matrix representation of the network, the desired photonic function is designed by fitting structural parameters according to an optimization procedure. We used this design scheme to demonstrate plasmonic structures that act as dichroic and trichroic routers in the infrared frequency range, splitting and routing bands of a broad spectrum along different waveguide channels. In 2012, we designed dielectric analogs to plasmonic resonant guided wave networks and showed that they can exhibit similar optical dispersion features but with considerable reduced material optical losses.

## 6. Broadband Polarization Independent Ultrathin Plasmonic Superabsorbers:

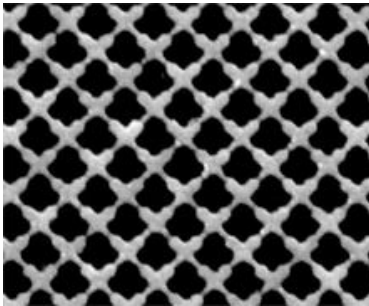


**Figure 1.** Scanning electron microscope image shows Ag/SiO<sub>2</sub> plasmonic super absorber nanostructures, which have a 400 nanometers period.

Resonant plasmonic and metamaterial structures allow for control of fundamental optical processes such as absorption, emission and refraction at the nanoscale. Considerable recent research has focused on energy absorption processes, and plasmonic nanostructures have been shown to enhance the performance of photovoltaic and thermophotovoltaic cells. Although reducing metallic losses is a widely sought goal in nanophotonics, the design of nanostructured ‘black’ super absorbers from materials comprising only lossless dielectric materials and highly reflective materials and highly reflective noble metals represents a new research direction. In the last grant period, we demonstrated an ultrathin (260 nm) plasmonic super absorber consisting of a metal– insulator– metal stack with a nanostructured top silver film composed

of crossed trapezoidal arrays. Our super absorber yields broadband and polarization-independent resonant light absorption over the entire visible spectrum (400–700 nm) with an average measured absorption of 0.71 and simulated absorption of 0.85. Proposed nanostructured absorbers open a path to realize ultrathin black metamaterials based on resonant absorption. Our work on plasmonics super absorbers was featured in *Technology Review* in November 2011 (see <http://m.technologyreview.com/energy/39106/>).

## Future Plans

The integration of nanostructures in photovoltaics significantly changes the mechanism of light absorption. In bulk semiconductors, light is absorbed exponentially from front to back. When nanostructures are introduced, however, the absorption in the film will depend on many effects such as scattering, localized modes, and guided modes, which significantly modify both the magnitude and the location of absorption within the photovoltaic absorber. We will investigate how inhomogeneous excitation and carrier generation in nanostructures affects the internal photocarrier collection efficiency and external radiative efficiency of photovoltaic absorbers.

## References to publications of DOE sponsored research from 2010-2012

1. "Plasmonics for improved photovoltaic devices," Harry A. Atwater and Albert Polman, *Nature Materials* **9**, 205, (2010).
2. "Design considerations for plasmonic photovoltaics," Vivian E. Ferry, Jeremy N. Munday, Harry A. Atwater, *Advanced Materials*, **22**, 43, 4794 (2010).
3. "Programming of Inhomogeneous Resonant Guided Wave Networks ", E. Feigenbaum, S.P. Burgos, H. A. Atwater, *Opt. Express* **18**, 25584-25595 (2010).
4. "Unity-order index change in transparent conducting oxides at visible frequencies", E. Feigenbaum, K. Diest, H. A. Atwater, *Nano. Lett.* **10**, 2111-2116 (2010).
5. "Light trapping in ultrathin plasmonic solar cells", V. E. Ferry, M.A. Verschuuren, H.B. T. Li, E. Verhagen, R. J. Walters, R. E. I. Schropp, H.A. Atwater, and A. Polman, *Opt. Express* **18**, A237 (2010).
6. "Light trapping in thin film plasmonic solar cells", V. E. Ferry, M. A. Verschuuren, H. B. T. Li, E. Verhagen, R. J. Walters, R. E. I. Schropp, H. A. Atwater, A. Polman, Proceedings of the 25<sup>th</sup> European Union Photovoltaic Solar Energy Conference, Valencia, Spain, 2010.
7. "Plasmonic light trapping for thin film a-Si:H solar cells," V. E. Ferry, M. A. Verschuuren, H. B. T. Li, E. Verhagen, R. J. Walters, R. E. I. Schropp, H. A. Atwater, A. Polman, Proceedings of the 35<sup>th</sup> IEEE Photovoltaics Specialist Conference, Honolulu, Hawaii, 2010.
8. "Large integrated absorption enhancement in plasmonic solar cells by combining metallic gratings and antireflection coatings," J. N. Munday and Harry A. Atwater, *Nano Letters* DOI: 10.1021/nl101875t (2011).
9. "Low Loss Plasmonic Metamaterials", Alexandra Boltasseva and H.A. Atwater, *Science* **331**, 290 (2011).
10. "Modeling Light Trapping in Nanostructured Solar Cells", Vivian E. Ferry, Albert Polman, and Harry A. Atwater, *ACS Nano*, **5** pp 10055–10064 (2011).
11. GaAs Passivation with Trioctylphosphine Sulfide for Enhanced Solar Cell Efficiency and Durability, Matthew T. Sheldon, Carissa N. Eisler, and Harry A. Atwater, *Adv. Energy Mater.* **2**, 339–344 (2012).
12. "Optimized Spatial Correlations for Broadband Light Trapping Nanopatterns in High Efficiency Ultrathin Film a-Si:H Solar Cells", Vivian E. Ferry, Marc A. Verschuuren, M. Claire van Lare, Ruud E. I. Schropp, Harry A. Atwater, and Albert Polman, *Nano Letters* **11**, 4239–4245 (2011).
13. "Plasmonic light trapping in thin-film Si solar cells", P Spinelli, V E Ferry, J van de Groep, M van Lare, M A Verschuuren, R E I Schropp, H A Atwater and A Polman, *J. Optics*, **14** 024002, (2012).
14. "Light trapping beyond the  $4n^2$  limit in thin waveguides", Jeremy N. Munday, Dennis M. Callahan, and Harry A. Atwater, *Appl. Phys. Lett.* **100**, 121121 (2012).
15. "Solar Cell Light Trapping beyond the Ray Optic Limit", Dennis M. Callahan, Jeremy N. Munday, and Harry A. Atwater, *Nano Letters* **12**, 214–218 (2012).
16. "Broadband polarization-independent resonant light absorption using ultrathin plasmonics super absorbers", Koray Aydin, Vivian E. Ferry, Ryan M. Briggs & Harry A. Atwater, *Nature Communications*, **2**:517, DOI: 10.1038/ncomms1528 (2012).
17. "Dielectric based resonant guided wave networks", Eyal Feigenbaum, and Harry A. Atwater, *Optics Express*, **20** 10674 (2012).

DOE award # DESC0000909, University of Utah

## Coherent control of spin states in organic electronics - Manipulation of electron-spin interactions for organic electronics and spintronics

PI: Christoph Boehme, co-PI: John M. Lupton  
University of Utah, Department of Physics and Astronomy,  
115S 1400E, Salt Lake City, Utah, 84112, [boehme@physics.utah.edu](mailto:boehme@physics.utah.edu)

### Program Scope or Definition

The current research of this project builds on the experimental demonstration of *electrically and optically detected coherent spin-motion* in organic semiconductor materials which has been accomplished in the course of the first three project years. New, pulsed electrically (pEDMR) and optically (pODMR) detected magnetic resonance techniques have proven to allow for the qualitative discrimination and individual quantitative determination of spin-exchange, spin-dipolar, hyperfine, and spin-orbit coupling involving spin states that influence optical and electrical materials properties. Based on these experimental breakthroughs, *the exploration of artificial pathways to the control of spin-coupling in organic semiconductors is pursued*. The goal of these activities is finding ways to manipulate electrical and optical materials properties by adjustment of spin-coupling (type and magnitude) between electron spins as well as electron and nuclear spins. This is achieved by: (i) *Control of spin interactions via materials structure and composition* through the investigation of novel organic and organic/inorganic hybrid materials structures and blends illustrating how chemical structure, morphological properties, and isotopic composition correlate with spin interactions qualitatively and quantitatively. (ii) *Control of spin-exchange and spin-dipolar interactions via electric fields*, which is explored through pEDMR experiments on organic field effect devices. (iii) *Control of hyperfine coupled nuclear spin states via electric current*, utilizing Overhauser spin-transfer as well as electrically generated polarons with the goal of testing the suitability of hydrogen nuclei in organic semiconductors for nuclear spin quantum storage. Methodologically, the different spin-spin coupling types are observed using pEDMR and pODMR, at excitation frequencies covering 6 orders of magnitude (1MHz to 330GHz). This previously inaccessible frequency range is achieved by utilization of the broadband range pEDMR/pODMR facilities in Utah and in collaboration with the National High Magnetic Field Laboratory in Tallahassee, Florida. The goal of this project is to introduce a new parameter set (exchange, dipolar, spin-orbit, and hyperfine interactions) into materials- and device design concepts of organic semiconductors. New pathways for organic electronics and spin-electronics are explored, including spin transistors, sensor concepts and organic microelectronic circuitry. In the long term, this fundamental research could also stimulate the development of the first organic quantum information devices.

### Recent Progress

During the first three years of this project, all technical requirements necessary for performing fast and efficient pulsed electrically detected and pulsed optically detected magnetic resonance experiments on organic semiconductor materials were implemented. This was accomplished by development of a photo-lithographically prepared organic sample template which defines device geometries of organic devices before the actual organic samples are deposited in an inert glove box environment in which lithography cannot be performed. These special templates are crucial to be able to apply high microwave fields to an organic device. Thus, the use of these templates allows a fast and well controlled pEDMR and pODMR sample preparation. After this initial development of experimental procedures, these techniques developed were then used for the electrical detection of spin coherence (Rabi flopping) in the device current of a  $\pi$ -

conjugated polymer OLED (poly-[2-methoxy-5-(2'-ethyl-hexyloxy)-1,4-phenylene vinylene], MEH-PPV) at room temperature [1-2, 4-5], which allowed a first estimate (a lower limit) to be placed on the spin coherence time of several hundred nanoseconds at room temperature, a result that was subsequently

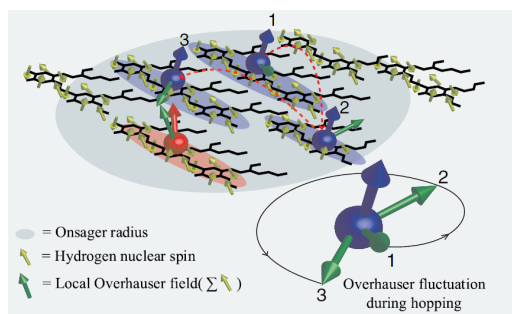


*Fig. 1: Illustration of charge carrier spin coherence decay. An electron (blue) and hole (red) form a carrier pair. As charges hop from site to site within the Onsager radius of the Coulombically bound pair, they experience an effective temporal fluctuation in the local magnetic field, even when the nuclear spin ensemble is quasistatic. The decoherence time therefore places an upper limit on the intersite hopping rate of charges within a pair [9].*

corroborated by electrically detected spin echo measurements [9]. The long room temperature coherence times are remarkable and for the first time, experimental data about this hardly accessible materials parameter became available. The extensive exploration of coherent spin motion effects in electric currents in organic semiconductor devices even at room temperature greatly helped to understand the physical nature (the microscopic model) behind spin-dependent processes in these materials [3-4,7,9]. Astonishing analogies to recent discussions in the field of quantum biology should be noted, where similar spin coherence times have been speculated to exist in retinal photosystems of migratory avian species [13]. Figure 1 displays a sketch illustrating the qualitative nature of the weakly spin coupled excitonic precursor states (so called polaron pairs) which are electron-hole systems whose spin manifold determines whether the pair will undergo transitions into the singlet or triplet exciton manifold. Our experiments allowed us to significantly scrutinize this model as the origin for pEDMR and pODMR signals, magnetoresistance effects and quantum efficiency limiting mechanism of both organic light emitting diodes as well as organic solar cells while, at the same time, excluding other spin-dependent processes (e.g. the bipolaron pair mechanism, or the triplet exciton-polaron pair) which had been speculated on in the literature as being responsible for the observed spin-dependent effects at room temperature [14,15]. Among these mechanisms, only the triplet exciton-polaron process could be verified in MEH-PPV using pEDMR, yet, only under the condition of an imbalanced injection of electrons compared with holes and at rather low temperatures (<80K) [7].

The polaron pair mechanism controls electric current via spin pair permutation symmetry states (singlet vs. triplet), not through spin polarization states. Because of this, variables which drastically influence polarization (magnetic field strengths, temperature) do not influence magnetic resonant current effects caused by the polaron pair process. This has dramatic consequences as it allows electrically detected magnetic resonance at room temperature and extremely low magnetic fields (as low as 1.5mT).

The polaron pair mechanism controls electric current via spin pair permutation symmetry states (singlet vs. triplet), not through spin polarization states. Because of this, variables which drastically influence polarization (magnetic field strengths, temperature) do not influence magnetic resonant current effects caused by the polaron pair process. This has dramatic consequences as it allows electrically detected magnetic resonance at room temperature and extremely low magnetic fields (as low as 1.5mT).

Figure 2 displays magnetoresistance measurements conducted on an MEH-PPV device. The two measurements are made under identical conditions except for the presence of an oscillating electromagnetic field (supplied by a stripline) whose frequency is 50MHz in one case (right) and 200MHz in the other case (left).

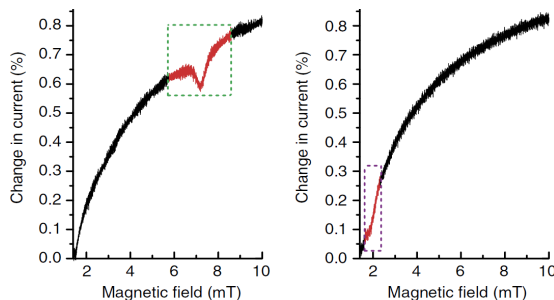


*Figure 2: The magnetic field response of a DC current (no modulation) in a bipolar MEH-PPV diode as a function of magnetic field as RF radiation (200 MHz (left); 50 MHz (right)) is applied. Reductions in the current are seen when magnetic resonance conditions are satisfied. These dips are more pronounced when the applied field exceeds the strength of local hyperfine fields in the material [8].*

The data is very similar for most magnetic fields. However, around distinct magnetic fields, the data sets differ, namely at those fields which establish magnetic resonance with the incident electromagnetic radiation. In the presence of magnetic resonance, which under the given continuous wave irradiation conditions drastically enhances spin mixing rates, a significant reduction of the current is observed. This effect is analogous to the magnetoresistance phenomenon which also reduces the current as magnetic fields lower than the hyperfine fields also cause a drastic enhancement of the spin mixing effect. The data in Fig. 2 is a remarkable example of how significant spin effects are for the properties of organic semiconductors. These materials obviously allow the observation of magnetic resonance by using a simple commercial current multimeter. Polaron EDMR is possible over a continuous frequency and magnetic field range. Figure 3 shows that the gyromagnetic ratio will always be constant, even at different temperatures and under degradation (oxidation) of the material. The gyromagnetic ratio is therefore an ideal natural magnetic field standard. By providing an accurate frequency (which is straightforward in the age of quartz oscillators), OLED devices can be used as highly accurate, calibration free, magnetic resonance low-cost thin-film magnetometers. Both, the patent [C. Boehme, D. R. McCamey, PCT International Application No. PCT/US12/20531, filed January 6, 2012], as well as the first demonstration [9] of this organic magnetic resonance based magnetometer (OMRM) device was an important but unexpected result of this project.

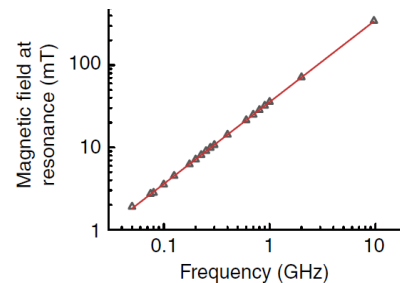


Figure 3: The peak magnetic field where maximal resonance-induced current changes are measured as a function of the applied excitation frequency, following a linear relationship (the error of the data points is below the size of the symbols) [8]. A linear fit yields a gyromagnetic ratio  $\gamma = 28.03(4)$  GHz/T and a corresponding  $g = 2.0026(4)$ . The near perfect linearity of the electrically detectable gyromagnetic ratio can be used for magnetometry as an absolute magnetic field standard.

Due to the simplicity and, at the same time, the sophistication of the pulsed optically-detected

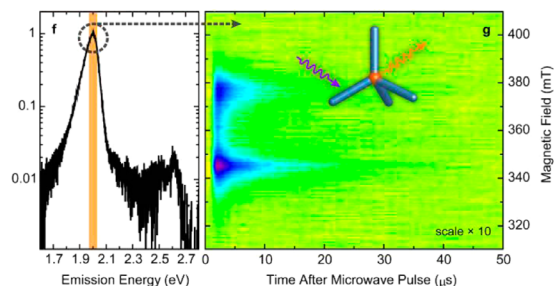


Figure 4, left: The photoluminescence intensity (arb. units) of CdS/CdSe tetrapod nanocrystals shows a distinct excitonic emission maximum. Right: The change of photoluminescence from a narrow band around this maximum observed after a brief pulsed magnetic resonant excitation as a function of time and magnetic field. The magnetic field dependence shows that several spin-dependent processes are present [11].

photoluminescence) magnetic resonance technique, we have also applied this technique to hybrid organic-inorganic semiconductor materials. These include CdS and CdSe nanocrystal quantum dot, quantum rod and light-harvesting tetrapod structures whose surfaces are terminated with organic ligands. [11-12]. A variety of spin dependent processes have been identified in these strong spin-orbit/ weak spin-orbit coupled heteromaterials. The results are intellectually stimulating due to their conceptual analogies to pure organic structures, but on very different  $g$ -factor scales. The results could also be significant for hybrid organic-inorganic devices such as improved solar cells. Figure 4 summarizes some of these recent results.

### Future Plans

In the coming project periods the main focus of this activity will be on the development of organic field effect transistor structures based on MEH-PPV, using Fullerene  $C_{60}$  and PEDOT as electron and hole

spin measurement scheme will be employed which is based on pEDMR. It is planned to combine electric field control of electron spin states and the previously demonstrated electrical detection of spin states in order to explore the technical prerequisites for spin transistors based on organic semiconductors. These devices would behave electrically similarly to inorganic spin transistors, yet their working principles depart radically from previous concepts. In parallel to this work, the general spectroscopic exploration (pEDMR/pODMR) of spin-coupling parameters in various (newly synthesized and well established) organic semiconductor molecules will continue as much as the exploration of electrical nuclear spin readout concepts for hydrogen and  $^{13}\text{C}$  nuclei.

### Published and accepted Publications of DOE sponsored research in 2010-2012

- [1] C. Boehme and D. R. McCamey, **Investigating spin-dependent processes in organic semiconductors** in *Organic Spintronics*. Z. V. Vardeny ed. (CRC Press, 2010).
- [2] J. M. Lupton, D. R. McCamey, C. Boehme, **Coherent Spin Manipulation in Molecular Semiconductors: Getting a Handle on Organic Spintronics**, *Chem. Phys. Chem.* 11 (14), 3040 (2010).
- [3] D. R. McCamey, S.-Y. Lee, S.-Y. Paik, J. M. Lupton, and C. Boehme, **Spin-dependent dynamics of polaron pairs in organic semiconductors**, *Phys. Rev. B* **82**, 125206 (2010).
- [4] D. R. McCamey, K. J. van Schooten, W. J. Baker, S.-Y. Lee, S.-Y. Paik, J. M. Lupton, and C. Boehme, **Hyperfine-field mediated spin beating in electrostatically-bound charge carrier pairs**. *Phys. Rev. Lett.* **104**, 017601 (2010). Reviewed in *Nature Materials* **9**, 288 (2010).
- [5] S.-Y. Lee, S.-Y. Paik, D. R. McCamey, J. Yu, P. L. Burn, J. M. Lupton, and C. Boehme, **Tuning hyperfine fields in conjugated polymers for coherent organic spintronics**, *JACS*, **133**, 2019, (2011).
- [6] D. Chaudhuri, H. Wettach, K. J. van Schooten, S. Liu, E. Sigmund, S. Höger, and J. M. Lupton, **Tuning the singlet-triplet gap in metal-free phosphorescent pi-conjugated polymers**, *Angew. Chem. Int. Ed.* **49**, 7714 (2010).
- [7] W. J. Baker, D. R. McCamey, K. J. van Schooten, J. M. Lupton, and C. Boehme, **Differentiation between polaron-pair and triplet-exciton polaron spin-dependent mechanisms in organic light-emitting diodes by coherent spin beating**, *Phys. Rev. B* **84**, 165205 (2011).
- [8] W. J. Baker, K. Ambal, D. P. Waters, R. Baarda, H. Morishita, K. van Schooten, D. R. McCamey, J. M. Lupton, and C. Boehme, **Robust Absolute Magnetometry with Organic Thin-Film Devices**, *Nature Communications* **3**, 898 (2012). Reviewed in *Nature Materials* **11**, 663 (2012) and *Nature Nanotechnology* **7**, 696–697 (2012).
- [9] W. J. Baker, T. L. Keevers, J. M. Lupton, D. R. McCamey, and C. Boehme, **Slow hopping and spin dephasing of Coulombically-bound polaron pairs in an organic semiconductor at room temperature**, *Phys. Rev. Lett.* **108**, 267601 (2012).
- [10] S.-Y. Lee, S.-Y. Paik, D. R. McCamey, C. Boehme, **Modulation frequency dependence of continuous-wave optically/electrically detected magnetic resonance**, *Phys. Rev. B* **86**, 115204 (2012).
- [11] K. J. van Schooten, J. Huang, W. J. Baker, D. V. Talapin, C. Boehme, J. M. Lupton, **Spin-Dependent Exciton Quenching and Spin Coherence in CdSe/CdS Nanocrystals** *Nano Letters* **13**, 65 (2013).
- [12] K. J. van Schooten, J. Huang, W. J. Baker, D. V. Talapin, C. Boehme, J. M. Lupton, **Spin-dependent exciton quenching and intrinsic spin coherence in CdSe/CdS nanocrystals**, *in press Phys. Rev. B* (2013), *arXiv:1210.5684* (2012).

### Other references

- [13] E. M. Gauger, E. Rieper, J. J. L. Morton, S. C. Benjamin, and V. Vedral, **Sustained Quantum Coherence and Entanglement in the Avian Compass**, *Phys. Rev. Lett.* **106**, 040503 (2011).
- [14] J. Shinar, A. V. Smith, P. A. Lane, K. Yoshino, Y. W. Ding, T. J. Barton, **UV-excited optically detected magnetic resonance (UV-ODMR) study of  $\pi$ -conjugated polymers**, *Mol. Cryst. Liq. Cryst.*, **256**, 691, (1994).
- [15] P. A. Bobbert, T. D. Nguyen, F. W. A. van Oost, B. Koopmans, M. Wohlgenannt, **Bipolaron mechanism for organic magnetoresistance**, *Phys. Rev. Lett.* **99**, 216801, (2007).

# First Principles Determination of Structure, Thermodynamics, and Transport in Metals and Oxides

Contract DE-FG02-96ER45571

Professor Gerbrand Ceder  
Department of Materials and Engineering  
Massachusetts Institute of Technology  
77 Massachusetts Avenue, Rm 13-5051  
Cambridge MA 02139

## Objective

The objective of this research is to:

- 1) Develop methods to predict structure in bulk and as function of particle size
- 2) Investigate and develop methods to understand the stability and morphology of materials in solution as function of pH and oxidation environment and integrate that with (1) to predict how structure selection can be modified by environment in aqueous solutions.

## Stability and morphology of materials in solution

Stability of materials in aqueous solutions is critically important for many materials applications: corrosion, catalyst stability in fuel cells, synthesis of materials from solution methods, etc. To address this problem we have developed an approach which enables us to directly combine ab initio calculated solids with experimental Gibbs free energies of arbitrary aqueous states. The method takes advantage of the fact that formation energies of solids are essentially transferable between energy reference systems. However, the transferability is contingent on the level of accuracy of the calculation and on consistent reference states. Depending on the complexity of the electronic state of the material, ab initio solid formation energies can differ from their respective experimental counterparts by up to  $\pm 0.5$  eV/atom. Reaction energies in water are typically on the scale of hundreds of meV which means that for example, shifting a simple dissolution reaction by 200 meV/atom is equivalent to changing the pH by several units, which is unacceptable in a method striving for predictive power. We have developed a novel model by referencing the energy of dissolved ions in water to the DFT solid state energies through the

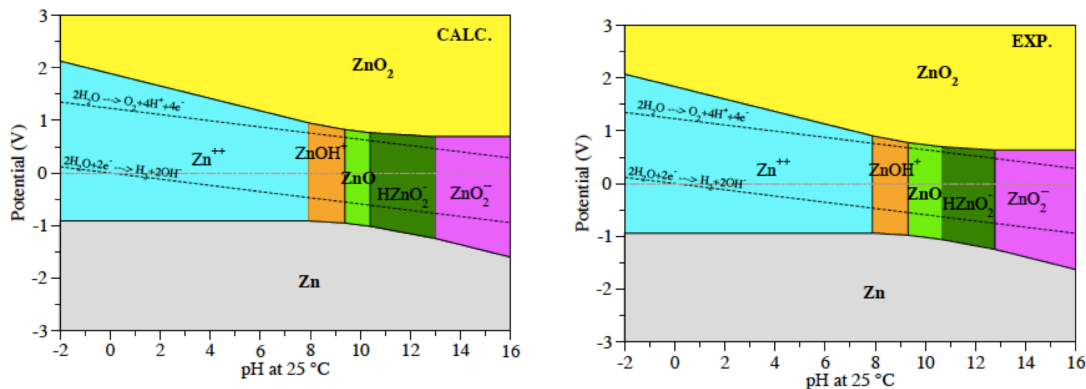


Figure 1: Calculated (left) and experimental (right) Pourbaix diagram showing excellent agreement

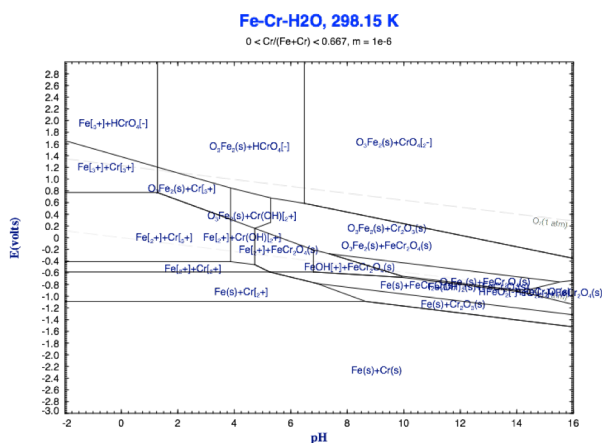
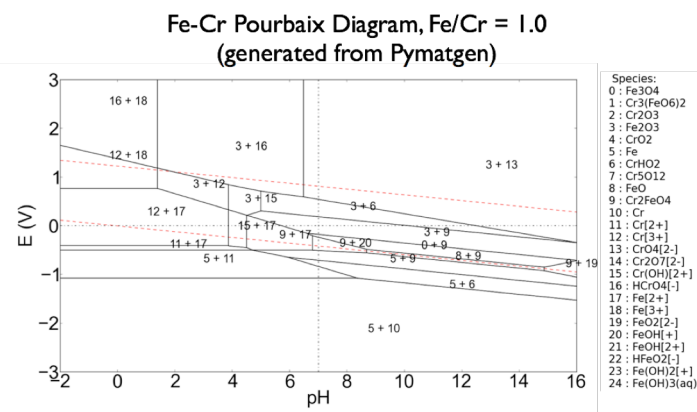


Figure 2: Comparison between the ab initio computed Pourbaix diagram of Fe-Cr alloys (top) and the experimental one (from FactSage (bottom))

experimentally know dissolution energies of the elements. This approach allows us now to predict for any compound the dissolution energy in water as function of pH and potential. The accuracy of the methodology relies on two simple facts: 1) ions in a dissolved state are always the same, irrespective of whether they come from a surface or a nanoparticle and 2) solid state errors in DFT tend to be systematic and will to a large degree cancel between phases within the same chemistry. We have tested the methodology on most elemental metal and have now extended the approach to any multi-component system. For example, Figure 2 shows the ab-initio Pourbaix diagram of Fe-Cr alloys. We can now generate such aqueous stability diagrams for any solid for which one can perform ab initio computations. In **Future Work** we plan to extend this approach to predict how solids can be synthesized from aqueous solutions. Many aqueous synthesis approaches start from soluble precursors which then react to form an insoluble product. Using Ab-initio computed Pourbaix diagrams we will be able to predict the conditions under which such synthesis reactions need to be executed. This capability will also be made available

through the Materials Project ([www.materialsproject.org](http://www.materialsproject.org))

## The Prediction of Surface Energies and Morphology in Aqueous Environments

An interesting interplay between surface chemistry and structure selection exists in solutions. By changing the composition and pH of a solution one can modify the surface energies of a compound (e.g. by modifying the surface adsorption). This gives one the ability to tailor morphology of particles in solutions, and even polytopism. Our objective is to develop an ab-initio approach to predict morphology and structure in aqueous solutions. As part of such an approach one needs to accurately determine the surface energy of nanoparticles with first-principles calculations. This requires the development of an approach that can predict all the stable surfaces of a material. In the past year we have developed robust surface slab generation algorithms that enable us to prepare generally oriented slabs for DFT calculations.

Since the development of the algorithm, we have successfully reproduced literature surface energy values for 6 structures, Anatase TiO<sub>2</sub>, Rutile TiO<sub>2</sub>, Monoclinic HfO<sub>2</sub>, Corundum Al<sub>2</sub>O<sub>3</sub>, Rocksalt NaH, and NaAlH<sub>4</sub> (Figure 3). Discrepancies between calculated and literature values are generally differ by less than 10%, which is typically under 0.1 J/m<sup>2</sup>, and the source of these discrepancies can generally be attributed to minor variations in input parameters.

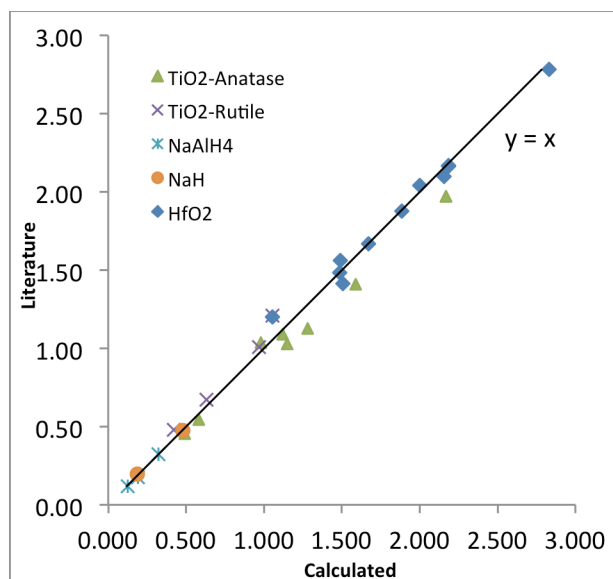


Figure 3. Literature vs. Calculated Surface Energies (J/m<sup>2</sup>)

Our **Future Plans** are to scale the surface algorithm to high-throughput and to develop models to study adsorption and reconstruction in aqueous environments. This will give us the capability to a) predict particle morphology in solution, and b) predict structure selectivity when materials form from solution. Figure 4 shows an example of the predicted LiFePO<sub>4</sub> morphology as function of ..

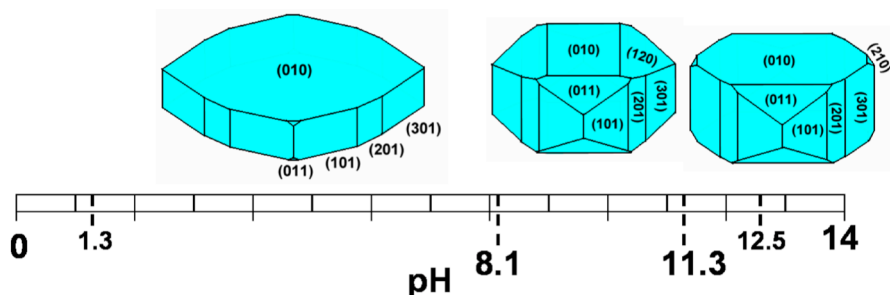


Figure 4: Computed shape of LiFePO<sub>4</sub> particles as function of pH in solution.

## Papers with DOE- Support

F. Zhou, G. Ceder, *First-Principles Determination of Charge and Orbital Interactions in Fe<sub>3</sub>O<sub>4</sub>*, Phys. Rev. B, 81 (20), 205113 (2010).

V.L. Chevrier, S.P. Ong, R. Armiento, et al., [Hybrid Density Functional Calculations of Redox Potentials and Formation Energies of Transition Metal Compounds](#), Physical Review B, 82 (7), 075122 (2010).

T. Mueller, G. Ceder, [Exact Expressions for Structure Selection in Cluster Expansions](#), Physical Review B, 82 (18), 184107 (2010).

G. Hautier, C. Fischer, V. Ehrlacher, A. Jain, G. Ceder, *Data Mined Ionic Substitutions for the Discovery of New Compounds*, Inorganic Chemistry, 50 (2), 656-663 (2011).

S.P. Ong, V. Chevrier, G. Ceder, *Comparison of Small Polaron Migration and Phase Separation in Olivine LiMnPO<sub>4</sub> and LiFePO<sub>4</sub> Using Hybrid Density Functional Theory*, Physical Review B, 83, 075112 (2011).

R. Sun, M.K.Y. Chan, G. Ceder, *First-Principles Electronic Structure and Relative Stability of Pyrite and Marcasite: Implications for Photovoltaic Performance*, Physical Review B, 83, 235311 (2011).

A. Jain, G. Hautier, C.J. Moore, S.P. Ong, C.C. Fischer, T. Mueller, K. Persson, G. Ceder, *A High-Throughput Infrastructure for Density Functional Theory Calculations*, Computational Materials Science, 50, 8, 2295-2310 (2011).

V.L. Chevrier, G. Ceder, *Challenges for Na-ion Negative Electrodes*, Journal of the Electrochemical Society, 158 (9), A1011-A1014 (2011).

A. Jain, G. Hautier, S.P. Ong, C.J. Moore, C.C. Fischer, K. Persson, G. Ceder, *Formation Enthalpies by Mixing GGA and GGA Plus U Calculations*, Physical Review B, 84 (4), 045115 (2011).

R. Sun, M.K.Y. Chan, S.Y. Kang, G. Ceder, *Intrinsic Stoichiometry and Oxygen-Induced P-Type Conductivity of Pyrite FeS(2)*, Physical Review B, 84 (3), 035212 (2011).

S.P. Ong, V.L. Chevrier, G. Hautier, A. Jain, C.J. Moore, S. Kim, X. Ma., G. Ceder, *Voltage, Stability and Diffusion Barrier Differences Between Sodium-Ion and Lithium-Ion Intercalation Materials*, Energy & Environmental Science, 4 (9), 3680-3688 (2011).

S.P. Ong, Y. Mo, G. Ceder, *Low Hole Polaron Migration Barrier in Lithium Peroxide*, Physical Review B, 85 (8), 081105 (2012).

A. Jain, G. Hautier, C. Moore, B. Kang, J. Lee, H. Chen, N. Twu, G. Ceder, *A Computational Investigation of Li<sub>9</sub>M<sub>3</sub>(P<sub>2</sub>O<sub>7</sub>)<sub>3</sub>(PO<sub>4</sub>)<sub>2</sub> (M = V, Mo) as Cathodes for Li Ion Batteries*, Journal of the Electrochemical Society, 159 (5), pp. A622-A633 (2012).

G. Hautier, S.P. Ong, A. Jain, C.J. Moore, G. Ceder, [Accuracy of Density Functional Theory in Predicting Formation Energies of Ternary Oxides from Binary Oxides and its Implication on Phase Stability](#), Physical Review B, 85 (15), 155208 (2012).

H. Chen, G. Hautier, A. Jain, C. Moore, B. Kang, R. Doe, L.J. Wu, Y.M. Zhu, Y.Z. Tang, G. Ceder, *Carbonophosphates: A New Family of Cathode Materials for Li-Ion Batteries Identified Computationally*, Chemistry of Materials, 24, 11, 2009-16 (2012).

K. Persson, B. Waldwick, P. Lazic, G. Ceder, *Prediction of Solid-Aqueous Equilibria: Scheme to Combine First-Principles Calculations of Solids with Experimental Aqueous States*, Physical Review B, 85, 235438 (2012).

T. Mueller, *Ab Initio Determination of Structure-Property Relationships in Alloy Nanoparticles*, Physical Review B, 86 (14), 144201 (2012).

S.P. Ong, W.D. Richards, A. Jain, G. Hautier, M. Kocher, S. Cholia, D. Gunter, C. Chevrier, G. Ceder, et al., *Python Materials Genomics (Pymatgen): A Robust, Open-source Python Library for Materials Analysis*, Computational Materials Science, 68, 314-319 (2013).

## Near-field thermal radiation between two objects at extreme separations (DOE grant no. DE-FG02-02ER45977)

PI: Gang Chen, co-PI: Mehran Kardar  
Massachusetts Institute of Technology  
Cambridge, MA 02139  
E-mail: [gchen2@mit.edu](mailto:gchen2@mit.edu) and [Kardar@mit.edu](mailto:Kardar@mit.edu)

**Program scope:** This project aims to investigate both experimentally and theoretically heat transfer between two surfaces when their separation changes from physical contact to tens of nanometers. It combines experimental investigation on near field thermal radiation in nanoscale gaps with the development of theoretical models to describe heat transfer between two surfaces in near contact, via both radiation and conduction mechanisms.

**Recent progress:** To experimentally probe heat transfer across narrow gaps we use a bimaterial AFM cantilever, which is made by two materials with different thermal expansion coefficients. This measurement technique uses the deflection of the cantilever due to mismatched thermal stresses to measure heat transfer and temperature change. Using this experimental technique, we previously measured near-field thermal radiation for sphere-plate separations down to  $\sim 30$  nm. We continued our experimental investigation by measuring near-field thermal radiation between a silica sphere and a silica substrate with separations as small as 1 nm. As we previously reported, the experimental results reasonably fit the theoretical calculation based on the proximity force approximation when the separation distances are larger than 100 nm. Below 100 nm, the experimental results start deviating from the theoretical calculation. Saturation in the near-field radiative conductance is observed below 30 nm. We have been investigating the possible reasons for this deviation, including the force effect, surface roughness, and the impurity of the sample material itself. The effect of the surface roughness is studied by doing measurements with spheres with varying surface roughness. The experimental results show that spheres with different surface roughness have very close near field conductance (Fig. 1a). Based on this result, hypothesis is made that the surface roughness has small influence on near field thermal radiation

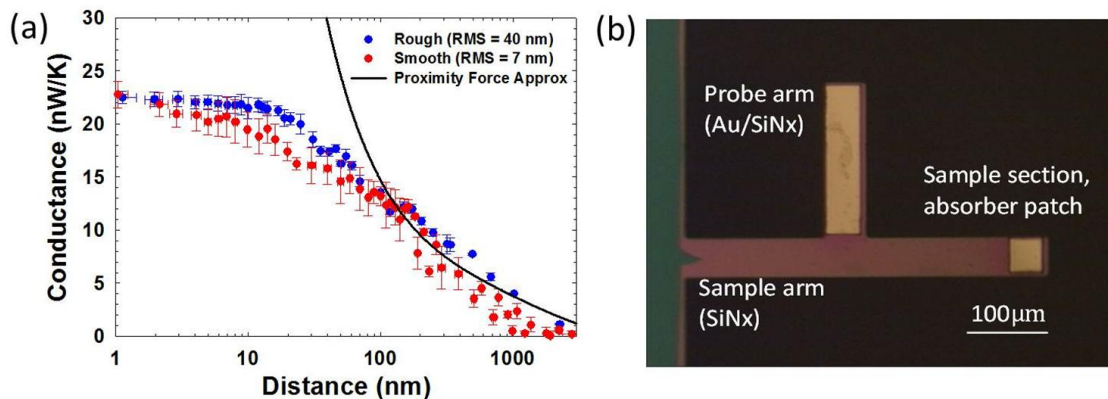


**Figure 1.** (a) Experimental results for near-field thermal conductance between a silica sphere (100 micron diameter) and a silica substrate for different levels of surface roughness of the sphere. (b) Optical microscopy image of a bi-arm cantilever, which prevents non-thermal bending effects by eliminating sample deflection and minimizing stray light absorption during heat flux measurements at the cantilever tip. Temperature difference between the sample section and chip base is maximized to enhance the sensitivity.

and we are continuing to cross examine the hypothesis by performing more experiments and improving the experimental system.

To measure near field thermal radiation more accurately, we have successfully fabricated and characterized a new type of cantilever which can decouple thermal and force signal to eliminate the parasitic deflection of the cantilever due to the force effect. In addition to enabling the force correction, the custom-designed bi-arm cantilever is over one order of magnitude more sensitive than current commercial cantilevers due to the significantly reduced thermal conductance of the cantilever sample arm. The proposed cantilever design is not commercially available and must be self-fabricated. By taking different material and process constraints into account, bi-arm cantilevers based on silicon nitride ( $\text{SiN}_x$ ) and gold (Au) were created on a silicon (Si) substrate. The sample arm is made up of nitride while the detector arm consists of a nitride/gold bilayer. An additional metal absorber patch is added to the tip of the sample arm to allow for laser absorption during calibration process (Fig.1b). For quantitative thermal measurements, the system requires three calibrations: temperature calibration, heating laser calibration, and detector laser calibration. The thermal conductances of the different bi-arm cantilever sections are extracted based on the sensitivities determined in the calibration measurements. The thermal conductance of the sample section with the appropriate error propagation equals  $G_S = 0.32 \text{ W/K} \pm 0.04 \text{ W/K}$ , which is much lower than that of the conventional triangular cantilever. The thermal conductance of the detector cantilever arm equals  $G_D = 4.06 \text{ W/K} \pm 9.48 \text{ W/K}$ . This complete characterization enables the system to be used to measure near field thermal radiation more accurately from tens of nanometers down to direct contact. We are now using these cantilevers to conduct near-field experiment.

In parallel, the group of Prof. Kardar developed analytical/numerical tools to compute heat transfer in different settings, including rough objects at proximity. In particular, a small distance

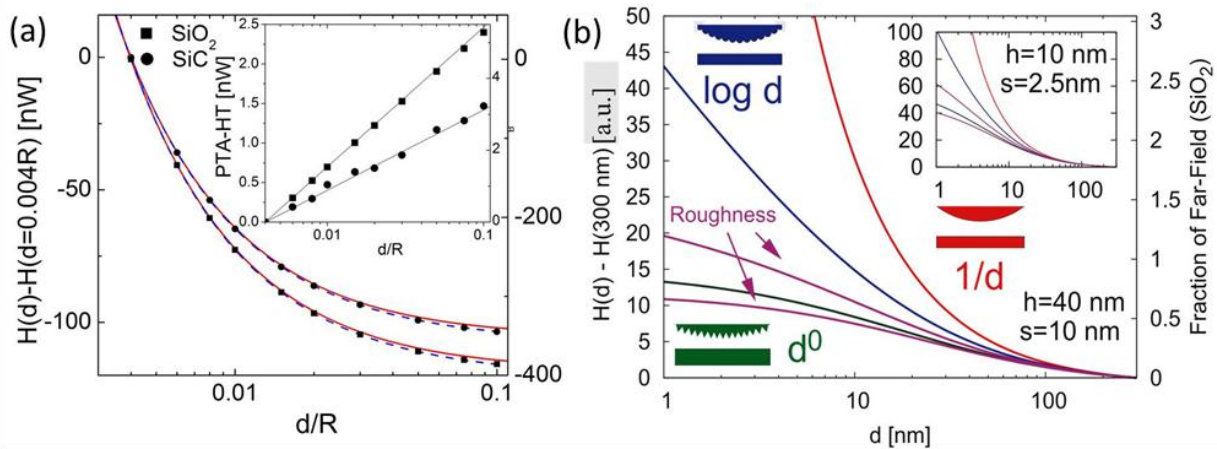


**Figure 2.** (a) Heat transfer near-field adjusted plot for a sphere in front of a plate for SiC (circles, left abscissa) and  $\text{SiO}_2$  (squares, right abscissa), and . Exact numerical data, PTA and gradient expansion are shown as data points, solid red and dashed blue lines, respectively. Inset depicts the deviation of PTA from the exact data, where lines show the analytical form which follows from the gradient expansion. All curves shown depend on only through . (b) Preliminary results modeling effect of roughness on near-field radiation heat transfer, showing drastic reduction of the divergence of heat transfer for sphere plate (red curve), due to modulations (blue for dome-like, or green for sharp pyramids) or roughness (magenta).

expansion for radiative heat transfer between gently curved objects was derived in terms of the ratio of distance to radius of curvature. A gradient expansion allows us to go beyond the lowest order proximity transfer approximation (PTA in Fig. 2a). The range of validity of such expansion depends on temperature as well as material properties. Generally, the expansion converges faster for the derivative of the transfer than for the transfer itself, which we use by introducing a near-field adjusted plot. Figure 2a demonstrates that the gradient expansion agrees remarkably with the exact numerical data for the case of a sphere in front of a plate. The expansion can be used to study arbitrary geometries, revealing the geometry dependence of the heat transfer at nano-scale.

When the spacing between two surfaces is less than the dominant wavelength of thermal radiation, heat transfer between the two surfaces can significantly exceed the blackbody limit. Radiative heat transfer at small spacing is described by Rytov's fluctuating electrodynamics formulation, whereas in the contact limit, heat transfer is described in terms of heat conduction and phonon transport. Today there is no unified theory that can describe the power transferred between two bodies as a function of their separation down to the contact limit. We developed an approach using lattice dynamics and the microscopic Maxwell equations to bridge the theories of conduction and radiation. We incorporated both short range and long range forces in a state of the art atomistic Green's function formalism to compute conjugate heat transfer due to both

conduction and radiation. This is the first application of the Green's function formalism to compute energy transmission including long range forces. Through this approach, we developed a comprehensive atomistic scale framework for predicting the interplay of short range and long range forces in transferring heat across very small gaps. This model is unique in that it is applicable for large gap spacing down to the contact limit, thus providing a unified theory of conduction and radiation. By using the developed model, we compared the transmission for the case of perfect contact with the one when a gap is introduced between two slabs. It can be seen in Fig. 3a that transmission drops sharply for the case of a gap. The integrated conductance data for several gap thicknesses shown in Fig. 3b. offers insight into the behavior of heat transfer as the slabs are spaced further and further apart. Our next steps is to extend the calculations for larger spacings, and to validate the model in this regime to the existing continuum approach based on fluctuating electrodynamic theory

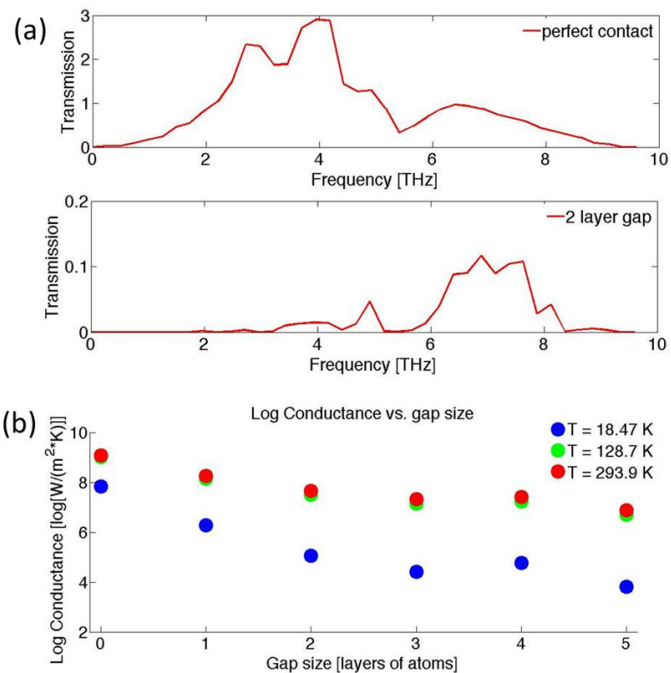


Figure 3. (a) Comparison of the integrated transmission for the cases of perfect contact (top) and for a gap of 2 atomic layers (bottom). A gap leads to a dramatic reduction in transmission and shifts the dominant modes that transmit from the acoustic regime to the optical regime, indicating the significant role played by long range electromagnetic forces. (b) Variation of the heat conductance as a function of the separation between two slabs. Increasing the separation diminishes the interaction forces, leading to the observed behavior above

based on macroscopic Maxwell's equations.

**Planned activities:** Our next steps include improving the accuracy of experiments to obtain reliable data on both near-field conductance and force by using bi-arm cantilever. On the theoretical part, we will extend the model that bridges conduction and radiation to dielectric materials. This will allow a direct comparison between theory and experiments, with the goal of furthering our understanding of heat transfer at nanometer length scales. A general method to compute heat transfer between curved and rough surfaces is also under development. While based on PTA, the approach provides in some cases exact asymptotic behavior, and in other cases qualitatively correct results, at short distances. The examples in Fig. 2b indicate the drastic reduction of the divergence of heat transfer for sphere plate (red curve), due to modulations (blue for dome-like, or green for sharp pyramids) or roughness (magenta). We are working out relations which allow inferring the of equilibrium properties from equilibrium fluctuations.

### **Publications:**

1. B. Burg, J. Tong, W.C. Hsu and G. Chen, Decoupled cantilever arms for highly versatile and sensitive temperature and heat flux measurements, *Rev. Sci. Instruments*, **83**, 104902, 2012.
2. S. Shen, A. Mavrokefalos, P. Sambegoro, and G. Chen. Nanoscale thermal radiation between two gold surfaces. *Appl. Phys. Lett.* **100**, 233114, 2012.
3. W.-C. Hsu, J.K. Tong, B.L. Liao, B.R. Burg and G. Chen, Direct and quantitative broadband absorptance spectroscopy on small objects using Fourier transform infrared spectrometer and bilayer cantilever probes, *Appl. Phys. Lett.*, **102**, 051901, 2013.
4. M. Krüger, G. Bimonte, T. Emig and M. Kardar, Trace formulas for nonequilibrium Casimir interactions, heat radiation and heat transfer for arbitrary objects, *Phys Rev. B* **86**, 115423, 2012.
5. V. A. Golyk, M. Krüger, M. T. H. Reid and M. Kardar, Casimir forces between cylinders at different temperatures, *Phys. Rev. D* **85**, 065011, 2012.
6. V. A. Golyk, M. Krüger, A. P. McCauley, and M. Kardar, Small distance expansion for radiative heat transfer between curved objects, *Europhys. Lett.* **101**, 34002, 2013.
7. T.F. Luo and G. Chen, Nanoscale heat transfer---from computation to experiment, *J. Phys. Chem. & Chem. Phys.*, **15**, 3389-3412, 2013.

## Electrochemically-Driven Phase Transitions in Battery Storage Compounds

D. B. Ravensbaek<sup>1</sup>, K. Xiang<sup>1</sup>, W. Xing<sup>1</sup>, C. Carter<sup>1</sup>, M. Tang<sup>2</sup> and Y. M. Chiang<sup>1</sup>

**PI: Yet-Ming Chiang**

**(Co-PI: W. Craig Carter)**

<sup>1</sup>Massachusetts Institute of Technology,  
Bldg. 13-4086, Cambridge, MA 02139

E-mail: [ychiang@mit.edu](mailto:ychiang@mit.edu)

**PI: Ming Tang**

<sup>2</sup>Lawrence Livermore National  
Laboratory, Livermore, CA 94550

E-mail: [tang25@llnl.gov](mailto:tang25@llnl.gov)

*Program scope:* Compounds of interest for ion storage in advanced batteries frequently exhibit phase transformations, driven by large and variable electrochemical driving forces inherent to practical use. The scope of this program is to develop a predictive understanding of the interaction between materials variables such as composition, crystallite size, especially at the nanoscale, as well as the electrochemical conditions driving the phase transition. This will be achieved through a combined experimental-theoretical study carried out by MIT and Lawrence Livermore National Laboratory using phospho-olivine materials,  $\text{LiMPO}_4$  ( $M = \text{Fe}, \text{Mn}$ ) as the main model system.

The phospho-olivine materials are attractive positive electrode materials for rechargeable Li-ion batteries due to their high theoretical capacity, high lithium intercalation voltage, excellent power performance and high stability.  $\text{LiFePO}_4$  is already widely utilized in power tools, electric vehicles and grid stabilization applications at up to MWh scale. The delithiation in this material typically occurs via a first order phase transition from the lithium-rich triphylite phase,  $\text{LiFePO}_4$  (LFP) to the lithium-poor heterosite phase,  $\text{FePO}_4$  (FP). Since the discovery of LFP as an electrode material much research has been devoted to elucidating the phase transformation mechanisms, which are of vital importance for practical applications as the reversibility and stability of the structural transformations determine the capacity, power, and lifetime of the system. Numerous models have been proposed to describe the phase transformation mechanism in LFP, including the core-shell model<sup>1,2</sup>, various phase boundary migration models<sup>3-5</sup>, solid-solution models<sup>6,7</sup> and spinodal-decomposition models<sup>8-10</sup>. It is hotly debated which is the “correct” model.<sup>11</sup> Limited experimental evidence exists to support some of the models, and where experimental data exists, the material composition, particle size and shape, structural defects, or electrochemical conditions such as applied overpotential differ.<sup>12</sup> It is not necessarily the case that there is a single correct model; more than one may be applicable depending on experimental conditions. Hence, in order to resolve these controversies and obtain a predictive understanding of mechanism(s) in phospho-olivines, it is necessary to investigate phase transformation behavior while systematically moving through the relevant parameter spaces.

Within this program several projects have been initiated: **1)** Electrochemical driven phase transitions in  $\text{LiMn}_y\text{Fe}_{1-y}\text{PO}_4$ , **2)** Time dependent stability and structural evolution of disordered and amorphous phases in nanoscale olivines, **3)** *In situ* TEM investigations of phase transformations in phospho-olivines and **4)** Structural analysis of nanoscale olivine cathodes after extensively cycling in commercial Li-ion cells. Wherever possible, multiple structure analysis techniques are being used, taking advantage of the various DOE beamlines, including *in situ* powder X-ray diffraction (PXD) at X14A, NSLS, BNL, *ex situ* PXD and pair distribution function (PDF) data at ID11-B, APS, and *ex situ* PDF at NPDF, LANL. In this abstract we mainly focus on our recent progress within project **1**.

*Recent progress:*

### **Electrochemical driven phase transformation in $\text{LiMn}_y\text{Fe}_{1-y}\text{PO}_4$**

The Mn-based olivine  $\text{LiMnPO}_4$  has a voltage plateau around 4.1 V vs.  $\text{Li/Li}^+$  compared to 3.45 V for  $\text{LiFePO}_4$ , and therefore has substantially higher energy density as a battery cathode. Unfortunately,  $\text{LiMnPO}_4$  exhibits slow charge-discharge kinetics even at nanoscale particle size, which has prevented its commercial use. However, with even a modest Fe addition, nanoscale  $\text{LiMn}_y\text{Fe}_{1-y}\text{PO}_4$  (LMFP) exhibits

amongst the highest rate capabilities of all the olivines. This has been explained by the existence of an intermediate solid solution (here denoted  $L_y\text{MFP}$ ,  $y = \text{Mn-content}$ ) that reduces the misfit strain by breaking the single phase transition (observed for LFP) into two stages, first a transition of MFP to an intermediate phase  $L_y\text{MFP}$ , then between  $L_y\text{MFP}$  and LMFP.<sup>13</sup> However, at this stage there is still no clear conclusion as to whether the transformations are two-phase first-order reactions or involve formation of a metastable solid solution. Significant discrepancies are found in the literature between the  $(x,y)$ -phase diagrams for  $\text{Li}_x\text{Mn}_y\text{Fe}_{1-y}\text{PO}_4$  determined experimentally (by chemical delithiation) versus computationally.<sup>14,15</sup>

Here we investigate a series of  $\text{LiMn}_y\text{Fe}_{1-y}\text{PO}_4$  ( $y = 0.1, 0.2, 0.4, 0.6$  and  $0.8$ ) powders with particle size of  $\sim 50$  nm (based on BET surface area). This system allows systematic exploration of phase space by varying lithium concentration (e.g. with electrochemical cycling) as well as Mn:Fe ratio. A systematic study of the effect of applied over- and undervoltage (OV and UV =  $E_{\text{appl.}} - E_{\text{eq}}$ ) on the phase transformation during charge and discharge, respectively has been conducted using *in situ* PXD at beamline X14A, NSLS, BNL.

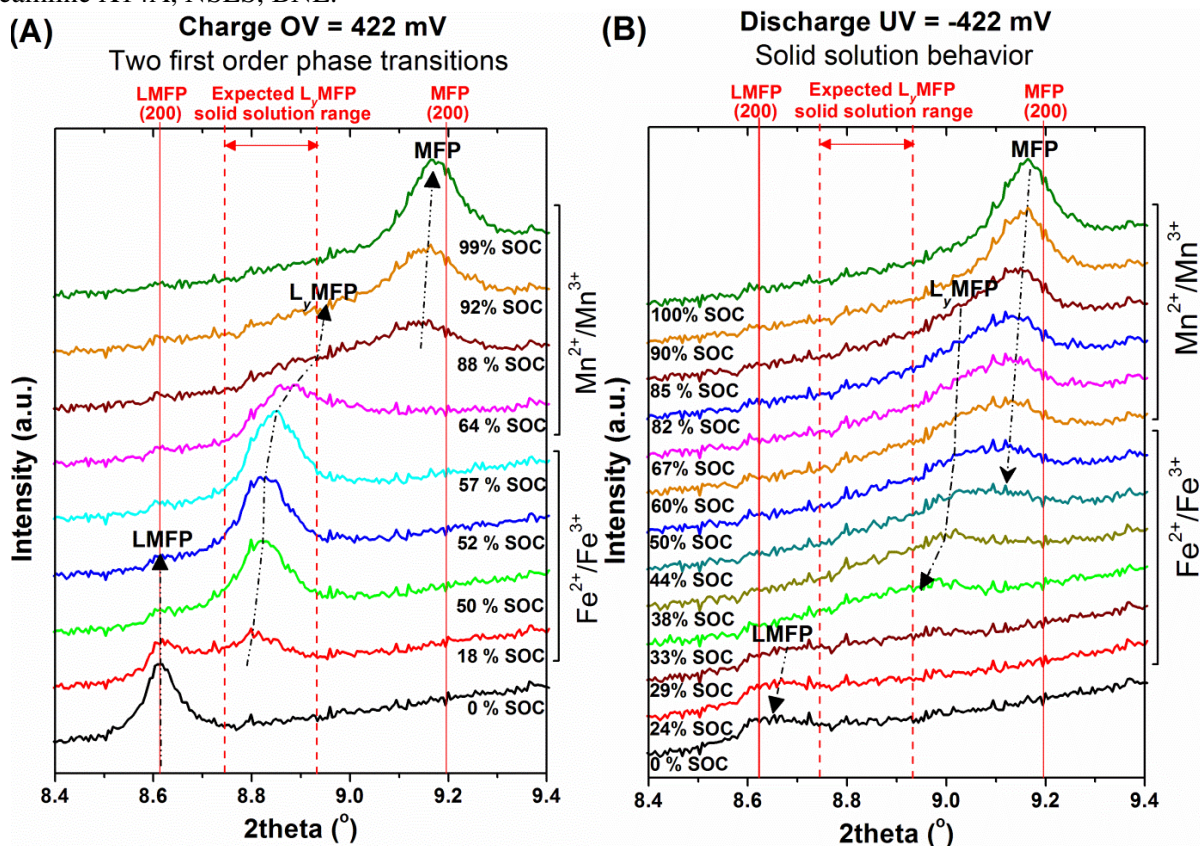


**Fig. 1** Example of typical *in situ* PXD data for  $\text{LiMn}_{0.4}\text{Fe}_{0.6}\text{PO}_4$  at selected state-of-charge (SOC) measured during charge (A) and discharge (B) at OV/UV =  $\pm 422$  mV. Charge and discharge were each carried out in two potential steps, i.e. at the selected OV/UV over/below the OCV for the  $\text{Fe}^{2+}/\text{Fe}^{3+}$  (3.473 V) and  $\text{Mn}^{2+}/\text{Mn}^{3+}$  (4.046 V) plateaus, respectively. Each step was terminated when the current response decreased to  $C/50$ . The solid red lines indicate the expected positions of the (200) peak for the LMFP and MFP end-members, while the dashed red line indicates the expected range for the observation of the (200) peak from the  $L_y\text{MFP}$  solid solution intermediate (based on ref. 14).

Our main focus has so far been on the composition  $\text{LiMn}_{0.4}\text{Fe}_{0.6}\text{PO}_4$  (i.e.  $y = 0.4$ ), which has been studied under three different OV/UV conditions, i.e.  $\pm 122$  mV, 272 mV and 422 mV. During charge (Fig. 1 A) two-phase reactions are observed at both the Fe- and Mn-plateau, and the phase evolution from LMFP to  $L_y\text{MFP}$  and  $L_y\text{MFP}$  to MFP, respectively are found (by peak integration) to follow the binary lever rule. Hence, these results suggest that LMFP is less prone to exhibit crystalline-to-amorphous phase transformation as compared to LFP.<sup>16</sup> It should be noted that  $L_y\text{MFP}$  exhibits pronounced solid solution

behavior at the Mn-plateau observed by peak broadening and change in position towards that of MFP. This indicates that the Li-miscibility gap between  $L_y$ MFP and MFP is significantly smaller than that between LMFP to  $L_y$ MFP or that in LFP-FP.

However, a significantly different phase transformation sequence is observed during discharge (Fig. 1 B). The relatively sharp MFP peak formed during charge changes position continuously with decreasing state-of-charge (SOC), indicating formation of a continuously varying solid solution. Moreover, starting at 90% SOC, a broad shoulder is observed at lower  $2\theta$  compared to the MFP peak. The  $2\theta$  position is higher than that of the  $L_y$ MFP intermediate phase, suggesting that it has an even greater concentration of Li vacancies. This peak broadens significantly upon discharge until between 40 and 30 % SOC it becomes hardly distinguishable from the background. The phase responsible is most likely a crystalline phase with large local variation in Li concentration rather than an amorphous phase. At end of discharge, a broad peak appears, located between the positions of equilibrium LMFP and the lower end of the solid solution range for  $L_y$ MFP expected from the published experimental phase diagram.<sup>14</sup> Thus this also appears to be a metastable crystalline phase with significant local variations in composition.

We have therefore observed, firstly, that the electrochemically-driven phase transformation is highly hysteretic between charge and discharge, and secondly, that two different metastable and locally non-uniform solid solution compositions form upon discharge. The phase transition sequence upon discharge may be correlated with the high rate capability of nanoscale LMFP, since the broad peaks and extended solid solutions occurring during each step in the two-stage transformation (MFP to  $L_y$ MFP and  $L_y$ MFP to LMFP) imply reduced misfit strain if the co-existing phases exist in the same particles.

We have observed very similar results for experiments conducted at lower OV and UV, as well as at different C-rates, the only difference being that the UV appears to affect the Li-content in the  $L_y$ MFP solid solution, especially at high SOC. The hysteresis in phase transformation behavior between charge and discharge may also explain the shape of the voltage curves obtained by galvanostatic cycling of these materials, i.e. during charge all compositions reveal two well divided plateaus suggesting two first-order phase transformations as observed by PXD, while during discharge the plateaus are only partly resolved and for large regions, especially at low SOC, the voltage is observed to decrease continuously.

To investigate the equilibrium phases in a wide  $(x,y)$ -space, *ex situ* PXD data was measured at beamline ID-11-B, APS. Samples of  $\text{Li}_x\text{Mn}_y\text{Fe}_{1-y}\text{PO}_4$  ( $y = 0.1, 0.2, 0.4, 0.6$  and  $0.8$ ) with varying  $x$  were prepared by electrochemical Li extraction or insertion at 1C. *Ex situ* PXD was measured approximately one week after sample preparation, hence allowing for long relaxation times towards equilibrium phases. From the data a  $(x,y)$ -phase diagram for  $\text{Li}_x\text{Mn}_y\text{Fe}_{1-y}\text{PO}_4$  has been constructed (Fig. 2). This study revealed significant differences between the phases observed during dynamic cycling conditions (*in situ*) and after relaxation (*ex situ*). For example, for  $y = 0.4$ , two-phase first order reactions are observed *in situ* during charge (Fig. 1A), while single phase solid solutions are observed over the entire Fe-plateau by *ex situ* PXD. This suggests that two coexisting phases, LMFP and  $L_y$ MFP, may relax to one equilibrium solid solution of composition  $\text{Li}_x\text{Mn}_y\text{Fe}_{1-y}\text{PO}_4$ . Also, the crystalline phase with large local variation in Li concentration, observed *in situ*

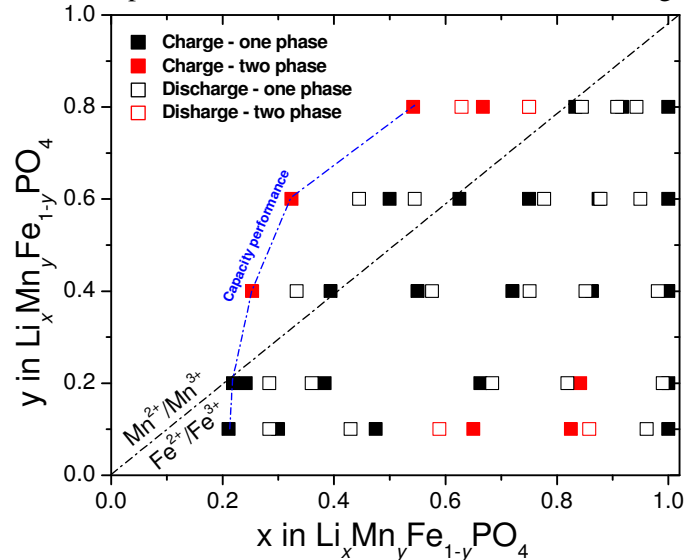


**Fig. 2**  $(x,y)$ -compositional phase diagram for  $\text{Li}_x\text{Mn}_y\text{Fe}_{1-y}\text{PO}_4$  based on *ex situ* PXD for samples prepared by charge and discharge at 1C. Black and red squares represents single- and two-phase regions observed in this study during charge (closed squares) and discharge (open squares).

during discharge (Fig 1B) is found to relax into a solid solution of homogeneous Li-content (i.e. sharp diffraction peaks). For the majority of samples *ex situ* PXD shows no hysteresis between charge and discharge. Only for  $y = 0.2$  minor hysteresis are observed at  $x \sim 0.82$ .

This clearly underlines the importance of observing these phenomena *in situ* to understand phase transformation behavior during real-world use, and points to the metastability of the phases obtained during dynamic cycling conditions, i.e. two coexisting phases. Metastability and time-dependent evolution may explain the significant differences between experimental and computational phase diagrams.

#### Future plans:

In order to gain more detailed insight into the structural changes during dynamic electrochemical conditions, *in situ* PXD will be measured for  $\text{LiMn}_y\text{Fe}_{1-y}\text{PO}_4$  compositions ( $y = 0.1, 0.2, 0.4, 0.6, .8$  and 1) during galvanostatic charge and discharge at selected C-rates at BM-17, APS (March 2013). The data will be collected using an image plate detector, which will allow for high time resolution and collection of data over a wide  $2\theta$  range, providing data suitable for analysis by Rietveld refinement. *In situ* powder neutron diffraction experiments will be performed at BL-7, ORNL (May 2013). The latter experiments are expected to first and foremost provide insight into the existence and effects of structural defects and disorder. Further PDF experiments are being planned to target the structural changes leading to instability in the composition space of high Mn- and low Li-content. In addition to these experiments conducted at DOE facilities, electroanalytical experiments such as GITT and PITT are being conducted at MIT, which will provide insight into transformation rates, limits of solid solution, and barriers to transition. And, we can already anticipate that the complex behavior observed experimentally will require new features in the corresponding theoretical models, under development with our colleagues at LLNL.

In parallel, we are initiating *in situ* TEM studies at EMSL, PNNL (April 2013) on the same family of olivines. *In-situ* TEM has recently been successfully used to investigate lithiation-induced behaviors of high capacity anode such as Si and  $\text{SnO}_2$ . However, our initial studies at MIT show that it is quite challenging to apply this state-of-art technique to cathodes where the transformation strains are significantly smaller. Using the superior instrumentation available at EMSL we expect to resolve phase transformation details of cathode materials in real time.  $\text{LiFePO}_4$ ,  $\text{LiMn}_y\text{Fe}_{1-y}\text{PO}_4$ , and oxide spinels, e.g.  $\text{LiNi}_{0.5}\text{Mn}_{1.5}\text{O}_4$  are targets for this study.

During fall 2012 we obtained *in situ* PXD data at NSLS providing evidence for metastability of amorphous intermediates in LFP cathodes during charge, i.e. recrystallization is observed during OCV conditions. Further *in situ* PXD experiments will be conducted at NSLS (March 2013) with the aim of studying the time-dependent structural relaxation of amorphous LFP phases. We have also initiated a study of size- and temperature-dependent phase behavior in LFP by *in situ* PXD (at NSLS). It has been suggested that the Li-miscibility gap will disappear at  $\sim 50$  °C for doped nanoscale LFP,<sup>17</sup> but this has never been demonstrated experimentally.

Finally, structure data on the electrodes in commercial nanoscale olivine Li-ion cells before and after many thousands of cycles, representing in-field service of an EV over its projected life, have recently been obtained. These results will show in detail the extent of structural stability of intercalation electrodes after an entire life cycle, and are the first of their kind.

#### References

1. A.S Andersson et al. *J. Power Sources* **2001**, 97–98, 498. 2. V. Srinivasan et al. *ECS* **2004**, 151, A1517. 3. G. K. Singh et al. *Elec. Acta* **2008**, 53, 7599. 4. C. Delmas et al., *Nat. Mater.* **2008**, 7, 665. 5. K. Weichert et al., *JACS* **2012**, 134, 2988. 6. P. Gibot et al., *Nat. Mater.* **2008**, 7, 741. 7. P. Bai et al. *Nano Lett.* **2011**, 11, 4890. 8. C.V. Ramana et al. *J. Power Sources* **2009**, 187, 555. 9. D. A Cogswell et al. *ACS Nano* **2012**, 6, 2215. 10. G. Chen et al. *Elec Sol. State Lett.* **2006**, 9, A295. 11.\* M. Tang, et al. *Annu. Rev. Mater. Res.* **2010**, 40, 469. 12.\* M. Tang, et al. *Electrochim. Acta* **2010**, 56, 769. 13.\* Y.-H. Kao, *Ph.D. thesis*, MIT, **2011**. 14. A. Yamada et al. *JECS* 2001, **148**, 10, A1153. 15. R. Malik et al. *PRB* **2009**, 79, 214201. 16.\* Y.-H. Kao, et al. *Chem. Mater.* **2010**, 22, 5845. 17. N. Meethong et al, *Adv. Func. Mater.* **2009**, 19, 1060.

\*) publication of DOE sponsored research 2010-2012

**Program Title:** Materials, Physics, and Nanostructures for Next Generation Spintronics

**Principal Investigator:** C. L. Chien

**Mailing Address:** Department of Physics and Astronomy, Johns Hopkins University  
3701 San Martin Drive, Baltimore MD 21218

**e-mail:** [clc@pha.jhu.edu](mailto:clc@pha.jhu.edu)

**Program Scope:** Spintronic phenomena, most notably giant magnetoresistance (GMR) in metallic multilayers, tunneling magnetoresistance (TMR) in magnetic tunnel junctions (MTJ), and spin transfer torque (STT) effects, have provided some of the most exciting developments in condensed matter physics. Equally impressive, these discoveries have led expeditiously to important technologies. The spin-valve GMR field sensors earlier, and the MTJ field sensors more recently, are now in virtually all hard-drives. Magnetic random access memories (MRAM) are poised to be the universal memories with the unique attributes of non-volatility, high speed, and unlimited rewritability. However, the first-generation devices driven by magnetic field are not site specific and the second-generation devices driven by electrical current require very high current densities.

The next generation spintronic phenomena depend on new physics, new materials, new mechanisms, and new nanostructures. They transcend the present paradigm of spintronics based on metallic ferromagnets with in-plane magnetization, transmission of spin information via partially spin polarized currents, and altering the magnetic state with either a magnetic field or a current with large current density ( $> 10^6$  A/cm<sup>2</sup>). We exploit materials with perpendicular magnetic anisotropy (PMA), ferromagnetic insulators, voltage or electric field controlled phenomena and devices, novel Rashba and spin Hall switching, pure spin currents generated by charge current or heat current.

**Recent Progress:** A pure current can be generated by a few mechanisms that include spin Hall effect (SHE) and spin pumping. When a charge current of density  $\mathbf{J}_e$  traversing through a metal with strong spin-orbit coupling (SOC), the SHE generate a pure spin current  $\mathbf{J}_S = \theta_{SH} (\boldsymbol{\sigma} \times \mathbf{J}_e)$  in the transverse direction, where  $\boldsymbol{\sigma}$  is the spin polarization unit vector, and  $\theta_{SH}$  is the spin Hall angle, which measures the efficiency of the conversion. Once generated, a pure spin current can be converted by the inverse spin Hall effect (ISHE) into a charge current and be detected by the charge accumulation on the sample edges. The ISHE has proven to be an indispensable tool for detecting pure spin current and confirming many pure spin current phenomena, most often employing Pt as the spin current detector.

Recently we have developed a new method to thermally inject a pure spin current using a ferromagnetic insulator into a number of  $5d$  metals (e.g., Pt and Au). The thermal injection method has the attributes of simple structure, very thin spin current detecting layer with a thickness comparable to, or less than, the spin diffusion length of only a few nanometers. We show that the thermal injection method can readily determine the sign of the spin Hall angle  $\theta_{SH}$  and the determined  $\theta_{SH}$  values are in good agreement with those determined by electrical means.

**Future Plans:** In spintronics, while the spin-polarized current enables the essential spintronic phenomena, the accompanying charge current generates heat. Indeed, the

large current density in spin transfer torque (STT) switching already threatens the integrity of the GMR or MTJ devices. The explorations of pure spin current are new advances.

A pure spin current carries no charge current. It efficiently delivers a maximal amount of spin angular momentum using a minimal number of charge carriers in a metal, or no carriers at all in an insulator. However, a pure spin current cannot be generated by electrical means except through a few special methods. In most cases, materials with a large spin-orbit coupling (SOC) play an essential role in generating, manipulating, detecting pure spin current, as well as controlling spin current devices. Some of our explorations include:

Rashba switching and spin Hall switching: We plan to study Rashba switching and spin Hall switching in suitable nanostructures. In these new mechanisms, unlike that in STT switching, the current does not flow through the device.

Thermally driven spintronic phenomena: Most electronic and spintronic devices involve electrical currents driven by electrical voltages. One can now in suitable situations use heat current to generate a pure spin current to explore new spintronic phenomena.

Voltage controlled spintronic devices: Recently we have demonstrated the first voltage-controlled spintronic devices consisting of MgO-MTJs using ferromagnetic layers with PMA [Nature Materials, **11**, 64 (2012)]. We demonstrate site-specific switching using low voltages ( $<1.5$  V), and mostly notably, with ultralow switching current densities ( $<10^4$  A/cm<sup>2</sup>), more than two orders of magnitude lower than previously achieved. We plan to exploit our initial success and further explore voltage-control spintronic phenomena and devices.

## Extreme Thermoelectric Behavior in Low-Dimensional Oxide Conductors

PI: Joshua L. Cohn, Department of Physics, University of Miami, P.O. Box 248046,  
Coral Gables, FL 33124

Contact: (305) 284-7123; [cohn@physics.miami.edu](mailto:cohn@physics.miami.edu)

### Program Scope

This program involves experimental studies of low-dimensional, bulk oxide conductors exhibiting extreme thermoelectric behavior. The investigations are motivated by preliminary research of the PI revealing a giant Nernst effect<sup>1</sup> at low T in quasi-one-dimensional (Q1D)  $\text{Li}_{0.9}\text{Mo}_6\text{O}_{17}$  (“Li-purple bronze” or LiPB), and very large Seebeck anisotropy near room temperature in both LiPB and the Q1D perovskite-related compound,  $\text{Sr}_5\text{Nb}_5\text{O}_{17}$ . It is argued that the novel characteristics of LiPB (Q1D electrons, large Fermi surfaces, bipolarity, low-D phonons, strong electron correlations) make it a model system for investigating the limits of conventional metals physics and the Nernst effect. Studies at room temperature and above are aimed at testing the PI’s hypothesis that extreme Seebeck anisotropy has its origin in interlayer (or interchain) resonant tunneling through defect states (e.g., via energy filtering). Additional studies are proposed to test recent band-structure predictions<sup>2</sup> of extreme Seebeck (thermopower or TEP) anisotropy in the delafossite compounds,  $\text{PdCoO}_2$  and  $\text{PtCoO}_2$ , for which interlayer transport is through coherent band motion.

While these compounds have in common highly anisotropic electronic structures, other, as yet unknown, material characteristics are clearly important to their extreme thermoelectric behavior. For example, TEP anisotropy of the magnitude observed is extremely rare in the many highly anisotropic bulk conductors that have been studied for decades (graphites, organics, other bronzes, cuprates, etc.). A central goal of this work is to determine which characteristics underlie this behavior by studying a spectrum of materials covering the range from coherent band to incoherent tunneling<sup>3,4,5</sup> inter-layer (or inter-chain) transport. Insight from this work may help to inform the “rational design” of functional thermoelectric materials.

The physics and physical properties of the materials targeted for study overlap research interests in both the correlated-electron and thermoelectrics communities. The extreme thermoelectric effects being investigated have potential in thermoelectric applications (cooling, power generation, or energy detection). The surprising magnitude of the Nernst coefficient in LPB motivates proposed examination of its potential for application in Ettingshausen cooling. The PI’s thermal conductivity measurements suggest that its thermomagnetic figure of merit might be significantly enhanced through a reduction of the thermal conductivity transverse to its conducting chains. Partial chemical substitution at the Li site by more massive Na, K, or Rb ions is proposed as a means to achieve

the desired effect. In addition, these chemical substitutions provide a means to alter the distribution and/or energy of interchain defect states, thereby enabling tests of Seebeck anisotropy hypotheses.

### Recent Progress

#### *Seebeck anomaly correlates with Structural changes in LiPB*

In parallel with our transport studies on the LiPB compound we have been using x-ray diffraction to determine lattice constants of individual single crystals. This work revealed a correlation between a large low-T (50 K) peak in the thermopower along the Q1D chains of LiPB and the crystallographic c-axis lattice parameter (Fig.'s 1). The c-parameter variations correlate with oxygenation (Fig. 2), suggesting that changes in the electronic structure associated with stoichiometric variations may explain the observations. Interchain couplings should be sensitive to lattice parameter variations, and thus oxygen content may tune the warping of the two Q1D Fermi surface sheets in this compound.

#### *Extension of Seebeck and resistivity measurements to 500 K*

We have completed construction of a high-temperature probe for measuring the thermopower and resistivity of small single crystals in vacuum to 500 K. Further modifications of the probe to extend the

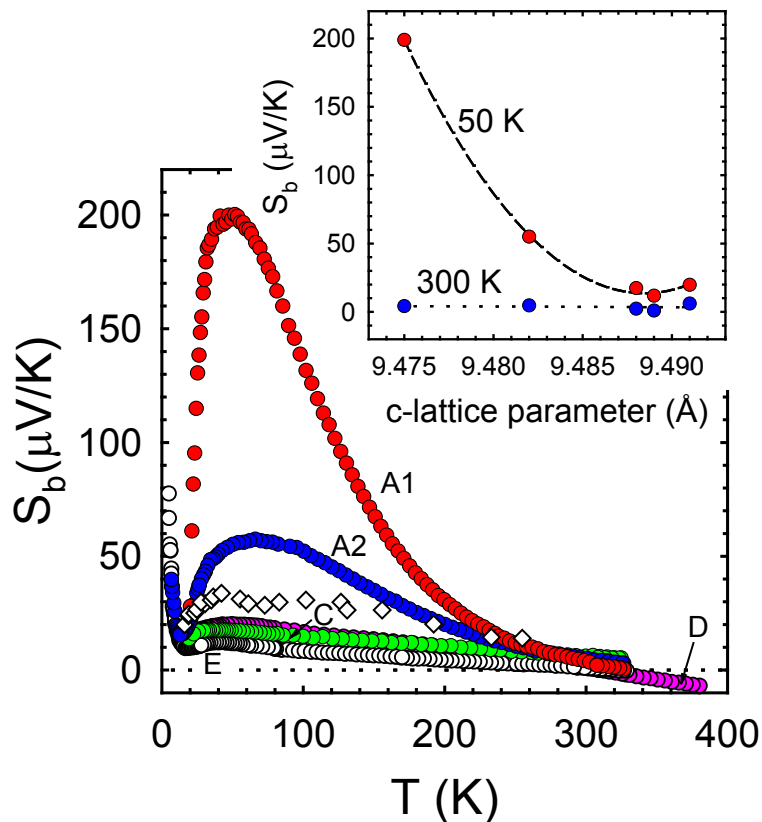


**Fig. 1** Seebeck coefficient (TEP) versus temperature along the Q1D chains (b-axis) for LiPB crystals (letter labels). Open diamonds are data from Ref. 6. Inset: correlation between  $T=50$  K peak in  $S_b$  and c-axis lattice constant.

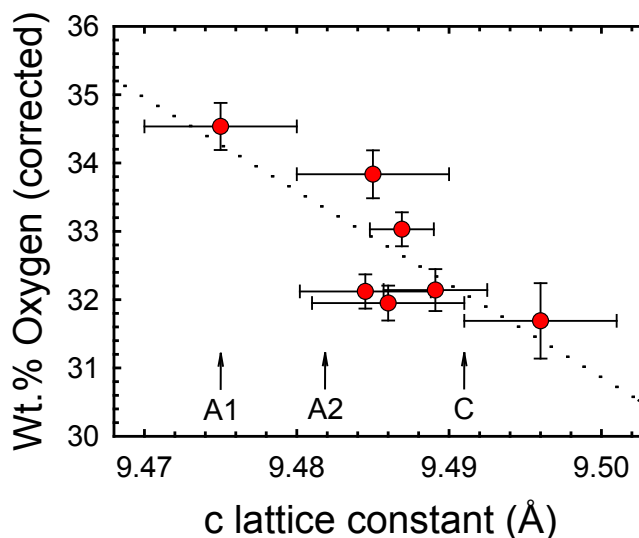


**Fig. 2** Correlation between EDS oxygen content and c-axis lattice constant for LiPB crystals. Arrows refer to specimens from Fig. 1.

measurement range to 800 K are in progress.

Preliminary measurements along (b-axis) and transverse (c-axis) to the Q1D conducting chains are shown in Fig. 3. The c-axis resistivity (right ordinate) exhibits metallic behavior at low T (dashed lines are linear-T), reaches a maximum near room temperature, and decreases with increasing T at higher T. This behavior has been widely observed for the interlayer or interchain resistivity in a variety of two-dimensional and Q1D metals, respectively.<sup>3</sup> Thought to be associated with interlayer (interchain) resonant tunneling, the thermopower has rarely been studied in such a regime. For LiPB it is remarkable that the c-axis TEP becomes as large as 200 mV/K or more while the b-axis TEP continues its linear-T decrease. The anisotropy of the TEP is among the largest known for any material -- our most recent data (light blue circles in Fig. 3) indicate a maximum in the c-axis TEP near 440 K. We will explore the prospect of LiPB in energy detection utilizing the transverse thermoelectric effect.

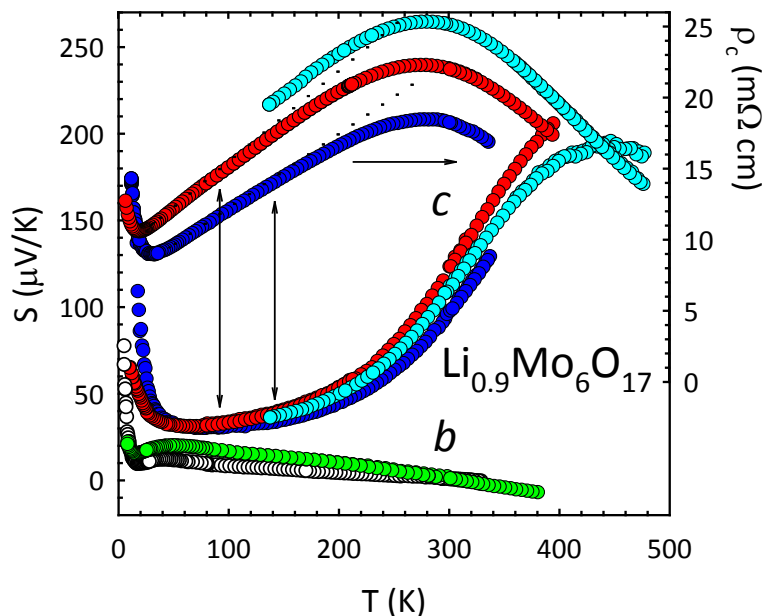


**Fig. 3** Thermopower and resistivity along the c-axis (transverse to chains) for three crystals and linear-in-T thermopower along the chains (b-axis) for comparison.

### Future Plans

Delivery of a new <sup>3</sup>He probe and 5-T magnet system supported by this program is expected in late April. This system will enable us to study the low-T limiting behavior of the Nernst coefficient well below its zero-field superconducting transition near T=2 K where novel physics is suggested. We will begin investigating the Nernst coefficient and thermal conductivity of Li-substituted crystals. Measurements of TEP anisotropy at room temperature and above will proceed on LiPB and on other compounds targeted for study.

### DOE-Sponsored Research Publications

J. L. Cohn, P. Boynton, J. S. Triviño, J. Trastoy, B. D. White, C. A. M. dos Santos, and J. J. Neumeier, *Stoichiometry, structure, and transport in the quasi-one-dimensional metal  $Li_{0.9}Mo_6O_{17}$* , Phys. Rev. B **86**, 195143 (2012).

## References

1. J. L. Cohn, B. D. White, C. A. M. dos Santos, and J. J. Neumeier, *Giant Nernst Effect and Bipolarity in the quasi-one-dimensional metal,  $Li_{0.9}Mo_6O_{17}$* , Phys. Rev. Lett. **108**, 056604 (2012).
2. Khuong P. Ong, David J. Singh, and Ping Wu, *Unusual Transport and Strongly Anisotropic Thermopower in  $PtCoO_2$  and  $PdCoO_2$* , Phys. Rev. Lett. **104**, 176601 (2010).
3. D. B. Gutman and D. L. Maslov, *Anomalous c-Axis Transport in Layered Metals*, Phys. Rev. Lett. **99**, 196602 (2007); *Boson-assisted tunneling in layered metals*, Phys. Rev. B **77**, 035115 (2008).
4. N. Kumar and A. M. Jayannavar, *Temperature dependence of the c-axis resistivity of high- $T_c$  layered oxides*, Phys. Rev. B **45**, 5001-5004 (1992).
5. P. Moses and R. H. McKenzie, *Comparison of coherent and weakly incoherent transport models for the interlayer magnetoresistance of layered Fermi liquids*, Phys. Rev. B **60**, 7998-8011 (1999).
6. M. Boujida, C. Escribe-Filippini, J. Marcus, and C. Schlenker, *Superconducting properties of the low dimensional lithium molybdenum purple bronze  $Li_{0.9}Mo_6O_{17}$* , Physica C **153-155**, 465 (1988).

# *In Situ* NMR to Understand Hydrogen Storage Chemistry

Mark S. Conradi  
[mcs@physics.wustl.edu](mailto:mcs@physics.wustl.edu)

Washington University Department of Physics, One Brookings Drive, Saint Louis, MO, 63130

## Program Definition:

We have used NMR to gain understanding of simple and complex (ionic-covalent) hydrogen storage solids. These are static, often *in situ* NMR measurements taken at the reaction conditions, typically involving high temperatures and high pressures. The work described here builds on our group's recent success with this technique in the discovery of a new mobile chemical species which evidently plays a key role in the dehydriding and rehydriding chemistry of NaAlH<sub>4</sub>, the archetype of complex hydrogen storage solids. Other hydrogen storage compounds have also been explored in depth, and some of the pertinent results will be mentioned, though here we focus principally on our work with NaAlH<sub>4</sub>.

## Recent Progress:

Recent DOE funded work<sup>1</sup> revealed the presence of an apparent new chemical species found to form in NaAlH<sub>4</sub> treated to high pressures and temperatures. The species was termed S105 (named after its <sup>27</sup>Al chemical shift), and was found to persist at ambient temperatures and pressures. We have made an in-depth study of the S105 species, in particular of the influence of impurities on its generation. We have used various methods of spectroscopy to identify its origin and identity, and studied the changes in the dehydride/rehydride cycling behavior of NaAlH<sub>4</sub> when S105 is present in the compound.<sup>2</sup>

We initially found that S105 can be reliably produced in undoped NaAlH<sub>4</sub> that has been briefly exposed to ambient air prior to heating above the 183 °C melting point under 200 bar of H<sub>2</sub> pressure (T-P treatment). Figure 1a shows an <sup>27</sup>Al NMR spectrum obtained from a sodium alanate sample *not* exposed to the air before T-P treatment, while Fig. 1b shows that obtained from a sample that *was* air-exposed prior to T-P treatment. Further investigation revealed that exposure to water vapor in particular plays a key role in the generation of the mobile species. For example, sodium alanate exposed to any dry gas (helium, nitrogen, argon, oxygen, carbon dioxide) prior to T-P treatment show spectra similar to Fig. 1a, while samples exposed to the same gases that have first been saturated with water vapor show spectra similar to Fig 1b. S105 is also generated in samples that have been mixed with dry hydroxide powders before heating under H<sub>2</sub> pressure (so, similar to Fig 1a), but not in samples of sodium alanate that have been mixed with dry oxide powders (resulting in spectra similar to Fig. 1b). The oxides and hydroxides of Al, Mg, and Na were tested and all found to exhibit the same behavior. Samples doped with TiCl<sub>3</sub> or ScCl<sub>3</sub> prior to T-P treatment were also able to generate S105, though it is not known whether these samples also contained the small amount of hydroxides necessary to generate S105 alone.

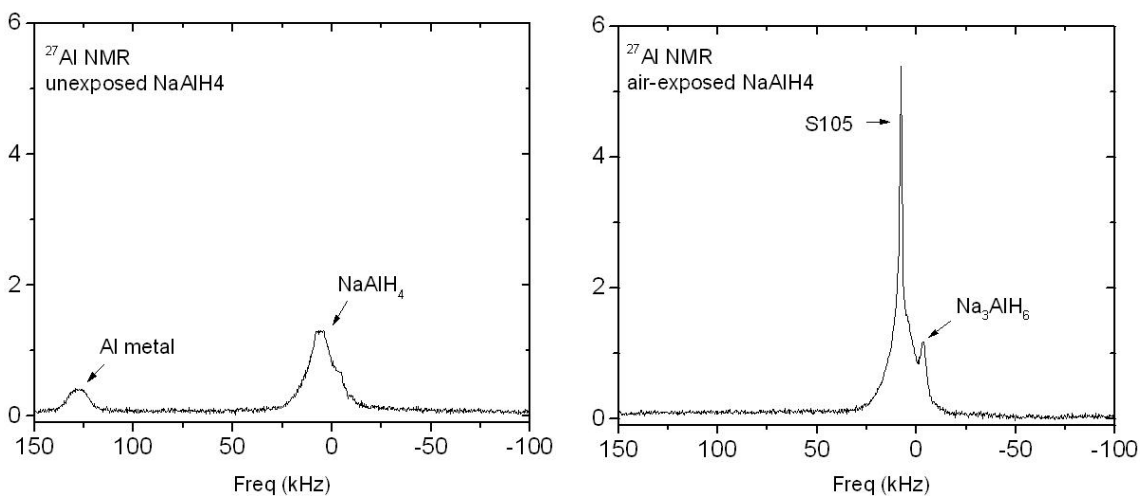


**Figure 1.**  $^{27}\text{Al}$  NMR (static) of samples at 22 °C after T-P treatment at 220 °C for 30 minutes under 210 bar of  $\text{H}_2$  pressure. (a)  $\text{NaAlH}_4$  sample unexposed prior to P-T treatment. (b)  $\text{NaAlH}_4$  sample air-exposed prior to P-T treatment.

No matter which of the above methods is used to form S105, the  $\text{Na}_3\text{AlH}_6$  peak is present with a comparable spectral intensity (area, or number of Al atoms) as that of the S105 resonance. Aluminum metal at 1640 ppm is generally found (after P-T treatment to 220 °C under 210 bar of  $\text{H}_2$  pressure) whenever S105 is *not* evident. Either  $\text{H}_2\text{O}$  or  $\text{NaOH}$  can react with  $\text{NaAlH}_4$  in strongly exothermic reactions,



forming hydroxide (or new hydroxide) species. These resultant hydroxide species are, at least in principle, compatible with the ionic nature of the parent  $\text{NaAlH}_4$ . Thus, it seems most likely that hydroxides, not water itself, are the major players in the formation of S105. The addition of hydroxide, following Eq. (2), results in  $\text{NaH}$ ; subsequently, the  $\text{NaH}$  can further react to yield the hexahydride evident in our spectra:



In the case of exposure to  $\text{H}_2\text{O}$ , reaction (1) results in hydroxide formation, which subsequently can yield  $\text{NaH}$  through (2) and  $\text{Na}_3\text{AlH}_6$ , through (3).

In attempting to identify and characterize the mobile S105 species, we used a variety of spectroscopic tools and characterization methods. X-ray diffraction on samples with and without S105 revealed no other crystalline chemical constituents apart from the  $\text{Na}_3\text{AlH}_6$  evident in the  $^{27}\text{Al}$  NMR. Raman and neutron spectroscopy on the same samples revealed the presence of amorphous hydroxide phases in the S105 bearing material, but no other chemical components apart from the sodium alanate and hexahydride companion in the S105 laden sample. DFT calculations were used to explore possible

atomic configurations, and concluded that only tetrahedral coordinations of  $\text{AlH}_4$  ions can exhibit chemical shifts in the range were S105 is found. Finally, analysis of the field-dependent quadrupole-induced chemical shifts of the  $\text{NaAlH}_4$   $^{27}\text{Al}$  MAS NMR at a variety of fields allowed us to show that the 101.6 ppm chemical shift of the S105 species is very close to that of the true chemical shift of sodium alanate (97.5 ppm), and almost identical to that of molten  $\text{NaAlH}_4$ . We therefore identify S105 as a very mobile version of  $\text{NaAlH}_4$ , with the mobility induced by the presence of hydroxide species in the samples. Despite the fact that S105 is simply  $\text{NaAlH}_4$  in more rapid motion than the bulk, Fig. 2 shows that the presence of the S105 nonetheless has a significant positive effect on the rate of hydrogen evolution in undoped sodium alanate.

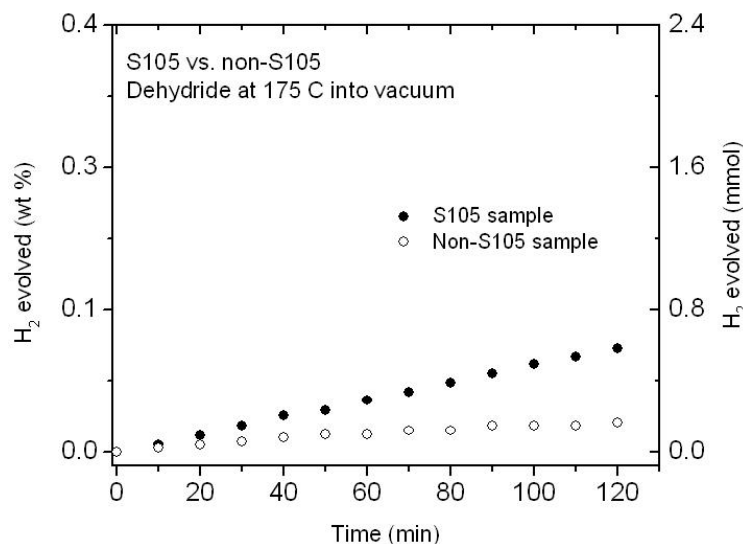


**Figure 2.**  $\text{H}_2$  gas evolved from S105-bearing and non S105-bearing sodium alanate solids as functions of time at 175 °C. Samples of approximately 1 g were heated into vacuum while the pressure buildup of  $\text{H}_2$  gas was monitored.

Beyond  $\text{NaAlH}_4$ , we have recently examined other solid hydrides. These include the borohydrides  $\text{LiBH}_4$ <sup>3,4</sup> and  $\text{Mg}(\text{BH}_4)_2$ <sup>5,6</sup> which we have studied with the aim of better exploiting their large mass fractions of reversible hydrogen (14% and 15%). Simple ionic hydrides such as  $\text{NaH}$ <sup>7</sup> have been studied and found to exhibit surprising atomic mobility in the presence of hydroxide impurities. Metallic hydrides such as palladium hydride<sup>8,9</sup> and magnesium hydride<sup>10</sup> were studied to determine their gas exchange rates, diffusion, and conductivity properties. Finally, more complex borane systems were studied in an effort to understand the volatile side products of their cycling properties.<sup>11</sup>

#### Future Plans:

Figure 2 shows that the presence of S105 in  $\text{NaAlH}_4$  enhances the hydrogen desorption kinetics in this material. As the slow rate of hydrogen evolution at reasonable temperatures is a major problem with many complex hydrides, we will examine other complex hydrides to see whether the mobile species are common to this class of solids. This will include other alanates ( $\text{LiAlH}_4$ ,  $\text{KAlH}_4$ ) because of their similar chemistry, and

the hexahydrides ( $\text{Na}_3\text{AlH}_6$ ,  $\text{Li}_3\text{AlH}_6$ ) because they are present whenever the alanates are cycled (or S105 is generated). The chemistry of the potassium system is the one most like sodium alanate but with the first dehydriding step at a higher temperature.  $\text{LiAlH}_4$  has a small endothermic reaction enthalpy, so the equilibrium  $\text{H}_2$  pressure of the first step is expected to be very high, suggesting very rapid dehydriding upon melting. Nevertheless, spectra of molten  $\text{LiAlH}_4$  have been reported; it appears that surface contamination may prevent the rapid dehydriding of the liquid. We will exploit this method in trying to generate the analogue to S105 from molten  $\text{LiAlH}_4$ .

## References

1. "Discovery of a New Al Species in Hydrogen Reactions of  $\text{NaAlH}_4$ " T.M. Ivancic, S.-J. Hwang, R.C. Bowman, Jr., D.S. Birkmire, C.M. Jensen, T.J. Udovic, and M.S. Conradi, *J. Phys. Chem. Lett.* 1, 2412-2416 (2010).
2. "Mobile Species in S105" E.G. Sorte R.C. Bowman, Jr., E.H. Majzoub, M. H. W. Verkuijlen, T. J. Udovic, and M.S. Conradi, (submitted, *J. Phys. Chem. C*).
3. " $\text{LiBH}_4$  in Carbon Aerogel Nanoscaffolds: An NMR Study of Atomic Motions", D.T. Shane, R.L. Corey, C. McIntosh, L.H. Rayhel, R.C. Bowman, Jr., J.J. Vajo, A.F. Gross and M.S. Conradi, *J. Phys. Chem. C* 114, 4008-4014 (2010).
4. "NMR Study of  $\text{LiBH}_4$  with C60" D.T. Shane, R.L. Corey, L.H. Rayhel, M. Wellons, J.A. Teprovich, Jr., R. Zidan, S.-J. Hwang, R.C. Bowman, Jr., and M.S. Conradi, *J. Phys. Chem. C* 114, 19862-19866 (2010).
5. "A Comprehensive NMR Study of Magnesium Borohydride" D.T. Shane, L.H. Rayhel, Z. Huang, J.-C. Zhao, X. Tang, V. Stavila, and M.S. Conradi, *J. Phys. Chem. C* 115, 3172-3177 (2011).
6. "NMR Investigation of Nanoporous Gamma- $\text{Mg}(\text{BH}_4)_2$  and Its Thermally Induced Phase Changes", M. Eagles, B. Sun, B. Richter, T.R. Jensen, Y. Filinchuk, and M.S. Conradi, *J. Phys. Chem.* 116, 13033-13037 (2012).
7. "NMR Studies of  $\text{NaH}$ " E.G. Sorte, R.L. Corey, R.C. Bowman, Jr., D. Birkmire, R. Zidan, and M.S. Conradi, *J. Phys. Chem.* 116, 18649-18654 (2012).
8. "Hydrogen NMR of Palladium Hydride to Measure the Hydride-Gas Exchange Rate" L.H. Rayhel, R.L. Corey, D.T. Shane, D.F. Cowgill, and M.S. Conradi, *J. Phys. Chem. C* 115, 4966-4970 (2011).
9. "NMR Measurement of Exchange of Deuterium between Palladium-Deuteride and Deuterium Gas" R.L. Corey, D.F. Cowgill, and M.S. Conradi, *J. Phys. Chem. C* 116, 4335-4339 (2012).
10. "Hydrogenation Rate Limiting Step, Diffusion and Thermal Conductivity in Cold Rolled Magnesium Hydride" J. Lang, J. Huot, M. Eagles, and M. S. Conradi (in preparation).
11. "Thermolysis and Solid State NMR Studies of  $\text{NaB}_3\text{H}_8$ ,  $\text{NH}_3\text{B}_3\text{H}_7$ , and  $\text{NH}_4\text{B}_3\text{H}_8$ " Z. Huang, M. Eagles, S. Porter, E. G. Sorte, B. Billet, R. L. Corey, M. S. Conradi, and J.-C. Zhao, *Dalton Transactions* 42, 701-708 (2013).

**Program Title:** Characterization of Functional Nanomachines

**Principal Investigator:** M. F. Crommie

**Mailing address:** University of California at Berkeley, Physics Department, 366 LeConte Hall #7300, Berkeley, CA 94720-7300

**e-mail:** crommie@berkeley.edu

**Co-investigators:** C. Bustamante, M. L. Cohen, S. G. Louie, G. Marriott, A. Zettl

**Program Scope / Definition:** The overarching goal of this program is to explore the fundamental science of nanomachines that are engineered at the atomic scale and that have the ability to control energy and information through mechanical transduction processes. We are following two paths toward this goal. First, we are exploring naturally occurring biomotors to take advantage of the molecular mechanisms provided by Nature. Second, we are purposefully designing new synthetic molecular machines in a molecule-by-molecule fashion. This research helps to clarify the mechanisms by which nanomachines convert different forms of energy into directed mechanical activity, as well as how these processes are affected by different environmental dissipation mechanisms. The program is aimed at creating new categories of functional nanomachines, such as bottom-up fabricated synthetic molecular machines that operate on surfaces, top-down fabricated carbon-based nanomachines that exploit the electromechanical properties of nanotubes and graphene, and hybrid nanomachines composed of integrated synthetic and biological components. These efforts will help to form the basis of new molecular-mechanical nanotechnologies with applications in areas of importance to DOE.

This project has six co-investigators whose expertise span physics, chemistry, and biology. The experimental tools utilized by our collaboration range from synthetic chemistry, surface science, and scanned probe techniques (**Marriott** and **Crommie**), to photolithography, wet biology, and laser tweezers (**Zettl** and **Bustamante**). **Cohen** and **Louie** provide theoretical support through the use of *ab initio* density functional techniques and molecular dynamics calculations.

**Recent Progress:** We have made recent progress in a wide range of experimental activities that span synthesis and actuation of new nanomachine molecular elements,<sup>1-4</sup> exploration of chemical-to-mechanical energy conversion in biomotors, and fabrication of nanotube-based nanomachines that operate on new nanomechanical principles (such as electromigration). Here I will highlight our activities in just one of these areas: optical actuation of molecular machine elements. The use of light to actuate molecular machines is an exciting topic because it has the benefit of not requiring nanoscale electrical contacts, of having extremely high bandwidth, and of having a wide range of optically active molecular candidates. Our work here is aimed at understanding and controlling the photomechanical properties of individual and combined nanomachine elements on different types of surfaces (including *active* surfaces). Recently we have made progress at developing a new STM-based technique for observing the response of molecular elements to infrared radiation (IR-STM), as well as exploring the behavior of molecular elements on electrostatically gated active substrates.

**IR-STM (PROGRESS):** The simplest molecular machine element is a single molecule adsorbed to a surface. To efficiently utilize such molecules for nanomachine applications we must be able to identify them, determine their surface conformations, and understand how they convert energy into mechanical (including vibrational) motion. Infrared (IR) spectroscopy is an extremely useful tool for extracting such information. A problem with applying it to molecular machines, however, is that it is an ensemble measurement with no spatial resolution. We have developed a new technique aimed to overcome this deficiency by combining scanning tunneling microscopy (STM) and infrared spectroscopy. This new technique, which we call “IR-STM”,

utilizes infrared light to excite molecules adsorbed to a surface while STM is used to detect their oscillatory response. IR-STM marries the energy resolution of infrared spectroscopy with the spatial resolution of STM in order to give a combined picture of molecular resonant energy absorption and sub-nanometer spatially resolved structure.

A frequency-tunable IR laser was set up outside of a variable temperature ultra-high vacuum (UHV) STM in **Crommie's** lab (in collaboration with **F. Wang**) and focused through a viewport onto a sample held at low temperature ( $T = 15$  K) containing diamondoid molecules adsorbed onto Au(111) in submonolayer amounts (see sketch in Fig. 1). The STM tip was brought into tunneling position over the molecules and the IR light was swept through an energy range that includes the vibrational modes of these molecules.

When the molecules on the surface absorb IR light in resonance with one of their mechanical modes, the photons' energy is converted into mechanical vibrational energy. This oscillatory motion caused sub-Ångstrom expansion of the surface ("Z"), thus allowing the STM to detect the infrared modes of the adsorbed molecules. Fig. 1 shows an IR spectrum obtained in this way for [121] tetramantane diamondoid molecules (a simultaneously obtained STM image of the molecules can also be seen in the figure). The IR-STM spectrum is shown in red, whereas the IR spectral lines of bulk tetramantane are shown as blue dashed lines. The solid blue line shows the result of traditional inelastic STM spectroscopy (IETS) on the same molecule/surface system measured at a lower temperature ( $T = 5$  K) and in the absence of IR light. The IR modes of the molecule are easily resolved by IR-STM, and clear differences can be seen between the IR-STM spectra and the bulk lines, showing the power of IR-STM to extract new spectral information. IR-STM is also seen to have significantly higher energy resolution compared to standard IETS (Fig. 1).

**Nanomachine Molecules on Active Substrates (PROGRESS):** Active substrates are surfaces whose properties can be dynamically tuned through an external control. By dynamically tuning active surface properties it should be possible to tune the behavior of molecular machine assemblies bound to the active surface. An example of such a surface is the top of an electrostatically gated graphene field effect transistor. We have performed the first STM imaging of molecular adsorbates bound to the surface of a gated graphene device (**Crommie, Zettl**). Molecules provided by **Marriott** and **F. Fischer** were deposited onto our gated graphene devices in UHV and imaged using a cryogenic STM (**Crommie**). Fig. 2 shows an STM image demonstrating that BTC molecules form a well-ordered monolayer on a gated graphene/BN device (BTC = 3,3',3''-(Benzene-1,3,5-triyl)tris(2-cyanoacrylonitrile), BN = boron nitride). STM spectroscopy of BTC (Fig. 2) reveals that the LUMO state of this molecule can be controllably tuned (i.e., shifted relative to

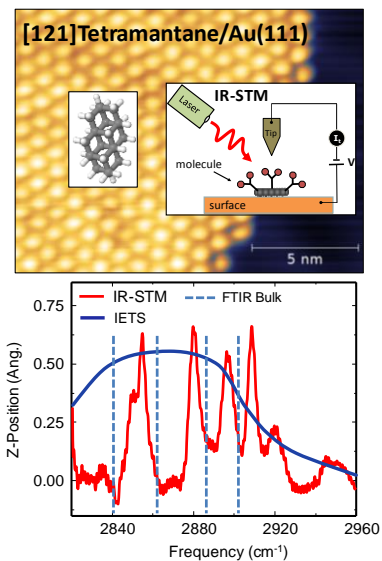


**Fig. 1:** Top: schematic of IR-STM and STM image of tetramantane on Au(111). Bottom: IR-STM spectrum of tetramantane on Au compared to bulk peak positions and IETS spectrum.

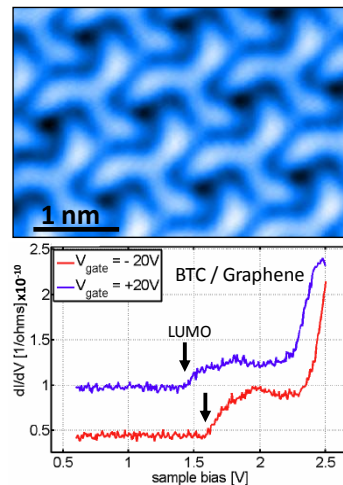


**Fig. 2:** Top: STM image of BTC molecules on gated graphene device. Bottom: STM spectroscopy shows LUMO shift with gate voltage.

$E_F$ ) via application of a backgate potential. Gating can thus be used to vary the charge state of molecules adsorbed to graphene and, potentially, to control their nanomechanical response.

**Future Plans:** Here we highlight future plans regarding two topics in this particular area of our Nanomachines Program: (a) Single Molecule IR-STM, and (b) Molecular Machine Self-assembly.

**Single Molecule IR-STM (FUTURE):** Our goal here is to perform single-molecule-resolved IR spectroscopy on individual nanomachine elements. Our preliminary results (described above, see Fig. 1) are encouraging, but although we have achieved submonolayer detection sensitivity we have not yet achieved single-molecule sensitivity. We intend to increase the spatial resolution of IR-STM in order to directly observe how isolated single-molecule structures on surfaces absorb infrared light and resonantly vibrate in response. Success in this project would be a major breakthrough providing a significant new tool for understanding molecular behavior at the nanoscale. **Louie** has performed preliminary estimates of the magnitude of the IR-STM response for a single molecule and finds that it should be well within the signal-to-noise limits of a high quality STM. Performing IR-STM at the single molecule level would provide new information compared to standard STM inelastic tunneling spectroscopy (IETS) since standard IETS provides no direct photonic information (i.e., such as optical absorption, optical polarization dependence, optical intensity dependence, and optically-induced lifetime effects). The IR-STM signal, on the other hand, is governed by an optical matrix element and has higher energy resolution than IETS. IR-STM should also allow investigation of a wider range of molecular systems than single-molecule Raman spectroscopy, which is mainly limited to dye molecules. We have several strategies that we will pursue to increase our experimental signal-to-noise sensitivity in order to achieve our goal of single-molecule IR-STM: (i) improve IR-laser stability, (ii) reduce scattered light in our STM chamber, (iii) modify STM electronics to allow dynamic subtraction of surface background, (iv) modulate IR light to induce an IR rectification signal, (v) develop a fundamental theory to explain IR-STM molecular response (**Cohen, Louie**).

**Molecular Machine Self-Assembly (FUTURE):** Our goal here is to use “click-chemistry” to self-assemble a multi-molecule synthetic nanomachine at a surface using individual photomechanically switching molecular building blocks. We intend to covalently bond three different photomechanically switching molecules in a stepwise surface reaction to obtain a three-molecule synthetic nanomachine capable of converting optical energy into self-propelled uni-directional motion on a surface. Such a nanomachine would be a molecular inchworm crawler powered completely by light. This synthetic crawler would be capable of operating on a surface under non-physiological conditions. Demonstration of this type of nanomachine would be a significant breakthrough, as it would show a higher order of functionality than has ever been demonstrated for a synthetic molecular machine in a non-physiological, non-fluidic environment. The bandwidth (i.e., speed) of such a

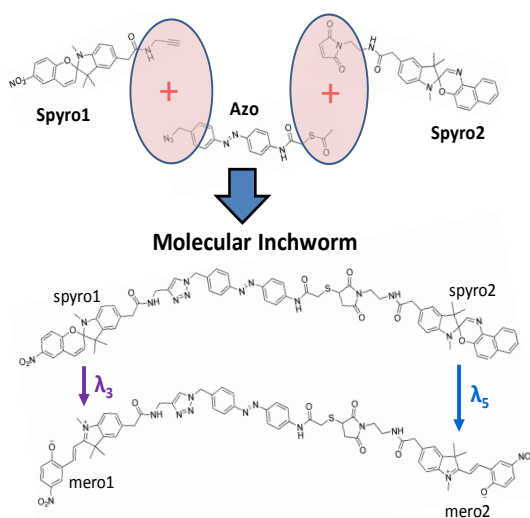


**Fig. 3:** Sketch of precursor elements of synthetic three-molecule inchworm nanomachine (above), and final reacted product (below). Sketches show inchworm with end pieces in low-dipole (unclamped) spiropyran state, as well as in high-dipole (clamping) merocyanine state.

nanomachine would not be limited by biological reaction times or catalytic activity, but rather by the intrinsic picosecond timescales of optical absorption and photo-isomerization. This is orders of magnitude faster than any known biological nanomotor or any known DNA-based nanomachine.

The inchworm will be composed of three components: a central “expansion/contraction” element and two “clamping” end pieces. The expansion/contraction element will be an azobenzene molecule (Fig. 3), capable of switching between *cis* (contracted) and *trans* (expanded) states when irradiated at wavelengths  $\lambda_1$  (*cis* to *trans*) and  $\lambda_2$  (*trans* to *cis*). The two clamping end pieces will be spiropyran molecules (Fig. 3) capable of switching between spiropyran (spiro1 and spiro2) and merocyanine (mero1 and mero2) states when irradiated at wavelengths  $\lambda_3$  (spiro1 to mero1),  $\lambda_4$  (mero1 to spiro1),  $\lambda_5$  (spiro2 to mero2), and  $\lambda_6$  (mero2 to spiro2). The clamping action will occur when the spiropyran is put into the merocyanine state, which lies flat and has a dipole moment an order of magnitude greater than spiropyran. Because of the flat geometry and large dipole moment, the merocyanine should bind to the surface (i.e., clamp) more effectively than the spiropyran isomer. Assuming the walker starts in a spiro1-azo(*cis*)-spiro2 state, then uni-directional inchworm motion will be induced by strobing the light source from  $\lambda_1$  to  $\lambda_6$  in order to cause the following actions: left-clamp ( $\lambda_3$ ), expand ( $\lambda_1$ ), right-clamp ( $\lambda_5$ ), left-unclamp ( $\lambda_4$ ), contract ( $\lambda_2$ ), right-unclamp ( $\lambda_6$ ), and repeat. We have chosen azide-alkyne click chemistry and maleimide coupling (Fig. 3) to assemble this nanomachine because we want the coupling reactions to occur on ultra-thin insulating layers on metal in order to increase molecular photoactivity while retaining the ability to image the working nanomachine via STM.

## References:

- [1] Matthew J. Comstock, David A. Strubbe, Luis Berbil-Bautista, Niv Levy, Jongweon Cho, Daniel Poulsen, Jean M.J. Fréchet, Steven G. Louie, and Michael F. Crommie, "Determination of Molecular Photoswitching Dynamics through Single-Molecule Chiral Mapping", *Phys. Rev. Lett.* **104**, 178301 (2010).
- [2] J. Cho, L. Berbil-Bautista, N. Levy, D. Poulsen, J. M. J. Fréchet, and M. F. Crommie, "Functionalization, self-assembly, and photoswitching quenching for azobenzene derivatives adsorbed on Au(111)", *J. Chem. Phys.* **133**, 234707 (2010).
- [3] J. Cho, L. Berbil-Bautista, I. V. Pechenezhskiy, N. Levy, S. K. Meier, V. Srinivasan, Y. Kanai, J. C. Grossman, K. P. C. Vollhardt, and M. F. Crommie, "Single-Molecule-Resolved Structural Changes Induced by Temperature and Light in Surface-Bound Organometallic Molecules Designed for Energy Storage", *ACS Nano* **5**, 3701–3706 (2011).
- [4] I. V. Pechenezhskiy, J. Cho, G. D. Nguyen, Luis Berbil-Bautista, B. L. Giles, D. A. Poulsen, J. M. J. Fréchet, and M. F. Crommie, "Self-Assembly and Photomechanical Switching of an Azobenzene Derivative on GaAs(110): Scanning Tunneling Microscopy Study", *J. Phys. Chem. C* **116**, 1052 (2012).

Program Title: Energy Transport in Graphene  
 Principal Investigator: Stephen Cronin  
 Institution: University of Southern California  
 Address: 3737 Watt Way, Los Angeles, CA 90089  
 Email: scronin@usc.edu  
 DOE Grant Number: DE-FG02-07ER46376  
 Collaboration: Prof. Li Shi, University of Texas, Austin

### Program Scope or Definition

The objective of this proposed research is to develop a better understanding of phonon transport and coupled electron-phonon transport in graphene. As a monatomic layer of  $sp^2$  carbon atoms, graphene is a promising material for future-generation energy-efficient electronic devices and thermal management solutions because of its superior charge mobility, mechanical strength, and thermal conductivity. This project aims to

- (i) Clarify whether the flexural vibration modes make an important or negligible contribution to thermal conductivity of graphene.
- (ii) Investigate the effects of inter-layer coupling, substrate interaction, stress and morphology on phonon transport in suspended and supported single- and few-layer graphene.
- (iii) Characterize the interfacial thermal transport between supported graphene and underlying dielectric, metallic, and polymeric substrates.
- (iv) Evaluate interfacial thermal transport between graphene and its surrounding gas environment;
- (v) Determine whether or not coupled electron-phonon transport in graphene is highly non-equilibrium as in carbon nanotubes.
- (vi) Reveal the effects of inter-layer coupling, substrate interaction, stress, morphology, and gas environment on electron-phonon coupling in graphene.

### Recent Progress

#### Low-Frequency Acoustic Phonon Temperature Distribution in Electrically Biased Graphene:

We have measured the low-frequency acoustic phonon temperature profiles in electrically biased graphene using Raman spectroscopy and scanning thermal microscopy (SThM). The obtained temperature maps reveal bias-dependent hot spots in the operating graphene devices that were considerably smaller than those reported by infrared (IR) thermal imaging measurements. In addition, the high temperature sensitivity of the SThM technique allows us to examine the thermal behavior of the graphene device in the low-power density regime that was not accessible by the optical techniques due to limited temperature sensitivity.

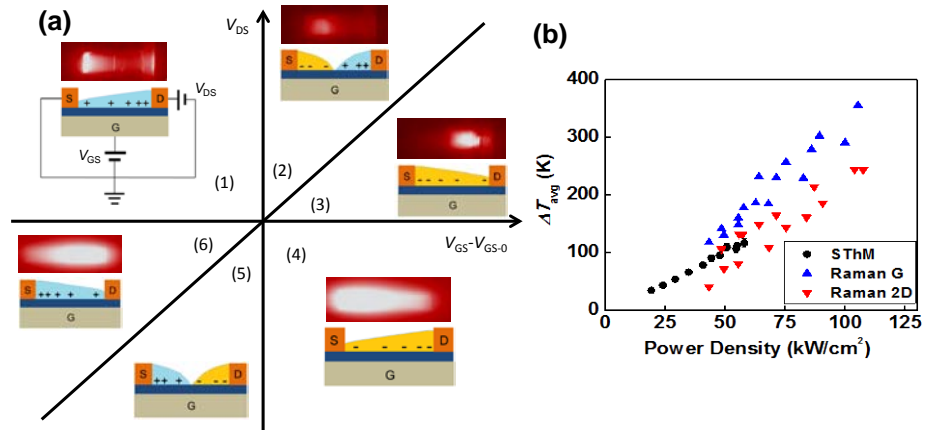


**Figure 1.** (a) Thermal images of a graphene device under different source-drain ( $V_{DS}$ ) and gate bias ( $V_G$ ) conditions, which result in different charge carrier distributions along the  $6.7\text{-}\mu\text{m}$  long graphene. (b) Average graphene temperature rise measured by SThM and Raman G and 2D peak as a function of power density in the device.

The measured acoustic phonon temperature was close to the anharmonic scattering temperature determined from the Raman peak shift on the same sample (Fig. 1b).

**Graphene-Silicon Schottky Diodes:** We have fabricated graphene-silicon Schottky junctions, which exhibit rectifying behavior and finite photocurrents. Figure 2 shows a schematic diagram, optical microscope image, and SEM image of one such device. This device represents the simplest device we can make between graphene and another material and is an important first step in the eventual integration of graphene with silicon and fabrication of graphene-based heterostructures. In the device shown in Figure 2, the graphene forms a Schottky junction with the underlying silicon on the left, and an Ohmic contact with the Au on the right. In order to obtain a clean interface between the graphene and the underlying silicon, the native oxide is etched and the silicon surface is passivated using reactive ion etching (RIE) and wet chemical etching. The  $I$ - $V$  characteristics of this device exhibit rectifying behavior at zero and positive gate voltages (Fig. 3a). The  $I$ - $V$  characteristics of these graphene-silicon junctions can be actively tuned from rectifying to Ohmic behavior by electrostatically doping the graphene with a polymer electrolyte top gate. Over the applied gate voltage range, the low bias conductance can be varied by more than three orders of magnitude. By varying the top gate voltage from  $-4$  to  $+4$  V, the Fermi energy of the graphene is shifted between  $-3.78$  and  $-5.47$  eV; a shift of  $\pm 0.85$  eV from the charge neutrality point. Since the conduction and valence bands of the underlying silicon substrate lie within this range, at

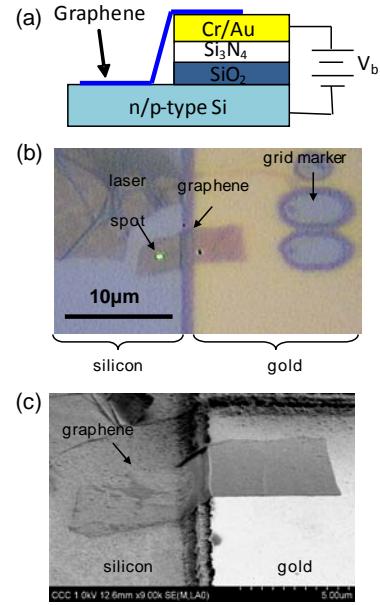


**Figure 2.** (a) Schematic diagram, (b) optical microscope, and (c) SEM image of a graphene-silicon Schottky diode.

$-4.01$  and  $-5.13$  eV, the Schottky barrier height and depletion width can be decreased to zero for both  $n$ - and  $p$ -type silicon under the appropriate top gating conditions.  $I$ - $V$  characteristics taken under illumination show that the photo-induced current can be increased or decreased based on the graphene-silicon work function difference, as shown in Figure 3b. This unique ability to tune the work function of graphene is a direct result of graphene's small density of states.

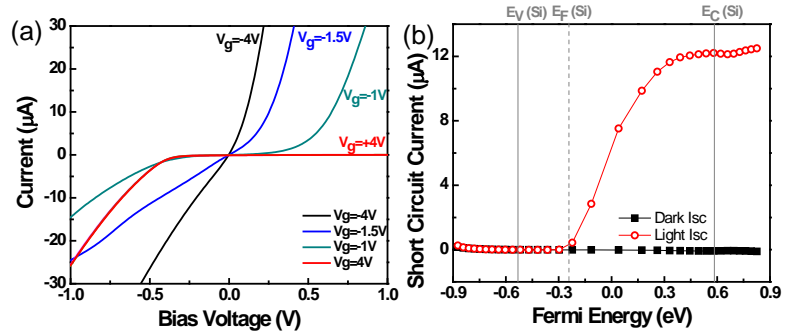


**Figure 3.** (a)  $I$ - $V$  characteristics for the graphene-silicon Schottky diode shown in Figure 2. (b) Short circuit photocurrent plotted as a function of graphene Fermi energy collected under an applied gate voltage range of  $-4$  to  $+4$  V.

**Negative Differential Resistance Observed in Suspended Carbon Nanotubes:** The  $I$ - $V$  characteristics of carbon nanotubes observed at high bias voltages exhibit negative differential resistance (NDR) and thermal non-equilibrium phonon populations. Figure 7 shows a sudden drop in current or “kink” and NDR occurring above  $0.4$  V. The kink corresponds to the threshold for optical phonon emission, when the electrons gain enough kinetic energy to emit optical phonons. The optical phonons cause scattering in the nanotube, which lowers the electric current as the voltage is increased beyond  $0.4$  V. After subtracting the voltage drop across the contact resistance, the kink bias voltage is found to occur at  $0.2$  V, which corresponds to the optical phonon energy. The corresponding Raman data (also plotted in Figure 4) shows an abrupt downshift of the  $G_+$  Raman mode at the position of the kink, which further corroborates the threshold emission of optical phonons. This behavior was observed consistently in a total of 25 nanotubes. In the proposed work, we will study the

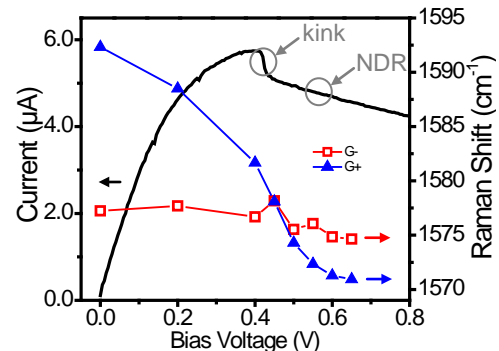


**Figure 4.** Electric current (solid line) and G band Raman shifts plotted as a function of bias voltage.

coupled electron-phonon transport of tunneling heterostructures, which may exhibit negative differential resistance and non-equilibrium phonon populations.

**Optical Measurement of Heat Transfer at Nanoscale Interfaces:** We have developed a new optical method to measure the thermal interface resistance between CNTs and their surrounding gas environment using a two-laser technique. In this approach, the temperature of an optically-heated suspended CNT is measured using Raman spectroscopy in air and in vacuum, as shown in Figure 5. One laser focused on the center of a suspended CNT (bottom) is used as a local heat source, while another laser (top) is used to measure the spatial temperature profile along the CNT by monitoring the  $G$  band downshifts in the Raman spectra. A constant temperature gradient is observed when the SWCNT is irradiated in vacuum, giving direct evidence of diffusive transport of the phonons probed by the Raman laser. In air, however, we observe an exponentially decaying temperature profile with a decay length of about  $7\mu\text{m}$ , due to heat dissipation from the SWCNT bundle to the surrounding gas molecules. Based on the exponential decay curves measured in air, the heat transfer coefficient between the SWCNTs and the surrounding air molecules is found to range from  $2.7 \times 10^3$  to  $8.7 \times 10^4$   $\text{W/m}^2\cdot\text{K}$ . This measurement is insensitive to the thermal contact resistance, since no temperature drops occur at the ends of the nanotube. It is also insensitive to errors in the calibration of the  $G$  band temperature coefficient. The optical absorption is also obtained from these results to be on the order of  $10^{-5}$ .

Using a similar approach, we have measured the temperature distribution of current-carrying,  $5\mu\text{m}$ -long, suspended carbon nanotubes in different gas environments. At the same heating power, the measured  $G$  band phonon temperature of the nanotube is found to be significantly lower in gaseous environments than in vacuum, indicating that approximately 57% of the heat dissipated in the suspended nanotube is removed by its surrounding gas molecules, and that the thermal boundary conductance is higher in carbon dioxide than in argon or helium, despite the lower thermal conductivity of carbon dioxide.

**Infrared Blackbody Emission Spectroscopy:** We have measured the thermal emission spectra from individual suspended CNTs under high voltage biases in the visible and near infrared wavelength ranges. Figure 6a shows an optical microscope image of one such nanotube suspended across a  $2\mu\text{m}$  trench under high bias conditions. The corresponding thermal emission spectra, shown in Figure 6b, deviate significantly from normal blackbody emission (Plank's Law) due to the  $E_{11}^M$  optical transition in the CNT that is thermally driven under these high applied bias voltages. Semiconducting nanotubes exhibit a similar peak corresponding to the  $E_{22}^S$  transition. Nevertheless, accurate measurement of the electron temperature can be obtained above 800K. At these temperatures, the blackbody radiation spectrum peaks at a wavelength of  $3.6\mu\text{m}$ . However, it is not necessary to resolve this peak in order to determine the temperature accurately. Fan et al. have shown that accurate temperature measurements can be made from the intensity of blackbody emission at 980 nm, which can be easily measured in our spectrometer.

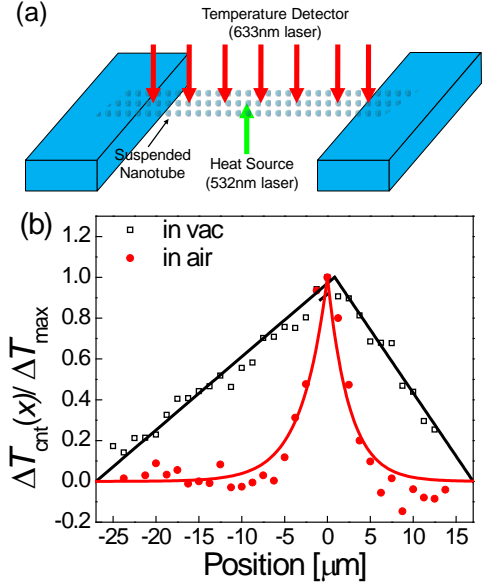


**Figure 5.** (a) Schematic diagram and (b) temperature profiles measured along an optically-heated suspended carbon nanotubes using Raman spectroscopy.

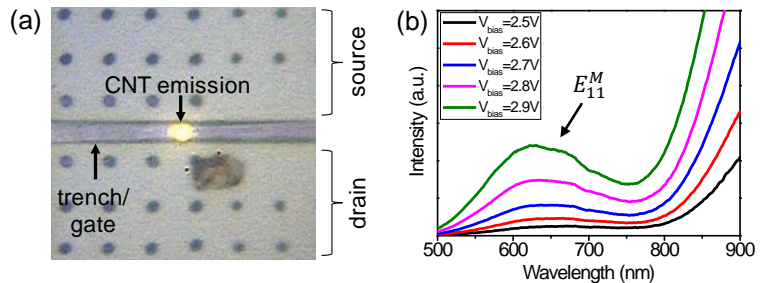


**Figure 6.** (a) Optical microscope image and (b) thermal emission spectra of an electrically heated suspended CNT.

## Future Plans

In the remaining funding period of this project, we will investigate non-equilibrium coupled electron-phonon transport in graphene and the effects of inter-layer coupling, substrate interaction, stress, morphology, and gas environment on electron-phonon coupling in graphene.

## References to publications of DOE sponsored research that have appeared in 2010-2012 or that have been accepted for publication.

1. Chia-Chi Chang, I-Kai Hsu, Mehmet Aykol, Wei-Hsuan Hung, Chun-Chung Chen, and Stephen B. Cronin, *A New Lower Limit for the Ultimate Breaking Strain of Carbon Nanotubes*, **ACS Nano**, 4, 5095 (2010).
2. I-Kai Hsu, Michael T. Pettes, Mehmet Aykol, Li Shi, and Stephen B. Cronin, *The Effect of Gas Environment on Electrical Heating in Suspended Carbon Nanotubes*, **Journal of Applied Physics**, 108, 084307 (2010).
3. Adam W. Bushmaker, Chia-Chi Chang, Vikram V. Deshpande, Moh. R. Amer, Marc W. Bockrath, Stephen B. Cronin, *Memristive Behavior Observed in a Defected Single-Walled Carbon Nanotube*, **IEEE Transactions on Nanotechnology**, 10, 582 (2011).
4. Insun Jo, I-Kai Hsu, Yong J. Lee, Mir Mohammad Sadeghi, Seyoung Kim, Stephen Cronin, Emanuel Tutuc, Sanjay K. Banerjee, Zhen Yao, and Li Shi, *Low-Frequency Acoustic Phonon Temperature Distribution in Electrically Biased Graphene*, **Nano Letters**, 11, 85 (2011).
5. Chun-Chung Chen, Mehmet Aykol, Chia-Chi Chang, A. F. J. Levi, and Stephen B. Cronin, *Graphene-Silicon Schottky Diodes*, **Nano Letters**, 11, 1863 (2011).
6. Chia-Chi Chang, Haitian Chen, Chun-Chung Chen, Wei-Hsuan Hung, I-Kai Hsu, Jesse Theiss, Chongwu Zhou, and Stephen B Cronin, *Tailoring the Crystal Structure of Individual Silicon Nanowires by Polarized Laser Annealing*, **Nanotechnology**, 22, 305709 (2011).
7. Mehmet Aykol, William Branham, Zuwei Liu, Moh R Amer, I-Kai Hsu, Rohan Dhall, Shun-Wen Chang and Stephen B Cronin, *Electromechanical Resonance Behavior of Suspended Single-Walled Carbon Nanotubes under High Bias Voltages*, **Journal of Micromechanics and Microengineering**, 21, 085008 (2011).
8. Zuwei Liu, Adam Bushmaker, Mehmet Aykol, and Stephen B. Cronin, *Thermal Emission Spectra from Individual Suspended Carbon Nanotubes*, **ACS Nano**, 5, 4634 (2011).
9. I-K. Hsu, M. T. Pettes, Mehmet Aykol, Chia-Chi Chang, Wei-Hsuan Hung, Jesse Theiss, Li Shi, and Stephen B. Cronin, *Direct Observation of Heat Dissipation in Individual Suspended Carbon Nanotubes using a Two-Laser Technique*, **Journal of Applied Physics**, 110, 044328 (2011).
10. Chun-Chung Chen, Wenzhong Bao, Chia-Chi Chang, Zeng Zhao, Chun Ning Lau, and Stephen B. Cronin, *Raman Spectroscopy of Substrate-Induced Compression and Substrate Doping in Thermally Cycled Graphene*, **Physical Review B**, 85, 035431 (2012).
11. Moh Amer, Adam Bushmaker and Steve Cronin, *Anomalous Kink Behavior in the Current-Voltage Characteristics of Suspended Carbon Nanotubes*, **Nano Research**, 5, 172 (2012).
12. R. Dhall, S.-W. Chang, Z. Liu, and S. B. Cronin, *Pronounced Electron-Phonon Interactions in Ultraclean Suspended Carbon Nanotubes*, **Physical Review B**, 86, 054527 (2012).
13. Moh. R. Amer, Adam Bushmaker, and Stephen B. Cronin, *The Influence of Substrate in Determining the Band Gap of Metallic Carbon Nanotubes*, **Nano Letters**, 12, 4843 (2012).
14. C.-C. Chang, C.-C. Chen, W.-H. Hung, I.-K. Hsu, M. A. Pimenta and S. B. Cronin, *Strain-Induced D Band Observed in Carbon Nanotubes*, **Nano Research**, 5, 854 (2012).
15. C.-C. Chen, C.-C. Chang, Z. Li, A. F. J. Levi, and S. B. Cronin, *Gate Tunable Graphene-Silicon Ohmic/Schottky Contacts*, **Applied Physics Letters**, 101, 223113 (2012).

## Proximity Effects in Charged Oxide Heterostructures

**PIs:** J.A. Eastman, P. Zapol, D.D. Fong, P.H. Fuoss  
 Materials Science Division  
 Argonne National Laboratory  
 9700 S. Cass Ave., Bldg. 212  
 Argonne, IL 60439  
 630-252-5141, jeastman@anl.gov

**Research Scope:** This program studies how to control heterointerfacial charge in epitaxial complex oxide thin film heterostructures to beneficially increase ionic conductivity and influence ferroelectric behavior. We create charged interfaces to enhance mobile oxygen vacancy concentrations and suppress oxygen vacancy ordering. Polarization in ferroelectric layers is used to control interfacial charge and oxygen transport in adjacent ionic conductor layers. Conversely, we explore how the electrical boundary conditions imposed by charged interfaces impact polarization behavior in ferroelectric films. Proximity effects associated with charged interfaces are amplified when heterostructure layer spacings are reduced below distances where the charges at neighboring interfaces strongly interact. The resulting knowledge is furthering basic understanding of charge interactions near interfaces and has great potential to impact energy-related technologies.

Our approach employs forefront in-situ synchrotron x-ray scattering and spectroscopy techniques. We determine depth-resolved atomic-level structure and composition in real-time, both during thin film growth and post-growth, in the elevated temperature, controlled oxygen pressure conditions where behavior is most interesting. The model heterostructures we create are based on fluorite- or perovskite-structured materials. Growth techniques that enable precise control of each atomic plane in a growing heterostructure of these materials are employed, including a new capability in sputter deposition. X-ray characterization of interfacial structure/chemistry, strain/composition gradients, and defect behavior is combined with in-situ electrical characterization to provide unique insight into structure-property relationships. The program integrates experimental measurements with a theoretical effort that uses first principles calculations to elucidate the factors that control growth behavior and properties.

**Recent Progress:** Our program has made significant progress in using in-situ synchrotron x-ray techniques during growth and characterization of ionically conducting and ferroelectric thin film oxide heterostructures, complemented with first-principles computations that are revealing the energetics of polar interfaces. In the following, we describe two brief highlights of our recent progress that demonstrate capabilities and phenomena that will continue to be exploited in our future plans.

**Oxygen Transport Behavior in Epitaxial Thin Film Heterostructures** Oxygen transport across interfaces is rate-limiting in many electrochemistry-based applications, adversely impacting performance in solar cells, batteries, and fuel cells, for example. Efficient energy conversion in those devices relies on limiting overpotential losses when charge is transported across interfaces. Understanding the series of electrochemical reaction steps associated with interfacial oxygen transport presents significant scientific challenges.

Oxygen transport behavior in thin film  $\text{La}_{0.6}\text{Sr}_{0.4}\text{Co}_{0.2}\text{Fe}_{0.8}\text{O}_{3-d}$  (LSCF) heterostructures exposed to controlled perturbations of temperature, oxygen partial pressure, and electrical potential was investigated at the Advanced Photon Source. Applying electrical potentials across the heterostructures resulted in significant expansion or contraction of the out-of-plane LSCF lattice parameter (Fig. 1), indicating changes in the LSCF oxygen vacancy concentration. Oxygen transport across the LSCF/atmosphere interface was found to be rate-limiting under both cathodic and anodic conditions.

The results of this study, which were published in *Applied Physics Letters* (101, 051603 (2012)), provide needed fundamental insight into the electrochemical behavior of

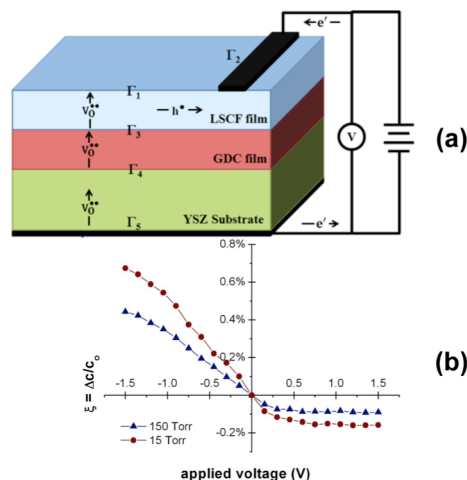


Fig. 1 (a) Oxygen transport was induced across five interfaces ( $\Gamma_1$ - $\Gamma_5$ ) by applying potentials under controlled conditions. (b) Lattice parameter responses revealed that transport across the film / atmosphere interface ( $\Gamma_1$ ) is rate-limiting.

interfaces in complex oxides. The techniques developed offer new avenues to study the electrochemical performance of surfaces and buried interfaces in thin film heterostructures.

**Equilibrium Polarization of Ultrathin  $\text{PbTiO}_3$  Films with Surface Compensation Controlled by Oxygen Partial Pressure** In this study we discovered that electrochemical interactions with the environment strongly modify the phase transition behavior of ultrathin ferroelectric films. The results were published in *Physical Review Letters* (**107**, 187602 (2011)). In particular, we found that the film's ferroelectric transition temperature and domain structure can be significantly varied by controlling the density of charged species at the film surface. The polarization structure of  $\text{PbTiO}_3$  films was characterized as a function of film thickness, temperature ( $T$ ), and the external oxygen partial pressure ( $p\text{O}_2$ ) by *in-situ* synchrotron x-ray scattering at the Advanced Photon Source. By studying the structure of the film during cooling at different values of  $p\text{O}_2$ , we were able to construct a ( $p\text{O}_2$ ,  $T$ ) phase diagram for each film thickness (Fig. 2). We found that high or low  $p\text{O}_2$  altered the sign of the charged species at the surface, and consequently led to positively or negatively polarized monodomain structures, respectively. However, intermediate  $p\text{O}_2$  resulted in the formation of a  $180^\circ$  stripe domain structure with significantly suppressed paraelectric-to-ferroelectric transition temperature ( $T_C$ ). The suppression of  $T_C$  was found to increase as film thickness decreased. These results are in agreement with a thermodynamic model regarding the effects of surface electrochemical reactions on the ferroelectric phase transition. The phase diagrams established by this study show that the nucleation-free switching of ultrathin ferroelectric films we previously discovered is an equilibrium, rather than a kinetic, phenomenon.

Control of charge at interfaces is crucial to widespread energy technologies such as batteries, fuel cells, and catalysts. It is also key to modulating transport behavior in nanoionic devices, a rapidly growing field of materials research. Progress in these areas depends on understanding the interaction between chemical environments and charged species. These studies of ultrathin ferroelectric complex oxides not only explored a potentially important

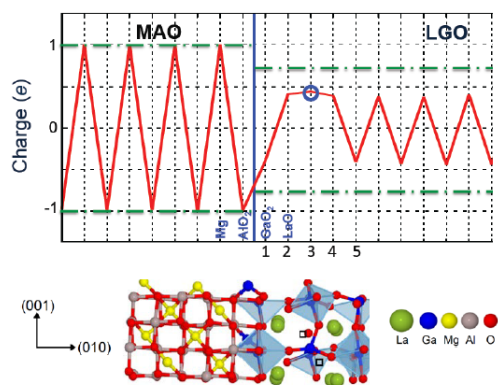


Fig. 3. Bader charge per plane (top) and DFT-optimized structure (bottom) of  $\text{LaGaO}_3/\text{MgAl}_2\text{O}_4$  heterostructure. Dashed lines are for respective bulk oxides. The positive charge (top, circle) for the most favorable vacancy positions (bottom, squares) indicates that the vacancies are doubly positively charged and provide compensating charge to excess negative charge at the interface (blue line).

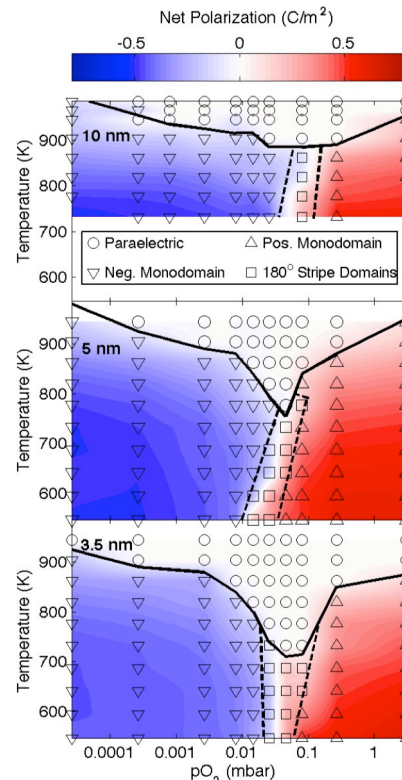


Fig. 2 Temperature vs  $p\text{O}_2$  phase diagrams for three thicknesses of  $\text{PbTiO}_3$  on  $\text{SrRuO}_3$  coherently strained to  $\text{SrTiO}_3$  (001). Color scale indicates net polarization. Symbols show points measured and phase observed. Solid lines indicate  $T_C$ , and dashed lines are boundaries of  $180^\circ$  stripe domain regions.

new class of catalytic materials but also identified a new approach for understanding the strength of the interactions between external chemistry, surface charge, and polarization, enabling the development of a predictive model of behavior. Our discoveries suggest new pathways in which surface chemistry can be used to control the stability of ferroelectrics, and ferroelectricity can be used to tune the chemical reactivity of surfaces.

**Future Plans:** Our planned research explores promising opportunities for creating and characterizing new oxide heterostructures possessing enhanced material properties through control of heterointerfacial charge. Two examples of planned and on-going research are briefly described in the following.

**Enhanced Ionic Conductivity in Oxide Thin Film Heterostructures:** Modifications of interfacial charge to manipulate properties of the space charge layer provide a venue of changing transport properties in proximity of an interface. If the density of the interfaces is such that

space charge layers overlap, one can expect emergent behavior of ionic transport properties that cannot be interpolated from the bulk counterpart behavior. One possible way of achieving enhanced in-plane interfacial ionic transport in systems is to induce oxygen vacancy enrichment layers. To guide and interpret experimental studies, we will explore computational models of such interfacial behavior. As an example, we consider LaGaO<sub>3</sub>, which is a poor ionic conductor intrinsically, but exhibits a high conductivity with heterogeneous doping. Provided that a negatively charged interface with another material can be synthesized, one would expect an increased oxygen vacancy concentration in LaGaO<sub>3</sub> to provide charge compensation. A negatively charged interface between the spinel MgAl<sub>2</sub>O<sub>4</sub> and perovskite LaGaO<sub>3</sub> would have only a limited number of possibilities for electronic compensation since each cation has only one valence state (Fig. 3). We will investigate different compensation mechanisms for excess negative charge at the interface to find conditions when the oxygen vacancy concentration in the interfacial region is increased and vacancy charge is retained.

Development of models based on first-principles calculations will help to create fundamental understanding of ionic transport in the vicinity of interfaces and to choose target materials and surface orientations for synthesis using computational materials design methods.

#### **Interplay between Ionic Conductivity and Ferroelectric Behavior:**

Studies of the interplay between different properties of complex oxides have drawn increasing attention in recent years. We have begun investigating coupled behavior in heterostructures containing a ferroelectric material in close proximity to an ionic conductor. Recent preliminary data (Fig. 4) indicate that the polarization in a ferroelectric PbTiO<sub>3</sub> layer affects the distribution of oxygen vacancies during growth of an adjacent layer of LaGaO<sub>3</sub>. We will explore whether such heterostructures exhibit ionic conduction localized to the space charge region of the heterointerface, i.e., determine whether they show the ionic conduction analogue of the quasi-two-dimensional electron gas (q2DEG) behavior reported in oxide heterostructures such as LaAlO<sub>3</sub> / SrTiO<sub>3</sub>. Our studies will determine how changing the magnitude and direction of the ferroelectric polarization (by either changing pO<sub>2</sub> or an applied electric field) affect the oxygen vacancy distribution in LaGaO<sub>3</sub> and the resulting ionic conduction behavior. Both experimental and theoretical studies of heterostructures consisting of undoped LaGaO<sub>3</sub> layered with PbTiO<sub>3</sub> will characterize the polarization-induced changes in oxygen vacancy concentration and distribution, and determine the possible effects of ferroelectric polarization on ionic transport behavior. A key question that will be addressed is whether the oxygen vacancies induced in proximity to ferroelectric/ionic conductor interfaces are sufficiently mobile to contribute to altering the oxygen diffusion rate in the ionic conductor.

Studies of interface charge in heterostructures containing both ionically conducting and ferroelectric materials not only provide an opportunity to enhance ionic conductivity, but also are of interest because of the possible effects of interfacial charge on the behavior of the ferroelectric. We thus will also continue to investigate the behavior of PbTiO<sub>3</sub>/YSZ heterostructures to determine the effects of ionic compensation on the switching behavior of PbTiO<sub>3</sub> films.

#### **Selected DOE Sponsored Publications (2010-2012)**

“In Situ X-Ray Studies of Oxygen Surface Exchange Behavior in Thin Film La<sub>0.6</sub>Sr<sub>0.4</sub>Co<sub>0.2</sub>Fe<sub>0.8</sub>O<sub>3-δ</sub>”, B. J. Ingram, J. A. Eastman, K.-C. Chang, S. K. Kim, T. T. Fister, E. Perret, H. You, P. M. Baldo, P. H. Fuoss, *Applied Physics Letters*, **101**, 051603(2012).

“Three-dimensional Quantitative Chemical Roughness of Buried ZrO<sub>2</sub>/In<sub>2</sub>O<sub>3</sub> Interfaces via Energy-filtered Electron Tomography,” X.Y. Zhong, B. Kabius, D.K. Schreiber, J.A. Eastman, D.D. Fong, A.K. Petford-Long, *Applied Physics Letters*, **100**, 101604 (2012).

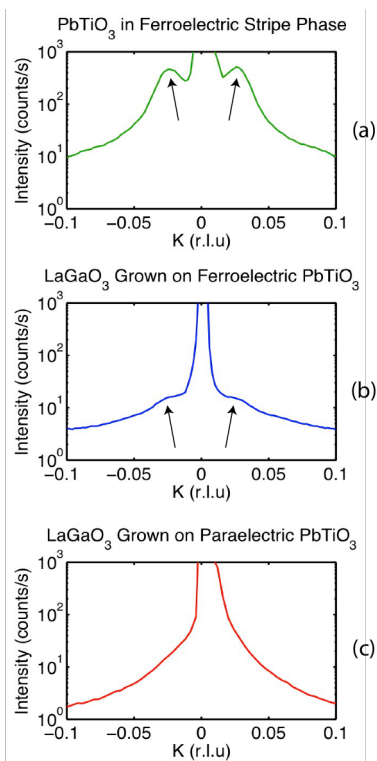


Fig. 4 In-plane X-ray scans through (a) the PbTiO<sub>3</sub> (304) Bragg peak, (b) the LaGaO<sub>3</sub> (304) Bragg peak in a film grown at 550°C, where the adjacent PbTiO<sub>3</sub> layer is ferroelectric, and (c) the LaGaO<sub>3</sub> (304) Bragg peak in a film grown at 650°C, where the PbTiO<sub>3</sub> is paraelectric. Arrows show the positions of diffuse intensity due to ordering, which is absent in the LaGaO<sub>3</sub> film grown on paraelectric PbTiO<sub>3</sub>.

- “Atomic Layer Engineering of Perovskite Oxides for Chemically Sharp Heterointerfaces”, W.S. Choi, C.M. Rouleau, S.S.A. Seo, Z. Luo, H. Zhou, T.T. Fister, J.A. Eastman, P.H. Fuoss, D.D. Fong, J.Z. Tischler, G. Eres, M.F. Chisholm and H.N. Lee, *Advanced Materials*, **24**, 6423 (2012).
- “Atomic-Scale Study of Ambient-Pressure Redox-Induced Changes for an Oxide-Supported Submonolayer Catalyst: VOx/ $\alpha$ -TiO<sub>2</sub>(110),” Z. Feng, L. Cheng, C.-Y. Kim, J. W. Elam, Z. Zhang, L. A. Curtiss, P. Zapol, and M. J. Bedzyk, *J. Phys. Chem. Lett.* **3**, 2845-2850 (2012)
- “First-Principles Calculations Of Surfactant-Assisted Growth Of Polar Cao(111) Oxide Film: The Case Of Water-Based Surfactant ,” X. Tan, P. Zapol, *Phys. Rev. B*, **86**, 045422 (2012)
- “First-Principles Study Of The Atomic And Electronic Structures Of Misfit-Layered Calcium Cobaltite (Ca<sub>2</sub>CoO<sub>3</sub>)(Coo<sub>2</sub>)(1.62) Using Rational Approximants ,” A. Rebola, R. Klie, P. Zapol, S. Ogut, *Phys. Rev. B* **85**,155132 (2012)
- “Synchrotron X-ray Scattering Studies of Oxide Heterostructures”, D. D. Fong, in *Multifunctional Oxide Heterostructures*, Eds. E. Y. Tsymbal, E. Dagotto, C. B. Eom, and R. Ramesh, Oxford University Press, New York (2012).
- “Tilt Transitions in Compressively Strained AgTa<sub>1/2</sub>Nb<sub>1/2</sub>O<sub>3</sub> Films,” R. L. Johnson-Wilke, D. S. Tinberg, C. B. Yeager, Y. Han, I. M. Reaney, I. Levin, D. D. Fong, T. T. Fister, S. Trolier-McKinstry, *Phys. Rev. B* **84**, 134114 (2011).
- “Metallic and Insulating Oxide Interfaces Controlled by Electronic Correlations,” H. W. Jang, D. A. Felker, C. W. Bark, Y. Wang, M. K. Niranjana, C. T. Nelson, Y. Zhang, D. Su, C. M. Folkman, S. H. Baek, S. Lee, K. Janicka, Y. Zhu, X. Q. Pan, D. D. Fong, E. Y. Tsymbal, M. S. Rzechowski, C. B. Eom, *Science* **331**, 886 (2011).
- “Equilibrium Polarization of Ultrathin PbTiO<sub>3</sub> with Surface Compensation Controlled by Oxygen Partial Pressure”, M.J. Highland, T.T. Fister, D.D. Fong, P.H. Fuoss, Carol Thompson, J.A. Eastman, S.K. Streiffer, G.B. Stephenson, *Physical Review Letters*, **107**, 187602 (2011).
- “Octahedral Tilt Transitions in Relaxed Epitaxial Pb(Zr<sub>1-x</sub>Ti<sub>x</sub>)O<sub>3</sub> Films,” D. S. Tinberg, R. L. Johnson-Wilke, D. D. Fong, T. T. Fister, S. K. Streiffer, Y. Han, I. M. Reaney, S. Trolier-McKinstry, *J. Appl. Phys.* **109**, 094104 (2011).
- “X-Ray Nanodiffraction of Tilted Domains in a Poled Epitaxial BiFeO<sub>3</sub> Thin Film”, S. O. Hruszkewycz, C. M. Folkman, M. J. Highland, M. V. Holt, S. H. Baek, S. K. Streiffer, P. Baldo, C. B. Eom, and P. H. Fuoss, *Applied Physics Letters*, **99**, 232903(2011).
- “Total-Reflection Inelastic X-Ray Scattering from a 10-nm Thick La<sub>0.6</sub>Sr<sub>0.4</sub>CoO<sub>3</sub> Thin Film”, T.T. Fister, D.D. Fong, J.A. Eastman, H. Iddir, P. Zapol, P.H. Fuoss, M. Balasubramanian, R.A. Gordon, K.R. Balasubramanian, P.A. Salvador, *Physical Review Letters*, **106**, 037401(2011). (*Editor’s Selection and Physics Synopsis*)
- “Tailoring a Two-Dimensional Electron Gas at the LaAlO<sub>3</sub>/SrTiO<sub>3</sub> (001) Interface by Epitaxial Strain,” C. W. Bark, D. A. Felker, Y. Wang, Y. Zhang, H. W. Jang, C. M. Folkman, J. W. Park, S. H. Baek, X. Q. Pan, H. Zhou, D. D. Fong, E. Y. Tsymbal, M. S. Rzechowski, C. B. Eom, *Proc. Nat’l. Acad. Sci.*, **108**, 4720 (2011).
- “In situ synchrotron x-ray characterization of ZnO atomic layer deposition”, D.D. Fong, J.A. Eastman, S.K. Kim, T.T. Fister, M.J. Highland, P.M. Baldo and P.H. Fuoss, *Applied Physics Letters*, **97**, 191904(2010).
- “Polarization Switching without Domain Formation at the Intrinsic Coercive Field in Ultrathin Ferroelectric PbTiO<sub>3</sub>”, M.J. Highland, T.T. Fister, M.-I. Richard, D.D. Fong, P.H. Fuoss, C. Thompson, J.A. Eastman, S.K. Streiffer, and G.B. Stephenson, *Physical Review Letters*, **105**, 167601(2010). (*Editor’s Selection and Physics Synopsis*)
- “Bragg coherent diffraction imaging of epitaxial nanostructures using focused hard x-ray ptychography, S. O. Hruszkewycz, M. V. Holt, D. L. Proffit, M. J. Highland, A. Imre, J. Maser, J. A. Eastman, G. R. Bai, and P. H. Fuoss, *AIP Conf. Proc.*, **1365**, pp. 235-238 (2011).
- “Phase Stabilization of  $\delta$ -Bi<sub>2</sub>O<sub>3</sub> Nanostructures by Epitaxial Growth onto Single Crystal SrTiO<sub>3</sub> or DyScO<sub>3</sub> Substrates,” D.L. Proffit, G.-R. Bai, D.D. Fong, T.T. Fister, S.O. Hruszkewycz, M.J. Highland, P.M. Baldo, P.H. Fuoss, T.O. Mason, J.A. Eastman, *Appl. Phys. Lett.*, **96**, no. 2, 021905 (2010).
- “X-Ray Probes for In Situ Studies of Interfaces,” D. D. Fong, C.A. Lucas, M.-I. Richard, and M.F. Toney, *MRS Bulletin* **35**, 504-513 (2010).

**Project Title:** Nanophotonics-enhanced solar cells

**DOE Grant:** DE-FG02-07ER46426

**Principal Investigators:**

- Prof. Shanhui Fan, Professor of Electrical Engineering, Spilker Building, Room 314, Stanford University, Stanford, CA 94305. Email: Shanhui@stanford.edu
- Prof. Mark Brongersma, Professor of Material Science and Engineering, McCullough Building, Room 349, Stanford University, Stanford, CA 94305. Email: Brongersma@stanford.edu

## 1. Program Scope

The objective of our program is to develop a fundamental understanding of optical physics of nanophotonic solar cells from a wave-optics perspective, and to use this understanding to develop pathways towards ultra-thin high-efficiency solar cells with thickness on the wavelength or deep sub-wavelength scales. This objective is accomplished by a collaboration of theory and experiments.

In our theoretical efforts, we are developing a formalism based entirely on the electromagnetic modal structure of the solar cells. This approach has reproduced the conventional  $4n^2$  limit for bulk solar cells, and moreover has pointed to the capabilities of ultra-thin nanophotonic solar cells to significantly exceed the conventional limit. In our experimental efforts, we have developed a testbed that enables systematic explorations of nanophotonic physics using very thin silicon photovoltaic structures. The combination of theory and experiments have enabled us to elucidate mechanisms of light trapping enhancement using aperiodic plasmonic structures on a ultra-thin silicon solar cells.

Building upon our previous accomplishments, in the next budget period we propose to direct the theoretical efforts towards understanding how nanophotonic engineering may impact both the open circuit voltage and the short-circuit current of ultra-thin solar cells, The theory efforts will be closely coupled with the experiments that explore a variety of ultra-thin absorber structures. The success of our project will open a pathway towards solar cell structures in a fundamentally different regime of performance as compared to conventional solar cells, with the potential to greatly enhance the efficiency/cost ratio.

## 2. Recent Progress

### 2.1. Thermodynamic constraint on broad-band light coupling

In the past budget period of 2007-2010 we have started the development of a light trapping theory based entirely on wave optics (Paper 1 in Section 4). However, the initial theoretical prediction was applicable only when the material absorption in the structure is infinitesimally small. For most of the solar spectral regime, solar cell materials have non-negligible absorption coefficient. Therefore, it is important to understand the upper limit of light trapping enhancement in the regime where material absorption is not infinitesimally small.

In this period we provided a definite wave optics theory of light trapping in the regime where material absorption is significant (Paper 12 in Section 4). In our statistical coupled mode formalism (Fig. 1a), each mode in the structure is characterized by both an intrinsic loss rate due to material absorption, and an external coupling rate due to radiation. Our key discovery here is to show that the external coupling rates are in fact subject to as an upper bound as dictated by the second law of thermodynamics. Using this upper bound, and combining with the statistical coupled mode theory formalism, we obtain the upper limit of light trapping absorption enhancement as:  $A \leq \frac{\alpha d}{\alpha d + 1/F}$ , where  $F$  is the light trapping enhancement factor in the limit where the single pass absorption is infinitesimal,  $\alpha d$  is the single pass

absorption. This result is consistent with and generalizes over the conventional light-trapping theory in the regime of non-negligible single-pass absorption.

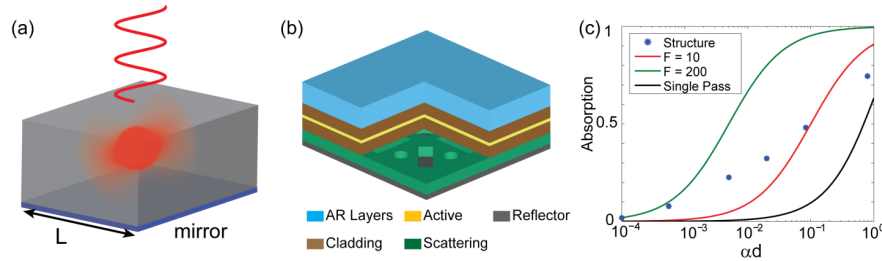


Fig. 1. (a) Schematic of an optical resonance coupling with free space through the top surface. b) Solar absorber structure (with cut-out showing the scattering layer pattern). It consists of cladding layers (brown color)

of thickness 125 nm and  $\epsilon = 12.5$ . The cladding layers surround the 5 nm active layer (yellow color) of  $\epsilon = 2.5$  on both sides. Below the lower cladding layer, we place a 150 nm thick scattering layer with  $\epsilon = 12.5$  (green color), with an air hole pattern of 1200 nm periodicity etched into it. Below the scattering layer we place a perfectly reflecting substrate. Finally, on top of the structure is an optimized four layer anti-reflection (AR) coating (blue color). c). Absorption as the function of single pass absorption  $\alpha d$  of the active layer. The black black curve is for single pass absorption. Dots are simulated results for the structure shown in b). The red and green curves are the conventional ray optics limit and the theoretical limit for the structure in b).

Our theory predicts that nanophotonic structure can achieve broad-band absorption enhancement beyond the conventional limit in non-negligible absorption regime. As numerical demonstration we consider the structure in Fig. 1b). The nanophotonic light trapping limit (green line in Fig 1c), and the actual simulated absorption (Blue dots in Fig. 1c) is indeed much higher than the conventional limit (red line in Fig. 1c) for most of the single pass absorption strength  $\alpha d$ .

## 2.2. Optimized design for simultaneous anti-reflection and light-trapping

We have applied our theory of nanophotonic solar cells to the design of ultra-thin crystalline silicon solar cells (Paper 8 in Section 4). Commercial crystalline silicon solar cell has thickness of 100's microns. However, there have been significant recent interests for the design of thin cell with a thickness of only a few microns for the purposes of cost reduction.

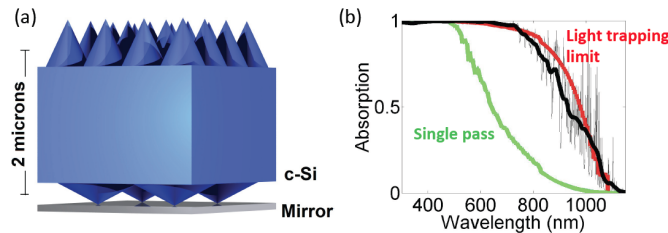


Fig. 2. (a) Crystalline silicon thin film structure. Blue represents silicon. The nanocones are placed in a two-dimensional square lattice on both the front and the back surfaces. (b) The gray line is actual absorption spectrum, and the black line is spectrally averaged absorption, for the structure shown in a). The green line is the single-pass absorption for a silicon layer of 2 micron thickness. The red curve is the upper limit of light trapping when light trapping is performed on such a 2-micron thick silicon film.

single-pass absorption for a silicon layer of 2 micron thickness. The red curve is the upper limit of light trapping when light trapping is performed on such a 2-micron thick silicon film.

The goal of our design is to reach the theoretical limit for short-circuit current for such ultra-thin silicon structures. To do so, one needs simultaneously achieve two different objectives: broadband anti-reflection and effective light trapping. Since these two objectives have very different design considerations, we employ a double-sided grating design (Fig. 2a), with a front-surface grating optimized for anti-reflection, and a back-surface grating optimized for light trapping purposes. The resulting structure has a performance very close to the theoretical limit (Fig. 2b). When illuminated with AM 1.5 solar spectrum, our design has a predicted current density of  $34.6 \text{ mA/cm}^2$ , as compared to the theoretical light trapping limit of  $35.5 \text{ mA/cm}^2$ . We have therefore shown that, by reaching the theoretical limit of light-trapping enhancement, there is indeed great potential for ultra-thin solar cell structures to achieve substantial efficiency.

### 2.3. Aperiodic plasmonic nanostructures

In a collaboration between the Brongersma and Fan groups, we have demonstrated the significant benefits of engineering non-periodic particle arrangements for broadband light trapping in ultrathin solar cells (Paper 19 in Section 4).

The importance of some amount of disorder has a recognized beneficial effect in PV cells. However, there has not been systematic strategy currently available to achieve the best light trapping structures. Full-field electromagnetic simulations are unfortunately computationally too time intensive. We developed a semi-analytical light trapping model that allows for a more rapid optimization and a deeper understanding why some non-periodic arrays outperform others. This model allows us to relate light trapping enhancement to the Fourier spectra of different structures.

Fig. 3 schematically shows how the light trapping performance of different non-periodic light trapping layers on ultrathin crystalline Si films were quantified and compared. When the resulting structures are top-illuminated with sunlight, photocarriers are produced in the thin Si layer. These carriers can be extracted via laterally-spaced contacts. Photocurrent spectrum measurements facilitate a quantitative assessment of the spectral light trapping properties.

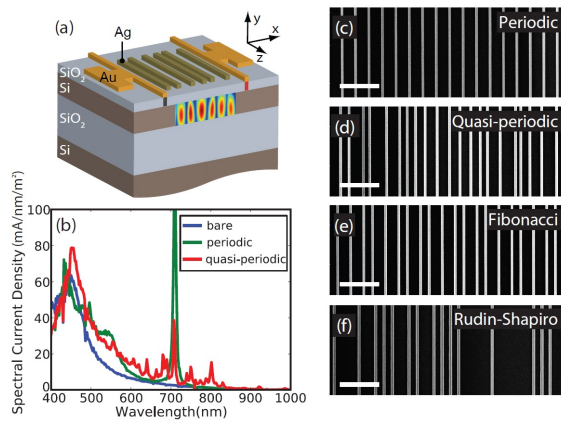


**Fig. 3. Optimized non-periodic stripe arrays facilitate enhanced light trapping in ultra-thin semiconductor layers. (a) A schematic of the SOI photodetector structure decorated with a quasi-periodic stripe array. (b) Simulated spectral short-circuit current density for the device with a periodic (green) Ag and a quasi-periodic (red) array of Ag stripes. The blue curve shows the simulated response for a reference device with a bare 50-nm-thick Si layer and 20-nm-thick SiO<sub>2</sub> layer on top. (c-f) SEM images of fabricated devices featuring (c) periodic, (d) Fibonacci, (e) quasi-periodic, and (f) Rudin-Shapiro arrays of Ag stripes. The scale bar is 1 μm.**

Fig. 3b shows the spectra for various light trapping structure as shown in Fig. 3c-f. We see that both the periodic and the quasi-periodic structure shows significantly enhancement over flat surfaces. The periodic structure features a few very sharp absorption peak, whereas the optimal quasi-periodic structures shows a much wider set of peaks. This is expected as the multiple periods present in the spatial Fourier transform of the quasi-periodic grating enable effective coupling at many wavelengths. By integrating the spectral photocurrent we find that the periodic array gives rise to a 40 % increase in the photocurrent over the bare Si film. The non-periodic array does even better and provides an enhancement of 55 %. We have accounted such enhancement by showing that the quasi-periodic array has the optimal scattering strength profile. Our results therefore indicate the important advantage of aperiodic structure for light trapping enhancement.

### 3. Future Plan

We propose to continue to explore the optical physics of nanophotonic solar cells and ultra-thin absorbers. In the development of solar cells, there has been a continuous effort in seeking to minimize thickness of the cell while preserving the efficiency. In this regard, a fundamental question arises as to whether one can achieve broad-band absorption of light with active layer thickness that is far smaller than the wavelength of light, and even approaching single-atomic layer scale. We propose to use our understanding of absorption enhancement to push towards such a frontier in light management in ultra-thin absorbers. Also, both current and voltage characteristics of a solar cell are important. While the majority of the previous works have focused on optimizing for the short-circuit current, there are in fact significant opportunities, especially in high-efficiency cells, to use the nanophotonic structure to control the open circuit voltage of the solar cell as well. Here we propose to develop a fundamental understanding of the basic thermodynamic constraints on voltage and current in nanophotonic structures.

#### 4. Publications in the budget period of 2010-2012

(Those that start with \* are solely funded with this grant.)

1. Z. Yu, A. Raman, and S. Fan, "Fundamental limit of nanophotonic light trapping in solar cells", Proceedings of the National Academy of Sciences, vol. 107, pp. 17491-17496 (2010).
2. \*Z. Yu and S. Fan, "Angular constraint on light-trapping absorption enhancement in solar cells", Applied Physics Letters, vol. 98, art. No. 011106 (2011).
3. Z. Ruan and S. Fan, "Design of subwavelength superscattering nanospheres", Applied Physics Letters, vol. 98, art. No. 043101 (2011). (Featured on cover)
4. E. S. Barnard, R. A. Pala, and M. L. Brongersma, "Photocurrent mapping of near-field optical antenna resonances," Nature Nanotechnology, 6, 588-593 (2011).
5. H. Wu, L. Hu, T. Carney, Z. Ruan, D. Kong, Z. Yu, Y. Yao, J. Cha, J. Zhu, S. Fan and Y. Cui, "Low reflectivity and high flexibility ITO Nanofiber Transparent Electrodes", Journal of the American Chemical Society (Communications), vol. 133, pp. 27-29 (2011).
6. \*P. B. Catrysse and S. Fan, "Transverse electromagnetic modes in apertures containing a meta-material with extreme anisotropy", Physical Review Letters, vol. 106, art. No. 223902 (2011).
7. Y. Yao, J. Yao, V. K. Narasimhan, Z. Ruan, C. Xie, S. Fan and Y. Cui, "Broadband light management using low-Q whispering gallery modes in spherical nanoshells", Nature Communications, vol. 3, art. No. 664 (2012).
8. \*K. X. Wang, Z. Yu, V. Liu, Y. Cui and S. Fan, "Absorption enhancement in ultra-thin crystalline silicon solar cells with anti-reflection and light-trapping nanocone gratings", Nano Letters, vol. 12, pp. 1616-1619 (2012).
9. \*L. Verslegers, Z. Yu, Z. Ruan, P. B. Catrysse, and S. Fan, "From electromagnetically induced transparency to superscattering with a single structure: a coupled-mode theory for doubly resonant structures", Physical Review Letters, vol. 108, art. No. 083902 (2012).
10. Z. Ruan, and S. Fan, "Temporal coupled-mode theory for light scattering by an arbitrary-shaped object supporting a single resonance", Physical Review A, vol. 85, art. No. 043828 (2012).
11. C. -M. Hsu, C. Battaglia, C. Pahud, Z. Ruan, F. -J. Haug, S. Fan, C. Ballif, and Y. Cui, "High-efficiency amorphous silicon solar cell on periodic nanocone back reflectors", Advanced Energy Materials, vol. 2, pp. 628-633 (2012).
12. Z. Yu, A. Raman and S. Fan, "Thermodynamic upper bound on broadband light coupling with photonic structures", Physical Review Letters, vol. 109, art. No. 173901 (2012).
13. A. P. Vasudev, J. A. Schuller, and M. L. Brongersma, "Nanophotonic light trapping with patterned transparent conductive oxides," Optics Express, vol. 20, A385-A394 (2012).
14. K. X. Wang, Z. Yu, S. Sandhu and S. Fan, "Fundamental Bounds on Decay Rates in Asymmetric Single-Mode Optical Resonators", Optics Letters, vol. 38, pp. 100-102 (2013).
15. \*S.B. Mallick, M. Agrawal, A. Wangperawong, E.S. Barnard, K.K. Singh, R.J. Visser, M.L. Brongersma, and P. Peumans, "Ultrathin crystalline-silicon solar cells with embedded photonic crystals", Applied Physics Letters, vol. 100, art. No. 053113 (2012).
16. S. Sandhu, Z. Yu and S. Fan, "Detailed balance analysis of nanophotonic solar cells", Optics Express, vol. 21, pp. 1209-1217 (2013).
17. \*P. B. Catrysse, and S. Fan, "Routing of deep-subwavelength optical beams and images without reflection and diffraction using infinitely anisotropic metamaterials", Advanced Materials, vol. 25, pp. 194-198 (2013).
18. A. Raman, W. Shin and S. Fan, "An upper bound on the material loss rate of modes in plasmonic and metamaterial systems", Physical Review Letters (accepted).
19. R. Pala, J. Liu, E. Barnard, D. Askarov, E. Garnett, S. Fan and M. Brongersma, "Optimization of non-periodic plasmonic light trapping layers for ultra-thin solar cells", Nature Communications (accepted).

## Abstract

---

### **“Elucidation of Hydrogen Desorption Mechanisms from Complex Metal Hydrides interacting with Carbon” Nanostructures**

**Jena, Purusottam**

#### **PROGRAM SCOPE**

The goal of our project is to provide a basic understanding of the interaction of hydrogen with metal atoms supported on carbon nanostructures and examine their physicochemical properties. Our theoretical work is a joint effort with the experimental group of Dr. Ragaiy Zidan at Savannah River National Laboratory. This study is aimed at attempting to predict and control material properties at the electronic, atomic and molecular level that can form the foundation of new energy technologies. Research is aimed at developing and characterizing novel class of hydride materials based on metal-carbon nanostructures. The formation of these nanocomposites (e.g.  $\text{Na}_x\text{C}_{60}$ ) has been of great interest for many researchers in various fields, seeking nano materials with novel properties such as hydrogen storage, high ionic mobility, and superconductors. Our work involves hydrogen storage and other properties of a series of  $\text{M}_x\text{-C-H}_y$  nanocomposites.

#### **RECENT PROGRESS**

The potential of a variety of nanostructures such as Li functionalized  $\text{BC}_3$  nanotubes, Pd atoms adsorbed on activated carbon nano-fibers, Ti-doped nano-porous graphene,  $\text{C}_{60}$  doped  $\text{LiBH}_4$  and Li-N-H systems, Sc- doped phthalocyanine sheet, COF-10,  $\text{Li}_3\text{N}$ -based nanostructures, Li functionalized  $\text{BC}_3$  nanotubes, functionalized boranes, highly porous borazine-linked polymers and  $\text{Li}_6\text{C}_{60}$ , for hydrogen storage, was examined. Several of these papers were published with experimentalists. The adsorbed metal atoms are found to store hydrogen in quasi-molecular form driven by the charge polarization mechanism introduced by the PI twenty years ago. The work on Li supported  $\text{C}_{60}$  was in support of the recent experiment in Dr. Zidan's group where the authors showed that  $\text{Li}_6\text{C}_{60}$  can store up to 5 wt% hydrogen reversibly. We provided the theoretical understanding of the structure of  $\text{Li}_6\text{C}_{60}$  and the sites hydrogen atoms bind to. A study of the energetics of the material revealed the manner in which hydrogen is desorbed and the energy necessary for the purpose. The PI also published an invited perspective in the Journal of Physical Chemistry Letters on Hydrogen Storage: Past, Present, and Future.

#### **FUTURE PLANS**

We are currently working with Dr. Zidan's group on the structure and properties of a new hydrogen storage material  $\text{KAl}(\text{BH}_4)_4$ . This compound is made from mixing two well-known salts  $\text{KBH}_4$  and  $\text{Al}(\text{BH}_4)_3$ . While the former releases hydrogen at elevated temperatures and the latter is a highly pyrophoric ionic liquid,  $\text{KAl}(\text{BH}_4)_4$  is a much safer and more stable solid

compound at ambient temperatures. The electronic structure of this compound will be analyzed to study if this can be classified as a hypersalt recently postulated by the PI on the basis of the discovery of the hyperhalogens by the PI and his colleagues. Work is also planned to examine hydrogen storage properties of functionalized graphene. The role of defects in graphene as catalysts for the production of H<sub>2</sub> from water will also be studied.

## REFERENCES TO PAPERS PUBLISHED in 2010-2012

1. Zhou, J., Sun, Q., Wang, Q., Jena, P., and Chen, X. S.: "Electric Field Enhanced Hydrogen Storage on BN Sheet", *Proc. Nat. Acad. Science* **107**, 2801 (2010).
2. Dolotko, O., Zhang, H., Li, S., Jena, P., and Pecharsky, V.: "Mechanochemically Driven Non-equilibrium Processes in MNH<sub>2</sub>-CaH<sub>2</sub> Systems (M=Li or Na)", *J. Alloys and Compounds*, **506**, 224 (2010).
3. Li, S. and Jena, P.: "Reaction Intermediates during Dehydrogenation of Metal Borohydrides: A Cluster Perspective", *J. Chem. Phys.* **114**, 16849 (2010).
4. Wu, M. M., Wang, Q., Sun, Q., Jena, P., and Kawazoe, Y.: "Firstprinciples study of hydrogen adsorption in metal doped COF-10", *J. Chem. Phys.* **133**, 154706 (2010).
5. Jiang, Z. P., Zhou, X., Sun, Q., Wang, Q., and Jena, P.: "Geometry, electronic properties, and hydrogen adsorption properties of Li<sub>3</sub>N-based nanostructures", *J. Phys. Chem. C* **114**, 19202 (2010).
6. Jena, P.: "Materials for Hydrogen Storage: Past, Present, and Future", *J. Phys. Chem. Letters* (invited) **2**, 206 (2011).
7. Zhou, J., Wang, Q., Sun, Q., and Jena, P.: "Enhanced Hydrogen Storage in Li Functionalized BC<sub>3</sub> Nanotube", *J. Phys. Chem. C* **115**, 6136 (2011).
8. Contescu, C. I., van Benthem, K., Li, S., Bonifacio, C. S., Pennycook, S. J., Jena, P., and Gallego, N. C.: "Single Pd Atoms in Activated Carbon Fibers and their Contribution to Hydrogen Storage", *Carbon* **49**, 4050 (2011)
9. Sa L., Zhao, H., and Jena, P.: "Ti-Doped Nano Porous Graphene: A Material for Hydrogen Storage and Sensor", *Frontiers of Phys.* **6**, 204 (2011).
10. Scheicher, R. H, Li, S., Arahujo, C. M., Blomqvist, A., Ahuja, R., and Jena, P.: "Theoretical study of C<sub>60</sub> as catalyst for dehydrogenation in LiBH<sub>4</sub>", *J. Nanotechnology* **22**, 335401 (2011)
11. Reich, T. E., Jackson, K. T., Li, S., Jena, P., and El-Kaderi, H. M.: "Synthesis and characterization of highly porous borazine-linked polymers and their performance in hydrogen storage applications", *J. Mat. Chem.* **21**, 10629 (2011).
12. Lu, K., Zhou, J., Zhou, L., Wang, Q., Sun, Q., and Jena, P.: "Sc-pthalocyanine sheet: Promising material for hydrogen storage", *Appl. Phys. Letts.* **99**, 163104 (2011)
13. Pathak, B., Pradhan, K., Hussain, T., Ahuja, R., and Jena P.: "Functionalized boranes for hydrogen storage", *Chem. Phys. Chem.* **13**, 300 (2012).
14. Wang, Q. and Jena, P.: "Density Functional Theory Study of the Interaction of Hydrogen with Li<sub>6</sub>C<sub>60</sub>", *J. Phys. Chem. Letters* **3**, 1084 (2012)
15. Zhao, Q., Li, S., Pathak, B., Araujo, C. M., Ahuja R., and Jena, P.: "C<sub>60</sub>-mediated hydrogen desorption in Li-N-H systems", *J. Nanotechnology* **23**, 485406 (2012).

## Abstract

---

### “Superhalogens and Beyond - Bare and Supported Clusters”

**Jena, Purusottam**

**Department of Physics, Virginia Commonwealth University, Richmond, VA  
23284-2000**

**pjena@vcu.edu**

#### **PROGRAM SCOPE**

The goal of the project is to provide a fundamental theoretical understanding of the structure-property relationships of a novel class of highly electronegative clusters in the gas phase, study their interaction with support and counter-ions, and explore their potential as building blocks of materials with tailored properties.

The project exploits the unique size and composition specific properties of clusters in the atom-by-atom design of a new class of super- and hyperhalogens with unusual composition and properties. They are designed by using simple electron counting rules, such as the octet, 18-electron, and Wade-Mingos and are used to guide experimentalists in their focused discovery. It deals with four interrelated thematic areas: (1) Using first principles theory we design new highly electronegative clusters whose electron affinities far exceed that of chlorine and validate their properties by working closely with experimentalists. These species, called super- and hyperhalogens, usually consist of a metal atom at the core surrounded by halogen or oxygen atoms. Our goal is to see if super- and hyperhalogens can also be created without a metal, halogen, or oxygen atom by tailoring their size and composition and if their electron affinities can be pushed to values even higher than that currently known. (2) Next we identify suitable counter ions and explore the ability of their corresponding salts to store hydrogen. (3) Superhalogens with magnetic moments are designed using transition metal atoms as key components. (4) Using electronegative species as building blocks we explore the potential of multifunctional nanoparticles with Janus anisotropy for clean energy solutions.

#### **RESEARCH PROGRESS**

In addition to the work on super and hyperhalogens, we have also studied some problems that were motivated by either exciting experiments or by novel properties of matter at the nanoscale. These include: functionalized graphene, metal oxide clusters, magnetism of zero (clusters), one (nanotubes, nanowires), and two (monolayers) dimensional materials. Functionalized graphene with multifunctional properties were also examined. Working closely with experimentalists we have been able to identify a new class of magnetic superhalogens with composition  $(\text{MnCl}_2)_x\text{Cl}$  ( $x=1, 2, 3, \dots$ ).

Unlike conventional superhalogens that contain a metal atom at the core, the core of these superhalogens is  $(\text{MnCl}_2)_x$  with each Mn carrying a magnetic moment of 5 Bohr magneton. Similar synergy has also led us to the discovery of hyperhalogens containing noble metal atoms (Cu, Ag, Au) at the core and  $\text{BO}_2$  superhalogen moieties as ligands. Our efforts have resulted in 63 publications during 2010-2012 with three more articles in press. An invited perspective by the PI entitled “Beyond the Periodic Table of Elements: Role of Clusters” is scheduled for publication in the Journal of Physical Chemistry Letters in April 2013. This article describes the design of specific clusters as superatoms whose chemistry mimics that of an atom in the periodic table and demonstrates how superatoms can serve as building blocks of a new three dimensional periodic table. The article also summarizes the advancements that have been made in this field and the future challenges.

## FUTURE PLANS

During the remainder of the project we will be studying an entirely new class of hyperhalogens that contain metal clusters or complexes as the core with  $\text{BO}_2$  as ligands. The objective is to extend the limits of negative ions to complex species so that new salts with uncommon properties can be formed. One such class of materials is  $\text{KAl}(\text{BH}_4)_4$  which is made from two well-known salts  $\text{KBH}_4$  and  $\text{Al}(\text{BH}_4)_3$ . One can view  $\text{KAl}(\text{BH}_4)_4$  as composed of a  $\text{K}^+$  cation and  $\text{Al}(\text{BH}_4)_4^-$  anion, the latter being as a hyperhalogen. These studies are complemented by simultaneous experimental investigations by our collaborators.

## PUBLICATIONS in 2010-2012

*Due to space limitation the following list includes publications only in 2011 and 2012. The list of publications in 2010 (17 original papers, 2 review articles, and one edited book) can be obtained from the PI.*

1. Zhou, J. Wang, Q., Sun, Q., and Jena, P.: “Stability and electronic structure of bilayer graphone”, *Appl. Phys. Letters* **98**, 063108 (2011)
2. Wu, M. M., Wang, Q., Sun, Q., and Jena, P.: “Reaction induced magnetic transition in  $\text{Mn}_2$  dimers”, *J. Phys. Chem. A* **115**, 549 (2011).
3. Wu, M. M., Wang, H., Ko, Y. J., Kandalam, A. K., B. Kiran, Wang, Q., Sun, Q., Bowen, K. H., and Jena, P.: “Manganese Based Magnetic Superhalogens”, *Angew. Chem. Int. Ed.* **50**, 2568 (2011).
4. Feng, Y., Xu, H-Guang, Zheng, W., Zhao, H., Kandalam, A. K., and Jena, P.: “Structures and Photoelectron Spectroscopy of  $\text{Cu}_n(\text{BO}_2)_m$  ( $n, m=1, 2$ ) Clusters: Observation of Hyperhalogen Behavior”, *J. Chem. Phys.* **134**, 094309 (2011).
5. Pradhan, K., Gutsev, G. L., Weatherford, C. A., and Jena, P.: “A systematic study of neutral and charged 3d-metal trioxides and tetraoxides”, *J. Chem. Phys.* **134**, 144305 (2011).
6. Zhou, J., Lv, K., Wang, Q., Chen, X. S., Sun, Q., and Jena, P.: “Electronic Structures and Bonding of graphyne sheet and its BN analog”, *J. Chem. Phys.* **134**, 174701 (2011).
7. Pradhan, K., Gutsev, G., Weatherford, C., and Jena, P.: “Interactions of a Mn atom with halogen atoms and stability of its half-filled 3d-shell”, *J. Chem. Phys.* **134**, 234311 (2011)

8. Musfeldt, J. L., Liu, Z., Li, S., Kang, J., Jena, P., Manson, J., Schlueter, J., Carr, L. G., Whangbo, M.: "Pressure-induced local structure distortion in  $\text{Cu}(\text{pyz})\text{F}_2(\text{H}_2\text{O})_2$ ", *J. Inorg. Chem.* **50**, 6347 (2011).
9. Zhou, J., Wang, Q., Sun, Q., and Jena, P.: "Intrinsic ferromagnetism in two-dimensional carbon structures: Triangular grapheme nanoflakes linked by carbon chains", *Phys. Rev. B. Rapid Commun.* **84**, 081402(R) (2011).
10. Pathak, B., Samanta, D., Ahuja, R., and Jena, P.: "Borane Derivatives: A new class of super and hyper halogens", *Chem. Phys. Chem.* **12**, 2422 (2011)
11. Gutsev, G. L., Weatherford, C. A., Pradhan, K., and Jena, P.: "Density Functional Study of Neutral and Anionic  $\text{AlO}_n$  and  $\text{ScO}_n$  with High Oxygen Content", *J. Comp. Chem.* **32**, 2974 (2011).
12. Pradhan, K. and Jena, P.: "Potential Candidates for Hyperhalogens: A Comparative Study of  $\text{BO}_2$ ,  $\text{AlO}_2$ , and  $\text{VO}_3$ ", *J. Chem. Phys.* **135**, 144305 (2011)
13. Samanta, D., Wu, M. M., and Jena, P.: " $\text{Au}(\text{CN})_n$  Complexes: "Superhalogens with pseudohalogens as building blocks", *J. Inorg. Chem.* **50**, 8918 (2011)
14. Li, X. W., Wang, Q., and Jena, P.: "Ferromagnetism in 2-D carbon chains linked by 1,3,5-benzenetriyl units", *J. Phys. Chem. C* **115**, 19621 (2011)
15. Paduani, C., Wu, M., Willis, M., and Jena, P.: "Theoretical Study of the Stability and Electronic Structure of  $\text{Al}(\text{BH}_4)_n$  and  $\text{Al}(\text{BF}_4)_n$  ( $n=1-4$ ) and their Hyperhalogen Behavior", *J. Phys. Chem. A* **115**, 10237 (2011).
16. Zhao, H. Wu, M. M., Wang, Q., and Jena, P.: "Effects of charging and doping on orbital hybridizations and distributions in  $\text{TiO}_2$  clusters", *Physica B* **406**, 4322 (2011).
17. Kan, M., Zhou, J., Wang, Q., Sun, Q., and Jena, P.: "Tuning the electronic and magnetic properties BN sheet impregnated with graphene flakes", *Phys. Rev. B* **84**, 205412 (2011)
18. Samanta, D. Wu, M. M., and Jena, P.: "Unique Spectroscopic Signature of Nearly Degenerate Isomers of  $\text{Au}(\text{CN})_3$  Anion", *J. Phys. Chem. Letters* **2**, 3027 (2011)
19. Wu, M. M., Zhong, X., Wang, Q., Sun, Q., Pandey, R., and Jena, P.: "Anisotropy and Transport Properties of Tubular C-BN Janus Nanostructures", *J. Phys. Chem. C* **115**, 23978 (2011)
20. Ko, Y. J., Wang, H., Pradhan, K., Koirala, P., Kandalam, A., Bowen, K., and Jena, P.: "Superhalogen Properties of  $\text{Cu}_m\text{Cl}_n$  Clusters: Theory and Experiment", *J. Chem. Phys.* **135**, 244312 (2011)
21. Li, X., Bowen, Jr., K. H., Jena, P., and Kandalam, A.: "Photoelectron Spectroscopic Study of Iron-Pyrene Cluster Anions", *J. Chem. Phys.* **135**, 204301 (2011)
22. Pradhan, K. and Jena, P.: "Double exchange mediated ferromagnetic coupling between Co atoms in di-cobalt complex", *Appl. Phys. Letters.* **99**, 153105 (2011)
23. Gutsev, G. L., Weatherford, C. A., Johnson, L. E., and Jena, P.: "Structure and properties of the aluminum borates  $\text{Al}(\text{BO}_2)_n$  and  $\text{Al}(\text{BO}_2)_n^-$  series ( $n=1-4$ )", *J. Comp. Chem.* **33**, 416 (2012).
24. Paduani, C. and Jena, P.: "A recipe for designing molecules with ever increasing electron affinities", *J. Phys. Chem. A* **116**, 1469 (2012).
25. Wang, Q., Sun Q., Ye, D.X, Kawazoe Y., and Jena, P.: "Adsorption of oxygen-containing functional groups on free and supported graphene", *Phys. Rev. B.* **85**, 085404 (2012).
26. Pradhan, K. and Jena, P.: "Doping induced magnetic transition in Mn-based molecular systems", *Chem. Phys. Lett.* **525-26**, 97 (2012)
27. Kan, M., Zhou, J., Sun, Q., Wang, Q., Kawazoe, Y., and Jena, P.: "Tuning Magnetic properties of Graphene Nanoribbons with Topological Line Defects: From Antiferromagnetic to ferromagnetic", *Phys. Rev. B.* **85**, 155450 (2012)

28. Li, X., Zhou, J., Wang, Q., Kawazoe, Y., and Jena, P.: "Magnetism of two-dimensional triangular nanoflakes based kagome lattices", *New J. Phys.* **14**, 033043 (2012)
29. Gutsev, G. L.; Weatherford, C.; Jena, P. ; Johnson, E.; and Ramachandran, B.: "Structural Patterns in Carbon Chemisorption on an Icosahedral Iron Cluster", *J. Phys. Chem. C* **116**, 7050 (2012)
30. Joseph, J., Pradhan, K., Jena, Wang, H., Ko, Y. J., Zhang, X., and Bowen, K. H.: "Evolution of the superhalogen properties in  $\text{PtCl}_n$  clusters", *J. Chem. Phys.* **136**, 194305 (2012).
31. Samanta, D. and Jena, P.: "Zinc in +III Oxidation State", *J. Am. Chem. Soc. (communications)* **134**, 8400 (2012)
32. Reich, T. E., Behera, S., Jackson, K. T., Jena, P., and El-Kaderi, H. M.: "Highly Selective  $\text{CO}_2/\text{CH}_4$  Gas Uptake by a Halogen-Decorated Borazine-Linked Polymer", *J. Mat. Chem.* **22**, 13524 (2012)
33. Behera, S. and Jena, P.: "Stability and Spectroscopic Properties of Singly and Doubly Charged Anions", *J. Phys. Chem. A* **116**, 5604 (2012)
34. Gupta, B., Konar, S., and Jena, P.: "Electrical transition of (3,3) carbon nanotube on patterned hydrogen terminated  $\text{Si}(001)\text{-}2\times 1$  driven by electric field", *J. Appl. Phys.* **111**, 123717 (2012)
35. Xiong, G., Zhou, L., Yawei, L., Sun, Q., and Jena, P.: "Design of metal-free dyes for dye-sensitized solar cells", *Phys. Letts. A* **376**, 2595 (2012)
36. Li, X. W., Zhou, J, Wang, Q., and Jena, P.: "Magnetic properties of two dimensional silicon carbide triangular nanoflakes based kagome lattices", *J. Nanoparticle Research* **14**, 1056 (2012)
37. Gupta, B. C., Konar, S., and Jena, P.: "Electric field induced metallic transition of (3,3) carbon nanotube supported on patterned hydrogen terminated  $\text{Si}(001)\text{-}1\times 1$  surface", *J. Nanoparticles Research* **14**, 909 (2012)
38. Paduani, C., and Jena, P.: "Super and hyperhalogen behavior in  $\text{MgX}_n$  and  $\text{GdX}_n$  ( $X = \text{F}, \text{BF}_4$ ) clusters", *J. Nanoparticles Research* **14**, 1035 (2012)
39. Gu, X, Zhou, L., Li, Y., Sun, Q., and Jena, P.: "Design of new metal-free dyes for dye-sensitized solar cells : A first-principles study", *Phys. Letters* **376**, 2595 (2012).
40. Zhou, J., Wang, Q., Sun, Q., Kawazoe, Y., and Jena, P.: "Strain induced spin crossover in phthalocyanine organometallic sheet", *J. Phys. Chem. Letters* **3**, 3109 (2012)
41. Wu, M., Burton, J. D.; Tsymbal, E. Y.; Zeng, X. .; and Jena, P: "Multiferroic Materials based on Transition Metal-Organo-metallic-Nanowires", *J. Am. Chem. Soc.* **134**, 14423 (2012).
42. Gutsev, G. L., Weatherford, C. A., Jena, P., Johnson, E., and Ramachandran, B. R.: "Structure and Properties of  $\text{Fe}_n$ ,  $\text{Fe}_n^-$ , and  $\text{Fe}_n^+$  clusters,  $n = 7 - 20$ ", *J. Phys. Chem. A* **116**, 10218 (2012)
43. Wu, M., Kandalam, A. K., Gutsev, G., and Jena, P.: "Origin of the Anomalous Magnetic Properties of  $\text{Fe}_{13}^+$  Cluster", *Phys. Rev. B* **86**, 174410 (2012)
44. Koirala, P., Pradhan, K., Kandalam, A., and Jena, P.: "Electronic and Magnetic Properties of Manganese and Iron Atoms Decorated with  $\text{BO}_2$  Superhalogens", *J. Phys. Chem. A* (invited) (in press)
45. Wu, M., Burton, J. D., Tsymbal, E. Y., Zheng, X., and Jena, P.: "Hydroxyl-decorated grapheme systems as candidates for organic metal-free ferroelectrics, multiferroics, and high-performance proton battery cathode materials", *Phys. Rev. B (Rapid Communication)* (in press)
46. Jena, P.: "Beyond the Periodic Table of Elements: Role of Superatoms", *J. Phys. Chem. Letters* (invited Perspective, in press).

## Optical and Electrical Properties of III-Nitrides and Related Materials

Hongxing Jiang and Jingyu Lin, Texas Tech University  
hx.jiang@ttu.edu; jingyu.lin@ttu.edu

### Project Scope

Among the members of the III-nitride material system, boron-nitride (BN) is the least studied and understood. Due to its extraordinary physical properties such as ultra-high bandgap ( $E_g \sim 6$  eV) and chemical stability, negative electron affinity, and a very large thermal neutron (0.025 eV) capture cross section, BN is very promising for applications of deep ultraviolet optoelectronic devices and solid-state neutron detectors to replace  $^3\text{He}$  gas detectors, which face serious issue of shortage. Moreover, hexagonal BN (hBN) has a close lattice match to graphene and is the most suitable substrate and dielectric/separation layer for graphene electronics and optoelectronics. Similar to graphene, low dimensional hBN is expected to possess rich new physics. Other potential applications of hBN include super-capacitors and electron emitters. However, our knowledge concerning the semiconducting properties of hBN is very scarce. The goal of this project is to study this “newest” family member of the III-nitride material system, hBN, and to address issues that have not yet been explored but are expected to profoundly influence our understanding on its fundamental properties and device applications. The research efforts include further development of epitaxial growth processes for achieving wafer-scale high crystalline quality hBN epilayers; to investigate the nature of band structures of different polytypes of hBN predicted by theoretical calculations; and to probe the two dimensional (2D) optical and electrical properties of hBN.

### Recent Progress

- Achieved the synthesis by MOCVD of wafer-scale (2-inch) hBN epitaxial layers with high crystalline quality - reflected by the realization of the narrowest linewidth of x-ray diffraction ( $0002$ ) *rocking curve* ( $<400$  arcsec).
- Realized room temperature band edge emissions in hBN with very high emission efficiency. The observed band edge emission efficiency in hBN epilayers is more than two orders of magnitude larger than that in *wurtzite* AlN.
- Investigated novel optical properties of hBN resulted from its unique layered structure. We have shown that the large  $p \rightarrow p$  transition rate combined with the large joint density of states of electron-hole pairs resulting from the 2D nature of hBN lead to high emission efficiency in hBN (in collaboration with Dr. Su-Huai Wei of NREL).
- Deduced exciton Bohr radius and binding energy in 2D hBN from the temperature dependent exciton recombination lifetime to be around 8 Å and 740 meV, respectively.
- Derived the effective masses of electrons and holes in 2D hBN from the dispersion relation of single sheet hBN to be  $0.54m_0$ , which is remarkably consistent with the 2D exciton reduced mass deduced from experiment.
- Demonstrated that hBN represents an ideal platform for probing 2D optical properties in semiconductors.

### List of Publications (The following published works have acknowledged DOE support):

1. B. Huang, X. K. Cao, H. X. Jiang, J. Y. Lin, and S. H. Wei, “Origin of the significantly enhanced optical transitions in layered boron nitride,” *Physical Review B* **86**, 155202 (2012).

2. S. Majety, X. K. Cao, J. Li, R. Dahal, J. Y. Lin and H. X. Jiang, "Band-edge transitions in hexagonal boron nitride epilayers," *Appl. Phys. Lett.* 101, 051110 (2012).
3. A. Sedhain, J. Y. Lin, and H. X. Jiang, "Nature of optical transitions involving cation vacancies and complexes in AlN and AlGaN," *Appl. Phys. Lett.* 100, 221107 (2012).
4. X. K. Cao, S. Majety, J. Li, J. Y. Lin and H. X. Jiang, "Optoelectronic properties of hexagonal boron nitride epilayers," *Proc. SPIE* 8631, 863128 (2013), invited.

# Light Trapping and Solar Energy Harvesting with Photonic Crystals

Sajeev John

Dept. of Physics, University of Toronto, 60 Saint George St., Toronto, Ontario, Canada M5S1A7  
[john@physics.utoronto.ca](mailto:john@physics.utoronto.ca) [www.physics.utoronto.ca/~john](http://www.physics.utoronto.ca/~john)

We have demonstrated that using photonic crystal light trapping effects it is possible to reduce the optimal amount of silicon in a solar cell from over 100 microns to about 1 micron (with a slight reduction, 95%→85%, in the overall fraction of absorbed sunlight). Our conical nano-pore silicon photonic crystal absorbs more sunlight than proposed by the  $4n^2$  Lambertian light trapping limit.

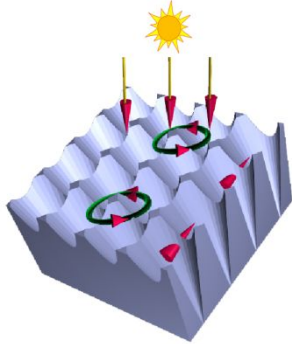


**Figure 1** Optimized slanted conical nano-pore photonic crystal yields MAPD of 36 mA/cm<sup>2</sup> with only 1 micron of silicon. Horizontal red arrows depict parallel to interface refraction of incident sunlight (downward arrows). Green circles depict optical cavity resonances where the electromagnetic Poynting vector exhibits vortex-like flow.

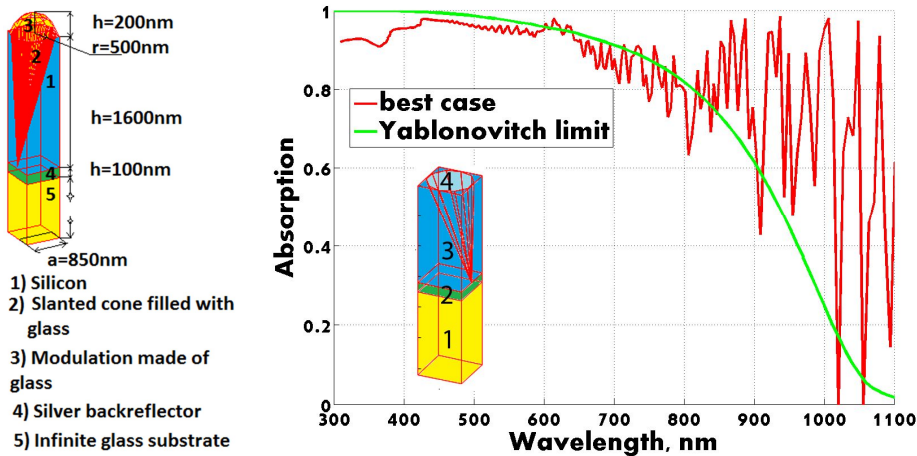


**Figure 2** Conical nano-pore photonic crystals consisting of one micron of silicon (left panel) reveal stronger light trapping than their nano-wire counterparts. Light absorption in the near infrared (850-1100 nm) exceeds the Lambertian statistical ray trapping (Yablonovitch) limit and yields a MAPD of 36 mA/cm<sup>2</sup> (right panel).

Our photonic crystal nano-pore solar cell designs, using only one micron of silicon, enable power conversion efficiencies in the range of 17.5-23% using lower quality silicon with a carrier diffusion length of only a few microns.

Our photonic crystal nanowire solar cell designs using only one micron of silicon enable power efficiencies in the range of 15-20% using lower quality silicon with a carrier diffusion length of only a few microns. For thick silicon solar cells similar efficiencies require very high quality (expensive) crystalline silicon with a diffusion length of about 100 microns.

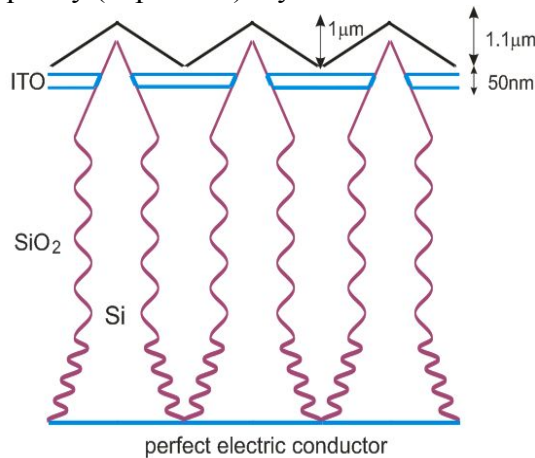


**Figure 3** Solar cell geometry consists of modulated silicon nanowires placed on a perfect reflecting back contact and connected to a transparent upper ITO contact. The entire structure is encased in a SiO<sub>2</sub> background that is weakly modulated at the top air interface. This modulation of the SiO<sub>2</sub> packaging serves as a graded refractive index and offsets solar reflection from the ITO contact.

Photonic crystal designs for silicon-based solar cells (utilizing one micron of silicon) provide exceptional angular response to incoming sunlight. Unlike thick silicon solar cells that require mechanical tracking of the sun, our power conversion efficiencies remain in the 15-20% range even when incident (direct) sunlight impinges on the photonic crystal solar cell at an angle of 60 degrees relative to the normal.

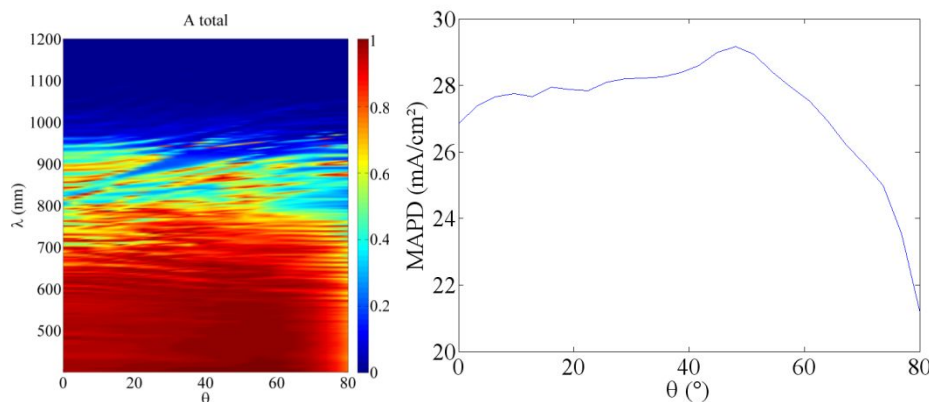


**Figure 4** Left panel depicts the total solar absorption over the entire nanowire. Right panel depicts the maximum achievable photocurrent density (MAPD) assuming that all incident sunlight is collimated at a particular angle of incidence.

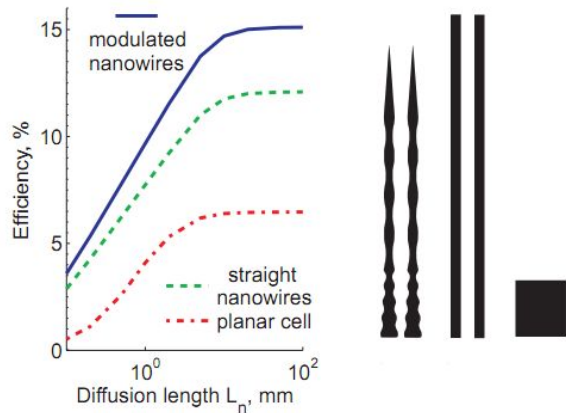


**Figure 5** Comparison of solar cell power efficiencies in three geometries (each with 1 micron equivalent bulk thickness of silicon) as a function of the carrier diffusion length (**measured in microns**). For a diffusion length of more than 3 microns, the modulated nanowire photonic crystal achieves 15% power efficiency, whereas the optimized straight nanowire photonic crystal exhibits 12% efficiency. A solid film with (hypothetical) perfect antireflection coating and perfect back-reflector yields less than 6% power efficiency.

Using optimized **GaAs photonic crystal nanowires and nano-pores**, it is possible to absorb about 95% of available sunlight above the electronic band gap using only 200 nm equivalent bulk thickness of GaAs. With 200 nm of GaAs, the MAPD is nearly 28 mA/cm<sup>2</sup>. For 100 nm of GaAs, this MAPD drops only slightly to 25 mA/cm<sup>2</sup>.

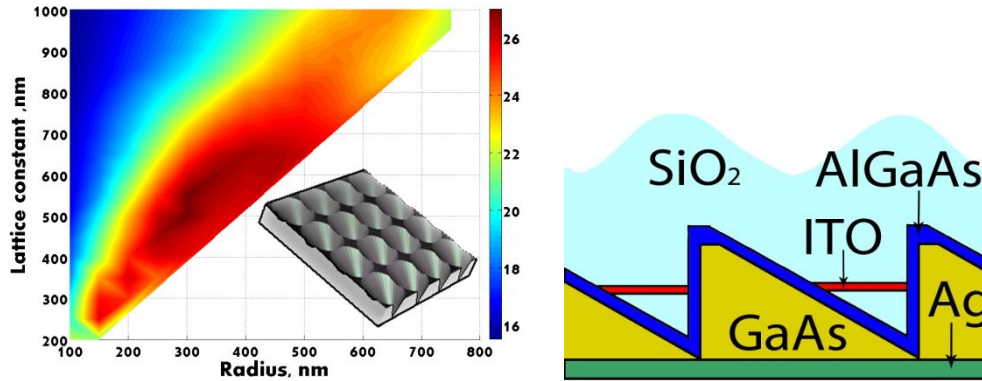


**Figure 6a** depicts a MAPD map revealing maximal short circuit current of 27 mA/cm<sup>2</sup> for the optimal lattice constant  $a=550$  nm and upper slanted cone radius of 300 nm. **Figure 6b** depicts this structure placed in a solar cell architecture with 10 nm AlGaAs surface passivation layer, SiO<sub>2</sub> packaging, a transparent ITO upper contact and a silver back-reflecting contact.

We studied various thicknesses of GaAs ranging from 50 nm to 500 nm and performed a similar optimization in each case. Unlike silicon, where the ideal thickness is about 1 micron, the ideal thickness of GaAs is 200 nm. Figure 7 shows that for very thin films (< 350 nm), the GaAs structure packaged with SiO<sub>2</sub> performs better than the unpackaged structure. Moreover, our optimization reveals that the MAPD saturates to its highest value when the GaAs equivalent bulk thickness reaches 200 nm. Negligible improvement in MAPD is found using more than 200 nm of GaAs. By halving the amount of GaAs to 100 nm, a relatively large MAPD of 25 mA/cm<sup>2</sup> is still obtained.

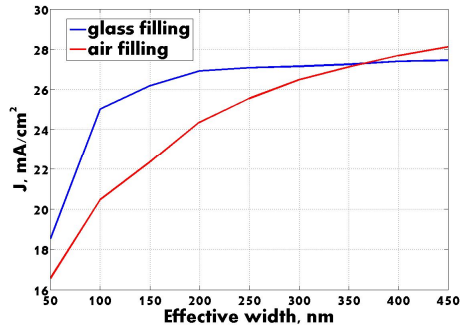


**Fig 7** The maximum achievable photo-current density (MAPD) is plotted for various optimized GaAs slanted conical pore photonic crystals resting on a perfect metallic back-reflector for various choices of the equivalent bulk thickness of GaAs (effective width) ranging from 50-450 nm. The blue curve corresponds to photonic crystals packaged in SiO<sub>2</sub>. The red curve corresponds to no SiO<sub>2</sub> packaging.

Photonic crystal based light trapping can improve the efficiency of dye-sensitized TiO<sub>2</sub> solar cells by at least 33%. This is not as large an improvement as in the case of silicon solar cells. The reason for the diminished role of light trapping is the absorption profile of current dyes that absorb very strongly above a certain cut-off frequency and then absorb virtually nothing below the cut-off. A broader and more gradual dye spectrum would lead to greater synergy with light trapping mechanisms. The 33% improvement is nevertheless quite significant for this industry.

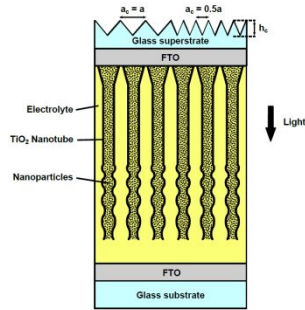


**Fig 8**

Cell geometry (not to scale) with linearly chirped sinusoidal modulation added to the lower portion of the nanotube array and triangular corrugation added to the air/glass interface. The modulation period increases towards the bottom of the array, with a constant amplitude  $A$ . The height of the modulated region is set to 0.52 times the total array height. The corrugation has height  $h_c$  and period  $a_c$ . We study the cases  $a_c = a$  (shown on the left of the diagram) and  $a_c = a/2$  (shown on the right).

1. A. Deinega and Sajeev John, "Effective optical response of silicon to sunlight in the FDTD method", Optics Letters Vol. 37, Issue 1, pp. 112-114 (2012).
2. G. Demesy and Sajeev John, "Solar energy trapping with modulated silicon nanowire photonic crystals" J. Appl. Phys., **112**, 074326 (2012)
3. A. Deinega and Sajeev John, "Solar power conversion efficiency in modulated silicon nanowire photonic crystals" J. Appl. Phys. **112**, 074327 (2012)
4. A. Deinega and Sajeev John, "Finite difference discretization of semiconductor drift-diffusion equations for nanowire solar cells" Computer Physics Communications: May 23 (2012) doi: 10.1016/j.cpc.2012.05.016
5. S. Eiderman, Sajeev John, A Deinega, "Solar light trapping in slanted conical pore photonic crystals: beyond statistical ray trapping" submitted to J. of Applied Physics
6. S. Foster and S. John, "Light Trapping in Dye-Sensitized Solar Cells", Energy and Env. Science (accepted)
7. A. Deinega, Sajeev John, and S. Eiderman, "Solar energy harvesting in conical pore silicon photonic crystals: power conversion optimization" to be submitted to J. of Applied Physics
8. S. Eiderman, Sajeev John, A Deinega, "Solar light trapping optimization in thin-film GaAs photonic crystals" to be submitted

## **Program Title: Bridging Atomistic and Continuum Scales in Phase-Field Modeling of Stressed Polycrystalline Materials**

**Principal Investigator:** Alain Karma

**Address:** Department of Physics and Center for Interdisciplinary Research on Complex Systems, Northeastern University, 360 Huntington Avenue, Boston, Massachusetts 02115

**Email:** a.karma@neu.edu

### **Program Scope**

This research focuses on the development of state-of-the-art scale-bridging phase-field methodologies to understand the physical behavior of stressed polycrystalline materials relevant for energy. A primary focus is the investigation of fundamental equilibrium and non-equilibrium properties of materials interfaces including solid-liquid interfaces, grain and compositional domain boundaries, and surfaces. This research takes advantage of a wealth of new observations from in situ imaging studies of those interfaces and recent advances in atomistic and continuum simulations. Conventional phase-field and phase-field-crystal (PFC) simulations are combined when possible with molecular dynamics (MD) simulations in an effort to bridge quantitatively atomistic and continuum length and time scales. MD simulations provide a direct quantitative link to interatomic force fields while PFC simulations access much longer diffusive time scales and provide a theoretical thermodynamics framework to understand generic behaviors. This makes the two approaches highly complementary. Specific phenomena under investigation include the formation of nanometer-thin intergranular liquid films at high homologous temperature and their impact on shear resistance that underlies important casting defects, fundamental mechanisms of curvature- and stress-driven grain boundary motion that impact the behavior of nanocrystalline materials, and the complex interaction of grain and compositional domain boundaries in the presence of large misfit strain. Multiscale modeling is expected to contribute new scientific understanding of interfacial processes relevant for the improved performance, design, and safety of diverse polycrystalline energy materials from structural alloys for the automotive and aerospace industries to energy storage materials.

### **Recent progress**

#### ***Premelting and shearing of hot grain boundaries in elemental materials and binary alloys.***

The atomic structure of a grain boundary (GB) can exhibit pronounced disorder at high homologous temperatures. This structural disorder commonly involves the formation of nanometer-scale intergranular films with liquid-like properties below the bulk melting point, a phenomenon commonly referred to as GB premelting. We have used PFC and MD simulations to investigate the equilibrium premelting and nonequilibrium shearing behaviors of [001] symmetric tilt GB at high homologous temperature in classical models of bcc Fe [12,13]. The premelting behavior was characterized using our previously developed methodology for computing the thermodynamic *disjoining potential*  $V(W)$  as a function of the width  $W$  of the disordered liquid-like intergranular layer. The derivative of this potential with respect to  $W$  is a direct measure of the structural force between crystal-melt interfaces due to the spatial overlap of crystal density waves. We find that low angle GBs with misorientation  $\theta$  less than about 15 degrees away from (100) or (110) planes display an

attractive potential with a shallow minimum (top of Fig. 1). Those GBs will therefore retain a finite layer width at the melting point, and remain “dry”. In contrast, GBs with a larger misorientation display a purely repulsive potential, and exhibit a diverging layer width at the melting point and become “wet”. The predicted misorientation ranges for dry and wet GBs PFC and MD simulations are in good agreement. We have also investigated the response to a shear stress of GBs as a function misorientation. We characterized this response by the coupling factor  $\beta = v_n/v_{||}$ , which is the ratio of the normal GB velocity  $v_n$  and the relative translation velocity  $v_{||}$  of two grains in a bi-crystal geometry, where the velocity is induced by an applied shear stress parallel to the GB plane. For small misorientation we find (Fig. 1) that the coupling factor follows well its geometrically predicted ideal value  $\beta_{ideal}$  corresponding to a pure glide motion of dislocations. In contrast, for larger misorientation, we find that pure coupling only occurs for homologous temperatures below about 0.8. Above this temperature, GBs exhibit partial or complete sliding, with the range of misorientation corresponding to sliding increasing with temperature. These results establish a clear relationship between GB premelting and sliding for symmetric tilt GBs at high homologous temperature. Our ongoing extension of those studies to alloys have revealed a strong dependence of the disjoining potential on solute addition that can shift grain coalescence to lower temperature, thereby promoting hot tearing.

***New methodology for extracting grain boundary mobilities from equilibrium fluctuations.*** In collaboration with Mishin’s group (supported by a in the Physical Behavior of Materials program), we have developed a new methodology to extract quantitatively the mobilities for GB migration (i.e. normal to the GB plane) and pure sliding from an analysis of equilibrium fluctuations [11]. Previous fluctuation analyses only predicted the migration mobility for high angle GBs that display an Edwards-Wilkinson  $1/k^2$  capillary fluctuation spectrum. Our new results provide the means to also calculate the pure sliding mobility of those

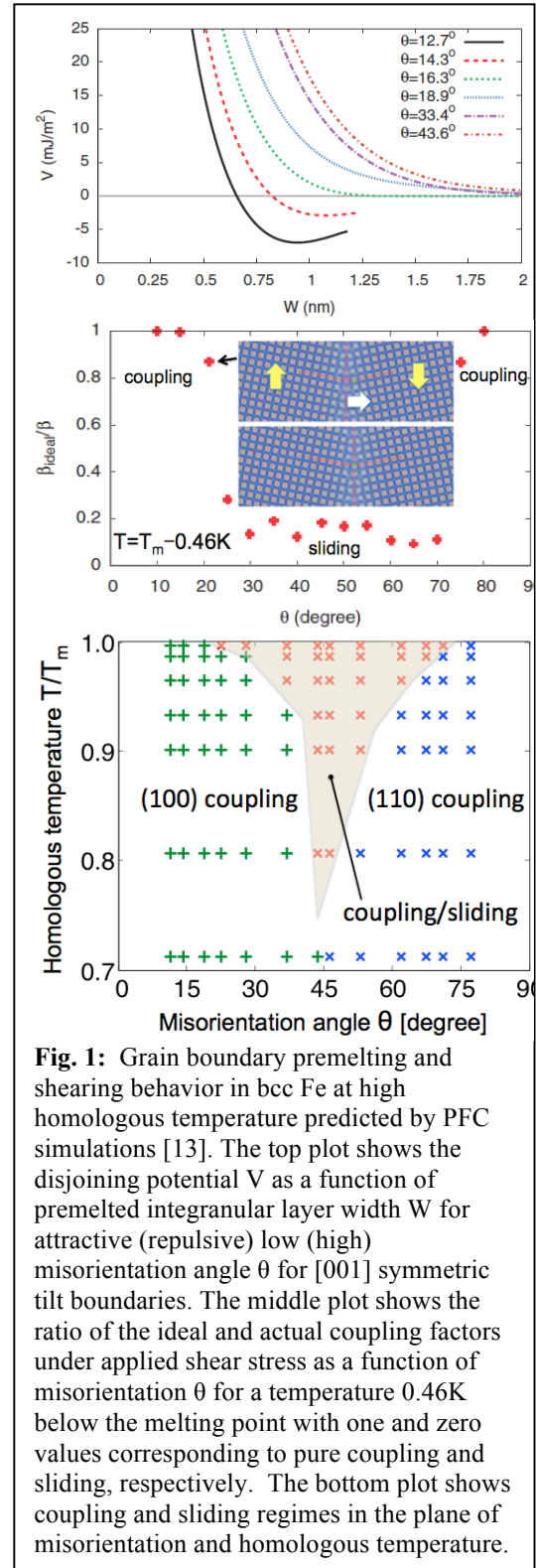


**Fig. 1:** Grain boundary premelting and shearing behavior in bcc Fe at high homologous temperature predicted by PFC simulations [13]. The top plot shows the disjoining potential  $V$  as a function of premelted intergranular layer width  $W$  for attractive (repulsive) low (high) misorientation angle  $\theta$  for [001] symmetric tilt boundaries. The middle plot shows the ratio of the ideal and actual coupling factors under applied shear stress as a function of misorientation  $\theta$  for a temperature  $0.46K$  below the melting point with one and zero values corresponding to pure coupling and sliding, respectively. The bottom plot shows coupling and sliding regimes in the plane of misorientation and homologous temperature.

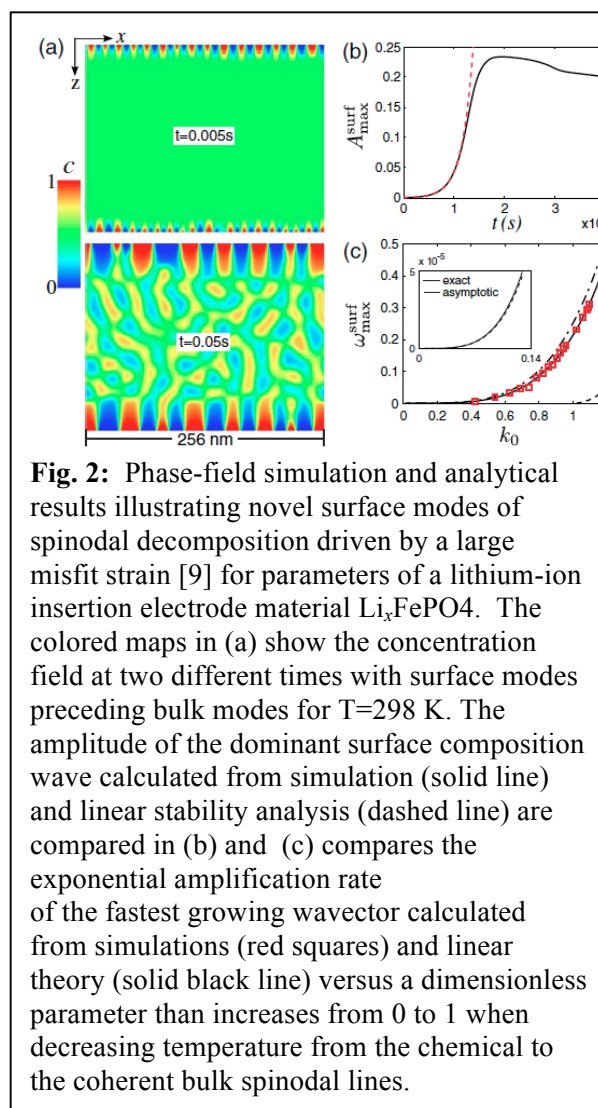
boundaries in response to a shear stress in the limit of vanishing driving force from an analysis of the random walk of the GB shear (i.e the relative translation of the two crystals). They also provide the means to calculate the migration mobility for low angle GBs that display a distinct  $1/k$  fluctuation spectrum dominated by elastic strain energy. These results shed light on the relationship between grain boundary fluctuation and motion coupled to shear deformation. Furthermore, they establish a new computational methodology for extracting nonequilibrium GB properties in the experimentally relevant limit of vanishing driving force that is notoriously hard to access by non-equilibrium MD simulations.

***Coupled motion of asymmetrical tilt grain boundaries: molecular dynamics and phase field crystal simulations.***

In a collaboration with Mishin’s group, we have carried out a joint PFC and MD simulation study of the stress-driven motion of asymmetrical GBs [10]. Our first main finding is that the coupling effect exists for most of the asymmetrical GBs. Our second main finding is that the coupling factor  $\beta$  exhibits a non-trivial dependence on both the misorientation and inclination angles. This dependence is characterized by a discontinuous change of sign of the  $\beta$ , which reflects a transition between two different coupling modes over a narrow range of angles. More importantly, we find that the magnitude of  $\beta$  becomes large or divergent within this transition region. This divergence gives rise to a sliding-like behavior that is present even at low homologous temperature, in contrast to symmetric tilt GBs that only display sliding at high homologous temperature (cf. Fig. 1). The simulation results agree well with existing experimental measurements and also allowed us to identify different dislocation mechanisms responsible for the motion of asymmetrical tilt GBs in the absence and presence of dislocation climb.

***Novel surface modes of coherent spinodal decomposition.***

In a collaboration with Ming Tang at LLNL, we have used linear stability theory and phase-field simulations to show that spontaneous phase separation in elastically coherent solids is fundamentally altered by the presence of free surfaces [9]. Due to misfit stress relaxation near surfaces, phase separation is mediated by unique surface modes of spinodal decomposition (Fig. 2). Those modes have faster kinetics than bulk modes and are unstable even when spinodal



decomposition is suppressed in the bulk. Consequently, in the presence of free surfaces, the limit of metastability of supersaturated solid solutions of crystalline materials is shifted from the coherent to chemical spinodal. Those novel surface modes are directly relevant to the phase separation kinetics of lithium-ion insertion electrode materials with a large misfit strain, and account for experimentally observed FePO<sub>4</sub>/LiFePO<sub>4</sub> domains on the surface of thin plate particles. They are also more broadly relevant to nanostructured materials.

### Future Plan

In our future studies, we plan to (i) extend our investigation of GB shearing to binary alloys for both symmetric and asymmetric tilt GBs, (ii) extend our new methodology to extract GB equilibrium and non-equilibrium properties from equilibrium fluctuations to GBs displaying mixed coupling and sliding behavior, (iii) use the identified dislocation mechanisms of GB motion for asymmetrical GBs as a basis to test the ability of the PFC approach to quantitatively model dislocation climb at high homologous temperature on diffusive time scales, (iv) extend the study of novel surface modes of spinodal decomposition to investigate the complex interaction of composition domain boundaries and GBs.

### References to DOE sponsored publications (2010-2012 and 2013 until 3/10/2013)

1. Phase-field crystal model for fcc ordering, K.-A. Wu, A. Adland, and A Karma, *Phys. Rev E* **81**, 061601 (2010).
2. Multi-phase-field analysis of short-range forces between diffuse interfaces, N. Wang, R. Spatschek, and A Karma, *Phys. Rev E* **81**, 051601 (2010).
3. Amplitude equations for polycrystalline materials with interaction between composition and stress, R. Spatschek and A Karma, *Phys. Rev B* **81**, 214201 (2010).
4. Structural disjoining potential for grain-boundary premelting and grain coalescence from molecular-dynamics simulations, S. J. Fensin, D. Olmsted, D. Buta, M. Asta, A. Karma, and J. J. Hoyt, *Phys. Rev. E* **81**, 031601 (2010).
5. Helical crack-front instability in mixed mode fracture, A. J. Pons and A. Karma, *Nature* **464**, 85-89 (2010).
6. "Phase-Field Modeling of Crack Propagation", R. Spatschek, E. Brener, and A Karma, *Phil. Mag.* **91**, 75-95 (2011).
7. "Dislocation-Pairing Transitions in Hot Grain Boundaries", D. L. Olmsted, D. Buta, A. Adland, S. M. Foiles, M. Asta, and A. Karma, *Phys. Rev. Lett.* **106**, 046101 (2011).
8. "Theoretical analysis of crack front instability in mode I+III", J.-B. Leblond, A. Karma, and V. Lazarus, *J. Phys. Mech. Solids* **59**, 1872-1887 (2011).
9. "Surface modes of coherent spinodal decomposition", M. Tang and A. Karma, *Phys. Rev. Lett.* **108**, 265701 (2012).
10. "Coupled motion of asymmetrical tilt grain boundaries: Molecular dynamics and phase-field crystal simulations", *Acta Materialia* **60**, 6528-6546 (2012).
11. "Relationship between Equilibrium Fluctuations and Shear-Coupled Motion of Grain Boundaries", A. Karma, Z.T. Trautt, and Y. Mishin, *Phys. Rev. Lett.* **109**, 095501 (2012).
12. "Structural short-range forces between solid-melt interfaces", R. Spatschek, A. Adland, and A. Karma, *Phys. Rev. B* **87**, 024109 (2013).
13. "Phase-field-crystal study of grain boundary premelting and shearing in bcc iron", A. Adland, A. Karma, R. Spatschek, D. Buta, and M. Asta, *Phys. Rev. B* **87**, 024110 (2013).

# Electron dynamics in nanostructures in strong laser fields

**Matthias F. Kling**

James R. Macdonald Laboratory, Department of Physics

Kansas State University, Manhattan, KS 66506

*Email: kling@phys.ksu.edu*

## Program Scope

The goal of our research is to gain deeper insight into the collective electron dynamics in nanosystems in strong, ultrashort laser fields. The laser field strengths will be strong enough to pull out and accelerate electrons from the nanoparticles and to transiently modify the materials electronic properties. We aim to observe, with sub-cycle resolution reaching the attosecond time domain, how collective electronic excitations in nanoparticles are formed, how the strong field influences the optical and electrical properties of the nanomaterial, and how the excitations in the presence of strong fields decay.

## Recent progress

Electron motion in condensed matter driven by intense light waves in the visible can proceed on attosecond timescales, where the propagation of electrons is restricted to nanometer dimensions. Laser pulses with well-defined electric field waveforms provide an ideal tool for manipulating this motion and offer unique spatio-temporal control on nanometer spatial and attosecond temporal scales [Hommelhoff et al.(2013)]. Such laser pulses in the few-cycle regime have been used to control the electron emission and acceleration from nanospheres [Zherebtsov et al.(2011)] and from nanotips and to control the electron emission from solids. Theoretical studies have furthermore predicted their application towards the control of the optical and electronic properties of solids [Durach et al.(2011)] and plasmonic fields in nanostructured surfaces for electron acceleration [Süßmann and Kling(2011)] and the generation of attosecond extreme-ultraviolet pulses [Yang et al.(2013), Feist et al.(2013)]. Consequently, the application of such laser fields to nanostructured materials has a high potential for the control of ultrafast nonlinear processes at the nanoscale, with important implications for enhancing laser-driven electron acceleration, the generation of extreme ultraviolet radiation at high repetition rates, and the design of lightwave driven electronic devices for information processing in optical communication.

The electric field of a laser pulse consisting of only a few optical cycles can be described as  $E(t) = E_0(t)\cos(\omega t + \phi)$ , where  $E_0(t)$  is the amplitude envelope function,  $\omega$  the angular frequency of the carrier wave, and  $\phi$  the carrier-envelope phase (CEP). The field evolution of such ultrafast laser fields critically depends on the value of the CEP. Our previous work and most of the work of others was based on the generation of few-cycle laser pulses with well-defined waveforms employing CEP stabilization. Within the last year, in collaboration with Gerhard Paulus (University Jena) and others, we have developed and implemented single-shot carrier-envelope phase tagging in conjunction with 3-dimensional velocity map imaging as an alternative to the detection of CEP-effects implementing carrier-envelope phase stabilization [Rathje et al.(2012)]. As a result, we were able to significantly improve the signal-to-noise ratio in CEP-dependent measurements and acquire high-quality, long acquisition time measurements at kHz repetition rates for the first time. We will highlight the attosecond control of the electron emission and acceleration from nanoparticles, reported in [Zherebtsov et al.(2012)]. We are in the process of completing a new VMI setup for studies at higher intensities and we have built the first part of an attosecond infrastructure for studies with attosecond time resolution. The progress on both fronts will be reported.

## Attosecond control of the electron emission and acceleration from nanoparticles

In our research on nanosystems, we have investigated the electron emission and acceleration from dielectric nanospheres in strong few-cycle laser fields. In our recent studies, intense ( $1 - 4.5 \times 10^{13}$  W/cm<sup>2</sup>) CEP-

stabilized laser pulses with a central wavelength of 720 nm and 5 fs pulse duration were focused onto a beam of 90 nm SiO<sub>2</sub> nanospheres [Zherebtsov et al.(2011)]. The nanoparticles were inserted into the gas phase by aerosol preparation and aerodynamic lens focusing and the momentum distribution of emitted electrons was obtained with a VMI spectrometer [Zherebtsov et al.(2011)]. By using a beam of isolated nanoparticles we can also explore the regime near, at and beyond the material damage threshold. The extremely short pulse duration of only a few cycles in our studies ensures that the electron dynamics responsible for the observed phenomena occurs before any nuclear dynamics. High kinetic energy electrons up to 100 eV were observed. The asymmetry of the electron emission in the direction of the polarization vector showed a pronounced CEP dependence in the energy range up to the cutoff energy [Zherebtsov et al.(2011)]. The intensity dependent measurements indicated a nearly linear dependence of the cutoff energy on laser intensity in the investigated intensity range with an average cutoff value of ca.  $50 U_p$  ( $U_p$  is the ponderomotive potential of an electron in the laser field). This number is about a factor of five over the classical  $10 U_p$  cutoff for above-threshold ionization of atoms.

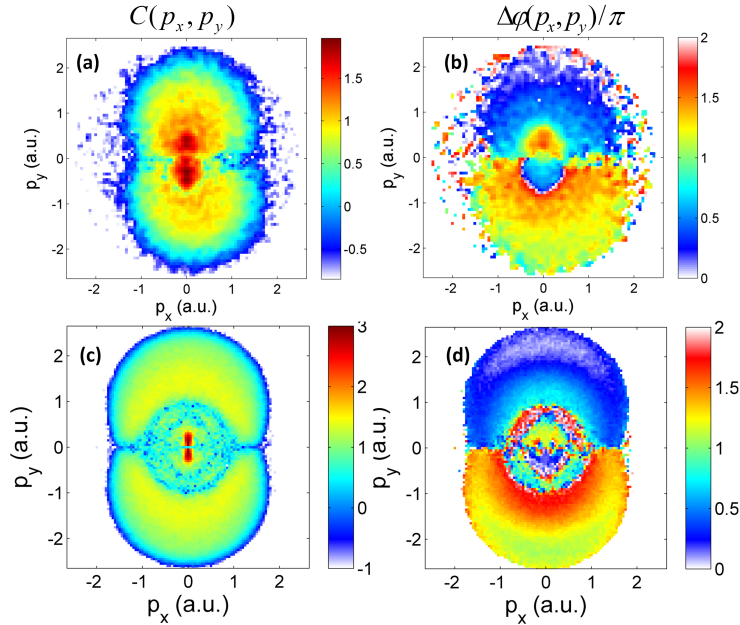


Figure 1: Amplitude (a) and phase (b) of the CEP dependent part of the electron emission obtained from the measurements of SiO<sub>2</sub> nanoparticles of 95 nm diameter for a laser intensity of  $3.7 \times 10^{13} \text{ W/cm}^2$ . Calculated amplitude (c) and phase (d) of the CEP dependent part of the electron emission. From [Zherebtsov et al.(2012)].

We have recently extended on these first results using our novel combined single-shot phase-tagged VMI approach [Süßmann et al.(2011)]. The phase-tagging approach allows efficient suppression of background contributions in the experimental data and the accurate retrieval of the CEP dependent electron yield amplitudes and phases for each point in the projected 2-dimensional momentum images. The advantage of working with the projected images is the absence of any assumptions on the symmetry of the electron momentum distribution, as imposed in the regular VMI-based photoemission analysis via the Abel inversion procedure. Furthermore, the direct analysis of the CEP dependent signal removes the cross-coupling of forward and backward emission channels in the usual analysis of forward-backward asymmetries.

The angle-resolved electron emission provided by the velocity-map imaging detection allows for a more detailed analysis of the CEP-dependent part of the electron emission. For each momentum projection on the detector plane,  $(p_x, p_y)$ , the CEP dependent electron yield was fitted with the function  $A(p_x, p_y) = C(p_x, p_y) * \cos(\phi + \Delta\phi(p_x, p_y))$ . From this fit, angular resolved amplitude,  $C(p_x, p_y)$ , and phase,  $\Delta\phi(p_x, p_y)$ , maps of the CEP dependent part of the electron emission were obtained. To increase the signal-to-noise-ratio, the image data was binned with a bin size of  $4 \times 4$  pixels (corresponding to an area of  $0.03 \text{ a.u.} \times 0.03 \text{ a.u.}$  in  $py-px$  momentum space). The CEP-dependent electron yields and electron emission asymmetries excellently agree with the results from semi-classical meanfield Monte-Carlo simulations [Zherebtsov et al.(2012)], see Fig. 1. The comparison of the momentum-resolved amplitudes and phases of the CEP dependent signal to theory offers unprecedented insights into the underlying electron acceleration mechanisms. The symmetry of the amplitude and phase maps with respect to the direction of laser propagation demonstrates that the

nanoparticle response is not affected by field propagation and retardation effects in the investigated size regime. The overall structure and symmetry properties of the amplitude and phase maps in the direction of the polarization axis show the phase-selectivity of the emission from different sides of the nanoparticle and confirm that electron backscattering from the surface is the major process for the CEP dependent generation of energetic electrons.

## Velocity-map imaging of high-energy electrons from nanostructures

Conventional velocity-map imaging (VMI) spectrometers with an einzel lens are typically able to image up to about 100 eV in electron energy while providing a resolution in the range of one percent or below. We have developed a new type of VMI with an achromatic thick lens to enable the detection of electrons up to 1 keV in energy with such a high resolution. The new design is advantageous for a range of experiments including high-energy electron imaging with mid-IR driver lasers and imaging high-energy electrons generated by field enhancement through nanolocalized fields near nanoparticles. In JRML we have designed and implemented a 'thick-lens' velocity map imaging (TL-VMI) spectrometer. The thick lens design consists of 11 electrodes (compared to 3 in the standard design) as depicted in the Simion simulation of the design in Fig. 2. The extension of the spectrometer's electric field allows for detecting charged particles with higher energies (up to 1 keV) with lower chromatic aberration using only up to 30 kV as the repeller voltage. Furthermore, simulations conducted by an REU student in the summer of 2012 have indicated that the resolution achievable with the TL-VMI is on the order of a few percent better than with the standard design. A full characterization of the TL-VMI and a technical paper on the design are underway.

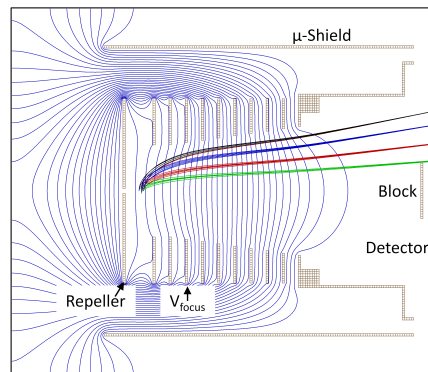


Figure 2: Schematic of the JRML 'thick-lens' velocity map imaging (TL-VMI) spectrometer.

## Work in progress and outlook

We have built and successfully tested a single-shot CEP meter at JRML. The new laser lab together with the 10-kHz PULSAR few-cycle light source has been completed. Currently, in combination with the single-shot phase meter, phase-tagged measurements are being tested. For this purpose the PULSAR pulses have been compressed with a new set of chirped mirrors down to a regular operation with about 4 fs pulses. An extension of the present experiments towards higher laser intensities holds the promise of becoming a fruitful approach for investigating the onset of a highly nonlinear processes of the dielectric medium, such as field-induced metallization [Durach et al.(2011)] or optical breakdown. Free nanoparticles will be particularly advantageous for exploring the nonlinear regime, as they provide constantly fresh samples for each laser shot. The CEP-dependent analysis used in our studies on the isolated 95 nm diameter nanospheres can further be applied to larger nanosystems, where the emission is expected to become asymmetric due to nanofocusing effects. Such experiments may elucidate the role of field propagation effects including nonlinear nanofocusing and local field distortions on the electron emission and acceleration.

We aim at tracing the electron dynamics in nanostructures with attosecond resolution using single attosecond XUV light pulses. In order to build a solid basis for our experimental studies, we have recently theoretically investigated the application of attosecond nanoplasmonic streaking for the real-time observation of collective electron motion in nanosystems for isolated nanoparticles [Süßmann and Kling(2011)]. One of

the key aspects in traditional attosecond streaking on e.g. gas phase atomic targets is the spatial homogeneity of the driving laser field. In contrast, noble metal nanoparticles exhibit strongly enhanced, but highly localized optical fields, such that the assumption of spatial homogeneity is no longer valid.

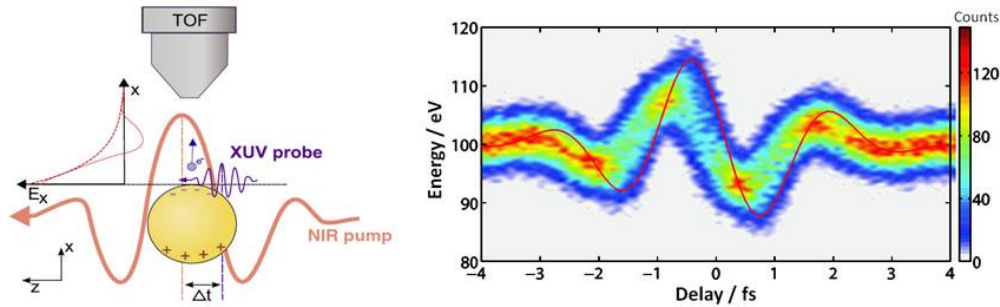


Figure 3: (left) Attosecond nanoplasmonic streaking principle. (right) Simulated streaking spectrogram for 10 nm Au spheres. The red line shows the contribution of electrons emitted on axis with the laser polarization vector. From [Süßmann and Kling(2011)].

When applying attosecond streaking spectroscopy to nanoparticles, the spatial decay of the near-field into free space will govern the streaking process. The principle of attosecond nanoplasmonic streaking for Au spheres is shown in Fig. 3 (left) and also applicable to other materials and to clusters. A few-cycle near-infrared (NIR) pulse is used to excite the collective electron motion, causing higher field amplitudes near the sphere as compared to the excitation field. Electrons will be photoemitted in the presence of the near-field resulting from the collective electron motion by an attosecond extreme-ultraviolet (XUV) pulse and detected by a time-of-flight (TOF) spectrometer. The change in the final drift velocity of the photoelectrons is measured as a function of the delay between the plasmonic field (locked in time to the excitation pulse) and the XUV pulse. Fig. 3 (right) shows the results of Monte Carlo simulations for 10 nm Au particles [Süßmann and Kling(2011)]. The collective oscillations were induced by a 5 fs laser pulse with stable electric field waveform at 800 nm (at an intensity of  $1.0 \times 10^{12}$  W/cm<sup>2</sup>) and an attosecond XUV pulse at 105 eV with 200 as duration. The resulting streaking spectrogram allows for the full spatio-temporal retrieval of the plasmonic field and in turn the retrieval of detailed information about the collective electron motion (see also [Süßmann and Kling(2011)]).

We aim at the real-time monitoring of collective electron motion for the first time. Importantly, the simultaneous measurements of the laser electric field (via attosecond streaking) and of the nanoplasmonic field (via attosecond nanoplasmonic streaking) will allow very detailed insight into the strongly driven collective electron dynamics [Süßmann and Kling(2011)]. The observed sub-cycle resolved differences between the two fields can be compared to simulations, giving insight into the complex multi-electron behavior. We will probe the collective electron motion in nanomaterials, studies that may reveal completely novel insight into how nanolocalized fields build-up and decay in the presence of ultrashort and intense laser fields. An extension of our experiments towards high laser intensities holds the promise of becoming a fruitful approach for investigating the onset of highly nonlinear processes (see e.g. [Durach et al.(2011), Yang et al.(2013), Feist et al.(2013)]).

## References

- [Hommelhoff et al.(2013)] P. Hommelhoff et al., *Ann. Phys.* **525**, A13 (2013).
- [Zherebtsov et al.(2011)] S. Zherebtsov et al., *Nature Phys.* **7**, 656 (2011).
- [Durach et al.(2011)] M. Durach et al., *Phys. Rev. Lett.* **107**, 086602 (2011).
- [Süßmann and Kling(2011)] F. Süßmann and M. Kling, *Phys. Rev. B* **84**, 121406 (2011).
- [Yang et al.(2013)] Y. Yang et al., *Opt. Exp.* **21**, 2195 (2013).
- [Feist et al.(2013)] J. Feist et al., *Phys. Rev. A* **in press** (2013).
- [Rathje et al.(2012)] T. Rathje et al., *J. Phys. B: At. Mol. Opt. Phys.* **45**, 074003 (2012).
- [Zherebtsov et al.(2012)] S. Zherebtsov et al., *New J. Phys.* **12**, 075010 (2012).
- [Süßmann et al.(2011)] F. Süßmann et al., *Rev. Sci. Instrum.* **82**, 093109 (2011).

## **Coupling electrons, phonons, and photon for nonequilibrium transport simulation**

Irena Knezevic  
University of Wisconsin- Madison  
Electrical and Computer Engineering  
1415 Engineering Dr, Madison, WI 53706  
knezevic@engr.wisc.edu

### **Program scope**

Time-dependent nonequilibrium transport in nanostructures offers a number of exciting basic science challenges, as well as real-world applications. While the low-field and steady-state quantum transport in nanostructures is theoretically well understood, there is incomplete theoretical understanding and a dearth of efficient computational techniques that can address time-dependent quantum transport in nanostructures, where electrons are excited either electrically (by applying a time-varying bias) or optically (by illumination with electromagnetic waves) and transport far from equilibrium that results from large applied biases or electromagnetic waves of high intensity.

In order to describe the generally time-dependent and far-from-equilibrium physics of the electronic system that is electrically or optically excited, a full picture of coupling between electrons, lattice, and electromagnetic wave dynamics becomes necessary. This three-pronged interplay, where simulations proceed in parallel at every time-step and drive each other, is what makes theoretical treatment of realistic transport problems far from equilibrium very different from the linear-regime transport and very challenging. This project addresses this knowledge gap.

The objective of this project is to develop a general and efficient multiphysics simulation framework where electron transport, phonon transport, and electrodynamics will be coupled self-consistently and provide insight into the time-dependent and nonlinear transport in optically or electrically excited low-dimensional electron systems. To achieve this objective, electronic transport [simulated by the Wigner Monte Carlo (WMC) technique] will be self-consistently coupled with the transport of phonons [described by the semiclassical ensemble Monte Carlo (EMC) technique] and electromagnetic field dynamics [described by the finite-difference time-domain (FDTD) technique and molecular dynamics (MD) for subgrid Coulomb interactions].

The proposed research program is organized into 3 thrusts, through which the expertise and tools will be developed gradually. In Thrust 1: Lateral transport, we investigate the electronic and optical response of quantum point contacts (QPCs) to GHz-frequency (microwave) illumination and *ac* biasing. In QPCs, quantum transport is nearly ballistic and the nonlocal nature of the density matrix plays a prominent role; it is a simple structure but with very rich physics, therefore ideal as a model system. In Thrust 2: Vertical unipolar transport, we address far-from-equilibrium transport in THz quantum cascade lasers. These structures are ideal test structures for the simulation of far-from-equilibrium vertical transport coupled with light as they operate at very high fields, while the electronic transport in them is decidedly quantum, with large coherent

currents. Finally, in Thrust 3: Vertical bipolar transport, we will address the interband transport in multijunction photovoltaics in the presence of light and significant nonequilibrium phonon generation.

The multiphysics simulation framework proposed here has the potential to greatly enhance our understanding of truly nonequilibrium, dissipative charge transport in semiconductor nanostructures in the presence of strong electron interaction with phonons and electromagnetic waves. The PI will also rely on established experimental collaborations for the validation of the proposed theoretical work.

### Recent progress

The project commenced in September 2012, so we have just completed 6 months of the study.

In Year 1, under Thrust 1, we have started working on solving the Wigner transport equation (WTE) using the stochastic Monte Carlo technique for a simple two-barrier tunneling heterostructure (Fig. 1). Wigner transport equation is the quantum generalization of the semiclassical Boltzmann transport equation (BTE) and is capable of treating nonlocal phenomena such as tunneling. In the stochastic Monte Carlo implementation, ballistic transport and carrier scattering are treated in the same way as in the semiclassical Monte Carlo that solves the BTE. Nonlocal phenomena are captured through the use of the fast-varying “quantum potential” terms and the concept of affinity that is ascribed to each simulated particle, and whose sign captures the instantaneous deviation of the particle’s behavior from the semiclassical picture.

Another line of work actively undertaken in Year 1 belongs to Thrust 2 and is the development of a coupled simulation of “hot” electron and “hot” phonon transport in quantum cascade lasers, using fully coupled simulation of electron and phonon transport; this is the first simulation of its kind. The electronic simulator includes a k.p band structure coupled with a Poisson solver to find the confined subbands. In the Monte Carlo simulation of electron transport, carriers can move freely in the plane normal to the heterostructure growth direction and hop between confined subbands in the

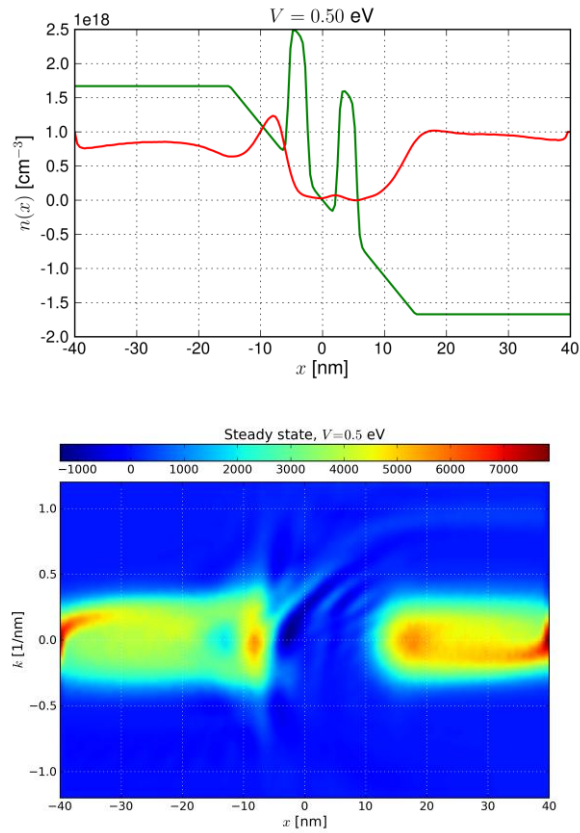


Fig 1. (Top) Potential profile (green) and charge density (red) in a two-barrier tunneling heterostructure, also known as the resonant tunneling diode (RTD) at 0.5 V across the structure and assumed linear potential drop. (Bottom) Wigner function  $f_W(x, k)$ , which is a function of position  $x$  and wave number  $k$ , in the steady state at the same biasing condition.

growth direction. Electron-electron and electron-phonon scattering is accounted for. Every time an optical phonon is emitted or absorbed, this event is recorded and the full phonon distribution is updated. The nonequilibrium phonon distribution further affects the scattering rates, an effect that is accounted for self-consistently in the electronic transport simulation. Nonequilibrium optical phonons undergo scattering of their own, with the most important process being anharmonic decay of the slow optical into fast acoustic phonons (Fig. 2). This process is directly recorded in the simulation and the phonon distribution modified accordingly. While the coupling of electrons and optical phonons is implemented locally, at the level of a single QCL stage, globally the heat transport is captured using the finite element solution of the heat diffusion equation (Fig. 3), where the optical phonons generated by the hot electron system act as a source (Fig. 2).

### Future plans

The work on electrothermal simulation of QCLs is expected to be completed by the end of 2013. RTD simulation with scattering included will be completed by the end of summer 2013, at which point the plan is to extend this work to full Maxwell-Bloch equations (essentially Wigner equations for multiple subbands coupled with the polarization vector) in order to work on the capability to capture the interaction with light. This step is critical for the completion of tasks in Thrusts 1-3.

Additionally, in the coming year we will start work on low-temperature quantum transport in split-gate quantum point contacts (QPC's), fabricated on Si/SiGe 2DEGs, under illumination by microwaves as well as under *ac* biasing (part of Thrust 1). QPCs, quantum transport is nearly ballistic and the nonlocal nature of the density matrix plays a prominent role. The main questions are how do highly delocalized carriers, such as electrons in QPC at low temperatures, couple with light and how do they respond to time-varying biasing. To answer these questions, a simulation that couples Wigner function Monte Carlo of electron transport, capable of capturing quantum transport of delocalized carriers, with FDTD solution of Maxwell's equations will be developed as the first fully self-consistent light/quantum transport simulation to date.

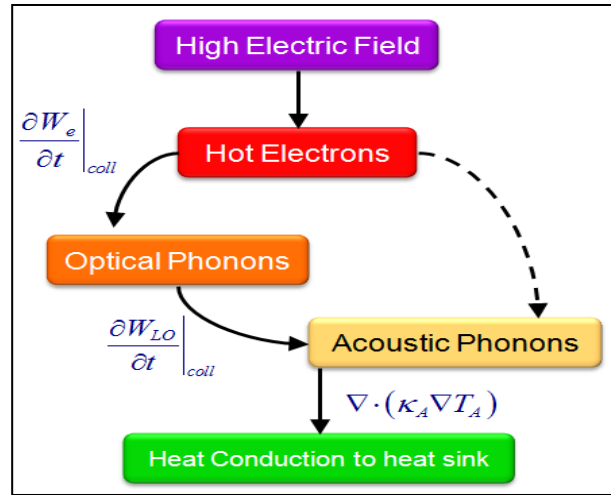


Fig 2. Schematic of the heat generation and flow in quantum cascade lasers under high bias.

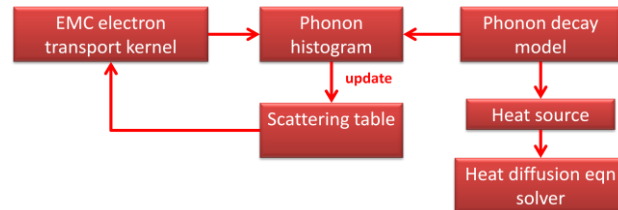


Fig 3. Coupled simulation flowchart. Electronic transport kernel generates phonons, which both affect the electronic scattering rates and act as a de facto source of acoustic phonons in the heat diffusion solver that covers the whole structure.

**PROGRAM TITLE:** Functional Imaging of Hybrid Nanostructures: Visualization of Mechanisms for Solar Energy Utilization

**PI:** Lincoln J. Lauhon, Department of Materials Science and Engineering, Northwestern University  
2220 Campus Drive, Evanston, IL 60208-3108. e-mail: lauhon@northwestern.edu

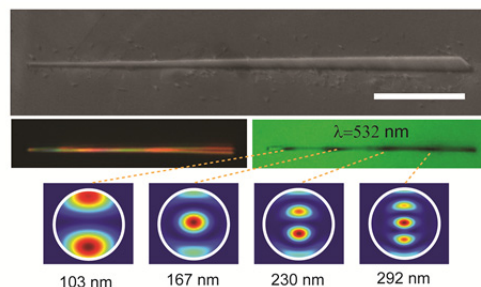
**PROGRAM SCOPE**

The program goal is to isolate and quantify various steps in the energy conversion process, including geometrically and plasmonically enhanced absorption, the generation of carriers with excess energy, and the efficiency with which the carriers can move to and perform useful chemistry at interfaces. The project utilizes Raman scattering, multi-wavelength optical excitation, and electrical transport measurements of nanowire-based hybrid materials structures to resolve, in energy and space, the absorption of light, the generation of excess energetic charge carriers, and the efficiency of their separation to generate electrical and chemical energy. Single nanostructure measurements on model nanowire hybrid systems are being extended to liquid environments and ensemble measurements to establish relationships between nanostructure, electronic structure, and photoelectrical and photoelectrochemical activity.

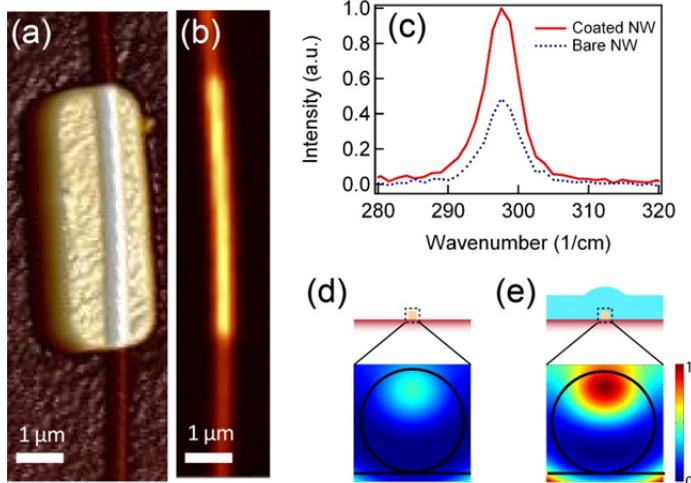
**RECENT PROGRESS**

**Light Absorption in Nanostructures** (*Nano Letters* **12**, 2266 (2012); *Optics Express* **20**, 5127 (2012))

In nanostructures with dimensions that are a fraction of the wavelength, the absorption of light is strongly modulated as a function of diameter. For perfect spheres and cylinders, these effects are well described by Mie theory, but for 'real' materials electromagnetics simulations are necessary to quantitatively account for light absorption. Furthermore, single nanostructure absorption measurements are difficult to perform. One approach is scanning photocurrent microscopy, in which the photocurrent generated by a nanostructured device is assumed to be proportional to absorption. We have successfully implemented spectrally resolved SPCM as described further below. Another approach to understanding light matter interactions is Raman spectroscopy. Raman spectroscopy has the advantage of not requiring the formation of electrical contacts, and in addition it provides a very stringent test of electromagnetics modeling due to its dependence on the fourth power of the field. In a recent *Nano Letters* publication, diameter dependent Raman scattering measurements in single tapered silicon nanowires were quantitatively explained by modeling with finite-difference time-domain simulations. Single crystal tapered silicon nanowires were grown by homoepitaxial radial growth concurrent with vapor-liquid-solid axial growth (see figure above right). The degree of taper was engineered to produce multiple electromagnetic resonances separated by a distance exceeding the optical resolution. Multiple resonances along the nanowire were thereby induced by broad-band light absorption and scattering. Observed Raman scattering intensities for multiple polarization configurations were reproduced by a model that accounts for the internal electromagnetic mode structure of both the exciting and scattered light. These studies provide a benchmark for our ability to describe absorption in ideal nanostructures, forming the basis for modeling studies that inform the design of advanced light harvesting systems.



Raman scattering in single nanowires can be significantly enhanced by the intrinsic geometric resonances described above, but extrinsic effects including background scattering and laser-induced heating can limit the analysis of intrinsic properties. For example, subtle changes in line-shape due to doping induced Fano resonances, quantum confinement, and defects can be obscured by heating, and lowering the excitation power reduces the signal to noise. To produce more light with less heat, we showed that a thin dielectric coating could be designed and deposited to enhance the Raman signal in a single Ge nanowire by light concentration.

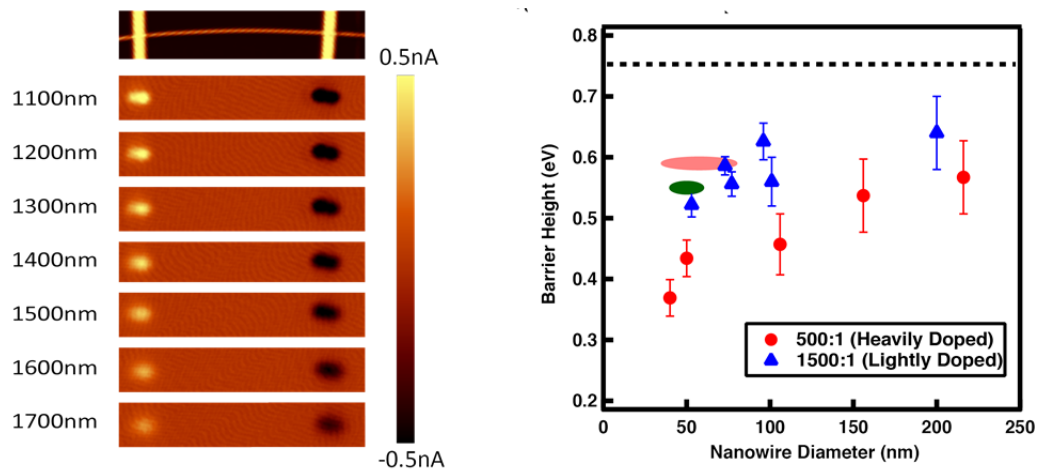


By surrounding the nanowire with a solid coating rather than air or vacuum, one can achieve higher signal intensities with less heating. The results demonstrate a simple and effective method to extend the limits of Raman analysis on single nanostructures and facilitate their characterization, and were reported in *Optics Express*. The figure above shows (a) the SiO<sub>2</sub> coating, (b) the Raman enhancement image, (c) the enhancement in the spectrum, and (d), (e) the field concentration modeled by finite difference time domain simulations.

### Resolving Hot Electron Transport at Nanoscale Metal-Semiconductor Contacts (*unpublished*)

Efficient charge injection and extraction through metal contacts to semiconductors is essential in most light emitting and solar energy conversion devices. Conventionally, internal photoemission spectroscopy (IPS) is used to measure the barrier height of Schottky contacts. However, the application of IPS has been limited to bulk and thin film semiconductor/dielectrics. As existing models of electrical contacts need to be modified for one-dimensional nanostructures (i.e. nanowires) due to significant deviations in geometries and electrostatics from conventional planar devices, methods are needed to measure barrier heights at reduced dimensions.

Spectrally resolved scanning photocurrent microscopy (SPCM) was used to measure the barrier height between metal contacts and a Si nanowire (see figure next page). Photoexcitation below the semiconductor bandgap in SPCM induces internal photoemission at the metal-semiconductor junction, enabling separation of the contacts response from that of the semiconducting channel. The scaling of the photocurrent with photon energy is consistent with internal photoemission, enabling extraction of a quantitative barrier height. Planar single nanowire devices were fabricated using n+ Si nanowires of varying diameters to systematically examine the influence of nanowire diameter on barrier height. As the diameter decreases, the measured effective barrier height decreases below the reported value for the Ni barrier height on bulk Si. Furthermore, we investigated the effect of near-surface doping, which is the primary method to achieve Ohmic contacts. For this purpose, Si nanowires were grown with an n+/i junction in the middle. With the same metallization, a Schottky contact was formed on the intrinsic portion, whereas an Ohmic contact was formed on the doped portion. As expected, the effective barrier height is lowered by the near-surface doping, which is expected to induce tunneling by reducing the barrier width.

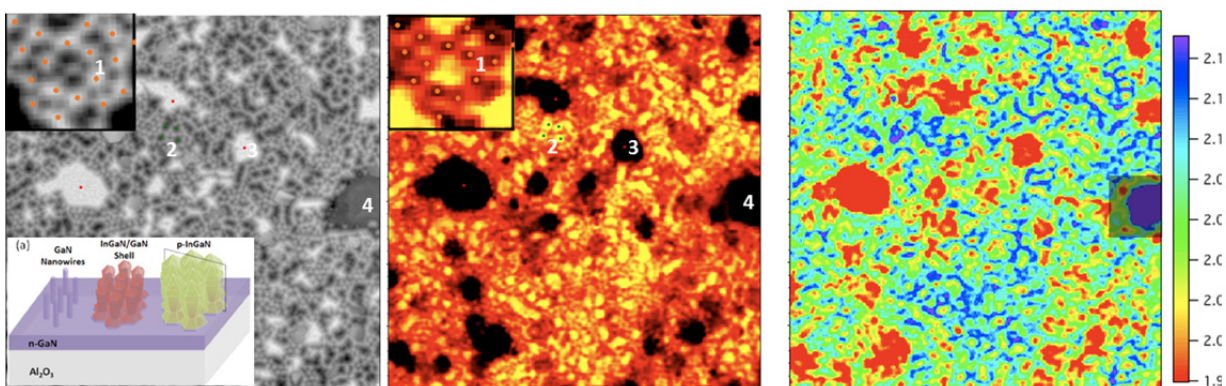


**Internal photoemission measurement of Schottky barrier height** of contact to semiconductor nanowire. At left is an image of the nanowire between two ohmic contacts, followed by photocurrent images at increasing wavelength ( $3 \times 15 \mu\text{m}^2$ ). The barrier height is extracted from dependence of the photocurrent yield on energy. At right, the measured barrier heights are plotted as a function of nanowire diameter for different doping densities.

The measurement of the barrier height of Schottky and Ohmic contacts on nanowires is an important step in understanding band profiles at nanoscale junctions, highlighting the potential for spectrally resolved SPCM measurements to investigate the physics of devices incorporating nanostructured materials with electronically active interfaces.

### **Spectrally Resolved Scanning Photocurrent Microscopy in Nanowire Array Solar Cells** (*unpublished*)

Nanowire core-shell heterostructures are of interest in photovoltaic applications because they can provide enhanced light trapping effects, elastic strain relief, and a decoupling of the absorption and carrier collection axes. For novel solar cell architectures that incorporate significant structural, chemical, and electronic heterogeneities, a detailed mechanistic understanding of spatial variations in external and internal quantum efficiency is essential to understand and improve device performance. Spatially resolved measurements of electronic properties are therefore necessary to the development of new generations of devices. We have applied spectrally resolved scanning photocurrent microscopy (SPCM) to characterize a nanowire solar cell consisting of an array of GaN-InGaN core-shell nanowires connected at the tops by a p-InGaN canopy layer and fabricated using scalable device fabrication techniques (figure next page). The spatially and spectrally resolved photovoltaic performance measured by SPCM is correlated with structure and composition inferred from (1) atomic force microscopy (AFM) topography; (2) scanning transmission electron microscopy (STEM) imaging; and (3) Raman microspectroscopy. AFM and SPCM images shown in the figure below reveal the contributions of individual nanowires to the external quantum efficiency within an array of  $\sim 500$  nm pitch, and identify structural defects that limit device performance. We find that the quantum efficiency is highest for illumination of the regions in between the nanowires, likely due to a combination of photonic effects and enhanced carrier collection in the generation region. The analysis is used to spatially decompose the overall device EQE and identify promising directions for optimization of performance.



**Spectrally resolved SPCM of a GaN/InGaN nanowire solar cell.** Left Panel: atomic force microscope topograph of solar cell adjacent to top contact. The total image size is  $30 \times 30 \mu\text{m}^2$ , and the pitch of the nanowire array is 500 nm. Inset: schematic of solar cell fabrication as described in Wierer, J. Jr., Wang, G.T., *et al*, *Nanotechnology* **23**, 194007 (2012). Top contacts are made to the p-InGaN capping layer. Middle Panel: SPCM image mapping the spatially resolved photocurrent with 405 nm excitation. Four characteristic regions are observed. Regions 1 and 2 exhibit high-efficiency for absorption on and between the nanowires. Right Panel: effective band gap map determined by extracting the absorption edge from aligned SPCM images at different wavelengths. Bright red regions correspond to areas of low bandgap, labeled region 3 in the middle panel. These are regions in which the rod arrays have coalesced prematurely, leading to a thick p-InGaN capping layer and absorption away from the junction regions. Region 4 is a defect from which negligible current is collected.

#### FUTURE PLANS

- Extend scanning photocurrent measurements into solution to probe local photoinduced electrochemistry in metal-semiconductor hybrid nanostructures.
- Extend SPCM capabilities to time-resolved measurements of nanostructured devices to access rate limiting steps in the utilization of photogenerated carriers for energy conversion.

#### PUBLICATIONS 2010-2012 (underline indicates student or postdoc supported by DOE)

- Justin G. Connell, KunHo Yoon, Daniel E. Perea, Edwin J. Schwalbach, Peter W. Voorhees, Lincoln J. Lauhon, "Facet-Dependent Dopant Incorporation in VLS-Grown Nanowires". *Nano Letters* **13**, 199 (2013).
- F. J. Lopez, J. K. Hyun, U. Givan, I. S. Kim, A. Holsteen, and L. J. Lauhon, "Diameter and Polarization Dependent Raman Scattering Intensities of Semiconductor Nanowires." *Nano Letters* **12**, 2266 (2012).
- J. K. Hyun, I. S. Kim, J. G. Connell, and L. J. Lauhon, "Raman Concentrators in Ge Nanowires with Dielectric Coatings." *Optics Express* **20**, 5127 (2012).
- F. J. Lopez, U. Givan, J. G. Connell, and L. J. Lauhon, "Silicon nanowire polytypes: identification by Raman spectroscopy, generation mechanism, and misfit strain in homostructures," *ACS Nano* **5**, 8958 (2011).
- Jerome K. Hyun and Lincoln J. Lauhon, "Spatially Resolved Plasmonically Enhanced Photocurrent from Au Nanoparticles on a Si Nanowire," *Nano Letters* **11**, 2731-2734 (2011).
- E. Koren, J. K. Hyun, U. Givan, E. R. Hemesath, L. J. Lauhon, and Y. Rosenwaks, "Obtaining Uniform Dopant Distributions in VLS-Grown Si Nanowires," *Nano Letters* **11**, 183-187 (2011).
- S. X. Zhang, F. J. Lopez, J. K. Hyun, & L. J. Lauhon, "Direct Detection of Hole Gas in Ge-Si Core-Shell Nanowires by Enhanced Raman Scattering," *Nano Letters* **10**, 4483-4487 (2010).

# Hydrogen Absorption in Pd-based Nanostructures

David Lederman

West Virginia University, Department of Physics, Morgantown, WV 26506-6315

david.lederman@mail.wvu.edu

## Program Scope/Definition

The goal of the project is to determine the intrinsic effects of hydrogen absorption on the electronic properties (i.e., changes in the Fermi level and/or band structure) of Pd-based nanostructures. Although it is known that hydrogen absorption can change the magnetic and dielectric properties of thin films when hydrogen is absorbed due to chemisorption in a Pd overlayer, the fundamental mechanisms of how this happens are not well understood. In particular, the effects of defects and crystallinity have not been quantitatively determined, mainly because the structures thus far have not been characterized sufficiently well, which makes it difficult to separate extrinsic (i.e., structural) effects from intrinsic (i.e. purely electronic) effects. This project deals with this issue by growing well-characterized thin films and nanostructures and measuring the magnetic, ferroelectric, and magnetoelectric properties, which are then correlated with direct measurements of hydrogen penetration. Another problem is that the amount of hydrogen absorption, both in the Pd overlayers and in the underlayers, is not measured directly, so it is sometimes difficult to assess whether a given change in the properties is due to hydrogen being absorbed in the underlayer or due to electronic changes at the interface. This is addressed by performing detailed polarized neutron reflectivity measurements that quantitatively determines the depth profile of hydrogen absorption, and at the same time, measures the depth profile of any magnetic changes induced by the hydrogen absorption. Magnetoresistance measurements were used to understand the role of hydrogen interstitials on the band structure of the material.

## Recent Progress

Co/Pd multilayer samples were fabricated and their electronic properties have been monitored by performing magnetization and magnetoresistance as a function of hydrogen absorption and temperature by the PI's group at West Virginia University, including graduate student [Kineshma Munbodh](#) and postdoctoral researcher [Felio Perez](#). Neutron reflectivity measurements, performed in collaboration with [Michael Fitzsimmons](#) and his group, including postdoctoral researcher [Mikhail Zhernenkhov](#), at the Los Alamos Neutron Science Center (LANSCE) spallation neutron source. Magnetoresistance measurements were carried out as a function of hydrogen pressure with the help of [Donovan Diaz-Droguett](#), a postdoc from the Pontificia Universidad Católica de Chile.

X-ray diffraction showed highly oriented growth along the Pd [111] direction. Multilayer periodicities obtained from the separation of the multilayer peaks (23.2 Å and 23.7 Å for samples A and B) agreed well with those obtained from x-ray reflectivity (XRR) and PNR data for sample A (23.5 ± 1.4 Å) and sample B (23.5 ± 2.5 Å). Quantitative analysis of XRR data was used to determine the non-magnetic structure.

Magnetization measurements for both samples are shown in Figure 1. By comparing the measurements with  $H$  perpendicular and parallel to the sample plane, we found that 35.7% and 53.8% of the magnetization was in the plane of the sample at  $\mu_0 H = 0.65$  for samples A and B, respectively. Square loops measured with the field applied out of the plane confirm the presence of a large out-of-plane anisotropy. SQUID magnetometry revealed that the in-plane saturation field of

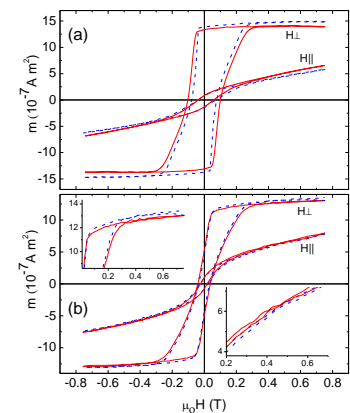


**Figure 1** Magnetic moment measurements in 1 atm of He (blue dashed curves) and  $\text{H}_2$  (red solid curves) with the magnetic field applied perpendicular ( $H_{\perp}$ ) and parallel ( $H_{\parallel}$ ) to the sample surface. (a) Data for sample A, (b) data for sample B. Top left and bottom right insets in (b) are close-up views of the data in (b) for the  $H_{\perp}$  and  $H_{\parallel}$  configurations, respectively.

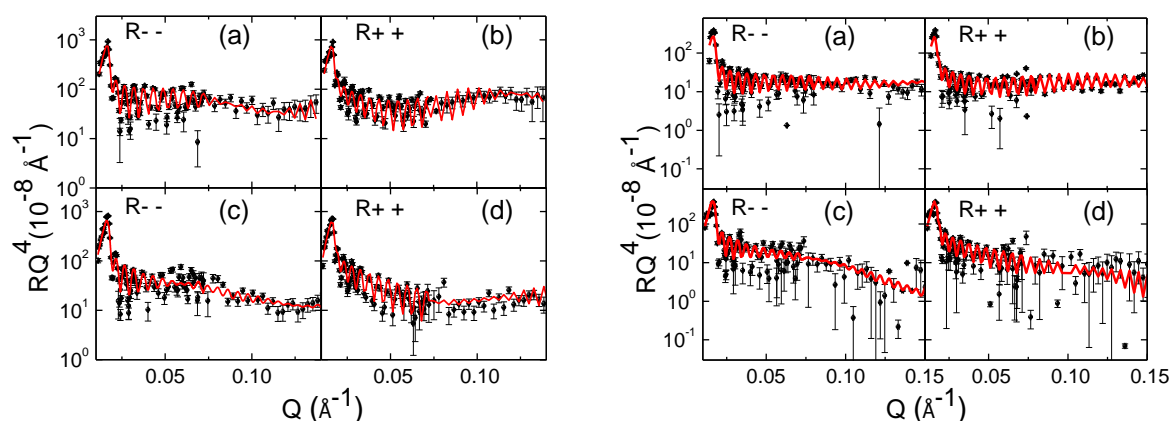


**Figure 2** PNR using neutrons with (- -) and (+ +) incoming and outgoing polarization states with the sample in helium [(a) and (b)] and deuterium [(c) and (d)] in 0.65 T (left) and 6.0 T (right) magnetic fields applied in the plane of sample A. Experimental data are black dots and the model fit is the red line.

sample A was 5.5 T. An observed decrease of the magnetization in sample B as the field decreased from saturation (for  $H > 0$  and  $H \perp$  to the sample surface) was due to the formation of magnetic domains. This was verified by MFM images of sample B, which indicated the presence of irregular striped domains characteristic of ferromagnetic Co/Pd multilayers with perpendicular magnetic anisotropy. Sample A displayed a larger remanence and coercivity than sample B, possibly as a result of greater atomic intermixing at the interfaces which is known to result in more pinning centers that obstruct domain growth and propagation. As a result, sample A showed no domain structure via MFM.

Magnetization measurements showed that when  $H$  was applied in the plane of the samples, there was a net increase in magnetization component along  $H$  upon  $H_2$  absorption at  $\mu_0 H = 0.65$  T, the increase being larger in sample A. When  $H$  was  $\perp$  to the sample surface, the saturation magnetization decreased in both samples, although the effect was once again greater for sample A. This means that the magnetization of the samples decreased upon  $H_2$  absorption. Therefore, the increase in the unsaturated state, with  $H$  in the plane of the samples, must be due to a decrease in the perpendicular anisotropy.

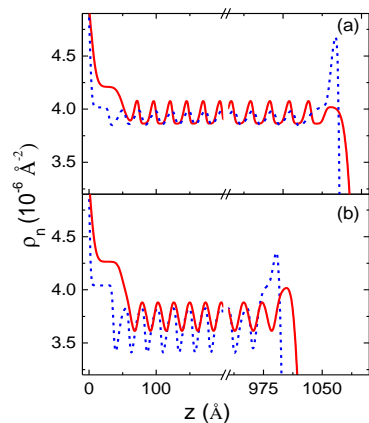


**Figure 3** Nuclear SLD profile in air (helium) (blue dashed curve) and in deuterium (red solid curve) for (a) sample A and (b) sample B at 0.65 T.

vertical dotted lines in Figure 4. Values of  $\rho_n$  were used to determine the stoichiometry of each layer independently. The Pd buffer and top layers' SLDs correspond to bulk Pd in both samples A and B.

PNR provided detailed magnetic information about the samples as a function of depth. PNR data obtained from sample A with the fit to the model are shown in Figure 2. Qualitatively, the decrease in the period of oscillations in the low- $Q$  regime upon  $D_2$  absorption indicates an increase in the total thickness of the sample. The same observation can be made for sample B. Figure 5 shows the high and low  $Q$  portions of the data and fits for sample B, respectively. The fact that the position of the multilayer peak at  $Q = 0.27 \text{ \AA}^{-1}$  remained unchanged indicates that the Co/Pd multilayer period did not change upon  $D_2$  absorption. Therefore, the increase in total sample thickness is solely due to an expansion of the Pd top and buffer layers.

Nuclear scattering length density (SLD) profiles  $\rho_n$  and their derivatives obtained from fits of the PNR data are shown in Figure 4 for sample B. Similar  $\rho_n$  profile was also obtained for sample A, but analysis of these data was less reliable due to the absence of the multilayer Bragg peak because we were unable to measure at high  $Q$ . Positions of the interfaces, determined from the locations of the maxima and minima in  $d\rho_n/dz$ , are indicated by

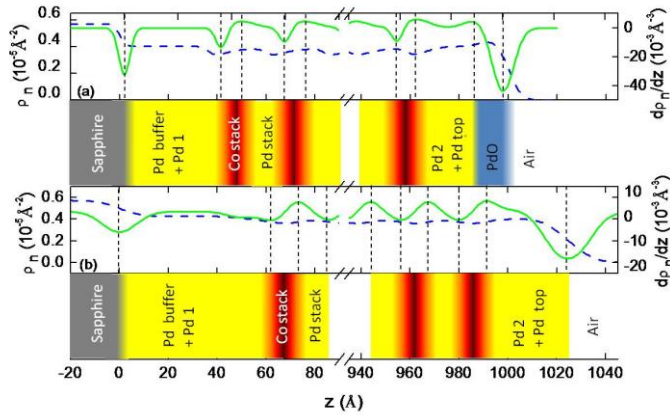


**Figure 4** Nuclear SLD profiles (blue dashed curve) and its derivative (green solid curve for sample B (a) in air and (b) for the sample in deuterium). The vertical dotted lines indicate the positions of the interfaces. The corresponding sample profile is shown.

deuterium atoms to Pd atoms,  $C_D$ , was estimated in each layer  $C_D$  was found to be 0.53 and 0.30 for sample A and 0.75 and 0.52 for sample B in the Pd buffer and Pd top layers, respectively, confirming that there was significant  $D_2$  absorption in these layers. The value of  $C_D$  for the Pd and Co stacks in sample A and B was approximately  $0.02 \pm 0.005$ . The relatively small value of  $C_D$  for the Pd and Co stack explains the lack of significant lattice expansion and implies that  $D_2$  was probably absorbed into interstitial sites.

The magnetic SLD profiles  $\rho_m$  for samples A and B are shown in Figure 4. The maxima in  $\rho_m$  correspond to Co layers and the minima represent Pd layers. Results indicated a doubling of the Sample B's multilayer magnetic period with respect to the nuclear period. Since the magnetization was not saturated, layers with weaker anisotropy tilted more strongly towards the field direction, causing a  $Q_{1/2}$  peak to appear. The results also indicate that the modulation grew stronger with  $D_2$  absorption, evident in Figure 5, which shows that the  $Q_{1/2}$  peak became more pronounced, and in the magnetic SLD profile in **Error! Reference source not found.** which shows the increase in magnetic contrast between adjacent minima, corresponding to Pd layers.

Magnetoresistance measurements a strong correlation of the changes in the extraordinary Hall effect (EHE). We found that, as expected, the resistivity  $\rho$  increased hydrogen was absorbed in the

Analysis indicates that in sample A, the center of the Pd stack layers consisted of 95% Pd and the Co stack layers are 12% Co. Sample B consisted of Pd stack layers with 89% Pd and Co stack layers with 30% Co, indicating the presence of interface disorder. Upon  $D_2$  absorption, there was a statistically significant increase in the thickness of the Pd buffer and top layers in both samples. Results also indicate statistically insignificant changes in the Co and Pd stack layer thicknesses. A noteworthy decrease of the PdO layer thickness occurred in both samples, which can be attributed reduction of the oxide due to deuterium absorption.

Comparing  $\rho_n$  and thickness change before and after  $D_2$  absorption (Figure 3), the ratio of the number of

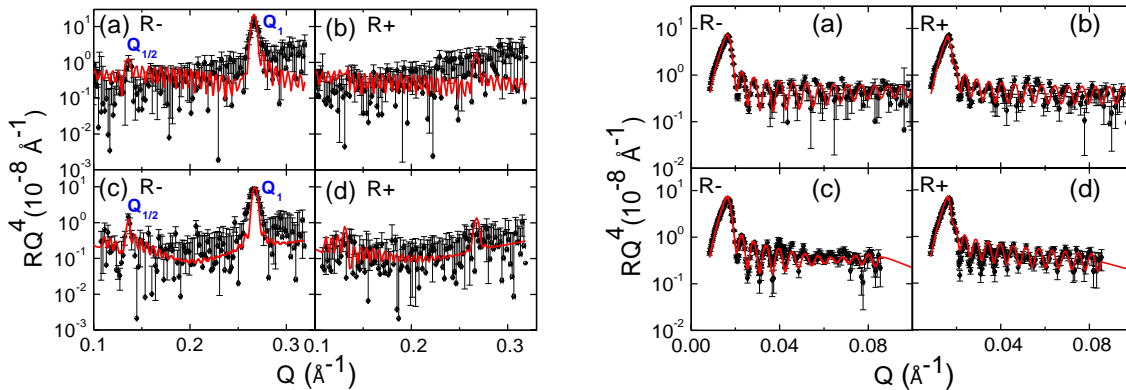


**Figure 5** Left: PNR using neutrons in the high-Q regime ( $Q > 0.1 \text{ \AA}^{-1}$ ) with (-) and (+) incoming polarization states with the sample in air [(a) and (b)] and deuterium [(c) and (d)] in a 0.65 T magnetic field applied in the plane of sample B. The positions of the single order ( $Q_1$ ) and half-order magnetic peaks ( $Q_{1/2}$ ) are indicated. Right: low-Q portion of same data. Experimental data are black dots and model fit is red line.

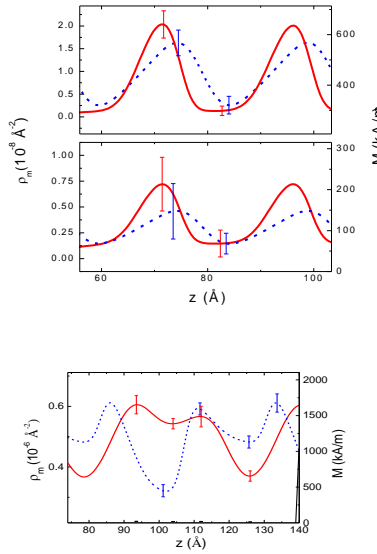


**Figure 6** Top: Magnetic SLD in air (blue dashed curve) and in D<sub>2</sub> (red solid curve) for sample A at (top) 6 T and (bottom) 0.65 T for two Co/Pd bilayer in the stack. The film-substrate interface is set at a thickness of zero. Bottom: data for sample B at 0.65 T.

sample. More importantly, however, is the fact that the increases in the EHE are proportional to  $\rho^2$  for low hydrogen pressures, indicating that this is due to an intrinsic change in the band structure of the material. This occurs in the pressure range where  $\rho \sim P^{1/2}$ , where  $P$  is the H<sub>2</sub> partial pressure. For larger hydrogen pressures, deviations appear that coincide with the onset of significant structural changes, that is, when deviations occur from the  $\rho \sim P^{1/2}$  relation. Data that confirm this are shown in Figure 7.

To summarize our most important experimental results, we have found that: 1) D<sub>2</sub> absorption occurs throughout the thickness of both samples; 2) the multilayer stack absorbs D<sub>2</sub> but does not expand along the growth direction; 3) both the Pd and Co layers are magnetized and their in-plane magnetization increases when the magnetization is not saturated in the plane but decreases at saturation; 4) These results indicate that electronic effects resulting from H<sub>2</sub> or D<sub>2</sub> absorption are responsible for a decrease in perpendicular anisotropy and saturation magnetization of the samples, and that strain effects are not significant.

### Future Plans

We are currently working on fabricating Pd/Co multilayers in a nanodot (< 100 nm diameter) in order to determine the importance of hydrogen absorption through the sides of the sample. Measurements require large volumes, and therefore we are attempting to create a large number of nanodots using polystyrene beads as a shadow mask. We are also planning to study the effect of hydrogen absorption in ferroelectric oxide thin films covered by Pd in order to attempt to control absorption via

electric voltages.

### Publications

1. D. Diaz-Droguett, K. Munbodh, F. A. Perez, A. L. Cabrera, and D. Lederman, "Hydrogen absorption and its effect on the extraordinary Hall effect in Co/Pd multilayers", *in preparation* (2013).
2. K. Munbodh, F. A. Perez, and D. Lederman, "Changes in the magnetic properties of Co/Pd multilayers induced by hydrogen absorption", *J. Appl. Phys.* **111**, 123919 (2012).
3. K. Munbodh, M. Cheon, D. Lederman, M. R. Fitzsimmons, and N. R. Dilley, "Interface coupling between ferromagnets and random and dilute antiferromagnets", *Phys. Rev. B* **84**, 214434 (2011).
4. K. Munbodh, F. A. Perez, C. Keenan, D. Lederman, M. Zhernenkov, and M. R. Fitzsimmons, "Effects of hydrogen/deuterium absorption on the magnetic properties of Co/Pd multilayers", *Phys. Rev. B* **83**, 094432 (2011).

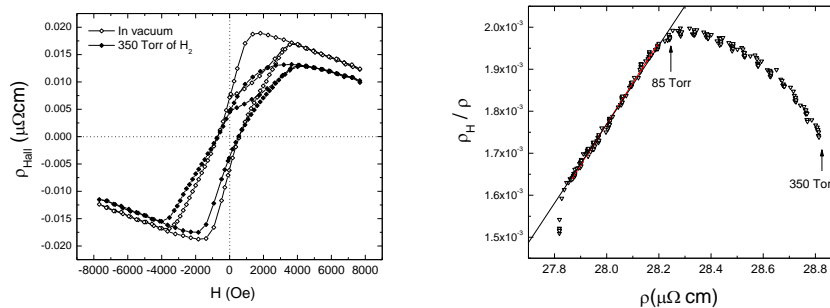


**Figure 7** Top: Hall voltage as a function of applied magnetic field for a 0.45 nm/1.5 nm Co/Pd multilayer. Bottom: Bottom: Hall voltage divided by resistivity as a function of resistivity for a 0.45 nm/2.0 nm Co/Pd multilayer. A linear dependence is indicative of intrinsic changes in the Hall conductivity.

## Physical Chemistry of Inorganic Nanostructures

Stephen R. Leone,<sup>1,2,4,5</sup> A. Paul Alivisatos (Program Leader),<sup>1,4</sup> Peidong Yang<sup>1,3,4</sup>

<sup>1</sup>*Departments of Chemistry, <sup>2</sup>Physics, and <sup>3</sup>Materials Science and Engineering, University of California, Berkeley, California 94720, United States*

<sup>4</sup>*Material Sciences and <sup>5</sup>Chemical Sciences Divisions, Lawrence Berkeley National Laboratory, Berkeley, California 94720, United States*

*srl@berkeley.edu, alivis@berkeley.edu, p\_yang@berkeley.edu*

### Program Scope:

Control of materials on the nanometer scale offers great opportunities to tailor the properties of energy conversion systems, yet the realization of these goals depends critically on improvements in our abilities to make complex nanostructures with precision. This program emphasizes the fundamental science of the synthesis of inorganic nanomaterials as well as the characterization of physical properties of these materials. The program consists of four subtasks: Physical Chemistry of Colloidal Nanocrystals, Fundamentals of Inorganic Nanowires, Microscopy Investigations of Nanostructured Materials, and Model Nanoscale Photo-catalytic Systems. The goal of the first subtask is to develop the science of colloidal inorganic nanocrystals with a special emphasis on understanding and controlling their synthesis. Particular attention is focused on investigating the fundamental optical, electrical, structural, and thermodynamics properties of these nanocrystals. The second subtask aims to establish and develop the core science and technology for semiconductor nanowires, with an emphasis on growth, assembly and fundamental optical and electronic properties characterization. This research effort is focused on two main categories: nanowire photonics and nanowires for energy conversion. The goal of the third subtask is to develop and use novel spectroscopic techniques to obtain a detailed understanding of charge carrier dynamics in nanostructured materials. This work is organized along two lines of inquiry: ultrafast x-ray transient absorption of excited-state dynamics in semiconductors and single-particle studies of quantum dot (QD) blinking and surface plasmon resonances. Subtask 4 is new and aims to understand the fundamental properties of charge transfer at the nanocrystal semiconductor interface to design an efficient photocatalytic system. This subtask is particularly interested in exploring the charge transfer phenomenon on a single particle level to better understand the effects of different numbers of quenchers on the surface, particle-to-particle heterogeneity, and single particle charge transfer kinetics.

### Subtask 1: Physical Chemistry of Colloidal Nanocrystals

Recent work in subtask 1 has included new synthesis strategies based on ion exchange reactions and facet control to obtain nanocrystals of greatly improved quality. Examples include highly monodisperse and crystalline covalent lattices such as III-V semiconductor nanocrystals<sup>1</sup>, highly luminescent ionic nanocrystals<sup>2,3</sup>, and interesting heterostructures.<sup>4,5</sup> We have also recently exploited novel in situ imaging techniques<sup>6-8</sup> to achieve unprecedented structural and mesoscale assembly dynamics of nanocrystals<sup>8</sup> and their growth in solution at atomic resolution with a graphene liquid cell.<sup>7</sup> Furthermore, the localized surface plasmon resonance, conventionally regarded as exclusive to noble metal nanocrystals, has been demonstrated and shown to be tunable in semiconductor nanocrystals through doping. Successful examples include Cu<sub>2</sub>S and WO<sub>3-δ</sub>. The position of the plasmon resonance can be tuned in both materials by altering the degree of oxygen deficiency.<sup>9,10</sup>

Future plans in subtask 1 will further use the ionic exchange method to synthesize previously unattainable nanocrystals with specific shape, size, and degree of doping if necessary. These crystals will serve as the platform for studying the structure-property relationship of nanostructures. We plan to address the mechanism for nanocrystal dynamic growth and assembly behaviors by engineering a multi-channel liquid cell design to enable the observation of multi-phase and multi-step reactions, such as cation exchange, metal tipping, growth and etching.

## Subtask 2: Fundamentals of Inorganic Nanowires

Nanowires have been identified as potential building blocks that mimic conventional photonic components such as interconnects, waveguides, and optical cavities at the nanoscale. To develop high-efficiency fluorescent nanowires, we have observed external quantum efficiency of photoluminescence (PL) as high as 20% from isolated ZnO nanowires measured at room temperature.<sup>11</sup> The efficiencies obtained here are significantly higher than those reported for ZnO materials in forms of bulk, thin films or powders. While semiconductor nanowires exhibiting strong PL offer promising solutions for miniaturized lasers, previously reported nanowire lasers suffer from emitting at multiple frequencies. By creating cleaved-coupled cavities in gallium nitride nanowires, we theoretically investigated and experimentally demonstrated single-frequency lasing in nanowires.<sup>12</sup> The agreement between theory and experiment presents design principles to rationally control the lasing modes in cleaved-coupled nanowire lasers. In addition to optically excited nanowires, we also demonstrated electrically driven, color tunable emission from epitaxially grown InGaN nanowire arrays.<sup>13</sup> Optically functional nanowires have also shown promises in biochemical applications. We showed that a nanowire waveguide attached to the tapered tip of an optical fiber can guide visible light into intracellular compartments of a living mammalian cell and can also be used to detect optical signals from subcellular regions with high spatial resolution.<sup>14</sup>

Semiconductor nanowires are promising for photovoltaic applications because of better charge collection and transport and the possibility of enhanced absorption through light trapping. Using a low-temperature solution-based cation exchange reaction, we created CdS-Cu<sub>2</sub>S heteroepitaxial junction nanowire solar cells with open-circuit voltage and fill factor values superior to those reported for equivalent planar cells.<sup>15</sup> In addition to photovoltaics, nanowires also offer advantages in solar energy conversion based on artificial photosynthesis. By growing single phase InGaN nanowires vertically on the sidewalls of Si wires, we obtained photocurrent density 5 times higher compared to the photocurrent density with InGaN nanowire arrays grown on planar Si.<sup>16</sup> Practical implementation of one-dimensional semiconductors into devices capable of exploiting their novel properties is often hindered by low product yields and high production cost. We demonstrated that large quantities of high quality, single crystalline TiO<sub>2</sub> nanowires with controllable dimensions and tunable transition metal doping can be synthesized using a molten-salt flux scheme.<sup>17</sup> In addition to material compositions, surface modifications of these nanowires are critical to their photocatalytic activity. We found that Atomic Layer Deposition (ALD) coating improves the charge collection efficiency from TiO<sub>2</sub> nanowires due to the passivation of surface states and an increase in surface area.<sup>18</sup> We also reported higher absorbed photon-to-current efficiency in Zn-doped GaP nanowire photocathodes' photoelectrochemical evolution of hydrogen using a surfactant-free solution-liquid-solid (SLS) synthetic method.<sup>19</sup> Using an epitaxial casting method, we created single-crystalline high surface area (Ga<sub>1-x</sub>Zn<sub>x</sub>)(N<sub>1-x</sub>O<sub>x</sub>) nanotubes, a promising candidate for a high efficiency photocatalyst for visible-light-driven overall water splitting with approximately 1.5–2 times higher photocatalytic activity than similar composition powders.<sup>20</sup> The ultimate goal of artificial photosynthesis is to imitate nature by using an integrated system of nanostructures, each of which plays a specific role in the sunlight-to-fuel conversion process. We demonstrated a fully integrated system of nanoscale photoelectrodes assembled from inorganic nanowires for direct solar water splitting.<sup>21</sup>

Future plans in subtask 2 will continue to explore nanowire laser cavity coupling physics and design semiconductor nanowire heterostructures with well-defined interfaces for solar energy conversion purposes. Systematic experiments will include designed nanostructure synthesis, detailed structural analysis, property and device performance measurements as well as ultrafast spectroscopic investigation.

## Subtask 3: Microscopy Investigations of Nanostructured Materials

Unlike visible and infrared spectroscopy, x-ray absorption can map the conduction band density of states with element- and oxidation-state specificity. A table-top apparatus has been developed that creates femtosecond pulses of soft x-rays from high-harmonic generation by a Ti:Sapphire amplifier. The 40 to 100 eV spectral range is ideal for studying the core-level absorption of transition metals and semiconductors. Photoexcitation of  $\alpha$ -Fe<sub>2</sub>O<sub>3</sub>, an earth-abundant photocatalyst for water splitting, at 400

nm causes the growth of an x-ray absorption feature consistent with a ligand-to-metal charge transfer (LMCT) state. The LMCT state rises initially in  $\sim 80$  fs and is followed by a 300 fs relaxation, highlighting the ability of this technique to probe ultrafast changes in electronic structure. The absorption spectrum of the photocatalyst  $\text{Co}_3\text{O}_4$  is composed of several distinct features attributed to metal-to-metal charge transfer between  $\text{Co}^{2+}$  and  $\text{Co}^{3+}$  ions, as well as LMCT transitions from  $\text{O}^{2-}$  to  $\text{Co}^{2+/3+}$ . A noncollinear optical parametric amplifier is being built for tunable visible pump wavelengths in order to selectively excite specific transitions, so that the excited state electronic structure and the relaxation pathways can be observed. Future work in subtask 3 will utilize transient x-ray absorption to study charge carrier dynamics, including electron/hole transfer and localization, of multicomponent nanostructures such as transition-metal doped nanowires in subtask 2 and seeded/cation-exchanged rods in subtasks 1 and 4.

Single particle fluorescence spectroscopy techniques are applied to study the fluorescence intermittency, or blinking, of single semiconducting nanostructures.<sup>22</sup> We have shown that rate fluctuations of the charge trapping process play an important role in the mechanism for QD blinking.<sup>23</sup> Further investigation into these fluctuations showed a strong correlation between on-state memory and distributed blinking kinetics, suggesting that the combined effect of two charge trapping processes (one fluctuation-based and one ionization-based) are responsible for blinking.<sup>24</sup> Blinking is also used as a probe of the nanoparticle-environment interaction. Surprising differences were found in the trap state distribution for QDs in two polymer hosts: the semiconducting *N,N'*-diphenyl-*N,N'*-bis(3-methylphenyl)-(1,1'-biphenyl)-4,4'-diamine (TPD) and the insulating poly(methylmethacrylate) (PMMA).<sup>25</sup> In coordination with subtask 1, fluorescence blinking statistics were used as a probe of the interaction between CdSe/CdS QDs and a new class of chalcogenidometalate (ChaM) ligands, specifically  $\text{Sn}_2\text{S}_6^{4-}$  or  $\text{In}_2\text{Se}_4^{2-}$ , revealing an increased density of charge trapping sites and increased stabilization of surface-trapped charges for the ChaM-capped QDs compared to oleylamine-capped QDs.<sup>26</sup> Current work aims to uncover the carrier dynamics of the charge-trapped off-state for single CdS nanorods by simultaneously measuring band-edge and trap-state blinking events.

Previous work on the localized surface plasmon resonance (LSPR) of rod-in-ring gold nanostructures showed that conductive coupling between the rod and ring leads to sharp quadrupolar and octupolar resonances.<sup>27</sup> Titanium is often used as an adhesion layer in electron-beam lithography, and this damping effect reduces the usefulness of LSPRs for sensing applications. We have shown that vapor-deposited (3-mercaptopropyl) trimethoxysilane performs well as an adhesion layer without damping the sharp plasmon resonances.<sup>28</sup> Dark-field scattering spectroscopy was used to study the coupling of  $\pi$  electrons in few-layer graphene to the LSPRs of gold disks illustrating that the resonance shift of plasmonic nanostructures on layered graphene can be used to measure the screening length of graphene films.<sup>29</sup>

#### **Subtask 4: Model Photocatalytic Nanostructures**

In subtask 4, we have examined the quenching efficiency of a variety of molecules whose redox potential falls within the band gap of nanocrystals. Previous work showed that the PL of a CdSe seeded CdS nanorod with a Pt tip was quenched via electron transfer to Pt.<sup>32</sup> We further explored other electron acceptors such as methyl viologen, a well-characterized electron acceptor with a long-lived radical state that makes it an attractive option for water reduction. Rapid electron transfer outcompetes hole scavenging and typically results in photo-oxidation and a blue shift of the particle fluorescence. We have also explored ferrocene as a hole scavenger for water oxidation, showing PL quenching with increased coverage of ferrocene ligands characterized by NMR. Current work is focused on elucidating the forward and backward rates of these processes with transient absorption.

Nanocrystal and quencher interactions have been examined on a single particle level using single particle fluorescence spectroscopy. Using a flow cell setup, we are able to observe a single particle's fluorescence trajectory over time as the quencher is introduced. Preliminary data shows that particles exhibit sudden to gradual drops in the discrete fluorescent levels, and increased off states. To eliminate blinking as a competing non-radiative pathway, we have synthesized nanocrystals with thick Type II

shells. Depending on the material, the thick shell will also slow down the forward and/or backward charge transfer rate by increasing the thickness of the tunneling barrier. We believe that slowing down this rate will allow us to monitor the forward and backward rates using on and off times on the single particle level.

## Publications:

1. B. J. Beberwyck and A. P. Alivisatos, *Ion Exchange Synthesis of III-V Nanocrystals*, *J. Am. Chem. Soc.* **134**, 19977 (2012).
2. P. K. Jain, B. J. Beberwyck, L. Fong, M. J. Polking, and A. P. Alivisatos, *Highly Luminescent Nanocrystals from Removal of Impurity Atoms Residual from Ion-Exchange Synthesis*, *Angew. Chem. Int. Ed.* **51**, 2387 (2012).
3. P. K. Jain, L. Amirav, S. Aloni, and A. P. Alivisatos, *Nanoheterostructure Cation Exchange: Anionic Framework Conservation*, *J. Am. Chem. Soc.* **132**, 9997 (2012).
4. J. B. Rivest, S. L. Swisher, L. K. Fong, H. Zheng, and A. P. Alivisatos, *Assembled Monolayer Nanorod Heterojunctions*, *ACS Nano* **5**, 3811 (2011).
5. H. Schlicke, D. Ghosh, L. K. Fong, H. L. Xin, H. Zheng, and A. P. Alivisatos, *Selective Placement of Faceted Metal Tips on Semiconductor Nanorods*, *Angew. Chem. Int. Ed.* **52**, 980 (2013).
6. J. M. Yuk, K. Kim, B. Alemn, W. Regan, J. Ryu, J. Park, P. Ercius, H. Lee, A. P. Alivisatos, M. Crommie, J. Lee, and A. Zettl, *Graphene Veils and Sandwiches*, *Nano Lett.* **11**, 3290 (2011).
7. J. M. Yuk, J. Park, P. Ercius, K. Kim, D. J. Hellebusch, M. F. Crommie, J. Y. Lee, A. Zettl, and A. P. Alivisatos, *High-Resolution EM of Colloidal Nanocrystal Growth Using Graphene Liquid Cells*, *Science* **336**, 61 (2012).
8. J. Park, H. Zheng, W. C. Lee, P. L. Geissler, E. Rabani, and A. P. Alivisatos, *Direct Observation of Nanoparticle Superlattice Formation by Using Liquid Cell Transmission Electron Microscopy*, *ACS Nano* **6**, 2078 (2012).
9. J. M. Luther, P. K. Jain, T. Ewers, and A. P. Alivisatos, *Localized Surface Plasmon Resonances Arising from Free Carriers in Doped Quantum Dots*, *Nature Materials* **10**, 361 (2011).
10. K. Manthiram and A. P. Alivisatos, *Tunable Localized Surface Plasmon Resonances in Tungsten Oxide Nanocrystals*, *J. Am. Chem. Soc.* **134**, 3995 (2012).
11. D. Gargas, H. Gao, and P. Yang, *High Quantum Efficiency of Band-Edge Emission from ZnO Nanowires*, *Nano Lett.* **11**, 3792 (2011).
12. H. Gao, A. Fu, S. C. Andrews, and P. Yang, *Cleaved-Coupled Nanowire Lasers*, *Proc. Natl. Acad. Sci.* (in press) (2013).
13. C. Hahn, Z. Zhang, A. Fu, C. Wu, Y. Hwang, D. J. Gargas, and P. Yang, *Epitaxial Growth of InGaN Nanowire Arrays for Light Emitting Diodes*, *ACS Nano* **5**, 3970 (2011).
14. D. Gargas, H. Gao, and P. Yang, *High Quantum Efficiency of Band-Edge Emission from ZnO Nanowires*, *Nano Lett.* **11**, 3792 (2011).
15. J. Tang, Z. Huo, S. Brittman, and P. Yang, *Solution Processed Core-Shell Nanowires for Efficient Photovoltaic Cells*, *Nature Nano* **6**, 568 (2011).
16. Y. Huang, C. Wu, C. Hahn, H. Jeong, and P. Yang, *Si / InGaN Core/Shell Hierarchical Nanowire Arrays and their Photoelectrochemical Properties*, *Nano Lett.* **12**, 1678 (2012).
17. B. Liu, H. M. Chen, C. Liu, S. C. Andrews, C. Hahn, C. H. Wu, and P. Yang, *A General Method for Large Scale Synthesis of Transition-Metal Doped Titanium Dioxide Nanowires*, *Nature* (submitted) (2013).
18. Y. Huang, C. Hahn, B. Lu, and P. Yang, *Photoelectrochemical Properties of TiO<sub>2</sub> Nanowire Arrays: A Study on the Dependence of Length and Atomic Layer Deposition Coating*, *ACS Nano* **6**, 5060 (2012).
19. C. Liu, J. Sun, J. Tang, and P. Yang, *Zn-Doped P-Type Gallium Phosphide Nanowire Photocathodes from a Surfactant-Free Solution Synthesis*, *Nano Lett.* **12**, 5407 (2012).
20. C. Hahn, M. A. Fardy, C. Nguyen, M. Natera-Comte, S. C. Andrews, and P. Yang, *Synthesis and Photocatalytic Properties of Single Crystalline (Ga<sub>1-x</sub>Zn<sub>x</sub>)(N<sub>1-x</sub>O<sub>x</sub>) Nanotubes*, *Israel J. Chem.* **52**, 1111 (2012).
21. C. Liu, J. Tang, H. Chen, B. Liu, and P. Yang, *A Fully Integrated Nanosystem of Semiconductor Nanowires for Direct Solar Water Splitting*, *Nature* (submitted) (2013).
22. A. A. Cordones, T. J. Bixby, and S. R. Leone, *Evidence for Multiple Trapping Mechanisms in Single CdSe/ZnS Quantum Dots from Fluorescence Intermittency Measurements over a Wide Range of Excitation Intensities*, *J. Phys. Chem. C* **115**, 6341 (2011).
23. A. A. Cordones, T. J. Bixby, and S. R. Leone, *Direct Measurement of Off-State Trapping Rate Fluctuations in Single Quantum Dot Fluorescence*, *Nano Lett.* **11**, 3366 (2011).
24. A. A. Cordones, K. L. Knappenberger, Jr., and S. R. Leone, *Linking On-State Memory and Distributed Kinetics in Single Nanocrystal Blinking*, *J. Phys. Chem. B: Paul F. Barbara Memorial* (2012).
25. T. J. Bixby, A. A. Cordones, and S. R. Leone, *CdSe/ZnS Quantum Dot Intermittency in the Semiconducting Polymer N,N'-diphenyl-N,N'-bis(3-methylphenyl)-(1,1'-biphenyl)-4,4'-diamine (TPD)*, *Chem. Phys. Lett.* **521**, 7 (2012).
26. A. A. Cordones, M. Scheele, A. P. Alivisatos, and S. R. Leone, *Probing the Interaction of Single Nanocrystals with Inorganic Capping Ligands: Time-Resolved Fluorescence from CdSe-CdS Quantum Dots Capped with Chalcogenidometalates*, *J. Amer. Chem. Soc.* **134**, 18366 (2012).
27. T. G. Habteyes; S. Dhuey; S. Cabrini; P. J. Schuck; S. R. Leone, *Theta-Shaped Plasmonic Nanostructures: Bringing "Dark" Multipole Plasmon Resonances into Action via Conductive and Capacitive Coupling*, *Nano Lett.* **11**, 1819 (2011).
28. T. G. Habteyes, S. Dhuey, D. Gargas, E. Wood, S. Cabrini, P. J. Schuck, A. P. Alivisatos, and S. R. Leone, *Analysis of Metallic Adhesion Layer Induced Plasmon Damping and Molecular Linker as a Non-Damping Alternative*, *ACS Nano* **6**, 5702 (2012).
29. H.-A. Chen, C.-L. Hsin, Y.-T. Huang, M. L. Tan, S. Dhuey, S. Cabrini, W.-W. Wu, and S. R. Leone, *Measurement of Interlayer Screening Length of Layered Graphene by Plasmonic Nanostructure Resonances*, (*J. Phys. Chem C* submitted) (2012).
30. A. A. Cordones and S. R. Leone, *Mechanisms for Charge Trapping in Single Semiconductor Nanocrystals Probed by Fluorescence Blinking*, *Chem. Soc. Rev.* (in press) (2012).
31. C. Hahn, A. A. Cordones, S. C. Andrews, H. Gao, A. Fu, S. R. Leone, and P. Yang, *Effect of Thermal Annealing in Ammonia on the Properties of InGaN Nanowires with Different Indium Concentrations*, *J. Phys. Chem. C* (in press DOI: 10.1021/jp311685x) (2013).
32. L. Amirav and A. P. Alivisatos, *Photocatalytic Hydrogen Production with Tunable Nanorod Heterostructures*, *J. Chem. Phys. Lett.* **1**, 1051 (2010).

# Superconducting Materials

Qiang Li (Principle Investigator)

Condensed Matter Physics & Materials Science Department, Bldg. 480  
Brookhaven National Laboratory, Upton, NY 11973-5000  
Phone: 631-344-4490, Fax: 631-344-4071, Email: [qiangli@bnl.gov](mailto:qiangli@bnl.gov)

## Program Scope:

This program studies basic relationships between nanostructures and the macroscopic properties of superconductors. Both basic understanding and understanding of materials aspects for practical use are sought. Emphasis is on improving the critical temperature  $T_c$ , the upper critical field  $H_{c2}$ , and the critical current density  $J_c$ , because they determine limits to energy applications. Because of recent developments and new opportunities, research activities focus on: (1) the response of superconductivity to chemical and structural tuning. This could provide new strategies for enhancing  $T_c$  and  $H_{c2}$ , and designing entirely new superconducting materials; (2) response and control of superconducting transport properties by structural tuning, where the simultaneous increase of  $J_c(H)$  and reduction of the  $J_c$  anisotropy ratio can be achieved by tuning the defect structures. This could lead to effective and practical superconductors, used for electricity transmission, wind power generation, and grid-scale energy storage. Coordinated studies involve synthesis, structural, transport, and magnetic property characterization. By exploiting the range of advanced experimental techniques available at Brookhaven National Laboratory (BNL), we seek to understand and control the transport properties of superconducting materials by tackling the key science issues, from the macroscopic to the atomic levels. These activities are aligned with the Grand Challenge for the BES Directorate to understand strongly correlated electron behavior in materials

## Introduction:

A vital mission of the US Department of Energy (DOE) is to advance the energy security of the United States. As the electricity demand increases, driven by continuing urbanization and economic activities, the challenge to the national electricity grid to provide reliable power reaches new heights. The superconductor's lossless current flow enables the design of highly power-dense and compact equipment, such as high capacity cables and fault-current limiters, and hence offers powerful opportunities for restoring the reliability of the power grid and increasing its capacity and efficiency.

In recent years, as renewable energy utilization grows, the increasing mismatch between variation of renewable energy resources and electricity demand makes it necessary to capture electricity generated by wind, solar and other renewable energy generation for later use. Superconducting magnet energy storage systems (SMES) use magnetic fields in superconducting coils to store energy with near zero energy loss, and have instantaneous dynamic response. Superconducting coils can also provide a lower cost alternative to the rare-earth permanent magnet or geared systems for high power (> 10 MW) direct drive wind turbines. During 2010-2012, DOE ARPA-E awarded several transformative projects to develop superconducting technologies capable of addressing many renewable energy challenges. Among them, are two projects awarded to BNL and its industrial partners. The first one is "Superconducting Magnet Energy Storage (SMES) System with Direct Power Electronics Interface" awarded in 2010 (Co-PI. Q. Li, also the PI of this FWP) to the team led by ABB, Inc. The nature of this ultra-high field SMES system is such that massive energy storage, fast response, and a nearly infinite cycling capability will be attained, representing a significant advantage over alternative energy storage devices, which are severely limited in terms of lifetime and environmental constraints when disposed. The second one is "Superconducting wires for direct drive wind generators" awarded in 2012 to the team led by BNL (Lead-PI Q. Li, also the PI of this FWP). The nature of this project is the development of a new generation of high temperature superconducting (HTS) wires capable of carrying critical current 4 times higher than the current state-of-the-art second generation (2G) wires, enabling cost-effective very large (10 MW+) direct-drive wind power gener-

ators. The key technology advance in the 2<sup>nd</sup> ARPA-E project is the combination of the solid-state “catalysis”-based synthesis approach – *A basic science discovery made in this BES program at BNL several years ago*, with a low-cost, long-length wire process at AMSC. Over the years, *this program* has not only made basic science discoveries, but also helped to facilitate critical transition from science discovery to transformative superconducting technology that has far reaching impact to the global energy landscape.

Although present HTS technology is positioned to play an important role in addressing our national and global energy challenges and can be deployed for some of the grid functions, significant barriers to achieving the full potential of superconductivity for transforming the power grid, renewable energy generations, and grid-scale energy storage have remained. The latter are primarily related to material properties. Bridging the gaps in performance improvement of superconductors and identifying the limiting factors requires a fundamental understanding of the microscopic origin of superconducting behavior.

This program continues the long-standing *BES funded Superconducting Materials program* at BNL to study basic relationships between nanostructures and macroscopic properties of superconductors. Both basic understanding and understanding of materials needs for practical use are sought. Several themes that extend from past work on HTS are retained, while research on emergent materials like iron-chalcogenides, and development of new characterization method are actively pursued. These include understanding of the origin and limits of critical temperature, upper critical field, vortex-pinning and critical current densities, and their response to structural and electronic tuning.

### Recent Progress (selected):

Superconducting iron-chalcogenide ( $\text{FeSe}_{0.5}\text{Te}_{0.5}$ ) epitaxial thin films were successfully grown on a variety of single crystal substrates and buffered metal substrates for the first time in our group by using pulsed laser deposition. We demonstrated that these films have significantly higher  $T_c$ , as compared to single crystal or bulk polycrystalline samples (bulk onset  $T_c \sim 15$  K) for the entire doping regime of  $\text{FeSe}_{1-x}\text{Te}_x$ . (Fig. 1). It was found that films made with  $\text{CeO}_2$  buffer layers on single crystal yttria-stabilized zirconia (YSZ) and bi-axial aligned Ni-W metal substrates have the highest  $T_c$  with an onset  $T_c$  above 20 K and zero resistance  $T_c$  above 18 K. Structural analysis by x-ray diffraction and high resolution transmission electron microscopy (TEM) reveal that these films generally have significantly smaller c-axis and a-axis lattice constant than the bulk value, suggesting that the crystal structure changes have a dominating impact on the superconducting transition in iron-based superconductors. [1][13][16]

Although HTS cuprates have been discovered for more than twenty five years, superconductors for high field application are still based on low temperature superconductors (LTS), such as  $\text{Nb}_3\text{Sn}$ . The high anisotropies, brittle textures and high manufacturing costs, limit the applicability of the cuprates. We demonstrate for the first time that the iron superconductors, without most of the drawbacks of the cuprates, have a superior high field performance over LTS at 4.2 K. With a  $\text{CeO}_2$  buffer, critical current densities  $J_c$  above  $10^6$  A/cm<sup>2</sup> were observed in iron-chalcogenide  $\text{FeSe}_{0.5}\text{Te}_{0.5}$  films grown on single crystalline and coated conductor (bi-axial aligned Ni-W metal substrates) substrates. As shown in Fig. 2, these films are robust and capable of carrying record high  $J_c$  exceeding  $10^5$  A/cm<sup>2</sup> under 30 T magnetic fields, which are much higher than those of LTS. Unlike cuprates, nearly isotropic  $J_c$  was observed at low temperature and high field, which is striking, considering both cuprates and iron-based superconductors have layered structure. High  $J_c$ , low magnetic field aniso-

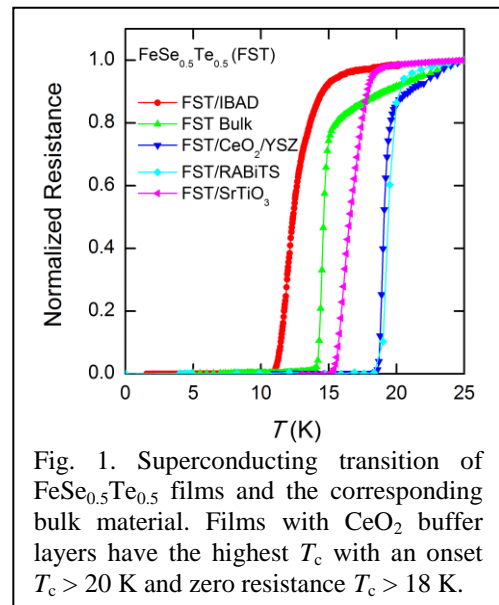


Fig. 1. Superconducting transition of  $\text{FeSe}_{0.5}\text{Te}_{0.5}$  films and the corresponding bulk material. Films with  $\text{CeO}_2$  buffer layers have the highest  $T_c$  with an onset  $T_c > 20$  K and zero resistance  $T_c > 18$  K.

tropies and relatively strong grain coupling, make iron-chalcogenide coated conductors particularly attractive for high field applications at liquid helium temperatures. [1]

Extensive structural characterization has been performed using analytical TEM and synchrotron-based light source at BNL in an attempt to understand the

structural origin of the record high performance  $\text{FeSe}_{0.5}\text{Te}_{0.5}$  films and the role of  $\text{CeO}_2$  buffer layer. Fig 3 shows the cross sectional view (a) of the films on  $\text{CeO}_2$  buffered single crystal YSZ substrates, and corresponding electron diffraction pattern (b). We found that the films with  $\text{CeO}_2$  buffer have similar c-axis lattice constant to the films without  $\text{CeO}_2$  buffer, while the a-axis lattice constant of the buffered films is substantially shorter. It appears that the compressive strain induced by  $\text{CeO}_2$  helps to enhance the flux pinning strength in the iron chalcogenides.

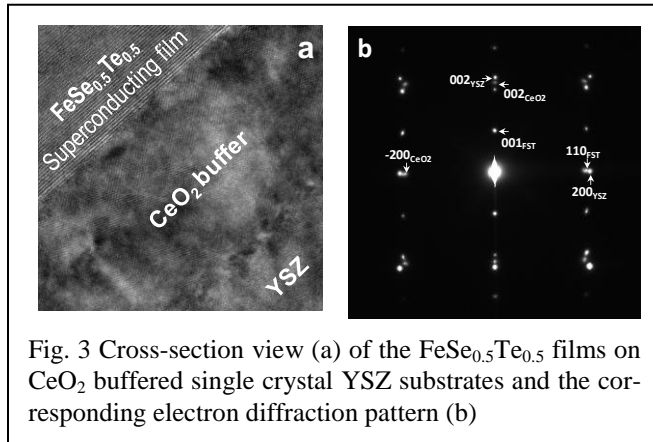


Fig. 3 Cross-section view (a) of the  $\text{FeSe}_{0.5}\text{Te}_{0.5}$  films on  $\text{CeO}_2$  buffered single crystal YSZ substrates and the corresponding electron diffraction pattern (b)

conductivity against high magnetic fields in the strongly-correlated iron-chalcogenide film  $\text{FeTe:O}_x$  - Below 2.52 K. Instead of saturating like a mean-field behavior with a single order parameter, the measured low-temperature upper critical field increases progressively, suggesting a large supply of superconducting states accessible via magnetic field or low-energy thermal fluctuations. We demonstrate that superconducting states of finite momenta can be realized within the conventional theory, despite its questionable applicability. Our findings reveal a fundamental characteristic of superconductivity and electronic structure in the iron-based superconductors. [20]

We carried out many detailed structural studies by synchrotron x-ray diffraction of several sets of  $\text{YBa}_2\text{Cu}_3\text{O}_7$  films that represent recent advances in flux-pinning design, containing various concentrations of artificial pinning centers: (i)  $\text{BaZrO}_3$  nanorods, (ii)  $\text{BaZrO}_3$  nanoparticles, and (iii)  $\text{Y}_2\text{O}_3$  nanoparticles. A statistical analysis was performed in order to separate the effects of foreign defect-induced and intrinsic (derivative phases) pinning. We found a statistically significant correlation between the orthorhombic distortion of the YBCO matrix and the pinning strength. Our result implies that the in-plane ordering of oxygen ions in the chain positions accounts for approximately 60% of the pinning force. The strain-induced pinning mechanism analysis, based on the Eshelby model of elastically strained composites, predicts that

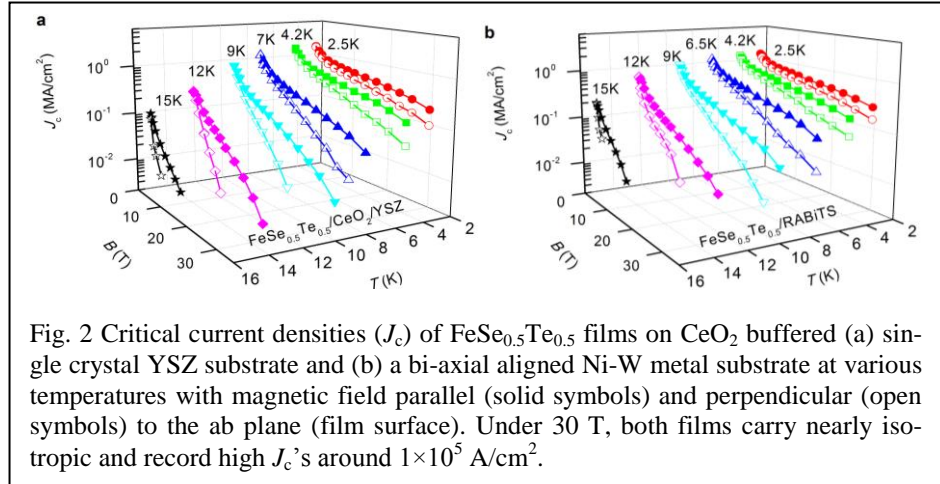


Fig. 2 Critical current densities ( $J_c$ ) of  $\text{FeSe}_{0.5}\text{Te}_{0.5}$  films on  $\text{CeO}_2$  buffered (a) single crystal YSZ substrate and (b) a bi-axial aligned Ni-W metal substrate at various temperatures with magnetic field parallel (solid symbols) and perpendicular (open symbols) to the ab plane (film surface). Under 30 T, both films carry nearly isotropic and record high  $J_c$ 's around  $1 \times 10^5$  A/cm<sup>2</sup>.

small YBCO grain size is a critical component of a strong pinning architecture that can enable critical current density values approaching the depairing limit. [2][4][14][19][21][23]

Neutron scattering, optical spectroscopy, x-ray absorption spectroscopy, point-contact spectroscopy, TEM, transport, and susceptibility measurements have been performed collectively on superconducting iron-chalcogenides. We reported several significant observations, including 1) strong correlation between superconductivity and magnetic order/fluctuations in  $\text{Fe}_{1+\delta}\text{Se}_x\text{Te}_{1-x}$ ; 2) The normal-state c-axis electronic response of  $\text{FeTe}_{0.55}\text{Se}_{0.45}$  is incoherent and bears significant similarities to those of mildly underdoped cuprates; 3) Enhanced second-nearest-neighbor Fe-Fe correlation below  $T_c$  identified in  $\text{K}_{0.8}\text{Fe}_{1.6+x}\text{Se}_2$  possibly due to changes in magnetic or local structural ordering; etc. [6][7][9][11][15][18][25][26]

### Future plans:

- 1) To investigate the response of superconductivity in iron-chalcogenides to proton and heavy iron irradiation - By controlling defect structure and landscape, we will gain understanding of the interaction between vortices and defects, so as to determine the most potent means of enhancing  $T_c$ ,  $J_c$  and  $H_{c2}$ .
- 2) To investigate the response of superconductivity in iron-chalcogenides to pressure and strain by bending or pulling iron-chalcogenide films on metal substrates, we will be able to create arbitrary amount of tensile and compressive strain, followed by transport and magnetization measurement.
- 3) To investigate the role of grain boundaries in iron-chalcogenides by measuring the mis-orientation angle dependence of critical current across various types of grain boundaries in the films made on bi-crystal substrates and bi-axial-aligned metal substrates, followed by detailed structural examination using TEM.
- 4) Novel superconducting materials grown on reconstructed polar surfaces - Polar surface is a termination with infinite surface energy (an example is  $\text{CeO}_2$ ), which is reduced by the surface reconstruction. The instability of polar surfaces can be utilized to create a rich variety of thermodynamically stable arrangements of surface atoms and vacancies. Some of the arrangements are shown by us previously to have high catalytic activity, i.e. ability to reduce the energy threshold for new phase formation. Traditionally, the polar terminations have been used for growing epitaxial structures. Little or no attention has been paid to the catalytic activity of the surface. By combining the template role of the polar surface with that of a catalyst, we plan to explore new avenues in synthesis of new and improved superconducting materials.

### Publications of this program, 2010-20102

- [1] W. Si et al, Nature Commun. **4**:1347 (2013).
- [2] V. Solovyov et al, Supercond. Sci. and Technol. **26** 013001 (2013)
- [3] Q. Jie et al, Physica C **481**, 46–54 (2012)
- [4] V. Solovyov et al, Phys. Rev. B **86**, 094511 (2012)
- [5] Q. Jie et al, Phys. Rev. B **86**, 11521 (2012)
- [6] H. Arham et al, Phys. Rev. B **85**, 214515 (2012)
- [7] C. Homes et al, Phys. Rev. B **85**, 134510 (2012).
- [8] H. Liu, et al, Nature Materials **11** 422 (2012)
- [9] T. A. Tyson, Phys. Rev. B **85** 024504 (2012)
- [10] J. Tao et al, PNAS, **108** 20941 (2012)
- [11] H. F. Hu et al, Phys. Rev. B **85** 064504 (2012)
- [12] J. Wen, et al, Phys. Rev. B **85**, 134513 (2012)
- [13] Q. Li et al, Rep. Prog. Phys. **74** 124510 (2011).
- [14] V. Solovyov et al, J. Appl. Phys. **110** 123904 (2011).
- [15] S. Moon, et al, Phys. Rev. Lett. **106**, 217001 (2011)
- [16] W. Si et al, Appl. Phys. Lett. **98**, 262509 (2011).
- [17] H. Hu et al, New Journal of Physics **13** 053031 (2011)
- [18] C. C. Homes, J. of Phys. and Chem of Solids, **72** 505 (2011)
- [19] V. Solovyov et al, J. Appl. Phys. **108**, 113912 (2010).
- [20] W. Si et al, Phys. Rev. B **81**, 092506 (2010)
- [21] V. Solovyov et al, J. Appl. Phys. **108**, 113912 (2010)
- [22] I. Dimitrov et al, Phys. Rev. B **81**, 17431 (2010)
- [23] V. Solovyov et al, Supercond. Sci. Technol. **23** 014008 (2010)
- [24] J. Wen et al, Phys. Rev. B **81**, 100513(R) (2010)
- [25] C. C. Homes, et al, Phys. Rev. B **81**, 220502(R) (2010)
- [26] Z. Xu et al, Phys. Rev. B **82**, 104525 (2010)

**Program Title:** “Light trapping, guiding and concentration for maximizing solar energy conversion”

Professor Shawn-Yu Lin  
Department of Physics, Applied Physics and Astronomy  
Rensselaer Polytechnic Institute, 110 8<sup>th</sup> street, Troy, NY 12180, Email: sylin@rpi.edu

## **Program scope**

Photovoltaics convert light directly into electric power. They can offer a virtually unlimited, clean, and renewable energy source provided that their light-capture capability and conversion-efficiency are improved while less semiconductor absorbing materials are used. In conventional silicon thin film solar cells, poor light trapping are a problematic issue, especially in the weakly or non-absorbing longer wavelength region of the solar spectrum. Therefore, thin film architecture is needed to collect and absorb a broadband spectrum of sunlight incident from all angles. Another benefit of using thin film architecture is the improved carrier collection efficiency. In this program, we use the *parallel-to-interface refraction* (PIR) effect in *three-dimensional* (3D) simple cubic photonic crystals to mold the flow of sunlight, to trap and absorb solar energy in submicron slab of semiconductor material, and to achieve a much improved solar cell device performance. Our program scopes, for sunlight collection and conversion, are to: (i) maximize solar trapping and absorption over a broad  $-\theta$  and  $-\lambda$  range; (ii) minimize solar reflection over a broad  $-\theta$  and  $-\lambda$  range; (iii) improve collection of photocurrent; and (iv) use less semiconductor materials with submicron thickness by utilizing standard semiconductor process and holographic technique.

## **Recent progress**

### **I. Fabrication of the simple cubic woodpile structures by standard semiconductor process**

To make the structures, hydrogenated amorphous silicon (a-Si:H) is first deposited on a four inch fused silica wafer by Plasma-enhanced chemical vapor deposition (PECVD). Then, resist patterns are created on top of the a-Si:H film by either electron-beam lithography or deep UV lithography. (Figure 1a) The grating patterns are transferred to the a-Si:H thin film by single-step deep RIE (DRIE) etching which provides relatively high silicon to resist selectivity and smooth silicon sidewall. (Figure 1b) After the pattern transfer and removal of the resist, Hydrogen silsesquioxane (HSQ) is spin-coated onto the pattern to provide a filling dielectric material with low refractive index ( $n \sim 1.45$ ) and no optical absorption. Excess HSQ is removed by RIE etching, and an one-layer grating structure of a-Si:H/HSQ is created. (Figure 1c) Another layer of a-Si:H film is deposited on the first layer structure, and a two-layer structure is fabricated by repeating the above process, with the second layer aligned orthogonally to the first one. (Figure



sustain nearly parallel propagation ( $90^\circ$  light bending) and strong resonances for the optical waves, and can lead to a very long photon dwell time. These resonant modes are more easily observed in the longer wavelength range with multiple absorption peaks beyond  $\lambda = 700$  nm.

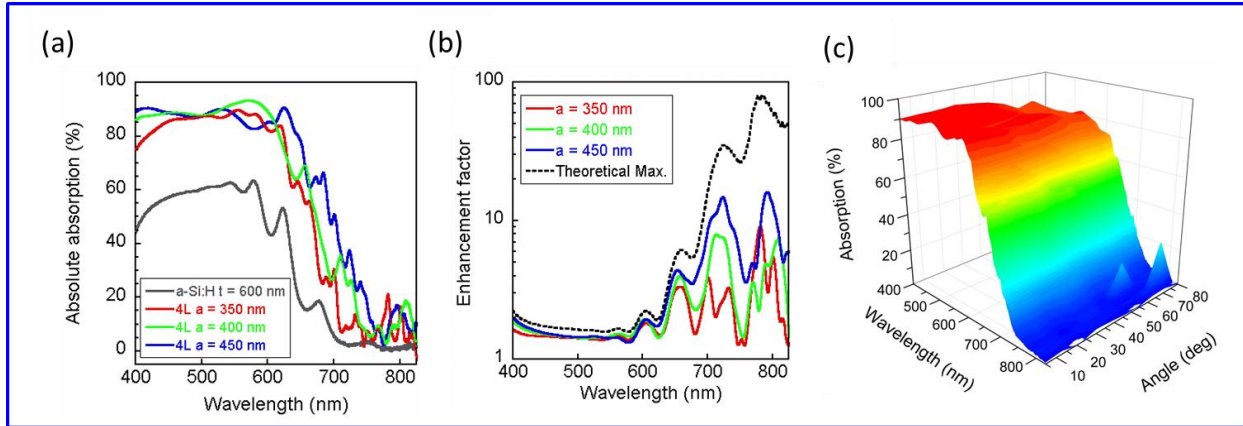


**Figure 2** (a) Absolute absorption of a 600 nm thick a-Si:H film and woodpile structures with lattice constant  $a = 350$  nm,  $a = 400$  nm, and  $a = 450$  nm. (b) Enhancement factors of the three 4L simple cubic woodpile structures compared to the 600 nm a-Si:H thin film. (c) Angular dependence of absorption of the 4L simple cubic woodpile structure with lattice constant  $a = 450$  nm at incident angles from  $5^\circ$  up to  $80^\circ$ .

We investigated the absorption enhancement factor of the 4L simple cubic woodpile structures by comparing to that of 600 nm thick a-Si:H thin film. As shown in Figure 2b, all three structures have enhanced absorption over the entire wavelength range. In the shorter wavelength range, the enhancement is about 1.5, which is already very close to the theoretical maximum of around 1.6. For longer wavelengths, significant enhancement is observed with multiple enhancement peaks for all three samples. The highest enhancement is  $\sim 17$  for  $a = 450$  nm sample at  $\lambda = 790$  nm. These enhancement peaks are evidence that there are resonant modes in the photonic crystal structures due to the PIR effect. Also, it clearly shows that the enhancement is dependent on the lattice constant of structures. As the lattice constant increases, the absorption enhancement is greater. The angular dependence of absorption was measured for  $a = 450$  nm sample. The absolute absorption measurements were taken with light of incident angle ( $\theta_i$ ) from  $5^\circ$  up to  $80^\circ$ . (Figure 2c) The results are depicted in a 3D surface plot in Figure 3c. The plot shows the absorption is sustained at around 90% in the shorter wavelength range even up to  $50^\circ$ . It is reduced only to 80% at  $70^\circ$ . At  $80^\circ$ , the absorption is still around 70%.

## Future Plans

1. In the near future, we plan to design, fabricate, and test 3D Simple cubic woodpile structures with aluminum back reflector to eliminate transmission and to improve the solar collection for  $\lambda = 350 - 900$  nm.
2. We plan to incorporate our 3D Simple cubic woodpile structures with ARC coating to minimize reflection at the surface and further improve the solar collection in the visible wavelength range.
3. We also plan to fabricate and test conical pore 2D photonic crystal structures proposed by Professor Sajeev John for further enhanced solar light trapping by PIR effect and Poynting vector circulation in certain high intensity hot spots. With only one micron equivalent thickness of silicon, such structures can show MAPD of  $J = 35.5$  mA/cm<sup>2</sup> over the spectral range  $\lambda = 300 - 1100$  nm, and this can lead to power conversion efficiency of 20% for silicon thin film solar cells.
4. We plan to advance our holographic light-diffraction approach such that the incident sunlight is bent 90 degree into a volume holographic film with an efficiency  $\geq 80 - 90\%$

## List of papers in which DOE support is acknowledged

1. Ping Kuang and Shawn-Yu Lin, "Optical absorption enhancement in three-dimensional simple cubic woodpile nanostructures for thin film solar cell applications", *SPIE Photonics West conference* (2013).
2. Ping Kuang, Alexei Deinega, Sajeev John, and Shawn-Yu Lin, "Experimental validation of parallel to interface refraction in three dimensional photonic crystals for absorption enhancement in thin film solar cell applications", to be submitted to *Nano Letters*.
3. Mei-Li Hsieh, James Bur, Yong-Sung Kim, and Shawn-Yu Lin, "A direct observation of quasi-coherent thermal emission by a three-dimensional metallic photonic crystal", *Optics Letters*, March 01 issue (2013).
4. Mei-Li Hsieh, Hong-Yu Chen, and Shawn-Yu Lin, "Observation of a large diffraction efficiency and efficiency enhancement of PQ/PMMA materials", submitted to *Applied Optics*, Jan (2013).

## Physical Behavior Associated with Mechanical Strain and Quantum Electronic Stress

Feng Liu (fliu@eng.utah.edu)  
Department of Materials Science & Engineering  
University of Utah, Salt Lake City, UT 84112

### Program Scope

This project focuses on three diverse but correlated research thrusts: (1) to continue our traditional efforts in the area of strain induced self-assembly of nanostructures in heteroepitaxial growth of thin films, (2) to expand a new research direction recently initiated by us in exploring the “quantum electronic stress” effect, a new conceptual extension over the conventional mechanical stress effect we developed recently, and (3) to foster a new research direction in studying the effect of strain on topological and electronic phases, such as topological insulator, of thin films. The common theme of our proposed research will remain focusing on fundamental understanding of stress/strain effect on physical behaviors of materials. The focused specific topics in the three thrusts include: (1) Nonlinear elastic effects on nucleation and growth of strained islands inside and outside a patterned pit, (2) Quantum electronic stress induced solid-state structural phase transitions, and (3) Effect of strain on topological and electronic phase transitions in Bi(111) and Sb(111) thin films.

### Recent Progress

Topic 1. First-principles Design of Organic Topological Insulators [1-3]. Topological insulators (TIs) are a recently discovered class of materials having insulating bulk electronic states but conducting boundary states distinguished by nontrivial topology. So far, several generations of TIs have been theoretically predicted and experimentally confirmed, but all based on inorganic materials. On the other hand, many conventional inorganic materials and devices have later found their way to organic counterparts, such as organic superconductors, light-emitting diodes, solar cells and field-effect transistors. In general, organic counterparts of inorganic materials have the added advantages of low cost, easy fabrication and mechanical flexibility. Recently, based on first-principles calculations, we predict a family of two-dimensional organic TIs made of organometallic lattices [1]. Designed by assembling molecular building blocks of triphenyl-metal compounds with strong spin-orbit coupling into a hexagonal lattice, this new classes of organic TIs are

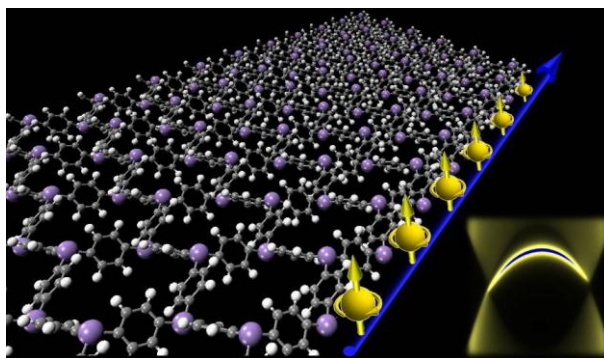


Fig. 1. Schematic illustration of an organometallic framework predicted from first-principles calculation to be an organic topological insulator, exhibiting nontrivial band topology and edge state, as shown by the calculated bands on the right.

shown to exhibit nontrivial topological edge states that are robust against significant lattice strain. Furthermore, by using different metal elements and molecular linkers, it is possible to also design organic magnetic TIs and topological flat-band materials [2,3]. We envision that organic TIs and topological materials will greatly broaden the scientific and technological impact of these interesting materials.

**Topic 2. Quantum Electronic Stress: Density Functional Theory Formulation and Physical Manifestation [9,6,20].** We recently introduced and formulated a new concept of “quantum electronic stress (QES)” within density functional theory (DFT) [9], to elucidate extrinsic electronic effects on the stress state of solids and thin films in the absence of external lattice strain. A formal expression of QES ( $\sigma^{QE}$ ) is derived in relation to the deformation potential of electronic states ( $\Xi$ ) and the variation of electron density ( $\Delta n$ ),  $\sigma^{QE} = \Xi(\Delta n)$ , as a quantum analog of classical Hook’s law of the relation of mechanical stress to strain, as illustrated in Fig. 2. Two distinct physical manifestations of QES have so far been demonstrated quantitatively by DFT calculations: (1) in the form of bulk stress induced by charge carriers [9,20]; and (2) in the form of surface stress induced by quantum confinement [6,9]. One interesting physical phenomenon is recognized to be associated with QES is the laser pulse induced graphite-to-diamond transition [9]. Broadly, QES may manifest in various physical phenomena and technological applications that are based on coupling of electronic structure with lattice stress, such as semiconductor doping and gating effects, quantum confinement in quantum wells, wires and dots, lasing and energy particle irradiation induced phase transitions, electroelastic effects, magnetoelastic effects and biological cell deformation due to charging and polarization.

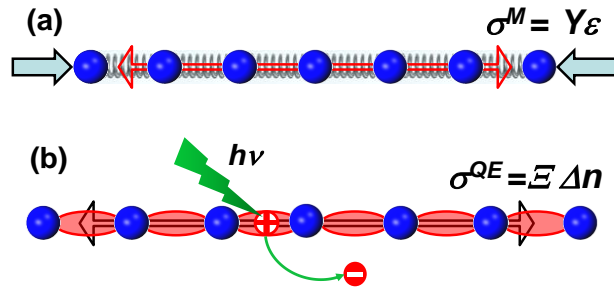


Fig. 2. Schematic illustration of mechanical stress ( $\sigma^M$ ) versus quantum electronic stress ( $\sigma^{QE}$ ). (a)  $\sigma^M$  induced by applying a compressive lattice strain ( $\epsilon$ ). Arrows indicate stress and force directions. (b)  $\sigma^{QE}$  induced by a hole excited by a photon in the absence of strain ( $\epsilon=0$ ).

**Topic 3. Non-equilibrium Composition Profiles of Alloy Quantum Dots and Nanowires and Their Correlation with Growth Mode [12-14].** Semiconductor alloy QDs and nanowires (NWs) with controlled composition profiles are promising nanoscale building blocks for modern nanophotonic and nanoelectronic devices. The overall composition profiles (CPs) of such low-dimensional nanostructures are usually far from equilibrium, because bulk diffusion is negligible for typical growth conditions. However, local equilibrium may be established in the near-surface regions via surface diffusion. Consequently, the kinetic growth mode, which dictates the manner of surface mass transport and alloy mixing at the growth front, becomes a key factor in determining the kinetically limited CP. Recent, we have developed an atomistic-strain-model Monte

Carlo method to directly simulate the non-equilibrium epitaxial growth of strained alloy QDs and NWs [12-14]. We discover a striking correlation between the CPs of strained semiconductor alloy QDs and NWs with the growth mode. The layer-by-layer growth (LG) mode results in spontaneously-formed, core-shell structures with the core rich in the unstrained component (relative to the substrate); while the faceted growth (FG) mode leads to nanostructures with the core rich in the strained component, as shown in Fig. 3. Our findings suggest a promising method for the control of the CP of semiconductor alloy QDs and NWs by selecting the growth mode [12-14].

### Future Plans

We will continue to expand our current studies as well as explore some new ideas. On the traditional topic of strain induced self-assembly of QDs, one interesting problem we are studying is the nucleation and growth of QDs next to a pit and their dependence of pit inclination angle as experimentally observed recently. We will develop a vigorous continuum model taking into account the nonlinear high-order elastic relaxation associated with large pit inclination and island facet angles, as well as perform atomistic-strain-model MC simulations to investigate the effect of composition distribution on the nucleation and growth of strained alloy islands. On the topic of quantum electronic stress effect, we are investigating the ultrafast crystal-to-amorphous phase transitions induced by pulse laser irradiation, by employing the concept of quantum electronic stress and first-principles DFT molecular dynamics simulations. In addition, we have taken on a new research direction studying the effect of strain on topoelectronic properties of Bi(111) and Sb(111) thin films. We have recently developed new computational tools in calculating the band topology and topological surface and edge states.

### The DOE Program Sponsored Publications (2010-present):

1. "Organic Topological Insulators in Organometallic Lattices", Z. F. Wang, Z. Liu and Feng Liu, *Nature Communications*, 4, 1471 (2013).
2. "Flat Chern Band in a Two-Dimensional Organometallic Framework", Z. Liu, Z. F. Wang, J.-W. Mei, Y.-S. Wu and Feng Liu, *Phys. Rev. Lett.* (in press), arXiv:1210.1826v2.
3. "Quantum Anomalous Hall Effect in 2D Organic Topological Insulators", Z. Liu, Z. F. Wang, and Feng Liu, arXiv:1302.1088v1.
4. "Quasiparticle Dynamics in Reshaped Helical Dirac Cone of Topological Insulators", L. Miao, Z. F. Wang, W. Ming, M. Yao, M. Wang, F. Yang, F. Zhu, A. V. Fedorov, Z. Sun, C. L. Gao, C. Liu, Q. Xue, Feng Liu, D. Qian, J. Jia, *PNAS* (in press).

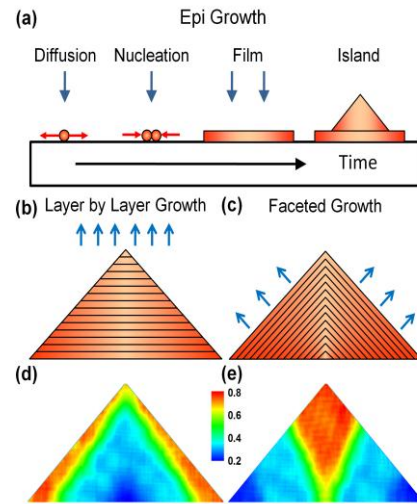


Fig. 3. (a) Schematic of the SK growth process. (b) and (c) Schematic of the LG and FG of a InGaN QD. (d) The CP of a QD with a triangle Ga-rich core. (e) The CP of a QD with a V-shape In-rich core. The color bar marks the In concentration.

5. "Anisotropic Strain Enhanced Hydrogen Solubility in bcc Metals: The Independence on the Sign of Strain", H.-B. Zhou, S. Jin, Y. Zhang, and G.-H. Lu, and Feng Liu, *Phys. Rev. Lett.* 109, 135502 (2012).
6. "Interplay between quantum size effect and strain effect on growth of nanoscale metal thin films", M. Liu, Y. Han, L. Tang, J. Jia, Q. Xue, and Feng Liu, *Phys. Rev. B* 86, 125427 (2012).
7. "Quantitative Model of Heterogeneous Nucleation and Growth of SiGe Quantum Dot Molecules", H. Hu, H. Gao, and Feng Liu, *Phys. Rev. Lett.* 109, 106103 (2012).
8. "Strain-less directed self-assembly of Si nanocrystals on patterned SiO<sub>2</sub> substrate", J. Ren, H. Hu, Feng Liu, S. Chu, and J. Liu, *J. Appl. Phys.*, 112, 054311 (2012).
9. "Quantum Electronic Stress: Density-Functional-Theory Formulation and Physical Manifestation", H. Hu, M. Liu, Z. F. Wang, J. Zhu, D. Wu, H. Ding, Z. Liu, and Feng Liu, *Phys. Rev. Lett.* 109, 055501 (2012).
10. "Spatial and Energy Distribution of Topological Edge States in Single Bi(111) Bilayer", F. Yang, L. Miao, Z. F. Wang, M.-Y. Yao, F. Zhu, Y. R. Song, M.-X. Wang, J.-P. Xu, A. V. Fedorov, Z. Sun, G. B. Zhang, C. Liu, Feng Liu, D. Qian, C. L. Gao, and J.-F. Jia, *Phys. Rev. Lett.* 109, 016801 (2012).
11. "Edge Stability of BN sheets and Its Application for Designing Hybrid BNC Structures", B. Huang, H. Lee, B.-L. Gu, Feng Liu, and W. Duan, *Nano Res.* 5, 62 (2012).
12. "Simulation of self-assembled compositional core-shell structures in In<sub>x</sub>Ga<sub>1-x</sub>N nanowires", X. B. Niu, G. B. Stringfellow, Young-Ju Lee and Feng Liu, *Phys. Rev. B* 85, 165316 (2012).
13. "Phase separation in strained epitaxial InGaN islands", X. B. Niu, G. B. Stringfellow, and Feng Liu, *Appl. Phys. Lett.* 99, 213102 (2011).
14. "Nonequilibrium Composition Profiles of Alloy Quantum Dots and their Correlation with the Growth Mode", X. B. Niu, G. B. Stringfellow, and Feng Liu, *Phys. Rev. Lett.* 107, 076101 (2011).
15. "Stress tensor: A quantitative indicator of effective volume and stability of helium in Metals", H.-B. Zhou, S. Jin, X.-L. Shu, Y. Zhang, G.-H. Lu and Feng Liu, *Euro. Phys. Lett.*, 96 66001 (2011).
16. "Giant Magnetoresistance in Zigzag Graphene Nanoribbon", Z. F. Wang and Feng Liu, *Appl. Phys. Lett.* 99, 042110 (2011).
17. "Atomic chemisorption on graphene with Stone-Thrower-Wales defects", L. Chen, H. Hu, Yu. Ouyang, H.Z. Pan, Y.Y. Sun, Feng Liu, *Carbon*, 49, 3356 (2011).
18. "Surface reconstruction transition of metals induced by molecular adsorption", J. T. Sun, L. Gao, X. B. He, Z. H. Cheng, Z. T. Deng, X. Lin, H. Hu, S. X. Du, Feng Liu, and H.-J. Gao, *Phys. Rev. B* 83, 115419 (2011).
19. "Controlled surface functionalization via self-selective metal adsorption and pattern transformation on the vicinal Si(111) surface", A. L. Chin, F. K. Men and Feng Liu, *Phys. Rev. B* 82, 201406(R) (2010).
20. "Strain-Enhanced Doping in Semiconductors: Effects of Dopant Size and Charge State", J. Zhu, Feng Liu, G. B. Stringfellow, and S.-H. Wei, *Phys. Rev. Lett.* 105, 195503 (2010).
21. "Tunable interfacial properties of epitaxial graphene on metal substrates", M. Gao, Y. Pan, C. Zhang, H. Hu, R. Yang, H. Lu, J. Cai, S. Du, Feng Liu, and H.-J. Gao, *Appl. Phys. Lett.* 96, 053109 (2010).
22. "Enhanced cation-substituted p-type doping in GaP from dual surfactant effects", J. Zhu, Feng Liu, and G. B. Stringfellow, *J. Crys. Growth* 312, 174 (2010).
23. "Growth Instability of Strained Film: An Elastic Green's Function Force Monopole Approach", H. Hu and Feng Liu, in "Surface Effects in the Mechanics of Nanomaterials and Heterostructures", IUTAM Bookseries, Volume 31, 59-70 (2013). (**Invited paper**)
24. "Nanomechanical Architecture of Semiconductor Nanomembranes", M. Huang, F. Cavallo, Feng Liu and M. G. Lagally, *Nanoscale*, 3, 96 (2011). (**Invited review**)

**Program Title:** Study of p-type ZnO and MgZnO Thin Films for Solid State Lighting

**Principal Investigator:** Jianlin Liu, Department of Electrical Engineering, University of California, Riverside, CA 92521. Email: jianlin@ee.ucr.edu.

**Program Scope:**

The objective of the program is to investigate high-quality p-type ZnO and MgZnO materials for solid state lighting. ZnO has a room-temperature band gap of 3.37 eV with a 60 meV free exciton binding energy. Its band gap can be tuned by alloying with Mg (MgZnO) and Cd (CdZnO). However, intrinsic ZnO shows n-type conductivity due to the presence of different defects in the crystal. The major obstacle is to control its p-type conductivity, that is, to obtain reliable p-type ZnO and alloys. To solve this problem, under this program, we utilized plasma-assisted molecular beam epitaxy (MBE) and chemical vapor deposition (CVD) to grow high-quality ZnO thin films and nanowires and studied the characteristics of p-type ZnO materials. We successfully grew high-quality antimony (Sb), silver (Ag) and nitrogen (N) doped p-type ZnO thin films in MBE. Hole concentrations of  $\sim 10^{16} \text{ cm}^{-3}$  (Ag doped) and  $\sim 10^{15} \text{ cm}^{-3}$  (N doped) were obtained from the Hall effect measurements. Strong donor-acceptor pair (DAP) recombination was observed in the low-temperature photoluminescence (PL) spectra. In the case of Sb doping of thin films, we used p-n-p structure to study the p-type behavior of Sb-doped ZnO thin films and further proved the p-type conductivity of Sb-doped ZnO and extracted hole densities. Furthermore, we achieved Sb-doped and N-doped ZnO nanowires by CVD and studied the p-type conductivity of these nanowires. Fabry-Perot (FP) type laser and random laser have been demonstrated based on the Sb-doped and N-doped p-type ZnO nanowires, respectively. The results indicate that both Sb and N are efficient dopants for p-type ZnO.

**Recent Progress:**

*Growth and characterization of high-quality Ag-doped ZnO thin films:* Ag was predicted in literature to be possible shallow acceptor in ZnO. The expected advantage is that Ag should act as a substitution dopant in ZnO. Although c-sapphire substrate has lattice mismatch of 18% with ZnO, we made progress on low-temperature buffer technology and achieved single-crystalline ZnO thin films on c-sapphire. Based on this, we achieved high-quality p-type ZnO thin film with Ag doping. Fig. 1(a) is an SEM image showing almost featureless surface of Ag-doped ZnO. The inset of Fig. 1(a) is RHEED pattern of the sample, with the streaky pattern indicating smooth surface. P-type conduction of  $\sim 1 \times 10^{16} \text{ cm}^{-3}$  hole concentration was obtained by Hall effect measurements. Further investigation into the p-type films was carried out through temperature dependent PL, as shown in Fig. 1(b). DAP peak at 3.217 eV can be clearly observed and identified through its stagnant peak position. Two bound exciton peaks were observed at 3.358 eV and 3.364 eV, respectively. The 3.358 eV peak is possibly an acceptor bound exciton.

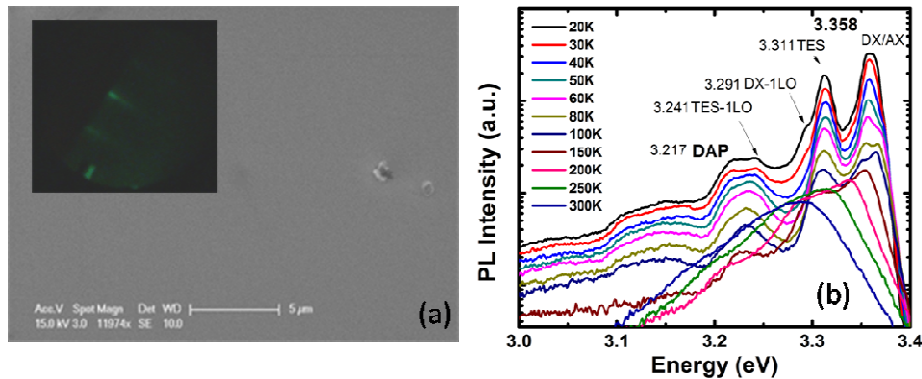


Fig. 1 (a) SEM image and RHEED pattern (inset) of Ag-doped ZnO, (b) Temperature dependent PL spectra of Ag-doped ZnO.

*Growth and characterization of high-quality N-doped p-type ZnO thin films:* We also explored p-type ZnO thin films by N doping. ZnO thin film on c-plane sapphire substrate was grown using MBE with nitrous oxide (N<sub>2</sub>O) gas as the doping source. We optimized the buffer layer to obtain single crystalline structure with very few defects. We achieved Zn-polar thin film, which is suitable for N doping, by controlling the thickness of the MgO buffer layer. Smooth surface was achieved (indicated by RHEED pattern in the inset of Fig. 2(b)). Prominent difference was observed in low-temperature PL spectra of N-doped ZnO with thinner MgO buffer layer and thicker MgO buffer layer. Fig. 2 shows low-temperature PL spectra of N-doped ZnO thin films. The sample in Fig. 2(b) has thicker (~30 nm) MgO buffer layer than that of in Fig. 2(a) (~5 nm). The near band edge (NBE) emission is more red shifted in Fig. 2(b) (3.351 eV) compared to Fig. 2(a) (3.356 eV). The DAP emission (around 3.23 eV) is much stronger in Fig. 2(b). The Hall bar measurement shows n-type conductivity of the sample in Fig. 2(a) with an electron concentration of around 10<sup>16</sup> cm<sup>-3</sup>. The sample of Fig. 2(b) shows p-type conductivity with a hole concentration of around 10<sup>15</sup> cm<sup>-3</sup>.

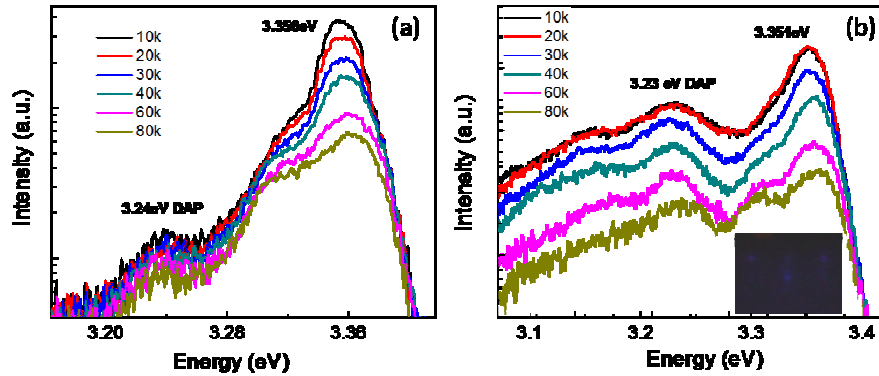


Fig. 2 Low-temperature PL spectra of N-doped ZnO thin films, (a) with thin MgO buffer and (b) with thick MgO buffer. Inset of (b): RHEED pattern.

*Study of p-type behavior of Sb-doped ZnO thin films using p-n-p structure:* P-type conductivities of p-ZnO thin films are normally investigated using Hall effect experiments. Nevertheless, higher-quality ZnO thin films require a ZnO buffer layer, which is usually n-type. Therefore, the Hall effect results would include multiple-layer effect, in many cases, the p-type conductivity of the active layer on top cannot be reliably extracted. We proposed to use photolithography and etching to fabricate a p-n-p structure based on the Sb-doped ZnO thin film on undoped n-ZnO on sapphire substrate. It was found by measuring electrical properties of this structure, the p-type conductivity of the ZnO thin film was extracted.

The sample was grown in a plasma-assisted MBE on c-sapphire substrate. Secondary ion mass spectrometry (SIMS) was used to obtain the elemental distribution of Zn, O, Sb, Mg, and Al, and the thickness information (Fig.3). The sharp staircase of Sb distribution between doped and undoped ZnO represents a good interface of the two layers of 350 nm each. The Al signal is from the sapphire substrate. Mg signal is seen at the film and substrate interface as MgO thin layer of 5 nm or so was deposited before the growth of ZnO layers.

Photolithography and etching were employed to etch away part of the top p-type film. As a result a “device” structure was formed between two p-type contacts with n-type ZnO layer lying underneath. Fig.4 shows high-frequency (1 MHz) C-V characteristics of the ZnO p-n-p structure (inset (a)). The capacitance was measured between the two Au/Ni contacts. The C-V sweep begins from 0V to 10V and then back to 0V. As the bias applied between the p-layers increases (forward sweep from 0V to 10V), the capacitance of the structure decreases. When the voltage is swept back, the capacitance of the structure is smaller than the value at the same voltage in the forward

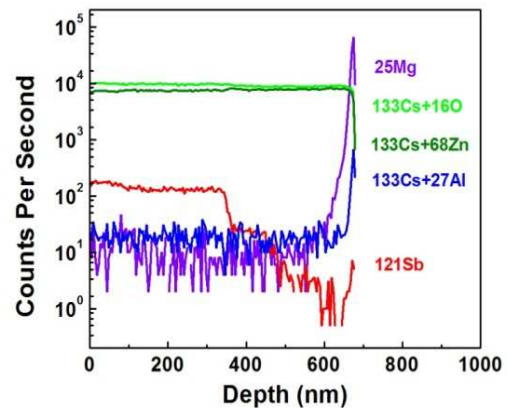


Fig. 3 SIMS spectra of Sb-doped ZnO/undoped ZnO on c-sapphire substrate. The elemental profiles of Zn, O, Sb, Mg, and Al can be seen.

sweep. The phenomena suggest the formation of p-type ZnO layer, and the structure is indeed a p-n-p device, which can be explained as follows. Insets (b) and (c) show the space charge regions and band diagram of the p-n-p structure at a thermal equilibrium state. When the bias is applied on the p-n-p structure, one p-n junction is reverse-biased while the other one is forward-biased. The electrons inside the n layer flow out of the structure from the forward-biased junction, leaving the positive space charges inside the potential well formed by the p-type and n-type layers and expanding the space charge region of the reverse-biased junction. As the bias increases, the width of the space charge region of the reverse-biased p-n junction increases and the capacitance of the junction decreases. The two p-n junctions are in series, therefore the total capacitance decreases as well. The extra positive space charges are trapped in the potential well in the n-type layer and develop the electric field, which tends to reverse both p-n junctions. So when the bias decreases back to 0V, the space charge region width of both junctions are larger than those of the junctions in fresh state and thus the capacitance is smaller. The decrease of the capacitance indicates that the extra space charges are trapped inside the potential well formed by the ZnO:Sb/ZnO/ZnO:Sb p-n-p structure. Such characteristics provide alternative evidence of the formation of p-type ZnO layers on n-ZnO buffer. With further information of the n-layer carrier concentration obtained from a reference sample, the p-layer hole carrier concentration can be extracted from the C-V characteristics to be around  $5 \times 10^{16} \text{ cm}^{-3}$ .

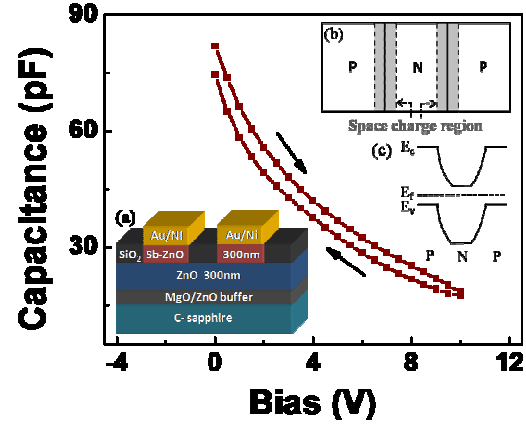


Fig. 4 C-V characteristics of ZnO p-n-p structure. C-V curve of p-n-p structure shows that the capacitance decreases as the bias increases and capacitance between forward and reverse sweeps is different. Inset (a) shows the p-n-p structure. Inset (b) is the schematic of the p-n-p structure showing the space charge regions of the p-n junctions in thermal equilibrium state and inset (c) is the corresponding energy band diagram.

*Realization of electrically pumped waveguide lasing based on Sb-doped p-type ZnO nanowires:* In this research, we studied the p-type conductivity of Sb-doped ZnO nanowires and demonstrated a homojunction laser diode, which consists of p-type Sb-doped ZnO nanowires on high-quality n-type ZnO film. The p-type conductivity of the ZnO nanowires was demonstrated by field-effect measurement. A hole concentration of  $4.5 \times 10^{17}$  to  $2.5 \times 10^{18} \text{ cm}^{-3}$  is extracted. The electrically pumped efficient Fabry-Perot (FP) type ZnO UV nanowire diode laser was realized at room temperature. Lasing was demonstrated by electroluminescence (EL) measurement. EL spectra under injection current from 20 mA to 70 mA is shown in Fig.5(a). The threshold of the laser device can be identified to be 48 mA in the integrated intensity versus current plot. The average spacing between modes is 2.52 nm and is close to the calculated value of 2.95 nm for this laser cavity. In addition to the spectra features, the side-view far-field microscope images for 60 mA and 70 mA injection current in Fig.5(b) shows another direct evidence of nanowire FP type lasing. The light emitting from both ends

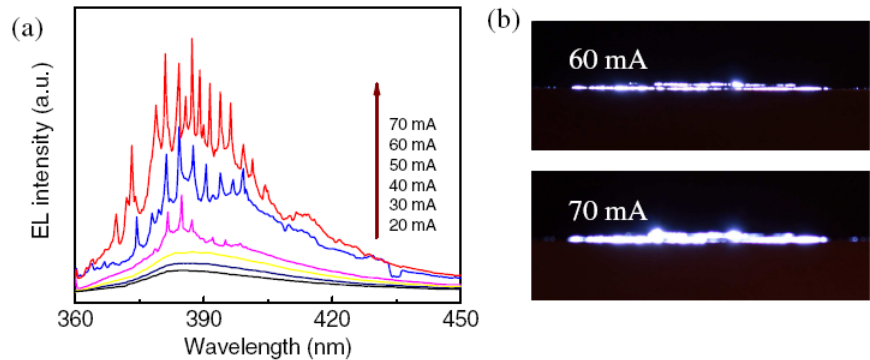


Fig.5 (a) EL spectra of nanowire laser operated from 20 mA to 70 mA. (b) Side-view microscope images of the device at 60 mA and 70 mA.

of nanowire is evident. This phenomenon is a strong proof of longitudinal lasing modes in a waveguide that has been constantly observed in nanowire optically pumped lasing. The laser diode is quite stable over the time suggesting that once Sb-doped p-type material is achieved, it appears robust.

*Study of p-type N-doped ZnO nanowires and realization of homojunction random laser:* We grew p-type N-doped ZnO nanowires by using CVD without any metal catalyst on ZnO seed layer on Si (SEM images in Fig. 6(a) and (b)). The p-type behavior was studied by the output characteristic and transfer characteristic of the nanowire back-gated FET (Fig. 6(c) and (d)), XPS (Fig. 6(b) inset) and PL. An acceptor activation energy of  $\sim 200\text{meV}$  was obtained. The formation of the p-n junction was confirmed by I-V and EBIC results. The lasing behaviors were studied by using both optical pumping and electrical pumping. Above the threshold pumping power/current, random lasing actions featuring a series of lasing peaks in the spectra were observed. The output power of the electrically pumped laser was measured to be 70 nW at a drive current of 70 mA. The angle dependant EL result shows that the emission has a broad angle distribution, further indicating the formation of ZnO nanowires p-n homojunction random laser and thus the p-type conductivity of the nanowires.

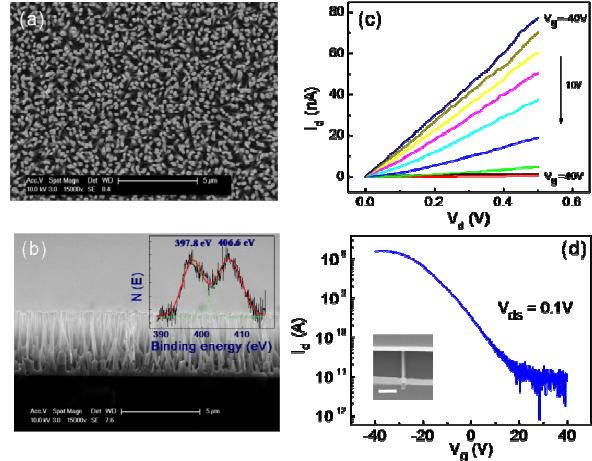


Fig.6 (a) Top view, and (b) Side view SEM image of N-doped ZnO nanowires. Inset: XPS spectrum of the sample, (c)  $I_d$ - $V_d$  curves, and (d)  $I_d$ - $V_g$  curves of N-doped nanowire back-gated FET. Inset: SEM image of the FET device. The scale bar is  $2\ \mu\text{m}$ .

### Future Plan:

The future research plan is to further enhance the p-type conductivity of high-quality ZnO materials. We will mainly focus on Sb, Ag and N doping and try to increase the hole concentration and mobility, and achieve highly conductive p-type ZnO thin films. In addition, the stability of the p-type ZnO will be carefully studied. Furthermore, band gap engineering of MgZnO will be studied. High quality p-type and n-type MgZnO will be achieve for future solid state lighting device applications.

### Publications (2010-present):

1. Z. Yang, S. Chu, W. V. Chen, L. Li, J. Y. Kong, J. J. Ren, P. K. L. Yu, and J. L. Liu, Appl. Phys. Express 3, 032101 (2010).
2. L. Li, Z. Yang, Z. Zuo, J. Y. Kong, and J. L. Liu, J. Vac. Sci. Tech. B 28(3), C3D13, 1071 (2010).
3. L. Li, Z. Yang, Z. Zuo, J. H. Lim, and J. L. Liu, Appl. Surf. Sci. 256, 4734 (2010).
4. L. Li, Z. Yang, and J. L. Liu, MRS Fall 2009, Boston, USA, Mater. Res. Soc. Symp. Proc. Vol. 1201, 1201-H01-09 (2010).
5. Z. Yang, H. Zhou, W. Chen, L. Li, J. Z. Zhao, P. Yu, and J. L. Liu, J. Appl. Phys. 108, 066101 (2010).
6. J. Y. Kong, L. Li, Z. Yang, and J. L. Liu, J. Vac. Sci. Tech. B 28(3), C3D10, 1071 (2010).
7. J. Z. Zhao, H. W. Liang, J. C. Sun, Q. J. Feng, J. M. Bian, L. Z. Hu, G.T. Du, J. J. Ren, and J. L. Liu, Physica Status Solidi A 208, 825 (2011).
8. S. Chu, J. Zhao, Z. Zuo, J. Kong, L. Li, and J. Liu, J. App. Phys. 109, 123110 (2011).
9. S. Chu, G. Wang, W. Zhou, Y. Lin, L. Chernyak, J. Zhao, J. Kong, L. Li, J. Ren, and J. Liu, Nature Nanotechnology 6, 506 (2011).
10. J. Huang, Z. L. Li, S. Chu, and J. L. Liu, Appl. Phys. Lett. 101, 232102 (2012).
11. J. Huang, S. Chu, J. Kong, L. Zhang, C. M. Schwarz, G. Wang, L. Chernyak, Z. Chen, and J. Liu, Adv. Opt. Mater., 2012, 10.1002/adom.201200062 (online).

## Amorphous Structures and Polymorphs of the Phase-Change Ge<sub>2</sub>Sb<sub>2</sub>Te<sub>5</sub> Alloy

E. Ma

Department of Materials Science and Engineering, Johns Hopkins University,  
Baltimore, MD 21218

ema@jhu.edu

### Program Scope

Phase-change multi-component chalcogenide materials, with Ge<sub>2</sub>Sb<sub>2</sub>Te<sub>5</sub> (GST) as a prototype alloy, are used as the media for high-density rewritable data storage. The amorphous (*a*-GST) and crystalline (*c*-GST) states possess significantly different optical and electronic properties. At the same time, GST can be rapidly switched between the two states (the crystallization of the *a*-GST happens on the time scale of several nanoseconds). Such characteristics are ideally suited for applications not only in rewritable optical data storage (CDs and DVDs), but also in electronic phase-change memory. The latter is a non-volatile memory that has fast data transfer rates and high storage densities, with the potential to replace flash memory in the future.

The desirable behaviors of GST must originate from the internal atomic structures of the amorphous and crystalline phases, as well as the unique chemical bonding features in these two states. Presumably, the reversible transformation between the *a*-GST and the *c*-GST only involves easy atomic rearrangements, such that the phase change process can be ultra-fast, while the changes in the chemical bonding are pronounced to produce a large contrast in optical and electronic properties. A thorough understanding of the atomic structure and its evolution, chemical bonding, possible competing phases in the transforming *a*-GST is highly important to the science of phase-change materials. The structural variations offer the room for controlling and optimizing the properties of GST materials, and are thus relevant to future development for their broadened data storage applications.

This project builds on our earlier success and experience in uncovering the atomic-level structure and poly(a)morphism [1], but shifting the emphasis from metallic glasses to GST. Our goals are three-fold. i) Understand the atomic structure and the chemical bonding in the GST glass; a comparison with those of the *c*-GST may help explain the ultra-fast (crystallization) switch speed and the large property contrast between the two phases. ii) Map out the phase relationships in the pressure (P)-temperature (T) space for GST. The crystalline polymorphs at the 2-2-5 composition, including new metastable phases, will be discovered and identified, to shed light on the phase transformation sequence. iii) Discover and understand the polyamorphic transitions between different *amorphous* states of the GST glass. We will explore the property changes associated with the different densities and electronic structures, to discover and expand the realm of possibilities for the GST properties.

### Recent Progress

During the past three years, our research used a two-pronged approach, composed of synchrotron measurements (*in situ* X-ray for structure, *in situ* pressure

experiments for phase transitions and resistivity measurements) on the experimental side, and *ab initio* molecular dynamics computer simulations on the modeling side. Our work has improved the understanding of the bonding and local structural motifs in as-prepared *a*-GST, and provided the first *in situ* monitoring of the pressure-induced evolution of the glassy structure, including its polyamorphism. Armed with our knowledge about the amorphous structure, we explained the rise of electrical conductance by four orders of magnitude, all in the amorphous state of *a*-GST.

- 1) Nature of chemical bonding and atomic structure in the phase-change amorphous  $\text{Ge}_2\text{Sb}_2\text{Te}_5$  (*Phys. Rev. Lett.* (2009) [2]).

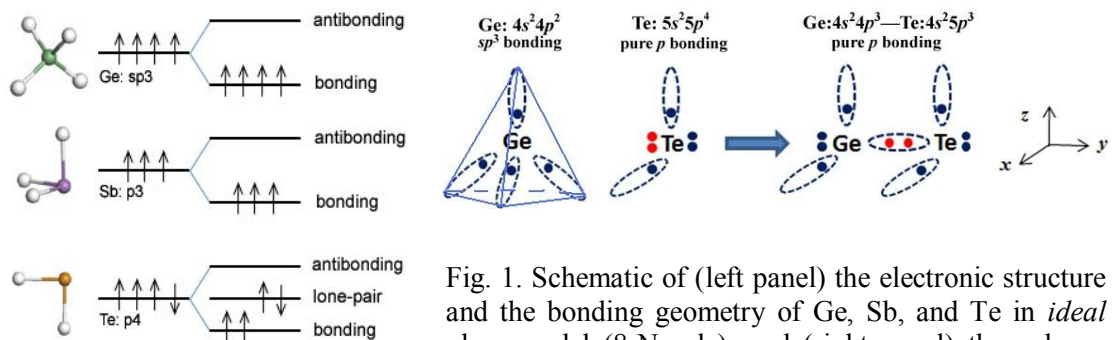
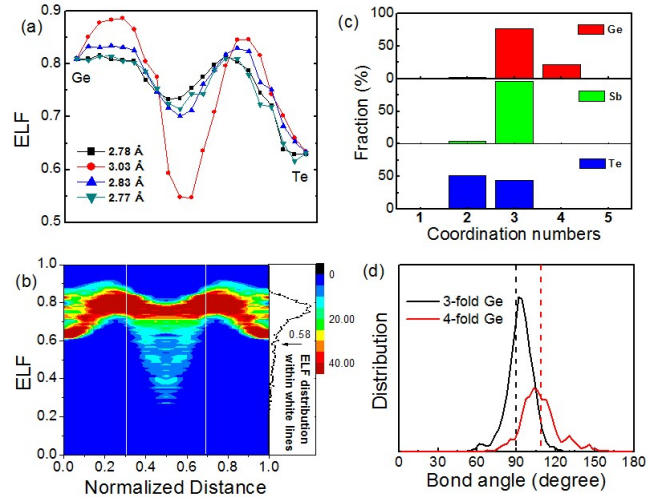


Fig. 1. Schematic of (left panel) the electronic structure and the bonding geometry of Ge, Sb, and Te in *ideal* glass model (8-N rule), and (right panel) the valence alternation process between Ge and Te. Te has the higher-energy non-bonding lone-pair electrons, as shown in (a), which interact with Ge, destabilizing the  $sp^3$  bonding for the latter. This leads to the formation of dative bond (red in dashed circle) between Ge and Te, see (b). In 3-D space, the  $sp^3$  bonds have the tetrahedral shape with bond angles of  $109^\circ$ , while the  $p$  bonds ( $p_x$ ,  $p_y$  and  $p_z$ ) are perpendicular to each other. In *a*-GST, the dative bonds change not only the true CN of the Ge and Te, but also the bond angle around Ge.

Using electronic structure calculations, we demonstrated a global valence alternation forming dative bonds in the *a*-GST at room temperature. The resulting  $p$  bonding profoundly influences the local atomic structure, leading to right-angle motifs. The dominance of  $p$  bonding is revealed by i) distributions of the coordination number (CN) and the bond angle, for truly bonded atoms determined based on the electron localization functions (ELF), and ii) a direct evaluation of the  $p$  (and  $s$ ) orbital occupation probability for the CN=3 Ge atoms that form  $90^\circ$  bonds with neighbors. Specifically, our *ab initio* MD simulations confirm that the *a*-GST is characterized by “right-angled” local atomic motifs and rationalized their origin from the nature of bonding on the level of electronic structures (dative bonds). This atomic structure is originated from the interaction between Ge and the lone-pair electrons of Te, which destabilizes the  $sp^3$  hybridization and promotes  $p$  bonding among all the constituent species. A schematic showing the proposed model is given in Fig. 1 and discussed in its caption. As a result (see Fig. 2), the CNs of Ge and Te both shift towards 3, and the bond angles around Ge become dominated by  $\sim 90^\circ$ . Some Ge atoms may retain the  $sp^3$  character with CN=4 and tetrahedral-like configuration. Our new method of basing the CN analysis on strongly bonded pairs determined using the ELF, as shown in Fig. 2, will be useful for studying other phenomena in GST.

Fig. 2. (a) Representative ELF profiles for a Ge atom and its neighbors, showing three strongly bonded and one weakly-bonded neighbors. (b) The ELF distribution between all atom pairs within a distance cutoff of 3.5 Å. The threshold ELF value (0.58) is labeled by an arrow, which cuts across the valley separating the truly bonded and not strongly bonded (tail). (c) The CN around each element, for strongly bonded neighbors. (d) Bond angle distributions for Ge atoms with CN=3 and CN=4, with the respective characteristic  $90^\circ$  or  $109^\circ$  angle (dashed lines). The majority of Ge atoms are in defective-octahedral environment with CN=3, with a small fraction of tetrahedrally bonded (CN=4) [1].



## 2) Pressure tunes electrical resistivity by four orders of magnitude in the amorphous $\text{Ge}_2\text{Sb}_2\text{Te}_5$ phase-change memory alloy (*PNAS*, (2012) [3])

Upon crystallization (e.g., by annealing at  $\sim 420$  K) from amorphous GST (*a*-GST) to crystalline rocksalt GST (*rs*-GST [4]), the electrical resistivity drops by at least two orders of magnitude, offering the desired contrast for memory applications. This scenario is shown in Fig. 3a (adapted from published work). The entire span of possible resistivity change by thermal annealing is about four orders of magnitude.

Instead of using temperature to induce phase transition and resistivity contrast, we have examined the structure and property changes in *a*-GST, entirely in the amorphous state, as a function of the other thermodynamic variable, “pressure” (P). Pressure and stresses are usually present in devices, and GST exhibits rich behavior in phase transformations under pressure [5,6]. The property excursion in *a*-GST under pressure (0 to  $\sim 28$  GPa in diamond anvil cell) offers an opportunity to observe the potential property window available in *a*-GST that may be useful for multi-state memory in this phase. Our discovery here is a dramatic decrease in electrical resistivity  $\rho$  under pressure, by as much as four orders of magnitude, in the glassy *a*-GST in the absence of crystallization, see Fig. 3b. This is comparable with the  $\rho$  range achievable by thermally induced phase transitions (Fig. 3a). Much of this large change is found to be accompanied by subtle changes in the parameters normally used to describe and monitor local structure, such as bond length, bond angle, and coordination number. Instead, we discovered an important structural indicator that changes fast with increasing P and correlates strongly with the  $\rho$  change: the volume fraction of low-electron-density (LED) regions, which are “vacant” local volumes analogous to voids or vacancies in crystalline materials. The obvious decrease of LED volumes resulting from electron charge density redistribution under increasing pressure offers a useful structural signature that can be monitored to represent all the important changes in atomic structure and bonding that mediate significant property variations. Our *ab initio* calculation suggests that the pressure-driven compression of the LED volumes in *a*-GST, by enhancing the interactions between local clusters, delocalizes electrons and narrows the band gap. We have also used ELF to provide evidence that at elevated P some originally trapped electrons indeed become less

localized. These suggest that it is the narrowing of the mobility gap, as the Peierls-like distortion is reduced, that results in the pronounced  $\rho$  decrease.

At high P,  $\rho$  levels off and is now close to the high end of metals. Different from the lower pressure regime where the *a*-GST largely retains its right-angled local motifs that bear some resemblance to the low-pressure rocksal *c*-GST (*rs*-GST), at P>8 GPa the bond angles start to be compressed to decrease. The glass eventually turns into a different amorphous state, characterized by a bond angle distribution starting around 55° and coordination numbers approaching 7~8. This local configuration now bears similarity to the local structure of the high pressure (~28 GPa) crystallization product, a body-centered-cubic (*bcc*) GST [5,6]. As such, this high-density, metallic-like *a*-GST can be identified as a new *bcc*-type polyamorph, and regarded as a precursor of the eventual *bcc*-GST upon high-pressure crystallization.

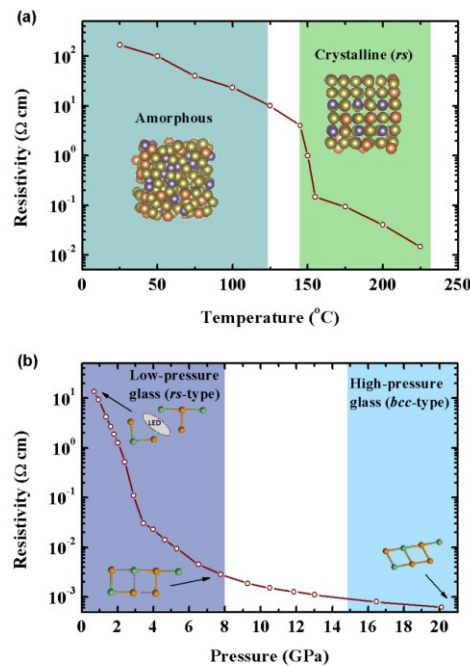


Fig. 3. (a) The electrical resistivity of  $\text{GeSb}_2\text{Te}_4$  as a function of temperature. The amorphous-to-crystalline transition occurs around 420 K, with a  $\rho$  drop by about two orders of magnitude. The *ab initio* models of these two structural configurations are displayed in the insets. (b) The  $\rho$  of amorphous  $\text{Ge}_2\text{Sb}_2\text{Te}_5$  (*a*-GST) with increasing P. The representative local motifs in the amorphous structure are shown schematically in the insets: the LED regions are compressed down first as the  $\rho$  decreases by orders of magnitude in the lower P regime (0 to 8 GPa), after which the characteristic bond angle starts to be compressed to decrease from around 90° towards ~55°, and the low-pressure *rocksalt*-type *a*-GST (*rs*-type *a*-GST) gradually transforms into a high-pressure *body-centered-cubic* type [5,6] polyamorph (*bcc*-type *a*-GST), before eventually crystallizing into the *bcc*-GST (>28 GPa).

1. Y.Q. Cheng and E. Ma, *Atomic-level structure and structure-property relationship in metallic glasses*, Progress in Materials Science, 56 (2011), pp. 379-473.
2. M. Xu, Y.Q. Cheng, H.W. Sheng and E. Ma, *Nature of atomic bonding and atomic structure in the phase-change  $\text{Ge}_2\text{Sb}_2\text{Te}_5$  glass*, Phys. Rev. Lett. 103 (2009) Art. No.195502.
3. M. Xu, Y. Q. Cheng, L. Wang, H. W. Sheng, Y. Meng, W. G. Yang, X. D. Han, and E. Ma, *Pressure tunes electrical resistivity by four orders of magnitude in amorphous  $\text{Ge}_2\text{Sb}_2\text{Te}_5$  phase-change memory alloy*, Proceedings of the National Academy of Sciences of the United States of America (PNAS), 109 (2012) E1055-E1062.
4. X.Q. Liu et al., *New Structural Picture of the Phase-Change  $\text{GeSbTe}$  Alloy*, Phys. Rev. Lett. 106 (2011) Art. No. 025501.
5. Y.Q. Cheng, M. Xu, H.W. Sheng, Y. Meng, X.D. Han and E. Ma, *A body-centered-cubic polymorph of the  $\text{Ge}_2\text{Sb}_2\text{Te}_5$  phase-change alloy*, Appl. Phys. Lett. 95 (2009) Art. No. 131904.
6. M. Xu, Y. Meng, Y. Q. Cheng, H. W. Sheng, X. D. Han, and E. Ma, *Pressure-induced crystallization of amorphous  $\text{Ge}_2\text{Sb}_2\text{Te}_5$* , J. Appl. Physics, 108 (2010) 083519.
7. Other publications under this grant: K. Zheng, C.C. Wang, Y.Q. Cheng, H. Yue, X.D. Han, Z. Zhang, Z.W. Shan, M. Ye, Y.D. Yin and E. Ma, *Electron-beam-assisted superplastic shaping of nanoscale amorphous silica*. Nature Communications 1:24 doi: 10.1038 / 1021 (2010); S. Li et al., *Inverse martensitic transformation in Zr nanowires*, Phys. Rev. B 81 (2010) 245433; M. Xu, J. Ding and E. Ma, *One-dimensional stringlike cooperative migration of lithium ions in an ultrafast ionic conductor*, Appl. Phys. Lett. 101 (2012) 031901.

# Surface Engineering by Simultaneous Action of Multiple External Fields

Principal Investigator: **Dimitrios Maroudas**  
Department of Chemical Engineering  
University of Massachusetts, Amherst, MA 01003-9303  
E-mail: [maroudas@ecs.umass.edu](mailto:maroudas@ecs.umass.edu); Phone: (413) 545-3617

## Program Scope

This research program aims at enabling surface engineering strategies based on a fundamental understanding and predictive modeling of the surface morphological response of solid materials subjected to the combined action of multiple external forces. Our research focuses on the surface morphological evolution and stability of electrically conducting and semiconducting solids under the simultaneous application of mechanical stresses, electric fields, and temperature gradients. We seek conditions under which the multiply driven surface morphology is stable and explore the complexity of the corresponding various morphologically stable surface patterns. We also emphasize on the driven evolution of nanoscale features, aiming at stabilizing and controlling nanoscale patterns on surfaces by their manipulation through simultaneously applied multiple external forces. Specifically, we address systematically the morphological response to the combined action of multiple external forces of bulk solid surfaces, surfaces of thin films grown epitaxially on thick or thin substrates, as well as nanoscale surface features such as coherently strained epitaxial islands on substrate surfaces. The research combines theoretical analyses of surface morphological stability with self-consistent dynamical simulations of surface evolution based on properly parameterized continuum and multiscale surface transport models.

## Recent Progress

***Current-Driven Surface Morphological Stabilization of a Coherently Strained Epitaxial Thin Film on a Substrate*** – We have analyzed systematically the surface morphological stability of a coherently strained thin film grown epitaxially on a solid substrate and subjected simultaneously to an external electric field. Due to its lattice mismatch with the substrate material, the planar surface of the epitaxial film may undergo a Stranski-Krastanow (SK) instability, resulting in formation of islands on the film surface. Our analysis aimed at examining the possibility for an externally applied electric field to stabilize the planar film surface morphology against the SK instability and at investigating the role of substrate engineering in the epitaxial film surface stabilization process. We examined three substrate types, namely, thick rigid substrates, thin elastically deformable substrates clamped onto rigid holders, and thin compliant substrates that can provide some elastic accommodation of the lattice-mismatch strain in the epitaxial film due to their ability to relax parallel to the interface with the epitaxial film.

We developed a three-dimensional (3D) fully nonlinear model for the surface morphological evolution of the epitaxial thin film, consisting of a surface height evolution equation coupled with the electrostatic and elastostatic boundary-value problems and accounting for surface diffusional anisotropy through a properly formulated diffusivity tensor. Based on this model, we conducted linear stability analysis to examine the morphological stability of the epitaxial film's planar surface state. The analysis has shown that *surface electromigration due to a properly applied and sufficiently strong electric field can inhibit SK-type instabilities, which can be used to control the onset of island formation on the epitaxial film surface* [1]. We have also determined the critical electric-field strength for surface stabilization as a function of material properties and heteroepitaxial system parameters (such as dimensions and mechanical properties of the film and the substrate), as well as the electric field's optimal direction for the most efficient stabilization of the surface morphology. Importantly, we have found that *optimal use of substrate engineering techniques can reduce by several orders of magnitude the critical strength of the electric field required to stabilize the planar surface morphology of the epitaxial film* with respect to the field strength required in the case of an infinitely thick substrate [1].

***The Effect of a Thermal Gradient on the Current-driven Surface Morphological Stabilization of Stressed Crystalline Solids and Epitaxial Thin Films on Crystalline Substrates*** – We have examined the surface morphological stability of electrically and thermally conducting crystalline elastic

solids in uniaxial tension under the simultaneous action of an electric field and an applied temperature gradient. We implemented a fully nonlinear surface mass transport model that accounts for surface electromigration and thermomigration induced by the applied fields and for surface diffusional anisotropy. Based on a systematic linear stability analysis according to this model, we found that a properly directed applied thermal gradient can reduce the critical electric-field strength requirement for stabilization of the planar surface morphology against Asaro-Tiller or Grinfeld (ATG) instabilities [2]; for the materials and systems of interest, a representative value of thermal gradient is around 500 K/cm.

We have also conducted a theoretical analysis of the surface morphological stability of a coherently strained thin film that has been grown epitaxially on a deformable substrate and is simultaneously subjected to an external electric field and a temperature gradient. We developed a 3D model for the surface morphological evolution of the thin film and carried out a linear stability analysis of the heteroepitaxial film's planar surface state. We accounted for the effect of the simultaneous action of multiple external fields on the anisotropy of the surface diffusivity tensor and considered various substrate types. We derived the condition for the synergy or competition of the two externally applied fields and determined the optimal alignment of the external fields that minimizes the critical electric-field strength requirement for the stabilization of the planar film surface [2]; this alignment is expressed by the angles formed on the film plane by the applied electric field and thermal gradient directions with a fast surface diffusion direction,  $\phi_E$  and  $\phi_T$ , respectively. In both problems (bulk crystalline solid and epitaxial film), we also examined the role of the temperature dependence of the thermophysical properties and focused on the strongest such dependence, namely, the Arrhenius dependence of the surface diffusivity. We showed that this temperature dependence does not affect the critical applied-field strength requirement for surface stabilization; it only amplifies the rate of growth or decay of the shape perturbation from the planar surface morphology [2]. Our analysis has established that the optimally synergistic effects of the simultaneous action of the externally applied electric field and thermal gradient can reduce further the critical electric-field strength requirement for epitaxial film planar surface stabilization against SK-type instabilities by a factor of over 2.5, which is a substantial improvement [2].

***Electromigration-driven Complex Dynamics of Void Surfaces in Stressed Metallic Thin Films under a General Biaxial Mechanical Loading*** – We have conducted a systematic computational study of the electromigration-driven complex surface dynamics of voids in thin films of face-centered cubic (fcc) metals with  $\langle 100 \rangle$ -oriented film planes subjected to an external electric field simultaneously with biaxial mechanical loading; the loading can be either purely tensile or compressive, ranging from isotropic to strongly anisotropic including uniaxial, or of a mixed type with both tensile and compressive stress components in the applied stress tensor. Our analysis was based on self-consistent dynamical simulations of driven void surface morphological evolution following a well validated, two-dimensional, and fully nonlinear model. Under purely isotropic tension, we found that a transition from steady to time-periodic states occurs at a critical stress level; the corresponding Hopf bifurcation is *supercritical* [3]. Under a general biaxial mechanical loading, we found that depending on the electromechanical conditions, void size, and surface diffusional anisotropy, two types of asymptotic states can be stabilized in the void surface dynamical response, namely, morphologically steady or time-periodic traveling voids, and film failure can be caused by void tip extension [3]. The loading mode as well as the loading anisotropy are found to be significant factors in determining the void morphological stability domains and can be tailored to stabilize steady or time-periodic states and to increase the film's resistance to failure. Under a mixed (tensile + compressive) loading mode, we found that it is impossible to stabilize steady states in the void morphological response and that the stress levels that the film can sustain prior to failure are much lower than those under purely tensile or purely compressive biaxial loading [3].

***Analysis of Current-Driven Morphological Response of Single-layer Epitaxial Islands on Crystalline Substrates*** – We have developed a fully nonlinear model for studying the current-driven morphological evolution of single-layer, coherently strained epitaxial islands on elastically deformable crystalline substrates. In the model, mass transport due to curvature- and stress-driven diffusion and electromigration is dominated by atomic migration on the island boundary (edge) and the anisotropy of such “periphery diffusion” is accounted for. We have also developed direct dynamical simulators of the driven morphological evolution of such islands based on this model. We have validated the model by comparing the simulation predictions for stable steady island morphologies and for the dependence of the

stable islands' migration speed on their size with recently reported results from an *in situ* STM experimental study for the current-driven response of single-layer homoepitaxial islands on Ag(111).

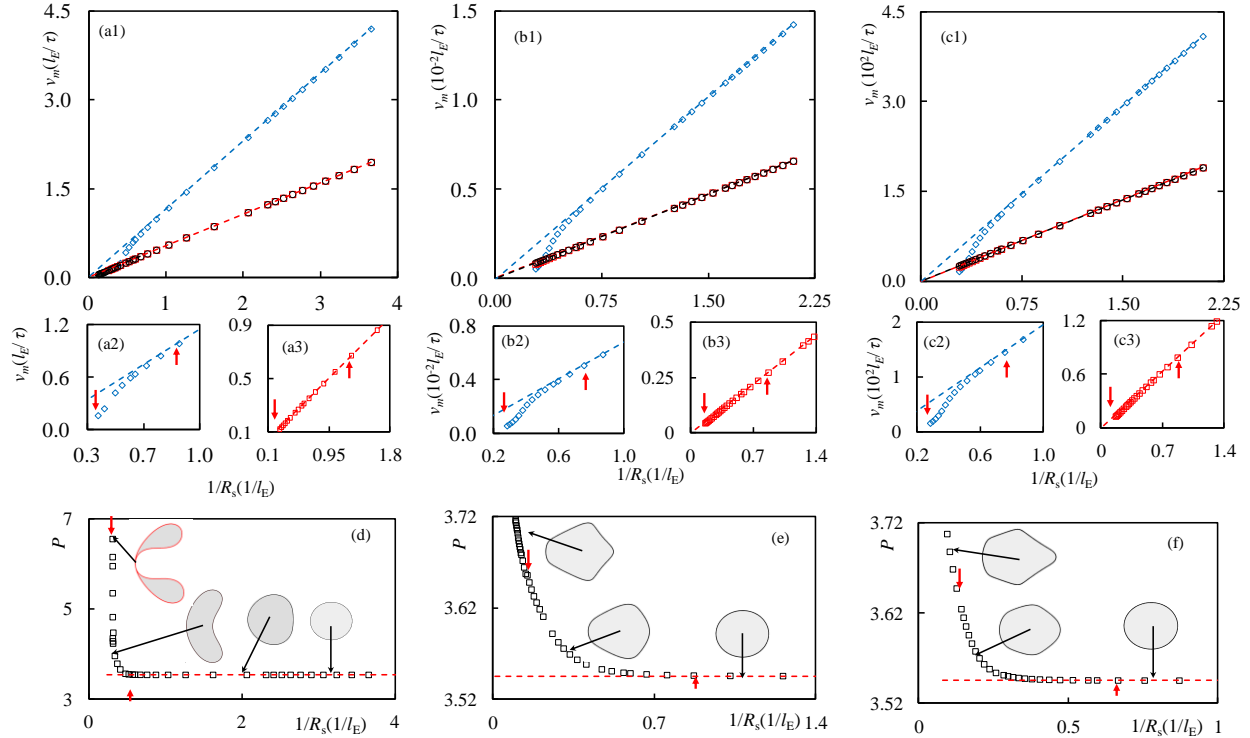


FIG. 1. Dependence of the migration speed,  $v_m$ , on the inverse of the island size,  $1/R_s$ , for the current-driven motion of (a) homoepitaxial and (b,c) coherently strained heteroepitaxial islands with tensile and compressive misfit strain due to lattice mismatch, (b)  $\varepsilon_m = +0.06$  and (c)  $\varepsilon_m = -0.06$ , respectively, on single-crystalline substrates of Ag at steady state;  $v_m$  is given in units of  $l_E/\tau$ , where  $l_E$  is a characteristic length scale and  $\tau$  is the diffusional time scale, and material properties typical of Ag have been used in the computations. The applied electric field is aligned with a fast direction for island edge diffusion. Open blue diamonds, red squares, and black circles give the current-driven response of islands on  $\langle 110 \rangle$ -,  $\langle 100 \rangle$ -, and  $\langle 111 \rangle$ -oriented substrate surfaces, respectively. The straight dashed lines give linear least-squares fits to the simulation results over the size range of smaller islands where the  $v_m(1/R_s)$  relation is clearly linear.  $\uparrow$  arrows mark the onset of nonlinearity in  $v_m(1/R_s)$ , which is accompanied by *island morphological transition* in  $\langle 110 \rangle$ - [(a2), (b2), and (c2)] and  $\langle 100 \rangle$ -oriented surfaces [(a3), (b3), and (c3)]. In (a2), (b2), and (c2),  $\downarrow$  arrows mark the onset of a *necking morphological instability*. In (a3), (b3), and (c3),  $\downarrow$  arrows mark the onset of a *fingering-like morphological transition*, beyond which the islands remain morphologically stable. In (d), (e), and (f), a morphological norm, the scaled island perimeter  $P = P_s/R_s$ , is plotted as a function of  $1/R_s$  at  $\varepsilon_m = -0.06$  for  $\langle 110 \rangle$ -,  $\langle 100 \rangle$ -, and  $\langle 111 \rangle$ -oriented surfaces, respectively; the  $\uparrow$  and  $\downarrow$  arrows have the same meaning as in (a), (b), and (c). The insets in (d)-(f) show representative island morphologies in the linear and nonlinear regimes of current-driven island migration.

We have conducted a systematic parametric study to examine effects of island size and misfit strain on the current-driven motion of stable single-layer epitaxial islands on crystalline substrates of fcc metals, including both homoepitaxial and coherently strained heteroepitaxial islands. The effects of strain due to lattice mismatch on the island periphery diffusion were quantified based on atomic-scale simulation results. Figure 1 shows representative simulation results for the dependence of the island migration speed,  $v_m$ , on the island size,  $R_s$ , given by the square root of the island's area, for current-driven epitaxial island motion on  $\langle 110 \rangle$ -,  $\langle 100 \rangle$ -, and  $\langle 111 \rangle$ -oriented surfaces of single-crystalline Ag that leads to *stable steady island morphologies*. We found the island migration speed to be directly proportional to the inverse of the island size for much of the island size range examined and starting from very small islands. For all three surface orientations, throughout the misfit strain range examined, and for an applied electric field aligned with a fast diffusion direction for island edge diffusion, we found that there exists a critical island size beyond which the  $v_m(1/R_s)$  dependence deviates from linearity; this onset of nonlinear behavior is accompanied by *island morphological transition*, as shown in Figs. 1(d), 1(e),

and 1(f). Increasing  $R_s$  further within this nonlinear migration regime leads to a *necking morphological instability* of the island's steady state for  $\langle 110 \rangle$ -oriented surfaces [Fig. 1(d)] and to a *finger-like morphological transition* for  $\langle 100 \rangle$ - and  $\langle 111 \rangle$ -oriented surfaces [Figs. 1(e) and 1(f), respectively]. Misaligning the direction of the applied electric field with a fast edge diffusion direction increases the complexity of the island morphological and dynamical response within the general framework of Fig. 1. Rescaling  $v_m$  with the proper island shape factor  $\beta$  leads to a linear relationship between  $v_m/\beta$  and  $1/R_s$ ; this linear scaling relationship is *universal* and is obeyed by islands of all sizes regardless of the complexity of the island stable morphologies for  $R_s$  beyond the onset of the nonlinear regime.

### Future Plans

Our current and future plans (work to be completed within the next 1-3 years) include: (1) Continuation of continuum-level analysis of surface morphological stability and evolution of stressed elastic crystalline solids [4] under surface electromigration and thermomigration conditions. (2) Analysis of field-driven surface morphological stabilization of coherently strained epitaxial films on elastically deformable substrates for further elucidation of thermal and geometrical effects. (3) Analysis of the driven dynamics of both isolated individual single-layer islands and pairs of islands driven into contact, emphasizing on collective dynamical phenomena, such as island coalescence and breakup. (4) Continuum-level exploration of complex (e.g., oscillatory, chaotic) dynamical response of surfaces under the combined action of electric fields, mechanical stresses, and thermal gradients. (5) Targeted atomistic computations for determining surface properties and parameterizing surface anisotropies for their incorporation into continuum-level models. (6) Incorporation into our fully nonlinear models of driven surface morphological evolution of thermal effects, such as the temperature dependence of material properties and Joule heating of metallic conductors for improving the predictive capabilities of the models. (7) Development of coarse-grained (micromechanical) kinetic models of strain relaxation based on analysis of molecular-dynamics simulations of metallic-film response to stress and using dislocation densities as dynamical variables to serve as constitutive models of plastic deformation phenomena. (8) Development of multi-scale models of driven surface morphological evolution involving kinetic Monte Carlo simulations for direct atomic-scale modeling of the propagation of epitaxial film surfaces and epitaxial island boundaries. (9) Development in collaboration with expert experimentalists of careful experimental protocols to test the modeling predictions for driven evolution of epitaxial film surfaces and epitaxial islands. (10) Exploration of other application areas in the study of the response of complex systems to the action of external fields, such as in problems of colloidal-particle assemblies [5].

### References to Publications of DOE Sponsored Research

1. G. I. Sfyris, M. R. Gungor, and D. Maroudas, "Electromigration-Driven Surface Morphological Stabilization of a Coherently Strained Epitaxial Thin Film on a Substrate," *Applied Physics Letters* **96**, 231911/1-3 (2010); "Analysis of Current-Driven Surface Morphological Stabilization of a Coherently Strained Epitaxial Thin Film on a Finite-Thickness Deformable Substrate," *Journal of Applied Physics* **108**, 093517/1-9 (2010); "The Effect of a Compliant Substrate on the Electromigration-Driven Surface Morphological Stabilization of an Epitaxial Thin Film," *Journal of Applied Physics* **111**, 024905/1-12 (2012).
2. D. Dasgupta, G. I. Sfyris, M. R. Gungor, and D. Maroudas, "Surface Morphological Stabilization of Stressed Crystalline Solids by Simultaneous Action of Applied Electric and Thermal Fields," *Applied Physics Letters* **100**, 141902/1-4 (2012); G. I. Sfyris, D. Dasgupta, and D. Maroudas, "The Effect of a Thermal Gradient on the Electromigration-Driven Surface Morphological Stabilization of an Epitaxial Thin Film on a Compliant Substrate," *Journal of Applied Physics* (under review).
3. V. Tomar, M. R. Gungor, and D. Maroudas, "Electromechanically Driven Chaotic Dynamics of Voids in Metallic Thin Films," *Physical Review B* **81**, 054111/1-10 (2010); G. I. Sfyris, M. R. Gungor, and D. Maroudas, "Effects of Applied Stress Tensor Anisotropy on the Electromechanically Driven Complex Dynamics of Void Surfaces in Metallic Thin Films," *Journal of Applied Physics* **110**, 063705/1-9 (2011); D. Dasgupta, G. I. Sfyris, and D. Maroudas, "Electromigration-Driven Complex Dynamics of Void Surfaces in Stressed Metallic Thin Films Under a General Biaxial Mechanical Loading," *Journal of Applied Physics* **112**, 083523/1-10 (2012).
4. D. Maroudas, "Surface Morphological Response of Crystalline Solids to Mechanical Stresses and Electric Fields," *Surface Science Reports* **66**, 299-346 (2011).
5. D. J. Beltran-Villegas, R. M. Sehgal, D. Maroudas, D. M. Ford, and M. A. Bevan, "A Smoluchowski Model of Crystallization Dynamics of Small Colloidal Clusters," *Journal of Chemical Physics* **135**, 154506/1-10 (2011); "Colloidal Cluster Crystallization Dynamics," *Journal of Chemical Physics* **137**, 134901/1-11 (2012).

## Using multiaxial magnetic fields to drive emergent behavior in magnetic platelet suspensions, James E. Martin and Kyle Solis, Sandia National Laboratories, Albuquerque, New Mexico

In the last several years we have begun to focus on the effect of multiaxial magnetic fields on magnetic platelet suspensions. The complex emergent behavior we have discovered arises from the complex magnetic interactions between the platelets and the field. A uniform magnetic field does not exert a force on a platelet, but it does exert a torque. This torque tends to align the particle such that the platelet director (surface normal) is perpendicular to the field. The field produced by each platelet also creates a significant torque and force on nearby particles. Each platelet is therefore subject both to the interaction forces and torques with nearby particles, and to torques that arise from the applied field. The particle rotations and translations are coupled hydrodynamically, and the combination of these magnetic and hydrodynamic interactions leads to a variety of emergent suspension dynamics. Some of the resultant flows enable vigorous, *noncontact* heat and mass transfer. There are essentially three types of emergent behavior: 1) flow lattices; 2) rotational flow and; 3) surface instabilities. Within each of these types there are a variety of effects, but in this abstract we will describe only some of the main effects.



**Figure 1.** A flow lattice stimulated by a 2:1 biaxial magnetic field.

**Flow lattices stimulated by biaxial fields.** We have found that a vigorous flow lattice results when platelet suspensions are subjected to certain types of biaxial magnetic fields. [1] For example, applying a biaxial field in the  $x$ - $y$  plane with a 2:1 frequency interval to a suspension that is roughly 4 vol% platelets induces the spontaneous flow symmetry breaking that gives rise to the flow lattice shown in Fig. 1. This lattice consists of a checkerboard of countercurrent flow columns parallel to the  $z$  axis, as illustrated in Fig. 2(left). We call this effect *Isothermal Magnetic Advection* (IMA) because unlike convection, this noncontact flow can be created without a thermal gradient. Although there is no component of the applied field in the direction of flow, the biaxial field in the  $x$ - $y$  plane *can* create torque around the  $z$  axis, and this torque can in principle lead to propulsion along this axis (a propeller is one familiar example). The detailed structure of this flow lattice is dependent on the phase angle between the two field components, which alters the trajectory of the field vector, Fig. 2(right). This phase angle is defined by  $\mathbf{H}(t) = H_x \sin(\omega t) \hat{\mathbf{x}} + H_y \sin(n\omega t + \phi) \hat{\mathbf{y}}$ , where  $n$  is a positive integer. Depending on the phase angle, the flow can be nonexistent, regular or writhing.

A biaxial field with a 3:1 frequency ratio also forms an advection lattice but with one significant difference: at phase angles where the Lissajous plot of the field vector is a forward or backward ‘S’ the fluid has a significant body torque around the  $z$  axis, clockwise or counterclockwise, indicating helical flow within. [1] This torque can be measured on a torsion balance and results in the fluid sloshing back and forth if the 3:1 field is phase modulated. Because of the chiral nature of the trajectory of the field vector (including its equivalent opposite) this body torque does not violate parity conservation.

**Controlling the lattice wavenumber.** We have recently demonstrated that IMA can be controlled to tailor the efficiency of heat and mass transfer. [3] The lattice wavenumber is proportional to the field frequency, Fig. 3(left), so low frequencies create coarse columns, which facilitate both mass *and* heat transfer, and high frequencies create fine columns, which would act as a counter-current heat exchanger, enabling mass transfer without heat extraction. The latter could be useful for feeding a reaction front without extracting heat. Increasing the field strength reduces the wavenumber, though this effect is relatively weak, scaling like the cube root of the field strength above a critical field required to initiate the instability, Fig. 3(right). Significantly, the lattice wavenumber is unaffected by the viscosity of the liquid phase, Fig. 4(left), so that if IMA were used to transfer heat across a thermal gradient, the lattice would remain commensurate. Such a defect-free lattice would facilitate efficient heat transfer. The liquid viscosity does, however, play an important role in the flow rate, which scales inversely with

the viscosity. Finally, studies of the dependence of the lattice wavenumber on the volume fraction of platelets shows only a weak dependence, Fig. 4(right).

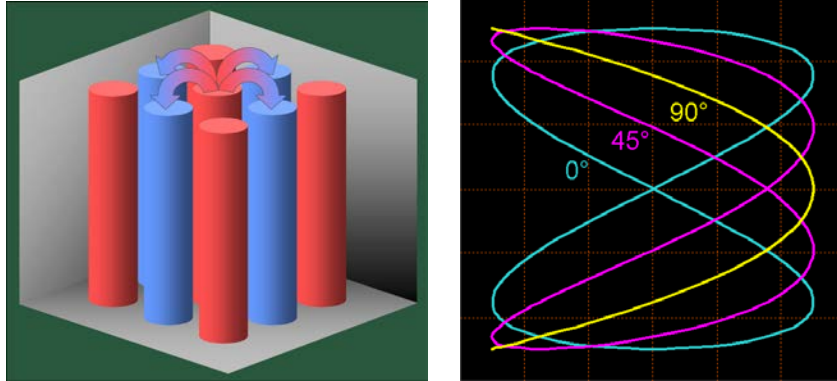


**Figure 3.** (left) Illustration of the basic *Isothermal Magnetic Advection* flow pattern, which is a checkboard lattice of counter-current flow columns. (right) Lissajous plot of the field vector for three phase angles.

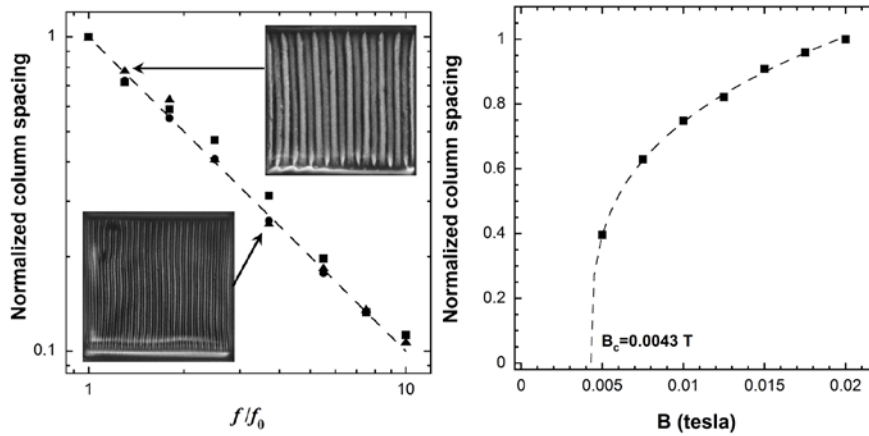


**Figure 4.** (left) The advection lattice column spacing is inversely proportional to the magnitude of the field frequency. Data are for 2:1 biaxial fields with a 45° phase angle, and an rms component induction of 0.015 T. Data are for volume fractions of ● 2.3%, ■ 5.8%, and ▲ 9.3%. (right) The column spacing increases as a power law of the induction field above a critical field strength.

These observations demonstrate that IMA has characteristics that make it attractive for applications. Gravity does not play a significant role in the formation of flow patterns, so the advection lattices can be created in any orientation. IMA could therefore be used to transfer heat in weightless environments, or anywhere else natural convection fails, such as under a hot object. IMA is also stimulated with uniform magnetic fields, so it can be scaled to any size, using only open-air Helmholtz coils to create the modest fields required. Finally, the wavenumber can be tuned by the field frequencies, the flow rate can be controlled by the strength of the field and the lattice wavenumber is independent of viscosity, and therefore of temperature, enabling a lattice to remain coherent across a thermal gradient.

**Surface instabilities.** Surface instabilities arise as the volume fraction of the particles increases to ~8%, and these are likely normal field instabilities of a complex type. To create these instabilities a biaxial field is applied in a vertical plane. Initially these instabilities appear as periodic stationary waves parallel to the horizontal component of the field. As the particle volume fraction increases, these waves become more pronounced and erupt into tall ridges within which one can observe an advection lattice. The dynamics of these ridges is affected by the phase relation between the field components. Phase modulating a 2:1 field causes pronounced wobbling of the ridge and phase modulating a 3:1 field causes the ridge to slosh back and forth parallel to the horizontal field component, due to the body torque.

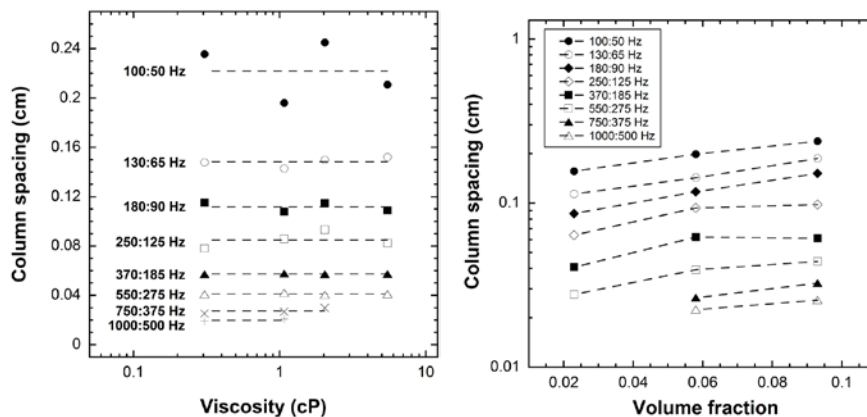


**Figure 4.** (left) For any given field frequency the column spacing is essentially independent of the liquid viscosity. (right) The column spacing is weakly dependent on the particle volume fraction.

**Effects produced by a third field component.** Applying a normal dc field to an advection lattice formed by an alternating biaxial field produces dramatic results. [2] If the dc field amplitude is relatively small, the field can substantially modify the flow lattice. But dc fields comparable to the biaxial field components can also *completely* obliterate the advection lattice and create rotational flows of surprising vigor, as shown in Fig. 5(a-c). (In the discussion below we will show that these flows are highly effective at heat and mass transfer.) An interesting aspect of these rotational flows is that the orientation of the vorticity axis is dependent on the whether the field frequency ratio is even or odd. For example, for a 2:1 field with a  $0^\circ$  phase angle the vorticity axis is parallel to the low frequency field component. In this case the vorticity can be reversed by either changing the biaxial field phase angle by  $180^\circ$  or by reversing the direction of the dc field.

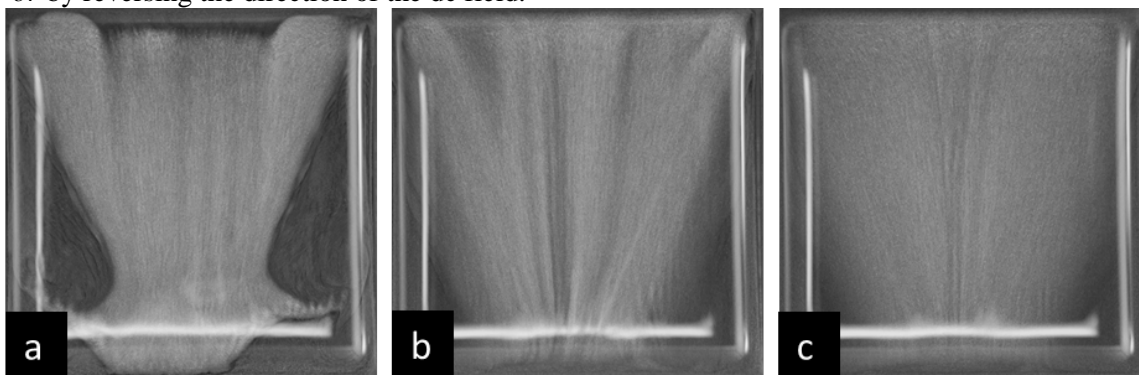


**Figure 5.** Temporal development of strong rotational flow for a 3.5 vol.% suspension subjected to a  $150 G_{\text{rms}}$ , 250:125 Hz/125  $G_{\text{dc}}$  ac/ac/dc triaxial field. (a) When the ac biaxial field is initially turned on, the platelet sediment erupts into plumes that quickly disperse throughout the supernatant. (b) Within a few seconds, the suspension is vigorously flowing from north to south at the surface. (c) After  $\sim 5$  seconds the flow is nearly fully developed.

This fluid rotation is due to the dc field causing chiral symmetry breaking of the trajectory of the field vector and its opposite, a point that requires a little explanation. For a 2:1 field with a  $0^\circ$  phase angle the Lissajous plot of the field vector is a figure eight, Fig. 2(right), with the zero field point at the center. The trajectory of the field vector will circulate in the opposite sense if the phase is shifted by  $180^\circ$ , so this field trajectory is chiral. However, the magnetic interactions are due to *induced* magnetic moments and thus scale as the square of the applied field. Inverting the sign of the total applied field will thus have no effect. So it is the combined trajectory of the applied field and its opposite that is the critical issue: in other words, the trajectory of a line. A little thought will convince one that for the figure eight trajectory of this “field line” is not chiral, so there is no reason to expect *deterministic* rotational flow, and in fact experiments show this does not occur. (However, one cannot rule out some mechanism of

spontaneous chiral symmetry breaking, which has indeed been observed as a weak effect in this case, but this does not lead to deterministic rotational flow.) If one applies a dc field orthogonal to the biaxial field plane, the zero point of the field shifts outside the plane of the figure eight. The field line now circulates on two figure eights separated by a gap, and this trajectory is now chiral. Changing either the *sign* of the dc field or *shifting the phase* of the biaxial field by  $180^\circ$  causes a change in the parity of this trajectory. The observations of rotational flow for the 2:1 field are in agreement with these parity considerations.

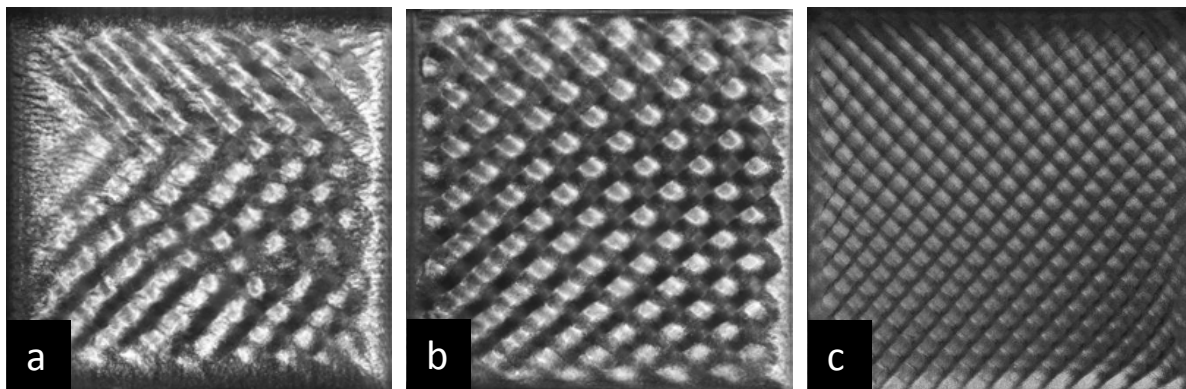


**Figure 6.** (a) A 250:125 Hz *ac/ac/dc* triaxial field produces a dynamic, disordered diamond vortex lattice pattern that becomes stationary and more ordered (b) when the high-frequency (vertical) component amplitude is reduced by half. (c) An ordered vortex pattern also emerges when the vertical component amplitude of a 125:250 Hz field is reduced. The axis of fluid vorticity is parallel to the plan view axis, which is in the vertical direction.

If the field frequency is 3:1 and the phase is  $90^\circ$ , strong rotational flow also occurs when a dc field is applied, but the axis of vorticity is the dc field. [2] In this case changing the phase of the biaxial field by  $180^\circ$  also reverses the flow, but altering the direction of the dc field does not. These observations are also consistent with parity considerations for the trajectory of the field line. The 3:1 field line trajectory is chiral even for the biaxial field itself, which is why a small deterministic body torque can be observed in this case. An orthogonal dc field component of either sign does not alter the parity of this pair trajectory, but changing the phase of the biaxial field by  $180^\circ$  does. It should be emphasized that such parity considerations are a necessary, but not sufficient, criterion for rotational flows.

**Formation of a vortex lattice.** Perhaps the most visually striking phenomenon we have observed is the formation of the vortex lattice shown in Fig. 6(a-c), which is due to spontaneous chiral symmetry breaking. This vortex lattice is most easily realized by subjecting an  $\sim 8$  vol.% platelet suspension to a triaxial field comprised of a 2:1 biaxial field in a vertical plane and an orthogonal dc field. Although it is not apparent from the image that the cells are vortices, dropping tracer particles onto the surface will convince one that this is in fact a checkerboard of vortices turning in opposite senses, like meshed gears. At lower particle volume fractions this same field creates rotational flow.

**Acknowledgements:** Sandia National Laboratories is a multiprogram laboratory operated by Sandia Corporation, a Lockheed Martin Company, for the United States Department of Energy under Contract No. DE-AC04-94AL85000. This work was supported by the Division of Materials Science, Office of Basic Energy Sciences, U.S. Department of Energy (DOE).

## References

- [1] *Isothermal Magnetic Advection: Creating Functional Fluid Flows for Heat and Mass Transfer*. K. J. Solis and J. E. Martin, *Appl. Phys. Lett.* **97**, 034101 (2010).
- [2] *Stimulation of vigorous rotational flows and novel flow patterns using triaxial magnetic fields*. Solis K J, Martin J E, *Soft Matter* **8**, 11989-94 (2012).
- [3] *Controlling the lattice spacing in isothermal magnetic advection to enable tunable heat and mass transfer*, Solis K J, Martin J E, *J. Appl. Phys.* **112**, 094912-7 (2012).

## Abstract

---

### Electronic Processes in Solid State Organic Electronic Materials

Richard L. Martin, Enrique R. Batista, and Darryl L. Smith

Theoretical Division, Los Alamos National Laboratory, MSB214, Los Alamos, NM 87545

rlmartin@lanl.gov

#### Program Scope

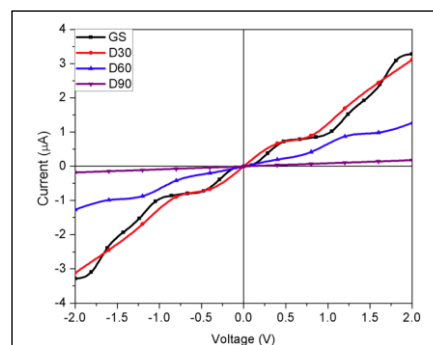
Organic electronic materials are of great intrinsic scientific interest because strong competing interactions produce a rich spectrum of tunable ground and excited states. This makes them an ideal vehicle for the study of flexible strongly correlated systems. The materials are also technologically important for a broad class of applications because of the tunability of their electronic properties, their facile thin film and heterostructure fabrication, and the possibility of creating nanoscale structures and devices through molecular assembly techniques. Because of the very large material and device structure phase space, there is a critical need for basic scientific research on the fundamental physical properties of organic electronic materials. The goal of this project is to provide an understanding of the fundamental physical processes that are important in determining the electrical and optical properties of organic electronic materials. We employ a closely coupled measurement/theory approach aimed at understanding fundamental physical processes in representative model systems and materials, including both conjugated polymers and small molecules. Our goal is to understand and control material structure and charge transport at the organic/inorganic and organic/organic interfaces. The experimental effort addresses optical and electrical characterization of model interfaces formed using solution or vacuum deposition techniques. The theory component connects with these experiments through a hierarchy of microscopic and macroscopic models, including large scale molecular dynamics calculations of the structure at the interface, quantum mechanical determination of the electronic structure associated with a subset of such configurations, and the development of appropriate device models.

#### Progress Report

- **Geometric distortions and polarization** in conjugated polymers has been examined for a number of electronic excitations in poly-p-phenylene vinylene. These include the lowest singlet (S1) and triplet (T1) excitons, as well as the positive and negative polarons. We also studied the effect of octyl side chains commonly found in the polymers used in actual devices. The localization of the S1 and T1 states was found to be driven by oligomer distortions, which are ubiquitous in amorphous materials. Computation of the binding energy of excitons show that the neutral excitons have higher binding energies compared to charged states. In contrast, the polaronic species exhibit larger coupling to the environment. These two behaviors can be

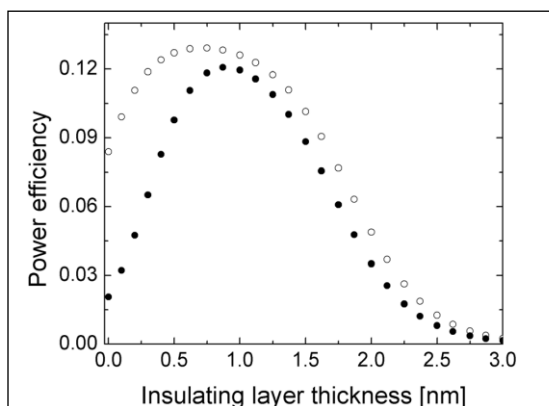
qualitatively rationalized from electrostatic arguments based on lower repulsion in the former and larger induction effects in the latter. An additional topic of interest in this work was a critical study of the dependence of density functional theory predictions on the form of the functional. In particular, it was shown that the new generation of hybrid functionals and range-corrected functionals are necessary to faithfully reproduce the delicate localization effects observed experimentally. Conventional functionals such as the local density approximation or generalized gradient approximations do not capture this behavior. This work is in press at the Journal of Chemical Theory and Computation.

- Electrical conductivity in organic polymers** can be separated into intra-oligomer mobility and inter-oligomer hopping events. In our past work we identified sites in the amorphous polymer that were associated with electron and hole trap sites. Those trap sites have strong binding energy for the charge carrier inhibiting the hopping process. In FY2012, we studied the conductivity along a single oligomer. We set up a geometry in which a strand of poly-p-phenylene-vinylene, with sulfur contact atoms, straddles gold leads. Ballistic transport was calculated and current vs. voltage (I-V) curves computed as function of a rotational defect introduced in the vinylene linkage. At zero angle (no defect) the perfect conjugation favors the transport and ohmic behavior is observed. As the rotational angle increases, the conjugation of the  $\pi$  orbitals is disrupted and the oligomer ceases to conduct current. The step like pattern observed in the I-V curve stems from the quantum nature of the calculated current, as the mobility stays almost constant when the voltage does not resonate with a molecular energy level and increases when a new energy level couples to the leads. This work has been submitted to the Journal of Chemical Physics.



I-V curve for a PPV oligomer as function of defect angle. At large angles the current is disrupted by the broken conjugation in the oligomer.

- Interfaces between different organic materials** can play a key role in determining organic semiconductor device characteristics. We developed a physics-based device model with the goal of exploring critical processes at organic/organic interfaces. Specifically, we considered a bilayer structure consisting of an electron transport layer (ETL), a hole transport layer (HTL), and the interface between them. Model calculations concentrated on: (1) the microscopic physical processes at the interface,



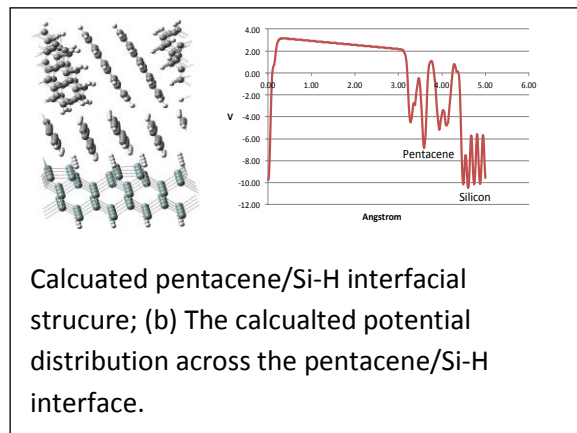
Calculated power efficiencies as a function of the insulating layer thickness. The circles are simulation results from the numerical device model for two sets of device parameters.

such as exciton formation/dissociation, exciplex formation/dissociation, and geminate/nongeminate recombination; (2) the treatment of the interface parameters; and (3) application of this model to different devices, such as organic light emitting diodes and photovoltaic cells. The relative impacts of the different processes on measurable macroscopic device characteristics were explored by varying the corresponding kinetic coefficients. We described results for an organic light emitting device with exciton or exciplex emission, and for a photovoltaic device with or without geminate recombination. This work appeared in *J. Appl. Physics*, **111**, 094507 (2012).

Motivated by the recent work of Campbell and Crone (I. H. Campbell and B. K. Crone, *Appl. Phys. Lett.* **101**, 023301 (2012)), who showed experimentally that inserting a thin insulating layer between the ETL and the HTL could improve the short-circuit photocurrent of a two layer organic solar cell, we used our interface device model to explore theoretically the effect of incorporating a thin tunnel barrier between the electron and hole transport layers of organic photovoltaic devices. We studied how macroscopic device characteristics (such as short-circuit current, open-circuit voltage, and power efficiency) are related to microscopic processes (such as exciton diffusion, dissociation, and recombination). We show that a tunnel barrier that alters the rates of different transfer processes at the interface between the electron and hole transport layers can significantly affect the operational characteristics. By optimally choosing the insulating layer thickness, the organic solar cell power efficiency can be significantly improved. The Figure below shows the calculated power efficiency from the numerical simulation as a function of the insulating layer thickness. The insulating layer can improve the short-circuit current and the open-circuit voltage and does not affect significantly the fill factor; therefore, the power efficiency can be significantly improved. This work appeared in *J. Appl. Physics*, **113**, 044516 (2013).

#### Future Plans

- Modeling the structural and electronic properties of polyacenes/Si-H.** The Organic/silicon interfacial properties are of considerable interests both from a perspective of fundamental research and for practical silicon-based optoelectronic devices. In this work, we theoretically explore the interfacial properties of the organic heterojunctions featuring solar cells, which are crucial to improving the performance of photovoltaic devices. Initially, we have targeted interfaces composed of polyacenes and hydrogen-passivated silicon (Si-H) surfaces. Molecular dynamics simulations using the semiempirical tight-binding DFT method yield the geometric structures at the interface. The MD results indicate that the organic phases are apt to order in herringbone structures



(illustrated in the following Figure 1a), as observed in crystals. With the predicted structures, the band alignments across the interfaces are calculated by taking a hybrid approach (Pasquarello et al. Phys. Rev. Lett. 2008, 101, 046405). The potential distributions across the interface are calculated with the generalized gradient density functional PBE. A significant potential difference along the interface was observed (as shown in Figure 1b), which might arise from a doping effect or strong surface dipole. The bandgaps of the silicon substrates and the organic phases have been calculated by a variety of approaches including PBE, HSE06, PBE0 and GW methods. The investigations of the source of potential distribution and the effect of the silicon slab thickness on the band alignment are ongoing. Based on this understanding of the surface states, the exciton recombination rate will be estimated and the characteristic I-V curves will be obtained. Moreover, larger supercells will be used in the simulations to eliminate the constriction effects on the interfacial structures and properties.

#### Publications related to this project

- Iffat H. Nayyar, Enrique R. Batista, Sergei Tretiak, Avadh Saxena, Darryl L. Smith, and Richard L. Martin. "Localization of Electronic Excitations in Conjugates Polymers Studied by DFT." *Journal of Physical Chemistry Letters* **2**, 566 (2011)
- Feilong Liu, P. Paul Ruden, Ian H. Campbell, and Darryl L. Smith. "Device Model for Electronic Processes at Organic/organic Interfaces." *J. Appl. Physics*, **111**, 094507 (2012).
- Feilong Liu, Brian K. Crone, P. Paul Ruden, and Darryl L. Smith. "Control of Interface Microscopic Processes in Organic Bilayer Structures and Their Effect on Photovoltaic Device Performance." *J. Appl. Physics*, **113**, 044516 (2013).
- Iffat H. Nayyar, Avadh Saxena, Richard L. Martin, Darryl L. Smith, Enrique R. Batista, and Sergei Tretiak. "Effect of trans and cis Isomeric Defects on the Localization of the Charged Excitations in  $\pi$ -Conjugated Organic Polymers", *Submitted to Advanced Functional Materials*. (2013)
- Svetlana Kilina, Enrique R. Batista, Avadh Saxena, Richard L. Martin, Darryl L. Smith, and Sergei Tretiak. "Effect of Packing on Formation of Deep Carrier Traps in Amorphous Conjugated Polymers." *Submitted to Journal of Physical Chemistry Letters*. (2013)

# Electronic and Optical Processes in Novel Semiconductors for Energy Applications

Angelo Mascarenhas

National Renewable Energy Laboratory, 1617 Cole Blvd., Golden, CO 80401

Angelo.Mascarenhas@nrel.gov

## Project Scope

The continued advancement of high-performance devices for energy-related applications requires the development of new materials with specifically tailored properties. The objective of this project is to investigate new semiconductor materials that transcend the existing limitations that constrain current photovoltaic and solid-state lighting (SSL) technologies. Particular emphasis is placed on developing high bandgap ( $> 2$  eV) and low bandgap (1 eV) absorbers for photovoltaics and efficient green-amber light emitters built on GaAs platforms. This work is based on understanding and controlling the fundamental electronic and optical processes in semiconductor alloys, including carrier localization in  $\text{GaAs}_{1-x}\text{N}_x$  and  $\text{GaAs}_{1-x}\text{Bi}_x$  alloys and spontaneous atomic ordering in  $\text{Ga}_x\text{In}_{1-x}\text{P}$  and  $\text{Al}_x\text{In}_{1-x}\text{P}$ . Additional activities focus on investigating bi-polar plasmons, charge and spin density excitations and long-range exciton diffusion in an effort to investigate how collective phenomena may be used to realize semiconductors with novel, useful properties. This project utilizes state-of-the-art resources in growth and spectroscopy through collaborative efforts with the BES Nanoscience Center at Sandia National Laboratory and the National High Magnetic Field Laboratory (NHMFL) at Los Alamos National Laboratory.

## Recent Progress

### *Metal-Insulator Transition in $\text{GaAs}_{1-x}\text{N}_x$*

Despite the loss of structural periodicity, an electronic state in a random alloy remains similar to that in an ideal crystal, in the so-called virtual-crystal approximation. However, the statistical fluctuations due to alloy disorder would suggest dilute alloys to be an archetype for investigating disorder-induced Anderson localization. Phosphorous doped silicon, which has served as the workhorse for studying this phenomenon for over three decades, suffers from the complexity of dealing with inherent electron-electron interactions associated with the long-range coulomb potential of the charged P dopants. The clear identification of the localized-delocalized Anderson transition and of the mobility edge in our recent study on  $\text{GaAs}_{1-x}\text{N}_x$ , suggests that these dilute isoelectronic alloys are an alternative that avoids such complexities. Photoluminescence (PL) and electroreflectance (ER) measurements identify the formation of a N-cluster impurity band below the host conduction band edge in GaAsN with 0.23% N (Fig. 1a). The interaction of this band with the conduction band states at N concentrations above 0.4% leads to the onset of a dramatic perturbation to the host GaAs electronic structure, as observed in the abrupt broadening of the ER transition (Fig. 1b), and signals the transformation from a heavily N-doped semiconductor to the  $\text{GaAs}_{1-x}\text{N}_x$  alloy.

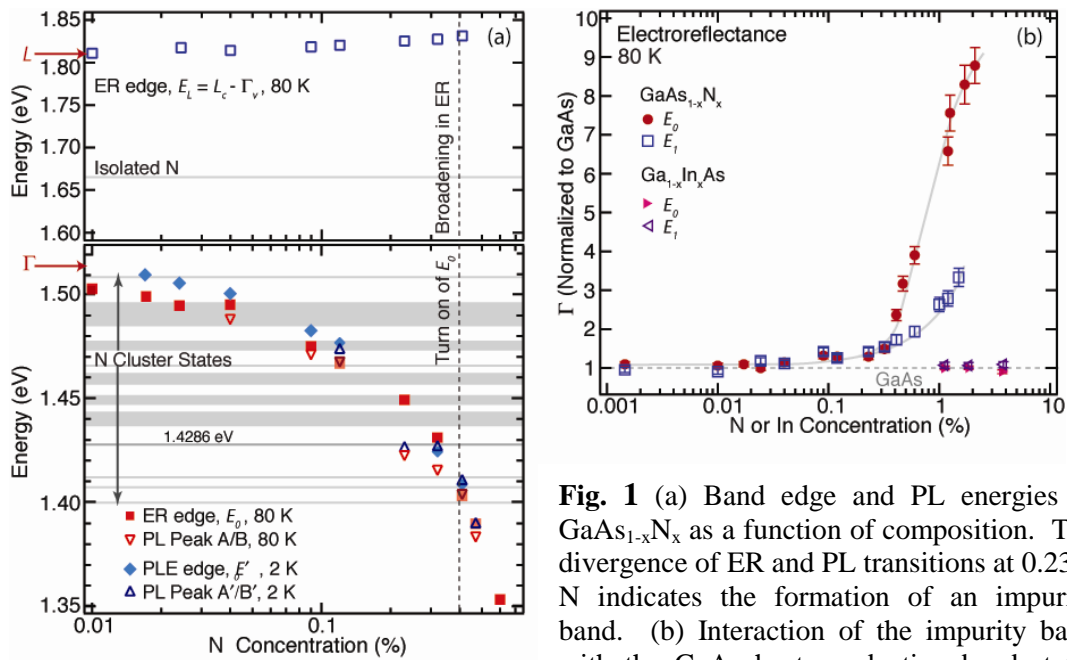


**Fig. 1** (a) Band edge and PL energies in  $\text{GaAs}_{1-x}\text{N}_x$  as a function of composition. The divergence of ER and PL transitions at 0.23% N indicates the formation of an impurity band. (b) Interaction of the impurity band with the GaAs host conduction band states results in a massive broadening of the ER transitions.

The localized-delocalized transition observed in  $\text{GaAs}_{1-x}\text{N}_x$  can be reversed at high magnetic fields. Photoluminescence measurements performed on the 60 T long pulse magnet at the Los Alamos NHMFL, shown in Fig. 2, reveal the dissolution of extended N supercluster states (lines D, E and F) into highly localized states as the exciton Bohr radius is reduced as well as expose resonant N cluster states (lines G, H and I) at high magnetic fields. These measurements provide new insights into the formation and evolution of mini-supercluster states in  $\text{GaAs}_{1-x}\text{N}_x$  and offer a new avenue for probing resonant states by ejecting them out of the conduction band.

Raman scattering measurements confirm the identification of N supercluster states in  $\text{GaAs}_{1-x}\text{N}_x$ . Resonance of the asymmetric line shape of the LO phonon as a function of excitation energy is attributed to the Fano type interference between the discrete LO phonon mode and an overlapping continuous distribution of Raman excitations. This phenomenon also exhibits a discontinuity in the resonance energy at the same N concentrations as observed in the PL and ER measurements and is conjectured to occur due to mixing of the  $\Gamma$  and L band states as the alloy forms.

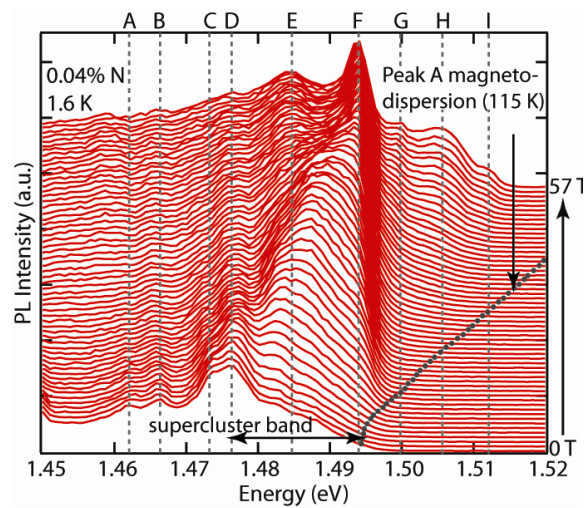


**Fig. 2** Magneto-PL spectra of the  $\text{GaAs}_{1-x}\text{N}_x$  sample with 0.04% N.

## Future Work

We are presently researching plasmon modes of separated-carrier structures as shown in Fig. 3. These are GaAs-based coupled (CQW) and multiple quantum well (MQW) systems that produce large spatial charge separation and result in exciton photoluminescence ring patterns. Because of this charge separation, they are suitable for combined optical and electrical control of electron-hole plasma density, and they exhibit characteristics of coupled plasmas. Coupled plasmas can arise from electrically-coupled layers, as in a MQW, and quantum-coupled layers, as in a CQW. Both systems exist in a ring structure, of which Fig. 1(a) shows the measured energies of the intersubband plasmon modes. The applied electric field changes the photo-generated carrier density through the recombination probability, and it also changes the MQW's intersubband energy spacing, both of which affect the plasmon frequency. The polarized modes show an anti-crossing behavior when the voltage pushes the plasmon energy near the LO-phonon energy, due to the dipole-coupling between phonon and charge-density wave. The depolarized data points do not show this coupling, identifying that mode as a spin-density wave. The control sample in Fig. 1(b) is designed without the CQW, eliminating the possibility of a quantum-coupled charge separation. The presence of multiple mode sets in the data of Fig. 1(b) suggests multiple carrier populations, or population of multiple subbands, although the latter is unlikely. Our future work will focus on the difference between the two structures' polarization behaviors near the anti-crossing, which will reveal information on the coupled plasmas.

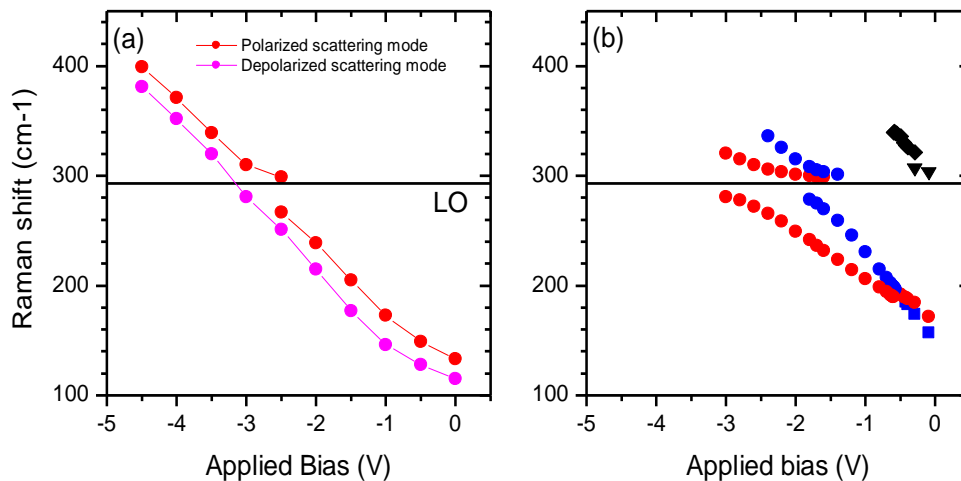


Figure 1. Plasmon energy as a function of gate bias in a combined MQW/CQW ring structure (a), and a MQW (b), both under reverse bias in a p-n junction. The ring structure shows contrasting behavior of the charge-density (polarized) and spin-density (depolarized) signals. The MQW in (b) shows multiple excitations entirely in the polarized scattering.

With respect to the localized delocalized transition dilute nitride alloys, since GaPN is distinctly different from GaAsN in that it is an indirect gap semiconductor alloy, we plan to perform similar high-magnetic field studies on the N isoelectronic impurity states and the evolution into an alloy with increasing N concentration

### Publications of BES-sponsored research (2010 – 2012)

1. “Magnetic field-induced delocalized to localized transformation in GaAs:N”, K Alberi, S.A. Crooker, B. Fluegel, D. A. Beaton, A. Ptak, and A. Mascarenhas. submitted to *Phys. Rev. Lett.*, (2012).
2. “Localization-delocalization transition of electrons at the percolation threshold of semiconductor GaAs  $1-xN_x$  alloys: The appearance of a mobility edge”, K Alberi, B. Fluegel, D. A. Beaton, A. Ptak, and A. Mascarenhas. *Phys. Rev. B*, **86**, 041201(R) (2012).
3. “Mechanism of asymmetric lineshape broadening in GaAsN Raman spectra”, A. Mialitsin, B. Fluegel, A. Ptak, and A. Mascarenhas. *Phys. Rev. B*, **86**, 045209 (2012).
4. “Delocalized state emission in GaAs $_{1-x}$ N $_x$  superclusters”, B. Fluegel, K. Alberi, D.A. Beaton, S.A. Crooker, A.J. Ptak, and A. Mascarenhas. *Phys. Rev. B*, **86**, 205203 (2012).
5. “Quaternary Bismide Alloy BGaAsBi Lattice Matched to GaAs”, D.A. Beaton, A. Ptak, K. Alberi and A. Mascarenhas, *J. Crystal Growth*, **351**, 37 (2012).
6. “Increase of substitutional boron incorporation in BGaAs with addition of a bismuth surfactant”, A. Ptak, D. Beaton and A. Mascarenhas. *J. Crystal Growth*, **351**, 122 (2012).
7. “Kinetically-limited growth of GaAsBi by molecular-beam epitaxy”, A.J. Ptak, R. France, D.A. Beaton, K. Alberi, J.D. Simon, C.-S. Jiang and A. Mascarenhas. *J. Crystal Growth*. **338**, **107** (2012).
8. “Exciton pattern generation in GaAs/AlGaAs multiple quantum wells”, B. Fluegel, K. Alberi, L. Bhusal, A. Mascarenhas, D. W. Snoke, G. Karunasiri, L.N. Pfeiffer and K. West, *Phys. Rev. B* **83**, **195320** (2011).
9. “Direct-Indirect Crossover in GaInP Alloys”, K. Alberi, B. Fluegel, M. Steiner, R. France, W. Ollavaria and A. Mascarenhas. *J. Appl. Phys.* **110**, **113701** (2011).
10. "Shubnikov-de Haas investigation of Bi:GaAs", B. Fluegel, R. Kini, A. Ptak, D. Beaton, K. Alberi, and A. Mascarenhas”, *J. Appl. Phys.* **99**, **162108** (2011).
11. “Eigenstate localization in an asymmetric coupled quantum well pair”, A. Mialitsin, S. Schmult, I. Soloyov, B. Fluegel and A. Mascarenhas, *Superlattices and Microstructures*, (submitted).
12. “Solid-State Lighting”, L. Bhusal and A. Mascarenhas, **Invited Book Chapter**, *Handbook of Luminescent Semiconductor Materials*, L. Bergman Ed. *CRC Press* (Sept. 2011).
13. “Effect of Bi alloying on the hole transport in the dilute bismide alloy, GaAs $_{1-x}$ Bi $_x$ ”, R. N. Kini, A. J. Ptak, R. France, R. C. Reedy and A. Mascarenhas, *Phys. Rev. B* **83**, 075307 (2011).
14. “Synthesis and photovoltaic effect of vertically aligned ZnO/ZnS core/shell nanowire arrays”, Wang K, Chen, J. J., Zeng, Z. M., Tarr, J., Zhou, W. L. Zhang, Y., Yan, Y. F. Jiang, C. S., Pern, J., Mascarenhas A., *Appl. Phys. Lett.* **96**, 123105 (2010).

# Interfaces in Electronic and Structural Materials

*Yuri Mishin, PI*

Department of Physics and Astronomy  
George Mason University, MSN 3F3  
4400 University Drive, Fairfax, VA

Phone: 703-993-3984  
Fax: 703-993-1269  
Email: [ymishin@gmu.edu](mailto:ymishin@gmu.edu)

## Program Scope

Many materials used in energy generation, conversion, storage and transmission are subject to high mechanical stresses pushing towards their theoretical strength and high temperatures approaching the melting point. The ability of materials to function under such extreme conditions depends critically on their microstructure, primarily on thermal and mechanical properties of grain boundaries and other internal interfaces. Development of revolutionary new materials for energy applications relies on fundamental knowledge of interfaces and our ability to design and control their properties.

The objective of the proposed research is to advance the fundamental understanding of interfaces and develop new methods for computational prediction of their properties. Some of the specific topics include: (1) investigation of the effect of crystallographic characteristics, applied stresses and high temperatures on thermodynamics and mechanical strength of internal interfaces, (2) dynamics and mechanisms of grain rotation at the nanoscale, and (3) interaction of moving grain boundaries with dislocations, and (4) nucleation and growth of new grains in nano-twinned materials. These topics are centered around the general problem of thermodynamic stability of interfaces as part of materials microstructure.

The proposed approach is a combination of theory and atomistic computer simulations, primarily molecular dynamics (MD) and a variety of Monte Carlo techniques, as well as first principles calculations. The atomistic approach will be combined, in a synergistic manner, with the phase-field and phase-field crystal (PFC) methods allowing us to extend the simulations to greater length and time scales. The project is expected to make a significant impact on the state of knowledge in interface science by improving the understanding of intrinsic physical limits of interfaces under mechanical and thermal extremes and suggesting ways of approaching such limits in energy technologies.

## Recent Progress

1. Structural transformations at interfaces are of profound fundamental interest as complex examples of phase transitions in low-dimensional systems. Despite decades of extensive research, no compelling evidence exists for structural transformations in high-angle grain boundaries (GBs) in elemental systems. We have shown that the critical impediment to observations of such phase transformations in atomistic modeling has been rooted in inadequate simulation methodology. The proposed new methodology allows variations in atomic density inside the GB and reveals multiple GB phases with different atomic structures. Reversible first-order transformations between such phases are observed by varying temperature or injecting point defects into the boundary region. Due to the presence of multiple metastable phases, GBs can absorb significant amounts of point defects created inside the material by processes such as irradiation. We have proposed a novel mechanism of radiation damage healing in metals which may guide further improvements in radiation resistance of metallic materials through GB engineering.

2. We have studied the phenomenon of GB premelting observed at high temperatures approaching the melting point of the material. GBs with relatively low energies can be superheated above the melting temperature and eventually melt by heterogeneous nucleation of liquid droplets. We proposed a thermodynamic model of this process based on the sharp-interface approximation with a disjoining potential. The distinct feature of the model is its ability to predict the shape and size of the critical nucleus using a variational approach. The model

reduces to the classical nucleation theory in the limit of large nuclei but is more general and remains valid for small nuclei as well. Contrary to the classical nucleation theory, the model predicts the existence of a critical temperature of superheating and offers a simple formula for its calculation. The model has been tested against MD simulations in which liquid nuclei at a superheated boundary were obtained by an adiabatic trapping procedure. The simulation results demonstrate a reassuring consistency with our model.

**3.** We have developed a rigorous thermodynamic theory of plane coherent solid-solid interfaces in multicomponent systems subject to non-hydrostatic mechanical stresses. The interstitial and substitutional chemical components are treated separately using chemical potentials and diffusion potentials, respectively. All interface excess quantities have been derived using Cahn's generalized excess method without resorting to geometric dividing surfaces. We have presented rigorous and accurate expressions for the interface free energy as an excess quantity and derived a generalized adsorption equation and an interface Gibbs-Helmholtz equation that does not contain the interface entropy. The interface stress tensor emerges naturally from our generalized adsorption equation as an appropriate excess over bulk stresses and is shown to be generally non-unique. Another interface property emerging from the generalized adsorption equation is the interface excess shear. This property is specific to coherent interfaces and represents the thermodynamic variable conjugate to the shear stress applied parallel to the interface. The theory reveals a number of Maxwell relations describing cross effects between thermal, chemical, and mechanical responses of coherent interfaces.

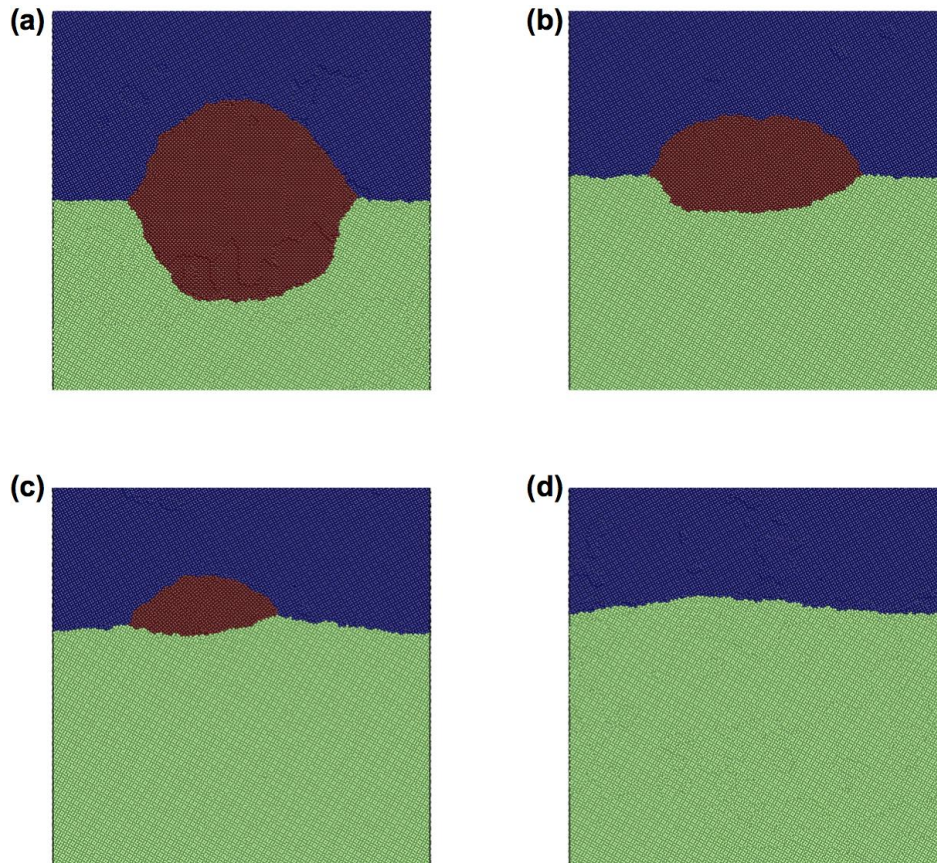
**4.** The thermodynamic theory of coherent interfaces discussed above has been applied to GBs subject to non-hydrostatic elastic deformations. We have derived expressions for the GB free energy as the reversible work of GB formation under stress. We have also presented a generalized adsorption equation whose differential coefficients define the GB segregation, GB stress tensor, GB excess volume, and GB excess shear. The generalized adsorption equation generates a set of Maxwell relations describing cross effects between different GB properties. The theory has been applied to atomistic simulations of symmetrical tilt GBs in Cu and Cu-Ag alloys. Using a combination of MD and Monte Carlo methods, we computed a number of GB excess quantities and their dependencies on the applied stresses, temperature and chemical composition in the grains. We have also tested several Maxwell relations and obtain excellent agreement between the theory and simulations.

**5.** We continued to study the so-called *coupling effect*, in which GBs are moved by applied stresses producing shear deformation of the lattice they traverse. This process is relevant to plastic deformation of nano-crystalline materials and can explain the stress-induced grain growth observed experimentally at room temperature and even at cryogenic temperatures. Previous simulation and experimental studies of the coupling effect were performed for symmetrical tilt GBs, even though most GBs in real polycrystalline materials are asymmetric. We have conducted a combined MD-PFC study in collaboration with Prof. A. Karma (Northeastern University) who is also sponsored by the Physical Behavior of Materials Program. The study has revealed that asymmetrical tilt GBs are indeed moved by applied shear stresses exhibiting the coupling effect. The GB motion occurs by glide of different types of dislocations on their slip planes and involves a chain for dislocation reactions. The observed agreement between the MD and PFC results points to the generic character of our results. It also demonstrates the ability of the PFC methodology to capture the most essential features of atomic processes and the fruitfulness of the multi-scale MD-PFC approach.

**6.** Coupled motion of curved GBs can produce grain rotation. We have studied the process of curvature-driven shrinkage and rotation of a cylindrical grain as a simple model of grain rotation in nano-crystalline materials. Geometrical rules of grain rotation have been derived, including high-angle misorientations and multiple coupling modes. At low temperatures, the coupling between GB migration and grain translation induces rotation of the grain towards higher or lower misorientation angles, depending on the initial misorientation. The direction of rotation depends on the sign of the coupling factor, which can change with the grain misorientation. The

grain rotation stops when the grain reaches a “frustration” angle at which the coupling factor changes sign. At very high temperatures, the grain rotation can cause GB premelting and eventually melting of the material. The dynamics of the GB motion and grain rotation have been studied as functions of the initial misorientation angle and temperature. The effects of imposed constraints blocking the grain rotation or exerting a cyclic torque have been examined.

7. In collaboration with Prof. A. Karma (Northeastern University), we have studied equilibrium fluctuations of GBs by analytical methods and MD simulations. The proposed analytical expressions has been validated by MD simulations for symmetrical tilt GBs. This study demonstrates that equilibrium fluctuations can be used to extract the misorientation dependence of the GB mobility. The results shed light on fundamental relationships between equilibrium and nonequilibrium GB properties and provide new means to predict such properties.



Molecular dynamics simulation of stress-driven motion of grain boundaries (GBs) in copper. The grains are color-coded by crystallographic orientation. The shear is applied parallel to the initially flat horizontal GB. The shear stress induces not only GB migration due to the coupling effect but also the motion of the *entire* grain upwards. Stress-driven motion of an entire grain has been observed in experiments but has never been seen in simulations before.

## Future Plans

1. We will continue to study the stress-driven GB motion, focusing on situations when the grains contain high concentrations of dislocations and/or vacancies. These cases are relevant to the processes of recovery, recrystallization and radiation damage of energy-related materials.

2. As a new direction, we will study the effect of GB phase transformations on GB diffusion. Recent diffusivity measurements in the symmetrical tilt  $\Sigma 5(310)$  GB in copper [Divinsky et al, PRB 2012] reported two distinct slopes on the Arrhenius plot of the diffusivity, suggesting a

possible structural transformation in this GB. Contrary to the experiment, previous MD studies concluded that the diffusivity followed the Arrhenius law with a single slope. We will modify the methodology of the MD simulations allowing the number of atoms in the boundary to adjust in order to observe structural transformations at high temperatures. The diffusivities of the different GB structures will be calculated using both the traditional methodology based on the Einstein equation and a novel approach based on the Fisher model assuming type-C diffusion kinetics. The goal of the study will be understand the effect of the structural transformation on the GB diffusion coefficient at high temperatures, and to reproduce and understand the non-Arrhenius behavior of the GB diffusivity seen in the experiment.

#### ***Publications of DOE sponsored research (2010-2012)***

1. T. Frolov, D. Olmsted M. Asta and Y. Mishin: Structural phase transformations in metallic grain boundaries, *Nature Communications*, under review.
2. A. Karma, Z. T. Trautt and Y. Mishin: Grain boundary fluctuations and coupling to shear deformation, *Phys. Rev. Letters* **109**, 095501 (2012)
3. Z. T. Trautt, A. Adland, A. Karma and Y. Mishin: Coupled motion of asymmetrical tilt grain boundaries: molecular dynamics and phase field simulations, *Acta Mater.* **60**, 6528-6546 (2012)
4. T. Frolov and Y. Mishin: Thermodynamics of coherent interfaces under mechanical stresses. I. Theory, *Phys. Rev. B* **85**, 224106 (2012)
5. T. Frolov and Y. Mishin: Thermodynamics of coherent interfaces under mechanical stresses. II. Application to atomistic simulation of grain boundaries, *Phys. Rev. B* **85**, 224107 (2012)
6. Z. T. Trautt and Y. Mishin: Grain boundary migration and grain rotation studied by molecular dynamics, *Acta Mater.* **60**, 2407-2424 (2012)
7. T. Frolov, and Y. Mishin: Liquid nucleation at superheated grain boundaries, *Phys. Rev. Letters* **106**, 155702 (2011)
8. Y. Mishin, M. Asta and J. Li: Atomistic modeling of interfaces and their impact on microstructure and properties, *Acta Mater.* **58**, 1117 - 1151 (2010)
9. T. Frolov and Y. Mishin: Stable nanocolloidal structures in metallic systems, *Phys. Rev. Letters* **104**, 055701 (2010)
10. T. Frolov and Y. Mishin: Effect of non-hydrostatic stresses on solid-fluid equilibrium. I. Bulk thermodynamics, *Phys. Rev. B* **82**, 174113 (2010)
11. T. Frolov and Y. Mishin: Effect of non-hydrostatic stresses on solid-fluid equilibrium. II. Bulk thermodynamics, *Phys. Rev. B* **82**, 174114 (2010)
12. T. Frolov and Y. Mishin: Orientation dependence of the solid-liquid interface stress: atomistic calculations for copper, *Model. Simul. Mater. Sci. Eng.* **18**, 074003 (2010)
13. C. A. Becker and Y. Mishin: Temperature dependence of the pre-wetting transition at the (111) anti-phase boundary in Ni<sub>3</sub>Al: an atomistic study, *Model. Simul. Mater. Sci. Eng.* **18**, 074004 (2010)
14. Y. Mishin and W. J. Boettinger: Thermodynamic model of hydride formation and dissolution in spherical particles, *Acta Mater.* **58**, 4968-4977 (2010)
15. T. Frolov, W. J. Boettinger and Y. Mishin: Atomistic simulation of hillock growth, *Acta Mater.* **58**, 5471-5480 (2010).

**“Optically Active 3-Dimensional Semiconductor Quantum Dot Assemblies in Heterogeneous Nanoscale Hosts” (DOE Award DE-FG02-ER46387)**

**A.V. Nurmikko, Brown University**  
 Division of Engineering, Providence, RI 02912  
[Arto\\_Nurmikko@brown.edu](mailto:Arto_Nurmikko@brown.edu)

**Jung Han, Yale University**  
 Department of Electrical Engineering, Yale University, New Haven, CT

**1. Project Scope:** The primary objective of this proposal is to advance the physics and application of colloidal quantum dots (CQD) for development of red-green-blue (RGB) *single material*-based light emitting thin solid films. Specifically, we look for means of discovering and implementing compact multi-color lasers and coherent emitters as compact devices where robust, optically active CQD thin films can be incorporated into new types of nanophotonic structures for applications such as scalable area projection displays.

**2. Recent Progress: Red, Green, and Blue Colloidal QD Lasers – Exploiting Single Exciton Gain in Densely Packed Films.** Current models for optical gain in nanocrystal wide gap semiconductor QDs show a fundamental obstacle for laser applications. These models (and experiments) argue that for ensembles of QDs samples, the light amplification requires more than one exciton per QD on average,  $\langle N \rangle \sim 1.5$ , thereby involving biexciton states. Yet the biexciton states suffer from the fundamental by non-radiative multiexciton Auger recombination process whose Coulomb interaction mechanism is largely enhanced in strongly confined systems. Because of Auger rate ( $\tau_{\text{Auger}} \sim 100$  ps) is about two orders faster than typical radiative recombination rates in such QDs, high power ultrashort pulse ( $\sim 100$  fs) laser systems are usually employed as pumping sources to overcome the large losses. We have surmounted this barrier by accessing optical gain in the single exciton regime, thereby benefiting from both the large optical cross-sections and diminished Auger effect.

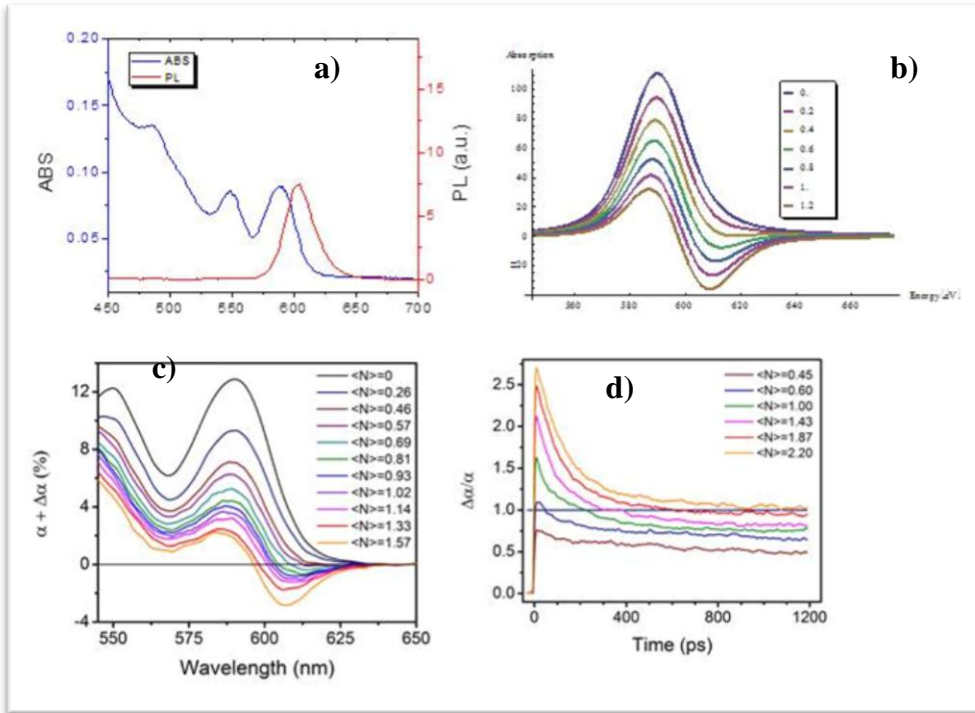


**Figure 1: Stokes shift of the first exciton transition enables single exciton optical gain.** *a*, Spectral analysis of absorbance and PL for a red CQD film shows a Stokes shift of 15 nm, while the linewidth of PL is 28 nm (full-width at half-maximum, FWHM). *b*, Model calculation of the first exciton absorption resonance at different excitation levels. (A negative absorption coefficient implies optical gain). *c*, spectral absorption (sum of linear absorption and differential absorption) of the CQD film measured at 2 ps after pump pulses shows optical gain threshold at  $\langle N \rangle \sim 0.50$ , a truly single exciton regime. *d*, Transient absorption of the CQD film at the wavelength of 614 nm, where the optical gain emerges, demonstrates the contributions of both single-exciton (slow decay) and multiexciton (fast decay) recombination. The optical gain regime corresponds to  $\Delta\alpha/\alpha > 1$ . (Horizontal lines in figure b, c, d are guides to the eye).

Our high quantum yield ( $> 80\%$ ) colloidal QDs (CdSe core and thin  $\sim 1$  nm  $\text{Zn}_{0.5}\text{Cd}_{0.5}\text{S}$  ternary shell), were optimized for a suitable Stokes shift between the ground state exciton absorption and emission. Figure 1a shows the linear absorbance and PL of our closely packed “epitaxial-like” spin-cast red QD film. This Stokes shift, about half width at half maximum (HWHM) of the PL peak, reduces the absorption and emission spectrum overlap to less than 50%, which significantly lowers the absorption losses under excitation conditions required for optical gain. Our model calculation in Fig. 1b shows that the optical gain occurs if average number of excitons generated in a QD is  $\langle N \rangle = 0.42$ . Experimental results of spectral absorption with different pumping levels at 2 ps after ultrafast pumping are presented in Fig. 1c. Pumping source is at 400 nm (3.1 eV), significantly higher than the lowest energy excitonic state of QDs (2.06 eV). The delay time of 2 ps is long enough for all excitons to relax (on the order of sub ps) and to occupy from their lowest energy states, similar to the model calculation. Auger process with time constant of 120 ps for our red QDs is the fastest recombination process, and the 2 ps delay time is short enough to neglect all the recombined excitons. The exciton number,  $n$ , in a QD has Poisson distribution:  $P(n, \langle N \rangle) = \frac{\langle N \rangle^n e^{-\langle N \rangle}}{n!}$ , similar to the model calculation in Fig. 1b. The model only considers the first atomic-like exciton transition with measured homogeneous and inhomogeneous broadenings in QDs. Finite background losses in the thin solid films slightly increase the experiment threshold value ( $\langle N \rangle = 0.50$ ) from the calculation one ( $\langle N \rangle = 0.42$ ). Yet, both threshold values clearly show the single exciton optical gain regime in our QD films. The dynamics of QD single exciton gain media was analyzed by transient absorption results in Fig. 1c (below). At low optical pumping levels, only a single exponential decay is observed as single exciton recombination. At high pump levels, an additional fast decay emerges ( $\sim 120$  ps) from Auger recombination. Yet, our model and experiments show how the rapid relaxation of the biexciton state to single excitons can contribute to the single exciton optical gain in a properly configured type-I colloidal QDs. We have achieved similar results *in the green and blue* as well.

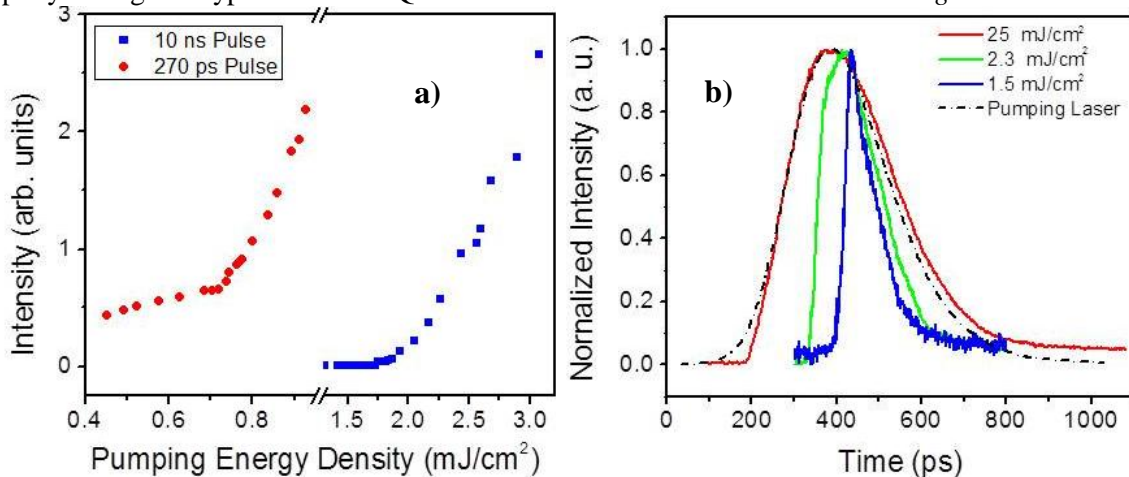


**Figure 2: Quasi-CW ASE of the red QD film pumping at the wavelength of 532 nm. a, Intensity of edge emission as a function of pump energy density per pulse with two different pumping sources: 270 ps and 10 ns pulse width. b, Transient ASE at different pumping energy densities, time referenced to the 270 ps pumping laser.**

With the advantages of single exciton gain and removal of the Auger competition, more pragmatic pumping conditions that approach those of realistic laser devices can be reached. We demonstrated this benefit here with red QD films while increasing the pump pulse duration to a steady state (quasi-continuous) regime, not accessed previously in any form of colloidal QD-based lasing. Two employed pump sources were 532-nm wavelength with pulse width of 270-ps and 10-ns (which are commonly available as compact YAG-lasers today). Figure 2 shows the edge emission of QD film in stripe excitation configuration. The ASE threshold for the red QD films is  $1.6 \text{ mJ/cm}^2$  and  $720 \mu\text{J/cm}^2$  for 10-nsec and 270-psec (Fig. 2a) pumping cases, respectively. The values are somewhat higher than our previous value when pumped by an ultrashort pulsed ( $\sim 100$  fs) laser. The differences are explained by

lower absorption coefficient of the red QD film at 532 nm (as opposed to a 400nm wavelength in ultrafast pumping case) and modest competition from finite Auger recombination during this quasi-steady state “slow” pumping process. Theoretically, the solutions of so-called “ladder rate equations” with all input parameters derived experimentally show that  $\langle N \rangle = 0.86$  and  $0.85$  for 270-pssec and 10-nsec cases, self-consistent with  $\langle N \rangle = 0.80$  acquired from ultrashort pulse excitation.

To focus on the tell-tale time dynamics, the time resolved ASE (Fig. 2b) was measured by a fast photodiode (25 GHz) and a digital sampling oscilloscope (50 GHz). The pulse width of ASE output is seen to increase with pumping level so as to finally reach the duration of the pump laser pulse width which in turn is more than twice of Auger time constant for this QD system. This result directly shows quasi-CW ASE from red QD film without the inhibition by the Auger process and invites further device development.

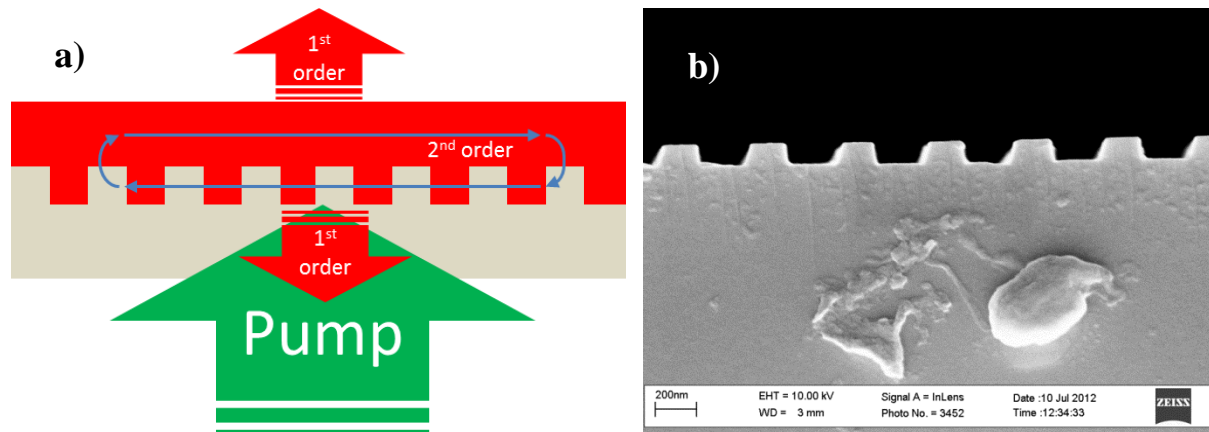


**Fig. 3: Second-order DFB laser with QD gain media.** *a*, Schematic of a QD-DFB laser in which the QD film is deposited on second-order glass grating. The pump beam is vertical. The second order of resonant grating provides feedback in the QD optical gain media, with first order of resonant grating as output channel, vertical to the grating surface. *b*, SEM image of a glass grating made by interference photolithography and ICP-RIE technique.

As the next step, the QD optical gain media (red) was employed in second order distributed feedback Bragg (DFB) laser structures which offer the vertical beam output (Fig. 3a). The larger pitch of a second order grating in comparison to the first order one is another advantage for fabrication. Our glass gratings were made by ICP-RIE technique with a square profile as presenting in Fig. 3b. The optimized depth of grating for QD-DFB laser was 75 nm. The hard-mask for etching was Cr which was defined by interference photolithography (for the red laser) or focus ion beam (for the green and blue lasers). The high concentration of QD solution was spun cast on the grating surface. A densely packed QD layer (250 nm) was formed on top of grating.

The pumping source was a compact sub-nanosecond pulsed laser with output at the wavelength of 1064 nm. The second (532 nm) and third (355 nm) harmonic were used to pump red, green and blue QD-DFB lasers. Figure 4a-e shows the top-view images of the red QD-DFB at different pumping levels. The pumping stripe on grating was made by cylindrical lens. Below the threshold, the QD photoluminescence shows a regular red stripe. When the pumping is exceeds the threshold level, the intensity abruptly increases from the center to the edge of the stripe. Figure 4e demonstrates the threshold behavior of the laser output. The threshold is about  $118 \mu\text{J}/\text{cm}^2$  - low in comparison to ASE threshold ( $720 \mu\text{J}/\text{cm}^2$ ). The strong feedback and low loss structure significantly reduce lasing threshold. Figure 3b presents the spectra of the red and green QD-DFB lasers. The single mode lasers at 610 nm and 568 nm provide a very narrow spatially coherent emission beyond our the spectrometer resolution.

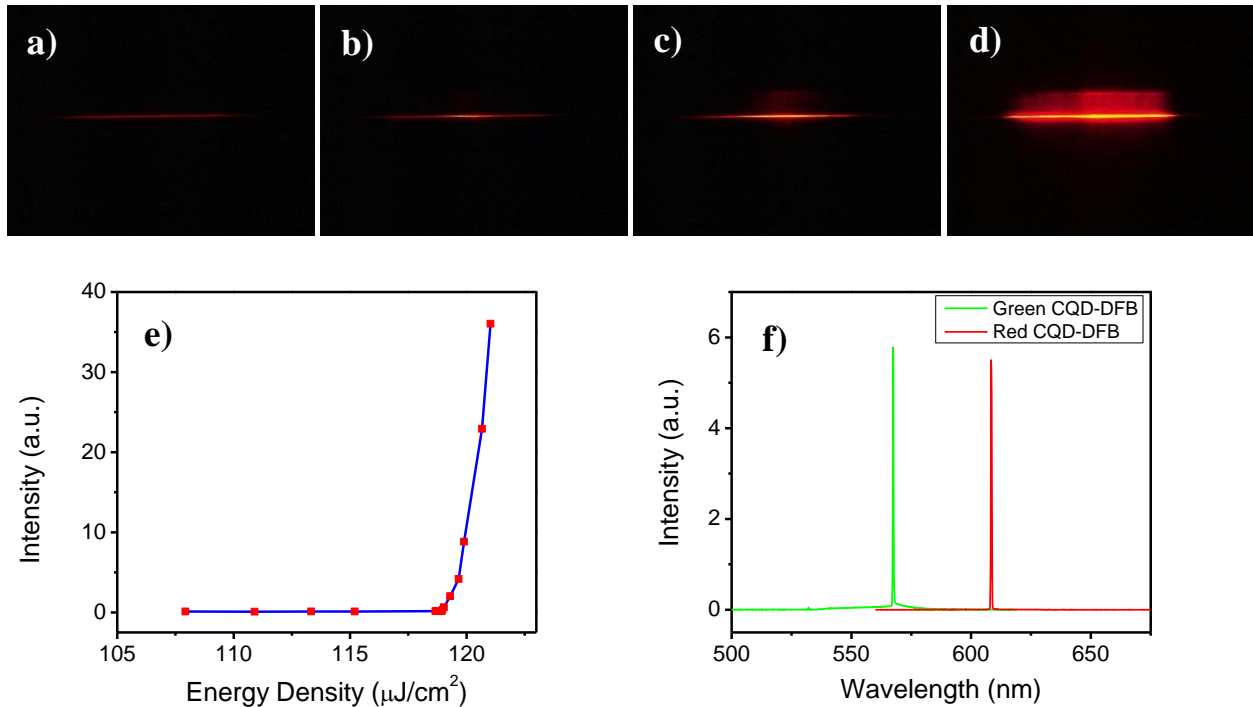


**Fig. 4: QD-DFB laser pumped by a compact sub-nanosecond pulse source.** *a-d*, Stripe pumping on the red QD-DFB laser from the top view at different excitation levels. The stripe length was 400  $\mu\text{m}$ . The grating direction is vertical (perpendicular to the pump stripe). *e*, The laser output as a function of pump pulse energy density shows a low threshold for the red QD-DFB laser. *f*, Spectral analysis of the red and green QD-DFB lasers pumped by the second (532 nm) and the third harmonic (355 nm) generation, respectively.

The spatial coherent outputs of the red and green QD-DFB lasers are shown in Fig 5. A second cylindrical lens was used to collimate the laser beam outputs to circular symmetry. Filters are used to remove the residue pumping laser beams. Figure 5a and 5c show laser spots projected on a screen. The top-view of the red QD-DFB laser on Fig. 5b shows strong output from a small point source - which might eventually be a pixel in a high intensity display or projector.

The current QD-DFB lasers provide two output beams on both sides of grating, with a total efficiency of red QD-DFB laser is 7%. However, as 75% of the pump beam power was unabsorbed, therefore the actual efficiency (output power vs absorption power) of the red QD-DFB laser is 28%.

**3. Plans Ahead:** With the discovery of gain and stimulated emission from closely packed arrays of quantum dots in host media, we next aim to better understand the nanoscale light-matter coupling effects that form a possible basis for collective radiative response of the epitaxial-like thin films. We also plan to advance the microcavity laser geometries from these RGB materials to explore the prospects of practical laser action across the entire visible system from the single component material which our CdSe/(Zn,Cd)Se system may offer. With the focus ion beam fabrication, smaller period gratings for QD-DFB laser in the green and the blue are possible and this work is under way.

- “Red, Green, and Blue Lasing enabled by Single-Exciton Gain in Colloidal, Densely Packed Quantum Dot Films”, C. Dang, J. Lee, A.V. Nurmikko, C. Breen, J. S. Steckel and S.Coe-Sullivan, *Nature Nanotechnology* 7, 335-339 (2012)
- “A Wafer-Level Integrated White Light Emitting Diode Incorporating Colloidal Quantum Dot as Nanocomposite Luminescent Medium”, C. Dang, J. Lee, Y. Zhang, J. Han, C. Breen, J. S. Steckel, S.Coe-Sullivan and A.V Nurmikko, *Advanced Materials*, 24 AUG 2012, DOI: 10.1002/adma.201202354
- Results of ongoing research have been submitted for publication and conferences..

## Complex hydrides – A new frontier for future energy applications

V.K. Pecharsky (presenting, vitkp@ameslab.gov), D.D Johnson, M. Pruski, and  
L.S. Chumbley  
Ames Laboratory, Iowa State University, Ames, IA 50011-3020

### Program Scope

Solid-state hydrogen storage is one of the critical enabling technologies required to ensure a successful future transition from fossil-based to hydrogen-based energy. We seek materials that afford substantially higher hydrogen content per unit mass and volume compared to compressed or liquefied hydrogen. Solids under consideration include alanates, and borohydrides of early alkali/alkaline earth metals, in which the Al or B atom is surrounded by four to six hydrogen atoms forming complex hydrogen-rich  $[MH_n]^{p-}$  anions, and the ammonia derivatives – amides and imides. We address issues related to their physical and chemical properties, and establish basic knowledge of the nature of mixed complex hydrides, hydrogenation-dehydrogenation mechanisms, equilibrium and nonequilibrium thermodynamics, and the kinetics of direct synthesis from the elements or intermediary compounds. Our focus is discovery of novel material systems/composites through innovative and facile processing methods leading to advanced ultra-high capacity hydrogen storage solids.

Although several light-weight, high-capacity complex hydride systems meet at least some of the DOE targets, none comes close to being reversible under practical temperature and pressure parameters. We strive to understand the underlying transformation mechanisms in such systems by comprehensive assessment of intermediates and final products during the hydrogen release cycle. By building such knowledge base we hope to address issues that may be critical for reversible hydrogen storage in these systems. This entails basic understanding of the mechanisms of hydrogenation/dehydrogenation transformations occurring in a ball mill, and differences between the mechanically- and thermally-induced transformations. To achieve the said goals we engage state-of-the-art characterization techniques such as X-ray diffraction, high resolution solid-state nuclear magnetic resonance, electron microscopy, supported by modeling and first principles theory. Following our strategies developed in the previous funding period we will:

- Continue to study mechano- and thermochemical transformations of selected complex hydride systems to establish relevant details of their mechanisms while focusing on events critical to achieving reversibility in these systems. Further, effect of varying stoichiometry and processing history (milling parameters) on their crystal and microscopic structures, thermodynamic, and kinetic properties will be evaluated.
- Continue to employ and improve characterization methods, such as gas-volumetric analyses, solid-state NMR spectroscopy (including in-situ), XRD, and electron microscopy to determine to the best extent possible the structure and properties of all materials developed in this project.
- Integrate experiments with theoretical modeling providing guidance toward the discovery of hydrogen-containing solids that would be unattainable using synthetic and processing methods alone. Theory, tested against reproducible experiments, will

lead to understanding of thermodynamics and kinetics of dehydrogenation and hydrogenation transformations in selected model systems

### Recent progress

#### Mechanically induced reactions, their progress and pathways.

We have successfully demonstrated that high yields of  $\text{Mg}(\text{BH}_4)_2$  can be obtained from a direct hydrogenation of  $\text{MgB}_2$  in a ball mill under high hydrogen pressure. Using  $^{11}\text{B}$  NMR we were able to identify various polyhedral borane anion salts as intermediates which improve our basic understanding of the mechanochemical pathway of this reaction. Magnesium borohydride,  $\text{Mg}(\text{BH}_4)_2$ , was synthesized at pressures between 50 and 350 bar  $\text{H}_2$  without the need for further isothermal hydrogenation at elevated temperature and pressure. The obtained products released  $\sim 4$  wt.%  $\text{H}_2$  below 390 °C, and a major portion of  $\text{Mg}(\text{BH}_4)_2$  transformed back to  $\text{MgB}_2$  around 300 °C, demonstrating the possibility of reversible hydrogen storage in an  $\text{Mg}(\text{BH}_4)_2$  -  $\text{MgB}_2$  system. Ability to carry out such *one-pot* hydrogenation under moderate temperature and pressure conditions and understanding of the physical behavior of such systems under mechanical stress significantly widens the scope of further investigation. For example, mechanochemical synthesis of mixed metal borohydrides such as  $\text{MgM}(\text{BH}_4)_n$  ( $\text{M}=\text{Sc}$ ,  $\text{Li}$  etc) may now be investigated systematically.

#### High resolution Solid-State NMR spectroscopy reveals the decomposition pathway of $\text{Li}_3\text{AlH}_6$ - $\text{NH}_3\text{BH}_3$ system

The mechanism of thermochemical dehydrogenation of the 1:3 mixture of  $\text{Li}_3\text{AlH}_6$  and  $\text{NH}_3\text{BH}_3$  (AB) has been established by the extensive use of solid-state NMR spectroscopy and theoretical calculations. Solid-state NMR measurements and theoretical calculations provided invaluable insights into the dehydrogenation mechanism of the  $\text{Li}_3\text{AlH}_6$ -3AB mixture. The key reactions involved in this process were identified by a suite of 1D and 2D NMR measurements, which provided coherent information about  $^{27}\text{Al}$  and  $^{11}\text{B}$  functionalities in samples treated at various temperatures. The DFT calculations were used to further refine the understanding of these functionalities, in cases when the spectroscopic information alone could not provide definite identification. These results revealed that the partial transformation of AB to LiAB yields the  $(\text{LiAB})_x(\text{AB})_{1-x}$  intermediate, which promotes the polymerization between AB and LiAB, and results in the lower activation energy for the dehydrogenation. The detailed reaction mechanism, in particular the role of lithium revealed in this study, open up opportunities for exploring new classes of hydrogen storage materials (both pure compounds and mixtures) and strategies for their utilization.

#### Density Functional Approach to Understanding Desorption Energetics.

*Nano structuring* and transition-metal (TM) catalytic doping are widely used concepts in hydrogen-storage materials to improve  $\text{H}_2$  sorption kinetics. However, mechanistic details behind these concepts remain poorly understood and thus detrimental to further improvements. We have successfully applied density functional theory in concert with nudged-elastic-band (NEB) calculations to elucidate the catalytic effect of Ti substitutional dopant on  $\text{H}_2$  desorption from  $\text{MgH}_2(110)$  surfaces. For a Ti-doped surface  $\text{H}_2$  desorption, we have identified a cooperative mechanism involving synchronized diffusion of two H atoms around Ti and bulk diffusion into the H vacancy sites (controlled by the bulk diffusion barrier of 0.70 eV) that replenish the surface H to restart

the desorption process once again (controlled by Ti-reduced barrier of 1.42 eV). Further, by employing density functional theory and simulated annealing, we studied initial H<sub>2</sub> desorption from semi-infinite stepped rutile (110) surface and Mg<sub>31</sub>H<sub>62</sub> nanoclusters, with(out) transition-metal catalyst dopants (Ti or Fe). We have given examples of stepped surfaces and nanoclusters, as well as full H-desorption, as compared to experiment. We demonstrated that local bonding controls the initial H-desorption energy from any stable MgH<sub>2</sub> surface or stable cluster configuration. The desorption energy is ruled not by whether H is removed from semi-infinite surfaces or an amorphous nanocluster, but instead by how many metal atoms to which the desorbing H is attached; namely, for undoped singly bonded (doubly bonded) H, the desorption energy is ~140 kJ/(mol H<sub>2</sub>) (~240 kJ/(mol H<sub>2</sub>)). Kinetic barriers also remain similar between undoped bulk and nanoclusters, i.e., ~1.83 eV. Hence, for removing a single surface H from MgH<sub>2</sub>, there is generally no effect from sample size on desorption energy. For doped cases, e.g., Ti, we find a reduction on desorption energetics (-24%) and barriers (-22%) as observed, showing that transition-metal dopants do provide a catalytic effect on H desorption.

### Future plans

Keeping in mind that there is a clear dearth of high hydrogen density systems that are reversible under practical conditions, we will continue to focus on innovative mechanochemical processing approaches to attain reversibility in a select few systems with demonstrated potential for reversibility. Further, such approaches will be applied to delve into promising but unexplored territory of mechanochemical hydrogenation of other classes of materials. Specifically, we will:

- Examine the mechanochemical regeneration of Li and Na-alanates starting from their decomposition products, Li(Na)H and Al or the intermetallic compounds in Li-Al system. Several aspects of liquid-assisted milling in polar and non-polar solvents under moderate hydrogen pressure will be investigated. Mechanochemical reaction of more complex systems such as Li<sub>3</sub>N-Al-H<sub>2</sub>, LiAlH<sub>4</sub>-MgB<sub>2</sub>-H<sub>2</sub> will be undertaken.
- Continue to investigate room-temperature, high H<sub>2</sub> pressure (up to 350 bar), mechanochemical synthesis of un-solvated AlH<sub>3</sub> (alane) via direct reaction of Al metal under H<sub>2</sub> pressure. Theoretically predicted role of Ti-dopant and lattice site defects in reducing the energy penalty during direct reaction of Al and H<sub>2</sub> will be scrutinized. Further, indirect routes to synthesis of AlH<sub>3</sub> via cation exchange reaction of alanates and metal halogenides will be developed to afford the “green” synthetic route (ongoing studies). Mechanical energy driven reaction pathway will be elucidated to further assist in selecting reaction components that may result in by-products that could be easily separated from the alane.
- Initiate investigation on mechanochemical hydrogenation of Al in the presence of graphite-like h-BN and a-BN structures.
- Study feasibility of hydrogen storage in chemically hybrid systems containing amides/alanates of Li and Na and conventional AB<sub>5</sub> and AB<sub>2</sub> metallic hydrogen absorbers.
- Extend our recently concluded investigation on mechanochemical MgB<sub>2</sub> ⇌ Mg(BH<sub>4</sub>)<sub>2</sub> transformation to include multiple cations leading to mixed-metal borohydrides with

potentially improved kinetics. For example, mechanochemical reaction of  $\text{LiH} + \text{B} + \text{MgB}_2$  or  $\text{LiB} + \text{MgB}_2$  will be evaluated. Using these as model systems, potential of nanoscale for improving reversibility at low temperatures will be scrutinized.

- Continue developing first principles calculations of clusters to model effects of nanostructuring on the properties of mixed complex hydrides.

#### **Publications of DOE sponsored research (2010-2012)**

1. O. Dolotko, J.W. Wiench, K.W. Dennis, V.K. Pecharsky, and V.P. Balema, "Mechanically Induced Reactions in Organic Solids: Liquid Eutectics or Solid-state Processes?" *New. J. Chem.* **34**, 25 (2010).
2. O. Dolotko, N. Paulson, and V.K. Pecharsky, "Thermochemical Transformations in  $2\text{MNH}_2\text{-}3\text{MgH}_2$  Systems (M = Li or Na)," *Int. J. Hydrogen Energy* **35**, 4562 (2010).
3. O. Dolotko, H. Zhang, S. Li, P. Jena, and V.K. Pecharsky, "Mechanochemically Driven Nonequilibrium Processes in  $\text{MNH}_2\text{-CaH}_2$  Systems (M = Li or Na)," *J. Alloys Compds.* **506**, 224 (2010).
4. O. Dolotko, T. Kobayashi, J.W. Wiench, M. Pruski, V. Pecharsky, "Investigation of the Thermochemical Transformations in the  $\text{LiAlH}_4\text{-LiNH}_2$  System," *Int. J. Hydrogen Energy*, **36**, 10626 (2011).
5. T.L. Tan, L.L. Wang, D.D. Johnson and K.W. Bai, "A Comprehensive Search for Stable Pt-Pd Nanoalloy Configurations and Their Use as Tunable Catalysts," *Nano Lett.* **12**, 4875 (2012).
6. N.K. Singh, T. Kobayashi, O. Dolotko, J.W. Wiench, M. Pruski and V.K. Pecharsky, "Mechanochemical Transformations in  $\text{NaNH}_2\text{-MgH}_2$  Mixtures," *J. Alloys Compds.* **513**, 324 (2012).
7. L.L. Wang and D.D. Johnson, "Hydrogen Desorption from Ti-Doped  $\text{MgH}_2(110)$  Surfaces: Catalytic Effect on Reaction Pathways and Kinetic Barriers," *J. Phys. Chem. C*, **116**, 7874 (2012).
8. T. Kobayashi, I.Z. Hlova, N.K. Singh, V.K. Pecharsky and M. Pruski, "Solid-State NMR Study of Li-Assisted Dehydrogenation of Ammonia Borane," *Inorg. Chem.* **51**, 4108 (2012)
9. J. M. Reich, L.L. Wang and D.D. Johnson, "Surface and Particle-Size Effects on Hydrogen Desorption from Catalyst-Doped  $\text{MgH}_2$ ," *J. Phys. Chem. C*, **116**, 20315 (2012)
10. S. Gupta, I.Z. Hlova, T. Kobayashi, R.V. Denys, F. Chen, I.Y. Zavaliiy, M. Pruski and V.K. Pecharsky, "Facile Synthesis and Regeneration of  $\text{Mg}(\text{BH}_4)_2$  by High Energy Reactive Ball Milling of  $\text{MgB}_2$ ," *Chem. Comm.* **49**, 828 (2013).

## Extraordinary Responsive Magnetic Rare Earth Materials

V.K. Pecharsky (presenting, vitkp@ameslab.gov), K.A. Gschneidner, Jr., G.J. Miller, and L.S. Chumbley  
Ames Laboratory, Iowa State University, Ames, IA 50011-3020

### Program scope

The overarching objective of this program is to *understand and manipulate* the responsiveness of materials that are sufficiently complex to facilitate control at length scales ranging from electronic interaction distances to atomic, nano- and microstructural scales; yet, remain simple enough to *develop predictive modeling tools*. Rare earth materials provide a unique and fertile resource by allowing for a subtle yet precise control of crystallography, electronic structure, and magnetic properties of a compound. Knowledge of the mechanisms of phase changes driven by a minor stimulus, followed by a major perturbation of properties, is of interest for understanding nonlinear relationships in the free energy and is *crucial for guiding the discovery of advanced energy materials*. It is the latter that is the focus of this research, building upon state-of-the-art synthesis, processing and characterization, and integrating with theory, modeling, and computations gauged and refined against reliable experimental data.

Our systematic research of the  $R_5(\text{Si}_x\text{Ge}_{1-x})_4$  and  $R_{1-x}\text{R}'_x\text{Al}_2$  systems brought to light a host of new phenomena. Combined with recent discoveries of other responsive systems, i.e.,  $\text{RCO}_2$ ,  $\text{RMn}_2$ , and  $\text{La}(\text{Fe}_{1-x}\text{Si}_x)_{13}$ , this leaves no doubt that multi-component rare earth intermetallic systems have the potential to become a remarkable source of the next generation magnetic materials, thus addressing many of the grand challenges in modern magnetism. To this end, we are pursuing the underlying basic science to achieve the precise control of intrinsic magnetism and magnetoelastic coupling, and, therefore, the materials' sensitivity to both strong (temperature,  $T$ , and pressure,  $P$ ) and weak (magnetic field,  $H$ ) stimuli by using electronic, atomistic, and microscopic tools. Development and validation of phenomenological models of transformations that range from magneto-volume to magnetic-martensitic is another goal. This will be attained through interdisciplinary basic research, seeking novel pathways to control the magnetic coupling between lanthanide and other magnetic and non-magnetic ions, and opening up new fields of study of the magnetic behaviors of rare earth-based intermetallics.

### Recent progress

All  $R_5\text{T}_4$  compounds are self-assembled multi-layers formed by subnanometer-thick, remarkably robust two-dimensional slabs. Their stacking (that leads to three distinct crystal structures known as OI, OII, and M) can be controlled by chemistry,  $T$ ,  $P$ , and/or  $H$ , thus defining their most interesting and unique physics. Regardless of  $x$ , the ground state of the  $\text{Gd}_5\text{Si}_x\text{Ge}_{4-x}$  system is OI-FM (ferromagnetic), i.e., it appears to be structurally and magnetically homogeneous over the whole range of concentrations, unlike the paramagnetic (PM) state, which has three structurally distinct single phase regions. From what little we know about the microscopic magnetism of Ge-rich compounds, the OI-FM state may not be completely uniform, since the easy magnetization axis is temperature-dependent, and changes from the  $a$ -axis for  $x = 1.7 - 2$ , to  $b$ -axis when  $x = 0$ . Furthermore, our recent neutron scattering study of  $\text{Gd}_5\text{Si}_x\text{Ge}_{4-x}$  alloys with  $0 \leq x \leq 0.9$  indicates no sign of long-range FM order below the OI  $\rightarrow$  OI structural transformation in zero magnetic field. It appears that an external magnetic field is required to establish long-range FM order, which may have been disrupted by disorder due to the massive displacive OII  $\rightarrow$  OI transformation.

Partial replacement of one lanthanide (R) with another (R') in  $R_{1-x}\text{R}'_x\text{Al}_2$  causes the evolution of unusual magnetic phenomena with  $x$  (spin reorientations that may be coupled to crystallographic transformations), as represented by first order peaks in the zero magnetic field heat capacities of the alloys below  $T_C$ . This occurs for certain critical concentrations of R' centered about  $x = 0.25$ . This behavior is a result of the competition between the exchange interactions, and magnetoelastic and quadrupolar effects due to the modification of the electronic structure by doping. Changes in the magnetic structures of the  $R_{1-x}\text{R}'_x\text{Al}_2$  systems are mainly caused by the  $4f$  charge densities of R being different from R' (i.e., prolate vs. oblate

spheroids that have different signs of the second order Steven's factor). The anomalies are observed when the solvent (R, e.g., Er) has a lower de Gennes factor than the solute (R', e.g., Dy). As  $x$  falls either below or above the critical concentration of  $x = 0.25$ , the additional heat capacity peaks in  $R_{1-x}R'_xAl_2$  vanish. The observed behavior strongly suggests that the Steven's coefficients may and should be used as a tool to predict magnetic reordering transitions in pseudo binary  $R_{1-x}R'_xAl_2$  alloys, and potentially, in other mixed lanthanide materials. Additional phenomena can be expected when heavy lanthanide (R) is combined with light lanthanide (R') because the  $4f$  orbital and spin moments are parallel in the former and antiparallel in the latter.

Recently, we showed that complexity is indeed the key towards achieving an unprecedented precision in manipulating magnetic behavior of an intermetallic compound. Thus,  $Gd_5Ge_4$  has three independent Gd sites. Theory predicts that loss of ferromagnetism is expected when magnetic Gd is replaced by nonmagnetic Y, La, or Lu in only one specific site inside a slab, while replacement of the other two crystallographically-independent Gd atoms has a less significant effect on the magnetism of the compound. This demonstrates that ferromagnetism in this alloy is uniquely associated with the Gd atoms inside the slabs, which, in the OI structure, interact with one another via the strong covalent-like -Gd-Ge-Ge-Gd- bonds *both within and between the slabs*. A unique crystallography of  $R_5T_4$  systems leads to a clear preference for the larger (e.g., La) and smaller (e.g., Lu) lanthanide atoms, as has been shown for mixed valence  $Yb_5T_4$  which has both large  $Yb^{2+}$  and small  $Yb^{3+}$  ions; hence, these theoretically-predicted substitutions have been realized experimentally. The smaller Lu selectively replaces Gd inside the slabs and suppresses ferromagnetism, even when added at impurity level concentrations in  $(Gd_{0.95}Lu_{0.05})_5Ge_4$ . On the other hand, equivalent substitutions of larger La for Gd only occur in the other two sites between the slabs. The result is that the magnetism of  $(Gd_{0.95}La_{0.05})_5Ge_4$  compared to pure  $Gd_5Ge_4$  is unchanged

Structural flexibility observed in the  $R_5T_4$  model system is based on the systematic changes of the electronic structure, as has been shown by first principles calculations. Four possible layered structures have been predicted for  $Gd_5Ge_4$ :  $Gd_5Si_4$ -type,  $Pu_5Rh_4$ -type,  $Sm_5Ge_4$ -type, and  $Tm_5Sb_2Si_2$ -type. One of the intermediate ( $Pu_5Rh_4$ -type) and one of the terminal ( $Tm_5Si_2Sb_2$  - type) structures are only stable when some of the Si or Ge atoms are replaced with trivalent Ga and pentavalent Sb, respectively. Here, both the size and valence electron concentration effects play a role in their stability. Theory predicts that three of the four structures have the FM ground state and only one has an antiferromagnetic (AFM) ground state. All of these theoretical conclusions are in good agreement with experiment.

Electronic structure calculations show that gain in the exchange energy due to the M-type to OI-type structural transformations in  $R_5Si_{4-x}Ge_x$  compounds decreases gradually, as R changes from Gd to Tb, Dy, and Ho. As a result, the structural transition in  $Gd_5Si_xGe_{4-x}$  is fully coupled with FM-PM ordering-disordering and is nearly complete.  $Tb_5Si_{4-x}Ge_x$  and  $Dy_5Si_{4-x}Ge_x$  compounds exhibit some decoupling between the crystallographic and magnetic transformations, and the structural transition becomes progressively less complete (~80 % completion for R = Tb, but only ~50% completion for Dy). Finally, in  $Ho_5Si_{3.5}Ge_{0.5}$ , as a result of low gain in the magnetic contribution to the total energy, there is no structural transition.

### Future plans

One of the keys to controlling physical behaviors is knowledge of the crystallography of the material along with an accurate analysis of interatomic interactions. The latter step is a challenging problem in metals. Yet, we believe meaningful results can be achieved *via* a coordinated theoretical and experimental effort. For example, consider the  $Gd_5(Si_xGe_{1-x})_4$  system. As Ge is replaced by Si, the magnetic and structural behaviors change substantially, which, in the first approximation, can be attributed to chemical pressure that enhances the ferromagnetism. However, since Ge and Si atoms carry no magnetic moment, an understanding of the magnetism of  $Gd_5(Ge_{1-x}Si_x)_4$  requires careful consideration of the behavior of the rare earth atoms carrying a magnetic moment. The complexity of this and other materials under study, and therefore, the potential sensitivity of their frameworks to the nature of the substituting atoms, opens a

pathway to an unprecedented precision in selective replacements of magnetically-active lanthanide atoms. Dilution effects may be avoided or minimized by low concentrations of substituents, thus experimentally clarifying the role that different sites play in defining the magnetism of these and other complex systems.

Thermodynamic feasibility of preferential substitutions will be established from the site preference energies computed *ab initio* from total energies. While selectivity of substitutions can be predicted, the question is: What, if any, would be the effect of such selective substitutions on magnetism? For example, in  $\text{Gd}_5\text{Ge}_4$ , each Gd atom has a  $4f$  moment totaling  $7 \mu_B$  that polarizes the conduction electrons through indirect Ruderman-Kittel-Kasuya-Yosida (RKKY) interactions. The magnetic moments of the conduction electrons (mainly  $5d$ ) of the three inequivalent Gd sites are different. RKKY interactions cause exchange splitting in the majority and minority spin bands of conduction electrons leading to site-specific  $5d$  magnetic moments. Lanthanides other than Gd exhibit crystal field splitting in addition to exchange splitting, affecting both the  $5d$  and the total  $4f$  moments differently for sites with different local environments. To date, we showed how to selectively suppress FM (and enhance AFM) states in a Gd-based compound. The issues in focus next are how to enhance FM in  $\text{R}_5\text{T}_4$ , and how to generalize our findings for other rare earth systems. Building on this example, we will concentrate on five model systems:  $\text{R}_5\text{T}_4$ ,  $\text{RAl}_2$ ,  $\text{RMn}_2$ ,  $\text{RCO}_2$ , and  $\text{La}(\text{Fe}_x\text{Si}_{1-x})_{13}$  families.

Observed differences in the spin reorientation behavior of  $\text{RAl}_2$  and  $(\text{R}_{1-x}\text{R}'_x)\text{Al}_2$  should be related to substantial variations of the exchange and crystal field splitting near the Fermi level. Our preliminary experiments indicate extremely high Schottky specific heat, show unexpected structural distortion in the ferromagnetic  $\text{PrAl}_2$ , and confirmed the Kondo effect in  $\text{CeAl}_2$ . These behaviors are dependent upon the applied magnetic field and are related to the crystal field splitting. On the other hand, pseudobinary mixed heavy rare earth dialuminides,  $(\text{R}_{1-x}\text{R}'_x)\text{Al}_2$ , exhibit an additional degree of complexity, since the quadrupolar moment may change as a function of composition, thus leading to the change of the sign of the anisotropy constant. In addition to the indirect  $4f$ - $4f$  exchange, itinerant electron magnetism and spin fluctuations play important roles in other Laves phases, i.e.,  $\text{RMn}_2$  and  $\text{RCO}_2$ . Understanding the hybridization between the  $3d$  and  $5d$  bands should help clarify interactions between Mn (Co) and R, and provide further insights on the nature of metamagnetic transitions observed in many of these and, potentially, other intermetallic compounds with lower symmetry and more complex magnetic behaviors.

Interactions critical for either inducing or suppressing the magnetism of layers, blocks, and clusters of atoms identifiable in all of these systems will be carefully analyzed. The thermodynamic feasibility of chemical replacements by magnetic and non-magnetic lanthanides, alkali-earth metals, main group elements, and transition metals with a broad range of both local and itinerant magnetic moments at the corresponding sites will be established. The role of different sites in determining magnetism, phase stability, and a potential for emergence or suppression of coupled phenomena will be analyzed using first-principles theory. Theoretical predictions will be validated experimentally and appropriate refinements of the modeling tools will be made.

The magnetism of physically or chemically heterogeneous nanoscale systems may be described by clusters, where the magnetism of a system depends both on the intrinsic properties of individual clusters and on their interactions. The former is determined by the structure of clusters, but the latter may be quite complex, since it depends on inter-cluster distances, the symmetry of their arrangements, and the nature of the space between the clusters. We believe our model systems are uniquely suited to better understand both contributions, and, therefore, achieve a more complete control over the coupling of the magnetic and crystal lattices in intermetallic compounds. Macroscopically, FM clustering may be enhanced (and controlled) by formation of a peculiar microstructure, as has been shown in a single crystalline  $\text{Gd}_5\text{Si}_2\text{Ge}_2$ . As follows from our recent work, platelet concentration in  $\text{R}_5\text{T}_4$  may be controlled, and, therefore, their role in bringing about the so-called Griffiths phase-like behavior may be better understood by varying processing conditions. Microstructure of the other model systems will be studied to establish its significance in affecting high temperature FM clustering. A systematic study of the role microstructure plays in defining correlation lengths will be initiated.

Of particular interest is our recent discovery that crystallography, and, therefore, magnetism of at least some of the  $R_5T_4$  alloys may be controlled by simple mechanical grinding. Thus, extended grinding of  $Er_5Si_4$  in a mortar with a pestle causes the transformation from the low-volume OI to the high-volume M structure. In this case,  $Er_5Si_4$  behaves as a metamaterial, increasing its volume under external pressure and shear. This behavior becomes even more intriguing in light of the fact that  $Er_5Si_4$  is extremely sensitive to hydrostatic pressure, which expectedly promotes the high volume M to low volume O(I) structural transition. Preliminary experiments indicate that magnetic properties of some other  $R_5T_4$  materials, i.e.,  $(Gd_{0.95}Sc_{0.05})_5Ge_4$ , may change upon grinding. This and other kinds of more energetic mechanical processing, e.g., in a ball mill, affect microstructure of materials. The latter will be examined in detail and correlated with the observed changes in magneto-structural behaviors.

**Publications of DOE sponsored research (67 total in FY2010-2012, only FY2012 publications are listed below)**

1. M. Khan, Ya. Mudryk, K.A. Gschneidner, Jr., and V.K. Pecharsky, "Magnetism of  $Ho_{1-x}Tb_xAl_2$  alloys: Critical dependence of a first order phase transition on Tb concentration," *Phys. Rev. B* **84**, 214437 (2011).
2. M. Khan, K.A. Gschneidner, Jr., and V.K. Pecharsky, "Spin reorientation transition in  $Ho_{1-x}Dy_xAl_2$  alloys," *J. Appl. Phys.* **110**, 103912 (2011)
3. Y. Mudryk, V.K. Pecharsky, and K.A. Gschneidner, Jr., "Extraordinary responsive intermetallic compounds: The  $R_5T_4$  family (R=rare earth, T-group 13-15 elements)," *Z. Anorg. Allg. Chem.* **637**, 1948-1956 (2011).
4. M. Khan, D.L. Schlagel, T.A. Lograsso, K.A. Gschneidner, Jr., and V.K. Pecharsky, "Magnetic and thermal properties of  $Er_{75}Dy_{25}$  single crystals," *Phys. Rev. B* **84**, 134424 (2011).
5. Y. Mudryk, N. K. Singh, V. K. Pecharsky, D. L. Schlagel, T. A. Lograsso, and K. A. Gschneidner, Jr., "Magnetic and structural properties of single-crystalline  $Er_5Si_4$ ," *Phys. Rev. B* **85**, 094432 (2012).
6. K. A. Gschneidner, Jr., Y. Mudryk, and V. K. Pecharsky, "On the nature of the magnetocaloric effect of the first-order magnetostructural transition," *Scr. Mater.* **67**, 572-577 (2012).
7. Y. Mudryk, D. Paudyal, V. K. Pecharsky, and K. A. Gschneidner, Jr., "Low-temperature crystal structure and magnetic properties of  $Gd_5Ge_3$ ," *Phys. Rev. B* **85**, 014116 (2012).
8. S. Yuce, M. Barrio, B. Emre, E. Stern-Taulats, A. Planes, J. L. Tamarit, Y. Mudryk, K. A. Gschneidner, Jr., V. K. Pecharsky, and L. Manosa, "Barocaloric effect in the magnetocaloric prototype  $Gd_5Si_2Ge_2$ ," *Appl. Phys. Lett.* **101**, 071906 (2012).
9. M. Khan, K. A. Gschneidner, Jr., and V. K. Pecharsky, "The effect of Er doping on the spin reorientation transition in  $Ho_{1-x}Er_xAl_2$ ," *J. Magn. Magn. Mater.* **324**, 1381-1384
10. S. Velez, J. M. Hernandez, A. Garcia-Santiago, J. Tejada, V. K. Pecharsky, K. A. Gschneidner, Jr., D. L. Schlagel, T. A. Lograsso, and P. V. Santos, "Anisotropic magnetic deflagration in single crystals of  $Gd_5Ge_4$ ," *Phys. Rev. B* **85**, 054432 (2012).
11. D. H. Ryan, N. R. Lee-Hone, J. M. Cadogan, K. Ahn, V. K. Pecharsky, and K. A. Gschneidner, Jr., "Doping-induced valence change in  $Yb_5Ge_{4-x}(Sb, Ga)_x$  : ( $x \leq 1$ )," *Hyperfine Inter.* **208**, 59-63 (2012).
12. A. Provino, Y. Mudryk, D. Paudyal, V. Smetana, P. Manfrinetti, V. K. Pecharsky, K. A. Gschneidner, Jr., and J. D. Corbett, "Crystal structure of  $Tb_5Ni_2In_4$  and  $Y_5Ni_2In_4$ , and magnetic properties of  $Dy_5Ni_2In_4$ ," *J. Appl. Phys.* **111**, 07e122 (2012).
13. N. Marcano, P. A. Algarabel, J. R. Fernandez, C. Magen, L. Morellon, N. K. Singh, D. L. Schlagel, K. A. Gschneidner, Jr., V. K. Pecharsky, and M. R. Ibarra, "Magnetism and magnetocaloric effect of single crystal  $Er_5Si_4$  under pressure," *Phys. Rev. B* **85**, 024408 (2012).
14. C. M. Bonilla, I. Calvo, J. Herrero-Albillos, A. I. Figueroa, C. Castan-Guerrero, J. Bartolome, J. A. Rodriguez-Velamazán, D. Schmitz, E. Weschke, D. Paudyal, V. K. Pecharsky, K. A. Gschneidner, Jr., F. Bartolome, and L. M. Garcia, "New magnetic configuration in paramagnetic phase of  $HoCo_2$ ," *J. Appl. Phys.* **111**, 07e315 (2012).

# High Performance Bulk Thermoelectric Materials

(DE-FG02-00ER45805)

PI: Zhifeng Ren

617 Science & Research Building 1, Department of Physics and TcSUH, University of Houston, Houston, Texas 77204-5005

[zren@uh.edu](mailto:zren@uh.edu)

**Program Scope:** solid-state thermoelectric energy conversion is a promising technology to convert waste heat into electricity, leading to significant energy savings and reduced environmental impact.

We have built up a strong foundation on which enhancing thermoelectric property is possible in a number of materials by using ball milling and hot pressing process to achieve nanocomposite with small grain size. The work involves enhancement of thermoelectric figure-of-merit (ZT) of the existing traditional good thermoelectric materials and potential new materials, which has resulted in publishing fifteen peer-reviewed papers [2-16] and one manuscript submitted for publication [1].

In addition to research, we have provided educational opportunities to five students who have graduated with PhDs, three PhD candidates who are still working on the project, six undergraduate students, one postdoc, and one visiting professor.

**Recent Progress:** during the last a couple of years, we have focused on studying the thermoelectric properties of p-type half-Heuslers  $\text{Hf}_{1-x}\text{Ti}_x\text{CoSb}_{0.8}\text{Sn}_{0.2}$  and  $\text{Hf}_{1-x-y}\text{Ti}_x\text{Zr}_y\text{CoSb}_{0.8}\text{Sn}_{0.2}$  based on our earlier work on  $\text{Hf}_{1-x}\text{Zr}_x\text{CoSb}_{0.8}\text{Sn}_{0.2}$  by exploring larger atomic size and mass differences to improve the thermoelectric figure-of-merit and also reducing the usage of the very expensive element Hf (Hf is at least 10 times more expensive than any other element used in half-Heusler compounds).

In 2011, we successfully enhanced ZT from 0.5 to 0.8 in p-type half-Heusler  $\text{Hf}_{0.5}\text{Zr}_{0.5}\text{CoSb}_{0.8}\text{Sn}_{0.2}$  by making grains smaller than 200 nm. The essence was to make the thermal conductivity lower due to stronger phonon scattering by increased grain boundaries while

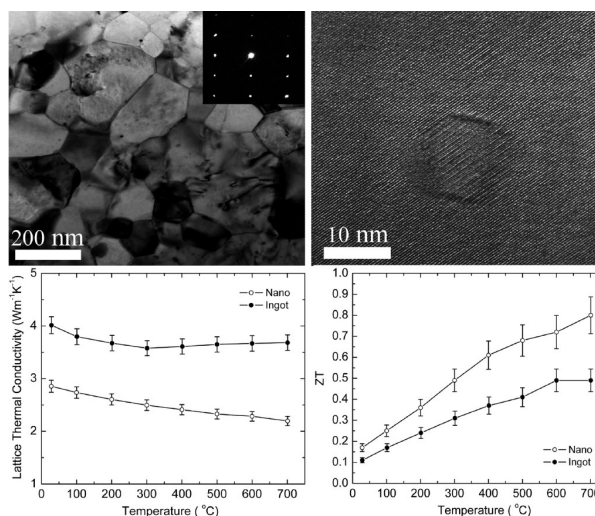


Fig. 1. (Top) TEM images showing the grain size (left) and nanoinclusion (right), and (bottom) lattice thermal conductivity (left) and ZT (right) dependence of temperature [8].

keeping the power factor unchanged, shown in Fig. 1.

Right after that we realized that larger atomic size and mass differences may produce stronger phonon scattering for even lower thermal conductivity. Therefore we studied the effect of combination of Hf and Ti on the thermoelectric properties in  $\text{Hf}_{1-x}\text{Ti}_x\text{CoSb}_{0.8}\text{Sn}_{0.2}$ . We found that 1) lower thermal conductivity was indeed achieved when a larger difference on atomic size and mass of Hf and Ti than Hf and Zr are used showing in Fig. 2 (left), and 2) higher ZT ( $\sim 1.0$ ) was indeed obtained with lower thermal conductivity, shown in Fig. 2 (right). However, the system involving Hf and Ti uses more Hf, which caused a significant increase in the cost of the material.

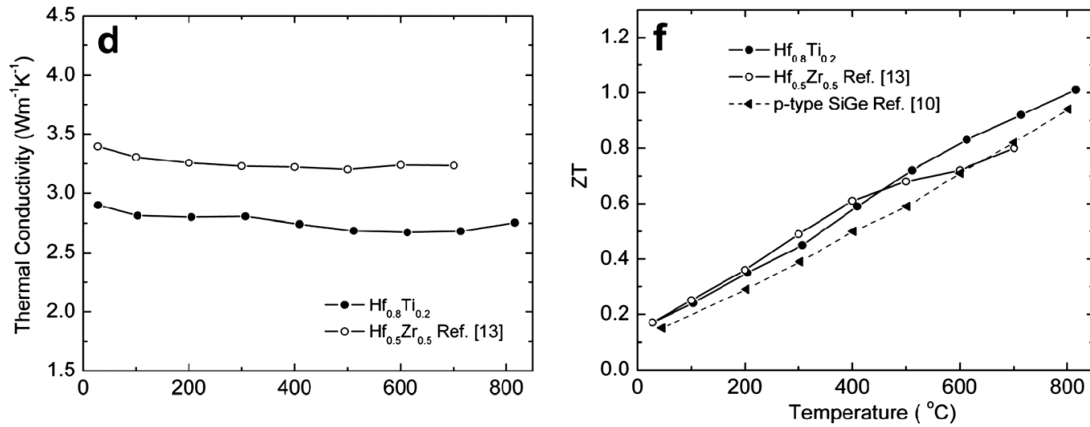


Fig. 2. (left) comparison of thermal conductivity of  $\text{Hf}_{0.8}\text{Ti}_{0.2}\text{CoSb}_{0.8}\text{Sn}_{0.2}$  with  $\text{Hf}_{0.5}\text{Zr}_{0.5}\text{CoSb}_{0.8}\text{Sn}_{0.2}$ , and (right) ZT dependence of  $\text{Hf}_{0.8}\text{Ti}_{0.2}\text{CoSb}_{0.8}\text{Sn}_{0.2}$  and  $\text{Hf}_{0.5}\text{Zr}_{0.5}\text{CoSb}_{0.8}\text{Sn}_{0.2}$  in comparison with SiGe alloy, which clearly shows the lower thermal conductivity because of the larger atomic size and mass differences, and higher ZT above 500 C [2].

In consideration of keeping the material cost low, we studied the effect of Ti on thermoelectric properties in  $(\text{Hf}_{0.5}\text{Zr}_{0.5})_{1-x}\text{Ti}_x\text{CoSb}_{0.8}\text{Sn}_{0.2}$ . We found that by adding only a very minor amount of Ti (0.12 per formula), a peak ZT of  $\sim 1$  was obtained in  $\text{Hf}_{0.44}\text{Zr}_{0.44}\text{Ti}_{0.12}\text{CoSb}_{0.8}\text{Sn}_{0.2}$  that has much less Hf than  $\text{Hf}_{0.8}\text{Ti}_{0.2}\text{CoSb}_{0.8}\text{Sn}_{0.2}$ , shown in Fig. 3, which is a big step towards studying the possible application of this material for waste heat recovery in vehicles and other industrial sites.

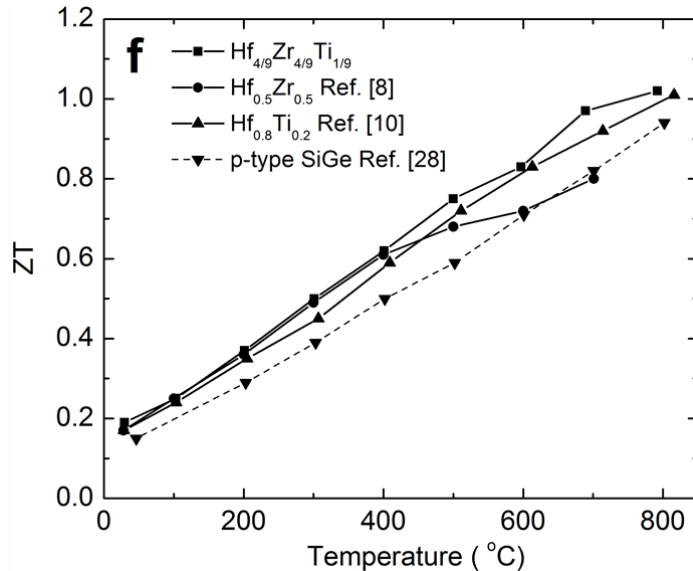


Fig. 3. ZT dependence of temperature of different materials to show the advantage of  $\text{Hf}_{0.44}\text{Zr}_{0.44}\text{Ti}_{0.12}\text{CoSb}_{0.8}\text{Sn}_{0.2}$  [1].

**Future Plans:** built on the progress we have achieved recently, we will focus our effort on further reducing the grain size to reduce the thermal conductivity. If we could reduce the grain size to below 50 nm, we may have a chance to achieve 30-50% reduction on thermal conductivity. We will study some very stable high temperature oxides as potential grain growth inhibitors to prevent grain growth during the hot pressing process.

**Publications appeared in 2010-2012 under the DOE sponsorship:**

1. Xiao Yan, Weishu Liu, Shuo Chen, Hui Wang, Qian Zhang, Hengzhi Wang, Dezhi Wang, Gang Chen, and Zhifeng Ren, "Thermoelectric property study of nanostructured p-type half-Heuslers  $\text{Hf}_{0.44}\text{Zr}_{0.44}\text{Ti}_{0.12}\text{CoSb}_{0.8}\text{Sn}_{0.2}$ ", *Advanced Energy Materials* (submitted).
2. Xiao Yan, Weishu Liu, Hui Wang, Shuo Chen, Junichiro Shiomi, Keivan Esfarjani, Hengzhi Wang, Dezhi Wang, Gang Chen, and Zhifeng Ren, "Stronger phonon scattering by larger differences in atomic mass and size in p-type half-Heuslers  $\text{Hf}_{1-x}\text{Ti}_x\text{CoSb}_{0.8}\text{Sn}_{0.2}$ ", *Energy and Environmental Science* **5**, 7543-7548 (2012).
3. Piotr Patoka, Tianyi Sun, Michael Giersig, Zhifeng Ren, and Krzysztof Kempa, "Nanoribbon Plasmonic Gratings and their Anomalous Interaction with Electromagnetic Waves", *Adv. Mater.* **24**, 3042-3045 (2012).
4. Yumin Ye, Yu Mao, Hengzhi Wang, and Zhifeng Ren, "Hybrid structure of pH-responsive hydrogel and carbon nanotube array with superwettability", *J. Mater. Chem.* **22**, 2449-2455 (2012).
5. Delaire, M. B. Stone, J. Ma, A. Huq, D. Gout, C. Brown, K. F. Wang, and Z. F. Ren, "Anharmonic phonons and magnons in  $\text{BiFeO}_3$ ", *Phys. Rev. B* **85**, 064405 (2012).
6. Yang Wang, Tianyi Sun, Trilochan Paudel, Yi Zhang, Zhifeng Ren, and Krzysztof Kempa, "Metamaterial-Plasmonic Absorber Structure for High Efficiency Amorphous Silicon Solar Cells", *NanoLetters* **12**, 440 - 445 (2012).
7. Feng-Jia Fan, Bo Yu, Yi-Xiu Wang, Yan-Long Zhu, Xiao-Jing Liu, Shu-Hong Yu, and Zhifeng Ren, "Colloidal Synthesis of  $\text{Cu}_2\text{CdSnSe}_4$  Nanocrystals and Hot-Pressing to Enhance the Thermoelectric Figure-of-Merit", *JACS* **133**, 15910-15913 (2011).
8. X. Yan, G. Joshi, W. S. Liu, Y. C. Lan, H. Wang, S. Lee, J. W. Simonson, S. J. Poon, T. M. Tritt, G. Chen, and Z. F. Ren, "Enhanced Thermoelectric Figure-of-Merit of p-Type Half-Heuslers", *NanoLetters* **11**, 556 - 560 (2011).
9. G. H. Zhu, Y. C. Lan, H. Wang, G. Joshi, Q. Hao, G. Chen, and Z. F. Ren, "Effect of selenium deficiency on the thermoelectric properties of n-type  $\text{In}_4\text{Se}_{3-x}$  compounds", *Phys. Rev. B* **83**, 115201 (2011).
10. Yucheng Lan, Yang Wang, and Zhifeng Ren, "Physics and Applications of Aligned Carbon Nanotubes", *Advances in Physics* **60**, 553 - 678 (2011).
11. J. M. Bao, I. Shalish, Z. H. Su, R. Gurwitz, F. Capasso, X. W. Wang, and Z. F. Ren, "Photoinduced oxygen release and persistent photoconductivity in ZnO nanowires", *Nanoscale Research Letters* **6**, 404 (2011).
12. T. Paudel, J. Rybczynski, Y. T. Gao, Y. C. Lan, Y. Peng, K. Kempa, M. J. Naughton, and Z. F. Ren, "Nanocoax solar cells based on aligned multiwalled carbon nanotube arrays", *Phys. Status Solidi A* **208**, 924 - 927 (2011).
13. Chetan Dhital, Clarina de la Cruz, C. Opeil, A. Treat, K. F. Wang, J.-M. Liu, Z. F. Ren, and Stephen D. Wilson, "Neutron scattering study of magnetic phase separation in nanocrystalline  $\text{La}_{5/8}\text{Ca}_{3/8}\text{MnO}_3$ ", *Phys. Rev. B* **84**, 144401 (2011).
14. Q. Hao, G. H. Zhu, G. Joshi, X. W. Wang, A. Minnich, Z. F. Ren, and G. Chen, "Theoretical studies on the thermoelectric figure of merit of nanograined bulk silicon", *Appl. Phys. Lett.* **97**, 063109 (2010).
15. Y. Peng, T. Paudel, W. C. Chen, W. J. Padilla, Z. F. Ren, and K. Kempa, "Percolation and polaritonic effects in periodic planar nanostructures evolving from holes to islands", *Appl. Phys. Lett.* **97**, 041901 (2010).
16. Y. C. Lan, A. J. Minnich, G. Chen, and Z. F. Ren, "Thermoelectric Figure-of-Merit Enhancement Using A Nanocomposite Approach", *Adv. Func. Mater.* **20**, 357 - 376 (2010).

## Nanostructured Materials for Thermoelectric Energy Conversion

Principal Investigator:

**Rachel Segalman**

Faculty Scientist

201 Gilman Hall, Berkeley, CA, 94720

Voice: 510-642-7998

Fax: 510-642-4778

RASegalman@lbl.gov

Direct thermal to electrical energy conversion using solid-state thermoelectric devices is attractive, but implementation has been slow due to both relatively low efficiency and scale-up challenges presented by the current non-abundant, expensive materials choices. A challenge lies in the fact that the thermopower,  $S$ , electrical conductivity,  $\sigma$ , and thermal conductivity,  $k$ , are all interdependent making optimization extremely difficult. Recent research on nanostructured materials has led to sharp increases in  $ZT$  attributed to: (i) quantum confinement of carriers in nanostructured materials modifying the density of states near the Fermi level, which increases  $S^2\sigma$ ; (ii) nanostructuring enhancing phonon scattering in the mid to long wavelength range, which thereby reduces  $k$ ; or (iii) a combination of both. While these significant gains have been achieved by nanopatterning of existing (non-earth abundant, expensive materials), there is a significant need for the development of new materials and novel design strategies for thermal energy conversion. This group will explore the basic science of thermoelectricity through the understanding and design of transport phenomena in new nanostructured materials with a particular eye to abundant materials and scalable processing. We will proceed with four approaches: (i) molecular, hybrid and polymeric thermoelectrics; (ii) Si-based nanostructures; (iii) superlattices; and (iv) ionocalorics, each with an integral effort in the theoretical development and understanding of the underlying physics. Each of these unique materials systems is designed specifically to test or develop new foundational concepts in thermoelectric transport, and the insights from each system is crafted to inform design in other team efforts.

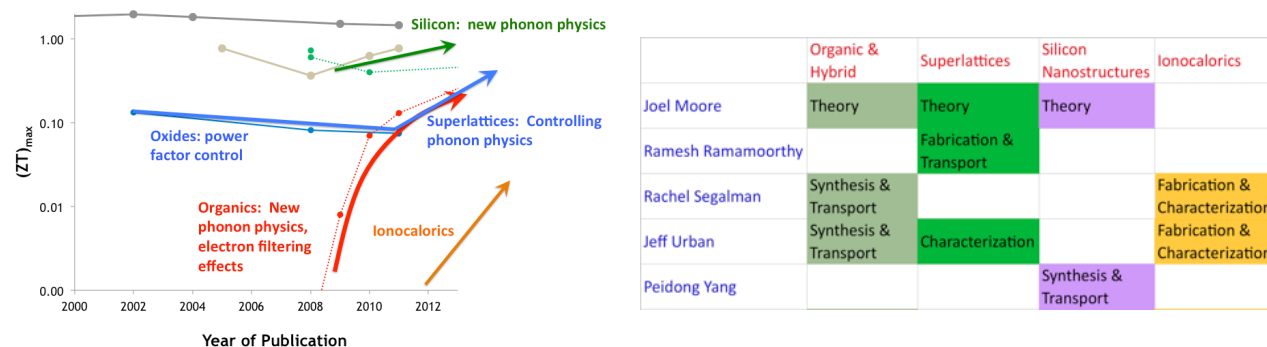


Figure 1: This interdisciplinary program is focused on the development of new materials with an eye towards scalability, manufacturability, and manifestation of new physical phenomenon.

### Approach 1: Molecular, Polymeric, and Organic-Inorganic Hybrid Thermoelectrics

Due to the band-like nature of carrier transport, the thermopower,  $S$ , and electrical conductivity,  $\sigma$ , in classical bulk inorganic thermoelectric materials exhibit opposing trends. The anti-correlation of  $S$  and  $\sigma$  in these materials means that the power factor  $S^2\sigma$  cannot be arbitrarily

increased. Our prior work with organic-inorganic thermoelectrics demonstrated that these fundamental rules do not apply to junctions with organic materials that possess discrete band structures, and elucidated paths for optimization that are not available in purely inorganic materials.<sup>[2,10]</sup> Results from our subsequent work with bulk organic-inorganic composites extended these insights from molecular junctions to the mesoscale, and strongly suggest that the properties of the inorganic-organic interface play a controlling role in the overall properties of the composite, leading to some of the highest performance hybrid thermoelectric materials reported.<sup>[6,17]</sup> Combined, these results naturally lead to the following fundamental questions: *i) What is the fundamental physics underlying the interfacial transport behavior in the hybrids? ii) Can we use our interface model to direct general design rules for organic-inorganic thermoelectrics?* Our ongoing work seeks to address these issues, by first developing simple model systems that allow us independent control over the interfacial bonding environment, interfacial morphology, and component energy levels. This future work will attack two aspects of this complex area: 1.) Testing our empirical design rules for hybrid materials to generate excellent n-type thermoelectrics and 2.) Using molecular design of both inorganic and polymeric components to craft tailored energy landscapes—elucidating how carrier transport occurs in hybrid materials.

A new effort approved for the program will study the effect of crystallinity and mesoscale structure on thermoelectric transport in purely polymeric systems. Here, we employ molecular scale design and self-assembly of polymers to explore the fundamental relationship between hierarchical structures (ranging from molecular to mesoscale) and thermoelectric performance of polymers. Semiconducting polymers and block copolymers will be used to control the structure of these materials at length scales ranging from  $\sim 1 \text{ \AA}$ –100 nm. Support from theory, will further enable fundamental, theoretical understanding of these systems.<sup>[4]</sup>

## **Approach 2: Si-based nanostructures**

Silicon is amongst the most abundant and inexpensive semiconductors, and an ideal scalable material. However, while a workhorse for microelectronics, silicon has not historically been considered for thermoelectric applications due to its large thermal conductivity (140 W/m-K at room temperature) which renders it an unlikely candidate for thermoelectrics. Our program has shown that nanostructures with roughness features close to and less than the phonon mean free path (10-100 nms in lateral width) could have a high thermoelectric figure of merit,  $ZT \sim 0.4$  to 1, but the physical mechanism underlying this roughness scattering has not been understood. In this project, we will continue to push the limits reducing the phonon component of the thermal conductivity by making nanostructures that have features of the order of the phonon wavelength.<sup>[8]</sup> Additionally, it is clear that in a highly harmonic crystal such as silicon, the possibilities for reducing the phonon contribution to the thermal conductivity do not end at incoherent scattering. Since the coherence of phonons can be preserved for relatively long distances in Si, correlated scattering of phonons could potentially reduce the thermal conductivity even further and push  $ZT$  far above 1. These new opportunities direct our future work, aimed at advanced fabrication methods for “holey” silicon nanostructures that will interact coherently with phonons in the wavelength regime spanning 1-10nm. Pairing with theory support in the program, we will fully explore the physics of controlled, coherent phonon scattering to drive the limits of reducing  $k$ .<sup>[9]</sup>

### Approach 3: Superlattices

The wavelength and mean free path of phonons in oxide systems are generally on the nanoscale, and thus, the inherently nanoscale structure of superlattices is an effective method to reduce the lattice contribution of thermal conductivity in these materials. With the exquisite control over feature sizes made possible by superlattice growth, we aim to achieve the first experimental demonstration of the crossover in phonon transport from an incoherent regime to a coherent regime.<sup>[3]</sup> This crossover in thermal transport is manifested by a minimum in thermal conductivity as a function of interface density. A realization of this thermal conductivity minimum in superlattices invites further investigations, such as exploring the role of acoustic impedance mismatch (AIM) between oxide materials, which provides an additional degree of freedom to tune the thermal conductivity and enhance the scattering of mid- to long wavelength phonons. Additionally, as a result of the low mobility of electrons in oxides, no significant degradation in electrical transport is anticipated as nanoscale structure is tuned, and hence, electron-doped oxides may lead to high thermoelectric figure of merit materials. These studies, paired with support from theory in the program, enable a path to quantum mechanically tuning  $k$  based on elementary physical considerations.

As an extension of the use of superlattice structures to access new material properties, we seek to use specific oxide superlattices to create an entirely new class of compound materials; *piezothermoelectrics* that can generate voltages from both primary thermal gradients (the thermoelectric effect) and also from thermally induced mechanical gradients (the piezoelectric effect). These compound piezothermoelectric materials will dramatically expand the types of thermal energy available for conversion.

### Approach 4: Ionocalorics

Taking stock of the progress made in thermoelectric science over the last two decades, it seems clear that new electron and phonon physics is needed to dramatically improve the performance of thermoelectric materials. It is worthwhile however to step back and ask: Are there other ways to achieve heating and cooling using charged particles? Here we propose a new approach—*ionocalorics*—that exploits the thermodynamics associated with ion condensation and expansion on a nanostructured dielectric surface for refrigeration and power generation. While the thermodynamic underpinnings have much in common with thermoelectrics, new mechanisms of manipulating correlations between entropy and temperature enable potentially larger power densities and application spaces to be accessed. In the ionocaloric approach, we wish to explore a new effect where an ionic solution is placed between two electrodes. In the absence of an electric field, the ions gain entropy producing a homogeneous state through diffusion. In the presence of an electric field, the ions are electrostatically attracted to the oppositely charged electrodes, which minimize the entropy of the ionic solution. We think this approach can provide the largest change in entropy of any known system. In this proposal, we will develop the theoretical framework of the ionocaloric effect, and establish relationships between the thermodynamic processes, such as changes in temperature and entropy, in terms of the properties of the fluid and the applied electric field. Once the theory and initial experiments on the ionocaloric effect bear results, we propose to utilize this effect in a novel device to demonstrate both refrigeration and power generation.

## Publications: 2010-2012

1. Scullin, M. L., Ravichandran, J., Yu, C., Huijben, M., Seidel, J., Majumdar, A., & Ramesh, R. *Journal of Materials Science* **58**, 457–463 (2010).
2. Malen, J. A., Yee, S. K., Majumdar, A., & Segalman, R. A. *Chemical Physics Letters* **491**, 109–122 (2010).
3. Ravichandran, J., Siemons, W., Heijmerikx, H., Huijben, M., Majumdar, A., & Ramesh, R. *Chemistry of Materials* **22**, 3983–3987 (2010).
4. Ghaemi, P., Mong, R., & Moore, J. *Physical Review Letters* **105**, 166603 (2010).
5. Bardarson, J., Brouwer, P., & Moore, J. *Physical Review Letters* **105**, 156803 (2010).
6. See, K. C., Feser, J. P., Chen, C. E., Majumdar, A., Urban, J. J., & Segalman, R. A. *Nano Letters* **10**, 4664–4667 (2010).
7. Ravichandran, J., Siemons, W., Oh, D. W., Kardel, J., Chari, A., Heijmerikx, H., Scullin, M., Majumdar, A., Ramesh, R., & Cahill, D. *Physical Review B* **82**, 165126 (2010).
8. Hippalgaonkar, K., Huang, B., Chen, R., Sawyer, K., Ercius, P., & Majumdar, A. *Nano Letters* **10**, 4341–4348 (2010).
9. Ravichandran, J., Siemons, W., Scullin, M. L., Mukerjee, S., Huijben, M., Moore, J. E., Majumdar, A., & Ramesh, R. *Physical Review B* **83**, 035101 (2011).
10. Yee, S. K., Malen, J. A., Majumdar, A., & Segalman, R. A. *Nano Letters* **11**, 4089–4094 (2011).
11. Ravichandran, J., Kardel, J. T., Scullin, M. L., Bahk, J. H., Heijmerikx, H., Bowers, J. E., & Majumdar, A. *Review of Scientific Instruments* **82**, 015108 (2011).
12. Oh, D. W., Ravichandran, J., Liang, C. W., Siemons, W., Jalan, B., Brooks, C. M., Huijben, M., Schlom, D. G., Stemmer, S., Martin, L. W., Majumdar, A., Ramesh, R., & Cahill, D. G. *Applied Physics Letters* **98**, 221904 (2011).
13. Lim, J., Hippalgaonkar, K., Andrews, S. C., Majumdar, A., & Yang, P. *Nano Letters* **12**, 2475–2482 (2012).
14. Tang, J., Wang, H.-T., Lee, D. H., Fardy, M., Huo, Z., Russell, T. P., & Yang, P. *Nano Letters* **10**, 4279–4283 (2012).
15. Dechaumphai, E., & Chen, R., *Journal of Applied Physics* **111**, 073508 (2012).
16. Yee, S. K., Coates, N. E., Majumdar, A., Urban, J. J., Segalman, R. *Physical Chemistry Chemical Physics* **11**, 4024–4032 (2013).
17. Coates, N. E., Yee, S. K., McCulloch, B., See, K., Majumdar, A., Segalman, R., Urban, J., *Advanced Materials*, (Accepted) (2013).

# Study of Materials and Interface Properties for High-Efficiency Spin Injection

Jing Shi

Department of Physics and Astronomy, University of California, Riverside

Jing.Shi@ucr.edu.

1. Program Scope: The program scope is to investigate the physical properties of materials and interfaces that are relevant to spintronics. Besides the high spin polarization half-metallic oxide films which was studied prior to this funding period, the research in this review period focuses on the growth and study of structural and magnetic properties of epitaxial ferrimagnetic insulator (FMI) films such as  $\text{Fe}_3\text{O}_4$  and  $\text{Y}_3\text{Fe}_5\text{O}_{12}$ . An important property of the FMI films is the magnetic proximity effect existing at the interface of the FMI film with another metallic, semi-metallic or semiconducting film. The magnetic proximity effect induced spin polarization is another way of generating spin polarization in non-magnetic materials. In addition, this research also studies both high and low spin-orbit coupling materials which are very useful for spintronics. The former includes topological insulators and the latter includes graphene and other carbon-based materials.

## 2. Recent Progress

- Epitaxial growth and physical property study of FMI films. We have successfully grown epitaxial  $\text{Fe}_3\text{O}_4$  on MgO and  $\text{Y}_3\text{Fe}_5\text{O}_{12}$  (YIG) films on gadolinium gallium garnet (GGG) substrates using laser molecular beam epitaxy. The former conducts at room temperature but the latter is a good insulator with the Curie

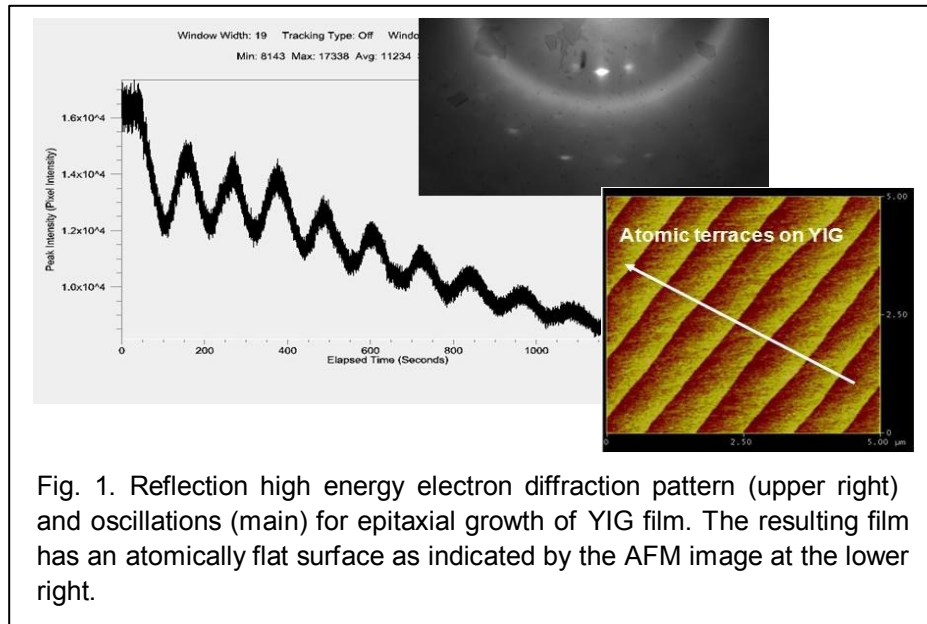


Fig. 1. Reflection high energy electron diffraction pattern (upper right) and oscillations (main) for epitaxial growth of YIG film. The resulting film has an atomically flat surface as indicated by the AFM image at the lower right.

temperature about 560 K. While  $\text{Fe}_3\text{O}_4$  is a good spin injector which has been shown to have high spin polarization, we focus YIG films for a different purpose: magnetic proximity effect

induced spin polarization. With the atomically flat surface, we grow thin metallic films on top. The first two films we have chosen are Pd and Pt, which are known to be at the verge of ferromagnetism due to large d-density of states. To ensure high quality, we have optimized the growth conditions so that the layer-by-layer mode is achieved in (110) orientation (Fig. 1). In (111) orientation, the window of parameters is much narrower, but we have also obtained epitaxy with atomically flat surface. The FMI films have strong in-plane anisotropy in both (110) and (111) orientations. The moment per formula unit is approximately  $5 \mu_B$  which agrees with the bulk value.

- Magnetic proximity effect and high-field effects in Pd/YIG and Pt/YIG. There has been a great deal of debate about the origin of a newly discovered effect in spintronics, i.e. the spin Seebeck effect (SSE) in FMI. It was shown that the magnetic proximity effect in the metal film

could contribute to the reported SSE. Pd and Pt both have strong spin-orbit coupling (Pt has stronger spin-orbit coupling than Pd), but both are prone to develop induced magnetization. We have deposited both Pd and Pt films on atomically flat YIG films using sputtering. At low in-plane magnetic fields, we have observed anisotropic magnetoresistance in both Pd and Pt films, a consequence of magnetic proximity effect (Fig. 2b). At high magnetic fields, there is still a much larger additional magnetoresistance effect and anomalous Hall effect

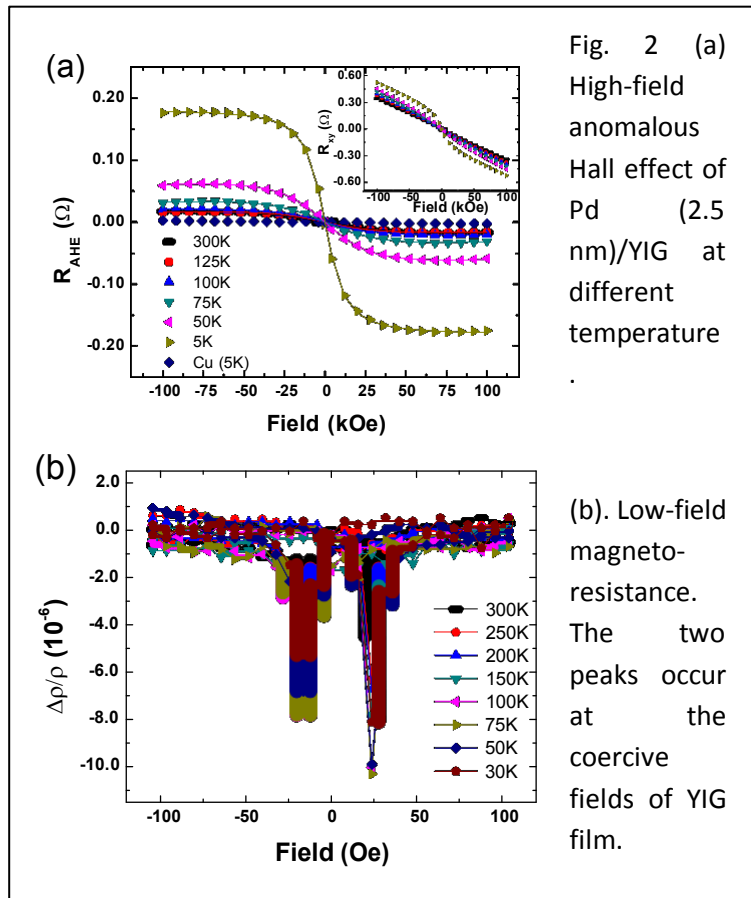


Fig. 2 (a) High-field anomalous Hall effect of Pd (2.5 nm)/YIG at different temperature

(b). Low-field magnetoresistance. The two peaks occur at the coercive fields of YIG film.

(Fig. 2a), both occurring at magnetic fields greater than the saturation field of YIG magnetization ( $<2,000$  Oe). The high-field effects (both magnetoresistance and anomalous Hall effect) cannot be possibly caused by the magnetic proximity effect. To study the physical origin of these high-field effects, we analyzed the field and temperature dependence of the anomalous Hall effect. The field dependence suggests that the anomalous Hall effect is likely

caused by independent magnetic moments that are aligned by an external magnetic field. By fitting the Brillouin function to the data, we have obtained the effective magnetic moment as a function of the temperature. The magnetic moment that is responsible for the field dependence is  $\sim 200 \mu_B$  at room temperature. We are still investigating the microscopic mechanism of these high-field effects.

- High-field transport properties of surface states in high-resistivity topological insulators. Topological insulators are potentially useful for spintronics applications due to the strong spin-orbit interaction which may enable the electric field control of the spins in the materials. We aim to demonstrate the unique transport properties of the surface

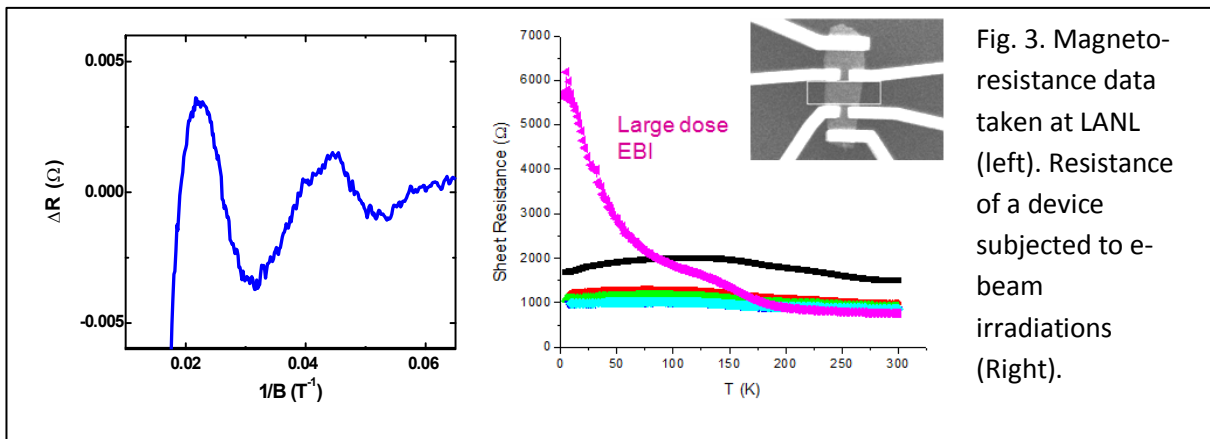


Fig. 3. Magneto-resistance data taken at LANL (left). Resistance of a device subjected to e-beam irradiations (Right).

states. To minimize the bulk contribution to the electrical conductance, we have grown high-resistivity crystals such as  $Bi_2Te_2Se$  and  $Bi_{2-x}Sb_xTe_{2-y}Se_{1+y}$ . The bulk resistivity reaches as high as  $5 \Omega cm$ . We have performed high-field transport measurements at Los Alamos National Lab's pulsed magnetic field facility and shown a low electron density ( $3 \times 10^{12} cm^{-2}$ ) on the surface from the Shubnikov-de Haas oscillations (Fig. 3, left). We will continue to use this high-field facility for our future investigations such as in gate-tunable devices. In the meantime, we have used electron beam irradiation as a tool to tune the carrier concentration in topological insulator devices (ref. 1). By varying the energy and dosage of the electron beam irradiation in low energies ( $< 16$  keV), we can control the position of the Fermi level without introducing measurable additional scattering. At higher energies, we have found a significant increase in scattering due to the introduced disorder from the e-beam irradiations. With large doses, we have observed indications of localization of bulk carriers as indicated by the diverging resistivity at low temperatures (Fig. 3, right). The resistivity approaches saturation at  $T=0$  K due to the metallic surface states. We will use both electron beam and ion beam to further tune bulk carrier concentration in order to reveal the topological surface states.

- Spin relaxation time in graphene and its relation to long- and short-range scattering. Non-local spin valve is an excellent device to study the spin diffusion and coherence in graphene. Room temperature graphene spin diffusion length has been shown to be as long as many microns which corresponds to a few hundred of pico-seconds in spin relaxation time. This is still significantly lower than what is expected from theory based on the fact that graphene has weak spin-orbit coupling and weak hyperfine interaction. In order to understand the fundamental limitations to the spin relaxation time, we have first focused on the effect of the charged impurities, i.e. long-range scattering potential. When we tuned the density of the charged impurities, we varied the momentum scattering time, but we did not find any effect on spin relaxation time (ref. 3). Currently, we are able to tune the carrier density to a high level (close to  $10^{15}\text{cm}^{-2}$ ) by using high-dielectric oxide gate insulator and reach the short range scattering dominated regime. We will investigate the effect of the short range scattering on spin relaxation time in graphene.

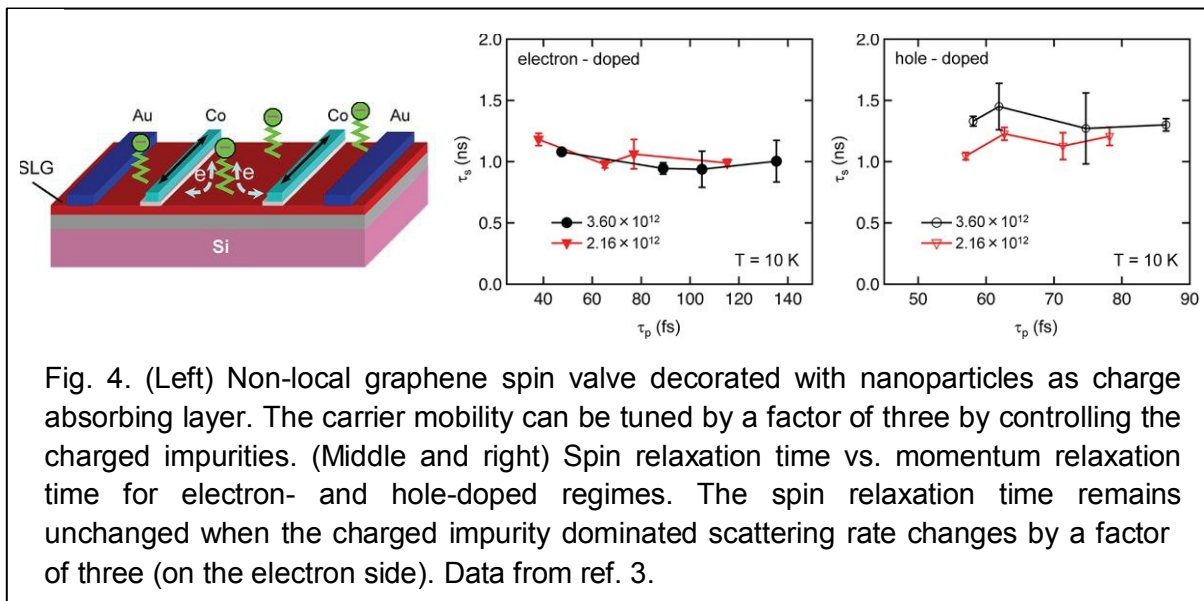


Fig. 4. (Left) Non-local graphene spin valve decorated with nanoparticles as charge absorbing layer. The carrier mobility can be tuned by a factor of three by controlling the charged impurities. (Middle and right) Spin relaxation time vs. momentum relaxation time for electron- and hole-doped regimes. The spin relaxation time remains unchanged when the charged impurity dominated scattering rate changes by a factor of three (on the electron side). Data from ref. 3.

- Future Plans: We will continue our work on magnetic proximity effect in structures with FMI films. We will extend the material system to graphene/YIG and topological insulator/YIG. We will use x-ray capabilities at ALS to directly measure/image the spin polarization induced at the interfaces. In the graphene project, we will study the effect of short-ranged impurities and other defects on the spin relaxation time in non-local graphene spin valves.

#### 4. References:

- (1). P. Wei, Z.Y. Wang, X.F. Liu, V. Aji, and Jing Shi, *Field-Effect Mobility Enhanced by Tuning the Fermi Level into the Band Gap of  $Bi_2Se_3$* , Phys. Rev. B Rapid Communications **85**, 201402 (2012).
- (2). X.F. Liu, D.Q. Wang, P. Wei, L.J. Zhu, and Jing Shi, *Effect of Graphene Mobility on Magneto-Thermoelectric Transport Properties*, Phys. Rev. B **86**, 155414 (2012).
- (3). W. Han, J.-R. Chen, D.Q. Wang, K. M. McCreary, H. Wen, A. G. Swartz, Jing Shi, and Roland K. Kawakami, *Spin Relaxation in Single-Layer Graphene with Tunable Mobility*, Nano Lett. **12**, 3443 (2012).
- (4). Y. Kim, X. Chen, Z. Wang, J. Shi, I. Miotkowski, Y.P. Chen, P.A. Sharma, A.L. Lima Sharma, M.A. Hekmaty, Z. Jiang, and D. Smimov, *Temperature Dependence of Raman-Active Optical Phonons in  $Bi_2Se_3$  and  $Sb_2Te_3$* , Appl. Phys. Lett. **100**, 071907 (2012).
- (5). X.F. Liu, D.Q. Wang, P. Wei, L.J. Zhu, and Jing Shi, *Derivation Relations between Electrical and Thermoelectric Quantum Transport Coefficients in Graphene*, Solid State Communications **152**, 469 (2012).
- (6). S. Wang, F. J. Yue, Jing Shi, Y. J. Shi, A. Hu, Y. W. Du, and D. Wu, *Room-Temperature Spin-Dependent Tunneling through Molecules*, Appl. Phys. Lett. **98**, 172501 (2011).
- (7). Z.Y. Wang, P. Wei, and Jing Shi, *Tuning the Fermi Level in  $Bi_2Se_3$  Bulk Materials and Transport Devices*, Frontier of Physics **7**, 160 (2012).
- (8). D.Q. Wang and Jing Shi, *Effect of Charged Impurities on Graphene Thermoelectric Power near the Dirac Point*, Phys. Rev. B **83**, 113403 (2011).

## Phase Transformations in Confined Nanosystems

Jeffrey E. Shield ([jshield2@unl.edu](mailto:jshield2@unl.edu))  
Department of Mechanical & Materials Engineering  
University of Nebraska-Lincoln, Lincoln, NE 68588-0526

### Program Scope

Alloy nanoparticles are important for a number of technologies, including catalysis, medical imaging, targeted drug delivery, and information technology. Additionally, they provide fundamental insight into physical properties at the nanoscale due to high surface areas relative to volume, quantum confinement effects, and the convergence of critical length scales in magnetism with system size. Furthermore, isolated nanoparticles allow us to probe phase and structural stabilities in finite-sized systems.

In this project, we have studied the phase formation and stability in nanoparticles in the Fe-Au system. Inert gas condensation has been utilized to produce sub-10 nm  $\text{Fe}_x\text{Au}_{1-x}$  alloy nanoparticles with  $x$  ranging from 0.3 to 0.8. Focus has been on the structure and magnetic properties of both as-formed and annealed nanoparticles. The as-deposited clusters were single-crystalline and displayed complete solid solubility, contradicting the equilibrium phase diagram. The as-deposited structures contained significant defect structures with expanded lattice parameters relative to elemental and rule-of-mixtures values, suggesting the presence of self-interstitials. The as-deposited clusters were ferromagnetic at room temperature.

Heat treatment at 600°C for 15 minutes followed by furnace cooling resulted in size-dependent transformation of the clusters into additional, non-equilibrium structures that depended on cluster composition, while larger clusters followed bulk behavior. At about 65 atom % Fe, clusters transformed to a well-ordered, single fcc phase with a lattice parameter of 0.364 nm, whereas the phase diagram predicted two-phase equilibrium. The stabilization of a single fcc phase was explained by a thermodynamic analysis. This analysis suggests that the single-phase stability in the Fe-Au nanoparticles arose from the fact that the introduction of a phase boundary was energetically opposed. Heat treatment of as-deposited nanoparticles resulted in  $L1_2$  and  $L1_0$  ordered structures near 1:3, 3:1 and 1:1 (Fe:Au) stoichiometries, respectively. Magnetically, the annealed nanoparticles displayed strong ferromagnetic behavior for Fe-rich compositions, and weak ferromagnetic behavior for Fe-poor compositions. The magnetism in the Fe-poor nanoparticles suggested a possible combination of an antiferromagnetic core with uncompensated spins at the surface providing the ferromagnetic signal. First-principles calculations are consistent with this explanation.

### As-Deposited Fe-Au Nanoparticles

Composition of 4 samples as measured by EDS in STEM mode were determined to be 79, 65, 53 and 33 atomic % Fe, relatively close to the compositions predicted based on sputtering yields and relative area fractions of Au and Fe on the target. These 4 compositions will be referred to as A1, A2, A3 and A4. Figure 1 shows TEM and HAADF STEM images of A4 that reveal both uniformity in size and composition. High-resolution images revealed that the clusters were single-crystalline, but with highly defective structures. Figure 2 shows a typical HRTEM image of A2. Note the wavy lattice fringes. The structures of the as-deposited nanoclusters were determined from both selected area electron diffraction patterns and FFTs of the HRTEM images. The two Fe-rich compositions were bcc with lattice parameters of 0.330 and 0.339 nm for A1 and A2, respectively. The A3 and A4

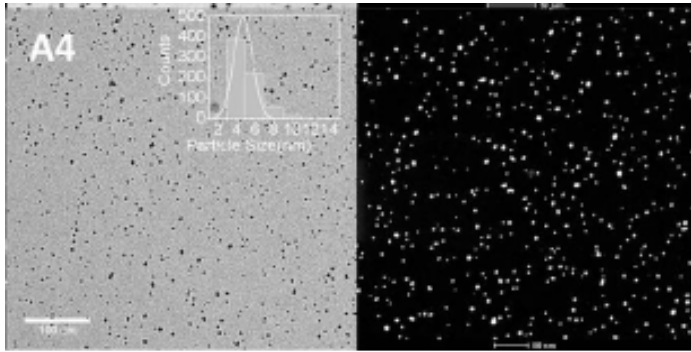


Figure 1. TEM (left) and HAADF STEM (right) images of Fe-Au nanoparticle. The size distribution is shown in the inset.

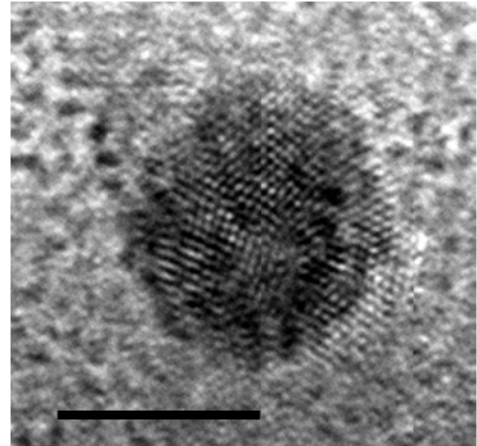
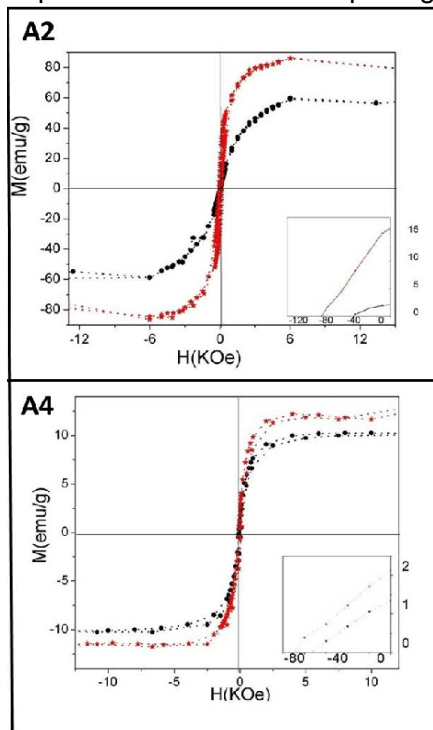


Figure 2. HRTEM image of an as-deposited Fe-Au nanoparticle showing a highly defected structure.

nanoparticles were determined to be fcc with lattice parameters of 0.415 and 0.427, respectively. All four lattice parameters were expanded significantly from simple “rule-of-mixtures” approximations. The expanded lattice parameters can be explained by the presence of self-interstitials. Calculated results using self-interstitial models agree well with experimental interatomic spacings.



The hysteresis behavior of all compositions was consistent with ferromagnetic ordering at both 10 K and 300 K. Figure 3 shows hysteresis curves for A2 and A4. Note the large difference in saturation magnetization. A4 is much lower than can be explained by pure dilution effects. Thus, it appears that the primary fcc structure is antiferromagnetic, and the ferromagnetic signal arises from uncompensated surface spins. A rough approximation of the magnetism arising from only surface Fe atoms is in good agreement with this hypothesis.

Figure 3. Hysteresis curves for A2 and A4 at 10 K (red) and 300 K (black). Insets show the second quadrant.

## Annealed Clusters

The nanoparticles were annealed at 600°C and then allowed to furnace cool in an attempt to reach an “equilibrium” structure. The A2 (65/35) composition was determined to form a well-ordered fcc structure with a lattice parameter of 0.364 nm, not far from a “rule-of-mixtures” approximation. Figure 4 shows both SAD and HRTEM images. Note the mostly defect-free structure, in stark comparison to the as-deposited structure.

From the equilibrium phase diagram, the expected phase constitution is two phases,  $\alpha$ -Fe+fcc Au. Evidently, the formation of equilibrium phases is inhibited by the size of the system (it should be noted that we are examining isolated nanoparticles). A simple model was considered that takes into account the various free energies of a single-phase nanoparticle and a two-phase nanoparticle, with the major difference being the introduction of an interphase (grain) boundary. Figure 5 shows the free energy calculations, where a positive value indicates single-phase stability and a negative value two-phase (bulk) stability. The critical transition size from “nano” to “bulk” behavior occurs at approximately 16 nm. The occurrence of two phases, one fcc and one bcc, was observed in agglomerated nanoparticles above 19 nm, in good agreement with our calculations.

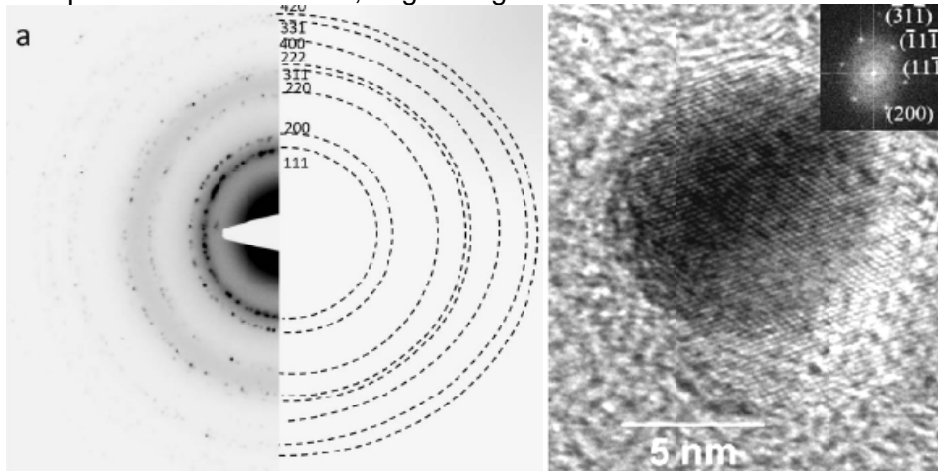


Figure 4. (a) Selected area diffraction pattern and (b) HRTEM image of Fe-35 Au nanoparticles after annealing. The structure is fcc. The inset in (b) shows its FFT.

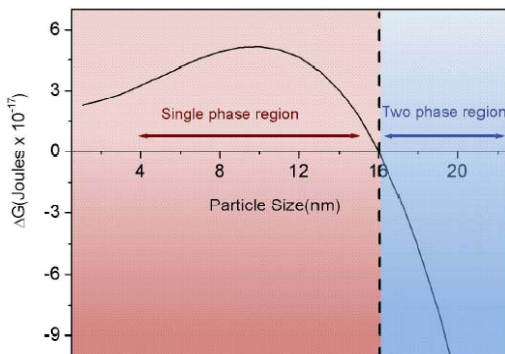


Figure 5. Free energy as a function of particle size for Fe-35 Au.

The inability for individual nanoparticles below a critical size to behave in “equilibrium” allows a pathway to new system energetics (i.e., the system can find local free energy minima that is not obtainable in bulk systems). In short, new atomic structures are possible. This was observed in A1, A3 and A4, which are reasonably close to 3:1, 1:1 and 1:3 stoichiometries. In all three of these nanoparticles, ordered atomic structures were

observed in Fe-Au. Figure 6 shows a HRTEM image and its FFT of the  $L1_0$  structure. Similar findings revealed the  $L1_2$  structure in the 3:1 and 1:3 stoichiometries. In fact,  $L1_0$  ordering was also observed via HAADF STEM imaging in some as-deposited nanoparticles.

The ordered structures displayed ferromagnetic behavior, though again the Fe-poor nanoparticles showed low magnetization values while the  $Fe_3Au$  compound showed high magnetization.

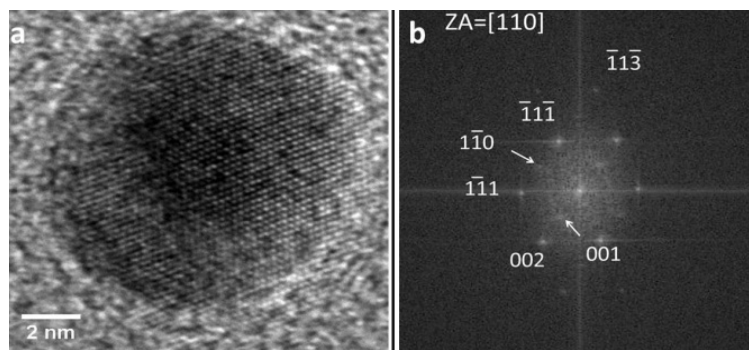


Figure 6. (a) HRTEM image and its (b) FFT of annealed 1:1 composition. The presence of the superlattice reflections indicates  $L1_0$  ordering. SAD (not shown) corroborated the structure.

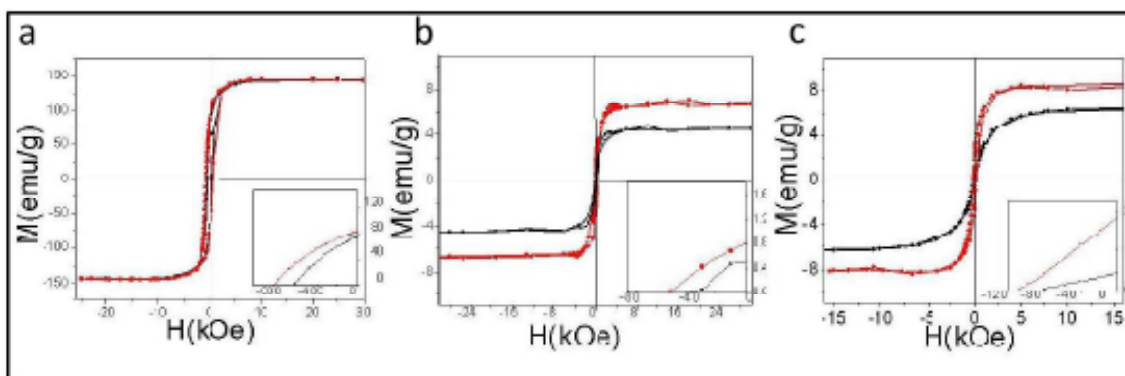


Figure 6. Magnetic Measurements of ordered nanoparticles: Hysteresis behavior of Au-Fe nanoparticles at 300K and 10K, for (a) near stoichiometric FeAu 3:1, (b) FeAu 1:1, and (c) FeAu 1:3 compounds. The insets show second quadrant behavior.

## Summary and Future Plans

Studies of isolated, sub-10 nm Fe-Au nanoparticles reveal the size-stabilization of non-equilibrium structures, including solid solutions and ordered compounds. Thus, studying the phase stabilities and structures in finite-sized systems provides a fundamental understanding of phase stability, while finite-sized systems are also a pathway to new structures that are not able to be stabilized in bulk systems. We are extending the work to other systems to determine the universality of our model.

## Publications

1. P. Mukherjee, Y. Zhang, M.J. Kramer, L.H. Lewis and J.E. Shield, "L1<sub>0</sub> Structure Formation in Slow-cooled Fe-Au Nanoclusters," *Appl. Phys. Lett.* **100**, 222405 (2012).
2. E. Folcke, J.M. Le Breton, W. Lefebvre, J. Bran, R. Lardé, F. Golkar, J. E. Shield, "Investigation of the magnetic properties of FeAu nanoclusters in a W matrix: evidence for exchange-bias phenomenon," *J. Alloys Cmpds.*, in revision.
3. P. Mukherjee, X. Jiang, Y. Wu, M.J. Kramer and J.E. Shield, "Nucleation-suppressed phase stabilization in nanoclusters," *Chem. Mater.*, in revision.

## **Project Title: Magnetic frustration and cooperative phenomena in correlated electron oxide materials**

**Principal Investigator: Prof. Hariharan Srikanth**

University of South Florida, Department of Physics, PHY 114

4202 East Fowler Ave, Tampa, FL 33620

E-mail: [sharihar@usf.edu](mailto:sharihar@usf.edu)

**Project Participants: Dr. M.H. Phan (Research Assistant Professor), Dr. Anis Biswas (Postdoctoral Researcher), Mr. Nicholas Bingham (Ph.D student), and Ms. Paula Lampen (Ph.D student)**

### **Program Scope:**

Transition-metal oxides exhibit rich complexity in their fundamental physical properties determined by the intricate interplay between structural, electronic and magnetic degrees of freedom. Our DoE funded effort during the past 3 years (2010-2013) have yielded new insights into the role of interplay between intrinsic strain, structural transitions, electronic phase separation, magnetic anisotropy and magnetic entropy in a broad range of correlated electron oxide materials such as  $\text{La}_{5/8}\text{Pr}_{3/8-x}\text{Ca}_x\text{MnO}_3$  (LPCMO) [1-3],  $\text{La}_{0.7-x}\text{Pr}_x\text{Sr}_{0.3}\text{MnO}_3$  [4],  $\text{La}_{0.7}\text{Ca}_{0.3-x}\text{Sr}_x\text{MnO}_3$  [5],  $\text{La}_{0.7}\text{Ca}_{0.3}\text{Mn}_{1-x}\text{Fe}_x\text{O}_3$  [6],  $\text{Pr}_{1-x}\text{Sr}_x\text{MO}_3$  ( $M=\text{Mn, Co}$ ) [7],  $\text{Sm}_{1-x}\text{Sr}_x\text{MnO}_3$  [8],  $\text{LaMnO}_{3+\delta}$  [9], and  $\text{Ca}_3\text{Co}_2\text{O}_6$  (CCO).

In particular, the current project period have addressed some of the outstanding issues in mixed phase manganites  $\text{La}_{5/8}\text{Pr}_{3/8-x}\text{Ca}_x\text{MnO}_3$  (LPCMO) with competing charge ordered and ferromagnetic phases strongly influenced by strain and low dimensionality;  $\text{AB}_2\text{O}_4$  type spinel ferrites with multiple spin re-orientation configurations and  $\text{Ca}_3\text{Co}_2\text{O}_6$  having Ising spin chains arranged on a triangular lattice geometry. All these systems are of current interest, and we have demonstrated the importance of combining conventional DC and AC magnetometry with relatively unconventional RF transverse susceptibility (TS) and magnetocaloric effect (MCE) methods to probe the ground state magnetic properties and glassy behavior in these systems. We present here selected representative results on LPCMO in different forms of single crystals, nanocrystals, and thin films and on CCO single crystals.

### **1. Multiphase coexistence and collective behavior in $\text{La}_{5/8}\text{Pr}_{3/8-x}\text{Ca}_x\text{MnO}_3$**

Bulk LPCMO exhibits a complex phase diagram due to coexisting charge-ordered antiferromagnetic (CO/AFM), charge disordered paramagnetic (PM), and ferromagnetic (FM) phases [10-13]. The different crystal structures of the FM and CO phases have been suggested to generate long-range strain interactions leading to an intrinsic variation in elastic energy landscape, which in turn leads to phase separation (PS) into the strain-liquid and strain-glass regimes [11,13]. Despite a number of previous studies, the effect of magnetic field on the strain-liquid and strain-glass states has not been studied in detail and the origin of the sharp change in the magnetization, resistivity, and magnetic entropy just below the Curie temperature ( $T_C$ ) in the strain-liquid region has remained exclusive.

To address these outstanding issues, we have performed MCE and TS experiments on  $\text{La}_{5/8-x}\text{Pr}_x\text{Ca}_{3/8}\text{MnO}_3$  ( $x = 0.275$  and  $0.375$ ) single crystals, which were synthesized in an optical floating-zone furnace and provided by Prof. Sang-Wook Cheong's group at Rutgers University. Systematic MCE studies, coupled with magnetic, transport and magnetic force microscopy (MFM) measurements, have evidenced the presence of multiphases with respectively dominant low-temperature FM and high-temperature CO phases [1,3]. The

“dynamic” strain liquid state is strongly dependent on magnetic field, while the “frozen” strain-glass state is almost magnetic field independent. The sharp increase of the magnetization below the Curie temperature occurs via the growth of FMM domain regions that are already present in the material even in zero magnetic field.

In addition to the MCE findings, TS experiments on LPCMO single crystals have revealed the unstable nature of the FM phase, the field-assisted kinetic arrest and frozen state at low temperatures just below 70 K, above which a strong phase separation occurs and field hysteresis are observed, leading to a new and comprehensive magnetic phase diagram (Fig. 1). We have also performed TS measurements on LPCMO thin films grown by Dr. Jian Shen at the Oak Ridge National Laboratory and discovered an important impact of strain and low dimensionality on the magnetism of LPCMO that in contrast to its bulk counterpart, the FM phase is stabilized and dominant over the CO phase in the entire temperature range in the films.

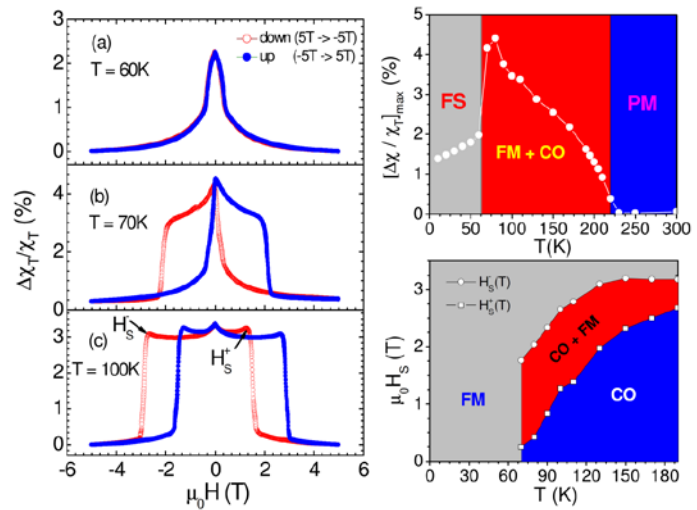


**Fig. 1** (Left panel) TS profiles taken at three representative temperatures  $T = 60$  K,  $70$  K, and  $100$  K for LPCMO; A strong phase separation accompanied by large field hysteresis occurs around  $70$  K, while a frozen state with kinetic arrest is observed at  $60$  K; (Right panel) Magnetic phase diagrams are constructed from the TS data.

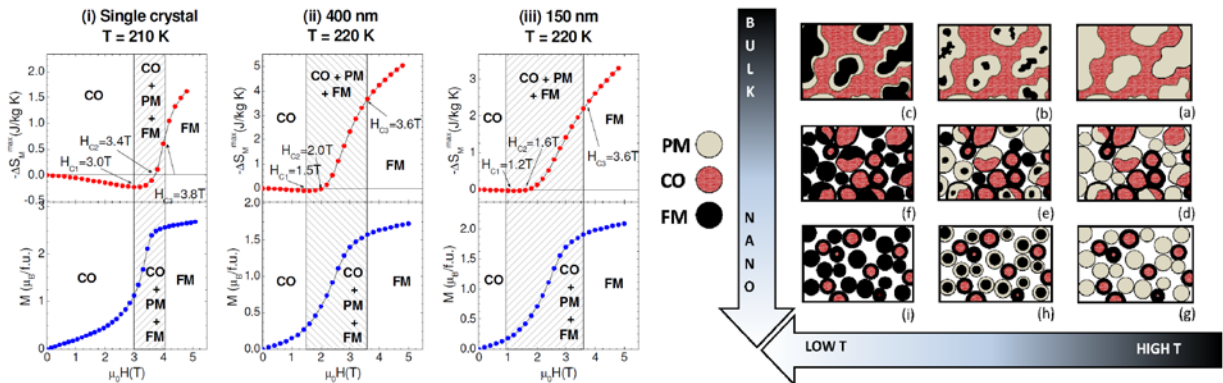


**Fig. 2** Magnetic field dependence of maximum magnetic entropy change ( $-\Delta S_M^{\max}$ ) (a) – (c) and magnetization (d) – (f) near the charge ordering temperature. Phase coexistence occurs between  $H_{C1}$  – the field at which the CO phase begins to melt – and  $H_{C3}$  – the field at which the CO phase is fully converted to FM. A simple “geometric” model is proposed to illustrate the effects of particle size on the phase coexistence in LPCMO.

Because phase separation in bulk LPCMO occurs on the *microscale*, reducing particle size to below this characteristic length is expected to have a strong impact on the magnetic properties of the system. Our first comprehensive study of the effects of reducing particle size to the *nanoscale* in  $\text{La}_{0.25}\text{Pr}_{0.375}\text{Ca}_{0.375}\text{MnO}_3$  have revealed that the conflicting trends that accompany size reduction in nanoparticles of FM and CO manganites in combination with the mitigation of long-range phenomenon (i.e. martensitic accommodation strains and microscale phase separation) result in strong modification of the magnetic and magnetocaloric properties of LPCMO as particle size is decreased [3]. The field-sensitivity and balance of the coexisting

phases is affected as the FM component is strengthened and becomes dominant below 100 nm. Our observation that the FM phase is stabilized on the nanoscale is contrasted with the earlier finding that charge disordered PM becomes dominant with grain size reduction on the microscale, demonstrating that in terms of the characteristic phase separation length, a few microns and several hundred nanometers represent very different regimes in microscale phase separated LPCMO.

From a magnetic cooling application perspective, we highlight that exploration of the large MCE and refrigerant capacity (RC) in magnetic refrigerant materials on the nanometer scale would lead to understanding functional responses in new nanomaterials and devices that could essentially impact a broad base of refrigeration technology. While the conventional trend is reduction of the magnetization that leads to the decrease in MCE and/or RC with nanostructuring, we have demonstrated the new possibility of enhancing both the MCE and RC in nanostructured mixed phase manganites like LPCMO [2]. A strong enhancement of MCE and RC and a strong reduction of thermal and field hysteresis losses are achieved in the nanocrystalline samples. This important finding opens up a new way of exploring nanostructured multiphase magnetic materials for energy-efficient magnetic refrigeration technology. These results have been reported at major conferences (MMM 2011, APS 2012, MMM-Intermag, 2013), featured in two invited talks (ICM 2012, MRS 2013), and summarized in three major publications (*Physical Review B* 2010; *Applied Physics Letters*, 2010; and *Physical Review B* 2012)

## 2. Complex magnetic phase diagram in $\text{Ca}_3\text{Co}_2\text{O}_6$

$\text{Ca}_3\text{Co}_2\text{O}_6$  is a system exhibiting low dimensionality and magnetic frustration [14,15]. Therefore it provides a very interesting case for us to study the cooperative phenomena of low-dimensional magnetism and topological magnetic frustration in a single material.  $\text{Ca}_3\text{Co}_2\text{O}_6$  has a rhombohedral structure composed of  $[\text{Co}_2\text{O}_6]_\infty$  infinite chains running along the  $c$  axis of the corresponding hexagonal cell, with the Ca cations located in between them. The chains are made of alternating, face-sharing  $\text{CoO}_6$  trigonal prisms and  $\text{CoO}_6$  octahedra. Each chain is surrounded by six equally spaced chains forming a triangular lattice in the  $ab$  plane. The intrachain Co-Co separation is  $\sim 0.26$  nm, while the interchain distance is  $\sim 0.52$  nm [14]. As a result, the intrachain coupling is ferromagnetic while interchain coupling is antiferromagnetic. Specific heat and magnetization measurements have revealed the onset of long-range magnetic order at  $T_N \sim 25$  K, below which antiferromagnetic interactions within the  $ab$  plane lead to a geometrical frustration of the magnetic structure and many degenerate spin configurations are possible, giving rise to highly susceptible dynamical states. Due to the geometrical frustration, the system only reaches a “partially disordered antiferromagnetic” (PDO) state at low temperatures. In this PDO state, two thirds of the ferromagnetic chains are coupled antiferromagnetically, while the remaining third remain incoherent (disordered chains with zero net magnetization). While a complex phase diagram has been proposed for  $\text{Ca}_3\text{Co}_2\text{O}_6$  [14-16], the true nature of the low temperature magnetic phase and complexity of interchain and intrachain interactions is under debate.

To better understand the magnetic nature of this interesting system, we have conducted

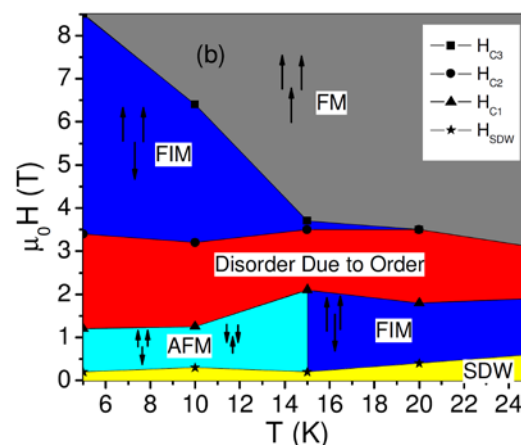


Fig. 3 A magnetic phase diagram constructed from the MCE data for  $\text{Ca}_3\text{Co}_2\text{O}_6$ .

systematic studies of MCE and TS measurements along with DC and AC magnetization on  $\text{Ca}_3\text{Co}_2\text{O}_6$  single crystals grown by Prof. Cheong's group at Rutgers University. Our MCE studies have revealed the signature of short-range FM ordering at  $T > T_N$ . At  $15 \text{ K} < T < T_N$ , the intrachain FM coupling is dominant over the interchain AFM coupling. In this region the FM coupling is stabilized, but the AFM coupling between nearest-neighbor and next-nearest neighbor chains is strong enough to slightly distort the FM ordering present in each chain, this can be thought of as a disorder induced by order. For  $T \leq 15 \text{ K}$ , the thermal fluctuations have stabilized the AFM phase. A new, comprehensive magnetic phase diagram has been constructed from the first time from the MCE data (Fig. 3), where  $H_{C1}$  is related to the maximum (minimum) in  $\Delta S_M$  before the induced disorder.  $H_{C2}$  represents the maximum disorder induced in the chains by magnetic field  $H$ .  $H_{C3}$  indicates the field at which the volume fraction of FM ordering starts to become the dominant phase. As  $T$  is decreased for 25 K it takes a significantly high value of  $H$  in order to achieve a large volume fraction of FM ordering, signifying the paradoxical notion that CCO becomes more disordered at  $T$  decreases.  $H_{C2}$  remains almost constant for all  $T$ , and is associated with the large step in  $M$ , present at all  $T$ . For  $H_{C1}$ , there is a crossover temperature, for  $T \geq 15 \text{ K}$  a relatively small  $H$  will globally align the material in the FIM state described above. However, for  $T < 15 \text{ K}$ , the system resides in the SDW state which gives rise to AFM like behavior. We presented our results in a poster presentation at MMM-Intermag (Chicago, 2013) conference, with the main results being written for publication in Physical Review B 2013.

Overall, our DC and AC magnetization, TS and MCE studies on a large class of correlated electron oxide systems have yielded deeper insights into the competing ground states and collective phenomena that can be correlated to their geometric frustration. Our studies point to the presence of competing CO and FM phases in bulk LPCMO and the importance of the low dimensionality and strain effects on these states in nanostructured LPCMO and thin films. Future work will continue to explore the ground magnetic states and collective phenomena in these oxides.

**Work at USF supported by DOE through grant number DE-FG02-07ER46438.**

## REFERENCES

- [1] M.H. Phan et al., Phys. Rev. B 81, 094413 (2010)
- [2] M.H. Phan et al., Appl. Phys. Lett. 97, 242506 (2010)
- [3] N. S. Bingham et al., Phys. Rev. B 86, 064420 (2012)
- [4] Y.D. Zhang et al., J. Appl. Phys. 111, 063918 (2012)
- [5] M.H. Phan et al., J. All. Compound. 508, 238 (2010)
- [6] P. Lampen et al., J. Appl. Phys. 112, 113901 (2012)
- [7] N. A. Frey et al., Phys. Rev. B 83, 024406 (2011)
- [8] N.S. Bingham et al., J. Appl. Phys. 111, 07D705 (2012)
- [9] S. Chandra et al., J. Phys. Condens. Matt. 24, 366004 (2012)
- [10] M. Uehara et al., Nature 399, 560 (1999)
- [11] W.Wu et al., Nat. Mater. 5, 881 (2006)
- [12] T. Z. Ward et al., Nat. Phys. 5, 885 (2009)
- [13] T. Dhakal et al., Phys. Rev. B 75, 092404 (2007)
- [14] V. Hardy et al., Phys. Rev. B 68, 014424 (2003).
- [15] S. Agrestini et al., Phys. Rev. B 77, 140403 (2008).
- [16] S. Agrestini et al., Phys. Rev. Lett. 106, 197204 (2011)

# Spin Polarized Functionality Through Complex Oxide Heteroepitaxy

PI: Yuri Suzuki

Department of Applied Physics, Stanford University

Geballe Laboratory for Advanced Materials

McCullough 341

Stanford University

Stanford, CA 94305-4665

ysuzuki1@stanford.edu

## PROGRAM SCOPE

The *main research objective* of the proposed program is to develop novel paradigms for the generation of quasi-two dimensional magnetic functionality in complex oxide thin films and heterostructures. In this program, we focus on the development of novel complex oxide thin films and heterostructures with spin functionality where surfaces/interfaces and coherent epitaxial strain play a critical role in the realization of the long range magnetic order. Complex oxides exhibit a wide range of electronic, magnetic and optical properties that can be tuned by parameters such as lattice strain and substitution. The tunability combined with the ability to control complex oxide interfaces with atomic accuracy makes them ideally suited for the exploration of *new quasi-two dimensional, magnetically functional materials systems*.

Our focus is on two classes of materials based on *3d, 4d and 5d transition metal oxide compounds* for:

- (a) heterostructures in which the interfaces gives rise to spin functionality not observed in the two constituent materials and engineered by *modulation doping of magnetic species, carrier mediated exchange interactions or valence discontinuities at ferromagnetic interfaces*.
- (b) thin films in which epitaxial strain can induce *spin-state transitions or metal-insulator transitions* to stabilize ferromagnetic and/or metallic ground states.

## RECENT PROGRESS

Highlights of recent work include (i) long range ferrimagnetic order in  $\text{PrCoO}_3$ , (ii) evidence of high spin Ru in epitaxial  $\text{SrRuO}_3$  thin films, and (iii) metal insulator transitions in epitaxial  $\text{LaVO}_3$  and  $\text{LaTiO}_3$  thin films.

*Long range ferromagnetic order in  $\text{PrCoO}_3$ .* We demonstrate an emergent ferrimagnetic ground state in heteroepitaxial  $\text{PrCoO}_3$  (PCO) thin films, where magnetic moment ordering occurs on both the Co and Pr sites. We find that the Co sublattice orders ferromagnetically, with significant evidence for HS Co, and it is aligned antiparallel to the ordered Pr sublattice. This is significant as ordering of Pr ions has not been observed in bulk cobaltites. The Pr ordering antiparallel to the Co ions accounts for the lower saturation magnetization for these PCO films compared to LCO films. We also observe a lower Curie temperature ( $T_C$ ), likely due to the greater stability of the low-spin state in bulk PCO. The ferromagnetic exchange mechanisms used to explain the behavior of metallic alkaline-earth doped bulk cobaltites is inconsistent with the insulating behavior of the PCO films obtained here. In our epitaxially strained films, the Pr moment appears to be strongly coupled to the HS/LS Co moments, unlike the bulk  $\text{Pr}_{1-x}\text{Sr}_x\text{CoO}_3$  IS Co

scenario. These findings are significant since they set these thin films apart from other cobaltites, and they represent the first evidence of an interaction of this type between high-spin Co ions and rare-earth ions, which results in novel ferromagnetic behavior.

The most remarkable finding of this investigation is the demonstration of two ferromagnetic sublattices: one of Co ions aligning with the applied magnetic field and another of Pr ions that is antiferromagnetically coupled to the Co moments. This reveals that these films are more appropriately described as ferrimagnetic and display a monotonic temperature dependence with a  $T_C$  of  $\sim 60$  K.  $\text{Pr}^{3+}$  ions in bulk PCO do not show any ordering down to 4 K. In doped  $\text{Pr}_{1-x}\text{Sr}_x\text{CoO}_3$ , long-range ferromagnetism associated with the Co ions is observed for  $x > 0.2$  and can be attributed to the double exchange interaction among intermediate spin Co moments in an intermediate valence, mediated by a mobile  $e_g$  electron.

*High spin Ru in  $\text{SrRuO}_3$  thin films.* We demonstrate that both enhanced saturated magnetic moment and strong uniaxial anisotropy can be induced simultaneously through the application of compressive epitaxial strain in epitaxial  $\text{SrRuO}_3$  (SRO) thin films. In (111)-oriented films, the resulting distortions of the Ru octahedral environment may cause electrons to populate the newly split  $e_g$  band, effectively placing the Ru in a high-spin state and enhancing the magnetic moment. We find an increase in the carrier concentration consistent with the presence of such high-spin Ru. SRO films grown under identical conditions on (100) and (110) substrates show similar behavior but are more consistent with a low-spin Ru state. All films with enhanced saturated moment also show strong uniaxial magnetic anisotropy with an OOP easy direction. By systematically varying the magnitude of the lattice distortions in the SRO samples, we conclusively show that these lattice distortions are the source of the enhanced Ru moment, larger carrier concentration, and strong magnetic anisotropy. We speculate that lattice distortions anisotropically alter the bonding in the Ru-O octahedra in a way that simultaneously reduces the quenching of the orbital moment and involves the  $e_g$  states in the magnetism, explaining all our observations.

Correlation of the lattice distortions, enhancement of saturated Ru moment and strong magnetic anisotropy in these SRO films lead us to conclude that it is the symmetry and magnitude of the lattice deformation that produces and controls these unusual magnetic properties. We find the degree of enhancement to be highly tunable and dependent only on the strain state.

*Metal insulator transitions in epitaxial  $\text{LaVO}_3$  and  $\text{LaTiO}_3$  thin films.* We demonstrate that the metallic ground state in  $\text{LaVO}_3$  (LVO)/  $\text{SrTiO}_3$  (STO) is qualitatively different from that in  $\text{LaTiO}_3$  (LTO)/ STO. In LTO/STO, the metallic state is found in the bulk of the LTO film and not just at the interface with STO. We demonstrate that the metallicity of LTO/STO is primarily from strain induced electronic structure modifications and is secondarily due to the polar discontinuity at the interface, thus reconciling previously contradictory reports on the origin of the metallicity. The small charge gap can be collapsed by the 1.67 % epitaxial mismatch strain imposed by the underlying STO substrate. Ab-initio studies with dynamical mean field modeling suggest that lattice distortions can indeed stabilize a metallic ground state in LTO. A careful study of epitaxial LTO films on  $\text{LaVO}_3$  buffered  $\text{DyScO}_3$  and  $\text{LaVO}_3$  buffered STO substrates reveal the importance of epitaxial strain induced electronic structure modification. LTO films on STO buffered  $\text{DyScO}_3$  substrates indicates that charge transfer at the LTO/STO interface may not be neglected and in the absence of epitaxial strain induced electronic structure modification

can become the dominant mechanism for the interface metallicity. The larger charge gap in LVO cannot be collapsed by lattice distortions alone. Metallicity is induced at the interface as is evident in the scaling of the sheet resistivity in LVO films of varying thicknesses grown on STO (not shown). A comparison of the low temperature transport behavior of the metallic ground state in LVO/STO and LTO/STO also suggests the different origins of the metallicity. In LTO/STO, there is a precipitous drop in the resistivity at low temperatures. In LVO/STO, the low temperature upturn in resistivity of LVO/STO shows signatures of weak localization. Moreover, the in-plane magnetoresistance (MR) shows a local maximum that is associated with strong spin-orbit coupling in the system as a result of the competition between weak localization and anti-localization in the presence of external magnetic field.

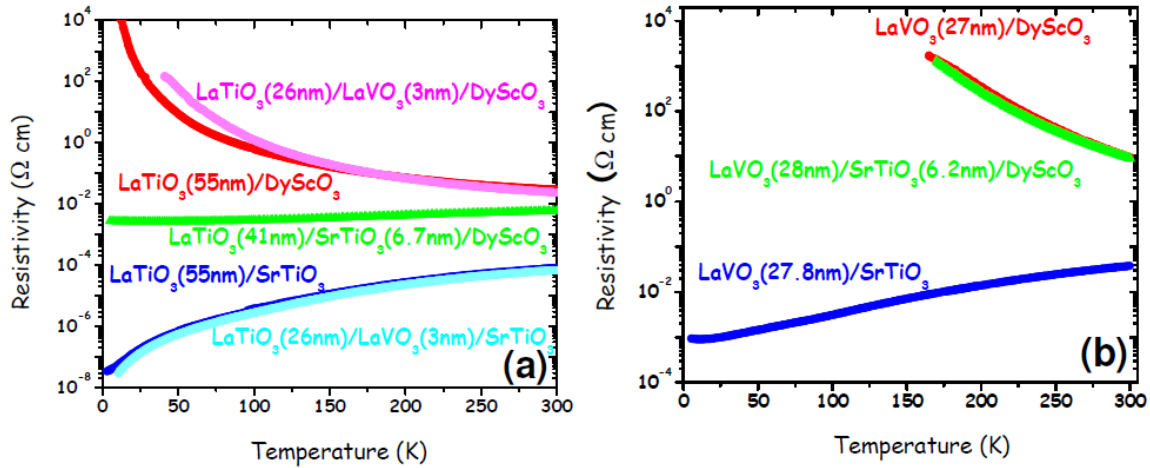


Figure 1. Temperature dependence of resistivity in zero field of (a) LaTiO<sub>3</sub> films and bilayers grown on SrTiO<sub>3</sub> and DyScO<sub>3</sub> and (b) LaVO<sub>3</sub> films and bilayers grown on SrTiO<sub>3</sub> and DyScO<sub>3</sub> show that metallicity in epitaxial LaTiO<sub>3</sub> and LaVO<sub>3</sub> films are different in nature.

## FUTURE PLANS

In each highlighted area above as well as our additional projects on other related complex oxide thin film materials, we plan to focus on some of the major challenges in the areas of oxide interfaces and spin based devices. One of the big challenges in the development of novel complex oxide thin films has been to identify or predict thin film behavior unattainable in the bulk a priori. More specifically, we will explore the generation of interfacial ferromagnetism at the interface of paramagnetic metal LaNiO<sub>3</sub> and antiferromagnetic CaMnO<sub>3</sub>, the universality of the generation of ferromagnetism in the undoped cobaltites and magnetic cation doping of the LaAlO<sub>3</sub>/SrTiO<sub>3</sub> (LAO/STO) interface to generate spin polarized quasi- two dimensional electron gas in the LAO/STO system.

## REFERENCES

Franklin J. Wong, Seung-Hyub Baek, Rajesh V. Chopdekar, V.V. Mehta, Ho Wan Jang, C.B. Eom, and Yuri Suzuki, "Metallicity in LaTiO<sub>3</sub> thin films induced by tetragonal lattice deformation," *Rapid Communications Physical Review B* **81** 161101 (2010).

Alexander Grutter, Franklin Wong, Elke Arenholz, Marco Liberati, Arturas Vailionis, Yuri Suzuki, "Enhanced Magnetism in Epitaxial SrRuO<sub>3</sub> Thin Films," *Applied Physics Letters* **96** 082509 (2010).

Alexander Grutter, Franklin Wong, Elke Arenholz, Marco Liberati, Yuri Suzuki, "Enhanced Magnetization in Epitaxial SrRuO<sub>3</sub> Thin Films via Substrate-Induced Strain," *Journal of Applied Physics* **107** 9E138 (2010).

B. B. Nelson-Cheeseman, F. J. Wong, R. V. Chopdekar, E. Arenholz, and Y. Suzuki, "Room Temperature Magnetic Barrier Layers in Magnetic Tunnel Junctions," *Physical Review B* **81**, 214421 (2010).

B. B. Nelson-Cheeseman, R. V. Chopdekar, M.F. Toney, E. Arenholz, and Y. Suzuki, "Modified Magnetic Ground State in NiMn<sub>2</sub>O<sub>4</sub> Thin Films," *Physical Review B* **82** 144419:1-7 (2010).

G. van der Laan, R. V. Chopdekar, Y. Suzuki, and E. Arenholz, "Strain-Induced Changes in the Electronic Structure of MnCr<sub>2</sub>O<sub>4</sub> Thin Films Probed by X-ray Magnetic Circular Dichroism," *Physical Review Letters* **105** 067405 (2010).

C. He, X. Zhai, V.V. Mehta, F. Wong, Y. Suzuki, "Interfacial magnetism in CaRuO<sub>3</sub>/CaMnO<sub>3</sub> superlattices grown on (001) SrTiO<sub>3</sub>," *Journal of Applied Physics* **109** 07D729 (2011).

V.V. Mehta and Y. Suzuki, "Ferromagnetism enhanced by structural relaxation of biaxially compressed LaCoO<sub>3</sub> films," *Journal of Applied Physics* **109** 07D717 (2011).

Franklin J. Wong, Shaobo Zhu, Jodi M. Iwata-Harms, and Yuri Suzuki, "Electronic Tuning of La<sub>2/3</sub>Sr<sub>1/3</sub>MnO<sub>3</sub> thin films via epitaxy," *Journal of Applied Physics* **111** 063920 (2012).

A. J. Grutter, F. J. Wong, E. Arenholz, A. Vailionis, and Y. Suzuki, "Evidence of high spin Ru and universal magnetic anisotropy in SrRuO<sub>3</sub> thin films," *Physical Review B* **85** 134429 (2012).

C. He, T. Sanders, M. Gray, F.J. Wong, V.V. Mehta, "Metal-insulator transitions in epitaxial LaVO<sub>3</sub> and LaTiO<sub>3</sub> films," and Y. Suzuki, *Physical Review B* **86** 081401 (2012).

C. He, A.J. Grutter, M. Gu, N.D. Browning, Y. Takamura, B.J. Kirby, J.A. Borchers, J.W. Kim, M.R. Fitzsimmons, X. Zhai, V.V. Mehta, F.J. Wong, and Y. Suzuki, "Interfacial ferromagnetism and exchange bias in CaRuO<sub>3</sub>/CaMnO<sub>3</sub> superlattices," *Physical Review Letters* **109** 197202 (2012).

Virat V. Mehta, Shameek Bose, Jodi Iwata-Harms, Elke Arenholz, Christopher Leighton, Yuri Suzuki, "Ferrimagnetism in PrCoO<sub>3</sub> Epitaxial Films," *Rapid Communications Physical Review B* **87** 020405 (2012).

## Electrochemically-Driven Phase Transitions in Battery Storage Compounds (MIT-LLNL collaborative research; LLNL part supported by DOE-BES FWP SCW1371)

Ming Tang (LLNL PI)

Condensed Matter and Materials Division, Lawrence Livermore National Laboratory  
7000 East Avenue, Livermore, CA 94550

Email: [mingtang@alum.mit.edu](mailto:mingtang@alum.mit.edu)

Yet-Ming Chiang (MIT PI), W. Craig Carter (MIT Co-PI)

Room 13-4086, Massachusetts Institute of Technology, Cambridge, MA 02139

Email: [ychiang@mit.edu](mailto:ychiang@mit.edu), [ccarter@mit.edu](mailto:ccarter@mit.edu)

**Program Scope:** Advanced battery storage compounds frequently exhibit phase transformations upon electrochemical cycling. Under the large electrochemical driving forces inherent to practical use, systems are often driven far from equilibrium where unusual phase transition phenomena occur. This program combines theoretical and experimental studies carried out at MIT and Lawrence Livermore National Laboratory (LLNL) to develop a predictive understanding of the collective influence of materials composition, transformation strain, crystallite size/shape, and the electrochemical conditions (e.g. the electrical overpotentials) on the phase transition behavior of electrodes at nanoscopic to mesoscopic scale. The systems that have been and will be studied include lithium transition metal olivines  $\text{LiMPO}_4$  ( $M=\text{Fe}$ ,  $\text{Mn}$ ) and oxide spinels,  $\text{LiNi}_{0.5}\text{Mn}_{1.5}\text{O}_4$ , which have both fundamental and practical interest. Phase-field modeling of phase stability, transformation pathways and morphological evolution is combined with in-situ experiments, in which electrochemical titration is conducted simultaneously with characterization by synchrotron X-ray diffraction, neutron scattering, and transmission electron microscopy at DOE facilities.

### Recent Progress:

In the LLNL's portion of the current program (starting September 2012), we have extended the phase-field model [1,2] developed during the previous award to MIT (grant no. DE-SC0002626) to understand the *morphological evolution of  $\text{LiFePO}_4/\text{FePO}_4$  two-phase microstructure* upon lithiation/delithiation. Recently, an intriguing periodic domain structure was discovered by Chen et al. [3] in  $\text{LiFePO}_4$  particles that were chemically delithiated, as shown by the transmission electron microscopy image (Figure 1(a)). The  $\text{LiFePO}_4$ - $\text{FePO}_4$  phase boundary appears to lie in the (100) plane, and alternating  $\text{LiFePO}_4$  and  $\text{FePO}_4$  stripes line up along (100). In the current work we use modeling to address two questions:

- 1) What is the kinetic process that leads to the formation of the observed domain structure?
- 2) Does the domain structure correspond to the thermodynamically equilibrium state?

Answers to these questions are fundamental to understand the origin of such phase morphology, the conditions for its formation, and its implications for Li intercalation kinetics.

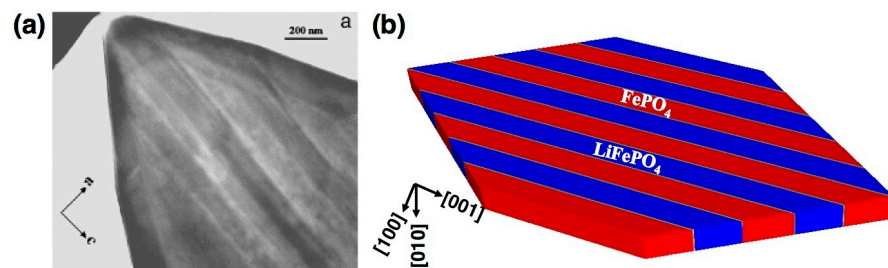


Figure 1 (a) TEM image of striped domains in a platelike partially delithiated olivine particle. Reprinted from ref. 3. (b) Schematics of a possible  $\text{LiFePO}_4/\text{FePO}_4$  two-phase structure corresponding to (a).

Our phase-field model [4] takes the anisotropic Li diffusivity, lattice mismatch, elastic moduli and phase boundary energy of olivine obtained from experiments or first-principles calculations as input parameters. Figure 2 shows a single-particle simulation that imitates the experimental condition under which the domain structure was observed. First, a  $\text{FePO}_4$  nanorod particle is lithiated under an overpotential  $\Delta\phi = 100$  mV until 50% of the Li sites are occupied. Next, Li flux from the electrolyte into the particle is stopped to let the particle “rest” under open circuit condition. Upon lithiation at relatively large overpotentials ( $\Delta\phi > 78$  mV), our model predicts that Li ions are inserted into all 1D Li channels through (010) surface at the same rate. Li composition is uniform along (010) plane and a gradient exists in the (010) direction. When lithium influx is terminated at the second “rest” stage, spontaneous phase separation occurs via spinodal decomposition in the simulation. After domain coarsening, a stable striped morphology is formed in (010) plane with [100] domain dimension  $\sim O(100\text{nm})$ , similar to experiments. The experimentally observed (100) phase boundary also appears in the simulation. Because the misfit strain in (100) plane is among the smallest, the alignment of phase boundary along (100) is favored by the reduction of the coherency strain energy. However, the simulated microstructure also contains (010) phase boundary. Such a morphology is due to one-dimensional Li diffusion in defect-free olivine [5]. At the beginning of the rest stage each (010) Li channel is 50% filled. Because Li ions can only move along but not across channels, phase separation has to occur along [010], forming (010) phase boundary.

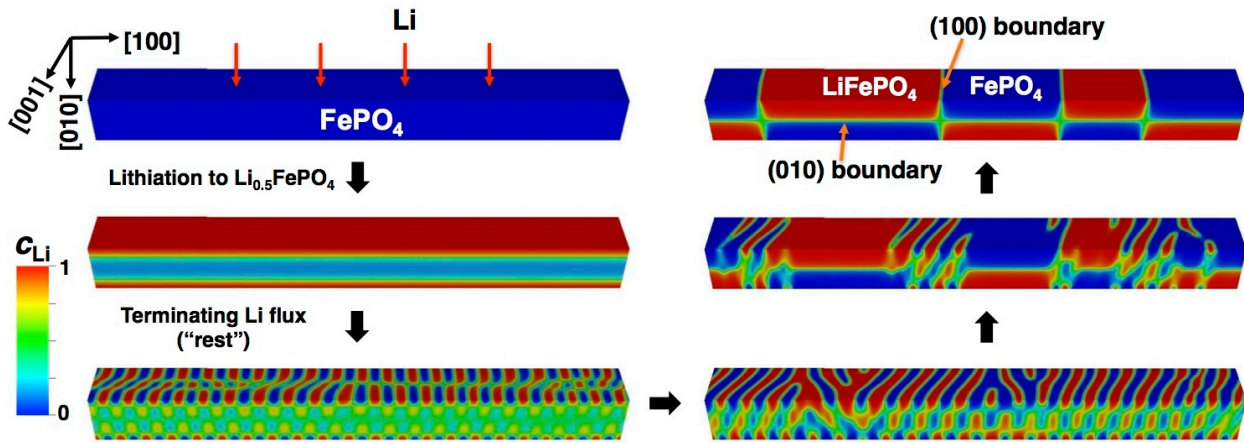


Figure 2 Evolution of Li composition distribution in a  $\text{FePO}_4$  nanorod particle ( $512 \times 50 \times 50 \text{ nm}^3$ ) upon lithiation to  $\text{Li}_{0.5}\text{FePO}_4$  followed by rest (i.e. no Li flux into the particle).

Notably, the spinodal decomposition process that leads to domain structure formation is found to initiate on (010) surface in the simulation (Figure 2); phase separation does not extend to the interior of the particle until later times. To understand this phenomenon, we develop a general linear stability theory to analyze the initial stage of spinodal decomposition in elastically coherent body with free surfaces [6]. Our analysis reveals the existence of a unique surface mode of spinodal decomposition. Because coherency stress induced by lattice mismatch between regions of different compositions is relaxed near free surfaces, the surface mode obtains a faster growth rate than the bulk mode and becomes unstable even when spinodal decomposition is suppressed in the bulk. A significant finding of our work is that when free surfaces are present, the metastability limit of supersaturated solid solution is no longer governed by the well-known coherent spinodal but the chemical spinodal as in bulk systems that do not have coherency stress. This result suggests that nanoparticles of materials with large misfit strains such as olivines are much easier to undergo spinodal decomposition and generate domain structure than their bulk counterparts. The combined linear stability analysis and numerical simulation clearly point out the importance of understanding the kinetics of surface-mode spinodal decomposition for controlling the two-phase microstructure in olivine particles.

While the (100) phase boundary from our simulation is consistent with the observation of Chen et al. [3], the predicted (010) interface between  $\text{LiFePO}_4$  and  $\text{FePO}_4$  remains to be confirmed by experiments. The (010) phase boundary possesses a larger misfit strain than (100); its formation is kinetically induced by the absence of Li diffusion along [100] and [001]. However, atomistic modeling by Malik et al. [7] shows that the presence of defects (e.g. Fe anti-site defects) can facilitate the hopping of Li ions between neighboring Li channels, resulting in non-negligible Li diffusion in (010) plane. When we consider such defect effect by assigning non-zero diffusivity to Li diffusion along [100] and [001] in simulation, the (010) phase boundary is eventually eliminated by inter-channel Li diffusion to minimize the coherent elastic energy. Therefore, we conclude that defect density has important influence on domain morphology in olivine particles, and (010) phase boundary should appear only in (near-)defect-free particles. Since  $\text{LiFePO}_4$  synthesized by the hydrothermal method, which was employed by Chen et al., usually contains a high population of defects, defect density could explain why only (100) phase boundary exists in such particles (viz. Figure 1(b)).

In a recent paper [8] Cogswell and Bazant suggest that the  $\text{LiFePO}_4/\text{FePO}_4$  domain structure observed by Chen et al. corresponds to an equilibrium morphology that minimizes the total free energy of the particle. The equilibrium stripe width in the [100] direction  $W$  is determined by the competition between the total phase boundary energy, which decreases with  $W$ , and the coherency strain energy, which increases with  $W$ . Nevertheless, the scaling argument and the phase-field model in their work uses the boundary condition of zero heterogeneous displacement on particle surface, which represents the condition of particles embedded in a rigid matrix. In battery composite electrodes in which individual particles are loosely bound by additives, it is appropriate to apply the traction-free boundary condition on particle surface. We employed this boundary condition in computing the elastic stress/strain fields in a platelike olivine particle resembling the sample of Chen et al. As is shown in Figure 3(a), the elastic stress field is localized around the phase boundary when the particle contains only two domains. With more domains in the particle, significant coherency stress also arises within each domain, resulting in an increasingly larger total elastic energy. Figure 3(b) shows that the average elastic energy density of the striped morphology decreases with the stripe width  $W$ . Therefore, both the phase boundary and the elastic energies are monotonically decreasing functions of  $W$  under the surface-traction-free boundary condition; the thermodynamically stable domain morphology in a particle with an average composition  $\text{Li}_{0.5}\text{FePO}_4$  should be two domains separated by a (100) phase boundary. However, Figure 3(b) also shows that when  $W$  is comparable to the [010] particle size  $L_{[010]}$  or larger, the average elastic energy density is well

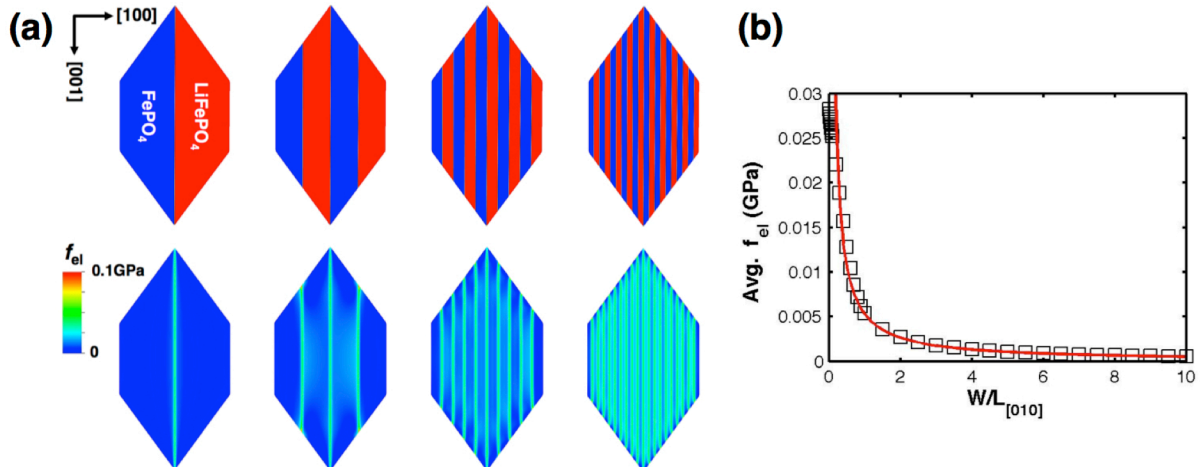


Figure 3 (a) A hexagonal platelike olivine particle accommodating different number of [100] stripes (top row), and the corresponding elastic energy density distribution in the particle (bottom row). (b) Average elastic energy density stored in the two-phase domain structure as a function of [100] stripe width ( $W$ ) normalized by [010] particle thickness ( $L_{[010]}$ ). Open squares are calculated results and the solid curve  $F_{el}^0/W$  (see text) describes the asymptotic behavior as  $W \rightarrow \infty$ .

described by the function  $F_{el}^0/W$  (solid line), where  $F_{el}^0$  is the coherency strain energy per unit area of a stand-alone (100) phase boundary. Such a trend indicates that the repulsive elastic interaction between two (100) phase boundaries becomes very weak when their separation is on the order of  $L_{[010]}$ , and further domain coarsening along [100] will become kinetically sluggish. This result explains the domain length scale observed in Figure 1(a), where  $W \sim L_{[010]}$  (200 nm).

In summary, we use phase-field simulation and analytical calculation to prove that the experimentally observed striped domain structure in partially lithiated (or delithiated) olivine particles is produced by surface-mode spinodal decomposition, and it represents a kinetically “frozen” state rather than the equilibrium morphology.

**Future Plans:** We next plan to:

- 1) Generalize phase-field simulations of olivine cathodes to a theoretical study of possible interface instability phenomena during electrochemically-driven ion intercalation into battery storage compounds and their implications for battery performance.
- 2) Develop a multi-particle phase-field model to investigate the effect of particle interaction on the phase transition pathways in  $\text{LiFePO}_4$  composite electrodes.
- 3) Begin to model the phase transition behavior in  $\text{Li}(\text{Mn}_y\text{Fe}_{1-y})\text{PO}_4$  with comparison to in-situ synchrotron X-ray diffraction experiments conducted by MIT investigators.

#### References:

1. M. Tang, W.C. Carter and Y.-M. Chiang, *Annu. Rev. Mater. Res.* 40, 469 (2010).
2. M. Tang, W. C. Carter, J. F. Belak, Y.-M. Chiang, *Electrochim. Acta* 56, 769 (2010).
3. G. Y. Chen, X. Song, T. J. Richardson, *Electrochem. Solid-State Lett.* 9, A295 (2006).
4. M. Tang, J. F. Belak, M. R. Milo, *J. Phys. Chem. C* 115, 4922 (2011).
5. D. Morgan, A. Van der Ven, G. Ceder, *Electrochem. Solid-State Lett.* 7, A30 (2004).
6. M. Tang and A. Karma, *Phys. Rev. Lett.* 108, 265701 (2012).
7. R. Malik, D. Burch, M. Bazant, G. Ceder, *Nano Lett.* 10, 4123 (2010).
8. D. A. Cogswell and M. Z. Bazant, *ACS Nano* 6, 2215 (2012).

#### Publications of DOE sponsored research in 2010-2012:

1. M. Tang, W.C. Carter and Y.-M. Chiang, “Electrochemically Driven Phase Transitions in Insertion Electrodes for Lithium-ion Batteries: Examples in Lithium Metal Phosphate Olivines”, *Annu. Rev. Mater. Res.* 40, 469 (2010).
2. M. Tang, W. C. Carter, J. F. Belak, Y.-M. Chiang, “Competing Phase Transition Pathways in Nanoscale Olivine Electrodes”, *Electrochim. Acta* 56, 769 (2010).
3. Y.-H. Kao, M. Tang, N. Meethong, J. Bai, W.C. Carter, Y.-M. Chiang, “Overpotential-Dependent Phase Transformation Pathways in Lithium Iron Phosphate Battery Electrodes”, *Chem. Mater.* 22, 5845 (2010).
4. M. Tang, J. F. Belak, M. R. Milo, “Anisotropic Phase Boundary Morphology in Nanoscale Olivine Electrode Particles”, *J. Phys. Chem. C* 115, 4922 (2011).
5. M. Tang and A. Karma, “Surface modes of Coherent Spinodal Decomposition”, *Phys. Rev. Lett.* 108, 265701 (2012).
6. M. Tang, B. W. Reed, M. Kumar, “Coarsening Kinetics of Topologically Highly Correlated Grain Boundary Networks”, *J. Appl. Phys.* 112, 043505 (2012).
7. M. Tang and W. C. Carter, “Branching Mechanisms in Surfactant Micelle Growth”, *J. Phys. Chem. B*, DOI:10.1021/jp309204t.

**Program Title:** Thermodynamic, Kinetic and Electrochemical Studies on Mixed Proton, Oxygen Ion, and Electron (Hole) Conductors  
DE-FG02-03ER46086  
PI: Prof. Anil V. Virkar  
University of Utah  
Email: [anil.virkar@utah.edu](mailto:anil.virkar@utah.edu)  
Phone: (801) 581-5396

**Program Scope or Definition:**

The goal of this project is to investigate multi-species transport in predominantly ion-conducting membranes, both theoretically and experimentally. While the primary materials selected are mixed proton, oxygen ion, and electron (hole) conductors, the results of this study are applicable to virtually all electrochemical systems. The selected materials are electrolytes for fuel cells, electrolyzers, batteries. Transport is examined in the general framework of non-equilibrium thermodynamics. A key feature of our work is the analysis of transport in which thermodynamic forces are expressed as functions of thermodynamic fluxes. This allows the determination of the chemical potentials of electrically neutral species in terms of the fluxes of electrically charged species. The significance is that although the chemical potentials cannot be easily measured, the fluxes of electrically charged species can be measured as electrical currents. The approach affords the determination of the chemical potentials of hydrogen or oxygen in fuel cell membranes; or of lithium in lithium-ion battery separators, in terms of experimentally measureable parameters; currents, voltages, transport parameters. Within the framework of linear non-equilibrium thermodynamics (Onsager equations), the analysis shows that whether or not the chemical potentials of electrically neutral species in the membrane are bounded by values at the electrodes is governed by the relative directions of electric currents (coulombs/second) in the membrane due to the transport the ionic species and the electronic species (electrons and/or holes). If the electric currents due to the ionic and the electronic species are parallel, the chemical potentials in the membrane can exceed electrode bounds. Should this occur, the membrane and the electrochemical device can degrade, and fail. The results explain why fuel cells, electrolyzers, lithium-ion batteries degrade – and under what conditions. Experimental verification of the analysis is achieved by the measurement of local thermodynamics using embedded probes in systems that are not in global thermodynamic equilibrium. The long-term impact of this work may lead to the development of degradation-resistant automotive batteries and hydrogen fuel cells – central to the development of the next generation of ‘clean’ energy technologies.

**Recent Progress: Why batteries, fuel cells fail?**

It is well known that batteries and fuel cells degrade or fail. In the case of batteries, failure is much more dramatic as fuel and oxidant are in close proximity separated by a thin membrane. Figure 1 shows photographs of a fire in a laptop Li-ion battery and a fire

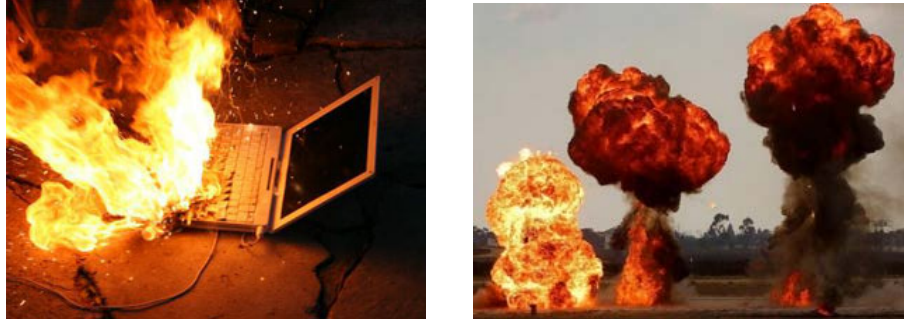


*Figure 1: (a) Laptop on fire because of a Li-ion battery failure. (b) NGK's Na-S several MW-class battery explosion and a fire in September 2011 in Tsukuba, Japan. Both photographs are taken from the internet.*

in a several MW-class Na-S battery. Recent grounding of Boeing 787 is a vivid reminder of issues related to battery failures. While there are many reasons for failures of electrochemical devices and many engineering solutions (e.g. cell balancing) are being sought, there is a fundamental scientific reason for their failures which is deeply rooted in non-equilibrium thermodynamics and transport. The focus of our work is on understanding the *science* behind such failures and eventually on developing novel materials and systems which will be resistant to such failures.

The focus of our work is on linear non-equilibrium thermodynamics and transport. Onsager equations form the fundamental basis of coupled transport. Much of the literature is on transport through fluids or membranes under chemical potential gradients. Our work is on transport in electrochemical systems (membranes) wherein coupling among the apparent fluxes of electrically neutral species occurs due to the application of the electro-neutrality condition on the actually transporting electrically charged species. Also, much of the literature is given with fluxes as dependent variables and thermodynamic driving forces (gradients in chemical potentials) as independent variables. In our approach, the transport equations are inverted so that fluxes are the independent variables and thermodynamic forces are the dependent variables. Upon integration, one can obtain the chemical potentials in terms of the fluxes, namely

$$\mu_i(\vec{r}) - \mu_i(\vec{r}_o) = \Delta\mu_i(\vec{r}, \vec{r}_o) = - \int_{\vec{r}_o}^{\vec{r}} \sum_k R_{ik} \vec{J}_k \cdot d\vec{r} \quad (1)$$

in which  $\vec{J}_k$  is the flux of  $k$ ,  $\mu_i$  is the chemical potential of species  $i$ ,  $\vec{r}$  is the position vector, and  $R_{ik}$  is the inverse Onsager cross coefficient. If for  $i \neq k$ ,  $R_{ik} \neq 0$ , then the fluxes are coupled. This formalism also allows us to obtain the chemical potentials of electrically neutral species (e.g.  $\mu_{O_2}$  in a solid oxide fuel cell or a solid oxide electrolyzer cell membrane or  $\mu_{Li}$  in a Li-ion battery electrolyte) in terms of the fluxes of electrically charged species (e.g.  $j_{O^{2-}}$  in a solid oxide fuel cell and  $j_{Li^+}$  in a Li-ion battery). If the  $\mu_{O_2}$  inside the dense membrane becomes too high, electrolyte cracking or electrode delamination will occur leading to failure of fuel cell/electrolyzer. Indeed, recent work has experimentally shown that the  $\mu_{O_2}$  can lie out of electrode bounds. If  $\mu_{Li}$  in a Li-ion battery separator or  $\mu_{Na}$  in Na-ion conducting solid electrolyte in a Na-S battery becomes

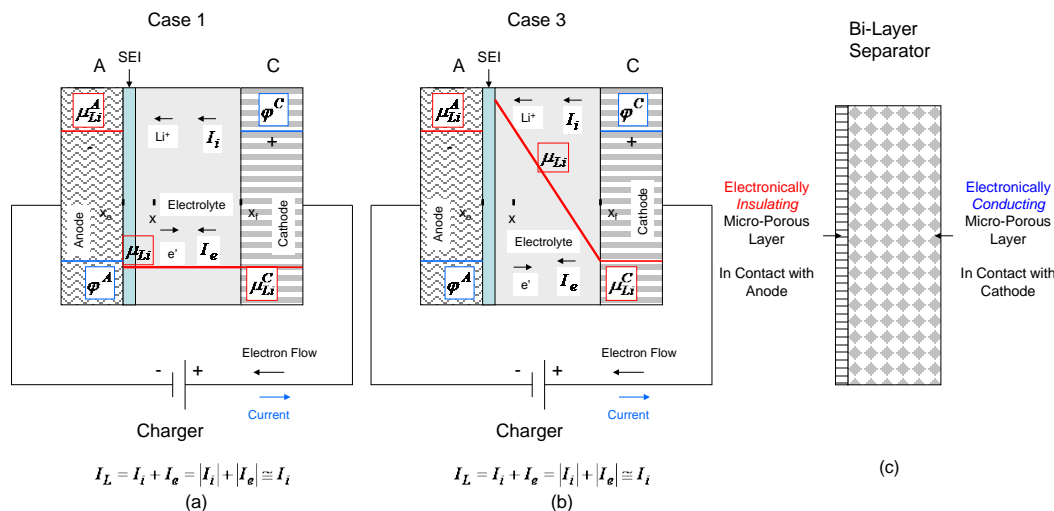


**Figure 2:** Chemical potential of Li in a Li-ion cell during charging: (a) Case 1: The SEI layer has negligible electronic conductivity. The  $\mu_{Li}$  (red line) in the electrolyte remains low. No dendrite formation, and no failure. (b) Case 3: The SEI layer has a relatively high electronic conductivity. The  $\mu_{Li}$  is high and can exceed the value in the anode. Li-dendrite and internal short is likely, leading to fires. (c) The  $\mu_{Li}$  can be maintained low if the separator is a bi-layer structure. Details are described in the paper (4) listed here.

too high, Li or Na dendrites can form which cause internal shorts leading to rapid chemical reactions and fires (Figure 1). We are able to describe the occurrence of these situations in terms of transport properties (ionic and electronic conductivities of the membranes), the kinetics of electrode reactions (exchange current densities), and the operating conditions (magnitudes and directions of fluxes; charging or discharging) in terms of the Onsager transport equations. In what follows, we give two representative examples of our approach as applied to Li-ion battery and reversible fuel cells (which can be operated as both fuel cells and as electrolyzers) and some key results.

**Lithium-Ion Battery:** Our theoretical analysis has identified that thermodynamic instabilities can occur during charging. By suitably choosing electrolyte/separator composition, it is in principle possible to modify properties of the SEI layer and of the electrolyte separator so that propensity to battery failures is drastically lowered. Specifically, we have shown that a bi-layer porous separator (in which electrolyte is impregnated) with one layer being a good electronic conductor and the other layer being a good electronic insulator should greatly lower the tendency for degradation (Figure 2).

**Reversible Fuel Cells:** We have examined transport in mixed proton, oxygen ion, and electron/hole conductors. Such membranes are candidates as electrolytes for fuel cells and electrolyzers. We have analyzed transport through such membranes within the framework of the Onsager transport theory. A key result is that Onsager reciprocity relations are always satisfied. In either the electrolyzer mode or the driven fuel cell mode (a phenomenon which occurs in batteries and fuel cell stacks), the chemical potentials of neutral species are not bounded by the electrode values. This is the source of thermodynamic instabilities leading to device failures. The cell performance can be described in four quadrant plots. Thermodynamic instabilities occur in quadrant 2

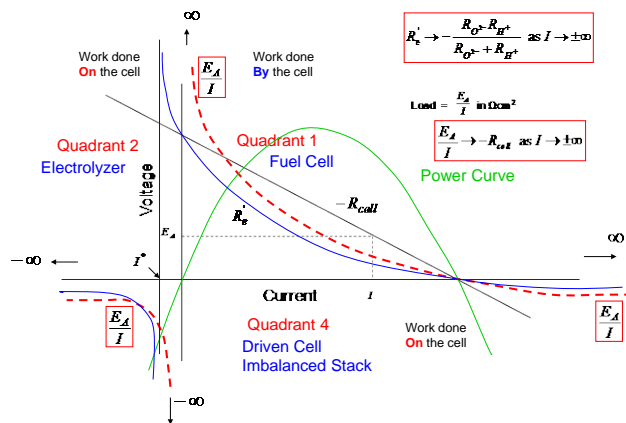


Figure 3: Cell behavior described in three of four quadrants. Details are given in the published paper (5) listed here.

(electrolyzer mode) and quadrant 4 (driven cell mode – cell imbalance). Figure 3 shows key features of the results.

**Future Plans:** Future plans are described below in a bullet form.

- 1) To theoretically analyze transport in fuel cells and Li-ion batteries. The analysis will be extended to transient cases, which is necessary to determine the rates (kinetics) at which thermodynamic instabilities occur.
- 2) To measure local thermodynamics within the electrolytes of fuel cells and batteries.
- 3) To measure Onsager coefficients in electrochemical systems; to relate them to fundamental transport properties (ionic and electronic conductivities) and electrocatalytic properties (exchange current densities).

**References to publications that have appeared in 2010-2012 or that have been accepted for publication:**

- 1) P. Parthasarathy and A. V. Virkar, “Electrochemical Coarsening of Copper Powder in Aqueous Media”, *J. Electrochem. Soc.*, **157** (5) B768-B775 (2010).
- 2) A. V. Virkar, F. F. Lange and M. A. Homel, “A simple analysis of current collection in tubular solid oxide fuel cells”, *J. Power Sources*, **195** 4816-4825 (2010).
- 3) J. H. Wright and A. V. Virkar, “Conductivity of porous Sm<sub>2</sub>O<sub>3</sub>-doped CeO<sub>2</sub> as a function of temperature and oxygen partial pressure”, *J. Power Sources*, **196** 6118-6124 (2011).
- 4) A. V. Virkar, “A model for degradation of electrochemical devices based on linear non-equilibrium thermodynamics and its application to lithium ion batteries”, *J. Power Sources*, **196** 5970-5984 (2011).
- 5) A. V. Virkar, “Transport through mixed proton, oxygen ion and electron/hole conductors: Analysis of fuel cells and electrolyzer cells using Onsager equations”, *Int. J. Hydrogen Energy*, **37** 12609-12628 (2012).
- 6) P. Parthasarathy and A. V. Virkar, “Electrochemical Ostwald ripening of Pt and Ag catalysts supported on carbon”, *J. Power Sources*, **234** 82-90 (2013).
- 7) J. Wright, A. V. Virkar, Q. Liu and F. Chen, “Electrical Characterization and Water Sensitivity of Sr<sub>2</sub>Fe<sub>1.5</sub>Mo<sub>0.5</sub>O<sub>6-δ</sub> as a Possible Solid Oxide Fuel Cell Electrode”, *J. Power Sources*, in-press (2013).

## Program Title: Nanocrystal-Based Dyads for Solar to Electric Energy Conversion

Principal Investigator: David Waldeck

Institution: University of Pittsburgh

Address: 219 Parkman Avenue, Pittsburgh PA 15260 USA

Email: dave@pitt.edu

Collaboration: D. N. Beratan, Duke University, and Ron Naaman, Weizmann Institute of Science.

### 1. Program Scope

We are exploring inorganic-organic hybrid materials that promise to provide a systematic and modular approach to creating a new generation of solar energy conversion devices. Figure 1 illustrates features of a device architecture that can be produced by self-assembly processes, in which the surface ligands of a semiconductor nanoparticle (NP) direct the NP to polymer interfaces in a bulk heterojunction material, and uses a modular set of nanomaterial components, so that each one can be optimized separately. While much is known about the properties of nanoparticles and conjugated polymers as separate entities, much less is known concerning their property evolution as they assemble into functional structures. For example, the charge transfer efficiency of any photo-electric device depends critically on the energy level alignment of its components, relative to each other and relative to the system's Fermi-level. In the past few years, our team has experimentally and computationally explored the important NP-ligand interactions and NP-electrode interactions, and we have used that knowledge to control energy level placements. Progress on this front is described in the section 'Recent Progress', and it enables us to move the research effort into a new phase in which we will explore how to create NP/NP interfaces and NP/polymer interfaces that enhance charge separation and inhibit charge recombination, (see the section 'Future Directions').

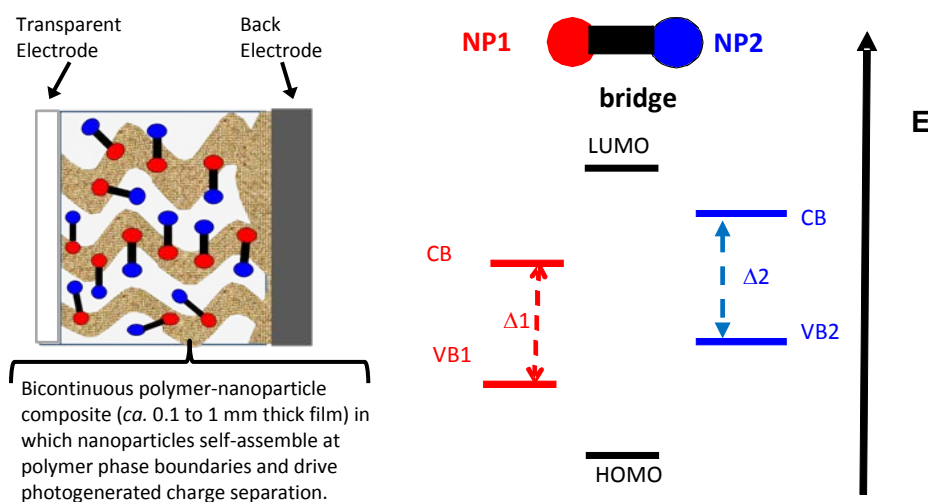


**Figure 1** The left panel illustrates a bulk heterojunction solar cell device architecture in which sets of linked nanoparticles act as *p-n* junctions with a tunable band gap. The panel on the right shows the intended band alignment for the nanoparticles.

### 2. Recent Progress

While the energy level structure of inorganic nanoparticles is known to depend on composition and physical size, the importance of the organic ligand shell and the local environment of the nanoparticle on its electronic energy levels are less appreciated. During the past few years, our research team has used computational and experimental methods to explore how the ligand shell affects a nanoparticle's energy-

level structure and how the interaction of the nanoparticle's ligand shell with an electrode affects its electronic energy level position. In addition to these fundamental studies, we have shown how this knowledge can be used to improve the design and performance of model photovoltaic devices and photoelectrochemical cells.

**Ligand effect on Nanoparticle Energetics.** We performed systematic DFT (B3LYP/Lan12dz) studies of the structural and electronic properties of  $\text{Cd}_n\text{Se}_n/\text{Cd}_n\text{Te}_n$  nanoparticles ( $n = 6, 9$ ), both bare and capped with amino, thiol, or phosphine oxide ligands (see [2, 5]). For  $-\text{OPH}_3$  and  $-\text{SCH}_3$  ligated NPs, changes in both the ligand structure (proton transfer either to NP atoms or to other ligands) and in the NP structure (bridge formation between NP atoms, breakage of Cd-Se/Cd-Te bonds, and opening of nanoparticles) were observed in the energy minimized structures, indicating the strong interplay between surface chemistry and NP structure.  $\text{NH}_3$  and  $\text{OPH}_3$  ligands cause HOMO/LUMO energy destabilization in capped NPs, which is more pronounced for the LUMOs than for the HOMOs. Orbital destabilization drastically reduces both the vertical ionization potential (IP) and the vertical electron affinity of the NPs, as compared to the bare species. For  $-\text{SCH}_3$  capped  $\text{Cd}_6\text{X}_6$  NPs, the formation of expanded structures was found to be preferable to crystal-like structures (see Fig 2).  $\text{SCH}_3$  groups destabilize the HOMOs and stabilize the LUMOs, which indicates a reduction of the IP of the capped NPs, as compared to the bare species. For the  $\text{Cd}_9\text{X}_9$  NPs, similar trends in stabilization/destabilization of frontier orbitals were observed in comparison with the capped  $\text{Cd}_6\text{X}_6$  species. The  $-\text{NH}_3$  and  $-\text{OPH}_3$  groups perturb the  $\text{Cd}_6\text{X}_6$  structures, but not very strongly (Fig. 2).

In parallel with this computational effort, we have used differential pulse voltammetry to examine the nanoparticle energetics as a function of the ligand coating for CdSe and CdTe. In particular, we have compared phosphonate, thiol, and amine groups to bind an organic phenyl group to the surface of the NP, and we find that we can systematically tune the HOMO (and correspondingly the LUMO) energy positions over a 0.4 eV range. The plots in Figure 3 show the HOMO and LUMO energy positions as a function of the NP size that we determined for the three different ligands (PPA is phenylphosphonate, TP is thiophenyl, and An is aniline). The HOMO positions were determined directly from the onset of the

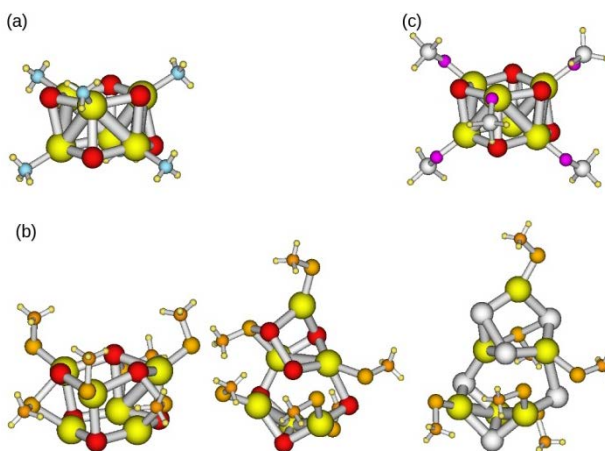


**Figure 2.** Structures of  $\text{Cd}_6\text{X}_6(\text{NH}_3)_6$  (a),  $\text{Cd}_6\text{X}_6(\text{SCH}_3)_6$  (b) ( $\text{Cd}_6\text{Se}_6(\text{SCH}_3)_6$  ‘closed’ and ‘open’, left and center, and  $\text{Cd}_6\text{Te}_6(\text{SCH}_3)_6$  ‘open’, right), and  $\text{Cd}_6\text{X}_6(\text{OPH}_3)_6$  (c).

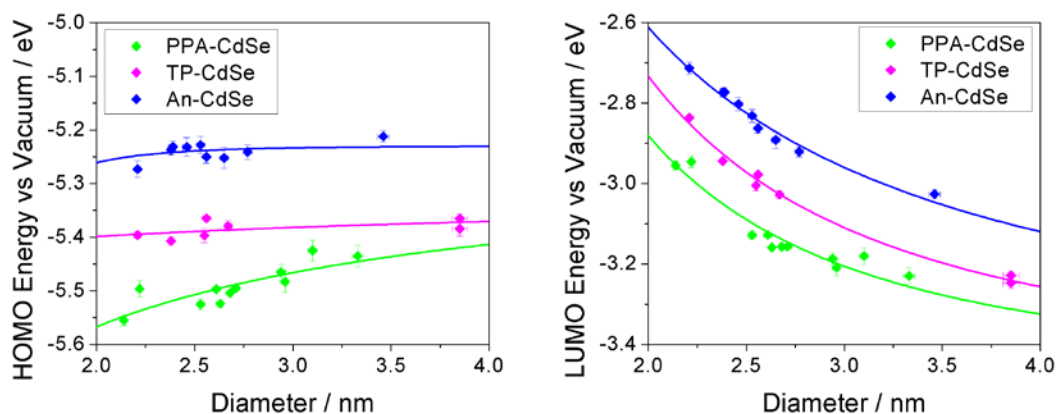


**Figure 3.** HOMO (left) and LUMO (right) positions of PPA (green), TP (magenta) and An (blue) capped NPs as a function of size. The solid curves represent power law fittings for each capping ligand.

oxidation wave in the voltammetry measurements, whereas the LUMO positions were determined by combining measurements of the optical bandgap with the HOMO position. This procedure gave good agreement with photoemission experiments in a related study [see reference 3 and Figure 4]. These data show that the nature of the chemical linkage between the capping ligand and the nanoparticle has a significant impact on the energetics, in agreement with the computational studies. This work is currently being prepared for publication.

**Fermi Level Pinning.** We have quantified the electronic energy level positions of nanoparticles when they are assembled onto electrodes with thiol linkers. Assemblies of CdSe NPs and CdTe NPs on a dithiol coated Au electrode were created, and their electronic energetics were characterized (see Figure 4) using cyclic voltammetry in an electrochemical cell and by photoemission spectroscopy *in vacuo* [3,7]. When placed on a common energy scale (by way of the 4.44 V absolute electrode potential), these data are found to be in excellent agreement. Importantly the HOMO energy of the NPs, when attached to the surface via thiol linkers, is ‘pinned’ (for sizes greater than 2.3 nm its energy does not vary). Although both the CdSe and the CdTe nanoparticles are each Fermi level pinned, the data show that they are pinned at different energies.

**Importance of the Energy Gradient.** We used our knowledge of the energy level alignment in the CdSe and CdTe NPs to examine how the energy offset between the NPs affects the charge transfer. To this end, we created organized bilayer assemblies of CdTe and CdSe nanoparticles for electrochemical systems and for solid-state photovoltaic devices. We controlled the energy level alignment by manipulating the NP size and linking the CdTe and CdSe NPs through dithiol molecules, and we combined this capability with control over the NPs spatial arrangement, either by sequential self-assembly onto an Au working electrode of an electrochemical cell or by sequential spin-coating onto an ITO substrate to create a photovoltaic (PV) device. A comparison of the photocurrent for the two cases shows that arranging the spatial and energetic hierarchy of the assemblies accounts for a factor of 75 in the maximum power output of the PV device (see [7] for details). This simple bilayer device shows how to exploit Fermi level pinning to create a multicomponent and hierarchically-structured device that collects light energy over a broad spectrum and converts it to separated charges.

### 3. Future Directions

We are examining the energy and charge transfer properties of nanoparticle/nanoparticle (NP/NP) and nanoparticle conjugated polymer (NP/CP) interfaces in order to promote the forward charge transfer and inhibit charge recombination. We will use model systems with CdSe and CdTe NPs and four different conjugated polymer (polyphenylvinylene (PPV), a donor-acceptor copolymer PDPPPV, polythiophene, and chiral polythiophene) materials. We are investigating how to use energy-level gradients, built-in electrostatic potentials, and symmetry/chirality properties to improve the charge-separation efficiency at the NP/NP and NP/CP interfaces. Our previous work shows the importance of the energy level offset at an NP/NP interface [7], and we are extending this work to the study of NP/CP interfaces and to trilayer structures in which we will tune and optimize the energy band offsets (by the organic linker groups, see Fig 3). In a second thrust we are investigating how to use an internal electrostatic field to inhibit charge recombination at NP/NP and NP/CP interfaces. Our initial work for electrostatic NP/NP aggregates in

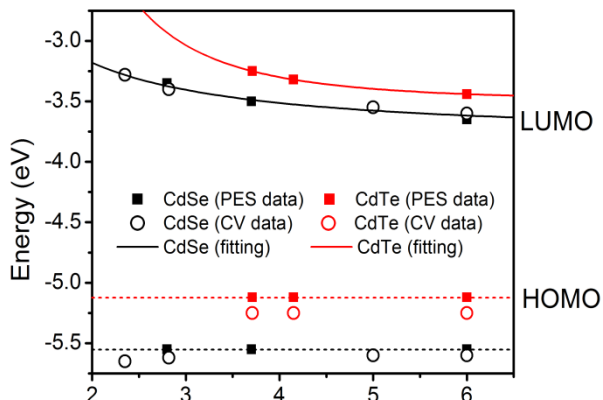


**Figure 4:** This figure shows the energetics for CdSe NPs (data in black) and CdTe NPs (data in red) that are immobilized onto a gold electrode by dithiol linkers. The filled squares are results from photoemission spectroscopy (PES) measurements, and the open circles are from cyclic voltammetry (CV) measurements. The dashed lines are the HOMO pinning level determined from PES; and the solid lines are the fitting to the LUMO energies.

solution [12] is being extended to include NP/CP interfaces and to allow for variation of the electrostatic field strength. In a third thrust we are exploring how to manipulate the electronic state's symmetry properties to inhibit charge recombination. In its initial phase, this work will build on recent results for chiral induced spin selectivity at chiral organic interfaces and exploit those symmetry constraints to enhance charge transfer efficiency.

#### 4. Publications for 2010 to 2012.

1. Chengyi Song, Yang Wang, and Nathaniel L. Rosi *Peptide-Directed Synthesis and Assembly of Hollow Spherical CoPt Nanoparticle Superstructures* *Angew. Chem. Int. Ed.* **52** (2013) ASAP.
2. Emmanuel Lim, Aleksey E. Kuznetsov, David N. Beratan. *Effects of S-containing Ligands on the Structures and Electronic Properties of Cd<sub>n</sub>Se<sub>n</sub>/Cd<sub>n</sub>Te<sub>n</sub> Nanoparticles (n=3, 4, 6, and 9)*. *Chemical Physics* **407** (2012) 97-109.
3. Y. Wang, Z. Xie, G. Gotesman, L. Wang, B.P. Bloom, T. Z. Markus, D. Oron, R. Naaman, and D. H. Waldeck *Determination of the Electronic Energetics of CdTe Nanoparticle Assemblies on Au Electrodes by Photoemission, Electrochemical, and Photocurrent Studies*. *J. Phys Chem C* **116** (2012) 17464-17472.
4. Gilad Gotesman, Rahamim Guliamov, and Ron Naaman, *Horizontal versus Vertical Charge and Energy Transfer in Hybrid Assemblies of Semiconductor Nanoparticles*, *Beilstein J. of Nanotechnology* **3** (2012) 629-636.
5. Aleksey E. Kuznetsov, Balamurugan Desinghu, Spiros S. Skourtis, David N. Beratan. *Structural and Electronic Properties of Bare and Capped Cd<sub>n</sub>Se<sub>n</sub>/Cd<sub>n</sub>Te<sub>n</sub> Nanoparticles (n = 6, 9)*. *J Phys Chem C* **116**, (2012) 6817-6830.
6. Zuoti Xie, Tal Z. Markus, Gilad Gotesman, Zvicka Deutsch, Dan Oron, Ron Naaman, *How isolated are the electronic states of the core in core/shell nanoparticles?*, *ACS Nano* **5** (2011) 863-869.
7. Y. Wang, L. Wang, and D. H. Waldeck *Electrochemically Guided Photovoltaic Devices: A Photocurrent Study of the Charge Transfer Directionality between CdTe and CdSe Nanoparticles* *J. Phys. Chem. C* **115** (2011) 18136-18141.
8. R. Naaman, *Molecular controlled nano-devices*, *Phys. Chem. Chem. Phys.*, **13** (2011) 3153.
9. Tal Z. Markus, Stella Itzhakov, Yafit Itzhaik Alkotzer, David Cahen, Gary Hodes, Dan Oron, Ron Naaman, *The Energetics of CdSe Quantum Dots Adsorbed on TiO<sub>2</sub>*, *J. Phys. Chem. C* **115** (2011) 13236–13241.
10. T. Aqua, H. Cohen, O. Sinai, V. Frydman, T. Bendikov, D. Krepel, O. Hod, L. Kronik, R. Naaman, *Role of Backbone Charge Rearrangement in the Bond-Dipole and Work Function of Molecular Monolayers*, *J. Phys. Chem. C*, **115** (2011) 24888–24892.
11. G. Gotesman and R. Naaman *Temperature-Dependent Coupling in Hybrid Structures of Nanoparticle Layers Linked by Organic Molecules* *J. Phys. Chem. Lett.* **1** (2010) 594-598.
12. M. Wu, P. Mukherjee, D. N. Lamont, and D. H. Waldeck *Electron Transfer and Fluorescence Quenching of Nanoparticle Assemblies* *J. Phys. Chem. C* **114** (2010) 5751-5759.

# Fundamental Piezotronic and Piezo-phototronic Effects in Nanowires

Zhong Lin Wang and Wenzhuo Wu

School of Materials Science and Engineering, Georgia Institute of Technology, Atlanta, GA 30332, (USA)

E-mail: [zhong.wang@mse.gatech.edu](mailto:zhong.wang@mse.gatech.edu)

## PROGRAM SCOPE

The goal of this project will be to investigate and utilize fundamental piezotronic and piezo-phototronic effects in nanowires for developing novel electromechanical devices and intelligently accessible interfaces between machine and human/environment.

Piezoelectricity is a phenomenon which produces electrical potential in the material upon variations of applied pressure/stress. The piezoelectric effect can be interpreted as the linear electromechanical coupling/interaction between mechanical and electrical state in materials which lack inversion symmetry. Piezoelectricity has been observed in a wide range of materials from ceramics, synthetic polymers to biological materials in response to applied mechanical stress. The most well-known piezoelectric material is Perovskite -structured  $\text{Pb}(\text{Zr}_x\text{Ti}_{1-x})\text{O}_3$  (PZT), which has numerous applications in electromechanical sensing, actuating and energy harvesting. PZT, however, is electrically-insulating and hence less useful for building electronic devices. In addition, the extremely brittle nature of ceramic PZT films and existence of lead impose issues such as reliability, durability and safety for long term sustainable operations and hinder its applications in areas such as biomedical devices. For Wurtzite-structured semiconductor materials lacking central symmetry, such as ZnO, GaN and InN, piezopotential is created in the crystal upon straining. For instance, Wurtzite ZnO crystal has a hexagonal structure with a large anisotropic property in  $c$ -axis direction and perpendicular to the  $c$ -axis. The  $\text{Zn}^{2+}$  cations and  $\text{O}^{2-}$  anions are tetrahedrally coordinated and the centers of the positive ions and negatives ions overlap with each other. If a stress is applied at an apex of the tetrahedron, the centers of the cations and anions are relatively displaced, inducing a dipole moment (Figure 1a). A constructive addition of all the dipole moments within all of the units in the crystal results in a macroscopic potential drop along the straining direction in the crystal. This is the piezoelectric potential (*piezopotential*) (Figure 1b)<sup>1</sup>.

Owing to the semiconducting and piezoelectric properties of these materials, strain-created inner-crystal piezopotential is capable of modulating characteristics of the contact formed between the NWs and the electrodes by modifying the height of local Schottky barrier and can hence serve as “gate voltage” to effectively modulate charge transport across metal-semiconductor interface or  $p$ - $n$  junction in as-fabricated devices. This is the *piezotronic* effect and electronic devices fabricated based on this general mechanism are *piezotronics*<sup>1-3</sup>. Additionally, *piezo-phototronic* effect is the tuning and controlling of charge carrier generation, separation or recombination at a  $p$ - $n$  junction by piezopotential, which can be used to effectively improve the performance of LEDs, solar cells, and photodetectors<sup>1-3</sup>. The above mechanism is different from the basic design of CMOS field effect transistor (FET) and has potential applications in force/pressure triggered/controlled electronic/optoelectronics devices, sensors, micro-electromechanical systems (MEMS), human-computer interfacing and nanorobotics. A better understanding of piezotronic effect can be obtained by comparing it with the fundamental concepts and device structures (Schottky barrier here) in conventional semiconductor physics (Figure 2).

It is well-known that transport of charge carriers across the Schottky barrier is sensitively dictated by the Schottky barrier height (SBH). Small amount of change in SBH can be reflected in the transport

characteristics of the device approximately through the exponential relation. It can therefore be seen from the band-diagrams shown in Figure 2 that piezopotential is able to effectively modulate the local contact characteristics through an internal field, depending on the crystallographic orientation of the piezoelectric semiconductor material and the polarity of the applied strain<sup>4</sup>. Consequently, the transport

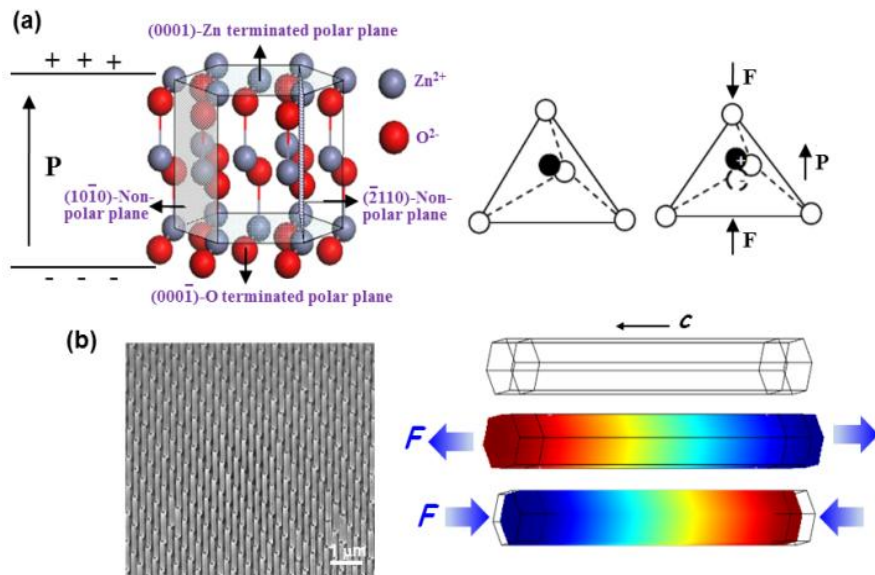
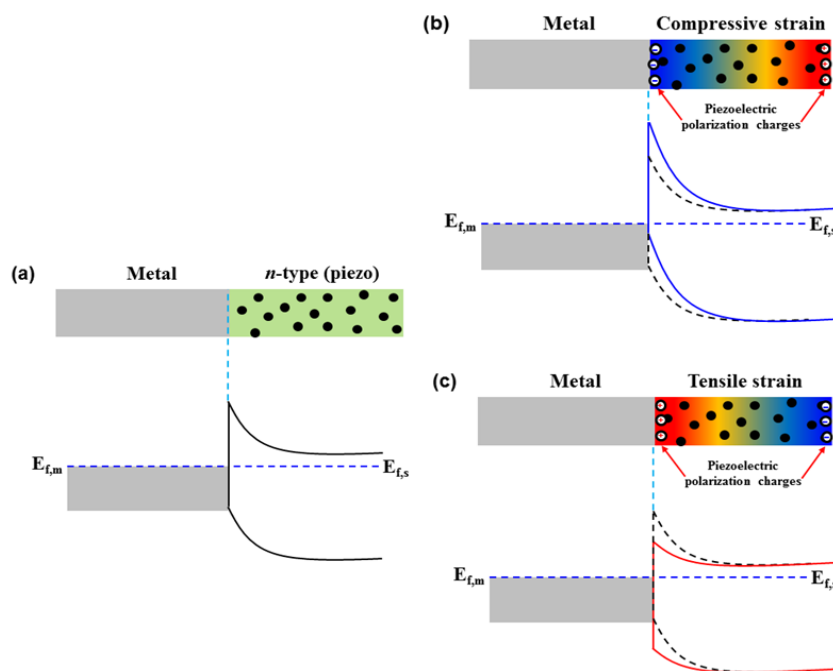


**Figure 1. Piezopotential in Wurtzite crystal.** (a) Atomic model of the Wurtzite-structured ZnO. (b) Left, large-scale aligned ZnO nanowire (NW) arrays by solution based hydrothermal approach<sup>5</sup>. Right, distribution of piezopotential along a ZnO NW under axial strain calculated by numerical methods. The growth direction of the NW is along *c*-axis. Color gradients represent the distribution of piezopotential.

of charge carriers across the contact can be effectively modulated by the piezoelectric polarization charges, or more specifically, the local contact characteristics can be tuned and controlled by varying the magnitude and polarity of externally applied strain. The modulation/gating of the charge transport across the interface by the strain-induced piezopotential is the core of piezotronics<sup>2-4</sup>. Similar discussions can also be applied to reveal the modulation effect of piezopotential on transport characteristics of *p-n* junctions.

**Figure 2. Energy diagram illustrating the effect of piezopotential on modulating the metal-semiconductor characteristics.** (a) Schottky barrier induced at the interface between metal and *n*-type piezoelectric semiconductor material, without strain applied. Black dots represent the free charge carriers in the bulk semiconductor. (b) With compressive strain applied, the negative piezoelectric polarization ionic charges induced near the interface (symbols with "-") increases the local SBH. (c) With tensile strain applied, the positive piezoelectric polarization ionic charges induced near the interface (symbols with "+") decreases the local SBH. Black dots represent the free charge carriers in the bulk semiconductor. The band diagrams for the M-S contact with and without the presence of piezotronic effect are shown using red solid and black dashed curves, respectively.



## RECENT PROGRESS

Much of the preliminary theoretical investigation for distribution of piezopotential and its modulation effect in electronic and optoelectronic processes have been developed by our group since 2010<sup>4,6</sup>. Central to this research are 1D Wurtzite-structured semiconductor nanomaterials, with enhanced piezoelectric and mechanical properties compared to their bulk counterparts, which are crucial for investigating piezotronic/piezo-phototronic effect and developing devices with characteristics such as superior sensitivity and responsivity. Our group has demonstrated the reproducible synthesis of 1D Wurtzite-structured ZnO nanowires with controlled morphology/properties, either in free-standing or ordered array form<sup>5</sup>.

In addition to the investigations in theory development and material synthesis, we have thus far successfully utilized the piezotronic/piezo-phototronic effects for various application purposes and demonstrated strain-gated piezotronic transistor of which the transport characteristics can be modulated by external mechanical strain<sup>7</sup>, strain-modulated piezotronic resistive memory which can record and store the information of applied strain for later access<sup>8</sup>, nanowire based biochemical sensors with enhanced sensitivity by piezotronic effect<sup>9,10</sup> and nanowire-based optoelectronics devices such as solar cells, photodetectors and LEDs with enhanced performance by piezopotential due to piezo-phototronic effect<sup>11-15</sup>. The modulation/control effect of piezopotential in electrochemical process has also been investigated<sup>16</sup>. We have also extended the investigations of piezotronic/piezo-phototronic effects to systems based on other inorganic material such as GaN, CdS and CdSe<sup>17,18 19,20</sup> as well as organic materials based devices<sup>11,15</sup>.

## FUTURE PLANS

Based on the progress our group has made in investigating and utilizing piezotronic/piezo-phototronic effects in nanowires, we intend to develop and modify more sophisticated theoretical framework along with experimental work. In the next period, we envision investigating piezotronic/piezo-phototronic effect in nanowire-based electronic, optoelectronic and electrochemical devices as well as array-based devices for more profound understanding and utilization of piezotronic/piezo-phototronic effects. We also intend to implement large-scale array piezotronic/piezo-phototronic systems.

In these proposed experiments, we will investigate and utilize the fundamentals and modulation effect of piezopotential in electronic, optoelectronic and electrochemical devices by controllably introducing strain and monitoring the change in performance of these devices. We will also extend current understanding/concept of piezotronics/piezo-phototronics, obtained from single-nanowire-based-devices, to functional devices based on large-scale ordered array. The long-term impact of this work will be to develop nanowire-based piezotronic/piezo-phototronic devices for sensing, intelligent micro/nano-systems and human-electronics interfacing.

## ACKNOWLEDGEMENT

The research was supported by U.S. Department of Energy, Office of Basic Energy Sciences.

## REFERENCES

- 1 Wang, Z. L. Piezopotential gated nanowire devices: Piezotronics and piezo-phototronics. **Nano Today** **5**, 540-552, (2010).
- 2 Wang, Z. L. Progress in Piezotronics and Piezo-Phototronics. **Adv. Mater.** **24**, 4632-4646, (2012).
- 3 Wang, Z. L. From nanogenerators to piezotronics-A decade-long study of ZnO nanostructures. **MRS Bull.** **37**, 814-827, (2012).
- 4 Zhang, Y., Liu, Y. & Wang, Z. L. Fundamental Theory of Piezotronics. **Adv. Mater.** **23**, 3004-3013, (2011).
- 5 Wei, Y. G. *et al.* Wafer-Scale High-Throughput Ordered Growth of Vertically Aligned ZnO Nanowire Arrays. **Nano Lett.** **10**, 3414-3419, (2010).
- 6 Zhang, Y. & Wang, Z. L. Theory of Piezo-Phototronics for Light-Emitting Diodes. **Adv. Mater.** **24**, 4712-4718, (2012).
- 7 Wu, W. Z., Wei, Y. G. & Wang, Z. L. Strain-Gated Piezotronic Logic Nanodevices. **Adv. Mater.** **22**, 4711-4715, (2010).
- 8 Wu, W. Z. & Wang, Z. L. Piezotronic Nanowire-Based Resistive Switches As Programmable Electromechanical Memories. **Nano Lett.** **11**, 2779-2785, (2011).
- 9 Yu, R. M., Pan, C. F. & Wang, Z. L. High performance of ZnO nanowire protein sensors enhanced by the piezotronic effect. **Energ. Environ. Sci.**, DOI: 10.1039/c2ee23718k (2012).
- 10 Pan, C. F., Yu, R. M., Niu, S. M., Zhu, G. & Wang, Z. L. Piezotronic Effect on the Sensitivity and Signal Level of Schottky Contacted Proactive Micro/Nanowire Nanosensors. **ACS Nano**, DOI: 10.1021/nn306007p (2013).
- 11 Yang, Y. *et al.* Piezotronic Effect on the Output Voltage of P3HT/ZnO Micro/Nanowire Heterojunction Solar Cells. **Nano Lett.** **11**, 4812-4817, (2011).
- 12 Yang, Q. *et al.* Enhancing Sensitivity of a Single ZnO Micro-/Nanowire Photodetector by Piezo-phototronic Effect. **ACS Nano** **4**, 6285-6291, (2010).
- 13 Yang, Q., Wang, W. H., Xu, S. & Wang, Z. L. Enhancing Light Emission of ZnO Microwire-Based Diodes by Piezo-Phototronic Effect. **Nano Lett.** **11**, 4012-4017, (2011).
- 14 Liu, Y., Yang, Q., Zhang, Y., Yang, Z. Y. & Wang, Z. L. Nanowire Piezo-phototronic Photodetector: Theory and Experimental Design. **Adv. Mater.** **24**, 1410-1417, (2012).
- 15 Yang, Q. *et al.* Largely Enhanced Efficiency in ZnO Nanowire/p-Polymer Hybridized Inorganic/Organic Ultraviolet Light-Emitting Diode by Piezo-Phototronic Effect. **Nano Lett.**, DOI: 10.1021/nl304163n (2013).
- 16 Xue, X. Y., Wang, S. H., Guo, W. X., Zhang, Y. & Wang, Z. L. Hybridizing Energy Conversion and Storage in a Mechanical-to-Electrochemical Process for Self-Charging Power Cell. **Nano Lett.** **12**, 5048-5054, (2012).
- 17 Dong, L. *et al.* Piezo-Phototronic Effect of CdSe Nanowires. **Adv. Mater.** **24**, 5470-5475, (2012).
- 18 Pan, C. F. *et al.* Enhanced Cu<sub>2</sub>S/CdS Coaxial Nanowire Solar Cells by Piezo-Phototronic Effect. **Nano Lett.** **12**, 3302-3307, (2012).
- 19 Yu, R. M. *et al.* Piezotronic Effect on the Transport Properties of GaN Nanobelts for Active Flexible Electronics. **Adv. Mater.** **24**, 3532-3537, (2012).
- 20 Hu, Y. F. *et al.* Piezo-Phototronic Effect on Electroluminescence Properties of p-Type GaN Thin Films. **Nano Lett.** **12**, 3851-3856, (2012).

Program Title: Synthesis and characterization of nanomaterial heterostructures and assemblies: investigation of charge and energy flow at nanostructured interfaces.

Principal Investigators: Stanislaus S. Wong and James A. Misewich, Brookhaven National Laboratory, CMPMSD Department, Building 480, Upton, NY 11973-5000; Email: [sswong@bnl.gov](mailto:sswong@bnl.gov); [misewich@bnl.gov](mailto:misewich@bnl.gov)

Collaborators: M.Y. Sfeir, R.M. Konik, Y. Zhu (BNL), J. Appenzeller (Purdue)

Program Scope: The ability to synthesize, functionalize, and purify nanomaterials and to understand their transport, optical and mechanical properties lies at the forefront of current materials science research and the foundation of rigorous device development. As highlighted in the DOE reports on Basic Research Needs for Solar Energy Utilization and for Solid-State Lighting, nanostructured materials offer several potential advantages for meeting the energy challenges in these areas by providing for relatively high electron and hole transport efficiencies, excitation multiplication possibilities, high surface-to-volume ratios, and short electron-hole diffusion lengths to junctions. Although it is tempting to combine distinctive nanomaterial components for solar conversion in order to take advantage of such attractive qualities, the fundamental role of nanoscale interfaces and heterojunctions in controlling charge and energy flow is not well understood and it is expected that junctions and interfaces between low dimensional materials will behave differently as compared with bulk junctions and interfaces. In order to develop an understanding of charge and energy flow at the interfaces of nanostructured materials and nanomaterial assemblies, we will investigate a key model system, namely the interface between a quantum dot (QD) and a quantum wire (such as a double-walled carbon nanotube (DWNT)) in a heterostructure configuration. We will address the important question of the efficiency of charge separation versus recombination. Furthermore, we will investigate the ability of nanomaterial assemblies to enhance optoelectronic properties of nanoscale components in order to advance their incorporation into functional device configurations. Complementary theoretical studies will help to clarify the role of interfaces and heterojunctions in heterostructured nanomaterial assemblies.

The overarching question that we seek to address in this work can be summarized as follows: *Can we design and synthesize well-controlled complex quantum-confined nanostructures so that we can manipulate the energy flow and charge transfer pathways in these materials in order to optimize not only the absorption of photons but also exciton harvesting for the production of useful work?*

In order to answer this question for our model system, we have undertaken a systematic series of studies wherein model nanomaterials are being synthesized and characterized structurally with their ensemble bulk optical properties determined. In addition, we will be providing insight into the transport and optoelectronic properties of these materials. Therefore, studies will be carried out on well-characterized individual materials in test structures where optoelectronic and transport properties are determined by making contact with the quantum wires. In effect, correlating the optical, transport, and opto-electronic properties with the structural characterization of the nanomaterial composite structures will allow us to unravel how competing pathways depend on the

nanomaterial composite synthesis parameters, such as the QD-DWNT linker length and the chemical composition of the ligand field around the QD.

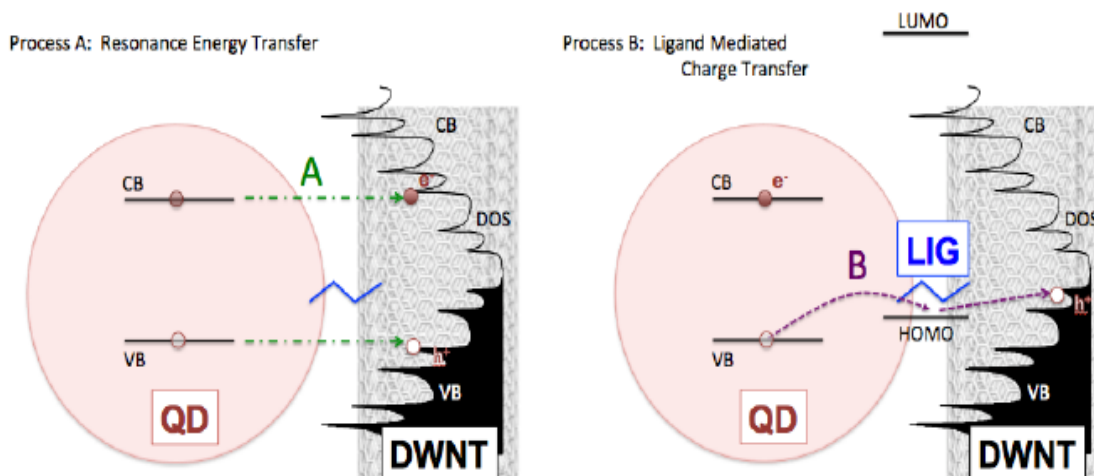


**Figure 1.** Schematic of energy and charge flow processes in ternary QD-LIGAND-DWNT heterostructures. In process A, both the photoexcited electron and hole are transferred simultaneously via near-field energy transfer. The ligand is a structural element only. In process B, the ligand is electronically active and functions to trap one of the carriers at the surface of the QD and tunneling (charge transfer) becomes the dominant kinetic interaction.

#### Recent Progress:

Promise for manipulating energy flow and charge transfer pathways is suggested in our previous studies of the optoelectronic properties of individual carbon nanotubes (CNTs). We have shown that the properties of the assembled 0D-1D composite system are different from and potentially better than the simple sum of its parts. A significant observation from our lab is the formation of a long-lived charge-separated state within DWNT-CdSe heterostructures, as illustrated by process B in Figure 1. This manifests itself as a significant quenching of the luminescence emission from the QD when in close spatial proximity to the CNT in conjunction with an *increase* in the photoluminescence lifetime. We have shown that only emission from a charged QD is consistent with this experimental observation, using kinetic models along with studies of surface termination effects. For example, by utilizing thin passivating shells to turn off the chemical interaction of the outer ligand with the CdSe core, we have been able to switch the primary electronic interaction from charge to resonance energy transfer (process A in Fig. 1). In this scenario, we observe quenching and a shortening of the emission lifetime. We believe that this charge transfer process is induced by hole-trapping ligands at the surface of the CdSe together with fast interfacial tunneling to a DWNT. A high coverage of aminoethanethiol molecules on the surface of the CdSe ensured not only the high efficiency of the trapping process but also the high statistical probability that one particular type of charge carrier localizes near the interface. This evidence for charge separation illustrates a potentially useful pathway that the proposed work aims to understand and optimize. For example, if process B illustrated in Figure 1 could be scaled up and generalized, such 0d-1d materials could become relevant and useful as alternative solar cell architectures to bulk heterojunction solar cells to improve overall efficiencies.

Nevertheless, as this DOE project was very recently funded and only began in September 2012, we have been working on a number of research tasks designed to address the key scientific issues posed in the program scope. We are learning to synthesize such 0d-1d heterostructures with reproducible control over important heterostructure design parameters such as: chemical composition, size, and shape of the nanoscale components, QD-CNT separation, and density of QD functionalization on CNTs. The experimental characterization tasks include an exploration of the absorption, photoluminescence, and time-resolved photoluminescence in ensembles of dispersed nanomaterial samples. Such ensemble studies will provide the fastest feedback to the synthesis team on promising materials. In order to elucidate the detailed pathways in the most promising material samples, we will apply high-sensitivity techniques to determine the structure, transport properties, and opto-electronic properties of well-characterized individual 0d-1d nanomaterial heterostructures. This task utilizes team expertise and experience in high-sensitivity individual nanowire characterization that was previously developed to study unfunctionalized carbon nanotubes. The experimental characterization team will work closely to correlate the optical properties of the ensemble samples with the structural and transport properties of individual 0d-1d nanomaterial heterostructures, in this way generating a comprehensive picture about the behavior of the 0D-1D system in order to provide critical feedback for additional chemical synthesis. The theoretical team will model the fundamental physical properties and help the experimentalists to correlate these physical properties with material structural properties. Further, as a more comprehensive model of the energy flow and charge transfer pathways emerges, an attempt will be made to provide additional guidance on creating better material structures to optimize these pathways for useful solar energy conversion.

In practical terms, thus far, for sample preparation, we have already produced, from the original literature, a series of DWNT-CdSe and single-walled carbon nanotube (SWNT)-CdSe samples, wherein the aminoethanethiol (AET)-capped CdSe QDs nominally measure ~3.1, 3.6, and 4.3 nm in diameter, respectively. We have also generated control samples consisting of AET-CdSe QDs, oleate-capped QDs, raw SWNTs, and raw DWNTs, as well as their oxidized, 'purified' counterparts. In all of this work, we are probing the effect of varying precursors and reaction times. Moreover, we are currently performing ligand exchange reactions on all QD samples. In a parallel effort, we have begun to work with higher-quality SWNT supplies from Helix Materials and Nanointegris, as well as quantum dots from NN Labs. Our intent is to create functional nanotube-QD heterostructures from these sources. Best samples will be further analyzed using high-resolution transmission electron microscopy (HRTEM).

One of the immediate objectives has been to determine if as-prepared samples are suitable for the requirements of both optical and transport measurements or if further tweaking is necessary from the synthesis point of view. One issue for instance might be that the tubes are not sufficiently long or clean enough for transport. Preliminary work has been conducted to establish that reliable, interpretable devices can be fabricated from as-prepared nanotube and nanocrystal samples; the idea will be to continue to optimize their fabrication and standardization techniques to derive reproducible data from individual devices. Another concern at this point is that the profile of either the

absorption or the photoluminescence spectrum may be unacceptable, e.g. the optical density and/or quantum yield of the QDs may be inordinately low. From the theory perspective, the initial system to model has been the SWNT-CdSe dot heterostructure in order to probe the effect of non-equilibrium phenomena, such as when the excitonic spectrum of tubes, for example, is perturbed by the presence of QDs and vice versa.

#### Future Plans:

The key point to emphasize here is that team members are actively involved with developing, optimizing, and cooperatively coordinating their part of the project, relevant to his area of expertise, whether it be ligand exchange, the development of relevant optical methods, theoretical modeling, tools for image interpretation in microscopy, or electronic device fabrication. The objective is to address the problem of energy and charge transfer in a consistent, uniform set of samples comprised of model nanoscale heterostructures through a comprehensive approach. In this light, additional goals include but are not limited to probing (a) the conjugation and characterization of nanotubes with surface-modified QDs, (b) the measurement of ensemble optical properties, (c) the use of TEM for high sensitivity structural characterization, (d) the evaluation of QD-DWNT hybrid devices, and (e) the theoretical limits of efficiency in these systems.

#### Relevant Selected Publications funded in part by Basic Energy Sciences (2010-present):

8. Lei Wang, Haiqing Liu, Robert M. Konik, James A. Misewich, and Stanislaus S. Wong, "Carbon nanotube-based heterostructures for solar energy applications", invited review, *Chem. Soc. Rev.*, submitted for publication.
7. Milena Jankulovska, Thomas Berger, Stanislaus S. Wong, Roberto Gómez, and Teresa Lana-Villarreal, "Trap States in TiO<sub>2</sub> Films Made of Nanowires, Nanotubes or Nanoparticles: an Electrochemical Study", *ChemPhysChem*, **13(12)**, 3008-3017 (2012).
6. Xiaohui Peng, James A. Misewich, Stanislaus S. Wong, and Matthew Y. Sfeir, "Efficient Charge Separation in Multidimensional Nanohybrids", *Nano Letters*, **11(11)**, 4562-4568 (2011).
5. Ming Shao, M. P. Garrett, Xinjun Xu, Ilia N. Ivanov, Stanislaus S. Wong, and Bin Hu, "Effects of single walled carbon nanotubes on the electroluminescent performance of organic light-emitting diodes", *Organic Electronics*, **12(6)**, 1098-1102 (2011).
4. Alexander C. Santulli, Christopher Koenigsmann, Amanda L. Tiano, Donald DeRosa, and Stanislaus S. Wong, "Correlating Titania Morphology and Chemical Composition with Dye Sensitized Solar Cell Performance", *Nanotechnology*, **22(24)**, 245402/1 - 245402/13 (2011).
3. Tae-Jin Park, Andrey A. Levchenko, Hongjun Zhou, Stanislaus S. Wong, and Alexandra Navrotsky, "Shape-dependent surface energetics of nanocrystalline TiO<sub>2</sub>", *J. Mater. Chem.*, **20(39)**, 8639-8645 (2010).
2. Teresa Lana-Villarreal, Yuanbing Mao, Stanislaus S. Wong, and Roberto Gómez, "Photoelectrochemical behavior of anatase nanoporous films: effect of the nanoparticle organization", *Nanoscale*, **2(9)**, 1690-1698 (2010).
1. Xiaohui Peng, Matthew Y. Sfeir, Fen Zhang, James A. Misewich, and Stanislaus S. Wong, "Covalent Synthesis and Optical Characterization of Double-walled Carbon Nanotube-Nanocrystal Heterostructures", *J. Phys. Chem. C*, **114(19)**, 8766-8773 (2010).

## Interband Cascade Photovoltaic Cells

DoE Award No: DE-SC0004523  
Principal Investigator: Rui Q. Yang  
Institution: School of Electrical and Computer Engineering, University of Oklahoma, Norman, OK e-mail: Rui.Q.Yang@ou.edu  
Address: 110 W. Boyd Street, Room 150, Norman, OK 73019  
Co-Principal Investigators: Michael B. Santos, Matthew B. Johnson  
Department of Physics and Astronomy, University of Oklahoma, Norman, OK  
Collaborator: J. F. Klem, Sandia National Laboratories, Albuquerque, NM  
Contributors: R. T. Hinkey, L. Li, H. Lotfi, Z. Tian, J. C. Keay, H. Ye, S. Rassel, L. Zhao, C. Niu, T. D. Mishima, University of Oklahoma, Norman.

### Program Scope

In this project, we are performing basic and applied research to systematically investigate our newly proposed interband cascade (IC) photovoltaic (PV) cells [1]. These cells follow from the great success of infrared IC lasers [2-3] that pioneered the use of quantum-engineered IC structures. This quantum-engineered approach will enable PV cells to efficiently convert infrared radiation from the sun or other heat source, to electricity. Such cells will have important applications for more efficient use of solar energy, waste-heat recovery, and power beaming in combination with mid-infrared lasers. The objectives of our investigations are to: achieve extensive understanding of the fundamental aspects of the proposed PV structures, develop the necessary knowledge for making such IC PV cells, and demonstrate prototype working PV cells. This research will focus on IC PV structures and their segments for utilizing infrared radiation with wavelengths from 2 to 5  $\mu\text{m}$ , a range well suited for emission by heat sources (1,000-2,000 K) that are widely available from combustion systems. The long-term goal of this project is to push PV technology to longer wavelengths, allowing for relatively low-temperature thermal sources.

Our investigations address material quality, electrical and optical properties, and their interplay for the different regions of an IC PV structure. These fundamental aspects include: systematic knowledge about the carrier absorption and recombination processes over the infrared spectral range; and how carrier transport is affected by scattering mechanisms involving defects, phonons, and electron-electron interactions. The tasks involve: design, modeling and optimization of IC PV structures, molecular beam epitaxial growth of PV structures and relevant segments, material characterization, prototype device fabrication and testing. At the end of this program, we expect to generate new cutting-edge knowledge in the design and understanding of quantum-engineered semiconductor structures, and demonstrate the concepts for IC PV devices with high conversion efficiencies.

### Recent Progress

We investigated interband cascade structures for the photovoltaic conversion of mid-infrared radiation using a blackbody radiation source. We conducted detailed studies of their performance characteristics at different temperatures. We demonstrated that these ICPV devices were able to achieve open-circuit voltages as high as 1.68 V with a cutoff wavelength of 4.0  $\mu\text{m}$

at 80 K. We showed that the quantum efficiency of these devices is insensitive to temperature, indicative of the advantage of circumventing the diffusion length limitation with the use discrete absorber architecture. We also performed an efficiency analysis by breaking the total power efficiency into a product of individual efficiencies in order to determine the power loss from each of the physical mechanisms involved in the conversion process. We found that at low temperature, the power conversion is limited by incomplete absorption of the incident light and a fill factor below 50%; while at higher temperature, the drop in open-circuit voltage limits the efficiency largely due to the significant increase of dark current density. We reported and discussed these results at the 38th IEEE Photovoltaic Specialists Conference in Austin, Texas on June 3-8, 2012 and in a paper published in the IEEE Journal of Photovoltaics (vol. 3, No. 2, IEEE website early access, 2013).

Based on our earlier studies, we recently designed and fabricated two- and three-stage ICPV devices with a cutoff wavelength near 3  $\mu\text{m}$  (bandgap of  $\sim 0.41$  eV) at room temperature (300 K). The absorber lengths of the cascade stages in these PV devices were varied across the structure in order to achieve better photocurrent matching between stages. The photovoltaic properties of these devices were investigated using both a broadband blackbody source and a mid-infrared IC laser with a photon energy slightly above (within  $k_B T$ ) of the absorber bandgap. Typical current density and voltage ( $J$ - $V$ ) curves for two-stage and three-stage devices, each with  $300 \times 300 \mu\text{m}^2$  square mesas, are shown in Fig. 1 for temperatures of 300 K and 340 K, obtained under illumination from the IC laser. The inset shows the emission spectrum of the laser used for the characterization compared to the electroluminescence (EL) spectrum of the PV device. Both the laser spectrum and the EL spectrum of the PV device peak near  $\sim 0.42$  eV.

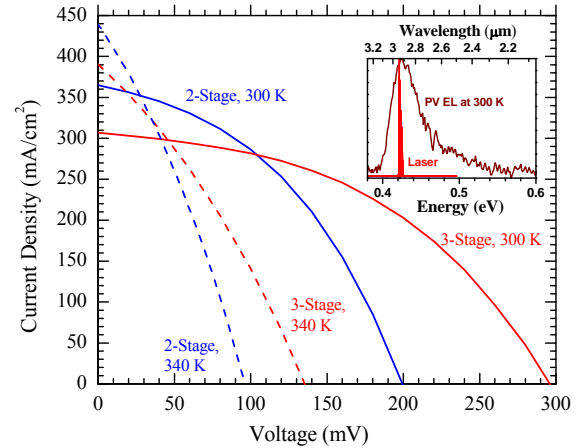


Fig. 1. Measured  $J$ - $V$  curves of two-stage and three-stage devices. Both devices had  $300 \times 300 \mu\text{m}^2$  square mesas. The inset shows the EL spectrum of the PV device at 300 K and the emission spectrum of the IC laser.

The three-stage device was able to achieve higher values of open-circuit voltage ( $V_{oc}$ ) and fill factor ( $FF$ ) than the two-stage device, as expected. However, the short-circuit current density ( $J_{sc}$ ) value was about  $\sim 16\%$  lower in the three-stage device, indicative of some mismatch of photocurrent between the different stages. There were similar differences in the  $J_{sc}$  values obtained under blackbody illumination for the two- and three-stage devices. This suggests that better performance of the three-stage device should be possible simply by improving the photocurrent matching between the stages. Nevertheless, the photocurrent matching was good enough for the three-stage devices to achieve higher output powers under equivalent illumination conditions. Under laser illumination, the three-stage device had  $J_{sc} = 310 \text{ mA/cm}^2$ ,  $V_{oc} = 295 \text{ mV}$ , and  $FF = 44\%$ . This  $V_{oc}$  value is comparable to those of the GaSb-based thermophotovoltaic (TPV) devices reported in Ref. 4. These values ranged from 239-313 mV for absorbers with bandgaps of 0.50-0.55 eV. In addition, the data for the GaSb-based devices was acquired under a much higher incident light intensity (the reported  $J_{sc}$  is  $3.5 \text{ A/cm}^2$  [4], which is about an order of magnitude higher than that of our device).

More recently, by using an IC laser with a lasing wavelength near  $4.3\ \mu\text{m}$ , we were able to operate 7-stage ICPV devices at room temperature and above with significantly higher open circuit voltage even though the bandgap of these devices is less than  $0.25\ \text{eV}$  (corresponding to a cutoff wavelength longer than  $5\ \mu\text{m}$ ). The  $J$ - $V$  characteristics for a  $200\times 200\ \mu\text{m}^2$  device at temperatures of 300 K and 340 K are shown in Fig. 2. The open-circuit voltage  $V_{oc}$  is as high as  $0.65\ \text{V}$  (with  $J_{sc}=1.4\ \text{A}/\text{cm}^2$ ), which is larger than a single bandgap determined value ( $\sim 0.25\ \text{V}$ ), indicative of a cascade advantage. The inset to Fig. 2 shows the EL spectra of an ICPV device at 300 and 340 K, and the lasing spectrum of the IC laser that was used to illuminate the PV devices. The dips in the EL spectra were caused by  $\text{CO}_2$  absorption in the air near  $4.23$ - $4.26\ \mu\text{m}$ . To the best of our knowledge, this is the first demonstration of TPV cells with the narrowest bandgap, operating at room temperature and above, yet still with a considerable open-circuit voltage, further validating the significant advantages of these ICPV devices for practical applications.

By varying the laser output power, we also obtained the relationship between  $J_{sc}$  and  $V_{oc}$  for devices at 300 and 340 K with different sizes and lasing wavelengths. The lasing wavelength of the IC laser was tuned from  $4.2$  to  $4.6\ \mu\text{m}$  by changing its operating temperature. We found that the  $J_{sc}$ - $V_{oc}$  relationship depends only on the PV device's operating temperature, and is essentially insensitive to the device size and the illuminating wavelength of the laser as shown in Fig. 3. This suggests that the attained  $J_{sc}$ - $V_{oc}$  relationship is a reflection of intrinsic properties of ICPV devices, which shall be investigated further in the future.

## Future Plans

Efforts will be devoted to studies of carrier transport and optical absorption with improved current matching between stages, and to the development of a theory for appropriate description of the  $J_{sc}$ - $V_{oc}$  relationship that was observed from ICPV devices. With improved understanding, we will design and fabricate new PV devices for achieving better device performance.

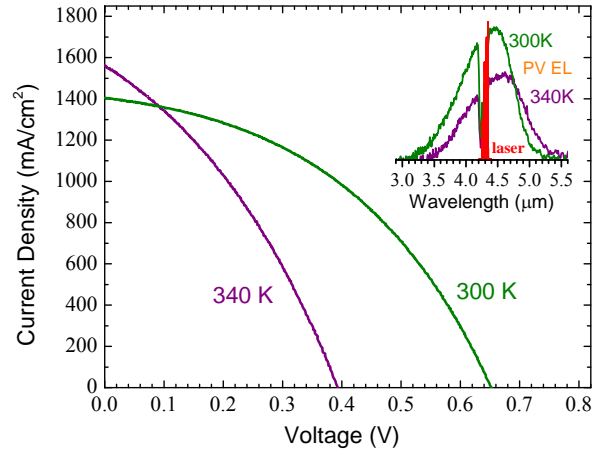


Fig. 2. Measured  $J$ - $V$  curves of a seven-stage ICPV device. The inset shows the EL spectrum of a PV device at 300 and 340 K, and the lasing spectrum of the IC laser used for characterization.

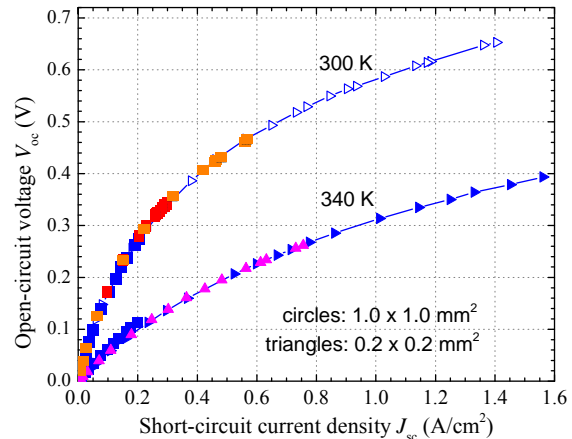


Fig. 3. Measured  $J_{sc}$ - $V_{oc}$  curves of seven-stage ICPV devices. Circles are for a  $1\times 1\ \text{mm}^2$  device and triangles are for a  $0.2\times 0.2\ \text{mm}^2$  device. Different colors stand for different illuminating wavelength emitted from the laser.

## References

1. R. Q. Yang, Z. Tian, J. F. Klem, T. D. Mishima, M. B. Santos, and M. B. Johnson, "Interband cascade photovoltaic devices", *Appl. Phys. Lett.* **96**, 063504 (2010).
2. R. Q. Yang, "Infrared laser based on intersubband transitions in quantum wells," at *7th Inter. Conf. on Superlattices, Microstructures and Microdevices*, Banff, Canada, August, 1994; *Superlattices and Microstructures*, **17**, 77-83, 1995; "Novel Concepts and Structures for Infrared Lasers", Chap. 2, in *Long Wavelength Infrared Emitters Based on Quantum Wells and Superlattices*, edited by M. Helm (Gordon & Breach Pub., Singapore, 2000); "Interband Cascade Lasers", Chap. 12, in *Semiconductor lasers: fundamentals and applications*, edited by A. Baranov and E. Tournie (Woodhead Publishing Limited, Cambridge, UK, 2013); and references therein.
3. I. Vurgaftman, W. W. Bewley, C. L. Canedy, C. S. Kim, M. Kim, C. D. Merritt, J. Abell, J.R. Lindle, and J. R. Meyer, "Rebalancing of internally generated carriers for mid-infrared interband cascade lasers with very low power consumption", *Nature Commun.*, **2**, 585 (2011).
4. C. A. Wang, H. K. Choi, S. L. Ransom, G. W. Charache, L. R. Danielson, and D. M. Depoy, "High-quantum-efficiency 0.5 eV GaInAsSb/GaSb thermophotovoltaic devices." *Appl. Phys. Lett.*, **75**, 1305 (1999).

## DOE Sponsored Publications in 2011-2012:

1. L. Li, J. C. Keay, H. Ye, T. D. Mishima, Z. Tian, R. Q. Yang, M. B. Santos, M. B. Johnson, "Suppression of Slip-Line Defect Formation in GaSb Substrates during Thermal Desorption of Oxide Layers", 28th North American Molecular Beam Epitaxy Conference, Aug. 14-17, 2011, La Jolla, CA.
2. Z. Tian, R. T. Hinkey, R. Q. Yang, J. F. Klem, M. B. Johnson, "Mid-IR photovoltaic devices based on interband cascade structures", Paper # 443 at The 38th IEEE Photovoltaic Specialists Conference, Austin, Texas, June 3-8, 2012.
3. R. T. Hinkey, Z. Tian, S. M. S. Rassel, R. Q. Yang, J. F. Klem, and M. B. Johnson, "Interband Cascade Photovoltaic Devices for Conversion of Mid-IR Radiation", *IEEE J. Photovoltaics*, **3**, No. 2 (IEEE website early access, 2013).

## Near-Field Thermal Radiation between Flat Surfaces with a Nanogap

Zhuomin Zhang [zhuomin.zhang@me.gatech.edu](mailto:zhuomin.zhang@me.gatech.edu)  
George W. Woodruff School of Mechanical Engineering  
Georgia Institute of Technology, Atlanta, GA 30332

### Program Scope

Evanescence waves and photon tunneling are responsible for the predicted near-field energy transfer being several orders of magnitude greater than that between two blackbodies, i.e., breaking Planck's law. The enhanced energy transfer may be used for improving the performance of energy conversion devices, augmenting laser cooling, developing novel nanothermal manufacturing techniques, and imaging structures with high spatial resolutions. Recent works by other groups have demonstrated significant enhancement of nanoscale radiation using sphere-plate geometry. We propose to fabricate ultrasmall gaps for measuring nanoscale radiation between flat surfaces with relatively large areas. The ultimate goal is to quantitatively demonstrate near-field radiation between relatively large flat surfaces at a distance of tens of nanometers for the application of near-field thermophotovoltaic (TPV) devices.

The activities progress summarized below include some theoretical calculations that enable the materials selection and geometric optimization. The results also help the fundamental understanding of nanoscale thermal radiation.

### Recent Progress

While near-field energy transfer between two bodies has been calculated as well as measured by researchers, only a few studies investigated the energy propagation direction in nanoscale thermal radiation. Unlike classical radiative heat transfer, the direction of energy propagation for nanoscale radiation cannot be determined using ray optics, since the refraction angle is not defined due to the coupling of evanescent waves during photon tunneling. The concept of energy streamlines (ESLs), based on the traces of Poynting vectors for a given parallel component of the wavevector ( $\beta$ ), is analogous to streamlines in fluid flow. Rather than assuming a planar wave incidence, the PI's group recently developed a more physical approach that uses fluctuational electrodynamics to directly calculate the emission from a thermal source with the assistance of Green's dyadic tensors, as illustrated in Fig. 1. The electromagnetic waves originated from a source layer may experience different energy transfer paths to reach another layer inside the emitter. A transfer function between each pair of layers is developed to fully capture the near-field radiative transfer [1].

Figure 2 illustrates the energy streamlines for a TM wave at  $\lambda = 10.5 \mu\text{m}$  (i.e.,  $\omega = 1.79 \times 10^{14}$  rad/s when SPhP is excited) between two SiC media with a vacuum gap  $d = 100$  nm. Here,  $\beta$  is 50 times that of the wavevector  $k_0 = \omega/c$  in vacuum. The streamlines are curved and a significant lateral shift exists in the emitter. The use of plane wave cannot fully describe the streamlines inside the emitter. The finding of a large lateral shift inside the emitter has important implications for the design of near-field TPV systems. Understanding the energy flow direction and lateral shift will also facilitate the design of experiments for measuring thermal radiation in both the near- and far-fields. It is also possible to extend the streamline method for multilayered media as well as for anisotropic media.

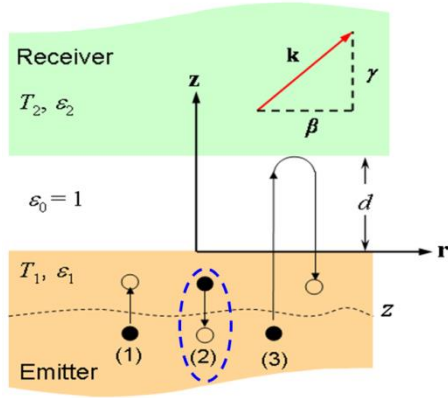


Fig. 1: Schematic of near-field radiation between parallel plates (medium 1 and 2), showing the different paths (1), (2), and (3) of energy propagation that contribute to the local field inside the emitter. Here,  $\varepsilon$  is the dielectric function and  $T$  is the temperature of each layer [1].

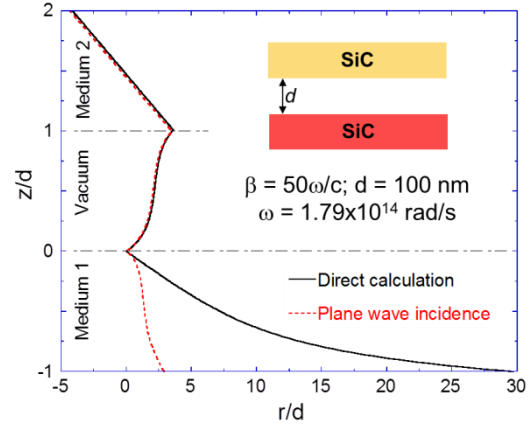


Fig. 2: Calculated energy streamlines between SiC plates at the SPhP resonance frequency [1]. The direct method allows an accurate model of the emission and reflection processes inside the emitter.

Kirchhoff's law has played an important role in thermal radiation analysis and for the calculation of radiative properties, particularly the emissivity. An outstanding question that has existed for a long time is about its validity to nonequilibrium systems. The PI's group [2] considered a multilayer structure with temperature variations and established the equivalence between the spectral-directional emissivity and absorptivity of each layer according to a generalized Kirchhoff's law. The results allow the calculation of thermal emission from a multilayered structure having a nonuniform temperature distribution without using the more complicated fluctuational electrodynamics [2]. The PI has studied near-field radiation and radiative properties of heavily doped Si [3,4]. The PI also modeled the near-field radiation between doped SiGe alloys and found that multiple peaks can exist in near-field spectra [5].

More recently, the PI and his former student [6] have predicted a large thermal rectification factor ( $r$ ) based on near-field radiation. The innovative aspect of this work is the use of intrinsic or lightly doped silicon whose carrier concentration is strongly temperature dependent. We have shown a strong thermal rectification effect between intrinsic Si and other materials (doped Si, SiO<sub>2</sub>, or Au) at various temperatures and vacuum gap distances. An example is given in Fig. 3 for thermal rectification between an intrinsic and a doped Si. When the intrinsic Si is at  $T_H = 1000$  K and the doped Si is at  $T_L = 300$  K, the dielectric functions of both media are dominated by free carriers, resulting in a greatly enhanced heat flux,  $q''_{\text{forward}}$ , particularly as the vacuum gap is at the nanoscales. In the reverse-bias scenario, the intrinsic Si at 300 K behaves like a non-absorbing medium at wavelengths longer than 1.1  $\mu\text{m}$ , except for some weak phonon absorptions. As shown in Fig. 3, the reverse heat flux  $q''_{\text{reverse}}$  is much lower at nanometer scales. The rectification factor  $R$  is defined as  $q''_{\text{forward}} / q''_{\text{reverse}} - 1$ . Rectification factors  $R = 0.71, 2.7,$  and  $67$  were predicted at  $d = 10, 5,$  and  $1$  nm, respectively. The strong enhanced near-field radiation for the forward bias is attributed to coupled SPPs, since the carrier concentration of intrinsic Si increases with temperature. Details can be found from Wang and Zhang [6].

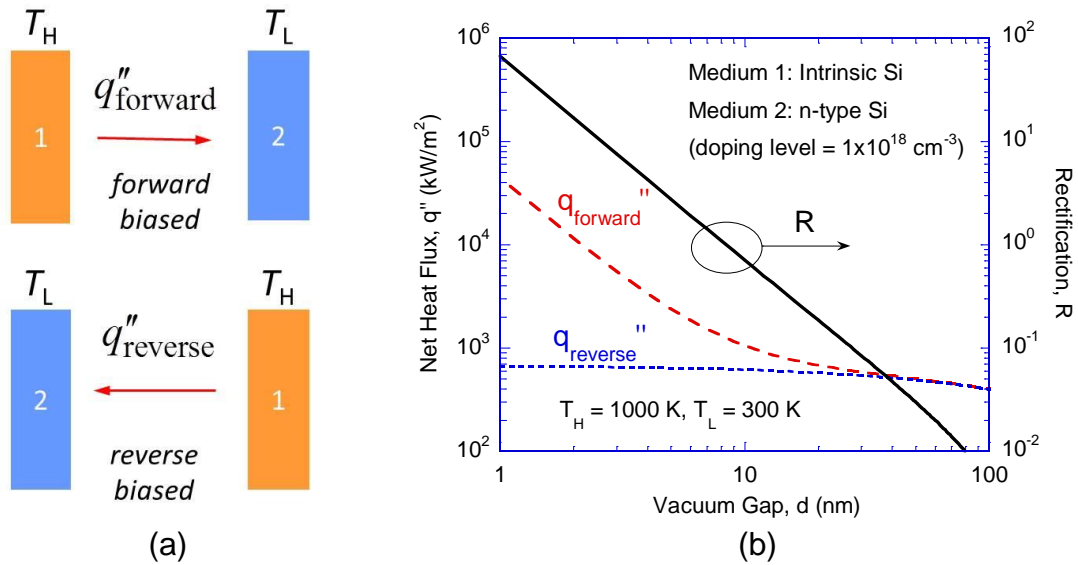


Fig. 3: (a) Schematic of the near-field thermal rectifier concept; (b) results between an intrinsic Si (medium 1) and a doped Si (medium 2) [6].

In addition, large thermal rectification between Si and SiO<sub>2</sub> and between Si and Au is also demonstrated. A rectification factor  $R = 9.9$  is predicted between intrinsic Si and SiO<sub>2</sub> with a 5-nm vacuum gap at temperatures of 1000 K and 300 K. A thermal rectifier made of gold and intrinsic Si is shown to have a rectification factor around 0.85 with temperatures of 600 K and 300 K at a wide range of vacuum gaps from 100 nm to 500 nm. Each of the proposed thermal rectifiers may have its own advantage for applications dealing with different temperatures and vacuum distances. The physical mechanisms of the rectification effect in the three configurations are different and elucidated by Wang and Zhang [6].

### Related Research

We have studied near-field effect on far-field radiative properties for a variety of nanostructured materials, both theoretically and experimentally [7,8]. Examples are the alignment dependent absorption coefficient of CNT arrays [9], Ag nanorods coated on a compact-disc [10], thermal emission control with microfabricated structures with cavity resonance modes and magnetic polaritons [11-14], Si nanowires [15,16], and optical constants of Si [17] and tungsten [18]. These studies have important applications in applications of solar energy as well as TPV devices.

### Future Plans

We will perform a fundamental investigation on nanoscale thermal radiation with a planar vacuum gap of large lateral extension using nanospacers. The experiments are well under way to fabricated nanometer to submicrometer scale spacers between Si wafers that may be coated with SiO<sub>2</sub> or doped. A cryostat system has been purchased and a heat conductance measurement system will be developed to determine near-field radiation heat flux experimentally. This study will facilitate applications of nanoscale thermal radiation to energy conversion devices, such as TPV and effective laser cooling. We also propose to study hyperbolic metamaterials made of doped Si nanowires for thermal radiation control in both the near and far fields.

### Selected Publications Supported by the DoE Contract

1. S. Basu, L.P. Wang, and Z.M. Zhang, "Direct Calculation of Energy Streamlines in Near Field Thermal Radiation," *J. Quant. Spectrosc. Radiat. Transfer* **112**, 1149 (2011).
2. L.P. Wang, S. Basu, and Z.M. Zhang, "Direct and Indirect Methods for Calculating Thermal Emission from Layered Structures with Nonuniform Temperatures," *J. Heat Transfer* **133**, 072701 (2011).
3. S. Basu, B.J. Lee, and Z.M. Zhang, "Infrared Radiative Properties of Heavily Doped Silicon at Room Temperature," *J. Heat Transfer* **132**, 023301 (2010).
4. S. Basu, B.J. Lee, and Z.M. Zhang, "Near-Field Radiation Calculated with an Improved Dielectric Function Model for Doped Silicon," *J. Heat Transfer* **132**, 023302 (2010).
5. Z.M. Zhang, E.T. Enikov, and T. Makansi, "Near-Field Radiative Transfer between Heavily Doped SiGe at Elevated Temperatures," *J. Heat Transfer* **134**, 092702 (2012).
6. L.P. Wang and Z.M. Zhang, "Thermal Rectification Enabled by Near-field Radiative Heat Transfer between Intrinsic Silicon and Other Materials," *Nanoscale Microscale Thermophys. Eng.* (accepted).
7. Z.M. Zhang and H. Ye, "Measurements of Radiative Properties of Engineered Micro/Nanostructures," *Ann. Rev. Heat Transfer*, G. Chen (ed.), Begell House, New York, Vol. 16 (2013). (Invited book chapter, in press).
8. Z.M. Zhang and L.P. Wang, "Measurements and Modeling of the Spectral and Directional Radiative Properties of Micro/Nanostructured Materials," *Int. J. Thermophys.*, available online: DOI: 10.1007/s10765-011-1036-5 (2011). In press.
9. H. Ye, X.J. Wang, W. Lin, C.P. Wong, and Z.M. Zhang, "Infrared Absorption Coefficients of Vertically-Aligned Carbon Nanotube Films," *Appl. Phys. Lett.* **101**, 141909 (2012).
10. X.J. Wang, A.M. Haider, J.L. Abell, Y.-P. Zhao, and Z.M. Zhang, "Anisotropic Diffraction from Inclined Silver Nanorod Arrays on Grating Templates," *Nanos. Micros. Thermophys. Eng.* **16**, 18 (2012).
11. L.P. Wang and Z.M. Zhang, "Wavelength-Selective and Diffuse Emitter Enhanced by Magnetic Polaritons for Thermophotovoltaics," *Appl. Phys. Lett.* **100**, 063902 (2012).
12. L.P. Wang, S. Basu, and Z.M. Zhang, "Direct Measurement of Thermal Emission from a Fabry-Perot Cavity Resonator," *J. Heat Transfer* **134**, 072701 (2012).
13. L.P. Wang, A.M. Haider, and Z.M. Zhang, "Effect of Magnetic Polaritons on the Radiative Properties of Inclined Plate Arrays," *J. Quant. Spectrosc. Radiat. Transfer* (in press).
14. L.P. Wang and Z.M. Zhang, "Measurement of Coherent Thermal Emission due to Magnetic Polaritons in Subwavelength Microstructures," *J. Heat Transfer* (accepted).
15. H. Wang, X.L. Liu, L.P. Wang, and Z.M. Zhang, "Anisotropic Optical Properties of Silicon Nanowire Arrays Based on the Effective Medium Approximation," *Int. J. Therm. Sci.* **65**, 62 (2013).
16. X.L. Liu, L.P. Wang, and Z.M. Zhang, "Wideband Tunable Omnidirectional Infrared Absorbers Based on Doped-Silicon Nanowire Arrays," *J. Heat Transfer* (in press).
17. H. Wang, X.L. Liu, and Z.M. Zhang, "Absorption Coefficient of Crystalline Silicon at Wavelengths from 500 nm to 1000 nm," *Int. J. Thermophys.* (in press).
18. J.I. Watjen, T.J. Bright, Z.M. Zhang, C. Muratore, and A.A. Voevodin, "Spectral Radiative Properties of Tungsten Thin Films," *Int. J. Heat Mass Transfer* **61**, 106 (2013).

## Elucidation of Hydrogen Interaction Mechanisms with Metal Doped Carbon Nanostructures

Ragaiy Zidan, Joseph A. Teprovich Jr., Douglas A. Knight, Brent Peters

Savannah River National Laboratory, Aiken, SC 29808

E-mail: [Ragaiy.Zidan@srnl.doe.gov](mailto:Ragaiy.Zidan@srnl.doe.gov)

In Collaboration with

Puru Jena

Department of Physics

Virginia Commonwealth University, Richmond, VA 23284

**Program Scope:** The objective of our work is to understand how the interaction of hydrogen with materials at the nanoscale affects the desorption/absorption properties of the bulk material. We investigated this phenomenon by examining the fundamentals of hydrogen interaction with two types of hydrogen storage materials, (1) carbon nanostructures intercalated with metal atoms and (2) complex metal hydrides. We are currently investigating the potential use of these novel materials as components of the next generation of energy storage and conversion devices.

The examination and characterization of these materials involved a systematic experimental approach complimented by relevant theoretical modeling studies. The goal of our study of metal intercalated carbon nanostructures is to develop a basic understanding of the physiochemical properties and the mechanisms by which these properties influence their interaction with hydrogen. In addition, our examination of complex metal hydrides focuses on understanding their formation and decomposition as well as the role catalysts play in enhancing both hydrogenation and dehydrogenation.

The hydrogen uptake and release from the materials was monitored by a Sieverts apparatus and a thermogravimetric analysis-residual gas analyzer (TGA-RGA). In order to characterize the bulk material as well as probe the immediate chemical environment of individual atoms contained in the material, a variety of spectroscopic tools including X-ray diffraction (XRD), nuclear magnetic resonance (NMR), Infrared (FT-IR), Laser Desorption Ionization-Time of Flight- Mass Spec (LDI-TOF-MS), Anelastic Spectroscopy, and Raman were utilized.

**Recent Progress:** Through our systematic examination of these materials, we recognized that carbon nanostructures (i.e. CNT and C<sub>60</sub>) behaved similar to transition metal catalysts (i.e. TiCl<sub>3</sub>) commonly used to enhance the kinetics of dehydrogenation and rehydrogenation of complex metal hydrides (i.e. NaAlH<sub>4</sub>, LiAlH<sub>4</sub>, LiBH<sub>4</sub>). We were able to synthesize unique nanocomposites formed from hydrides and carbon nanostructures through novel solvent-assisted mixing in organic solvent. This method maintains the structural integrity of the carbon nanostructures and eliminates the introduction of metal contaminants. This is a significant departure from the common practice of ball-milling complex metal hydrides with catalysts (transition metals or carbon nanostructures) which has been known to irreversibly damage the carbon nanostructures and introduce iron and other metal contaminants.

### Effect of alkali metal doping on the hydrogen storage properties of fullerene (C<sub>60</sub>)

- A nanocomposite of LiAlH<sub>4</sub>-C<sub>60</sub> (60:1) demonstrated that the complete decomposition of LiAlH<sub>4</sub> (Equations 1-3) occurs below 300 °C in the presence of C<sub>60</sub> and that the resultant material can reversibly store hydrogen (Figure 1).<sup>[1]</sup>



- The complete 3 step decomposition of  $\text{LiAlH}_4$  was unexpected since the 3<sup>rd</sup> decomposition step is (Equation 3) typically does not occur until  $T > 670^\circ\text{C}$
- It is believed that the active hydrogen storage material is  $\text{Li}_x\text{C}_{60}\text{H}_y$  (Al behaves as a spectator metal) in this composite and that simple metal hydrides (i.e. LiH) can be utilized as an alkali metal doping sources for  $\text{C}_{60}$
- A lithium doped fullerene was successfully prepared from LiH and  $\text{C}_{60}$  via solvent assisted mixing and annealing
  - TGA-RGA demonstrated that a 6:1 mol ratio (Li: $\text{C}_{60}$ ) was optimal for hydrogen storage with 5 wt%  $\text{H}_2$  reversibly absorbed with no release of  $\text{CH}_4$ . The onset of desorption is also lowered to  $275^\circ\text{C}$  from  $500^\circ\text{C}$  with lithium doping (Figure 2).<sup>[2,3]</sup>
  - XRD of the material showed that rehydrogenation at temperatures below  $250^\circ\text{C}$  results in the expansion of the *fcc*  $\text{C}_{60}$  lattice due to formation of C-H bonds. At rehydrogenation temperatures greater than  $350^\circ\text{C}$  there was also a reversible phase transition from *fcc* to *bcc* (Figure 3)
  - $^7\text{Li}$  MAS NMR demonstrated that there is a highly shielded Li species in the material and is consistent with the migration of a Li inside the  $\text{C}_{60}$  upon hydrogenation (Figure 4, blue circle).

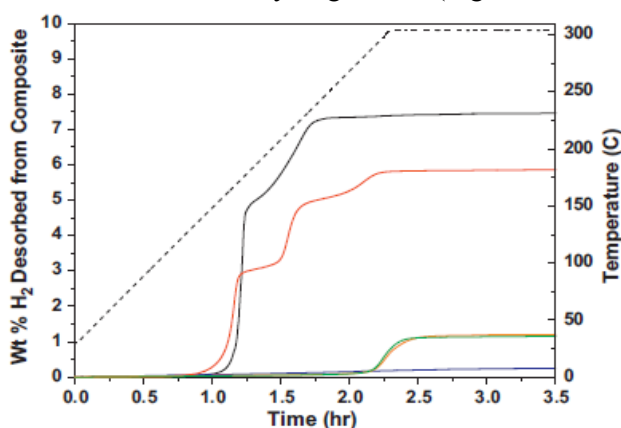


**Figure 1.** TPD study of the  $\text{LiAlH}_4\text{-C}_{60}$  nanocomposite. Black (pure  $\text{LiAlH}_4$ ), Blue (2<sup>nd</sup> desorption of pure  $\text{LiAlH}_4$ ), Red (1<sup>st</sup> desorption of  $\text{LiAlH}_4\text{-C}_{60}$ ), Orange (2<sup>nd</sup> desorption of  $\text{LiAlH}_4\text{-C}_{60}$ ), and Green (3<sup>rd</sup> desorption of  $\text{LiAlH}_4\text{-C}_{60}$ ).

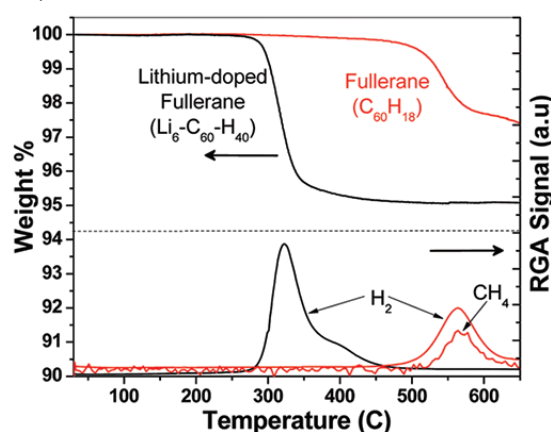


**Figure 2.** TGA-RGA comparison of the lithium doped fullerene ( $\text{Li}_6\text{C}_{60}\text{H}_{36}$ , black) and a pure undoped fullerane ( $\sim\text{C}_{60}\text{H}_{18}$ , red) hydrogenated at  $350^\circ\text{C}$  and 105 bar  $\text{H}_2$ .

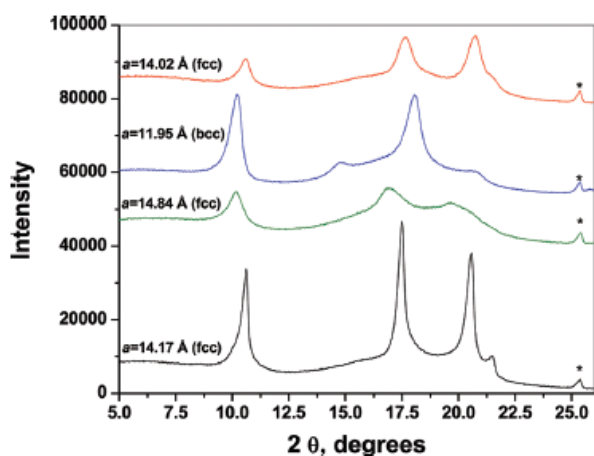


**Figure 3.** XRD of the lithium doped  $\text{C}_{60}$  at various stages of the hydrogen absorption/desorption process. Black- as prepared, green- rehydrogenated at  $250^\circ/105$  bar  $\text{H}_2$ , blue- rehydrogenated at  $350^\circ/105$  bar  $\text{H}_2$ , and red- dehydrogenated. (\*)  $\text{Al}_2\text{O}_3$  internal standard.

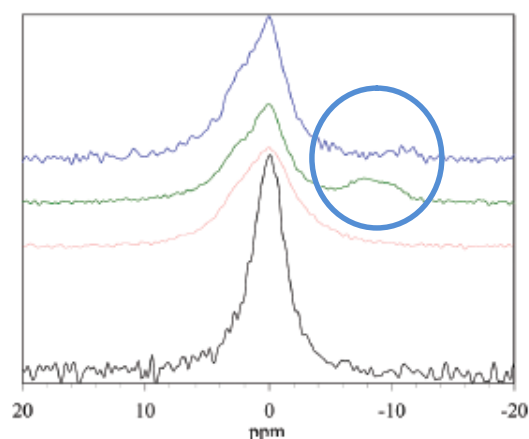


**Figure 4.**  $^7\text{Li}$  MAS NMR of the lithium doped  $\text{C}_{60}$  at various stages of the hydrogen absorption/desorption process. Black- as prepared, red- dehydrogenated, green- rehydrogenated at  $250^\circ/105$  bar  $\text{H}_2$ , and blue- rehydrogenated at  $350^\circ/105$  bar  $\text{H}_2$ .

- Anelastic spectroscopy indicated that a polymeric network forms upon rehydrogenation of the material in the presence of Li and Na as indicated by the absence of a transition at 150 K (Figure 5).<sup>[4,5]</sup>
- FT-IR, Raman, SS-NMR, and LDI-TOF-MS were also used to show the reversible formation of C-H bonds as well as charge transfer from the Li to the C<sub>60</sub>.
- Theoretical modeling of the Li<sub>6</sub>C<sub>60</sub>H<sub>40</sub> system suggesting the migration of the Li inside the C<sub>60</sub> cage upon rehydrogenation (Figure 6), which is consistent with the <sup>7</sup>Li MAS NMR data.<sup>[6]</sup>

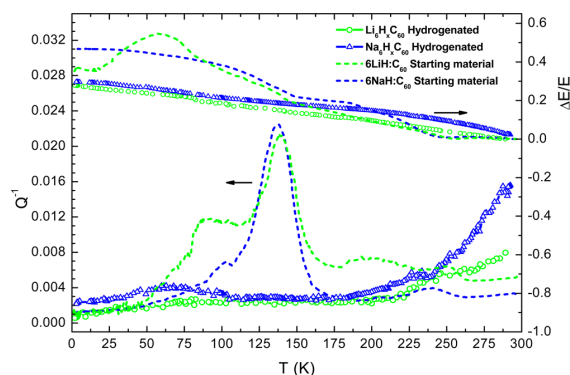


**Figure 5.** Temperature dependence of the variation of the Young modulus and of the elastic energy dissipation in the starting materials and in the rehydrogenated compounds: 6LiH:C<sub>60</sub> starting material (green line); 6NaH:C<sub>60</sub> starting material (blue line); Li<sub>6</sub>C<sub>60</sub>H<sub>4</sub> (open green dots); Na<sub>6</sub>C<sub>60</sub>H<sub>4</sub> (open blue triangles).

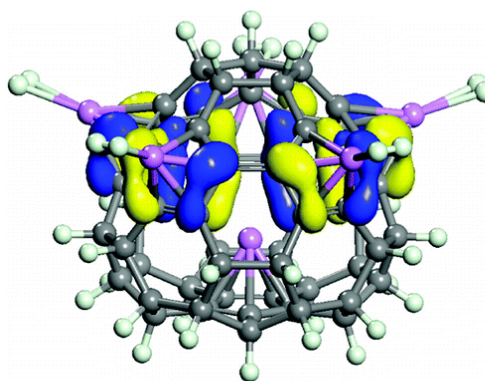


**Figure 6.** Theoretical modeling of the Li<sub>6</sub>C<sub>60</sub>H<sub>40</sub> system. White- hydrogen, grey- carbon, purple- lithium.

- This methodology has also been recently extended to a sodium doped fullerene prepared from NaH and C<sub>60</sub> via solvent assisted mixing and annealing.<sup>[7]</sup>
  - This system has shown a reversible hydrogen capacity of 2.1wt% over 10 cycles through the reversible formation of a hydrogenated fullerene.

#### Determining the hydrogen storage properties ion mobility in a LiBH<sub>4</sub>-C<sub>60</sub> nanocomposite

- We have investigated the hydrogen storage properties of the LiBH<sub>4</sub>-C<sub>60</sub> composite and determined that a 70:30 weight ratio is optimum for this purpose.<sup>[8]</sup>
  - The temperature at which the maximum rate of H<sub>2</sub> desorption of LiBH<sub>4</sub> is lowered by ~125°C in the presence of C<sub>60</sub>.
  - Reversible hydrogenation is achieved by the reformation of LiBH<sub>4</sub> (Figure 7) as well as through C-H bonds.
  - This system is unique versus the commonly utilized nanoconfinement technique in that the carbon material (in our case C<sub>60</sub>) actively participates in the hydrogen storage process unlike other commonly used carbon materials (i.e. aerogels) in nanoconfinement experiments.
- NMR experiments were designed and performed to examine how ion mobility changes in a material from the as prepared and annealed samples.<sup>[9]</sup>
- Hydrogen, <sup>6,7</sup>Li, <sup>11</sup>B, and <sup>13</sup>C NMR experiments were used to analyze ion mobility in the LiBH<sub>4</sub>-C<sub>60</sub> (60:1) nanocomposite
  - The hydrogen NMR shows two components, a broad line from immobile BH<sub>4</sub> anions and a narrow resonance from rapidly moving ions. Heat treatment to 300 °C results in a much larger narrow component, which is ~36% of the total intensity already at 22 °C

- The increase in mobile  $\text{BH}_4$  anions upon heat treatment could be attributed to the formation of a polymeric carbon network of  $\text{C}_{60}$ , in addition to a catalytic effect.
- After heat treatment at  $300\text{ }^\circ\text{C}$ , the  $^7\text{Li}$  spectrum at  $22\text{ }^\circ\text{C}$  is much narrower by about a factor of 5 compared to those of the bulk and as-mixed materials, indicating a highly mobile Li species in the material (Figure 8).

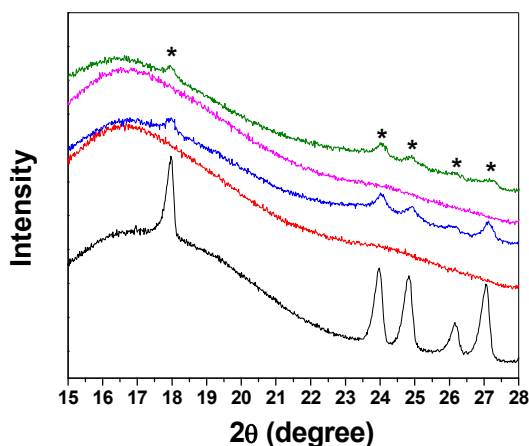


**Figure 7.** XRD of the  $\text{LiBH}_4\text{-C}_{60}$  (70:30 wt %) in the as prepared (black), 1<sup>st</sup> dehydrogenation (red), 1<sup>st</sup> rehydrogenation (blue), 2<sup>nd</sup> dehydrogenation (pink), and 2<sup>nd</sup> rehydrogenation (green). (\*)  $\text{LiBH}_4$ .

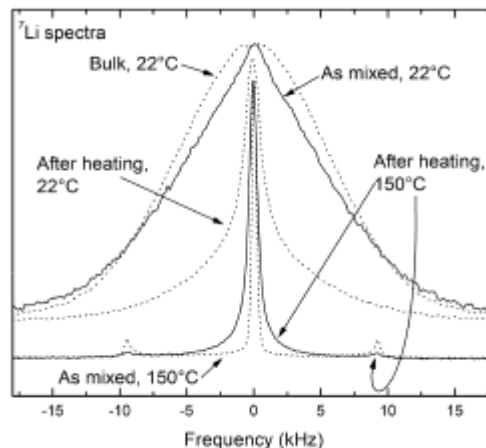


**Figure 8.**  $^7\text{Li}$  spectra acquired at indicated temperatures of pure  $\text{LiBH}_4$ ,  $\text{LiBH}_4\text{-C}_{60}$  as prepared, and  $\text{LiBH}_4\text{-C}_{60}$  after heating (at  $300\text{ }^\circ\text{C}$  for 1 hour)

**Future Plans:** Our future research efforts are aimed at understanding how hydrogen interacts with carbon nanostructures (in particular alkali fullerides) at the atomic level to form these nanocomposites. We are looking beyond the hydrogen storage capabilities of these materials and exploring their potential use in other energy storage and conversion devices. This includes the measurements and systematic evaluation of the electrochemical, electrical, and magnetic properties through the variation of alkali metal and hydrogen doping in the carbon nanomaterial.

#### Publications

1. J.A. Teprovich Jr., D.A. Knight, M.S. Wellons, R. Zidan *J. Alloys Compd.* 2011, 509, S562-S566.
2. J.A. Teprovich Jr., M. Wellons, R. Lascola, S. Hwang, P. Ward, R. Compton, R. Zidan. *Nano Letters*, 2012, 12, 582-589.
3. J.A. Teprovich Jr., D.A. Knight, B. Peters, R. Zidan *J. Alloys Compd.*, 2013 (In Press)
4. A. Paolone, F. Vico, F. Teocoli, S. Sanna, O. Palumbo, R. Cantelli, D.A. Knight, J.A. Teprovich Jr., R. Zidan. *J. Phys. Chem C.*, 2012, 116, 16365-16370.
5. A. Paolone, O. Palumbo, F. Leardini, R. Cantelli, D.A. Knight, J.A. Teprovich Jr., R. Zidan, *J. Alloys Compd.*, 2013 (In Press)
6. Q. Wang, P. Jena, *J. Phys. Chem Lett.* 2012, 3, 1084-1088.
7. D.A. Knight, J.A. Teprovich Jr., A. Summers, B. Peters, P.A. Ward, R.N. Compton, R. Zidan, *Nanotechnology* (submitted)
8. P.A. Ward, J.A. Teprovich Jr, B. Peters, J. Wheeler, R.N. Compton, R. Zidan, *Carbon* (submitted)
9. D.T. Shane, R. Corey, L. Rayhel, M. Wellons, J.A. Teprovich Jr., R. Zidan, S. Hwang, R.C. Bowman, Jr., M.S. Conradi, *J. Phys. Chem. C*, 2010, 114, 19862-19866



# **Author Index**



## Author Index

Ager, Joel W. ....	13, 17	Grigoropoulos, C. P. ....	33
Alberi, Kirstin .....	125	Gschneidner, Karl A., Jr.....	25, 260
Ali, Naushad.....	127	Han, Jung.....	252
Alivisatos, A. Paul.....	208	Hanrath, Tobias .....	104
Appenzeller, J.....	304	Hinkey, R. T. ....	308
Atwater, Harry A. ....	77, 131	Jarillo-Herrero, P. ....	73
Balke, Nina .....	41	Javey, Ali.....	13
Barnett, S. A.....	45	Jena, Purusottam.....	177, 179, 316
Bartelt, Norman.....	29	Jiang, Hongxing.....	183
Batista, Enrique R.....	240	Joannopoulos, J.....	73
Beratan, D. N.....	296	John, Sajeev.....	185
Bergman, Leah .....	21	Johnson, D. D. ....	256
Bingham, Nicholas .....	280	Johnson, Matthew B. ....	308
Biswas, Anis.....	280	Kardar, Mehran.....	143
Boehme, Christoph.....	135	Karma, Alain .....	189
Borca-Tasciuc, T. ....	73	Keay, J. C. ....	308
Broido, D.....	73	Kellogg, Gary .....	29
Brongersma, Mark.....	173	Khachatryan, Armen .....	87
Bustamante, C. ....	161	Kim, S.-G. ....	73
Carter, W. Craig .....	147, 288	Klem, J. F. ....	308
Ceder, Gerbrand .....	139	Kling, Matthias F. ....	193
Chen, Gang.....	73, 143	Knezevic, Irena.....	197
Chen, Youping .....	91	Knight, Douglas A. ....	316
Chiang, Yet-Ming.....	147, 288	Konik, R. M.....	304
Chien, C. L. ....	151	Lampen, Paula .....	280
Chrzan, Daryl C.....	13, 33	Lauhon, Lincoln J. ....	200
Chumbley, L. S.....	256, 260	Law, Matt .....	95
Cohen, M. L. ....	161	Lederman, David .....	204
Cohn, Joshua L.....	153	Leone, Stephen R.....	208
Conradi, Mark S. ....	157	Li, L.....	308
Crommie, M. F. ....	161	Li, Qiang .....	212
Cronin, Stephen.....	53, 165	Lin, Jingyu.....	183
Delaire, O. ....	73	Lin, Shawn-Yu .....	216
Dresselhaus, M. S.....	73	Liu, Feng .....	220
Dubón, Oscar D.....	13	Liu, Jianlin.....	224
Eastman, J. A.....	169	Look, David C. ....	49
Egami, T.....	79	Lotfi, H. ....	308
El Gabaly, Farid .....	29	Louie, S. G. ....	161
Engstrom, Jim .....	104	Luk, Ting S. (Willie).....	108
Fan, Shanhui.....	173	Lupton, John M.....	135
Feibelman, Peter.....	29	Ma, E.....	228
Fitzgerald, E. A. ....	73	Majetich, Sara.....	61
Fong, D. D.....	169	Marks, L. D. ....	45
Fuoss, P. H. ....	169	Maroudas, Dimitrios .....	232
Garcia, Robert .....	37	Marriott, G.....	161
Gokirmak, Ali .....	112	Martin, James E. ....	236

Martin, Richard L. ....	240	Solis, Kyle .....	236
Mascarenhas, Angelo .....	244	Soljadic, M. ....	73
Mason, T. O. ....	45	Srikanth, Hariharan .....	280
McCarty, Kevin .....	29	Stadler, Shane .....	127
McCluskey, Matthew D. ....	21	Stockman, Mark I. ....	5
Miller, G. J. ....	260	Suzuki, Yuri .....	284
Minor, A. ....	33	Swartzentruber, Brian .....	29
Misewich, James A. ....	304	Tang, Ming .....	147, 288
Mishima, T. D. ....	308	Teproovich, Joseph A., Jr. ....	316
Mishin, Yuri .....	248	Thürmer, Konrad .....	29
Missert, Nancy .....	29, 37	Tian, Z. ....	308
Naaman, Ron .....	296	Tyson, Trevor A. ....	65
Nelson, K. A. ....	73	Velmurugan, Jeyavel .....	37
Niu, C. ....	308	Viehland, Dwight .....	87
Nurmikko, A. V. ....	252	Virkar, Anil V. ....	292
Ohta, Taisuke .....	29	Voorhees, P. W. ....	45
Opeil, C. P. ....	73	Waldeck, David .....	296
Padilla, Willie J. ....	8	Walukiewicz, Wladek .....	13
Pecharsky, V. K. ....	256, 260	Wang, E. N. ....	73
Persson, Kristin .....	26	Wang, Yu U. ....	83
Peters, Brent .....	316	Wang, Zhong Lin .....	300
Phan, M. H. ....	280	Wise, Frank .....	104
Poepelmeier, K. ....	45	Wong, Stanislaus S. ....	304
Priya, Shashank .....	87	Wu, Junqiao .....	13, 33
Pruski, M. ....	256	Wu, Wenzhuo .....	300
Ramanath, G. ....	73	Wu, Yiying .....	100
Ramesh, R. ....	33	Wuttig, Manfred .....	99
Rassel, S. ....	308	Xi, Xiaoxing .....	69
Ravnsbaek, D. B. ....	147	Xiang, K. ....	147
Ren, Shenqiang .....	99	Xing, W. ....	147
Ren, Z. F. ....	73	Yablonovitch, Eli .....	1
Ren, Zhifeng .....	264	Yang, Peidong .....	208
Santos, Michael B. ....	308	Yang, Rui Q. ....	308
Scarpulla, Mike .....	57	Ye, H. ....	308
Schuh, C. A. ....	73	Yu, Kin Man .....	13, 33
Segalman, Rachel .....	267	Zapol, P. ....	169
Sekaric, Lidija .....	117	Zavadil, Kevin .....	29
Sfeir, M. Y. ....	304	Zettl, A. ....	161
Shao-Horn, Y. ....	73	Zhang, Xiang .....	1
Shen, Yuen-Ron .....	1	Zhang, Zhuomin .....	312
Shi, Jing .....	271	Zhao, L. ....	308
Shi, Li .....	53, 165	Zhu, Y. ....	304
Shield, Jeffrey E. ....	276	Zidan, Ragaiy .....	316
Silva, Helena .....	112		
Singh, D. J. ....	73		
Smith, Darryl L. ....	240		

# **Participant List**



## Participant List

Name	Organization	E-Mail Address
Ager, Joel	Lawrence Berkeley National Laboratory	jwager@lbl.gov
Alberi, Kirstin	National Renewable Energy Laboratory	Kirstin.Alberi@nrel.gov
Atwater, Harry	California Institute of Technology	haa@caltech.edu
Balke, Nina	Oak Ridge National Laboratory	balken@ornl.gov
Bergman, Leah	University of Idaho	Lbergman@uidaho.edu
Boehme, Christoph	University of Utah	boehme@physics.utah.edu
Ceder, Gerbrand	Massachusetts Institute of Technology	gceder@mit.edu
Chen, Gang	Massachusetts Institute of Technology	gchen2@mit.edu
Chen, Youping	University of Florida	ypchen2@ufl.edu
Chiang, Yet-Ming	Massachusetts Institute of Technology	ychiang@mit.edu
Chien, Cia-Ling	Johns Hopkins University	clc@pha.jhu.edu
Click, Tammy	Oak Ridge Institute for Science and Education	tammy.click@orise.orau.gov
Cohn, Joshua	University of Miami	cohn@physics.miami.edu
Conradi, Mark	Washington University in Saint Louis	msc@wustl.edu
Crommie, Mike	University of California, Berkeley / Lawrence Berkeley National Laboratory	crommie@berkeley.edu
Crockett, Teresa	U.S. Department of Energy	teresa.crockett@science.doe.gov
Cronin, Stephen	University of Southern California	scronin@usc.edu
Dang, Cuong	Brown University	Cuong_dang@brown.edu
Eastman, Jeffrey	Argonne National Laboratory	jeastman@anl.gov
Egami, Takeshi	University of Tennessee / Oak Ridge National Laboratory	egami@utk.edu
Gersten, Bonnie	U.S. Department of Energy	Bonnie.Gersten@science.doe.gov
Gokirmak, Ali	University of Connecticut	gokirmak@enr.uconn.edu
Greer, Julia	California Institute of Technology	jrgreer@caltech.edu
Gschneidner, Karl	Ames Laboratory	cagey@ameslab.gov
Hanrath, Tobias	Cornell University	th358@cornell.edu
Horton, Linda	U.S. Department of Energy	linda.horton@science.doe.gov
Javey, Ali	Lawrence Berkeley National Laboratory	ajavey@berkeley.edu
Jena, Purusottam	Virginia Commonwealth University	pjena@vcu.edu
Jiang, Hongxing	Texas Tech University	hx.jiang@ttu.edu
John, Sajeev	University of Toronto	john@physics.utoronto.ca
Karma, Alain	Northeastern University	a.karma@neu.edu
Kellogg, Gary	Sandia National Laboratories, New Mexico	gkello@sandia.gov
Kling, Matthias	Kansas State University	klings@phys.ksu.edu
Knezevic, Irena	University of Wisconsin-Madison	knezevic@enr.wisc.edu

Kortan, Refik	U.S. Department of Energy	refik.kortan@science.doe.gov
Kuang, Ping	Rensselaer Polytechnic Institute	kuangp2@rpi.edu
Lauhon, Lincoln	Northwestern University	lauhon@northwestern.edu
Law, Matt	University of California, Irvine	lawm@uci.edu
Lederman, David	West Virginia University	david.lederman@mail.wvu.edu
Leone, Stephen	Lawrence Berkeley National Laboratory/ University of California, Berkeley	srl@berkeley.edu
Li, Qiang	Brookhaven National Laboratory	qiangli@bnl.gov
Lin, Jiangyu	Texas Tech University	jingyu.lin@ttu.edu
Lin, Shawn	Rensselaer Polytechnic Institute	sylin@rpi.edu
Liu, Feng	University of Utah	fliu@eng.utah.edu
Liu, Jianlin	University of California, Riverside	jianlin@ee.ucr.edu
Look, David	Wright State University	david.look@wright.edu
Luk, Ting Shan (Willie)	Sandia National Laboratories, New Mexico	tsluk@sandia.gov
Ma, Evan	Johns Hopkins University	ema@jhu.edu
Majetich, Sara	Carnegie Mellon University	sara@cmu.edu
Maroudas, Dimitrios	University of Massachusetts, Amherst	maroudas@ecs.umass.edu
Martin, James	Sandia National Laboratories, New Mexico	jmartin@sandia.gov
Martin, Richard	Los Alamos National Laboratory	rlmartin@lanl.gov
Mascarenhas, Angelo	National Renewable Energy Laboratory	angelo.mascarenhas@nrel.gov
McCluskey, Matthew	Washington State University	mattmcc@wsu.edu
Miahin, Yuri	George Mason University	ymishin@gmu.edu
Missert, Nancy	Sandia National Laboratories, New Mexico	namisse@sandia.gov
Padilla, Willie	Boston College	willie.padilla@bc.edu
Pecharsky, Vitalij	Ames Laboratory / Iowa State University	vitkp@ameslab.gov
Persson, Kristin	Lawrence Berkeley National Laboratory	kapersson@lbl.gov
Priya, Shashank	Virginia Polytechnic Institute and State University	spriya@vt.edu
Ravnsbaek, Dorthe	Massachusetts Institute of Technology	dorthe@mit.edu
Ren, Shenqiang	University of Kansas	shenqiang@ku.edu
Ren, Zhifeng	University of Houston	zren2@central.uh.edu
Rhyne, James	U.S. Department of Energy	james.rhyne@science.doe.gov
Santos, Michael	University of Oklahoma	msantos@ou.edu
Scarpulla, Michael	University of Utah	scarpulla@eng.utah.edu
Schwartz, Andrew	U.S. Department of Energy	andrew.schwartz@science.doe.gov
Sekaric, Lidija	U.S. Department of Energy	Lidija.Sekaric@hq.doe.gov
Shi, Jing	University of California, Riverside	jing.shi@ucr.edu
Shi, Li	University of Texas at Austin	lishi@mail.utexas.edu
Shield, Jeff	University of Nebraska	jshield2@unl.edu
Sorte, Eric	Washington University in Saint Louis	esorte@physics.wustl.edu

Srikanth, Hariharan	University of South Florida	sharihar@usf.edu
Stadler, Shane	Louisiana State University	stadler@phys.lsu.edu
Stockman, Mark	Georgia State University	mstockman@gsu.edu
Suzuki, Yuri	Stanford University	ysuzuki1@stanford.edu
Thiyagarajan, Thiyaga P.	U.S. Department of Energy	p.thiyagarajan@science.doe.gov
Tyson, Trevor	New Jersey Institute of Technology	tyson@njit.edu
Urban, Jeff	Lawrence Berkeley National Laboratory	jjurban@lbl.gov
Viehland, Dwight	Virginia Polytechnic Institute and State University	viehland@mse.vt.edu
Virkar, Anil	University of Utah	anil.virkar@utah.edu
Voorhees, Peter	Northwestern University	voorhees@northwestern.edu
Waldek, David	University of Pittsburgh	dave@pitt.edu
Wang, Yu	Michigan Technological University	wangyu@mtu.edu
Wang, Zhong-Lin	Georgia Institute of Technology	zhong.wang@mse.gatech.edu
Wise, Frank	Cornell University	frank.wise@cornell.edu
Wong, Stanislaus	Brookhaven National Laboratory	sswong@bnl.gov
Wu, Junqiao	University of California, Berkeley	wuj@berkeley.edu
Wu, Wenzhuo	Georgia Institute of Technology	wenzhuowu@gatech.edu
Wu, Yiyang	The Ohio State University	wu@chemistry.ohio-state.edu
Wuttig, Manfred	University of Maryland	wuttig@umd.edu
Xi, Xiaoxing	Temple University	xiaoxing@temple.edu
Yablonovitch, Eli	University of California, Berkeley	eliy@eecs.berkeley.edu
Yang, Rui	University of Oklahoma	Rui.Q.Yang@ou.edu
Yu, Zongfu	Stanford University	zfyu@stanford.edu
Zapol, Peter	Argonne National Laboratory	zapol@anl.gov
Zhang, Zhuomin	Georgia Institute of Technology	zhuomin.zhang@me.gatech.edu
Zidan, Ragaiy	Savannah River National Laboratory	ragaiy.zidan@srnl.doe.gov